FREQUENCY SELECTIVE SURFACES

Theory and Design

This Page Intentionally Left Blank

FREQUENCY SELECTIVE SURFACES

This Page Intentionally Left Blank

FREQUENCY SELECTIVE SURFACES

Theory and Design

BEN A. MUNK
Professor of Electrical Engineering, Emeritus
The Ohio State University
Life Fellow IEEE

A Wiley-Interscience Publication
JOHN WILEY & SONS, INC.
New York • Chichester • Weinheim • Brisbane • Singapore • Toronto

This text is printed on acid-free paper. ♾

Published simultaneously in Canada.

For ordering and customer service, call 1-800-CALL-WILEY.

Library of Congress Cataloging-in-Publication Data:

Munk, Ben (Benedikt A.)
Frequency selective surfaces : theory and design / by Ben Munk.
p. cm.
"A Wiley-Interscience Publication."
ISBN 0-471-37047-9 (alk. paper)
1. Frequency selective surfaces. I. Title.
TK7872.F5M84 2000
621.381'3—dc21 99-39545

Printed in the United States of America

10 9 8 7 6 5 4 3 2

This book is dedicated to all of my students and colleagues who have taught me so much, and to all my sponsors, who not only taught me but paid me.

This book would not have been possible had it not been for the constant support of my family, and especially that of my wife, Aase.

This Page Intentionally Left Blank

CONTENTS

FOREWORD I

In the early 1950s the Air Force Avionics Laboratory[1] was involved in efforts to quantify the aircraft characteristic known as the radar cross section (RCS) or radar echoing area which had eluded a solution since WWII. In order to do the calculations and measurements, one had to know how to make an appropriate model, which meant that the features that dominated RCS had to be discovered. In time, a number of these "echo sources" were identified, which subsequently allowed the construction of the needed models and the routine cataloging of RCS of all types of military vehicles.

In the course of these studies, the thought began to grow that it might be possible to reduce the radar size of these prominent echo sources. This started the program on radar signature reduction. The Avionics Lab was the leader in this work of the Department of Defense for many years, but it clearly did not have the manpower to conduct in-house studies and simultaneously look into the treatment of every kind of echo source, which involved long-term development of technology of many types. It was only with the tremendous assistance of a number of organizations that the current state of the art came about.

The first efforts toward echo reduction were devoted to radar absorber materials (RAM) (it seemed reasonable that absorbing incident radar signals from the bad guys was a good thing to do). One particular type of RAM studied was called the circuit analog absorber because it depended on layers of geometric arrays of conductive material which acted like combinations of resistive, capacitive, and inductive circuit components. Chapter 9 of this book treats this topic nicely.

At the same time, one very important echo source was identified that provided an interesting challenge—the large antenna featured so prominently on the nose of most aircraft. The problem was that while we (the good guys) only needed the antenna to

[1] Names of organizations changed frequently over the years, but the most familiar are used herein.

work in a certain small range of frequencies, the bad guys were provided with a big echo source at virtually any frequency they chose to use. Obviously, putting RAM over this could reduce the echo, but we had a feeling that some people on our side might not like the idea too much. It was then (in the late 1950s) that the possibility of using "high Q" (highly conductive) elements, similar to the resistive ones in the circuit analog absorber, was conceived. The idea was to at least severely limit the range of frequencies over which the antenna would be an echo source by substituting a surface that only reflected in a narrow band for the conventional metallic surface that reflected at all frequencies.

At the time the Ohio State University ElectroScience Laboratory was providing major assistance to the Avionics Lab in the RCS activity. The investigation of the "tuned surface" concept was requested because it seemed that a major effort would be required to develop it. At first, progress was slow and not very promising, partly because some of the key players at OSU had doubts about the concept and partly because it was easy to get mired in the complex mathematics (method of moments) chosen as the path to success. After a year or more of frustration, along came Ben Munk, then nearing completion of his doctorate in electromagnetics. To say that Ben was a breath of fresh air would be an understatement.

He immediately took a different tack on the approach, using array theory combined with the detailed method of moments (which became the "Periodic Moment Method" in this book) to handle the problem from a macro rather than a micro view. The results were startling, and the potential of this concept became the source of continued support.

Since that time, Ben has been the worldwide guru of this technology, providing support to applications of all types. His genius lies in handling the extremely complex mathematics while at the same time seeing the practical matters involved in applying the results. As this book clearly shows, Ben is able to relate to novices interested in using frequency selective surfaces and to explain technical details in an understandable way, liberally spiced with his special brand of humor.

Over the years there have been people who were made aware of this work, who proceeded to publish their own ideas on the subject based on "advanced" mathematical analysis. While it is possible to manipulate equations to produce new and interesting theoretical results, most of these publications are of little use. As mentioned earlier, it is in the understanding of the real world design problem that the mathematics produces truly useful results. As this book by Ben Munk clearly demonstrates, he and the team he guided have been able to do just that. His many discussions of "common misconceptions" and little, but very important, factors like "dielectric underwear," serve to demonstrate his mastery of this technology in its most practical form (and his wonderful sense of humor).

Make no mistake about this—Ben Munk has written a book that represents the epitome of practical understanding of frequency selective surfaces. He deserves all honors that might befall him for this achievement. (Continued support for his future work would no doubt be gratefully accepted too.)

WILLIAM F. BAHRET

Mr. W. Bahret was with the United States Air Force but is now retired. From the early 1950s he sponsored numerous projects concerning radar cross section of airborne platforms, in particular antennas and absorbers. Under his leadership grew many of the concepts used extensively today, for example, the metallic radome. In fact he is considered by many to be the father of stealth technology.

B.A.M.

This Page Intentionally Left Blank

FOREWORD II

As early as 1947 George Sinclair, the founder of the Ohio State University Antenna Laboratory (which later became the ElectroScience Laboratory), realized that antennas placed on aircraft represented significant scatterers. Ed Kennaugh led much of the subsequent research on control of the radar cross section of antennas. This was initiated by a white paper on the "Echoing Area of Antennas" in 1961. One of the concepts introduced for this task was that of frequency selective surfaces, which became the major topic under investigation and which has continued to the present. However, Kennaugh had become deeply involved in transient scattering, complex natural resonances, and the like, and he asked to be replaced as principal investigator on these projects. As a result the laboratory's director asked me to take over this role in 1965. This was a very fortunate event for me in that I became associated with a number of great students. Two of these Ph.D. students, Ben Munk and Randy Ott, focused their research on the analysis of frequency selective surfaces. Both were successful; however, our sponsor (Bill Bahret) commented, "I need two solutions like a turtle needs air brakes!" Randy used more traditional electromagnetic computational moment methods, whereas Ben, from the very beginning of his career, had a very unique viewpoint with respect to this analysis and incorporated the basic physics of interaction between elements into his solution. The four of us (Bill, Ben, Randy, and I) agreed that Ben's approach, which is the same approach he uses in this book, was the most adaptable and thus the most useful. History has demonstrated that the correct choice was made. Since physical concepts are deeply embedded in the analysis of frequency selective surfaces, his approach has subsequently provided useful results for many FSS configurations that weren't even considered in his earlier research. Ben would take over as principal investigator several years after he received the Ph.D. and has remained our FSS guru ever since.

I have a few comments concerning the development of this book. Ben's Danish education has had a strong influence on his writing. His dissertation and subsequent reports were all very well organized. The organization of this book is even better than his earlier works. Also, unfortunately for me, Ben always used a single letter when a double letter occurred in a word, and vice versa. To this day, I sometimes have to go to the dictionary to obtain the correct spelling of certain words. It seems that by the looks of it, Ben has mastered the spelling lesson as the spelling in the present work shows none of this early problem!

This book compiles under one cover most of his research over the past three decades. It is woven with the physical insight that he has gained and further developed as his career has grown. Ben uses mathematics to whatever extent is needed, and only as needed.

This material is written so that it should be useful to engineers with a background in electromagnetics. I strongly recommend this book to any engineer with any interest in phased arrays and/or frequency selective surfaces. The physical insight that may be gained from this book will enhance their ability to treat additional array problems of their own.

LEON PETERS JR.

Leon Peters Jr. was a professor at the Ohio State University but is now retired. From the early 1960s he worked on, among many other things, RCS problems involving antennas and absorbers. In fact he became my supervisor when I joined the group in the mid-1960s.

B.A.M.

PREFACE

The material in this book represents part of the work I performed with my colleagues and students from the mid-1960s to the present time. Much of that work was classified. In fact even my 1968 Ph.D. dissertation became classified. Fortunately, many of these restrictions (but not all) have now been lifted, and I am grateful for this opportunity to publish this book.

Most of the work was sponsored by the U.S. Air Force. However, in the last couple of years funding has primarily come from the U.S. Navy, which has actually made this book possible.

BEN MUNK

November 1999

This Page Intentionally Left Blank

ACKNOWLEDGMENTS

Many individuals have supported and inspired me over the years. To list all of them would be impossible, but certain people stand out. Foremost are Mr. William F. Bahret, Dr. Leon Peters, Jr., and Dr. Robert Kouyoumjian. Without a doubt, they are the three individuals who had the greatest influence on my work in stealth technology. Later, they were joined or followed by Dr. Carl Mentzer, Dr. Brian Kent, and Mr. Ed Utt.

While the U.S. Air Force primarily was interested in band pass filters, the U.S. Navy typically was more interested in band stop designs. Immense, valuable guidance and support was given to me by Mr. Jim Logan, Dr. John Meloling, and Dr. John Rockway.

My gratitude is also extended to my good friend Mr. Clyde L. Hoots from the Marion Composite (formerly Brunswick) Corporation. He taught me many practical aspects of radome design.

I am also indebted to my friend and colleague Prof. John Kraus for the constant encouragement and advice he has given me over the years.

Numerous students have assisted me over the years and many of them are referenced in the text. A special thank you goes to Mr. Ethan Saladin, Mr. Jonothan Pryor, and Mr. Dan Janning for running many of the computed cases. I am further indebted to the students in my last EE910 class. They corrected numerous errors and made many good suggestions.

Finally, my deep felt thanks goes to Miss Ann Kelly who typed the entire manuscript and to Mr. Jim Gibson who drafted all the manually-generated drawings. They both did a superb job.

B.A.M.

This Page Intentionally Left Blank

SYMBOLS AND DEFINITIONS

a	Horizontal distance between column q and point of observation $\bar{R}$
a, a_1	Wire radius of elements
a	Side length of square elements
$d\bar{A}$	Vector potential for double infinite array of Hertzian elements
$d\bar{A}_q$	Vector potential of Hertzian elements located in column q
$d\bar{A}_{qm}$	Vector potential of a single Hertzian element located in column q and row m
b_{m-1}	Location of the front face of dielectric slab m in dipole case
b_m	Location of the back face of dielectric slab m in dipole case
C_p	Equivalent shunt capacitance from the orthogonal elements in a circuit analog absorber
d	Diameter of circular plate element
d_m	Thickness of dielectric slab in dipole case
D_N	Determinant of admittance matrix for N slot arrays

D_x	Inter-element spacings in the x-direction
D_z	Inter-element spacings in the z-direction
$\bar{e} = [\hat{p} \times \hat{r}] \times \hat{r} = {}_{\perp}\hat{n}_{\perp}e + {}_{\parallel}\hat{n}_{\parallel}e$	Field vector for infinite array of Hertzian elements
$\bar{E}_m(\bar{R})$	Electric field at $\bar{R}$ in medium m
$\bar{E}^i_m(\bar{R})$	Incident electric field at $\bar{R}$ in medium m
$\bar{E}^r_m(\bar{R})$	Reflected electric field at $\bar{R}$ in medium m
f	Frequency
f_g	Onset frequency of grating lobe
$F(w)$	Fourier transform of $f(t)$, not necessarily a function of time
$\bar{H}_m(\bar{R})$	Magnetic field of $\bar{R}$ in medium m
$\bar{H}^i_m(\bar{R})$	Incident magnetic field at $\bar{R}$ in medium m
$\bar{H}^r_m(\bar{R})$	Reflected magnetic field at $\bar{R}$ in medium m
$H^{(2)}_n(x)$	Hankel's function of the second kind, order n and argument x
$I_{qm}(l)$	Current along element in column q and row m
k, n	Indexes for the spectrum of plane, inhomogeneous waves from an infinite array
l	Distance from a reference point to an arbitrary point on the element
$2l_1$	Total element length
dl	Infinitesimal element length
Δl	Element length of Hertzian dipoles
$\bar{m}_{\pm} = \bar{E} \times \hat{n}_{D\pm}$	Magnetic current density
$\bar{M}_{\pm}$	Total magnetic current in slots
$\hat{n}_D$	Unit vector orthogonal to dielectric interface pointing into the dielectric medium in question
${}_{\perp}\hat{n}_m = \frac{\bar{n}_D \times \hat{r}}{\lvert n_D \times \hat{r} \rvert}$	Unit vector(s) orthogonal to the planes of incidence or reradiation in medium m
${}_{\parallel}\hat{n}_m = {}_{\perp}\hat{n}_m \times \bar{r}$	Unit vector(s) parallel to the planes of incidence or reradiation in medium m.
$n, n_0, n_1, n_2, \ldots$	Integers

$\hat{p}$	Orientation vector for elements
$\hat{p}^{(p)}$	Orientation vector for element section p
$\hat{p}^{p,n}$	Orientation vector for element section p in array n
$P^{(p)}$	Scattering pattern function associated with element section p
$P^{(p)t}$	Transmitting pattern function associated with element section p
$P_m^{(p)}$	Scattering pattern function associated with element section p in medium m
$\underset{\parallel}{\overset{\perp}{P}}{}_{m\pm}^{(p)} = \hat{p}^{(p)} \cdot \underset{\parallel}{\overset{\perp}{\hat{n}}}_{m\pm} P_{m\pm}^{(p)}$	Orthogonal and parallel pattern components of scattering pattern in medium m
$P_m^{(p)t}$	Transmitting pattern function associated with element section p in medium m
$\underset{\parallel}{\overset{\perp}{P}}{}_m^{(p)t} = \hat{p}^{(p)} \cdot \underset{\parallel}{\overset{\perp}{\hat{n}}}_{m\pm} P_{m\pm}^{(p)t}$	Orthogonal and parallel pattern components of transmitting pattern in medium m
$\mathcal{P}_n$	Polynomial for a band-pass filter comprised of n slot arrays
q, m	Position of a single element in column q and row m
$\hat{r}_\pm = \hat{x} r_x \pm \hat{y} r_y + \hat{z} r_z$	Direction vectors of the plane wave spectrum from an infinite array
$\hat{r}_{m\pm} = \hat{x} r_{mx} \pm \hat{y} r_{my} + \hat{z} r_{mz}$	Direction vectors in medium m of the plane wave spectrum from an infinite array
$r_\rho = \sqrt{1 - \left(s_z + n\frac{\lambda}{D_z}\right)^2}$	ρ-Component of $\hat{r}_\pm$
$\hat{s} = \hat{x} s_x + \hat{y} s_y + \hat{z} s_z$	Direction of incident field
$\hat{s}_m = \hat{x} s_{mx} + \hat{y} s_{my} + \hat{z} s_{mz}$	Direction of incident field in medium m
t	Variable used in Poisson's sum formula
$\underset{\parallel}{\overset{\perp}{T}}{}_m$	Orthogonal and parallel transformation functions for single dielectric slab of thickness d_m
$\underset{\parallel}{\overset{E}{\perp}} T_m$	Orthogonal and parallel transformation function for the E-field in a single dielectric slab of thickness d_m
$\underset{\parallel}{\overset{H}{\perp}} T_m$	Orthogonal and parallel transformation function for the H-field in a single dielectric slab of thickness d_m

$\underset{\parallel}{\perp} T_{m-m'}$	Orthogonal and parallel generalized transformation function when going from one dielectric slab of thickness d_m to another of thickness $d_{m'}$, both of which are located in a general stratified medium
$T.C._{\pm 1}$	Transmission coefficient at the roots $Y_{1\pm}$, etc.
$V^{1',1}$	Induced voltage in an external element with reference point $\bar{R}^{(1')}$ caused by all the currents from an array with reference element at $\bar{R}^{(1)}$
$V_{Di\pm}^{(1')}$	Induced voltage in an external element with reference point $\bar{R}^{(1')}$ caused by a direct wave only from the entire array
$V_{D\pm}^{(1')}$	Induced voltage in an external element with reference point $\bar{R}^{(1')}$ caused by double bounced modes ending in the $\pm$ direction
$V_{S\pm}^{(1')}$	Induced voltage in an external element with reference point $\bar{R}^{(1')}$ caused by a single bounded mode ending up in the $\pm$ direction
w	Dipole or slot width
$\underset{\parallel}{\perp} W_m$	Orthogonal and parallel components for the Wronskian for a single dielectric slab of thickness d_m
$\underset{\parallel}{\perp} W_m^e$	Orthogonal and parallel components for the effective Wronskian for a single dielectric slab of thickness d_m and located in a general stratified medium
Y	Intrinsic admittance
y	Variable defined by (6.29)
$y_{1\pm}, y_{2\pm}, \cdots$	Roots of polynomial for band-pass filter
Y_A	Scan admittance as seen at the terminals of an element in the array
Y_L	Load admittance at the terminals of the elements
$Y_0 = \frac{1}{Z_0}$	Intrinsic admittance of free space
$Y_m = 1/Z_m$	Intrinsic admittance of medium m
$Y^{1,2}$	Array mutual admittance between array 1 and 2
Z	Intrinsic impedance

$Z = \frac{a+bz}{c+dz}$	Dependent variable as a function of the independent variable z in a bilinear transformation
$Z_0 = 1/Y_0$	Intrinsic impedance of free space
$Z_A = R_A + jX_A$	Scan impedance as seen at the terminals of an element in the array
Z_L	Load impedance at the terminals of the elements
$Z_m = 1/Y_m$	Intrinsic impedance of medium m
$Z^{n,n'}$	Array mutual impedance between a reference element in array n and double infinite array n'
$Z^{q,q'}$	Column mutual impedance between a reference element in column q and an infinite line array at q'
$Z_{q,q'm}$	Mutual impedance between reference element in column q and element m in column q'
α	Angle between plane of incidence and the xy-plane
$\beta_m = \frac{2\pi}{\lambda_m}$	Propagation constant in medium m.
Δl	Total element length of Hertzian dipole
ϵ	Dielectric constant
ϵ_{eff}	Effective dielectric constant of a thin dielectric slab as it affects the resonant frequency
ϵ_m	Dielectric constant in medium m
ϵ_{rm}	Relative dielectric constant in medium m
η	Angle of incidence from broadside
η_g	Angle of grating lobe direction from broadside
θ_m	Angle of incidence from broadside in medium m
$\begin{matrix} E \\ \perp \\ \parallel \end{matrix} \Gamma_{m+} = \begin{matrix} E \\ \perp \\ \parallel \end{matrix} \Gamma_{m,m+1}$	Orthogonal and parallel Fresnel reflection coefficient for the E-field when incidence is from media m to $m+1$
$\begin{matrix} H \\ \perp \\ \parallel \end{matrix} \Gamma_{m+} = \begin{matrix} H \\ \perp \\ \parallel \end{matrix} \Gamma_{m,m+1}$	Orthogonal and parallel Fresnel reflection coefficient for the H-field when incidence is from media m to $m+1$
$\begin{matrix} E \\ \perp \\ \parallel \end{matrix} \Gamma^e_{m+} = \begin{matrix} E \\ \perp \\ \parallel \end{matrix} \Gamma^e_{m+1}$	Orthogonal and parallel effective reflection coefficient for the E-field when incidence is form media m to $m+1$

$\begin{matrix} H \\ \perp \\ \parallel \end{matrix} \Gamma^e_{m+} = \begin{matrix} H \\ \perp \\ \parallel \end{matrix} \Gamma^e_{m,m+1}$	Orthogonal and parallel effective reflection coefficient for the H-field when incidence is from media m to $m+1$
λ_m	Wavelength in medium m
μ_m	Permeability in medium m
μ_{rm}	Relative permeability in medium m
$\begin{matrix} E \\ \perp \\ \parallel \end{matrix} \tau_{m+} = \begin{matrix} E \\ \perp \\ \parallel \end{matrix} \tau_{m,m+1}$	Orthogonal and parallel Fresnel transmission coefficient for the E-field when incidence is from media m to $m+1$
$\begin{matrix} H \\ \perp \\ \parallel \end{matrix} \tau_{m+} = \begin{matrix} H \\ \perp \\ \parallel \end{matrix} \tau_{m,m+1}$	Orthogonal and parallel Fresnel transmission coefficient for the H-field when incidence is from media m to $m+1$
$\begin{matrix} E \\ \perp \\ \parallel \end{matrix} \tau^e_{m+} = \begin{matrix} E \\ \perp \\ \parallel \end{matrix} \tau^e_{m,m+1}$	Orthogonal and parallel effective transmission coefficient for the E-field when incidence is from media m to $m+1$
$\begin{matrix} H \\ \perp \\ \parallel \end{matrix} \tau^e_{m+} = \begin{matrix} H \\ \perp \\ \parallel \end{matrix} \tau^e_{m,m+1}$	Orthogonal and parallel effective transmission coefficient for the H-field when incidence is from media m to $m+1$
$\omega = 2\pi f$	Angular frequency
$\omega_1 \omega_0$ and ω_1	Variables used in Poisson's sum formula (not angular frequencies)

1

GENERAL OVERVIEW

1.1 WHAT IS A PERIODIC SURFACE?

A *periodic surface* is basically an assembly of identical elements arranged in a one- or two-dimensional infinite array. An example is shown in Fig. 1.1, where simple *"dipoles"* loaded at their centers with a load impedance Z_L have been arranged in a rectangular array with inter-element spacings D_x and D_z.

1.2 PASSIVE VERSUS ACTIVE ARRAYS

Fundamentally, any *periodic array* can be excited in two ways: by an incident plane wave $\bar{E}^i$, as shown in Fig. 1.1 top (passive array), or by individual generators connected to each element, as shown in Fig. 1.1 bottom (active array). In the latter case, the voltage generators must have the same amplitude and a linear phase variation across the active array in order for it to qualify as a periodic surface. (This constraint produces one or more radiated plane waves.)

In the passive array case (Fig. 1.1 top), the incident plane wave will be partly transmitted in the forward direction ($\bar{E}^t$) and partly reflected in the specular direction ($\bar{E}^r$). Under resonant condition and for no *grating lobes* (see Section 1.9) the amplitude of the reflected signal may equal E^i while $E^t = 0$. It is customary to define the specular reflection coefficient as

$$\Gamma = \frac{E^r}{E^i}, \tag{1.1}$$

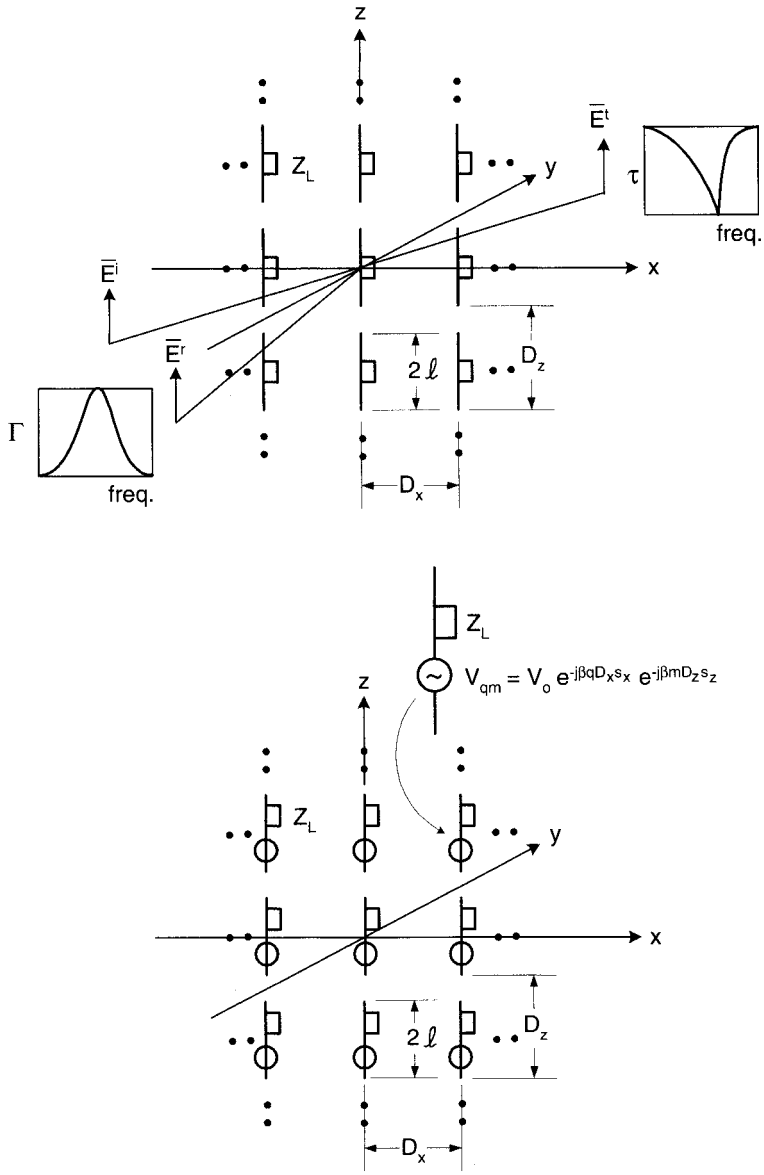

FIGURE 1.1. *Periodic structure* of electric conductors (*dipoles*) with load impedances Z_L. *Top:* Passive case. The structure is excited by an incident plane wave $\bar{E}^i$ which is being partly reflected in the specular direction ($\bar{E}^r$) and partly transmitted in the forward direction ($\bar{E}^t$). *Bottom:* Active case. Each element is excited by individual generators with the same amplitude and each has a linear phase variation across the aperture as shown. (s_x and s_z denote the directional cosines along the x- and z-axes, respectively).

where E^r and E^i in general are referenced to the plane of the array. Similarly the transmission coefficient is defined as

$$\tau = \frac{E^t}{E^i}. \tag{1.2}$$

1.3 DIPOLE VERSUS SLOT ARRAYS

Instead of arrays of dipoles with electric currents as shown in Fig. 1.1, we may also consider arrays of slots with magnetic currents as shown in Fig. 1.2.[1] This type of array can also be driven either passively by an incident plane wave or actively by individual generators. The main difference between the dipole and slot cases is that we excite electric currents on the wires in the *dipole* case while we excite "magnetic

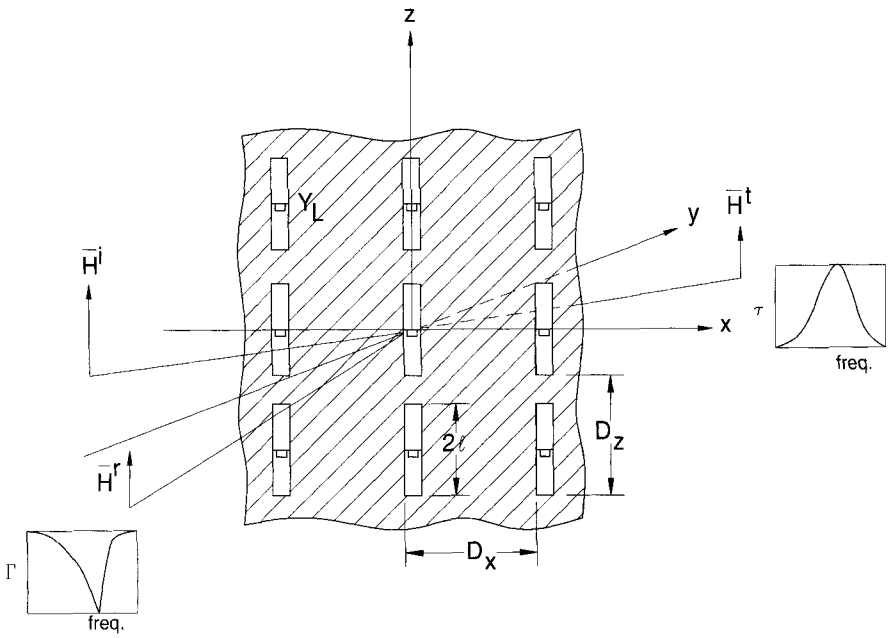

FIGURE 1.2. *Periodic structure* of *slots* with load-admittance Y_L. It is passively excited by an incident plane wave $\bar{H}^i$ which is being partly reflected in the specular direction ($\bar{H}^r$) and partly transmitted in the forward direction ($\bar{H}^t$).

[1]Magnetic currents are fictitious; that is, they do not really exist. However, the electric field $\bar{E}$ present in the *slots* can by the equivalence principle be shown to be equivalent to a magnetic current density $\bar{m} = \bar{E} \times \hat{n}$, where $\hat{n}$ is normal to the screen pointing into the medium in question. The magnetic current approach leads to a very desirable symmetry relationship between the *dipole* and *slot* cases, as explored in Chapters 6 and 7.

currents" in the *slot* case (i.e., there is a voltage distribution in the *slots*). As will be shown later, the two cases become quite similar and symmetric if we compare the electric field in the dipole case and the magnetic field in the slot case.

1.4 COMPLEMENTARY ARRAYS

Complementary arrays may be defined as dipole and slot arrays with elements of similar shape such that if the two complementary arrays are put on top of each other a "complete" perfectly conducting plane is obtained. An example is given in Fig. 1.3, with the dipole array at the top and the complementary slot array at the bottom.

It can be shown that the specular reflection coefficient for one array equals the transmission coefficient for the complementary array. This is a simple case of the general "Babinet's principle." Based on this observation it is often expected that a potential designer need only investigate one of the two cases. However, the reader should be warned that this is in general not the case. First of all, the conducting screen must be a perfect conductor and "infinitely" thin, typically less than 1/1000

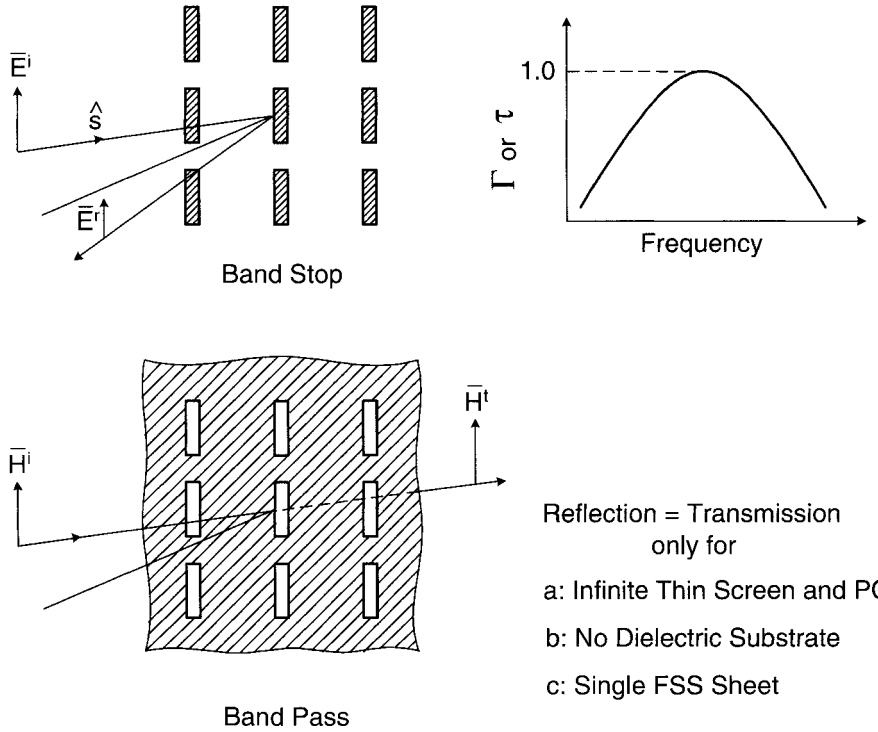

FIGURE 1.3. Simple example of *complementary arrays*: The *dipole* array at the top and the *slot* array at the bottom. The reflection coefficient Γ for the top equals the transmission coefficient T for the bottom. (This is an example of Babinet's principle.)

wavelength. If the screen is thicker, the bandwidth of the dipole array will be larger while the bandwidth of the slot array will be smaller. Further, if a thin layer of dielectric is added, the resonant frequency will be lowered somewhat for both the dipole and the slot arrays, but for a dielectric thickness of the order of $\lambda/4$ or more, the two cases behave vastly different, as explained later (see Section 1.6.3 and Chapter 7).

Finally, if two or more arrays are cascaded, we can in both cases obtain a band filter characteristic with a flat top and sharp fall off. However, the calculations for the two cases are vastly different and lead to vastly different results, as explained in Chapters 4, 7, and 8.

1.5 A LITTLE HISTORY WITH PHYSICAL INSIGHT

At this point many readers might wonder about the puzzle illustrated in Fig. 1.4. At the top we show an array of infinitely long rods, while we at the bottom show an array of elements of finite length $2l$ but of the same interelement spacings D_x. Thus the top array has more "conducting area" than the bottom one. Nevertheless, only the case with the finite-length rods may have a reflection coefficient magnitude equal to one (i.e., when $2l \sim \lambda/2$), while the infinitely long rod case will only at "DC." The explanation is readily understood by inspection of the equivalent circuits shown to the right. While the long rods are inductors, the finite elements have series capacitances associated with the gaps between the elements, resulting in the equivalent circuit of a series LC circuit as shown. Obviously only the latter will act like a true ground plane at the resonant frequency with no leakage, while the long rod case cannot.

This observation is far from new. In fact, while it is true that a rather intense (although not widely publicized) study of periodic surfaces got started in the mid-1960s because of the great potential for military applications, the general principle was known long before. Actually, the oldest reference known to this writer is a patent granted in 1919 to the famous Marconi and Franklin (the one with the antenna, not the kite!). It is reproduced in part in Fig. 1.5(a) and (b). They produced a parabolic reflector of wire sections rather than "infinitely" long rods. Although these inventors claimed improvement (see line 27) that sounds a bit high (possibly because the long rod case was purely designed), they nevertheless were the first to present the concept of "tuned elements" (see lines 38–42). To paraphrase, they state that the length of the sections should be preferably $\lambda/2$ but may be made greater or less by inserting in it either a condenser or an inductance.

The author was unaware of the above facts when his patent on a "periodic surface for large scan angles" was filed on October 16, 1968 (it was under secrecy order until it was granted on January 29, 1974). Basically this patent, reproduced in part in Fig. 1.6, showed that in order for any periodic surface to have a stable resonant frequency with angle of incidence, the interelement spacings D_x and D_z must be small ($< 0.4\lambda$). The required elements of small size can be obtained by using elements with some sort of loading (see Section 2.3.1). Another patent concerning three-legged loaded elements was issued in 1975 to Pelton and Munk (U.S. Patent

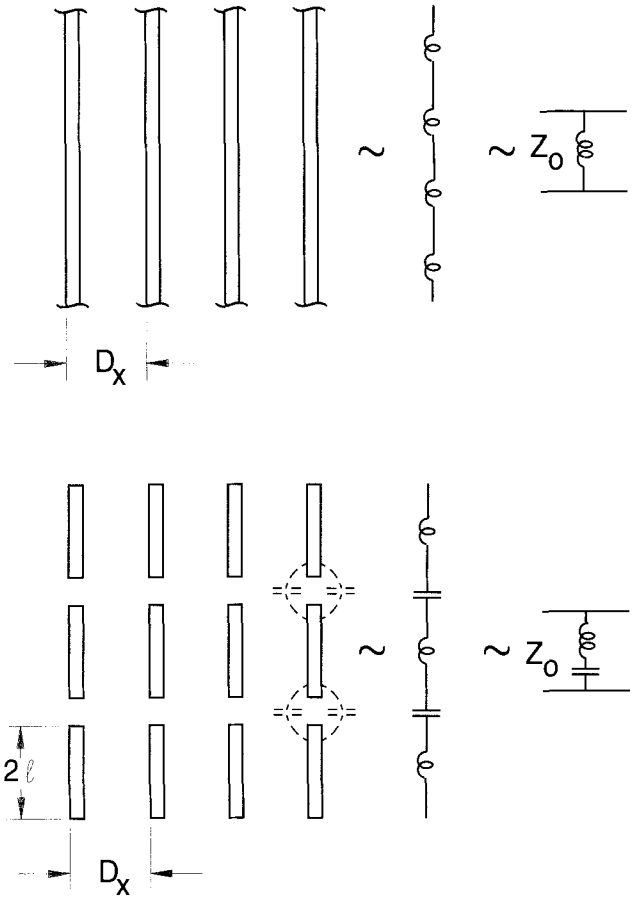

FIGURE 1.4. *Top: Periodic surface* of infinitely long rods with its equivalent circuit to the right. *Bottom: Periodic surface* of elements of length $2l$ and its equivalent circuit to the right. (Desspite a greater conducting area in the top case, only the bottom case can produce perfect reflection without any leakage, namely at the resonant frequency.)

3,975,938). In some respects this element is superior to the four-legged loaded element. A detailed survey of various element types is given in Chapter 2, where the requirements for a "good" element are also given.

Incidentally, the mono-polarized version of the loaded element shown in Fig. 1.6 bottom-left is only for the purpose of presenting the concept of loading. It may have cross-polarization deficiencies at higher angles of incidence and so is not in general recommended. However, the bi-polarized version shown in Fig. 1.6 bottom-right does not have that problem because of its symmetric shape (see also Section 2.3.1).

UNITED STATES PATENT OFFICE.

GUGLIELMO MARCONI AND CHARLES SAMUEL FRANKLIN, OF LONDON, ENGLAND, ASSIGNORS TO MARCONI WIRELESS TELEGRAPH COMPANY OF AMERICA, OF NEW YORK, N. Y., A CORPORATION OF NEW JERSEY.

REFLECTOR FOR USE IN WIRELESS TELEGRAPHY AND TELEPHONY.

1,301,473. Specification of Letters Patent. Patented Apr. 22, 1919.

Application filed February 26, 1919. Serial No. 279,410.

To all whom it may concern:

Be it known that we, GUGLIELMO MARCONI, a subject of the King of Italy, and CHARLES SAMUEL FRANKLIN, a subject of the King of Great Britain, and both residing at Marconi House, Strand, London, England, have invented new and useful Improvements in Reflectors for Use in Wireless Telegraphy and Telephony, of which the following is a specification.

This invention relates to improvements in reflectors used with transmitters and receivers in wireless telegraphy and telephony.

According to this invention a reflector is constructed of two or more sets of rods (which term includes strips and wires) arranged on a parabolic surface around the transmitting or receiving aerial as a focus, each rod being tuned to the aerial and the rods of the different sets being preferably in line with each other. By this means the efficiency and effect of the reflector are very largely increased for example, by making the reflector of three sets of rods arranged on a parabolic surface and having a focal distance of one-quarter wave length, the range may be increased from 400% to 500% as against 80% obtained with the simple reflectors before known.

The reflector may be described in other words as follows:—

On a parabolic surface surrounding a transmitter or receiver and in the correct direction having regard to the polarization of the transmitted waves is arranged a number of long wires which are divided up into elements each in tune with the transmitter. The length of each element is preferably about half a wave length, but may be made either greater or less than this by inserting in it either a condenser or an inductance. The adjacent ends of these elements may be insulated from each other or joined by inductance coils or condensers, the controlling factor being that each element when in its working position in the reflector is in tune with the aerial.

In practice we find that some of the elements may be removed slightly from the true parabolic surface provided that those elements of the reflector which are nearer the focus than they would be if on the parabolic surface are tuned to a rather longer wave, and those elements which are farther to a rather shorter wave.

For very short waves no earth connections are required or desirable, but for longer waves it is an advantage to earth the aerial and the lower elements of the reflector.

Very good results can be obtained by arranging the elements on a cylindrical parabolic surface, but better results can be obtained by arranging them on a true paraboloid, particularly when using a reflector having a focal length equal to three-quarter wave length or more.

Our invention is illustrated by the accompanying drawings. In said drawings Figure 1 is a plan, Fig. 2 a rear view and Fig. 3 a side view of a reflector constructed in accordance with this invention.

Figs. 4, 5 and 6 are plan view, rear view and side view respectively, of a second form of reflector embodying our invention.

Figs. 7, 8 and 9 are plan view, rear view and side view respectively, of a third form of reflector embodying our invention.

Figs. 10 and 11 are diagrammatic detail views each illustrating a single set of rods or wire reflector elements of which the reflectors may be built up.

Referring to the drawing more in detail, the reflector illustrated in Figs. 1, 2 and 3 has three sets of parallel rods *a* arranged on a cylindrical parabolic surface with an aerial or antenna *b* at the focus. This arrangement is for concentrating vertically polarized waves in the horizontal direction.

In the arrangement shown in Figs. 4, 5 and 6, the individual reflector members are placed in parallel planes which are spaced apart vertically instead of being spaced horizontally as in Figs. 1, 2 and 3. This arrangement is for concentrating horizontally polarized waves in the horizontal direction. In the arrangement of Figs. 7, 8 and 9, there is a reflector having three sets of parallel rods arranged on a true paraboloid instead of a cylindrical parabola; this will concentrate both vertically and horizontally polarized waves in the horizontal direction.

These figures illustrate reflectors made with three sets of parallel rods, or, stated otherwise, reflectors made up of a number of wires each divided into three elements,

FIGURE 1.5(a). Presumably the oldest patent concerning *periodic surfaces* was issued in 1919 to Marconi and Franklin. Note in lines 38–42 that they were quite aware of the concept of tuned elements and made them potentially shorter or longer than $\lambda/2$.

each element being in tune with the transmitted or received wave. As illustrated, each of these elements should be nearly half a wave length long; alternatively each of these wires may be divided up into a larger number of elements connected together by condensers.

Fig. 10 shows one wire divided into three elements each in tune with the desired wave.

Fig. 11 shows one wire divided into a number of shorter elements connected together by condensers. The capacity of each condenser must be such that if joined in circuit with the inductance of the wire joining it to the next condenser it would form a circuit in tune with the desired wave.

What we claim is:—

1. In wireless telegraphy, a reflector comprising a plurality of reflector members arranged on a substantially parabolic surface, each of said members including a plurality of elements, each element being in tune with the aerial.

2. In wireless telegraphy, a reflector comprising a plurality of reflector members arranged on a parabolic surface, said members lying in planes arranged parallel but separated a finite distance, each of said members including a plurality of elements, each element being in tune with the aerial.

3. In wireless telegraphy, a reflector comprising a plurality of sets of rods arranged on a parabolic surface around an aerial at the focus, each rod being in tune with the aerial, and the rods of each set being in line with one another.

GUGLIELMO MARCONI.
CHARLES SAMUEL FRANKLIN.

Witnesses:
GEORGE J. TRUSTY,
LEON DE SOUSA.

G. MARCONI & C. S. FRANKLIN.
REFLECTOR FOR USE IN WIRELESS TELEGRAPHY AND TELEPHONY.
APPLICATION FILED FEB. 26, 1919.

1,301,473. Patented Apr. 22, 1919.

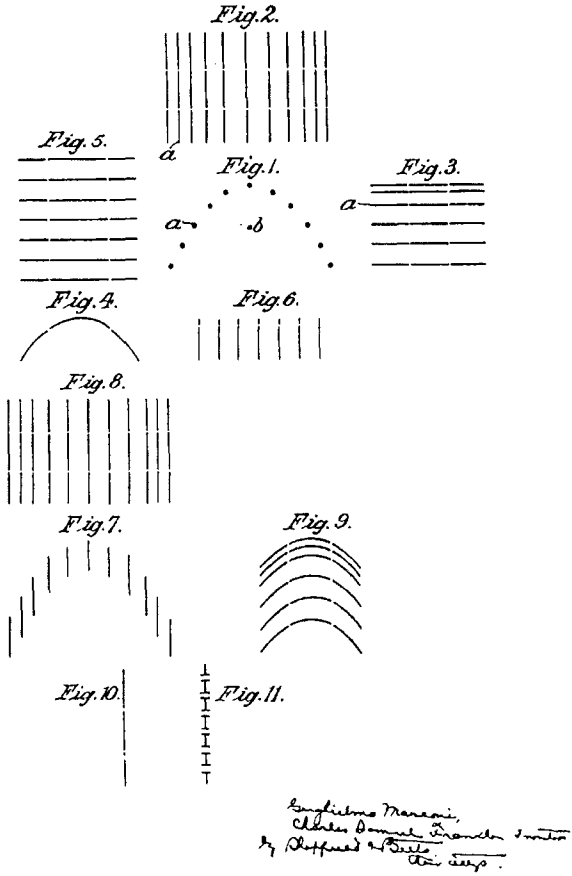

FIGURE 1.5(b). Continuation of Fig. 1.5(*a*).

United States Patent [19]
Munk

[11] **3,789,404**
[45] ***Jan. 29, 1974**

[54] **PERIODIC SURFACE FOR LARGE SCAN ANGLES**

[75] Inventor: **Benedikt A. Munk**, Columbus, Ohio

[73] Assignee: **The Ohio State University Research Foundation**, Columbus, Ohio

[*] Notice: The portion of the term of this patent subsequent to Aug. 29, 1989, has been disclaimed.

[22] Filed: **Oct. 16, 1968**

[21] Appl. No.: **768,142**

[52] **U.S. Cl.** ..... **343/18 B**, 343/18 A, 343/872
[51] **Int. Cl.** **H01q 15/14**
[58] **Field of Search** ..... 343/18 A, 18 B, 872

[56] **References Cited**
UNITED STATES PATENTS

2,478,463	8/1949	De La Sablonieve	343/18 A
3,273,062	9/1966	Raabe	343/18 B
3,309,704	3/1967	Klingler	343/18 A
3,381,293	4/1968	Tarpley, Jr.	343/18 B

OTHER PUBLICATIONS

Wiekhorst, Absorption and Transmission of Electromagnetic Waves, 7, 1957 pp. 1–4, 23.

Luis L. Oh et al., Slotted Metal Radome Cap For Rain, Hail, and Lightning Protection, Microwave Journal, Mar. 1968 pp. 105–108.

Primary Examiner—T. H. Tubbesing
Attorney, Agent, or Firm—Anthony D. Cennamo

[57] **ABSTRACT**

The invention is for a tuned resonant surface utilizing an array of short, loaded dipoles to obtain unity reflection or transmission coefficient over a narrow bandwidth about the desired frequency with said coefficient substantially independent of the angle of incidence of the impinging or radiated electromagnetic signal. Reference is made to the claims for a legal definition of the invention.

12 Claims, 17 Drawing Figures

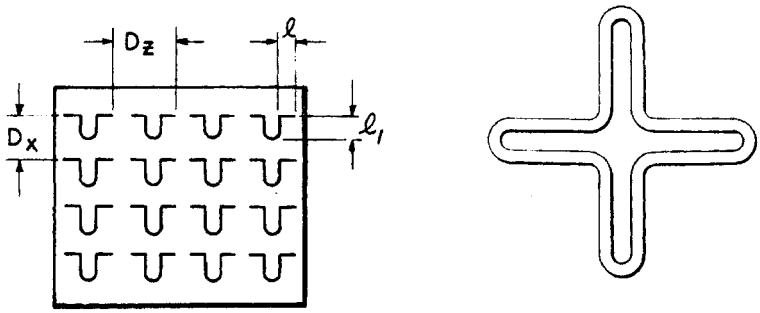

FIGURE 1.6. Part of the patent concerning loaded elements for large scan angles filed in 1968 and issued in 1974. The four-legged loaded elements, shown bottom-right, became one of the key elements for making *periodic surfaces* for high angles of incidence. Later in 1975 another patent concerning three-legged loaded elements was issued to Pelton and Munk.

1.6 HOW DO WE "SHAPE" THE RESONANT CURVE?

The periodic surfaces shown so far exhibit perfect reflection or transmission only at resonance. However, many applications call for a resonant curve with a flat top and faster roll off. There are essentially two ways to accomplish this goal:

1. Use two or more *periodic surfaces* cascaded behind each other without dielectrics.

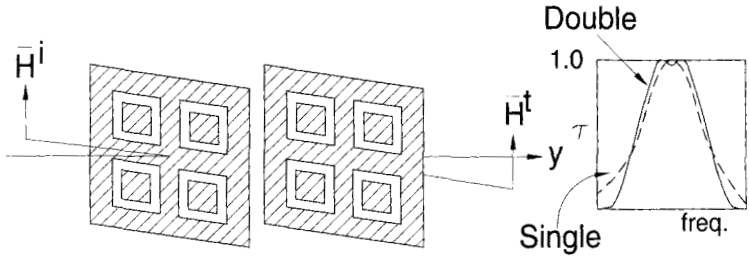

FIGURE 1.7. By using cascaded *periodic structures* we can obtain a broader top and faster roll-off. However, the bandwidth will vary considerably with angle of incidence.

2. Use dielectric slabs sandwiched between cascading periodic surfaces, which leads to the so-called hybrid periodic surfaces.

1.6.1 Cascading Periodic Surfaces without Dielectrics

An example of two periodic surfaces of slots cascaded behind each other is shown in Fig. 1.7. Inspection of the transmission curves clearly shows that the double layer has a much flatter top and faster roll-off as compared to the single layer. However, such a simple surface has considerable bandwidth variation as a function of angle of incidence and polarization. It is in general not recommended for precision work. (See also Fig. 7.5.)

1.6.2 Single Periodic Surface with Dielectric Slabs

A single periodic surface of slots provided with dielectric slabs of equal thickness and dielectric constant on each side is shown in Fig. 1.8. With such a surface typically

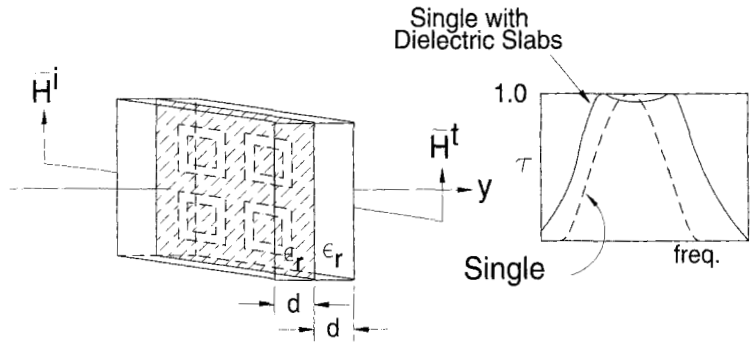

FIGURE 1.8. Adding dielectric slabs to each side of a single slotted surface can produce a considerable bandwidth that is almost constant with angle of incidence (see Fig. 1.18 bottom-right for details).

we can obtain a bandwidth that is considerably larger than that of a single structure. However, the flatness of the transmission curve is usually inferior and it is in general not recommended for precision work even if the bandwidth can be designed to be rather constant with moderate angle of incidence and polarization. (For details see Fig. 1.18 bottom-right, Section 1.8, as well as Fig. 7.5.)

1.6.3 Real Hybrid Periodic Structures

It is not uncommon that a periodic structure be designed first without any dielectric (sometimes called "free standing"). Then a dielectric structure is added (almost as an afterthought) mainly for mechanical reasons in hopes that the original design "won't change much!" This is fundamentally wrong. As seen above, dielectric slabs can have a profound effect on the transmission or reflection curves. (See Section 1.8 as well as Fig. 7.9.)

Two things happen when a dielectric slab is added next to a periodic structure: First, the resonant frequency f_0 changes. If the periodic structure had been completely surrounded by an infinite dielectric material of infinite extent and with relative dielectric constant ϵ_r, it is easy to see from Maxwell's equations that the resonant frequency would reduce in frequency with the factor $\sqrt{\epsilon_r}$, as illustrated in Fig. 1.9 top. If the extent of the infinite dielectric is reduced into dielectric slabs of a small, finite thickness $2d$, as shown in Fig. 1.9 bottom-left curve, the resonant frequency will change to somewhere between f_0 and $f_0/\sqrt{\epsilon_r}$. The interesting fact is that even for slab thicknesses as small as $d \sim 0.05\lambda_\epsilon$, the resonant frequency is fairly close to $f_0/\sqrt{\epsilon_r}$ (for more details, see Appendix E). If we only have dielectric to one side of the periodic structure, as shown in Fig. 1.9 bottom-right curve, the largest frequency shift downward would be $f_0/\sqrt{(\epsilon_r+1)/2}$. This resonance shift for thin dielectric slabs is essentially the same whether we are considering periodic surfaces of the dipole or slot type. However, if the slabs become thicker, for example, $\lambda_\epsilon/4$ or more, the two types behave quite differently. The dipole type will have a resonant frequency independent of the slab thickness, while the slot type will show unit transmission at frequencies varying around $f_0/\sqrt{\epsilon_r}$ for symmetric dielectric slabs. The reason for this is simply that the *dipoles* act like a short circuit across a transmission line, while the slots act like "open circuits" (i.e., they can be easily affected by dielectric slabs). It is obvious from the preliminary discussion above that a stratified dielectric medium can profoundly change not only the resonant frequency but also the shape and the angle of incidence variation of the resonant curves. (See also Fig. 1.18 later.)

More specifically, while simple cascading of periodic surfaces without dielectric was covered in the patent for large scan angles shown in Fig. 1.6, another patent was issued in 1978 concerning cascading and included dielectric slabs, as shown partly in Fig. 1.10 (details are given in [1]). This specific design is comprised of two slotted periodic surfaces sandwiched between three dielectric slabs. Each dielectric slab serves a very specific purpose: The two outer ones preferably should be identical and are responsible for providing a constant bandwidth for angle of incidence and polarization. Similarly the slab in the middle determines the flatness of the top of

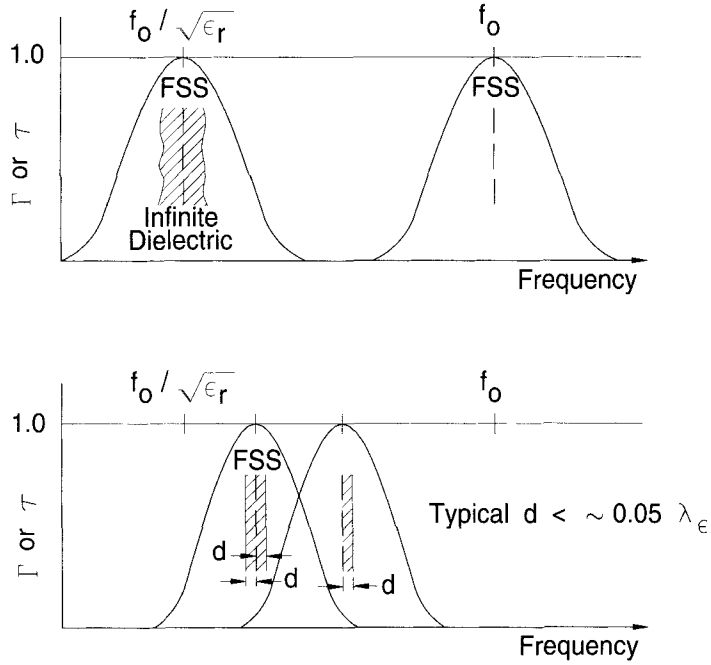

FIGURE 1.9. Effect of dielectric upon the resonant frequency. *Top:* If an FSS is immersed in an infinite medium of relative dielectric constant ϵ_r, the original resonant frequency f_0 will change to $f_0/\sqrt{\epsilon_r}$. *Bottom*: For slabs of thickness d on both sides the resonant frequency will be somewhere between f_0 and $f_0/\sqrt{\epsilon_r}$; however, even for $d \sim 0.05\lambda_\epsilon$ we are close to $f_0/\sqrt{\epsilon_r}$. For a single sheet see also Appendix E.

the transmission curve. Finally the FSS determines the bandwidth and the resonant frequency. As can be seen from the typical transmission curves in Fig. 1.10 bottom for the E- and H-planes, the bandwidth remains remarkably constant for all angles of incidence, even up to 80° for both polarizations. This is quite remarkable considering that we would obtain a bandwidth variation of the order of 30:1 without dielectric compensation.

The designer is warned not to expect this kind of performance simply by slapping a couple of dielectric layers between a pair of FSS that happens to be found in the shop! Nor is one likely to obtain these results simply by putting a computer to work unless he or she has a pretty good idea where to start the optimization.

The finer design details cannot be properly appreciated without understanding the *plane wave expansion* for periodic surfaces as given in Chapters 3, 4, 5 and 6. This theory is then applied to hybrid radome design (band-pass filters) given in Chapter 7. It is important to understand that the two outer dielectric slabs must act like quarter-wave transformers, that is, they must have a thickness of the order of $\lambda_\epsilon/4$ or more, regardless of the number of FSSs or the element type. Similarly, band-stop filters will usually be made of periodic surfaces of the dipole type. They too will often

United States Patent [19] [11] **4,125,841**
Munk [45] **Nov. 14, 1978**

[54] **SPACE FILTER**

[75] Inventor: **Benedikt A. Munk**, Columbus, Ohio
[73] Assignee: **Ohio State University Research Foundation**, Columbus, Ohio

[21] Appl. No.: **797,798**
[22] Filed: **May 17, 1977**
[51] Int. Cl.² **H01R 15/10**
[52] U.S. Cl. **343/909**; 343/872
[58] Field of Search ..... 343/909, 781 CA, 781 P, 343/779, 831, 872, 18 A, 18 B

[56] **References Cited**
U.S. PATENT DOCUMENTS

2,747,184	5/1956	Kock	343/909
3,295,131	12/1966	Hollingsworth	343/909
3,754,271	8/1973	Epis	343/909

Primary Examiner—Alfred E. Smith
Assistant Examiner—David K. Moore
Attorney, Agent, or Firm—Sidney W. Millard

[57] **ABSTRACT**

An improved space-filter formed as a composite multi-layered structure. Utilizing a periodic slot array structure nested between first and last strata of a dielectric material, the filter exhibits a constant bandwidth characteristic over a broad range of angles of incident radiation. Where two slot arrays are utilized in parallel relationship, an intermediate dielectric layer is provided which has an effective dielectric function selected to achieve critical array component coupling.

17 Claims, 18 Drawing Figures

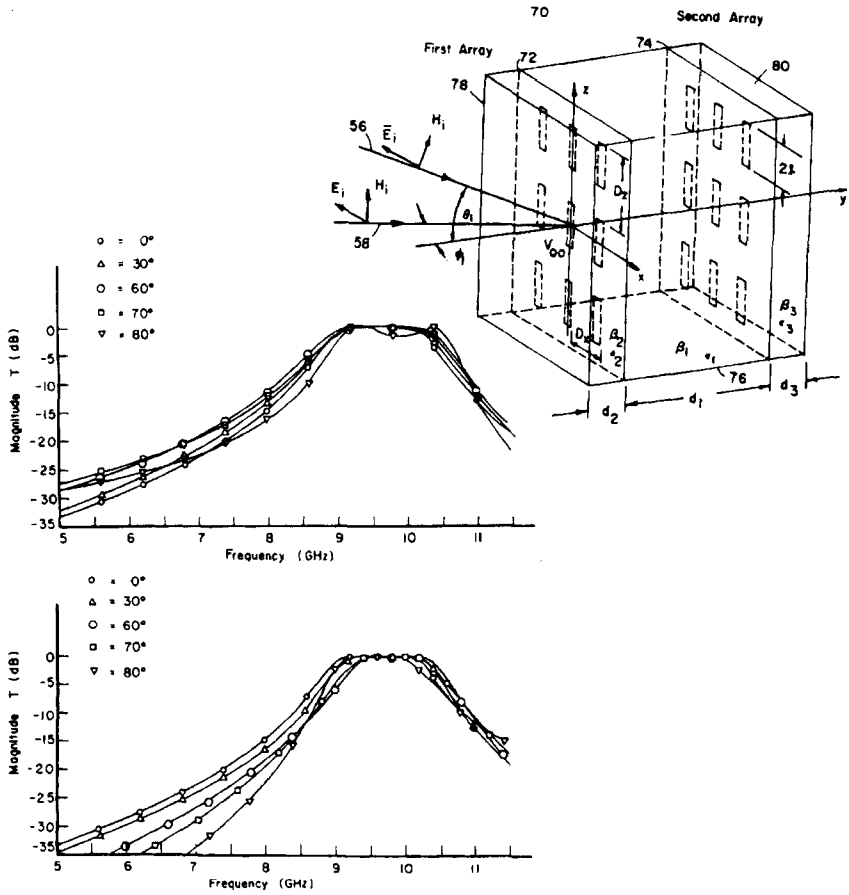

FIGURE 1.10. Excerpts of patent for the "space filter" with constant bandwidth and resonant frequency with angle of incidence and polarization; usually called a *hybrid radome*. (See Chapter 7 for details.) These curves were shown for the first time in the open literature in 1976, see [1].

involve dielectric materials that can be very crucial in controlling the shape of the reflection and transmission curves. However, the designer should be warned that no simple relationship exists between the slot and dipole cases as was the case for a single periodic structure discussed earlier (see Fig. 1.3, Babinet's principle). Thus the band-stop filter theory is treated separately in Chapter 8.

1.7 APPLICATION OF PERIODIC STRUCTURES

At this point the reader will be justified in asking: What is all that good for? Well, the answer is simply: A multiplicity of very important things!

1.7.1 Hybrid Radomes

Perhaps the first thing that comes to mind is the application of band-pass radomes used to reduce the radar cross section (RCS) of antennas outside their operating band.[2]

A typical situation is shown in Fig. 1.11 top where the radar antenna mounted at the front of an airplane has been covered with a shaped radome with a band filter characteristic as shown at the bottom of the same figure. When the radome is opaque and exposed to an incident field most signals will be reflected in the bi-static direction because of the radome's shape and thus produce a very weak signal in the backscatter direction, that is, we have a low RCS. On the other hand, if the incident signal has a frequency where the radome is transparent, the radome is ineffective in reducing the antenna RCS. It is essentially determined by the antenna itself and the question then becomes how low can that become? In general, it is expected to be anything but low, and often that is the case. However, in Chapter 9 we will investigate this question in more detail and show that certain antennas, namely arrays, can in principle be designed to be "invisible" in the backscatter direction over a considerable bandwidth. In practice, the lower level is determined by the tolerance level obtainable by the components. See also Section 9.9.2.

1.7.2 Band-Stop Filters

Another situation is shown in Fig. 1.12 top where antennas in general have been mounted on a mast. This entire assembly has been covered by an FSS of some sort in order to deflect out of band signals while the desired signals go through. In other words, a low RCS is obtained the same way as for the case shown earlier in Fig. 1.11. However, there is an important difference. Typical radar installations for shipboard applications often operate below 3 GHz and so do most communication systems.

[2]Using a band-pass radome to reduce the antenna RCS seems first to have appeared in an internal memorandum written by the late Prof. E. M. Kennaugh of the Ohio State University. He gave a copy to this author sometime after 1970, noting that the memorandum was written around 1961. However, it appears that W. F. Bahret had similar ideas before that.

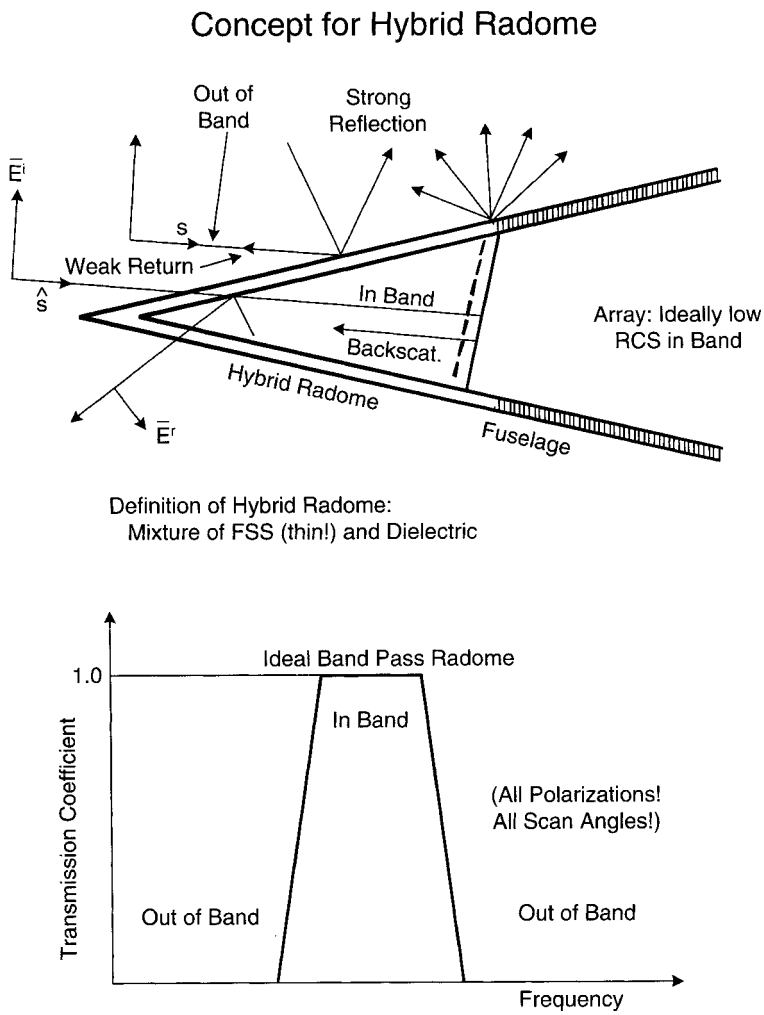

FIGURE 1.11. Use of a hybrid radome with band-pass characteristic to reduce the antenna RCS out of band.

Thus one might be tempted to merely scale the hybrid radome in Fig. 1.11 (typical X-band) to a lower frequency. This is in general a bad idea, partly because a slotted radome operating, say, at 3 GHz would have higher-order resonances that could be a problem somewhere in X-band and higher. But most important, there would likely be multiple grating lobes (see Section 1.9) at the higher frequencies. These can produce undesirable high levels of RCS at some frequencies and some angles of incidence.

For this reason it is better to design instead a broadband band-stop filter, as indicated at the bottom of Fig. 1.12. The dipole elements for such a filter would typically resonate at X-band, leading to much smaller elements with much smaller inter-

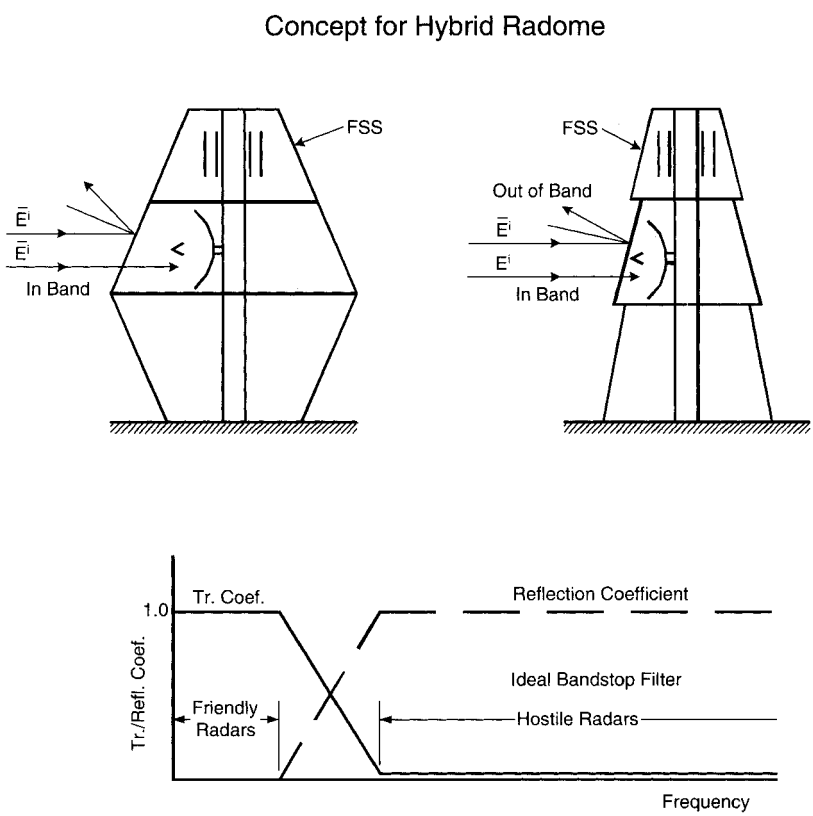

FIGURE 1.12. Band-stop filter used to reduce the RCS of ship-borne antennas. It is transparent from DC up to the cutoff frequency.

element spacings; that is, the onset of grating lobes would be significantly delayed to higher frequencies. A detailed design procedure of such band-stop filters is given in Chapter 8.

1.7.3 Dichroic Subreflectors

Another application is shown in Fig. 1.13 where a Cassegrain system has the subreflector made of a so-called dichroic structure. This simply refers to a periodic surface that is transparent at a frequency band f_1 and opaque at another frequency band f_2. This enables us to place one feed horn operating at f_1 at the focal point of the main reflector and another feed horn operating at f_2 at the Cassegrain focal point. The net result is that two frequency bands f_1 and f_2 can be accommodated by the same main reflector, which not only may take up valuable space but also weigh heavily on the financial scale.

The subreflector does not necessarily have to be a hyperboloid but can be flat. An example that is also offset is shown in Fig. 1.14. The designer should be aware

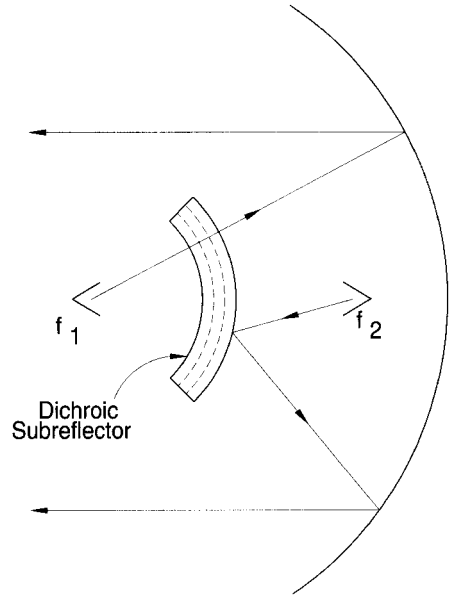

FIGURE 1.13. Use of a *periodic structure* as a Cassegrain subreflector.

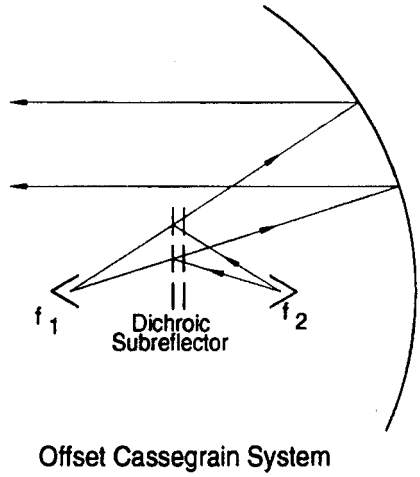

FIGURE 1.14. Similar to Fig. 1.13 but offset and with a flat reflector instead of hyperbola.

that although the flat reflector may be simpler to build than a convex one, it must nevertheless, like all reflecting surfaces, maintain its mechanical shape with high tolerance at all times. In general, this is simpler to accomplish for a convex surface than a flat surface, which often must be held in place by a substantial support structure. An example of a dichroic surface is given in Chapter 8.

1.7.4 Dichroic Main Reflectors

Another interesting application is shown in Fig. 1.15 where we have placed an X-band array to the left that radiates through a polarizer (see Section 1.7.6) and a dichroic main reflector. Besides being transparent at X-band the dichroic reflector is opaque at Q-band. The entire assembly had a diameter of only 6 inches and was designed to be located in the periscope of a submarine. Measurements taken on a model actually built showed negligible transmission loss through the dichroic surface; a slight narrowing of the X-band beam was noted due to a lens like effect of the dichroic reflector. The radiation pattern at Q-band was virtually indistinguishable from that obtained from a solid metallic reflector.

1.7.5 Circuit Analog Absorbers

So far we have considered only lossless structures. However, periodic surfaces not only can be made of lossy material but at the same time can be very useful. An ex-

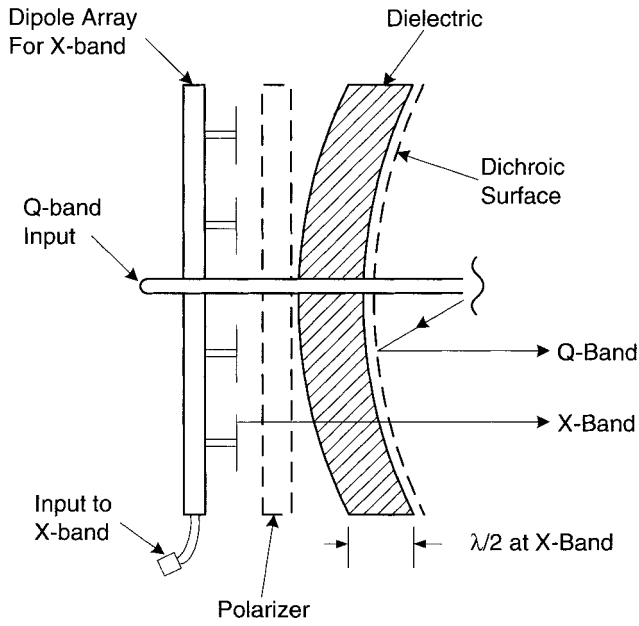

FIGURE 1.15. X-band array (*left*) looking through a polarizer and a dichroic main reflector reflecting Q-band.

ample is shown in Fig. 1.16, a so-called circuit analog absorber. It is seen to consist of crossed elements made of a resistive material backed by a ground plane. Such surfaces are reminiscent of the classical Salisbury screen. They are, however, superior to them by the fact that the periodic surfaces exhibit a reactive component that to a large extent can be designed to produce a larger bandwidth, particularly as more layers are added. These surfaces will be discussed in detail in Chapter 9. Note that

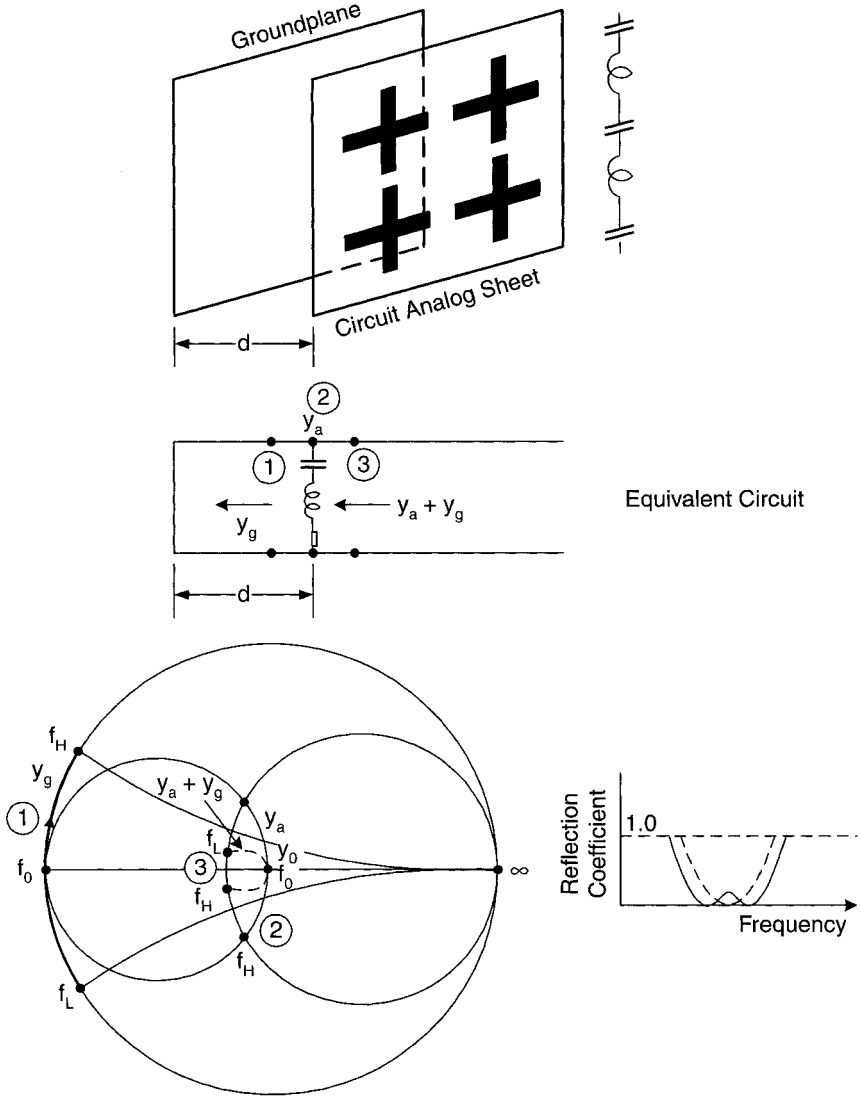

FIGURE 1.16. Circuit analog absorbers are made of periodic structures of very lossy material. They have more bandwidth per given thickness than most other absorbers.

while we in general advise designers not to use simple crossed lossless elements, it's okay for the lossy case (see also Fig. 2.37).

1.7.6 Meanderline Polarizers[3]

A simple single-layer meanderline polarizer is shown in Fig. 1.17. To an incident signal with vertical E-field, the meanderlines will act like a shunt inductance over

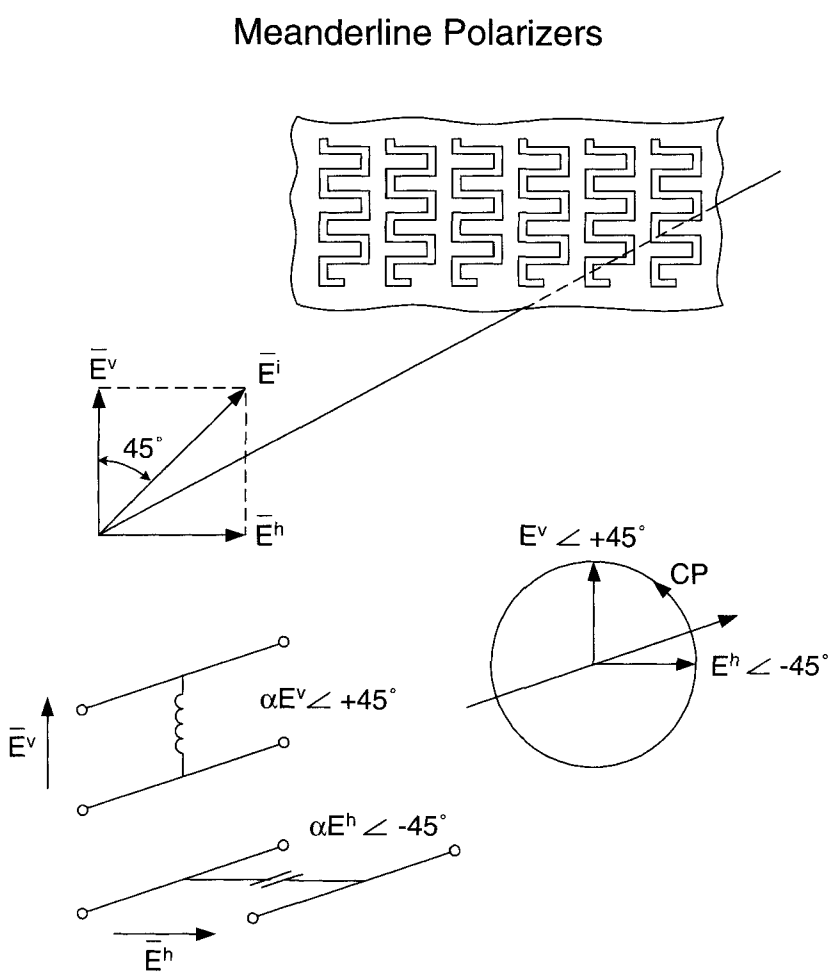

FIGURE 1.17. A meanderline structure acts like a shunt inductance for vertical polarization and as a capacitance for horizontal. For a net difference of 90°, a signal tilted 45° as shown will be transformed into a circular polarized signal.

[3]U.S. Patent 3,754,271, James J. Epis (inventor, Sunnyvale, California), "Broadband Antenna Polarizer," August 21, 1973. This patent appears to be an improvement patent over the "prior art."

an equivalent transmission line while a horizontal polarized wave is affected in a capacitive way. Thus, if an incident wave is linear polarized and tilted 45°, it may be decomposed into vertical and horizontal components where the former is delayed and the latter advanced. If after passing through the polarizer the net difference between the two components is 90°, they will simply recombine into a circular polarized wave. Cascading two or more polarizer sheets can improve the bandwidth. Adding dielectric slabs can improve the angle of incidence stability. At any rate, it is a periodic structure that can easily be analyzed with the theory developed in Chapters 3, 4, and 5.

1.8 COMMON MISCONCEPTIONS

Perhaps the biggest problem of a periodic structure is the fact that it conceptually is so simple that almost everyone understands it instantly. However, the designer soon realizes that one has to produce more than just some calculated curves! Basically, while a classical filter is subjected only to change of frequency, a "space filter" must deal with signals of various angles of incidence as well as polarizations. This will typically result in some variation of the resonant frequency and also in general a variation of the bandwidth as well as the shape of the transmission and reflection curves. For example, when facing the task of producing a radome with band-pass characteristics for camouflage purposes, the underlying thinking often goes like this: "Why don't we just take a standard $\lambda_\epsilon/2$ radome and add an FSS either on the inside or outside?" Transmission curves for a typical $\lambda/2$ radome only is shown in Fig. 1.18 top-left for various angles of incidence. Similarly the typical transmission curves for a thin slotted surface is shown in Fig. 1.18 top-right. Comparison of these two sets of curves shows that they both vary very similarly with angle of incidence; namely they both become narrower with higher-incidence angles for the E-field being orthogonal to the plane of incidence (i.e., H-field is parallel). Note also, however, that the resonant frequency is moving upward for the dielectric and downward for the metallic surface. Thus, when the two surfaces are combined as shown in Fig. 1.18 bottom-left, it is not too surprising that we may obtain a very stable resonant frequency with angle of incidence (note we now boldly show 75° instead of 70° earlier). However, we also note that the bandwidth is still changing dramatically with angle of incidence, which in general makes this design unsuitable for stealth purposes (see Fig. 1.11 earlier).

While many would expect this kind of behavior based on the performance of the dielectric and metallic radome panels individually, this is not necessarily so. For example, we show in Fig. 1.18 bottom-right the case where we have placed the slotted surface in the middle of the $\lambda_\epsilon/2$ radome. We now obtain a considerably more stable bandwidth with angle of incidence as seen. However, while the top looks fairly flat, it is just not good enough for making a quality radome unless the radome panel varies with angle of incidence. The problem is that a radome in general not only should have good transmission properties but also low reflection in order to keep "image lobes" to a very low level as indicated by the reflected field E_r in Fig. 1.11. For a

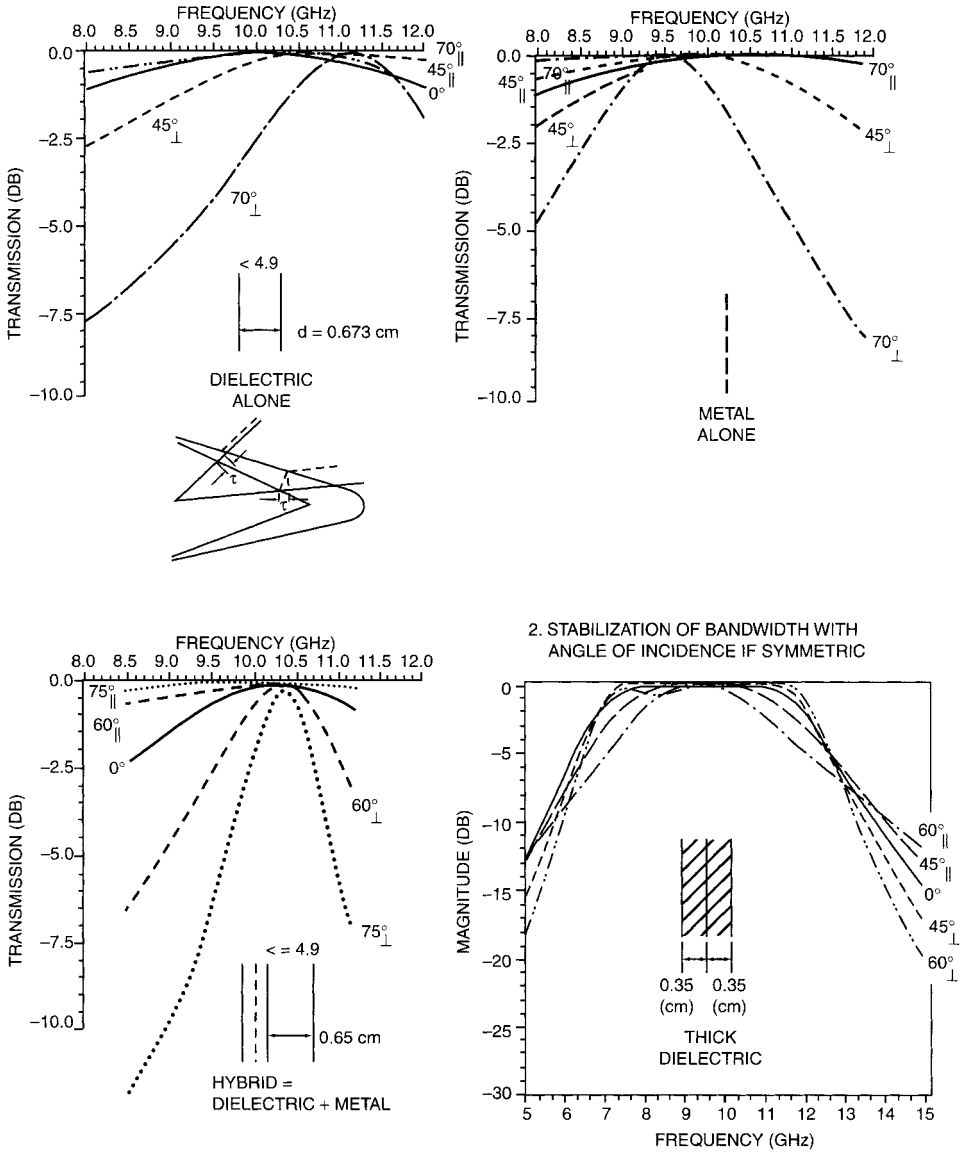

FIGURE 1.18. The transmission coefficient curves for various angles of incidence for: *Top-left*: A dielectric only $\lambda_\epsilon/2$ radome panel. *Top-right*: A slotted surface only panel. *Bottom-left*: Combination of the $\lambda_\epsilon/2$ and metal mounted to one side with thin layers of dielectric on both sides. *Bottom-right*: With the slotted surface placed in the middle of a $\lambda_\epsilon/2$ radome panel. Note the difference in bandwidth variation in the two bottom cases.

lossless radome panel, conservation of energy simply requires for the reflection and transmission coefficient Γ and $\mathcal{T}$, respectively, that

$$\Gamma^2 + \mathcal{T}^2 = 1. \tag{1.3}$$

Thus, from Eq. (1.3) we readily see that a high value of $\mathcal{T}$ automatically leads to a low value of Γ as desired. However, as explained in more detail in Chapter 7 on advanced radome design, we must in general require for a quality radome the reflection coefficient Γ to be so low that the transmission coefficient $\mathcal{T}$ will be so close to a magnitude of one it cannot be seen in the transmission curves; see Section 7.7.1. And on that account the design of Fig. 1.18 bottom-right falls far short. However, compared to its counterpart in Fig. 1.18 bottom-left, it has the advantage that it always will produce unit transmission regardless of the dielectric slab thickness, while the asymmetric version requires a dielectric slab thickness very close to $\lambda_\epsilon/2$ at the resonant frequency of the slotted surface; otherwise, a reflection loss will occur and make for a rather mediocre radome design even for general purposes. See also Problem 7.1.

The conclusion of the discussion above is that the design presented in Fig. 1.18 can be used for less demanding jobs such as communication or where reducing the RCS of an antenna is not an issue. However, when designing a radome with constant bandwidth and low reflection like the one shown in the insert of Fig. 1.10, the reader should consult Chapter 7 concerning hybrid radome design. Unfortunately, this cannot be fully comprehended without first studying the general theory presented in Chapters 3, 4, 5, and 6.

1.9 GRATING LOBES

Although a very general treatment of grating lobes will be encountered in Chapters 4 and 5 where we will deal with the general theory of periodic surfaces, the physical understanding of grating lobes is so fundamental and so important that a simple derivation will be given already here in the simple one-dimensional case. In Fig. 1.19 top we show a plane wave incident upon a one-dimensional periodic structure with interelement spacing D_x. Denoting the angle of incidence by η, it is clear that each element will be delayed in phase by $\beta D_x \sin\eta$ with respect to its neighbor to the left. However, in the forward as well as the specular directions, the same element will be ahead in phase with the same amount; that is, all the wavelets from the elements will always be in phase or we will always obtain plane waves that can propagate in these directions.

However, there are possibly other directions where propagation can take place as illustrated in Fig. 1.19 bottom. Here the incident wave is the same as before, and a possible grating lobe direction is denoted by η_g. From the figure we readily see that the total phase delay of an element (with respect to its neighbor to the left) is going to be $\beta D_x(\sin\eta + \sin\eta_g)$. If this delay equals a multiple of 2π, all signals from the elements will be in phase in the direction η_g; that is, propagation is possible. In other words:

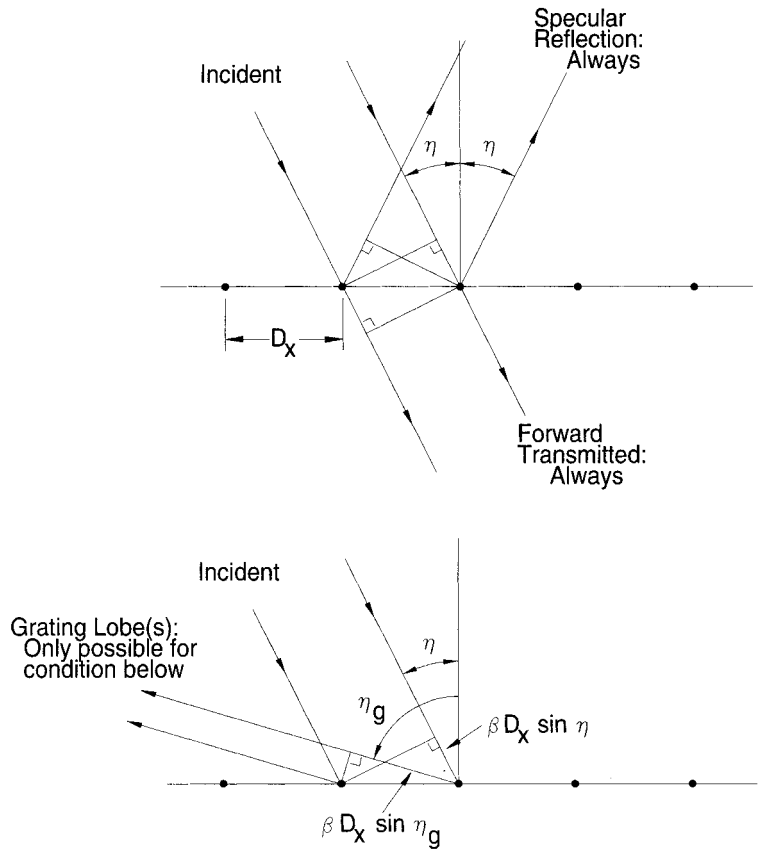

FIGURE 1.19. *Top:* Plane wave incident upon a periodic structure will always have propagation possible in the forward and specular directions. *Bottom:* Propagation in direction η_g is possible if $\beta D_x(\sin\eta + \sin\eta_g) = 2\pi n$.

Grating Lobe Condition

$$\beta D_x(\sin\eta + \sin\eta_g) = 2\pi n, \tag{1.4}$$

where

$$\beta = \frac{2\pi}{\lambda_g},$$

$$D_x = \text{interelement spacing (m)},$$

$$f_g = \frac{c}{\lambda_g} = \frac{nc}{D_x(\sin\eta + \sin\eta_g)}\ (\text{Hz}), \quad c = 3 \cdot 10^8\ \text{m/s}. \tag{1.5}$$

The lowest frequency f_{g0} where a grating lobe is encountered is when it is grazing the array, that is, for $\eta_g = 90°$ leading to:

Onset Grating Lobe Condition

$$f_{g0} = \frac{nc}{D_x(\sin\eta + 1)} \text{ (Hz)}. \tag{1.6}$$

Note: f_{g0} depend only on the angle of incidence η and the inter-element spacing D_x, and nothing else!

For grating lobe conditions in the general two-dimensional case including dielectric slabs, see Sections 4.6, 5.12, 5.13, and 5.14.

1.10 PROBLEMS

1.1 On Onset of Grating Lobes The condition for onset of grating lobes is very important. For a simple one-dimensional array with interelement spacing D_x, plot D_x/λ as a function of the angle of incidence η for $n = \pm 1$ and ± 2.

Almost equally important is the condition for a grating lobe being reflected in the direction of incidence. On the same graph as above, plot D_x/λ as a function of η for $n = \pm 1$ and ± 2. Compare the two cases!

This problem is by far the simplest in this book. However, it also may well be the most important!

1.2 On Element Loading It is desirable that an array of straight dipole elements resonate at 10 GHz.

a. Find the approximate element length, $2l$.

b. The elements are loaded at their center with an impedance $\sim j100$ ohm. Should the elements be made longer or shortened to still resonate at 10 GHz?

If you are unable to do this problem you are not as good as Marconi and Franklin. However, you have the benefit of being able to read Chapter 2.

2

ELEMENT TYPES: A COMPARISON

2.1 INTRODUCTION

When designing either a band-pass or band-stop FSS, the choice of the proper element may be of utmost importance. Some elements are inherently more broadbanded or more narrow-banded than others, while some can be varied considerably by design. In this chapter we present the typical behavior of the most common element types available to the FSS designers of today. All the curves are shown at 45° angle of incidence for orthogonal as well as parallel polarization with a resonant frequency around 10 GHz. Other cases can usually be "gleaned" by inter- and extrapolation. Further the FSSs have a 20 mil $\epsilon = 2.2$ dielectric slab placed on both sides. A word of caution: When judging an element type, one might be tempted to prefer an element where the bandwidth around the first resonance varies as little as possible with polarization. However, it should be kept in mind that in general, at least for mechanical reasons, all FSS eventually must be supported by a substantial assembly of dielectric slabs. These can, as discussed in Chapters 1 and 7, have a profound effect on the bandwidth variation with angle of incidence. Or, more to the point, what is most stable without a substantial dielectric slab may not be the proper choice in the final FSS design. Also the bandwidth of any FSS can in general be varied significantly by variation of the inter-element spacings D_x and D_z: A larger spacing will in general produce a narrower bandwidth, and vice versa. However, two things must in this case be watched closely: earlier onset of grating lobes (see Sections 1.9 and 5.14) and greater variation of the first resonant frequency with angle of incidence and polarization.

The curves presented in the following are mostly for small inter-element spacings resulting in a rather large bandwidth and stable resonant frequency with respect to

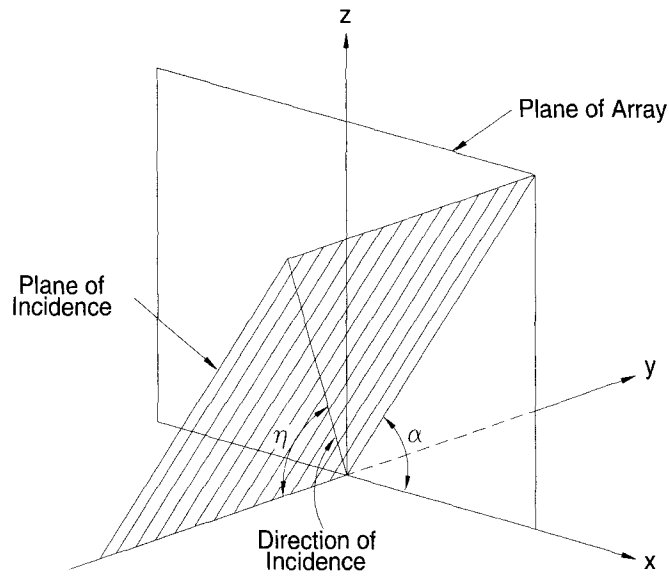

FIGURE 2.1. The plane of incidence determined by α and the direction of incidence by η.

angle of incidence. The plane of incidence and direction of incidence are defined in Fig. 2.1. All the cases presented in the following have been computed by use of the computer program, "Periodic Moment Method" (PMM). It was written by Dr. Lee Henderson as part of his doctoral dissertation in 1983 [2, 3] and is based on the plane wave expansion and mutual impedance approach developed in Chapters 3, 4, 5, and 6, as well as [4, 5]. It has stood its ground over the years and is considered to be one of the most reliable programs available being able to handle elements of arbitrary shape, slot as well as dipole arrays mixed together in an arbitrary dielectric profile that may include loss.

The elements are arranged into four groups as shown in Fig. 2.2:

Group 1: The center connected or N-poles, such as the simple straight element, three-legged element; anchor elements; the jerusalem cross; and the square spiral.

Group 2: The loop types such as the three- and four-legged loaded elements; the circular loops; and the square and hexagonal loops.

Group 3: Solid interior or plate types of various shapes.

Group 4: Combinations. The list is endless!

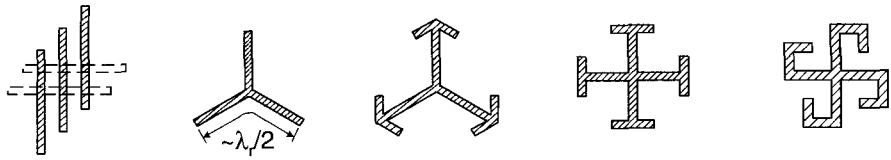

Group 1: "Center Connected" or "N-Poles"

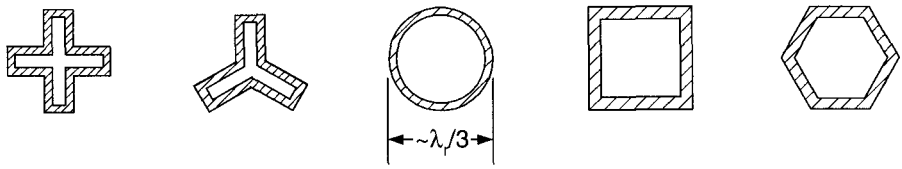

Group 2: "Loop Types"

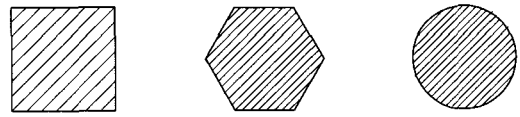

Group 3: "Solid Interior" or "Plate Type"

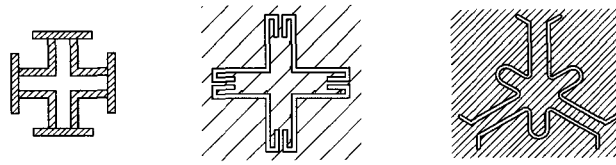

Group 4: "Combinations"

FIGURE 2.2. Typical element types arranged in groups.

2.2 GROUP 1: CENTER CONNECTED OR *N*-POLES

2.2.1 "Gangbuster" Surface

A simple example of the so-called gangbuster surface first presented in Kornbau's dissertation [6] is shown in the insert of Fig. 2.3. Basically it consists of simple straight dipoles arrayed in a fashion explained in Fig. 2.4. Here we show a simple rectangular grid with inter-element spacings $D_x = D_z$. The reference element in a "type n" surface is simply defined as having one end at an arbitrary point (x, z) and the other end at $(x + D_x, z + nD_z)$. If we let D_x, D_z remain constant, it is clear that the length of the dipole elements becomes larger; that is, the fundamental resonance becomes lower with increasing n. However, since the inter-elemental spacings are

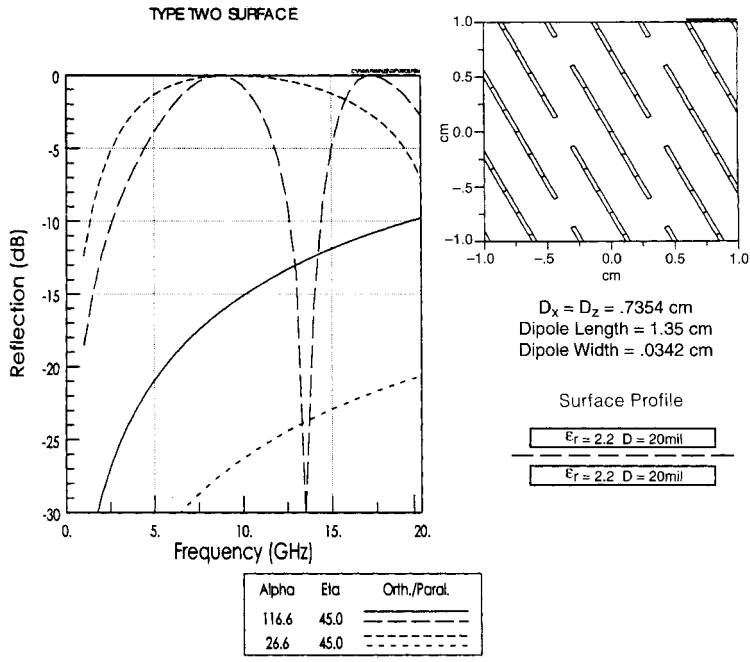

FIGURE 2.3. Gangbuster FSS type 2 made of simple straight dipoles arrayed to delay the onset of *grating lobes* (see Fig. 2.4). For general polarization, use two closely spaced surfaces twisted 90° with respect to each other. The four curves are for orthogonal and parallel polarization at 45° angle of incidence in the E-plane as well as the H-plane. The low reflection values are from the substrate alone (i.e., the incident field vector is orthogonal to the elements during the computation).

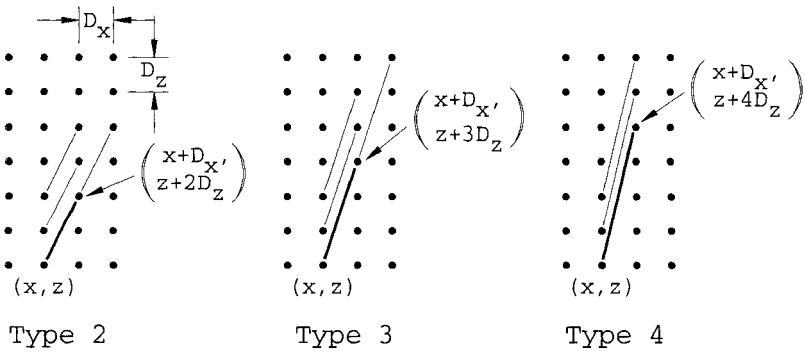

FIGURE 2.4. Construction of various gangbuster types. If $D_x = D_z$ is kept constant, higher type numbers will resonate at a lower frequency. However, the onset of grating lobes is always at the same frequency. Conversely, if the element length is kept constant, we must reduce D_x and D_z leading to delayed onset of grating lobes as the type number increases; see Figs. 2.3, 2.5, and 2.6.

the same regardless of n, the onset frequencies for grating lobes are also the same. (Grating lobes depend only on D_x, D_z and the incidence angle; see Sections 1.9 and 5.14.) On the other hand, if we keep the dipole length the same and reduce D_x and D_z for increasing n, the resonant frequency remains essentially constant while the onset of grating lobes is delayed. Examples of the reflection curves for types 2, 3, and 4 with constant dipole length are shown in Figs. 2.3, 2.5, and 2.6, respectively, in the frequency range 0 to 20 GHz. We observe that as the type number increases, the array gets more densely packed; that is, we obtain a larger and larger bandwidth, as mentioned earlier. In fact in Fig. 2.7 we show the reflection curves for type 4 in the larger-frequency range (0–40 GHz). Notice that the magnitude of the reflection is close to unity except for some very sharp nulls, for example, around 13 GHz. The location of this null is observed to be pretty much independent of the type number. It is explained in Fig. 2.8 as follows:

The fundamental mode seen in Fig. 2.8 (top) can always be strongly excited provided that the element length is about $\lambda/2$ long, and the incident E-field has a com-

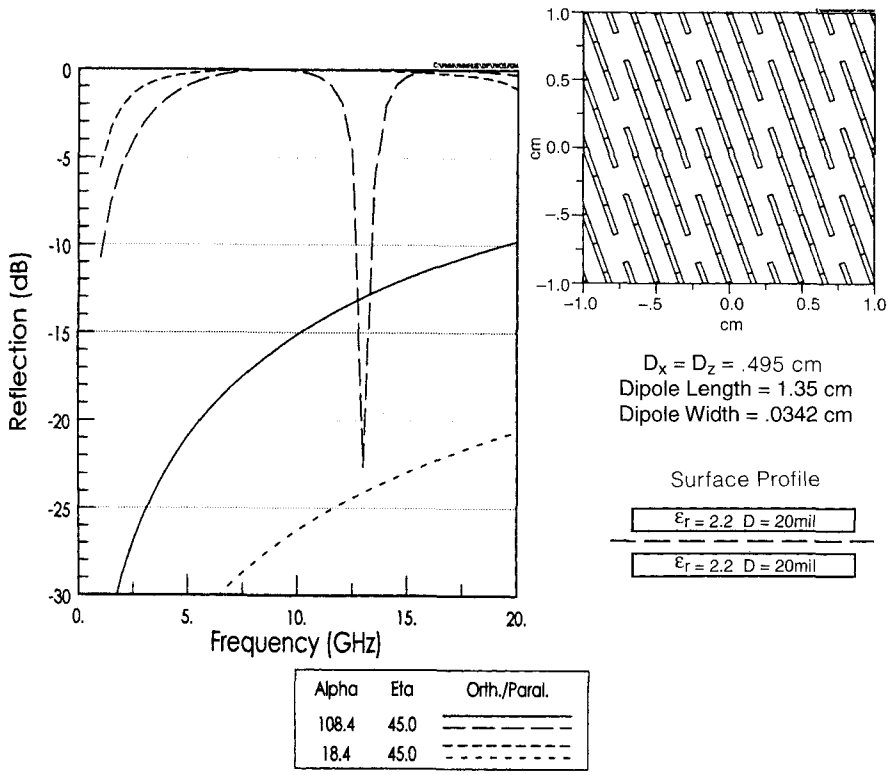

FIGURE 2.5. Gangbuster FSS type 3 is more closely packed than type 2, leading to broader reflection bandwidth and a narrower null. Higher-order types will have a null so narrow that they may be inconsequential for many applications.

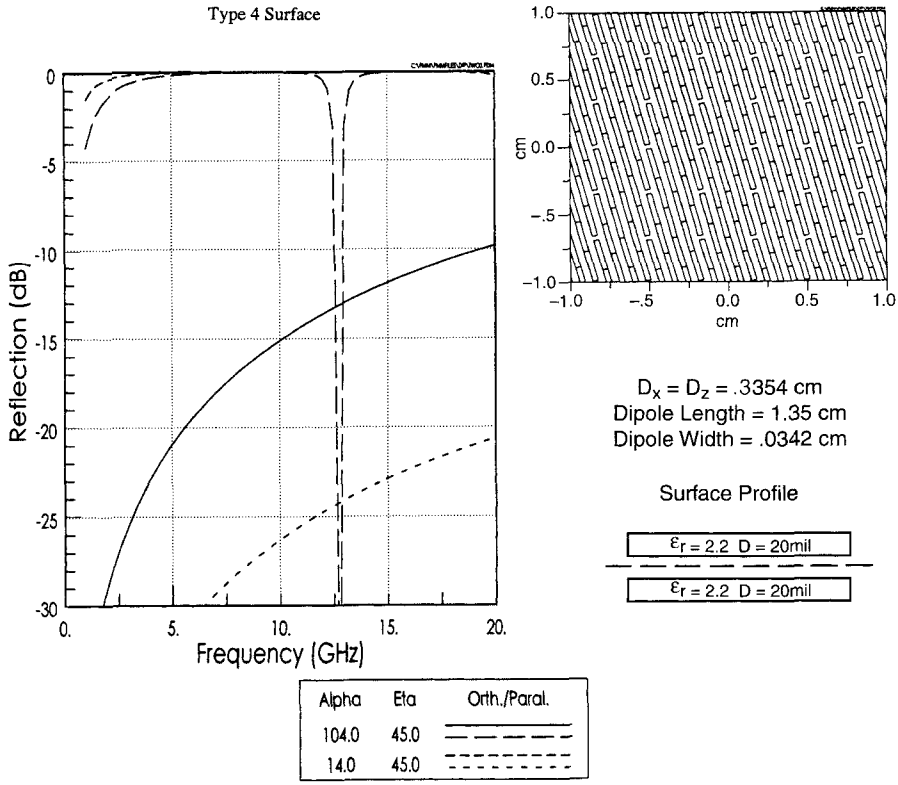

FIGURE 2.6. Gangbuster type 4 leading to broader bandwidth and a narrower null.

ponent parallel to the elements. The odd mode shown in Fig. 2.8 (bottom) is only excited for oblique angle of incidence and when the element length is approximately λ. In Figs. 2.3 to 2.7 we observe these two frequencies to be around 9 and 17 GHz, respectively. It is now a simple consequence of Foster's reactance theorem that between two poles will always be a null, in this case about 13 GHz. We usually denote this type of null as a modal interaction null. There is not much that can be done to avoid this null, but the good news is that it becomes more and more narrow as the surface type number increases. In fact for many practical applications it is so narrow that it is of minor consequence (e.g., see Fig. 2.7). Also a slight amount of loss will strongly reduce the depth of the null.

Obviously a single gangbuster surface can only handle linear polarization with the E-field being in the plane of the element. However, arbitrary polarization can easily be handled if we use two gangbuster surfaces twisted 90° with respect to one another. It is important, however, that the two surfaces are mounted close to each other, since some cross-polarization in the cardinal plane will occur. The smaller the separation, the lower the cross-polarization. (For details, see Schneider's dissertation [7].)

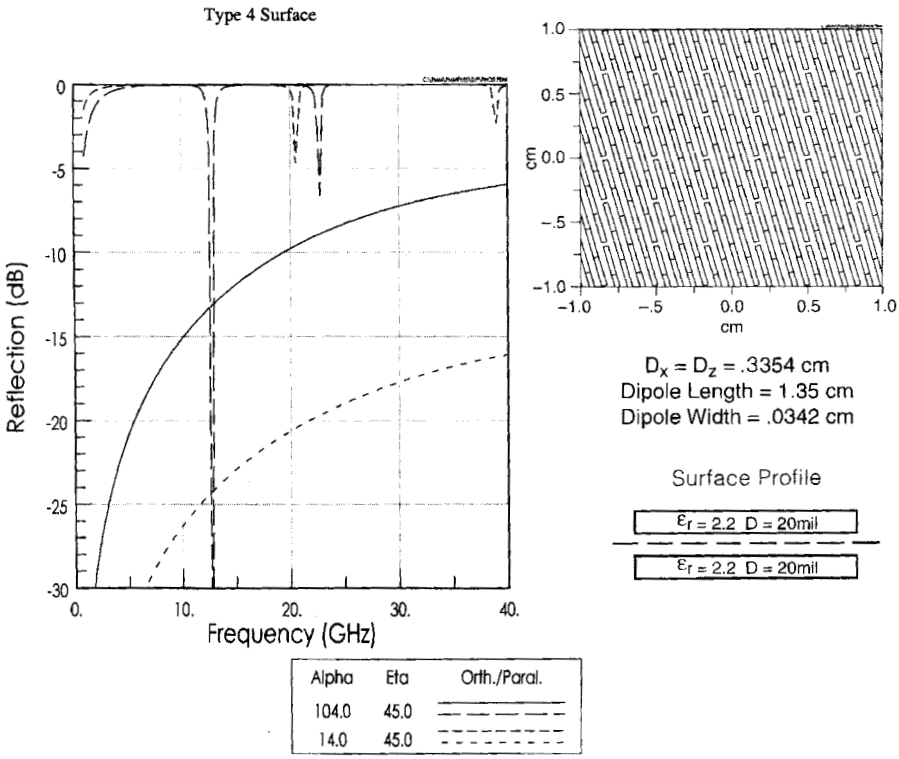

FIGURE 2.7. Same as Fig. 2.6 but shown over a broader band (0–40 GHz).

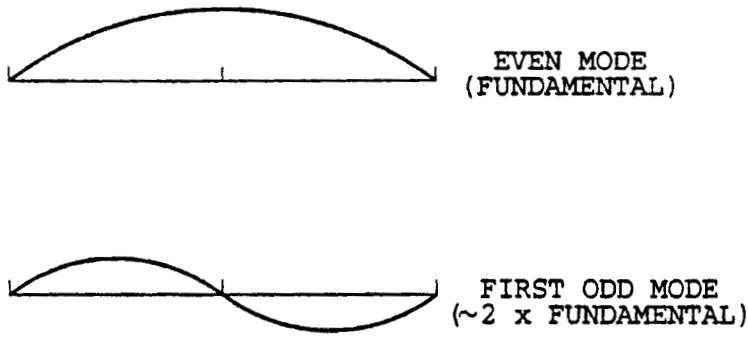

FIGURE 2.8. Any element can be excited at the fundamental frequency f_f for any incidence (top), while the first odd resonance at about $2f_f$ may be excited only for oblique angles of incidence (bottom). The odd resonance may occur at frequencies different from $2f_f$ depending on element shape. A modal interaction null will be located somewhere between f_f and $2f_f$ (for no grating lobes).

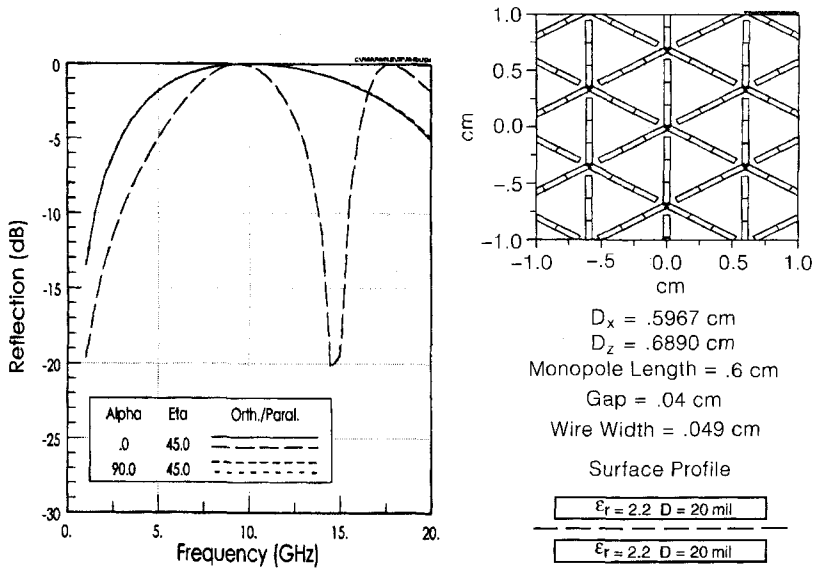

FIGURE 2.9. Reflection coefficient curves for a closely packed array of simple unloaded tripoles. Note the odd mode resonance at 17.5 GHz leading to the null at 14.5 GHz.

2.2.2 Unloaded Tripole Array

Although not particularly small in terms of wavelength, the unloaded tripole element has a very favorable feature: It can be packed tightly, thereby making the interelement spacings small and the bandwidth large. An example is shown in Figs. 2.9 and 2.10, where we have packed unloaded tripoles as closely as possible. The bandwidth is seen to be comparable to a gangbuster of type 2 (Fig. 2.3). It does, however, suffer from the same problem as the gangbuster element in general, namely excitation of the second harmonic for parallel polarization (although the modal interactive null now occurs around 15 GHz rather than 13 GHz; see Figs. 2.3–2.7). It does not produce hybrid radomes as superior with respect to constant bandwidth as do the three- and four-legged loaded elements; see Sections 2.3.1 and 2.3.2. In contrast to the gangbuster elements, it cannot be packed closer—unless more closely spaced layers of tripoles are used. This leads to so-called super-dense surfaces. They are discussed in detail in Schneider's dissertation [7]. These surfaces have the advantage of a much lower cross-polarization than the gangbuster type, but they are somewhat more complicated to manufacture due to registration requirements between the various layers.

2.2.3 Anchor Element

A simple modification of the unloaded tripole leading to increased bandwidth is to add an end capacity (as shown in Fig. 2.11). This type is usually called the *anchor*

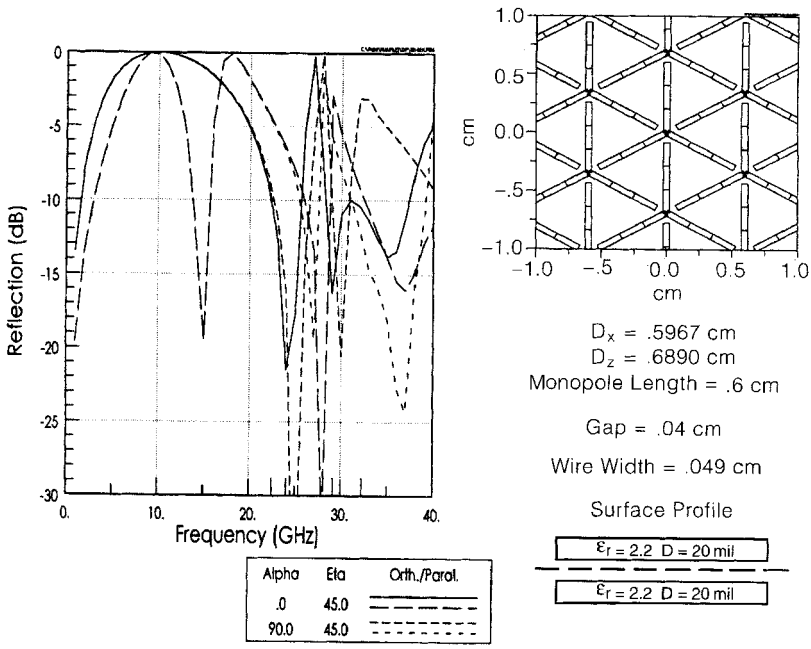

FIGURE 2.10. Same as in Fig. 2.9 but frequency range is 0 to 40 GHz.

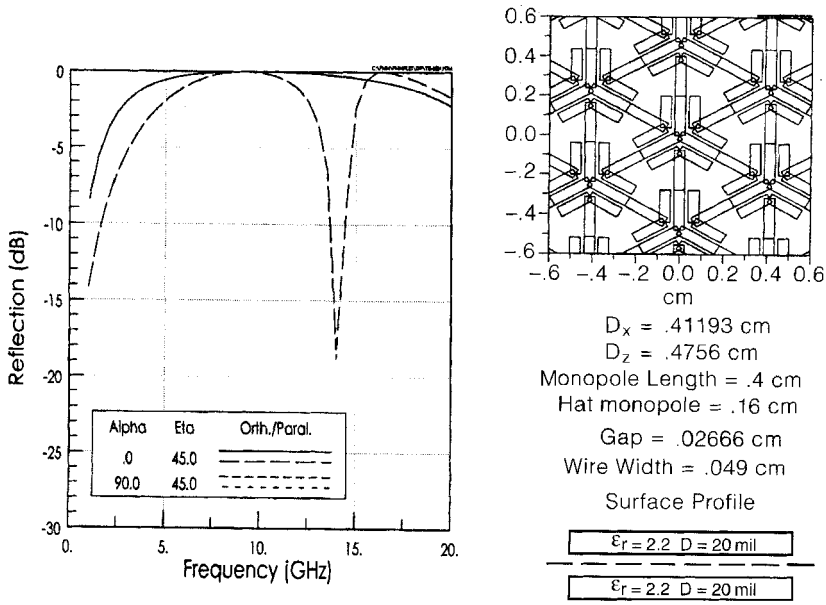

FIGURE 2.11. Reflection coefficient curves for a closely packed array of end-loaded tripoles, the so-called anchor elements. Note the broader bandwidth than for the simple tripoles in Figs. 2.9 and 2.10, but the null location has not changed significantly.

element. It naturally leads to smaller elements resulting in a significantly smaller inter-element spacing (D_x is seen to be reduced from about 0.60 cm in Figs. 2.9 and 2.10 to about 0.42 cm in Fig. 2.11). As seen, this not only results in a significantly larger bandwidth but also in a much delayed onset of *trapped* as well as *free space grating lobes*. The bad news is, however, that the modal interaction nulls still occur around 15 GHz (a slightly less dense packing of the elements can produce nulls slightly above 15 GHz but with smaller bandwidth).

2.2.4 Jerusalem Cross

One of the oldest elements used in FSS work is the Jerusalem cross, seen in Fig. 2.12. Basically it consists of a pair of crossed dipoles with end loading. We observe a null around 17 GHz (parallel polarization only) and another one around 24 GHz.

The first null is easily explained by inspection of the modal picture shown in Fig. 2.13. To the left we show the fundamental mode and note a large difference in potential across the end capacitance, namely, a significant downward pull of the fundamental frequency. In the middle we show the modal picture of the so-called

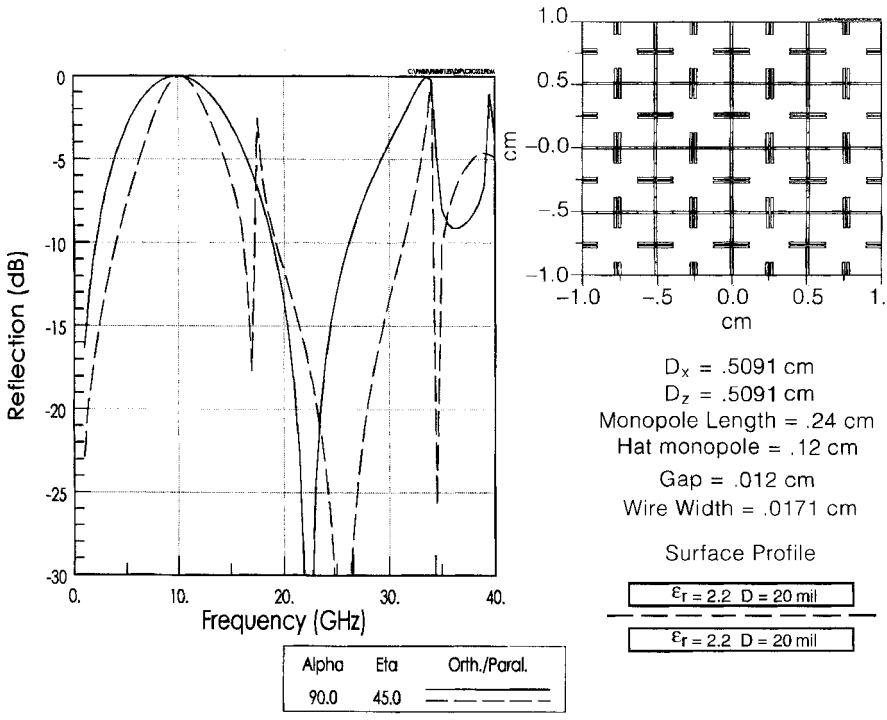

FIGURE 2.12. Reflection coefficient curves for an FSS of Jerusalem crosses. Angle of incidence equals 45°, orthogonal and parallel polarization. Note the null at about 17 GHz for parallel polarization.

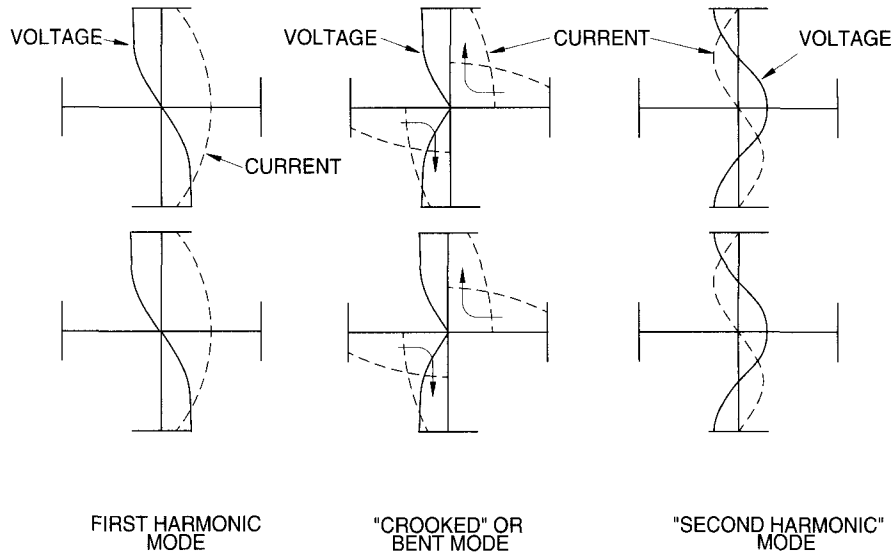

FIGURE 2.13. Current and voltage distribution on a Jerusalem cross at the first (fundamental) harmonic, the "bent mode," and the "second" harmonic.

crooked or bent mode. Note that in the top half of the vertical element the current is shown going upward being drawn from the horizontal part, while similarly it is going downward in the bottom half. This mode can only exist for oblique angle of incidence and parallel polarization. Although the total length of the bent mode is equal to that of the fundamental (or straight) mode, we note the lack of any difference in potential across the end capacitors. Thus only the fundamental mode is being pulled downward, not the bent mode. In fact, if the end capacitances are completely removed such that we are left with only a simple cross, the two resonances move very close to each other for parallel polarization (still with a null between them!) but not for orthogonal. *This is one good reason not to use a simple cross.* Of course, if the vertical and horizontal dipoles are printed on each side of a dielectric substrate, the bent mode simply cannot exist and the nulls associated with this mode simply disappear. However, registration requirements between the two sides make this approach somewhat cumbersome, and it is impossible to perform that "trick" when working with slots!

The behavior of the "second" harmonic mode, shown to the right in Fig. 2.13, is being complicated by the fact that a trapped grating lobe is "popping up" around 27 GHz. Simply put, this phenomenon is identical to forced surface waves and will at one frequency become a free surface wave as explained in Section 5.12. Although the latter typically is associated with reflection nulls, the null at 27 GHz is merely a modal interaction null between the bent and the second harmonic modes. At any rate, inspection of the modal picture clearly indicates that no difference in potential across the end capacitor is present for the second harmonic which explains why it

is resonating so high in frequency. Note further that a *free space grating lobe* is emerging at 36 GHz: All resonances higher than that frequency have loss associated with them.

2.2.5 Square Spiral Element

This element seems to have originated among a group of the author's former students now working at the Mission Research Corporation, Dayton, Ohio.

A typical response is seen in Fig. 2.14. It's bandwidth is significantly approaching that of the gangbuster element (Section 2.2.1). However, its "claim to fame" is that it can be made into both a reflecting and transparent FSS, a feature the gangbuster does not have (can only reflect by using two surfaces).

The modal interaction null is remarkably high, namely about 24 GHz. This feature combined with the fact that $D_x = D_z = 0.3454$ cm leads to the onset of trapped grating lobes slightly below 40 GHz which makes this element extremely interesting. It can be made somewhat broader by adding more turns to the spiral and using closer spacing to increase the end capacitance. In that respect it is reminiscent of the anchor

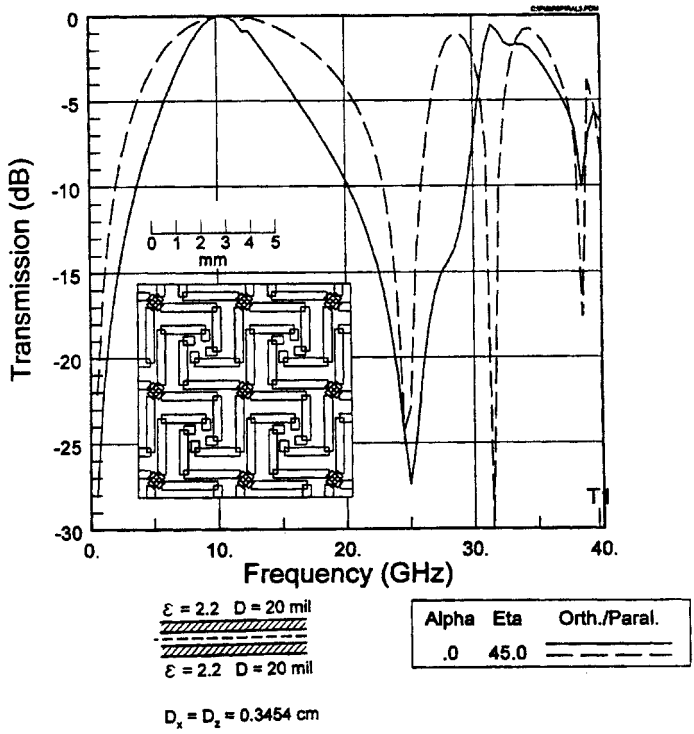

FIGURE 2.14. Typical frequency response for the square spiral. Note this is transmission rather than reflection. Angle of incidence equals 45°, orthogonal and parallel polarization.

element and the Jerusalem cross, which explains why the modal interaction null is so relatively high.

2.3 GROUP 2: LOOP TYPES

2.3.1 Four-legged Loaded Element

Development Examples of surfaces of four-legged loaded elements are shown in Figs. 2.15, 2.16, and 2.17 [8]. The development of this element is quite instructive. In Fig. 2.18 we show a simple $\lambda/2$ dipole with load impedance Z_L under receiving condition; that is, its equivalent circuit is a generator connected to its radiation impedance $Z_A = R_A + jX_A$ in series with the load impedance Z_L. Under resonant conditions $jX_A \sim 0$; that is, we obtain the strongest current for $Z_L = 0$. Making an element smaller is usually a good idea because it enables us to pack the elements closer together, resulting generally in better resonance stability with angle of incidence and possibly greater bandwidth. Thus in Fig. 2.18*b* we have shortened the total length of the dipole to about $\lambda/4$, thereby changing the radiation impedance to $R_a - jX_a$; it is now strongly capacitive. However, if we choose the load impedance to be inductive, $Z_L = +jX_a$, we again obtain maximum current and can actually

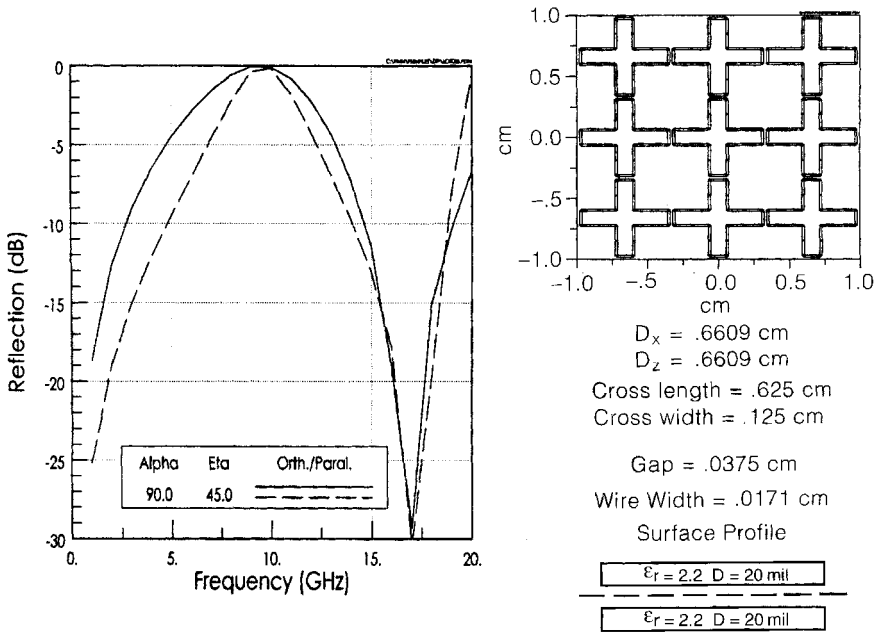

FIGURE 2.15. Reflection coefficient curves for an array of four-legged loaded elements. Angle of incidence equals 45°, orthogonal and parallel polarization (0–20 GHz). Note the load null at about 17 GHz for both polarizations.

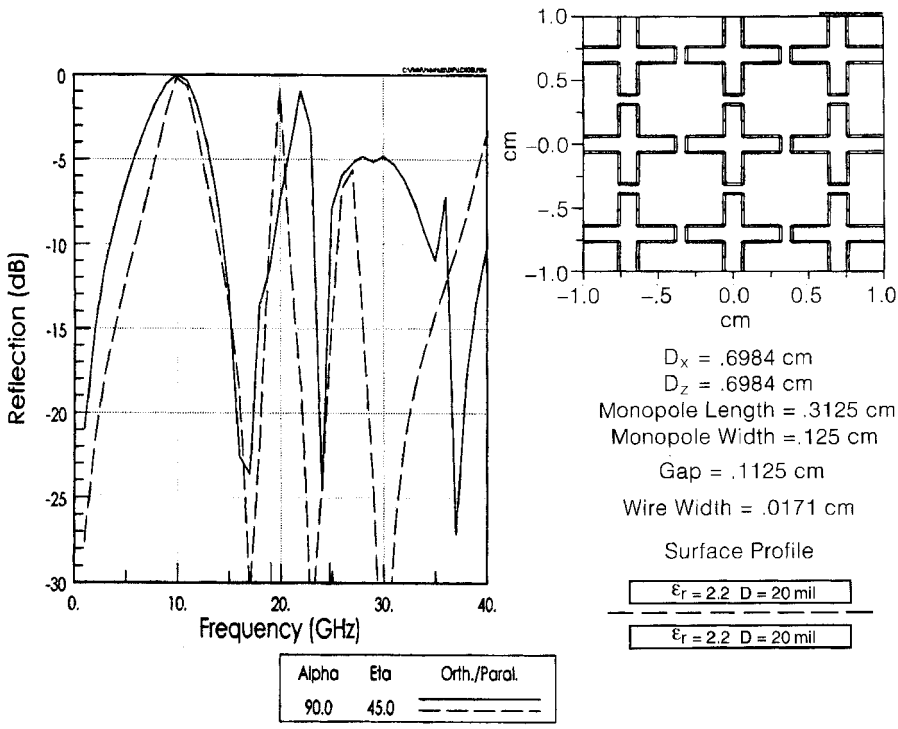

FIGURE 2.16. Essentially the same array as in Fig. 2.15 but for larger frequency range (0–40 GHz).

receive just about as much power as for case *a*. The practical execution of the load impedance Z_L is shown in Fig. 2.18*c*, top, namely in the form of a two wire transmission line of length $l \sim \lambda/8$ and characteristic impedance Z_0. In Fig. 2.18*d* we have placed two dipoles with loads next to each other, which primarily has the effect of cutting the effective load impedance in half. However, it is interesting to note that the tips of the two dipoles will have essentially the same potential; that is, without any change we can freely add a short between them as illustrated in Fig. 2.18*e*. The net result is that we now have obtained the four-legged loaded element equally capable of interacting with vertical as well as horizontal polarized fields (in fact arbitrary polarization).

Typical Reflection Curves The reflection curves for a surface of four-legged loaded elements arranged in a simple rectangular grid is shown in Fig. 2.15 from 0 to 20 GHz, and in Fig. 2.16 we show essentially the same array except with a slightly larger gap spacing between adjacent elements in the frequency range 0 to 40 GHz. This difference results in a slightly higher resonant frequency and slightly smaller bandwidth in the latter case as we would expect. Finally we show in Fig. 2.17 an interlaced example in the frequency range 0 to 40 GHz. One feature is common for

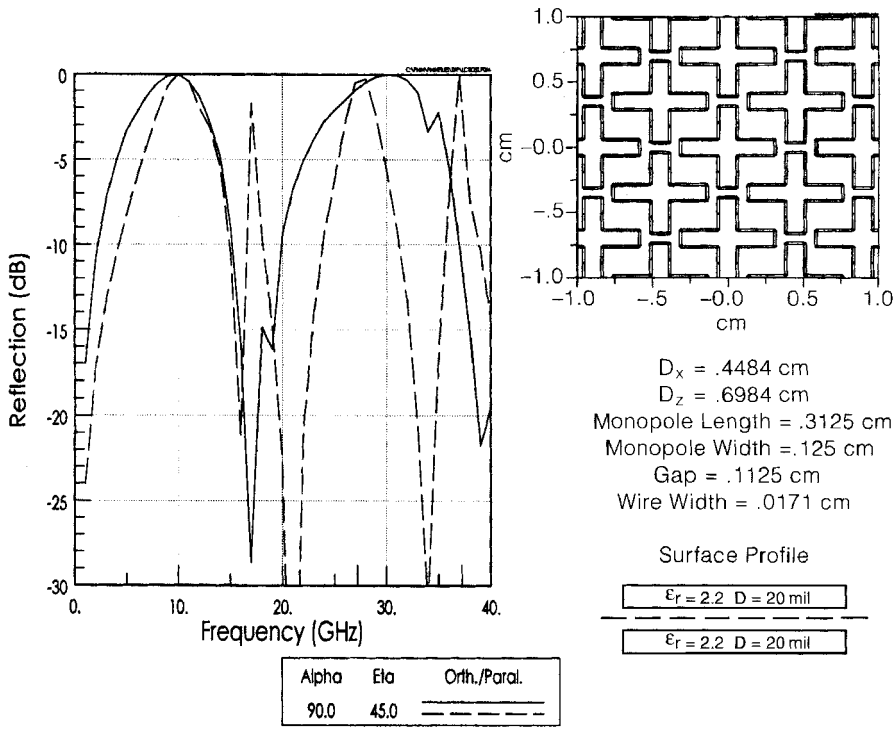

FIGURE 2.17. Reflection curves for an FSS of four-legged loaded elements arranged in an interlaced grid. Angle of incidence equals 45°, orthogonal and parallel polarization. The load null is still at around 17 GHz.

all these surfaces: They all have a null for both parallel and orthogonal polarization at around 17 GHz. This is easily explained by the fact that the lengths of the "loads" are about $\lambda/4$ long at that frequency; that is, the transmission line load impedance Z_L becomes infinite, effectively preventing any essential element current to flow, namely no interaction. These kind of nulls (called load nulls), for both polarizations are typical for elements with loads as opposed to for example the center-connected elements where the first null may be present only for parallel polarization (e.g., see Figs. 2.1–2.8).

However, note also that the 3 dB bandwidth of the reflection curves still differ significantly, being much narrower for the parallel than for the orthogonal case. This is ideal when designing hybrid radomes (a mixture of slotted FSSs and dielectric slabs, see Chapters 1 and 7). In fact the four-legged loaded element is one of the best-suited elements for designing band-pass radomes with moderate bandwidth.

Bandwidth Control Another feature of loaded elements in general is their ability to control bandwidth by modification of the load impedance $Z_L = j\frac{1}{2}Z_0 \tan \beta l$. For example, in Figs. 2.19 and 2.20 we show the reflection curves for another array of

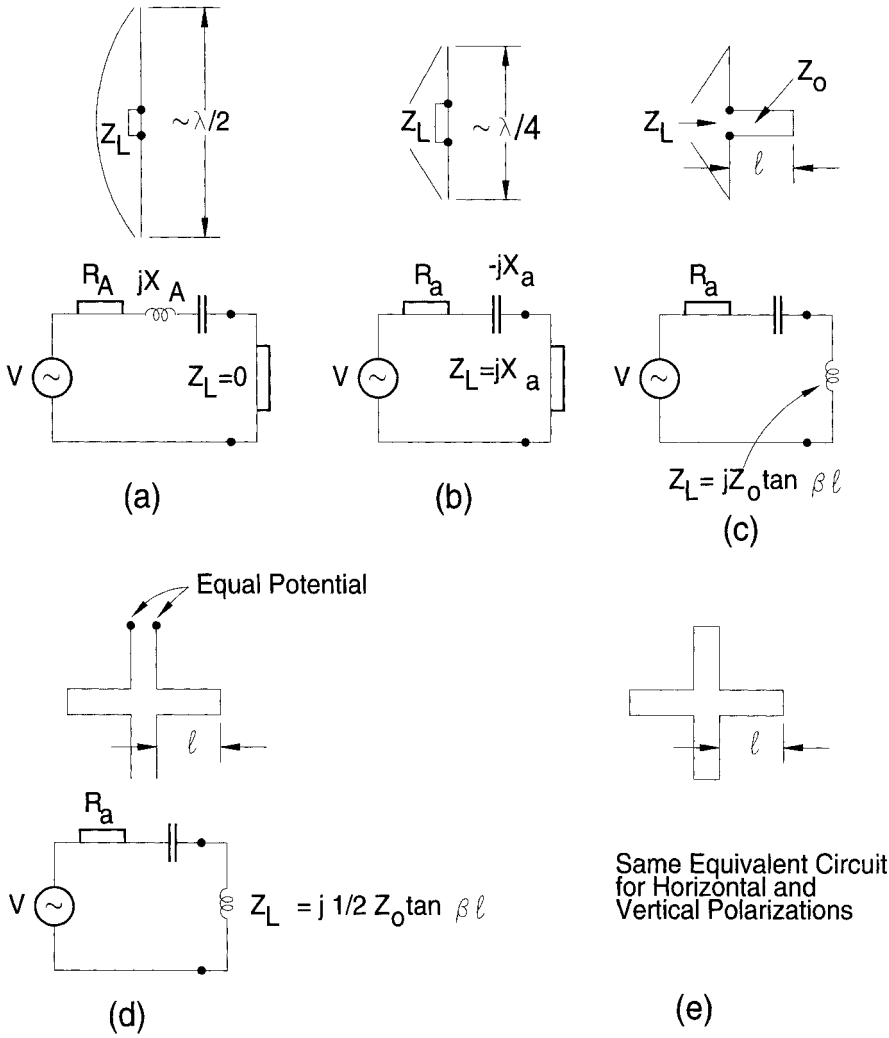

FIGURE 2.18. Development of the four-legged loaded element starting from a simple $\lambda/2$ dipole (*a*) that is shortened into a $\lambda/4$ dipole (*b*) that is loaded with an inductive impedance in the form of a two wire transmission line (*c*). Next, two elements are placed side by side to each other (*d*). Since the potential of the tips of the two dipoles are the same, they can readily by connected and the four-legged loaded element is complete (*e*).

four-legged loaded elements where the wire distance (cross width) is half of what it was in Figs. 2.15 and 2.16; that is, we make Z_0 lower. Note that the null is located at about the same frequency in all cases (about 16–17 GHz) as we would expect (the load impedances will again go to infinity when the leg lengths are about $\lambda/4$). However, note also that the 3 dB bandwidth has been reduced by about 30% to 40%

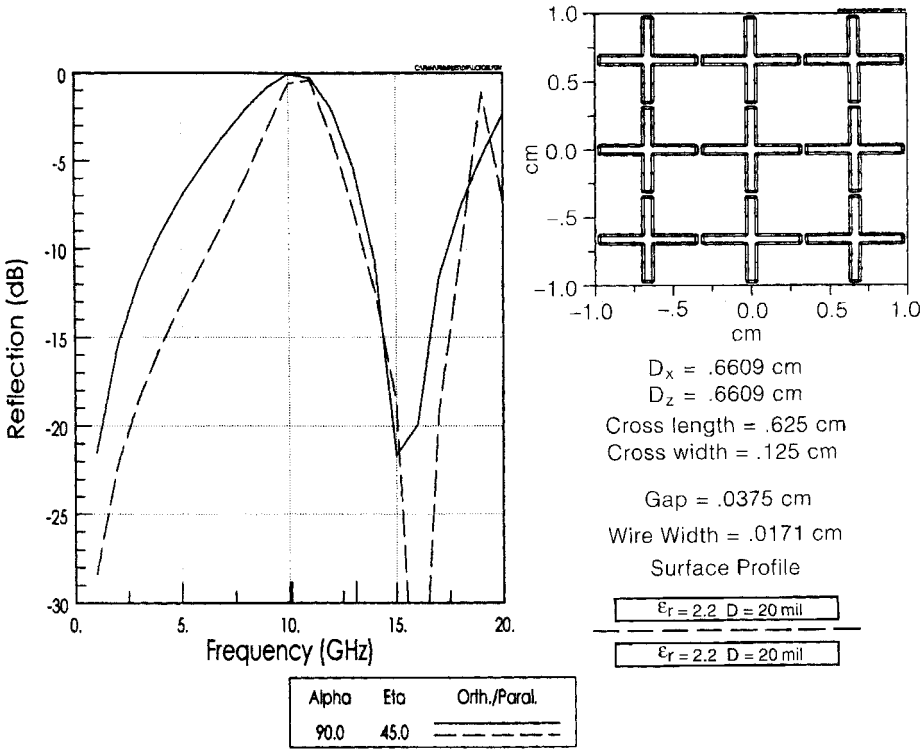

FIGURE 2.19. By cutting the distance of the transmission line spacings in half compared to Fig. 2.15, the bandwidth can be reduced by around 40%. (Note: D_x and D_z are unchanged.)

despite the fact that the inter-element spacings, D_x and D_z, are precisely the same in all cases. Thus the onset of *grating lobes* occurs at the same frequency in all three cases. This is a very convenient way to vary the bandwidth without worrying about onset of grating lobes.

Behavior above the First Null The general behavior of the reflection curves at frequencies above the first (load) null around 16 GHz is best understood by first studying the case for normal angles of incidence, as shown in Fig. 2.21. We observe a second resonance around 22.5 GHz. This is caused by the fact that the element impedance is now somewhat inductive while the load impedance $j\frac{1}{2}Z_0 \tan \beta_\epsilon l$ is somewhat capacitive; that is, a resonance will occur in this neighborhood. If we next consider the oblique case in Fig. 2.20, we note that the orthogonal case retains its second resonance just slightly lower at 21.5 GHz (which is expected since the inter-element spacings are rather large in terms of wavelength in this frequency range). The parallel case, however, shows a first odd resonance at around 19 GHz. This is simply caused by the lowest odd mode that can only be excited for oblique angle of incidence. More specifically, the direction of the current flow in the element is

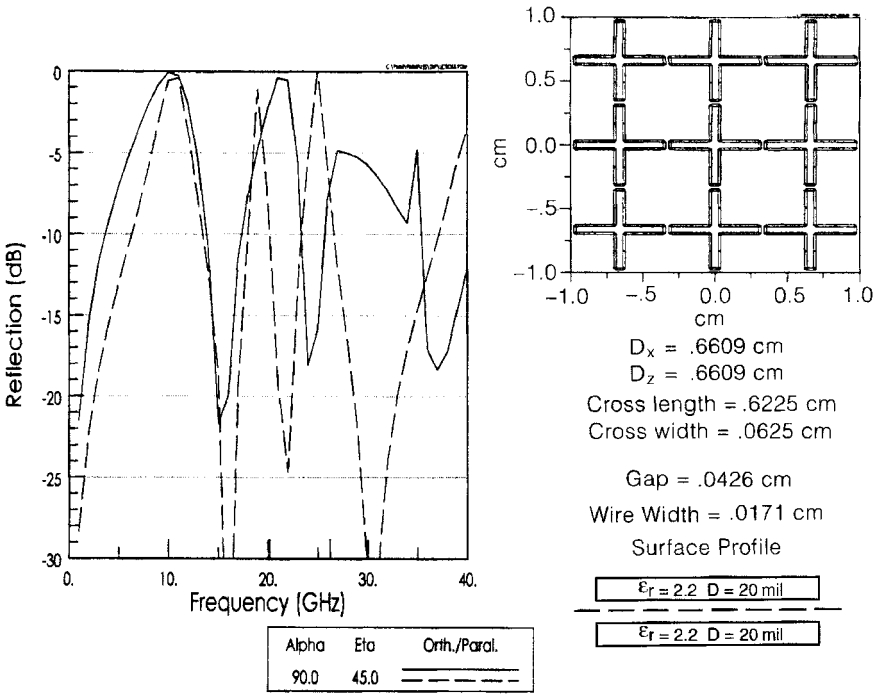

FIGURE 2.20. Same case as Fig. 2.19 but frequency range 0 to 40 GHz.

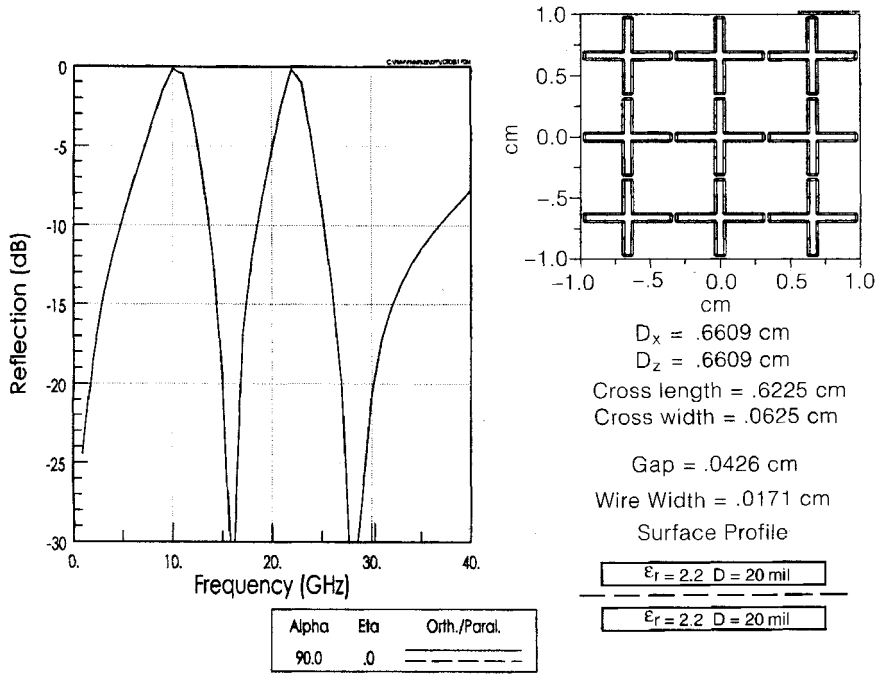

FIGURE 2.21. Same case as Fig. 2.19 but normal angle of incidence.

opposite on the top and bottom, which forces the currents on the loads to operate in the push-push rather than the push pull mode. In other words, the loads no longer act like loads and are ineffective in choking the element currents. The original second resonance is simply pushed upward by this odd mode resonance and becomes a third resonance at around 25 GHz. These two resonances are separated, as discussed earlier, by a deep null, since a *free space grating lobe* is not encountered before around 26.5 GHz. At frequencies above this threshold, all maximum values have reflective coefficients smaller than unity because additional power must be directed to the grating lobe directions.

2.3.2 Three-legged Loaded Element

Typical Reflection Curves A surface of three-legged loaded elements is shown in Figs. 2.22 to 2.24. It was developed as a direct consequence of the four-legged loaded element (Figs. 2.15–2.17), although it is not as easy to explain [9, 10]. However, the fact remains that both of these elements resonate when their circumferences are approximately one full wavelength, and they show a load null at the frequency where the legs are approximately $\lambda/4$ long (see the element discussion in Section 2.3.1 on development).

The bandwidth variation with polarization is suited quite well for use in a hybrid radome (better than the three-legged unloaded element). It is considerably more

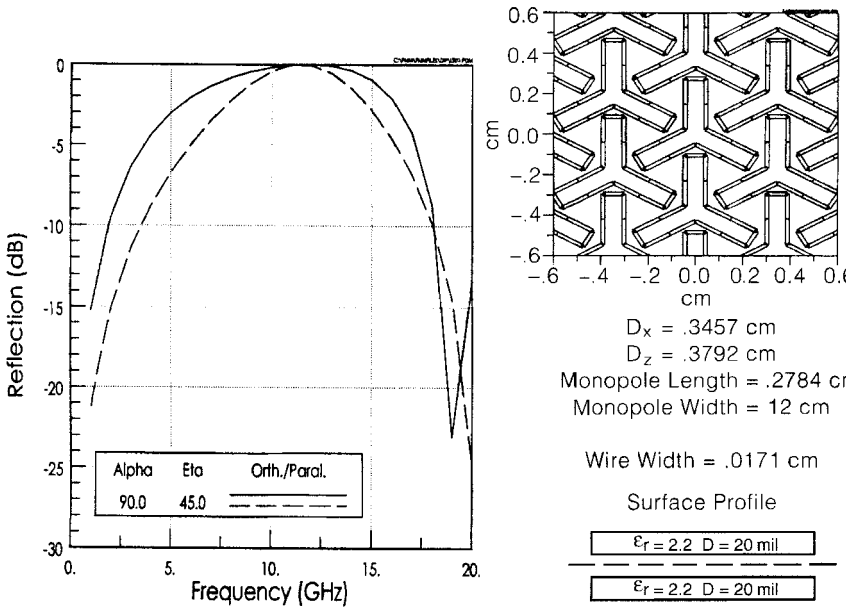

FIGURE 2.22. Reflection coefficient curve for closely packed FSS of three-legged loaded elements. Angle of incidence equals 45°, orthogonal and parallel polarization. Note the load null at about 19 GHz for both polarizations.

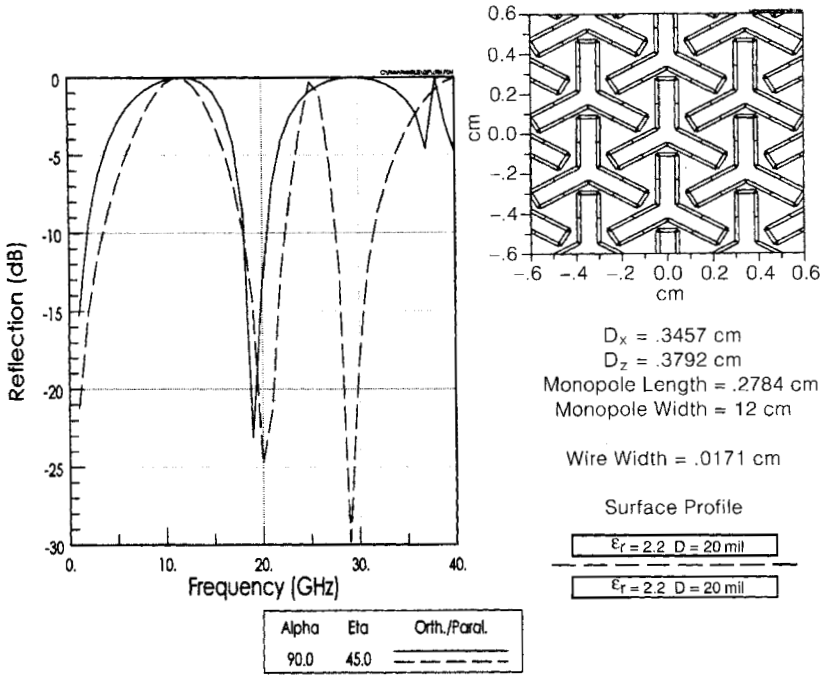

FIGURE 2.23. Same as in Fig. 2.22 but frequency range 0 to 40 GHz.

broadbanded than the four-legged cases in Figs. 2.15 to 2.17, the primary reason being that the inter-element spacings D_x, D_z are considerably smaller; in other words, an increase in D_x, D_z could reduce the bandwidth considerably. (See also the earlier discussion about bandwidth of the four-legged loaded element in Section 2.3.1 on bandwidth control.) We finally show in Fig. 2.23 the reflection curves of the same three-legged loaded element in the larger frequency range 0 to 40 GHz. Here the plane of incidence is along the vertical leg, $\alpha = 90°$ (see Fig. 2.1). It is worth mentioning that we have also run the reflection curves in the horizontal plane ($\alpha = 0°$). However, since these two curves are practically indistinguishable, we do not show the latter case.

Behavior above the First Null Like the four-legged loaded element, the behavior of the three-legged loaded element at higher frequencies is best understood if one considers the reflection curve for normal angle of incidence as shown in Fig. 2.24. We observe a second resonance around 30 GHz where the current distribution typically looks like the one shown in Fig. 2.25*b* while Fig. 2.25*a* shows the distribution at the first resonance (around 11 GHz). Both of these distributions are even; that is, they may be excited for all angles of incidence. However, the mode shown in Fig. 2.25c represents the lowest-order odd mode. It will only be excited for oblique

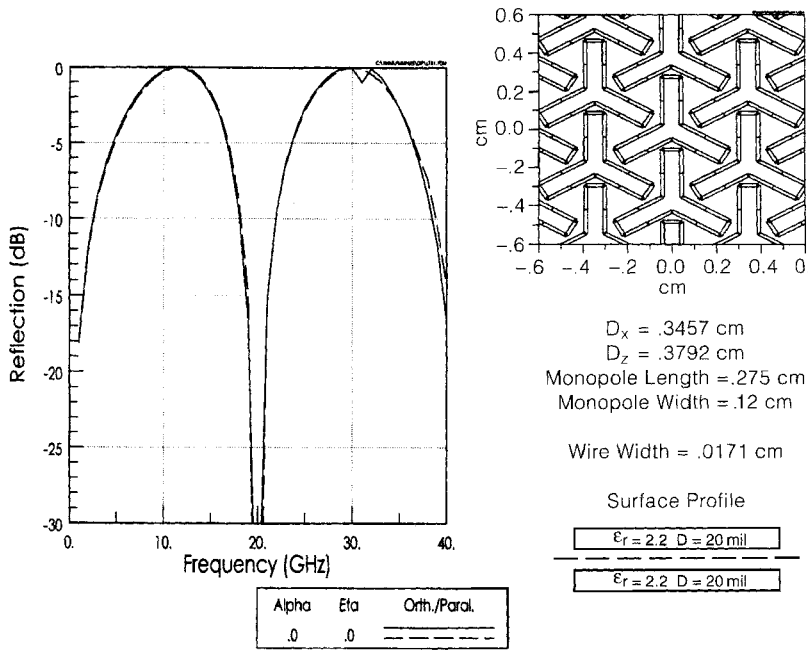

FIGURE 2.24. Same FSS as in Fig. 2.22 but normal angle of incidence and frequency range 0 to 40 GHz.

angles of incidence and parallel polarization. Inspection of Fig. 2.23 shows this to happen at 25 GHz, while the second even resonance is now being pushed up to 40 GHz (as usual with a null between). Finally note that grating lobes are not excited before around 40 GHz for 45° incidence angles. If this feature is important, the three-legged loaded element is hard to beat (a competitor would be a Gangbuster of higher order and an interlaced four-legged loaded element). See also the hexagon element discussion in Section 2.3.3.

Bandwidth Control It was shown earlier how the four-legged loaded element can change bandwidth simply by varying the transmission line spacings, for example, as demonstrated in Figs. 2.19 and 2.20. Similarly the three-legged loaded element has exactly the same feature. An example is shown in Fig. 2.26.

2.3.3 Hexagon Element

Typical Reflection Curves The physical appearance of the hexagon array is shown in Fig. 2.27 for close inter-element spacing and in Fig. 2.28 for wider spacing, where we also show the reflection curves at 45° angles of incidence for orthogonal and parallel polarization, respectively [11]. Note that the frequency range in both cases is 0 to 40 GHz, not just 0 to 20 GHz. This is done to fully show the superior behavior

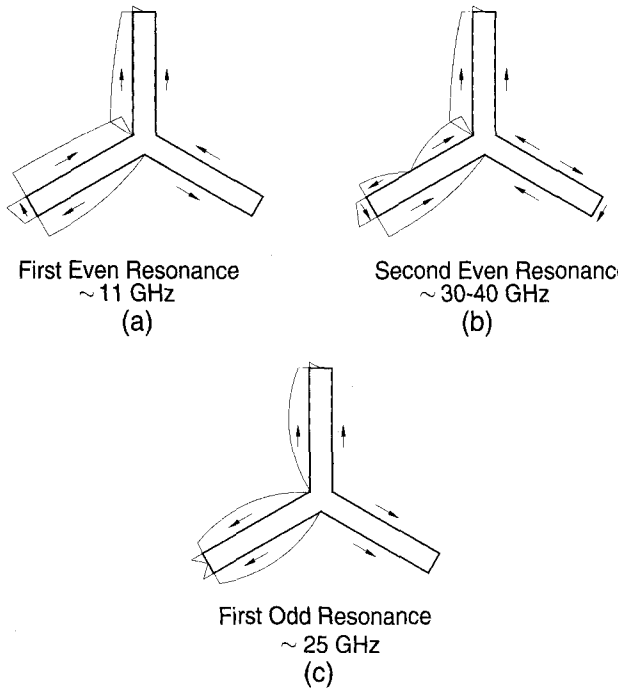

FIGURE 2.25. Current distribution on a three-legged loaded element at the (*a*) first even resonance at about 11 GHz; (*b*) second even resonance from about 30 to 40 GHz; (*c*) first odd resonance at about 25 GHz.

of the hexagon array, namely the location of the first modal interaction null at about 29 GHz; this is about twice as high as anything seen earlier with the exception of the square spiral element. Also the difference in inter-element spacing is seen to lead to a rather significant change of bandwidth and also a difference in element circumference: 1.5 cm compared to 1.98 cm.

An explanation for this somewhat unexpected behavior of the second resonance is given in Fig. 2.29. To the left we show the equivalent circuit of the hexagon element where we have associated inductance with the four side segments and capacitance with the top and bottom segments of adjacent elements. Note that for series resonance the entire array will at resonance act essentially like a short circuit, that is, like a ground plane. To the right in Fig. 2.29, we depict the current and voltage distribution along the wire at the fundamental resonance mode as well as at the second resonance (which as we saw above could occur at about three times the fundamental resonance). Note how the voltage distribution for the fundamental mode leads to a strong voltage difference across the "capacitor," that is, the fundamental frequency will be greatly pulled downward. However, inspection of the voltage distribution at the second harmonic shows no voltage difference across the capacitor, that is, no

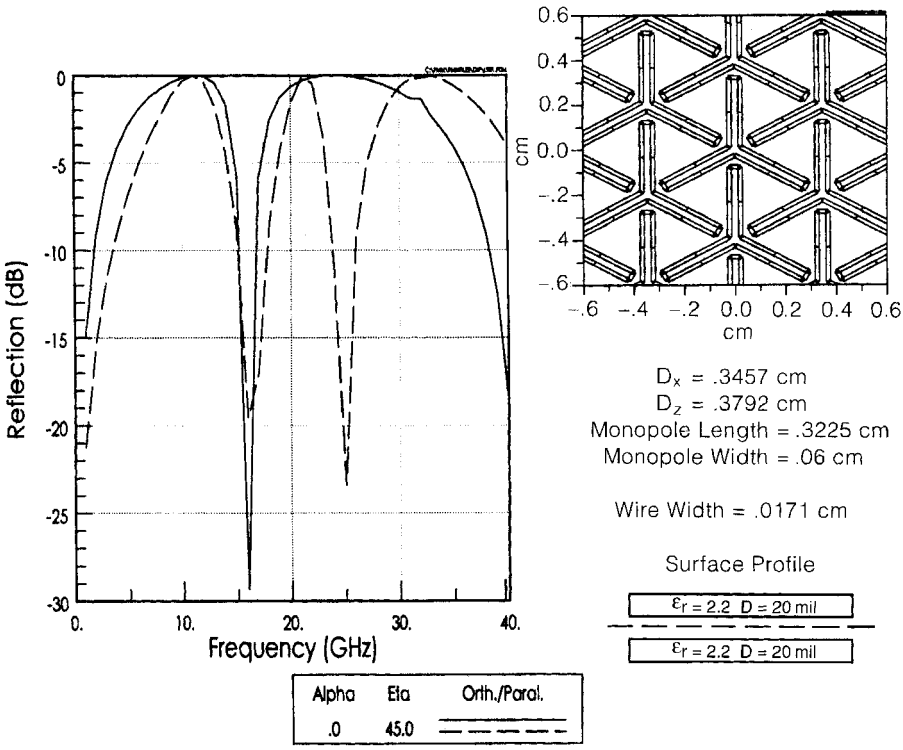

FIGURE 2.26. By reducing the transmission line spacing we obtain a significant reduction in bandwidth compared to Fig. 2.23. With the same D_x and D_z, we preserve the same onset frequency of the grating lobes.

downward pulling of that frequency. This explains how the second resonance of the hexagon element may be approximately three times the fundamental.

It should be noted that other loop elements act similar, but none are superior to the hexagon. For example, a circular loop [12] has the second resonance about twice the fundamental, unless the elements are almost touching each other. One may finally wonder: Why is it that the end capacity of the anchor element does not similarly produce a large difference in frequency pulling of the fundamental and the second harmonic (see Fig. 2.11) as we just saw for the hexagon element (see Figs. 2.27 and 2.28)? The answer to this question is obtained by inspection of the current and voltage modes for the anchor element as depicted in Fig. 2.30. Note that a significant voltage difference between the element tips and the center of the adjacent elements are present for *both* the first and second harmonics; that is, they are both pulled significantly downward.

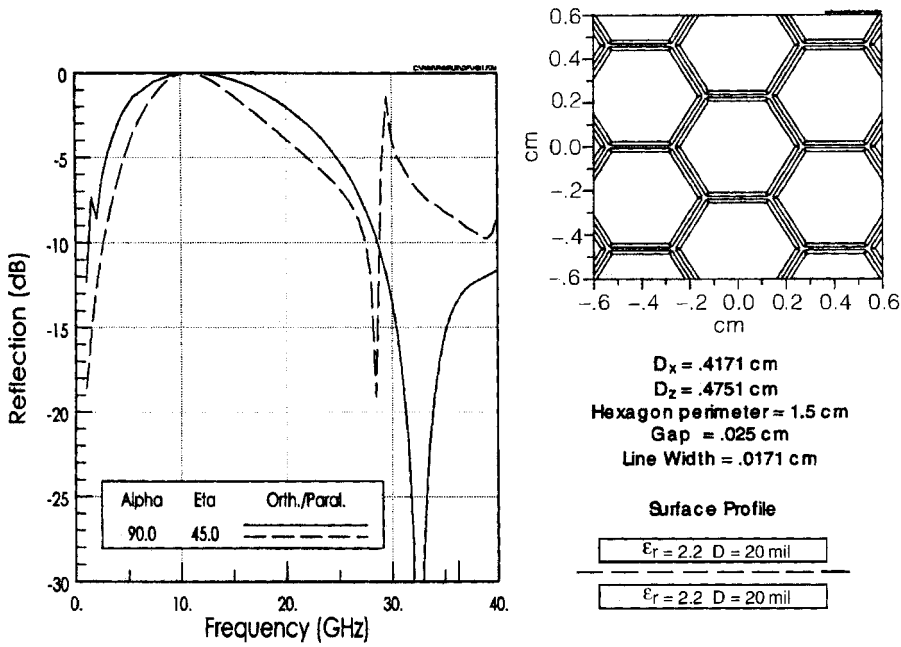

FIGURE 2.27. Reflection coefficient curves for an FSS of closely packed hexagon elements. Angle of incidence equals 45°, orthogonal and parallel polarization. Note that the location of first null is unusually high (around 28 GHz).

2.4 GROUP 3: SOLID INTERIOR TYPES

The third group of elements are comprised of plates of simple shapes such as squares, hexagons, circular disks, and the like, as shown in Fig. 2.31 (top) for the reflecting case and shown at the bottom of the same figure for the transparent case. These types can be characterized as being made with solid interior as opposed to the loop types discussed above such as the three- and four-legged loaded elements as well as the hexagon element.

These plate elements were actually among the first to be investigated, for example, by Kieburtz and Ishimaru [13] who considered a periodic surface of square apertures. Later contributions were made by Lee [14] and Chen [15]. Unfortunately, this class of surfaces leads to element dimensions close to $\lambda/2$; that is, the inter-element spacing must be somewhat large leading to angle of incidence sensitivity and early onset of grating lobes.

Although some relief can be obtained by arrangement in a triangular grid (see Problem 5.4) as well as by the use of dielectric loading (see Chapter 5), their performance is summed up well in Chen's own conclusions: "Shift of resonant frequency

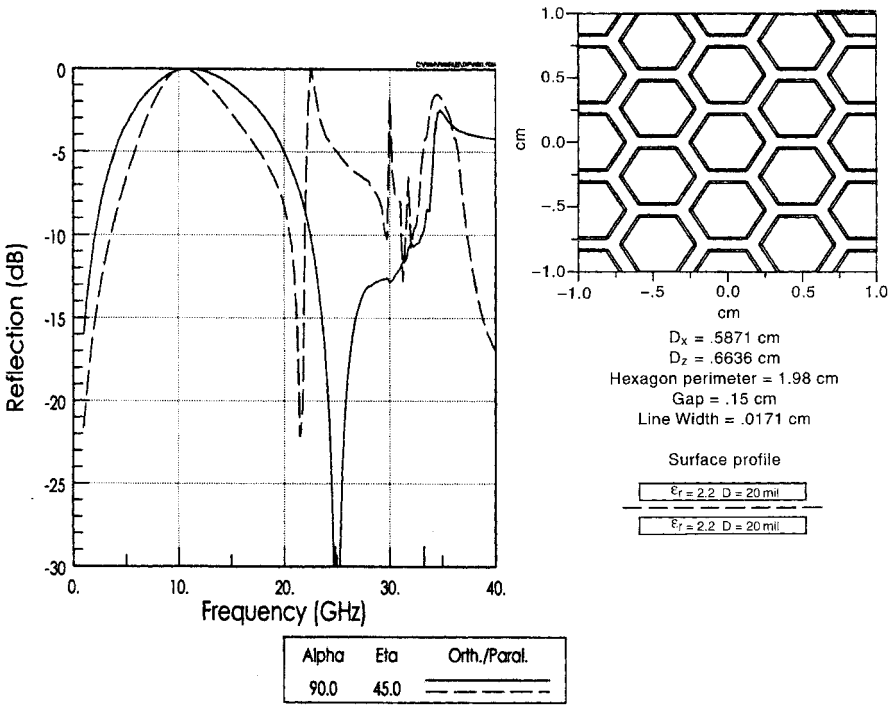

FIGURE 2.28. Reflection coefficient curves for an FSS of not so tightly packed hexagons resulting in narrower bandwidth as compared to Fig. 2.27.

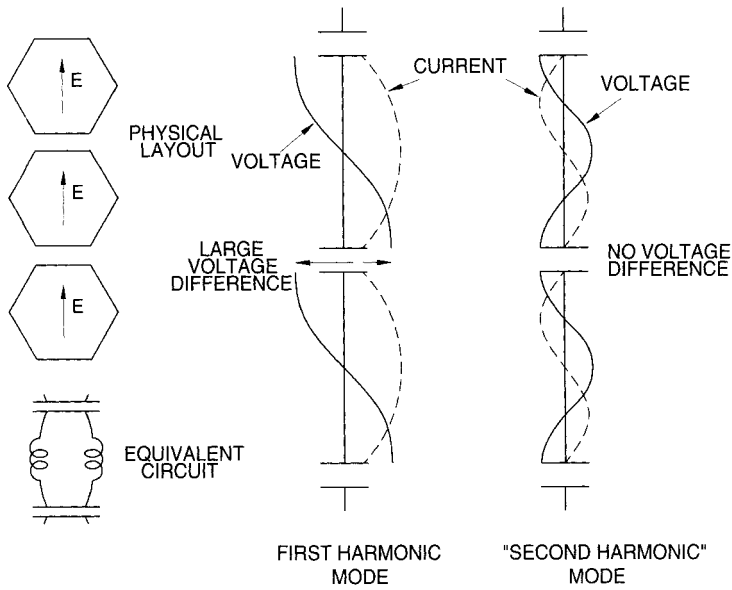

FIGURE 2.29. Voltage and current distribution along the circumference of a typical hexagon element. These explain why the second harmonic may be more than twice the first harmonic.

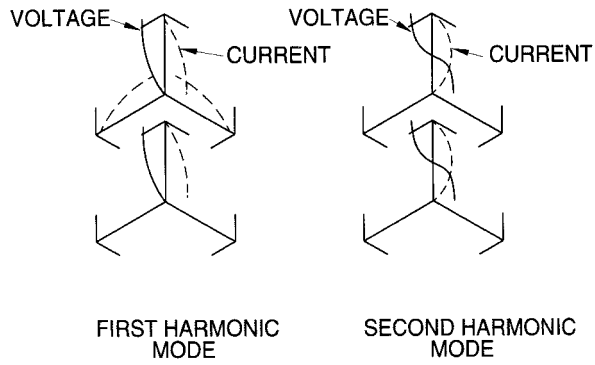

FIGURE 2.30. Voltage and current distribution along the legs of a typical anchor element.

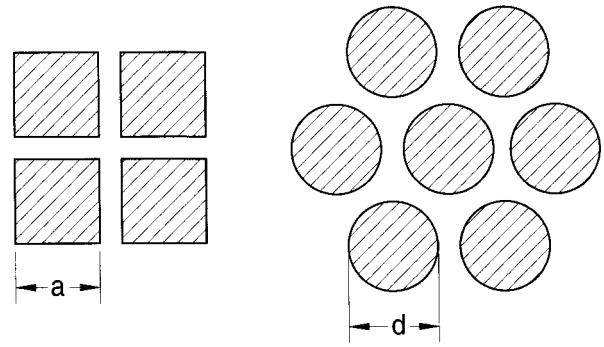

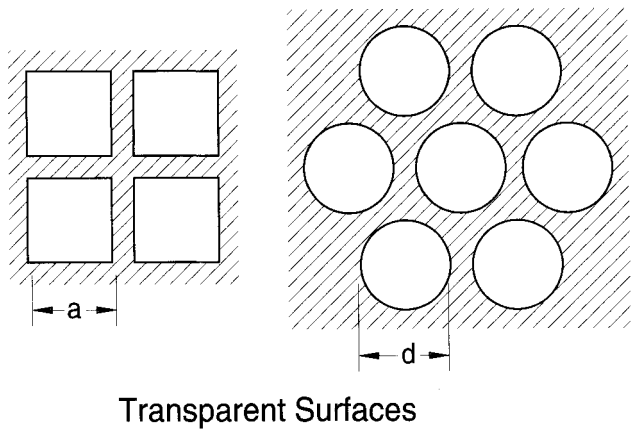

FIGURE 2.31. Examples of simple solid interior type elements, namely, elements without any form of loading. Sometimes called plate elements.

and changes of bandwidth in opposite sense for the perpendicular and the parallel polarizations as functions of incident angle limit many useful applications of this perforated plate" [15]. Since we agree with this conclusion, we see no need to present any results here but refer interested readers to the references cited above.

It is, however, interesting to speculate on the physical reasons for this shortcoming and thereby perhaps alleviate this problem. Figure 2.32 attempts to do just that. At the top left we show a periodic surface made of simple square apertures. For a vertical polarized signal this surface can be envisioned as composed of infinitely long rods leading to inductors across an equivalent transmission line as shown in Fig. 2.32 middle-left. The horizontal bars will act primarily like capacitors in parallel with the inductors. At resonance we would then obtain perfect transmission. The problem is, however, that due to the large separation of the horizontal bars the equivalent capacitance C is too small to produce a "real" resonance. In fact, when a resonance does occur it is typically only because the lowest-order evanescent mode becomes very strong shortly before it "jumps" out into real space as a grating lobe (for more on this subject, see Chapter 4). In other words, the simple equivalent circuit in Fig. 2.32 is really not valid in this case.

An increase of the capacitance is possible in a number of ways. Perhaps the simplest is to place a solid plate inside each aperture as shown in Fig. 2.32 top-right. Due to the smaller distances between the pertinent conductors, the capacitances are strongly increased and a strong resonance is now obtained at a lower frequency. Of course this should not surprise anyone, since we have merely loaded the original square with a solid square and thereby modified it into a member of the excellent loop family, namely a square loop! Placing complementary arrays next to each other is sometimes justified if the elements are very small and tolerance is a problem. In this way we simply substitute a potential thin slot with a small gap between the arrays. Also only one artwork is needed, positive and negative. If one aperture array and one solid interior are placed next to each other, a small mismatch loss will occur. However, if we place, for example, one aperture, one solid, and finally another aperture array in any symmetric fashion, no loss will occur.

A circular aperture may similarly be loaded simply by placing a smaller circular disk in the middle as shown in Fig. 2.33*a*. This simply results in the circular loop case as shown in Fig. 2.2, group 2, middle. Alternatively we may, as suggested by Orta et al. [16], replace the circular disk with a tripole as shown in Fig. 2.33*b*. Finally the circular aperture can be slightly modified into a tripole shaped aperture as shown in Fig. 2.33*c*, and we are now transformed into the loaded tripole shown in Fig. 2.2, group 2, second from left. One of the great advantages of the latter is its ability to be packed close in an array and thereby delay the onset of grating lobes (see Section 1.9). And, as all members of the loop family, it is small in terms of wavelength.

It should finally be mentioned that transparent designs of the plate group have been made with substantial screen thickness and where the apertures are filled with dielectric plugs. First of all, increasing the screen thickness leads to a higher resonant frequency (this is opposite of the reflecting case). While this is unfortunate since it effectively leads to higher inter-element spacings in terms of wavelength, it can be

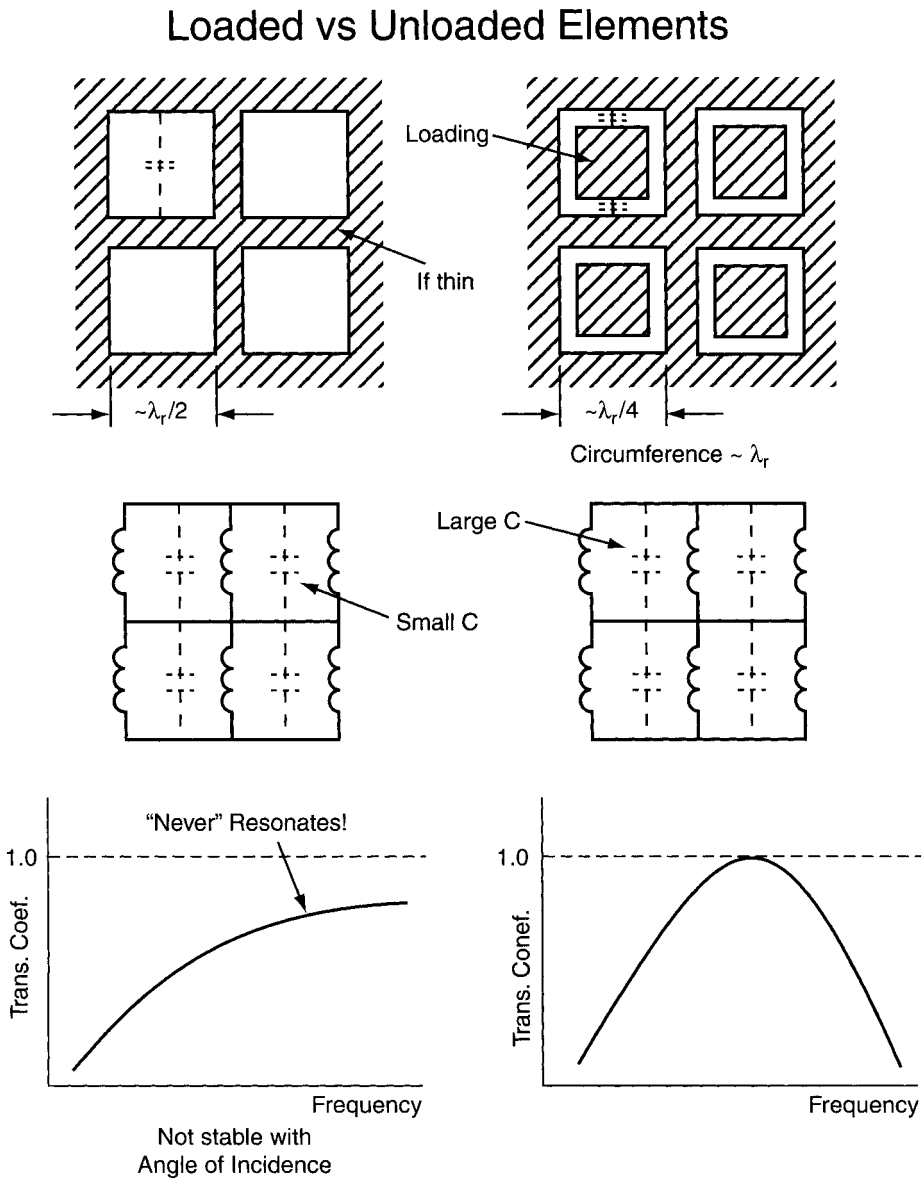

FIGURE 2.32. *Left-top:* Square aperture without any loading. *Middle:* Equivalent circuit. *Bottom:* Typical transmission curve. *Right-top:* Square aperture with loading. *Middle:* Equivalent circuit. *Bottom:* Typical transmission curve.

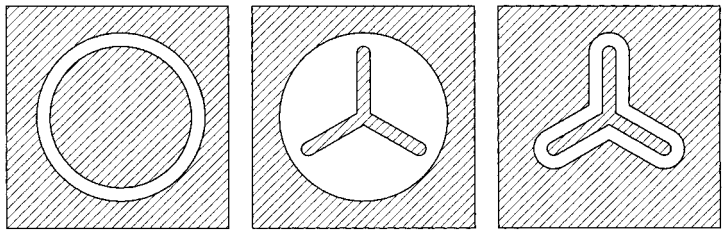

FIGURE 2.33. A circular aperture can be (*a*) loaded with a solid conducting disk, (*b*) loaded with a conducting tripole, Orta et al. [16], and (*c*) slightly reshaped into a loaded tripole.

greatly compensated for by using dielectric plugs with very high dielectric constants (about 30 or more).

While this approach may lead to designs that look acceptable from a theoretical point of view, they are in general not to be recommended. First of all they are very labor intensive to produce. Second, the most minute air gap between the screen and the dielectric plug has a significant effect upon the resonant frequency (see also Section 1.6.3 and Appendix E). Since the thermal expansion coefficient for most metals and dielectric materials usually are vastly different, air gaps will easily develop with disastrous results. This calamity is further augmented when the dielectric constant is particularly high. More specifically, any time a material with a high dielectric constant is placed next to a *periodic surface*, a significant change of resonant frequency will occur that is very tolerance-sensitive. (See also Section 7.6 for further discussion.)

2.5 GROUP 4: COMBINATION ELEMENTS

The list of elements above is not complete, only typical. Endless combinations and variations are possible and can easily be contemplated by anyone familiar with the state-of-the-art. An example is shown in Fig. 2.34 where a four-legged loaded element (see Fig. 2.16) has been provided with end-loading similar to a Jerusalem cross (see Fig. 2.12). Comparison of Figs. 2.16 and 2.34 shows that the first null is located almost at the same frequency in the two cases (about 16–17 GHz). The inter-element spacing is lower in the latter case; that is, the onset of grating lobes is higher in frequency. However, by interlacing the four-legged loaded elements as shown in Fig. 2.17, this problem can easily be alleviated if needed. Interlacing of the end-loaded elements in Fig. 2.34 does not seem practical.

When an FSS is produced by simple photo-etching, the shape of the elements is immaterial. However, if the surface is produced by an electroforming process, it may be a problem if parts of the elements are "isolated," for example, the interior loading of the loop type elements. To alleviate this problem, several loaded elements have been developed without a "floating" interior. Two examples are shown in Fig. 2.35.

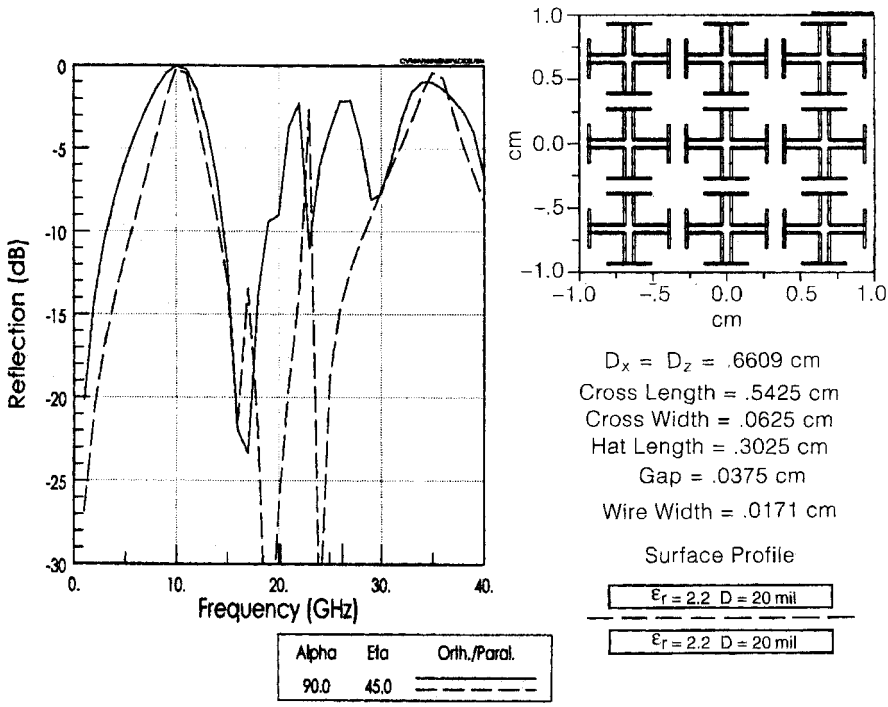

FIGURE 2.34. Reflection coefficient curves for an FSS made of elements being a mixture of the four-legged loaded element and the Jerusalem cross.

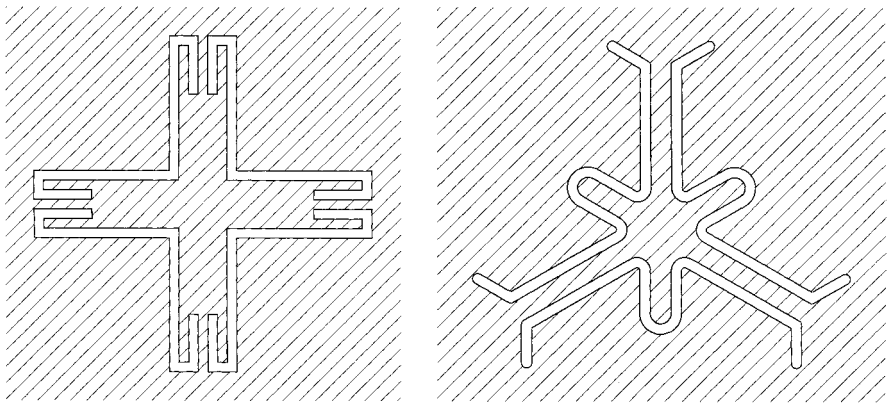

FIGURE 2.35. *Left:* Slot version of the MK element where the open-circuited transmission line load has been elongated by folding the ends inward. *Right:* Loaded tripole comprised of three 120° V-slots loaded capacitively at the center and inductively at the ends.

To the left is the so-called MK element (named after the inventor Mike Kastle, a former student). Instead of making the load legs equal to $\lambda/8$ and terminated in a short as in Fig. 2.19, they are effectively made longer by folding the ends inward and instead left open-circuited. Fig. 2.35 right, shows a three-legged nonfloating type invented by Pelton (U.S. Patent 4,126,866). It is seen to be made of three 120° V-slots loaded capacitively at the centers and inductively at the ends.

2.6 SOME COMMON MISCONCEPTIONS ABOUT ELEMENTS

2.6.1 Array versus Element Effect

The performance of an FSS is often attributed entirely to the elements. This is not quite so. The elements must also be arranged in the proper grid. A very important example is shown in Fig. 2.36 [7]. At the top left we show the co-polarized reflection curves for an array of tripoles arranged in a rectangular grid and just below the same tripoles arranged in a triangular grid.[1] Although the two cases at first glance look similar, a closer look reveals that the rectangular case at the top has up to almost 1 dB loss at resonance. And, if we consider the cross-polarized reflection shown to the right for the same two cases, the difference is spectacular, namely about 13 dB for the rectangular case and about 40 dB for the triangular case.

The conclusion of this discussion is that tripoles should always be arranged in a triangular grid. If for some reason it is desirable to use a grid of isosceles rather than equilateral triangles, and if the angle between two of the element legs is changed, it is still possible to keep the cross-polarization low. For details of this technique, see [17].

It should finally be mentioned that the cross-polarization for the triangular case always goes to zero when the plane of incidence falls along the element legs and not as in Fig. 2.36 between the legs.

Not only tripoles but other elements in general should be arrayed with some care. Consider, for example, a simple cross, that is, a simple four-legged unloaded element. It can be considered as a degenerate case of the Jerusalem cross (see Section 2.2.4) where the end loading bars have shrunk into nothing. As shown there, such an element has for oblique incidence and parallel polarization two resonances, one at the fundamental (10 GHz) and one at around 18 GHz with a null in between around 17 GHz. As the end bars shrink, the fundamental and the higher resonance move very close to each other. The bad part is that they still have a null between them. This fact makes designing simple arrays of unloaded fourpoles very tricky, and this author does not in general recommend them (that is why not one picture of a single unloaded fourpole is shown in this book!).

However, if we instead tilt the elements and move them closer together as shown in Fig. 2.37, we introduce an extra end capacity similarly to the endbars of a

[1] The elements in the rectangular case are not touching each other but are etched on each side of a very thin dielectric substrate.

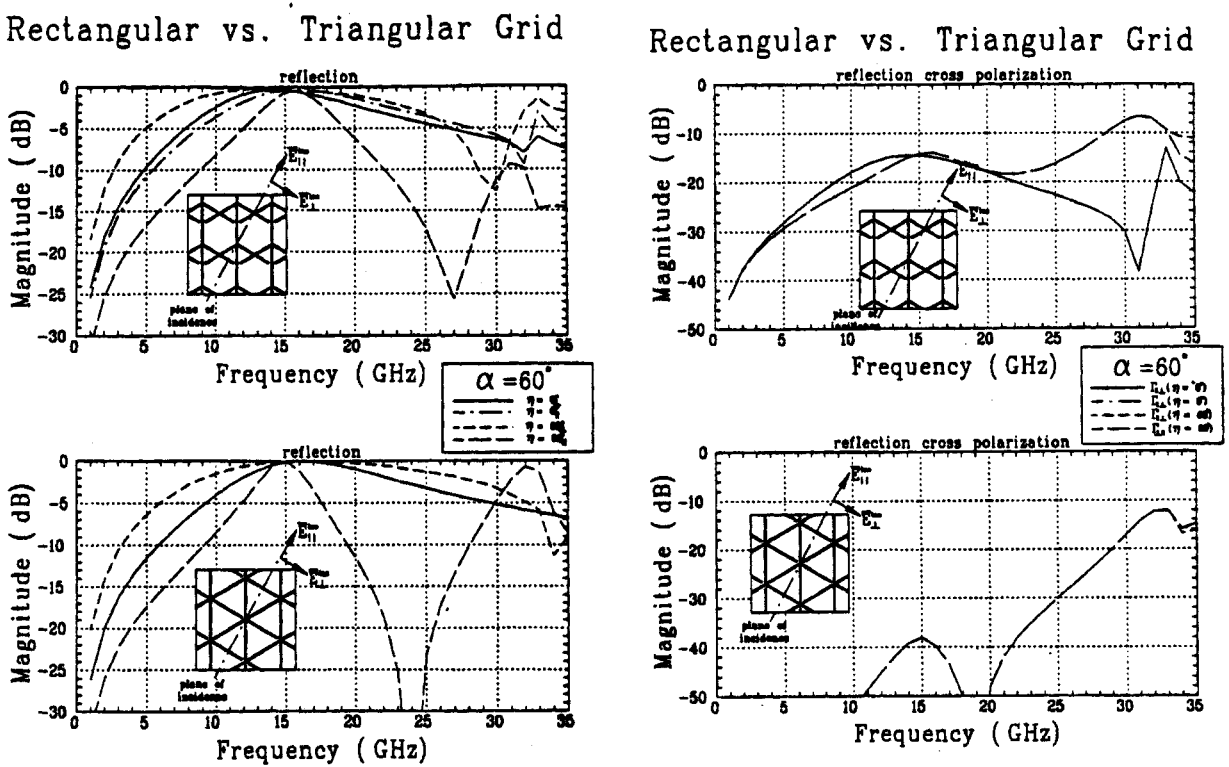

FIGURE 2.36. *Left:* Co-polarized reflection coefficient at various angles of incidence for a doubly infinite array of tripoles in a rectangular grid (*top*) and in an equilateral triangular grid (*bottom*). The tripoles in both cases are identical. *Right:* Cross-polarized reflection coefficient at various angles of incidence for a doubly infinite array of tripoles in a rectangular grid (*top*) and in an equilateral triangular grid (*bottom*). The tripoles in both cases are identical. (From Schneider [7].)

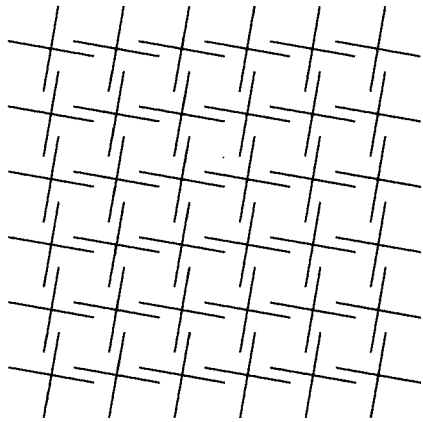

FIGURE 2.37. Simple unloaded crossed element, in general, with two resonances close to each other and a null between. Thus this configuration is not recommended in general. However, increasing the end capacity as shown above alleviates the problem.

Jerusalem cross. In other words, the two resonances move away from each other and the element is okay. It is conceptually similar to the square spiral in Section 2.2.5. For details, see Kornbau's Ph.D. dissertation [6].

2.6.2 Bandwidth versus Width of the Elements

Every antenna engineer knows that the bandwidth of a wire antenna in general increases with wire radius. And up to a point, the same is true for a dipole FSS. However, as the "fat is beautiful" doctrine is pursued, we eventually reach a point where we have reduced the element inductance to the extent that it is insufficient to create a resonance with the element capacitance. This is not a startling new revelation, since it is well documented that the impedance of "fat" dipole antennas usually stays in the capacitive region where they normally should cross the real axis when their length is around $\lambda/2$. However, this is not necessarily a disaster, since the impedance eventually can be "yanked" to the center of the Smith chart by a proper matching network. Although a similar arrangement is possible in the FSS case, it will in general not lead to a large bandwidth as originally desired. However, if a large bandwidth is desired, it will in general be advantageous to go to a loop element with a large opening (see the discussion in Sections 2.3 and 2.4).

It would be a fundamental mistake, for example, to assume that a square loop behaves like a square solid type (or fat dipole). When these elements resonate, it is simply because the onset of grating lobes pushes through resonance. Or, more precisely, they have a relatively narrow band and are very sensitive to the angle of incidence.

The PMM code was primarily developed for wires and slot elements. However, it can also be modified for "solid elements" (see Chapter 9 and Appendix F). However,

I prefer not to go into that, since there has been enough time spent on that subject already by people who know more about how to push buttons than about the physics of their problems. (See also Problem 2.3 concerning bandwidth of an array versus the bandwidth of the elements.)

2.7 COMPARISON OF ELEMENTS

Based on our investigation of some of the most common and typical elements, we are able to reach some interesting conclusions by comparison. The *grade* of an element will of course depend on the ultimate application of the FSS. However, certain features stand out as being desirable for most applications.

First, a quality element should have a stable resonant frequency with angle of incidence. Most elements presented in this chapter behave quite well in that respect, but it must be emphasized that the primary reason for this is simply that the inter-element spacings are kept small in terms of wavelength. Spacings larger than $\lambda/2$ will lead to early onset of grating lobes (see Section 1.9) which always will push the fundamental resonance downward with angle of incidence, no matter what type of element.

The logical conclusion of this observation is simply that a "good" element should be small in terms of wavelength (see grating lobe conditions, Section 1.9). Leading candidates with this feature are seen to be all the members of group 2, namely the loop types such as the three- and four-legged loaded elements, the simple circular and square loops and in particular, the hexagon element for broadband applications. Although all of these may look quite different at first glance, they are really all elements of the loop type resonating when their circumference is about a full wavelength or somewhat smaller (hexagon); that is, their size is typically less than about 0.3λ without dielectric. It is further observed that the "shaping" of these loops can give the designer a wide range of bandwidths from the narrow (the four- and three-legged loaded element) to the super wide (the hexagon). Although all FSSs can change bandwidth by variation of the inter-element spacings, the four-legged and three-legged elements are capable of considerable variation by changing the elements themselves. This is significant, since keeping D_x and D_z small delays the onset of grating lobes. (The three-legged loaded element is particularly outstanding in that respect.)

In contrast to the loop family stands the center-connected group as typically represented by the gangbuster, the three-legged unloaded elements, the anchor element, the Jerusalem cross, and the square spiral. Typical for most of these elements are the onset of the second resonance for oblique incidence and parallel polarization leading to nulls as low as only half an octave over the fundamental frequency. However, by packing the elements very close together, for example, as in the gangbuster designs, it is not only possible to experience extremely large bandwidths but to obtain modal interaction nulls so narrow that they are rather inconsequential for many applications. Furthermore it should be emphasized that the gangbuster surface will decrease the inter-element spacings, D_x and D_z, for increasing type number; that is, the onset of grating lobes is greatly delayed.

The square spiral element is extremely interesting because not only is it able to reflect but can also be transparent (the gangbuster can only reflect by using two orthogonal arrays). It has a very large bandwidth approaching that of the hexagon element. Further the inter-element spacings D_x and D_z are typically smaller than those of the hexagon element because the spirals are "locked" into each other. This leads to a higher onset frequency of the trapped grating lobe. It is definitely the best center-connected element for many applications. Note also that the bandwidth varies more with polarization than it does in the hexagon case. This may or may not be an advantage for some applications.

In contrast, not much can be done about the location nor the width of the modal interaction null for the three-legged unloaded as well as end loaded (anchor) element. However, it is possible to place several layers of FSS precisely positioned with respect to each other, leading to the so-called super-dense surfaces explored by Schneider [7]. This can lead to a significant increase in the 3 dB bandwidth but the modal interaction null is only moved slightly upward in frequency. The great advantage of the super-dense surfaces lies in their potential for extremely low cross-polarization.

The Jerusalem cross has its first modal interaction null about $1\frac{3}{4}$ octave above the fundamental mode and not much can be done about it. Decreasing the end-loading moves the null downward while increasing the length of the end loading moves the null upward; however, the end bars themselves will eventually start to scatter. Thus, despite the fact that the Jerusalem cross is a small element, it is used mostly for narrowband applications.

The solid interior or plate type element is seldom used alone but mostly in conjunction with a "complementary" FSS adjacent to it, see Fig. 2.32. Finally the list of combination elements is endless and is growing longer every day.

The author's favorite?	The loop family!
And the least favored?	The plate family!

Finally those who merely wish to estimate the resonant frequency of a periodic surface are referred to Appendix E, where a summary is presented of what primarily determines the resonant frequency and what determines the bandwidth. In particular, the change of the resonant frequency as caused by a dielectric substrate is given in the form of curves as a function of slab thickness. Also the effect of a small air gap between the elements and the dielectric substrate is discussed. However, it should be emphasized that a more exact description of a periodic surface is only possible by use of a well-tested program like, for example, the PMM code.

2.8 PROBLEMS

2.1 The Straight Wire Element: Effect of Substrate An FSS of straight wires in air as shown above in Fig. P2.1 is exposed to an incident plane wave. Sketch

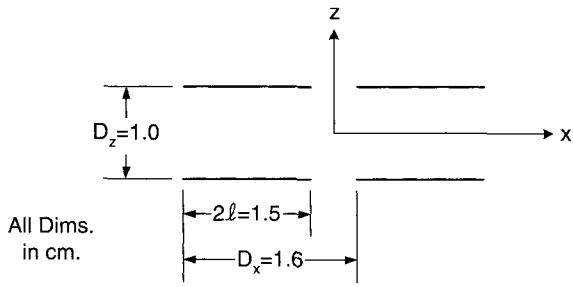

Fig. P2.1

the current distribution along the elements for the cases $\bar{E}^i = \hat{x}E^i$ and $E^i = \hat{z}E^i$. Estimate the resonant frequency for both cases.

If we add a substrate to one side only with $\epsilon_r = 2.4$ and thickness 1 mm, estimate the change in resonant frequency. *Hint:* See Appendix E.

2.2 The Chevron Element A passive dipole array of so-called Chevron elements in air as shown above in Fig. P2.2 is exposed to an incident plane wave at normal angle of incidence. Sketch the current distribution for the cases $\bar{E}^i = \hat{x}E^i$ and $\bar{E}^i = \hat{z}E^i$.

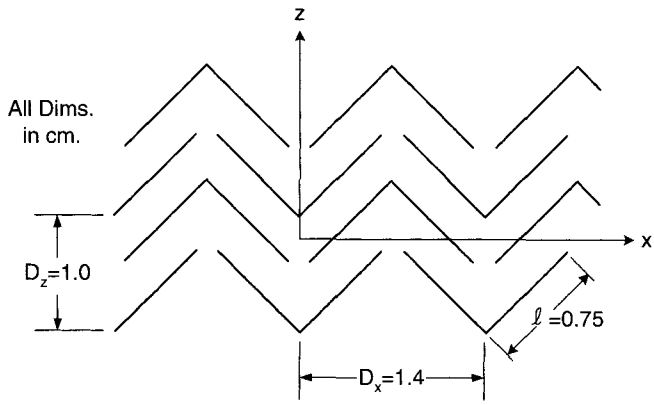

Fig. P2.2

Estimate the resonant frequencies for the two polarizations. (This example goes to show that while it is true that all periodic surfaces make at least fair-looking wallpaper designs, not all wallpaper designs make good FSSs.)

2.3 Bandwidth of Elements versus an Array: Another Common Misconception It has often been suggested that designing a broadband array starts with developing a broadband element. And one of the most broadbanded elements is the flat spiral shown above in Fig. P2.3. The circumference of a single spiral

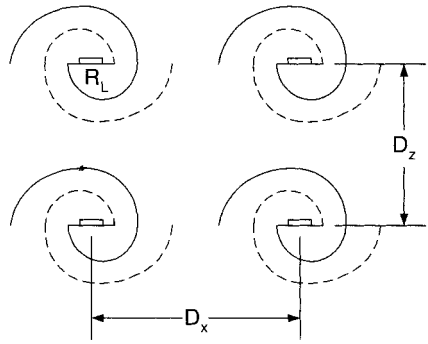

Fig. P2.3

is approximately 1λ at the lowest frequency (disregarding the dielectric substrate). Assume further that the inter-element spacings D_x and D_z are both 10% larger than the element diameter.

If the lowest frequency is 1 GHz, what is the onset frequency of the first grating lobe(s) when

a. The incident wave is normal to the array?

b. The incident wave has an angle of incidence equal to 60° in one of the principal planes?

Most active arrays have a ground plane such that we have only one mainbeam. If the spacing between the array and the ground plane is $\lambda/4$ at the center frequency f_0, the effect of the ground plane will be to add an inductive shunt reactance for $f < f_0$, and a capacitive shunt reactance for $f > f_0$ (for more about this, see Chapter 9 on absorbers).

If the antenna impedance without a ground plane happened to behave in an opposite manner as a function of frequency, it is quite feasible that the effect of the ground plane will be to make the combined array impedance more broadbanded. However, the typical impedance for a spiral will go around the Smith chart many times as a function of frequency, that is, alternate between the capacitive and inductive half-planes and not track the ground plane reactance very well.

Conclusion: Even if the presence of grating lobes is treated in a high-handed way (!), the bandwidth of an array of spirals will somewhat lack the performance of the single element. However, arrays of dipoles can be made extremely broadbanded! The trick is to pack them close together, thereby reducing the stored EM energy. See also Chapter 9.

3

EVALUATING PERIODIC STRUCTURES: AN OVERVIEW

3.1 INTRODUCTION

There are basically two ways to determine the scattering and impedance properties of periodic structures:

1. The *mutual impedance approach*, also sometimes called the *element to element approach* and is closely associated with the method of moments.
2. The *plane wave expansion* or the *spectral approach.*

Both methods have advantages and disadvantages. For this reason it is highly recommended that the reader becomes familiar with both approaches. In fact the approach taken in this book is really a mixture of both of these approaches.

Consider the *finite* array shown in Fig. 3.1. Since a periodic structure by definition must be infinite in extent, this array is strictly speaking not a periodic structure; however, it may be a realistic approximation of a periodic structure provided that all inter-element spacings are the same, D_x as well as D_z. Let us for a moment assume that this array is actively fed by voltage generators $V_1 \cdots V_9$ as shown in the figure.

The definition of the element mutual impedance between two single elements is illustrated in Fig. 3.2. Here the current $I_2(z)$ in antenna 2 will produce a field at antenna 1 which in turn results in an impressed voltage defined as $-Z_{1,2}I_2$, where $Z_{1,2}$ is called the *element mutual impedance* between antennas 2 and 1. If antenna 1 also has a generator impressing the voltage V_1 at its terminals, then the total impressed voltage will be $V_1 - Z_{1,2}I_2$. According to Ohm's law, this total impressed voltage must be equal to the self-impedance $Z_{1,1}$ plus the load impedance Z_{L1}, multiplied

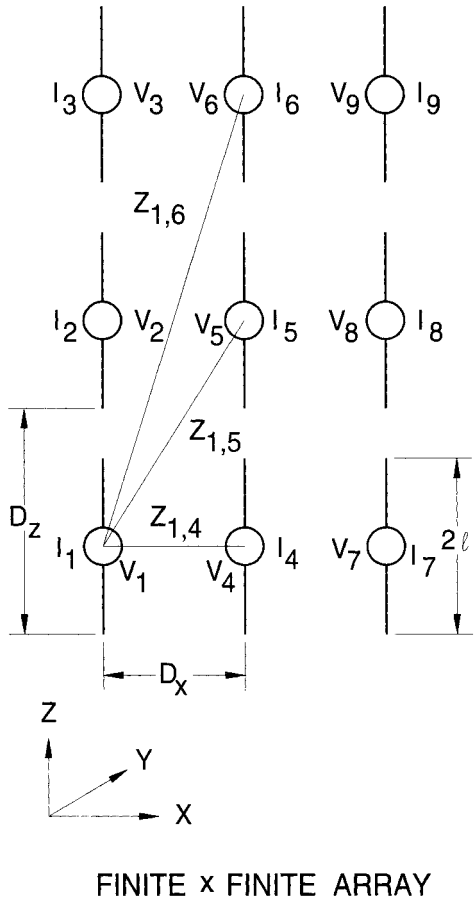

FIGURE 3.1. A *finite* × *finite* array is a realistic approximation of a truly periodic structure as long as all inter-element spacings (D_x as well as D_z) and element length $2l$ are the same.

by the current I_1,

$$V_1 - Z_{1,2}I_2 = (Z_{1,1} + Z_{L1})I_1, \tag{3.1}$$

or, writing (3.1) in the more conventional form,

$$V_1 = (Z_{1,1} + Z_{L1})I_1 + Z_{1,2}I_2. \tag{3.2}$$

For the multi-element case in Fig. 3.1, we then similarly obtain the following equations:

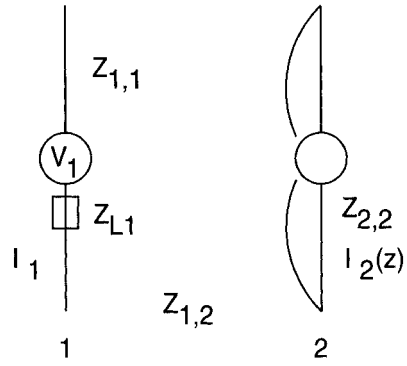

FIGURE 3.2. Element mutual impedance $Z_{1,2}$ between two single elements simply defined as $Z_{1,2} = -V_{1,2}/I_2(0)$, where $V_{1,2}$ is the voltage induced in element 1 due to a terminal current $I_2(0)$ in antenna 2.

$$
\begin{aligned}
V_1 &= (Z_{1,1} + Z_{L1})I_1 + Z_{1,2}I_2 + Z_{1,3}I_3 + \cdots + Z_{1,9}I_9 \\
V_2 &= Z_{2,1}I_1 + (Z_{2,2} + Z_{L2})I_2 + Z_{2,3}I_3 + \cdots + Z_{2,9}I_9 \\
&\vdots \\
V_9 &= Z_{9,1}I_1 + Z_{9,2}I_2 + Z_{9,3}I_3 + \cdots + (Z_{9,9} + Z_{L9})I_9.
\end{aligned}
\tag{3.3}
$$

Note that the mutual impedance terms in (3.3) may not be quite the same as for the two-element case shown in Fig. 3.2. The reason is that the *shape* of the current distribution $I(z)$ may change because of the presence of the other elements, in particular, if we scan the beam by changing the relative phases of the voltage generators $V_1 \cdots V_9$ and if the lengths, $2l$, of the elements are somewhat large in terms of the wavelength. This fact does not change the mutual impedance concept per se. It is sufficient here to state that all these concerns will be taken care of automatically when we later break the elements up in appropriate short sections as is always the case in the method of moments. Also, while the *shape* of the current distributions may change with scan or angle of incidence, it is always a good bet that the *amplitude* will change merely by being placed in the array environment (more about these subjects later).

While (3.3) is simple, there are practical problems. First of all, the element mutual impedance terms $Z_{k,m}$ for the individual elements are relatively time-consuming to evaluate whether they are determined by King's general formulation for linear antennas [18] or obtained by numerical integration. Furthermore the number of elements in a typical array can easily run up to several thousand. In addition we may have several arrays cascaded after each other (see Fig. 1.12). Finally, as indicated above, we will in general have to split the elements into sections corresponding to even more arrays. In other words, the size of the matrix of (3.3) will soon grow to be uncomfortably large as the array gets larger. In view of this, it will therefore sound ridiculous

to make the array as big as possible, namely infinite. However, this is precisely what we are going to do in two steps.

3.2 SINGLE INFINITE CASE

First we are going to extend the array in the vertical direction (i.e., along the z-axis) to $\pm\infty$ as shown in Fig. 3.3. We will also denote each infinite column by a number q going from 1 to Q. We will require the inter-element spacings in the z-direction to be the same (D_z) for all the columns; however, the spacings in the horizontal plane along the x-axis need not be uniform. In fact we do not even require the array to be

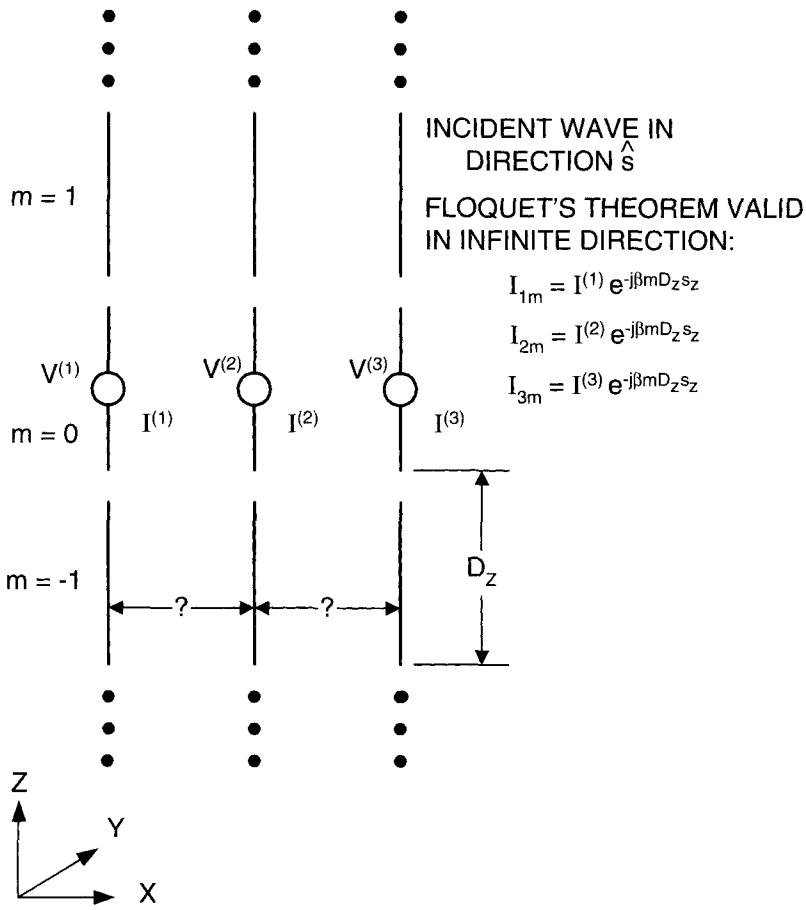

FIGURE 3.3. An array that is finite in the x-direction and infinite in the z-direction with identical inter-element spacing D_z is truly a periodic structure in the z-direction, but not in the x-direction.

planar in the x-direction (see Chapter 9). What is important is that this structure be a true periodic structure along the z-axis and not necessarily along the x-axis.

If this structure is exposed to an incident plane wave propagating in the direction

$$\hat{s} = \hat{x}s_x + \hat{y}s_y + \hat{z}s_z, \tag{3.4}$$

it will induce the currents $I^{(1)}, I^{(2)}, \ldots, I^{(Q)}$ in the arbitrarily chosen reference elements of columns $1, 2, \ldots, Q$, respectively. Furthermore the element currents in a particular column will have the same amplitude as that of its reference element and a phase matching the phase velocity of the incident signal in the z-direction,

$$I_{qm} = I_q e^{-j\beta m D_z s_z}, \qquad q = 1 \ldots Q, \tag{3.5}$$

where m equals the element number in the z-direction with $m = 0$ corresponding to the reference element in the respective column.

Equation (3.5) is usually easy to accept for people with an engineering background. However, those that prefer a mathematical proof should consult the original classical paper by Floquet [19]. To be sure, it has very little direct connection with our kind of periodic structure but addresses the mathematical problem concerning differential equations with periodic coefficients. Floquet's theorem simply states that the solution will have the same periodicity.

Equation (3.5) results in a significant simplification of (3.3). In fact, if we arrange the currents according to the columns and write Ohm's law for each reference element, we readily obtain the following system of equations:

$$\begin{aligned}
V^{(1)} &= (Z^{1,1} + Z_{L1})I^{(1)} + Z^{1,2}I^{(2)} + \cdots + Z^{1,Q}I^{(Q)} \\
V^{(2)} &= Z^{2,1}I^{(1)} + (Z^{2,2} + Z_{L2})I^{(2)} + \cdots + Z^{2,Q}I^{(Q)} \\
&\vdots \\
V^{(Q)} &= Z^{Q,1}I^{(1)} + Z^{Q,2}I^{(2)} + \cdots + (Z^{Q,Q} + Z_{LQ})I^{(Q)},
\end{aligned} \tag{3.6}$$

where

$$Z^{q,q'} = \sum_{m=-\infty}^{\infty} Z_{q,q'm} e^{-j\beta m D_z s_z} \tag{3.7}$$

is called the *array mutual impedance*. It is made of a sum of element mutual impedances $Z_{q,q'm}$ where we use subscript while the array mutual impedance uses superscript. The evaluation of (3.7) is shown in Fig. 3.4. We observe that if the *finite* $\times$ *finite* array in Fig. 3.1 had $Q \times Q$ elements, we have Q^2 unknowns. This is a sharp contrast to the *finite* $\times$ *infinite* array of Q columns that has only Q unknowns.

Although this leads to some reduction in computer time it should be emphasized that the evaluation of the array mutual impedances $Z^{q,q'}$ is still time-consuming if we evaluate them by use of (3.7). This is simply because they rely on evaluating

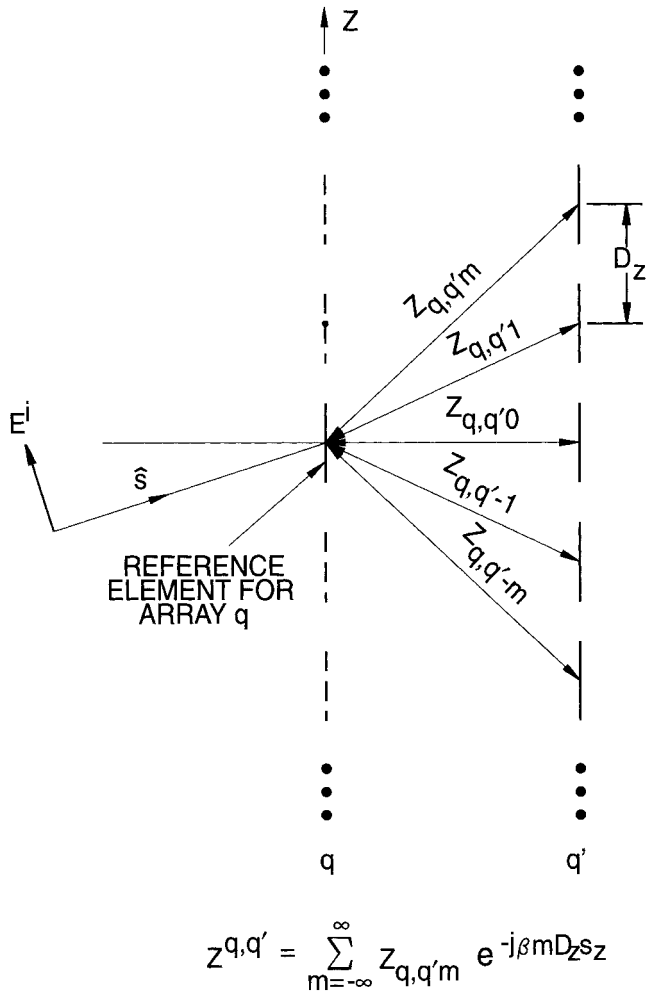

FIGURE 3.4. Evaluation of the array mutual impedance $Z^{q,q'}$ between the reference element in array q and all the other elements in array q' by using the mutual impedance approach.

element mutual impedances. In addition the infinite series (3.7) is in general very slowly convergent requiring the incorporation of many elements, namely high values of m.

Fortunately there are alternative approaches. In fact it will be shown later that the array mutual impedance between two columns with co-linear elements located in a cylindrical coordinate system at ρ and ρ' can be evaluated by another infinite series, namely

$$Z^{q,q'} = \frac{\beta z}{4D_z} \sum_{n=-\infty}^{\infty} r_\rho^2 P_z^{(q)} P_z^{(q')t} H_0^{(2)} \left(\beta r_\rho \left|\rho' - \rho\right|\right), \tag{3.8}$$

where

$$r_\rho = \sqrt{1 - r_z^2} = \sqrt{1 - \left(s_z + n\frac{\lambda}{D_z}\right)^2}, \tag{3.9}$$

and the pattern functions

$$P_z^{(q)} = \frac{1}{I^{(q)}} \int_{-l}^{l} I^{(q)}(z'') e^{-j\beta z'' r_z} dz'', \tag{3.10}$$

$$P_z^{(q')t} = \frac{1}{I^{(q')t}(z^{(q')})} \int_{-l'}^{l'} I^{(q')t}(z'') e^{-j\beta z'' r_z} dz'', \tag{3.11}$$

and $H_0^{(2)}\left(\beta r_\rho \left|\rho' - \rho\right|\right)$ = Hankel function of second kind of order 0 and argument $\beta r_\rho \left|\rho' - \rho\right|$. Equation (3.8) will be derived and discussed in much detail in a future book. It is sufficient here to note that as long as the argument in the Hankel function is real, the magnitude will for reasonably large distances ($>\sim \lambda/4$) decrease monotonically as $1/\sqrt{|\rho' - \rho|}$. However, if the argument becomes imaginary, $H_0^{(2)}$ becomes a modified Bessel function (K_0-function) that falls off exponentially with the argument (i.e., the distance $|\rho - \rho'|$); in other words, only the $H_0^{(2)}$ term is important. Inspection of (3.9) further shows that r_ρ is always real for $n = 0$ and, if D_z is large, is also real for a finite number of n. It will be shown later that this corresponds to the bistatic reflected and transmitted directions as well as the grating lobe directions (see Section 1.9), respectively. They will all propagate away from the array as opposed to all other values of n that lead to evanescent waves (the K_0-function). The bottom line is that evaluation of $Z^{q,q'}$ using (3.8) requires just a few terms unless the distance $|\rho - \rho'|$ is small, typically if it is less than about $\lambda/4$.

Equation (3.8) is an example of the spectral approach yielding the array mutual impedances $Z^{q,q'}$ which is then subsequently used in the mutual impedance approach in (3.6). The value of this mixed approach is not only that we can investigate *finite* × *infinite* arrays but also arrays that are nonplanar in the x-direction. A typical example is shown in Fig. 3.5 where we have modeled an array of three planar surfaces including the finite ground planes. These were modeled by an FSS surface with elements twice as close as the active dipoles (the open "dots"). This was done to obtain more bandwidth around the resonant frequency for the FSS. It should finally be noted that the case above is called for the longitudinal case namely when the elements are pointed in the z-direction. Similarly, the transverse case will be treated in a future book. These cases are of utmost importance when we study corner and edge effects in finite arrays.

3.3 DOUBLE INFINITE CASE

Just as we earlier extended our array along the z-axis to $\pm\infty$, we are now going to extend it to $\pm\infty$ in the x-direction as well; in other words, the array will now

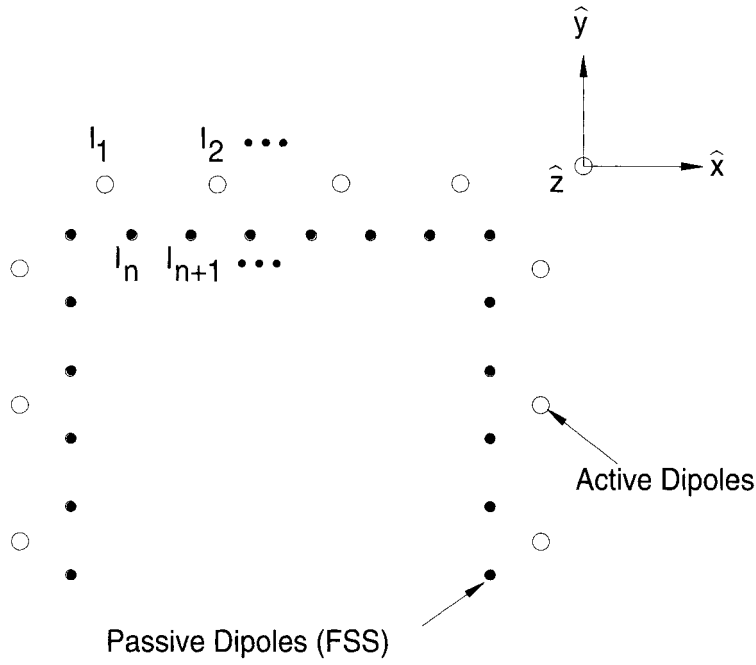

FIGURE 3.5. A *finite* × *infinite* array of three facets of active dipoles with ground planes made of passive elements acting as reflective FSS surfaces.

truly be an *infinite* × *infinite* periodic structure, as long as we keep the inter-element spacings D_x and D_z constant. Also the array must be planar, as shown in Fig. 3.6. If this configuration is exposed to an incident plane wave propagating in the direction $\hat{s}$ as indicated by (3.4), then the amplitude of all the element currents will be the same, while their phases will match the phase of the incident field. Put formally, for the element current in column q and row m,

$$I_{qm} = I_{0,0} e^{-j\beta q D_x s_x} e^{-j\beta m D_z s_z}. \tag{3.12}$$

As in the single infinite case above, this is a direct consequence of Floquet's theorem [19].

Use of (3.12) results in a very significant simplification of the general equation, (3.3). Writing Ohm's law for reference element 0, 0 yields

$$V^{0,0} = \left[Z_L + \sum_{q=-\infty}^{\infty} \sum_{m=-\infty}^{\infty} Z_{0,qm} e^{-j\beta q D_x s_x} e^{-j\beta m D_z s_z} \right] I_{0,0}. \tag{3.13}$$

Thus we have reduced the determination of the element current $I_{0,0}$ to only one equation, (3.13). However, as in the single infinite case above, the evaluation of the

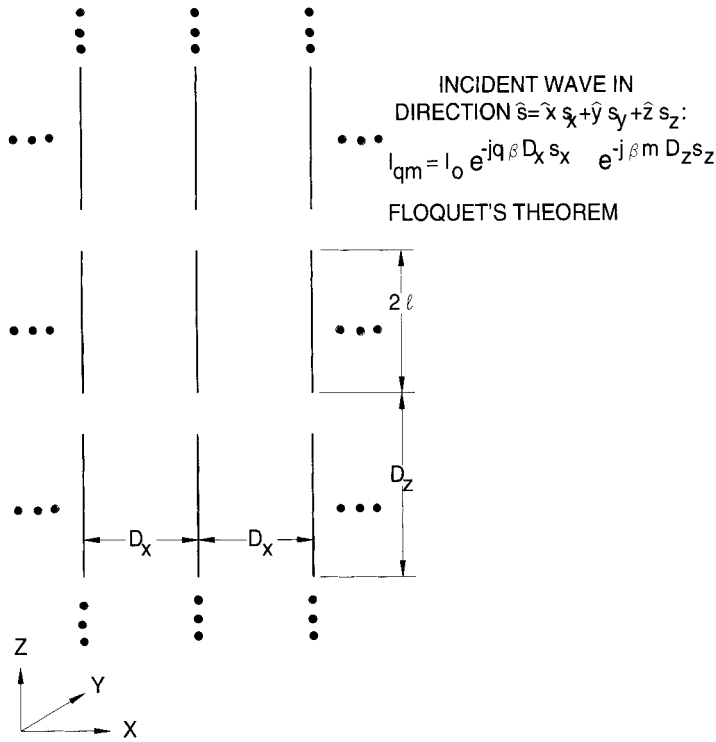

FIGURE 3.6. An *infinite* × *infinite* truly periodic structure with inter-element spacings D_x and D_z and element length $2l$.

array scan impedance

$$Z^{0,0} = \sum_{q=-\infty}^{\infty} \sum_{m=-\infty}^{\infty} Z_{0,qm} e^{-j\beta q D_x s_x} e^{-j\beta m D_z s_z} \tag{3.14}$$

is time-consuming; it converges relatively slowly.

Fortunately it will be shown in great detail in Chapter 4 that alternative ways can be used. In fact we illustrate in Fig. 3.7 the most general case where the array elements are oriented completely arbitrarily along $\hat{p}^{(1)}$ and where the reference point for the reference element of the array is denoted by $\bar{R}^{(1)}$. Furthermore the "external" element, which typically could be the reference element of another array not shown, is oriented along $\hat{p}^{(2)}$ with reference point $\bar{R}^{(2)}$. If we assume element currents as indicated by (3.12), we can determine the voltage $V^{2,1}$ induced in the external element by all the array currents. The mutual array impedance is simply defined as

$$Z^{2,1} = -\frac{V^{2,1}}{I_{0,0}}. \tag{3.15}$$

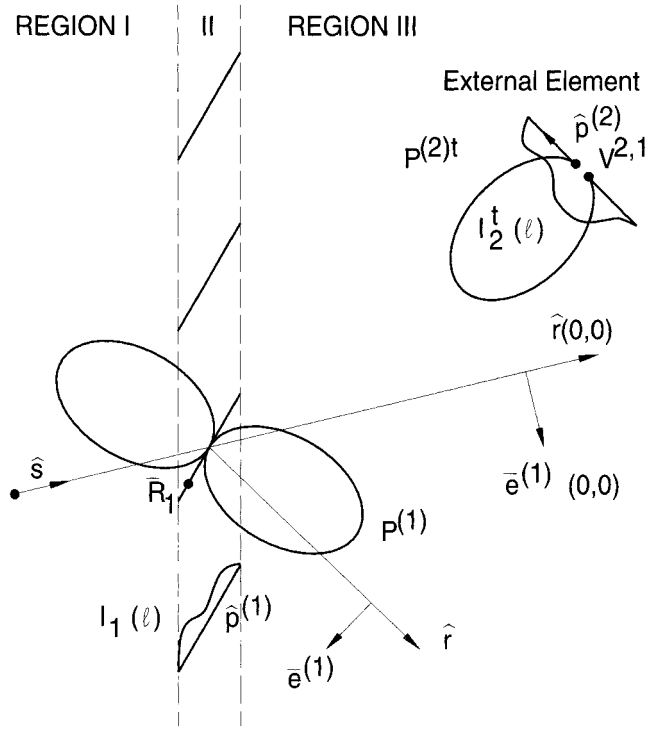

FIGURE 3.7. Array mutual impedance $Z^{2,1}$ between an array with element orientation $\hat{p}^{(1)}$ and an external element with orientation $\hat{p}^{(2)}$ is readily obtained by the plane wave expansion, (3.16) (i.e., the spectral approach).

As shown in Chapter 4, we obtain

$$Z^{2,1} = \frac{Z_0}{2D_x D_z} \sum_{k=-\infty}^{\infty} \sum_{n=-\infty}^{\infty} \frac{e^{-j\beta(\bar{R}^{(2)}-\bar{R}^{(1)})\cdot\hat{r}}}{r_y} \left[{}_{\perp}P^{(1)}\, {}_{\perp}P^{(2)t} + {}_{\parallel}P^{(1)}\, {}_{\parallel}P^{(2)t} \right], \tag{3.16}$$

where

$$\hat{r} = \hat{x}\left(s_x + k\frac{\lambda}{D_x}\right) \pm \hat{y} r_y + \hat{z}\left(s_z + n\frac{\lambda}{D_z}\right) \quad \text{for} \quad y \gtrless 0, \tag{3.17}$$

$$r_y = \sqrt{1 - \left(s_x + k\frac{\lambda}{D_x}\right)^2 - \left(s_z + n\frac{\lambda}{D_z}\right)^2}, \tag{3.18}$$

$$\underset{\parallel}{\perp} P^{(1)} = \hat{p}^{(1)} \cdot \underset{\parallel}{\perp} \hat{n} P^{(1)}, \tag{3.19}$$

$$\underset{\parallel}{\perp} P^{(2)t} = \hat{p}^{(2)} \cdot \underset{\parallel}{\perp} \hat{n} P^{(2)t}, \tag{3.20}$$

and where the pattern factors are defined similarly to (3.10) and (3.11) as

$$P^{(1)} = \frac{1}{I_0^{(1)}\left(\bar{R}^{(1)}\right)} \int_{-l_1}^{l_1} I_0^{(1)}(l) e^{j\beta l \hat{p}^{(1)}\cdot\hat{r}} dl, \tag{3.21}$$

$$P^{(2)t} = \frac{1}{I_0^{(2)t}\left(\bar{R}^{(2)}\right)} \int_{-l_2}^{l_2} I_0^{(2)t}(l) e^{-j\beta l \hat{p}^{(2)}\cdot\hat{r}} dl, \tag{3.22}$$

and ${}_{\perp}\hat{n}$ and ${}_{\parallel}\hat{n}$ are orthogonal and parallel unit vectors associated with $\hat{r}$ (see Chapter 4). The physical interpretation of (3.16) is actually quite simple.

First of all the exponential terms $e^{-j\beta(\bar{R}^{(2)}-\bar{R}^{(1)})\cdot\hat{r}}$ are closely associated with a bundle of inhomogeneous plane waves emanating at the array plane going through the reference point $\bar{R}^{(1)}$ and propagating in the directions $\hat{r}$ as given by (3.17) and (3.18). These directions are seen to depend strongly on the summation indices k and n where we note that the values $k = n = 0$ yields $\hat{r} = \hat{x}s_x \pm \hat{y}s_y + \hat{z}s_z$ corresponding to the forward and bistatic reflected propagating waves, respectively. Depending on the inter-element spacings D_x and D_z, most other values of (k, n) will lead to imaginary values of r_y corresponding to evanescent waves; that is, they are attenuated as we move away from the array. Only when D_x and/or D_z are sufficiently large will there be a finite number of (k, n) where r_y is real. These cases correspond to grating lobes propagating away from the array (see Chapter 4 and Section 1.9).

Finally, this plane wave spectrum is multiplied by pattern components for reference elements 1 and 2, namely ${}_{\perp}P^{(1)}{}_{\perp}P^{(2)t} + {}_{\parallel}P^{(1)}{}_{\parallel}P^{(2)t}$. It will be shown in Chapter 4 that this sum of pattern components is always pure real. The conclusion of the discussion above is simply that the array mutual impedance is simply calculated from (3.16) primarily by just the leading term ($k = n = 0$) and then a few imaginary terms (low values of k, n). The array self-impedance is obtained by putting $\hat{p}^{(1)} = \hat{p}^{(2)}$ and moving the external element toward the array reference element to a distance equal to a wire radius. Typically in that case only do we need to incorporate higher values of k, n (typically 20–40). Still the plane wave expansion will in general converge much faster then the array mutual impedance sum given by (3.14).

3.4 EXAMPLE

As a typical example of how to use this mixed approach, consider two cascaded arrays of dipoles as shown in Fig. 3.8. They are exposed to an incident plane wave which induces the voltages $V^{(1)}$ and $V^{(2)}$ in the respective reference elements. The array mutual impedances $Z^{1,2}$ and $Z^{2,1}$ are determined by the plane wave expansion (3.16). The array self-impedances $Z^{1,1}$ and $Z^{2,2}$ are obtained from the same formula simply by placing an external element, with the same orientation and element length and one wire radius, away from the respective reference elements. Denoting the currents on the reference elements by $I^{(1)}$ and $I^{(2)}$, we readily obtain from the mutual

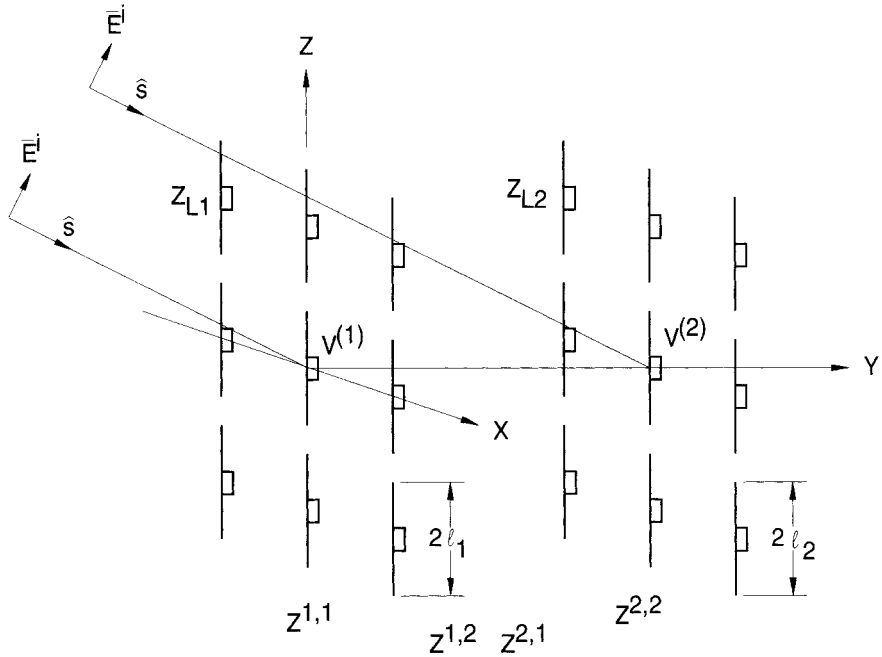

FIGURE 3.8. Two cascaded arrays of dipoles exposed to an incident plane wave inducing the voltages $V^{(1)}$ and $V^{(2)}$ in the respective reference elements. The array self and mutual impedances $Z^{1,1}$, $Z^{2,2}$, $Z^{1,2}$, and $Z^{2,1}$ are determined by the plane wave expansion, (3.16), while the reference currents $I^{(1)}$ and $I^{(2)}$ are determined by the mutual impedance approach, (3.23).

impedance approach

$$\begin{bmatrix} V^{(1)} \\ V^{(2)} \end{bmatrix} = \begin{bmatrix} (Z^{1,1} + Z_{L1}) & Z^{1,2} \\ Z^{2,1} & (Z^{2,2} + Z_{L2}) \end{bmatrix} \begin{bmatrix} I^{(1)} \\ I^{(2)} \end{bmatrix}. \tag{3.23}$$

Solving (3.23) yields the terminal currents $I^{(1)}$ and $I^{(2)}$. If we assume that we know the shape of the currents along the respective elements, we know the current on the structure everywhere. Finding the scattered field is then a simple matter.

For further accuracy read the next section.

3.5 COMMON MISCONCEPTIONS

The mutual impedance approach is sometimes dismissed as being inaccurate. This can be the case if proper precautions are not taken. The problem is simply that we in general do not know the current distribution along the elements well enough. In fact

the shape may well change with angle of incidence and even become asymmetric. See, for example, Fig. 2.8.

The remedy for this problem is simply to split up the elements into mathematical segments, each so short that the exact shape of the assumed current distribution on each section is of minor importance (characteristic for the method of moments). An example is shown in Fig. 3.9 where a single array of wire elements has the total currents on each element modeled by the overlapping current segments or modes. This arrangement leads to three arrays (one for each mode) with current amplitudes $I^{(1)}$, $I^{(2)}$, and $I^{(3)}$. If this configuration isexposed to an incident plane wave, there will be

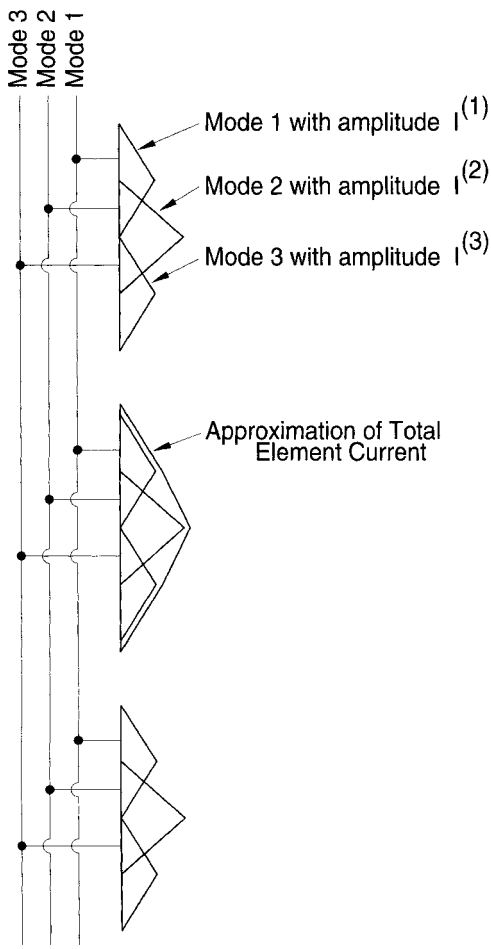

FIGURE 3.9. How the total current distribution is modeled by three mathematical segments or modes which leads to three arrays that can be calculated in a similar manner to the cascaded arrays in Fig. 3.8

voltages $V^{(1)}$, $V^{(2)}$, and $V^{(3)}$ induced in each respective segment as shown in Section 4.12. If, on the other hand, the array is driven by generators connected to merely the center of each physical element, then the center terminals only have a voltage $V^{(2)}$, while all the other segment voltages $V^{(1)}$ and $V^{(3)}$ equal zero. In either case, the current amplitudes are readily found by the mutual impedance approach outlined above, (3.23). Note that by modeling the total current distribution by segments, we can readily approximate any current distribution, even asymmetric ones.

It should further be noted that the segments do not have to be parallel; that is, we can readily model elements of arbitrary shape. This is precisely what is used in the "Periodic Moment Method" (PMM) as shown in Section 4.12 and [2, 3, 4, 5]. It will handle planar elements, dipole, and/or slot types, of completely arbitrary piecewise linear shape placed in a completely arbitrary stratified medium of arbitrary complex ϵ and μ. However, the array(s) in the PMM program must be planar.

One word of caution about segments (modes): From our encounter with integral calculus early in life, we are often led to assume that use of more segments on the elements leads to greater computational accuracy. This is not necessarily the case. The problem lies in the way we evaluate the self-impedance of each segment. It is obtained as the mutual impedance between two current fibers placed at a distance of one wire radius from each other (see Section 4.10). This amounts to an approximation that fails when the length of each segment becomes comparable to the wire radius. Thus, when dividing an element of a certain length up into more and more segments, they become shorter and shorter until they simply become too short for a given wire radius.

So how many segments should we typically use? Well, for elements $\lambda/2$ long or shorter, we can actually get by with just one segment (sinusoidal) if one is willing to accept calculated resonant frequencies that are typically 10% too high. In general, however, it is fairly prudent to use three for a $\lambda/2$ long element and then go to five or seven for greater accuracy. Only longer elements in terms of wavelength really require more segments.

Another common misconception is that reciprocity applies to the array mutual impedances. This is not necessarily the case. In other words, while the mutual impedance $Z_{1,2}$ between two individual elements obey reciprocity,

$$Z_{1,2} \equiv Z_{2,1},$$

it is valid only under certain circumstances for the array mutual impedances.

3.6 SUMMARY OF OUR COMPUTATIONAL APPROACH

Our approach is really a mixture of the mutual impedance and the plane wave expansion approaches where we use the latter to evaluate the array mutual impedances to be used in the former. By dividing the elements up into overlapping segments, we can use a method of moments approach adapted to periodic surfaces with a very high degree of accuracy and great computational speed.

It should be pointed out, however, that the actual determination of the current distribution often is unnecessary when analyzing certain aspects of periodic structures. We merely have to assume that the elements have "some" current distribution (although unknown). In this manner many important features of a periodic structure may be determined, for example, the very important dielectric profile of a hybrid radome; see Chapter 7. Of course, ultimately we must find the current. We will go deeper into these aspects in Chapters 4, 5, 6, and 7.

3.7 PROBLEMS

3.1 Active Array: The Mutual Impedance Approach

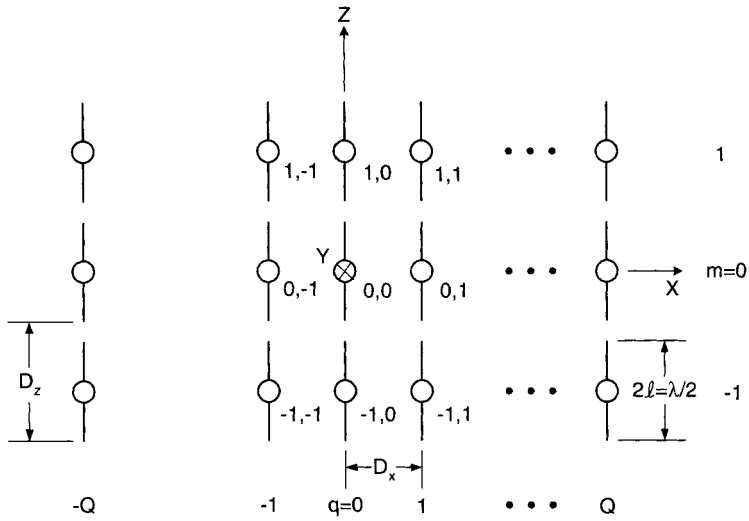

Fig. P3.1

The array scan impedance for an infinite array of z-oriented dipoles, as shown above in Fig. P3.1, is given by (3.14):

$$Z^{0,0} = \sum_{q=-\infty}^{\infty} \sum_{m=-\infty}^{\infty} Z_{0,qm} e^{-j\beta q D_x s_x} e^{-j\beta m D_z s_z}.$$

In this problem we study the effect of truncating this infinite series. Assume that the element self-impedance $Z_{0,00} = 70$ ohm, and use a suitable subroutine for $Z_{0,qm}$.

We will scan only in the H-plane (i.e., the xy-plane) with the scan angle going from broadside to grazing. We will limit the number of rows to merely $m = \pm 1$ as shown in the figure.

Plot the following cases for $Z^{0,0}$ as a function of scan angle:

Case 1:	$D_x = 0.35\,\lambda$	$D_z = 0.60\,\lambda$	$Q = 20$
Case 2:	$D_x = 0.70\,\lambda$	$D_z = 0.60\,\lambda$	$Q = 10$
Case 3:	$D_x = 0.70\,\lambda$	$D_z = 0.60\,\lambda$	$Q = 11$

[Do not forget the contributions from elements (0, 1) and (0, −1).]

The cases above also represent the array self impedance (rigorously) for the center element of a *finite* × *finite* array fed by *constant current* generators with phases following Floquet's theorem (3.12). Had we instead fed the individual elements by constant voltage generators, the element currents would no longer obey Floquet's theorem because the element terminal impedances in a finite array would vary from element to element. Realistically the voltage generators will in general have a generator impedance different from zero. This would correspond to a case somewhere between the constant current and constant voltage generator cases. If the element voltages were caused by an incident plane wave, we would have ideal constant voltage generators (see Section 4.7).

Finally, calculate the onset of the grating lobes and mark them in your figures.

3.2 The Fejèr Kernel As demonstrated in Problem 3.1, the convergence of $Z^{0,0}$ as given by (3.14) is not terribly good (compare cases 2 and 3). It is well known that the convergence of this kind of series can often be improved by use of a "window" or kernel.

We suggest a reevaluation of cases 1, 2, and 3 in Problem 3.1 when using the Fejèr kernel:

$$Z^{0,0} = \sum_q \sum_m Z_{0,qm} \left(1 - \frac{|q|}{Q}\right) e^{-j\beta q D_x s_x} \cdot e^{-j\beta m D_z s_z}.$$

Note: The kernel is not dependent on m and is equal to zero for $|q| \geq Q$.

Similarly to Problem 3.1, this will constitute an approximation to an infinite array. It will also rigorously depict the impedance of the center element (0, 0) in a finite array fed with constant current generators with a triangular aperture taper in the x-direction.

Plot your results along with the cases in Problem 3.1 and observe the changes caused by the kernel.

4

SPECTRAL EXPANSION OF ONE- AND TWO-DIMENSIONAL PERIODIC STRUCTURES

4.1 INTRODUCTION

In this chapter we first determine the vector potential $d\bar{A}$ as well as the field $d\bar{E}$ from a two-dimensional infinite array of Hertzian elements of length dl and arbitrary orientation $\hat{p}$ as shown in Fig. 4.1. The array is located in the xz-plane and the inter-element spacings are denoted by D_x and D_z in the x- and z-directions, respectively. The reference element is located at the origin (0, 0, 0) with its current denoted by I_{00}, while the current of an arbitrary element located in column q and row m is denoted by I_{qm}.

We consider such a configuration both under scattering and transmitting conditions.

In the first case we will assume that the array is exposed to an incident plane wave propagating in the direction

$$\hat{s} = \hat{x}s_x + \hat{y}s_y + \hat{z}s_z. \tag{4.1}$$

According to Floquet's theorem (see Section 3.2), Eq. (4.1) results in element currents I_{qm} of equal amplitudes and a phase relationship matching that of the phase velocity of the incident plane wave along the array:

$$I_{qm} = I_{00}e^{-j\beta qD_xs_x}e^{-j\beta mD_zs_z}. \tag{4.2}$$

Similarly radiation from this array will take place when each element is connected to individual current or voltage generators. We always assume that these generators have equal amplitudes and a phase relationship as given by Eq. (4.2). In other words, (4.2) will be satisfied whether we consider the scattering or transmission case. In

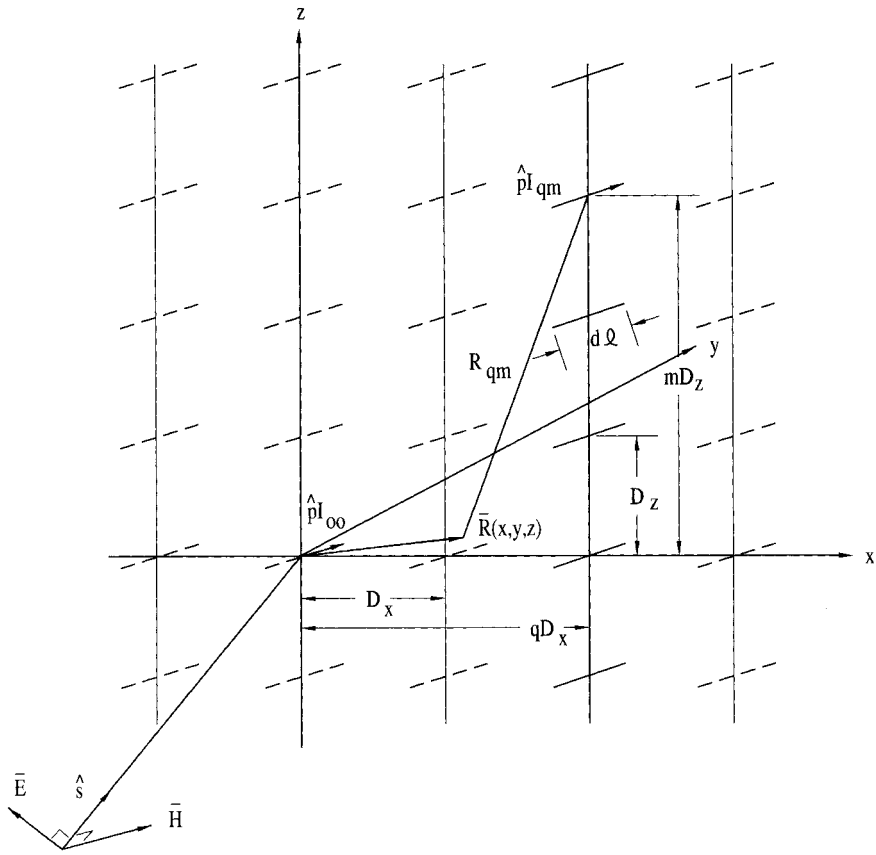

FIGURE 4.1. A double infinite array of Hertzian elements with arbitrary orientation $\hat{p}$ and inter-element spacings D_x and D_z is exposed to an incident plane wave resulting in the element currents $I_{qm} = I_{00}e^{-j\beta q D_x s_x}e^{-j\beta m D_z s_z}$ (Floquet's theorem).

the latter case we will later show that the radiated field will consist of plane waves propagating in the directions

$$\hat{r}_{\pm} = \hat{x}s_x \pm \hat{y}s_y + \hat{z}s_z \tag{4.3}$$

and eventually grating lobe directions if D_x and/or D_z are large enough in terms of wavelength (see Section 1.9).

Some readers will be delighted to notice that we are in effect determining Green's functions for a two-dimensional periodic surface (and a dyadic one at that!). Others might feel slightly intimidated. Whichever category the reader is in, do not worry. Our approach will be straightforward; we will not assume any special mathematical knowledge with the exception of Poisson's sum formula (explained later). Further our approach will be as rigorous and "exact" as the method of moments. In fact our

approach is often referred to as the "Periodic Moment Method" (PMM), for example, see the work of Hansen [20], pp. 246 and 280.

We will simply start with the vector potential $d\bar{A}_{qm}$ of the single element q, m and use this to obtain the vector potential $d\bar{A}_q$ for the entire column located at $x = qD_x$ (shown in full line in Fig. 4.1). Next we will be adding the vector potentials from all the column arrays from $q = -\infty$ to $q = +\infty$ and thereby obtain the vector potential $d\bar{A}$ for the entire array.

We will later determine the total field $\bar{E}$ from a double infinite array of elements with arbitrary orientation $\hat{p}$ and length $2l$. Also we will find the array mutual and self-impedances.

4.2 THE VECTOR POTENTIAL $d\bar{A}_q$ FROM A SINGLE INFINITE COLUMN ARRAY OF HERTZIAN ELEMENTS WITH ARBITRARY ORIENTATION $\hat{p}$

The determination of the vector potential $d\bar{A}_q$ for a single column array is important not only as a step for obtaining the vector potential $d\bar{A}$ for the entire array but also because it enables us to consider arrays that are infinite in one dimension and finite in another. (The x-direction in the present case.) In fact, this finite array is really only required to have all infinite column arrays parallel with the z-axis, but it can otherwise be of arbitrary shape, such as, a nonplanar array. This opens up the possibility of treating curved as well as faceted arrays being infinite only in the z-direction. This subject will be covered in a future book. Let the point of observation be denoted by $\bar{R}(x, y, z)$; see Fig. 4.1. Further the distance from this observation point $\bar{R}$ to an arbitrary element q, m is denoted by R_{qm} where we readily observe that

$$R_{qm}^2 = a^2 + (mD_z - z)^2, \tag{4.4}$$

where

$$a^2 = y^2 + (qD_x - x)^2. \tag{4.5}$$

The vector potential $d\bar{A}_{qm}$ for a single Hertzian element with current I_{qm}, length dl and arbitrary orientation $\hat{p}$ is well known:

$$d\bar{A}_{qm} = \hat{p}\frac{\mu I_{qm} dl}{4\pi}\frac{e^{-j\beta R_{qm}}}{R_{qm}}. \tag{4.6}$$

Since all the elements in the entire array are oriented in the same direction $\hat{p}$, the total vector potential of the line array as well as the double infinite array is obtained by simple addition of the vector potentials of the single elements. Thus, for the line array, we find that

$$d\bar{A}_q = \hat{p}\frac{\mu dl}{4\pi}\sum_{m=-\infty}^{\infty} I_{qm}\frac{e^{-j\beta R_{qm}}}{R_{qm}}. \tag{4.7}$$

Substituting Eq. (4.2) into Eq. (4.7) obtains

$$d\bar{A}_q = \hat{p}\frac{\mu I_{00} dl}{4\pi} e^{-j\beta q D_x s_x} \sum_{m=-\infty}^{\infty} e^{-j\beta m D_z s_z} \frac{e^{-j\beta R_{qm}}}{R_{qm}}. \tag{4.8}$$

Equation (4.8) will converge to a finite value except when a grating lobe emerges. In that case it will in general correctly become infinite. The problem is that the series in general is very slowly convergent.

We will transform the infinite series (4.8) into another infinite series in the hope that the new series converges faster than the old one. This will be accomplished by the use of Poisson's sum formula. Many engineers encounter this formula for the first time in a communications course where it is widely used to relate the time domain to the frequency domain; for example [21],

$$\sum_{m=-\infty}^{\infty} e^{-jmw_0 t} F(mw_0) = T \sum_{n=-\infty}^{\infty} f(t + nT), \tag{4.9}$$

where $F(w)$ denotes the Fourier transform of $f(t)$, namely $F(w) = \mathcal{F}[f(t)]$ and

$$T = \frac{2\pi}{w_0}. \tag{4.10}$$

We emphasize that the present application of Poisson's sum formula has nothing to do with time nor frequency. These quantities are for our purpose purely mathematical, used just the way Poisson originally intended.

Thus we will start by finding a suitable Fourier transform pair. From Bateman [22] we obtain from Section 1.13 formula (1.42), for $\nu = \frac{1}{2}$,

$$\frac{e^{-j\beta\sqrt{a^2+w^2}}}{\sqrt{a^2+w^2}} = \mathcal{F}\left[\frac{1}{2j} H_0^{(2)}\left(a\sqrt{\beta^2 - t^2}\right)\right], \qquad -\infty < t < \infty. \tag{4.11}$$

Applying the shift theorem [23]

$$\mathcal{F}(w - w_1) = \mathcal{F}\left[e^{-jw_1 t} f(t)\right]$$

to Eq. (4.11) yields the Fourier transform pair:

$$\frac{e^{-j\beta\sqrt{a^2+(w-w_1)^2}}}{\sqrt{a^2+(w-w_1)^2}} = \mathcal{F}\left[\frac{e^{-jw_1 t}}{2j} H_0^{(2)}\left(a\sqrt{\beta^2 - t^2}\right)\right]. \tag{4.12}$$

Comparison of Eqs. (4.8) and (4.9) and application of Eqs. (4.4), (4.10), and (4.12) now suggest that we put

$$w_0 = D_z, \quad T = \frac{2\pi}{w_0} = \frac{2\pi}{D_z}, \quad t = +\beta s_z, \quad w_1 = z. \tag{4.13}$$

Application of Poisson's sum formula (4.9) readily yields for Eq. (4.8),

$$d\bar{A}_q = \hat{p}\frac{\mu I_{00} dl}{4\pi}\frac{2\pi}{D_z} e^{-j\beta q D_x s_x} \sum_{n=-\infty}^{\infty} e^{-jz(\beta s_z + n(2\pi/D_z))} \frac{1}{2j} H_0^{(2)}\left(a\sqrt{\beta^2 - \left(\beta s_z + n\frac{2\pi}{D_z}\right)^2}\right) \tag{4.14a}$$

or

$$d\bar{A}_q = \hat{p}\frac{\mu I_{00} dl}{4jD_z} e^{-j\beta q D_x s_x} \sum_{n=-\infty}^{\infty} e^{-j\beta z(s_z + n(\lambda/D_z))} H_0^{(2)}(\beta r_\rho a), \tag{4.14b}$$

where

$$r_\rho = \sqrt{1 - \left(s_z + n\frac{\lambda}{D_z}\right)^2}. \tag{4.15}$$

4.3 VECTOR POTENTIAL $d\bar{A}$ FOR A DOUBLE INFINITE ARRAY OF HERTZIAN ELEMENTS WITH ARBITRARY ORIENTATION $\hat{p}$

4.3.1 Rectangular Grid

The vector potential $d\bar{A}$ for a two-dimensional infinite array of Hertzian elements is obtained by adding the vector potentials $d\bar{A}_q$ of all the column arrays from $q = -\infty$ to $+\infty$:

$$d\bar{A} = \sum_{q=-\infty}^{\infty} d\bar{A}_q. \tag{4.16}$$

Substituting Eq. (4.14b) into (4.16), we find that

$$d\bar{A} = \hat{p}\frac{\mu I_{00} dl}{4jD_z} \sum_{n=-\infty}^{\infty} e^{-j\beta z(s_z + n(\lambda/D_z))} \sum_{q=-\infty}^{\infty} e^{-j\beta q D_x s_x} H_0^{(2)}(\beta r_\rho a). \tag{4.17}$$

The infinite summation over q is now transformed into another infinite series by application of Poisson's sum formula. Comparison of Eqs. (4.17) and (4.9) suggests that we put

$$w_0 = D_x, \quad T = \frac{2\pi}{w_0} = \frac{2\pi}{D_x}, \quad t = +\beta s_x. \tag{4.18}$$

From Bateman [24, sec. 1.13] for $\nu = 0$ we obtain the transform pair

$$H_0^{(2)}\left(\beta r_\rho \sqrt{y^2 + w^2}\right) = \mathcal{F}\left[\frac{e^{-jy\sqrt{(\beta r_\rho)^2 - t^2}}}{\pi\sqrt{(\beta r_\rho)^2 - t^2}}\right], \qquad -\infty < t < \infty. \tag{4.19}$$

Application of the shift theorem as earlier (4.19) yields

$$H_0^{(2)}\left(\beta r_\rho \sqrt{y^2 + (w - w_2)^2}\right) = \mathcal{F}\left[e^{-jw_2 t}\frac{e^{-jy\sqrt{(\beta r_\rho)^2 - t^2}}}{\pi\sqrt{(\beta r_\rho)^2 - t^2}}\right]. \tag{4.20}$$

We now note that βr_ρ occuring in the argument of the Hankel function of Eq. (4.17) is constant with respect to q while "a" as given by Eq. (4.5) suggests that we put

$$w_2 = x. \tag{4.21}$$

Applying Poisson's sum formula (4.9) with summation indexes k on Eq. (4.17) and making use of Eqs. (4.18), (4.20), and (4.21) yields:

$$d\bar{A} = \hat{p}\frac{\mu I_{00} dl}{4jD_z}\sum_{n=-\infty}^{\infty} e^{-j\beta z(s_z + n(\lambda/D_z))}\frac{2\pi}{D_x}\sum_{k=-\infty}^{\infty} e^{-jx(\beta s_x + k(2\pi/D_x))}\frac{e^{-jy\sqrt{(\beta r_\rho)^2 - (\beta s_x + k(2\pi/D_x))^2}}}{\pi\sqrt{(\beta r_\rho)^2 - (\beta s_x + k(2\pi/D_x))^2}}. \tag{4.22}$$

Substituting r_ρ^2 as given by Eq. (4.15) into (4.22) yields

$$d\bar{A} = \hat{p}\frac{\mu I_{00} dl}{2j\beta D_x D_z}\sum_{k=-\infty}^{\infty}\sum_{n=-\infty}^{\infty} e^{-j\beta z(s_z + n(\lambda/D_z))} e^{-j\beta x(s_x + k(\lambda/D_x))}\frac{e^{-j\beta y\sqrt{1 - (s_x + k(\lambda/D_x))^2 - (s_z + n(\lambda/D_z))^2}}}{\sqrt{1 - (s_x + k(\lambda/D_x))^2 - (s_z + n(\lambda/D_z))^2}}.$$

Written in compact form,

$$d\bar{A} = \hat{p}\frac{\mu I_{00} dl}{2j\beta D_x D_z}\sum_{k=-\infty}^{\infty}\sum_{n=-\infty}^{\infty}\frac{e^{-j\beta \bar{R}\cdot\hat{r}_\pm}}{r_y} \qquad \text{for } y \gtrless 0, \tag{4.23}$$

where

$$\begin{aligned}\hat{r}_{\pm} &= \hat{x}r_x \pm \hat{y}r_y + \hat{z}r_z \\ &= \hat{x}\left(s_x + k\frac{\lambda}{D_x}\right) \pm \hat{y}r_y + \hat{z}\left(s_z + n\frac{\lambda}{D_z}\right) \qquad \text{for } y \gtrless 0, \end{aligned} \tag{4.24}$$

and where

$$r_y = \sqrt{1 - \left(s_x + k\frac{\lambda}{D_x}\right)^2 - \left(s_z + n\frac{\lambda}{D_z}\right)^2}. \tag{4.25}$$

The physical interpretation of (4.23) to (4.25) will be given in Section 4.6.

4.3.2 Skewed Grid

The section above deals with a rectangular grid. However, there are numerous applications where our array grid is skewed as shown in Fig. 4.2. This case was solved by Kornbau [25] by extension of the approach above. He found that (4.24) should simply be modified to

$$\hat{r}_{\pm} = \hat{x}\left(s_x + k\frac{\lambda}{D_x} - n\frac{\Delta z}{D_z}\frac{\lambda}{D_x}\right) \pm \hat{y}r_y + \hat{z}\left(s_z + n\frac{\lambda}{D_z}\right); \tag{4.26}$$

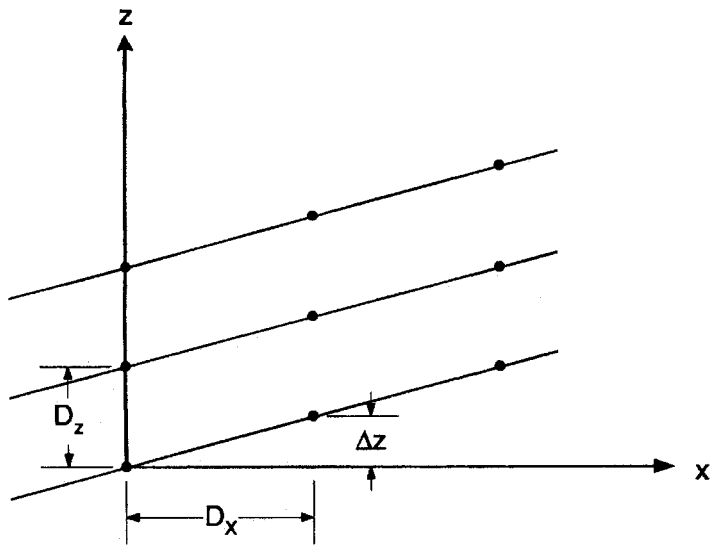

FIGURE 4.2. Elements placed in a skewed grid produced by shifting the elements $\Delta z q$ in the z-direction.

Note that *only* r_x is modified; everything else remains the same! See also Sections 5.14.2 and 5.14.3.

4.4 VECTOR FIELDS $d\bar{H}(\bar{R})$ AND $d\bar{E}(\bar{R})$ FOR A DOUBLE INFINITE ARRAY OF HERTZIAN ELEMENTS WITH ARBITRARY ORIENTATION $\hat{p}$

Having determined the vector potential $d\bar{A}$ for a double infinite array, it is now a simple matter to find the fields $d\bar{H}$ and $d\bar{E}$.

Substituting Eq. (4.23) into $d\bar{H} = \frac{1}{\mu}\nabla \times d\bar{A}$ readily yields

$$d\bar{H} = \frac{I_{00}dl}{2j\beta D_x D_z} \sum_{k=-\infty}^{\infty} \sum_{n=-\infty}^{\infty} \nabla \times \left(\hat{p} \frac{e^{-j\beta \bar{R}\cdot\hat{r}_\pm}}{r_y} \right) \qquad \text{for } y \gtrless 0. \quad (4.27)$$

Applying the vector identity,

$$\nabla \times (\bar{A}\phi) = \phi \nabla \times \bar{A} - \bar{A} \times \nabla\phi \quad (4.28)$$

[note that $\bar{A}$ is any vector in (4.28)] to Eq. (4.27), and notice that $\nabla \times \hat{p} = 0$, we have

$$d\bar{H} = \frac{I_{00}dl}{2D_x D_z} \sum_{k=-\infty}^{\infty} \sum_{n=-\infty}^{\infty} \frac{e^{-j\beta \bar{R}\cdot\hat{r}_\pm}}{r_y} \hat{p} \times \hat{r}_\pm \qquad \text{for } y \gtrless 0. \quad (4.29)$$

Finally we substitute Eq. (4.29) into $\bar{E} = (1/jw\epsilon)\nabla \times \bar{H}$, and again applying Eq. (4.28), we obtain

$$d\bar{E} = I_{00}\, dl \frac{Z}{2D_x D_z} \sum_{k=-\infty}^{\infty} \sum_{n=-\infty}^{\infty} \frac{e^{-j\beta \bar{R}\cdot\hat{r}_\pm}}{r_y} \bar{e}_\pm \qquad \text{for } y \gtrless 0 \quad (4.30)$$

where $Z = \sqrt{\mu/\epsilon}$ and the field vector

$$\bar{e}_\pm = [\hat{p} \times \hat{r}_\pm] \times \hat{r}_\pm. \quad (4.31)$$

4.5 VECTOR FIELD $\bar{E}(\bar{R})$ FOR A DOUBLE INFINITE ARRAY OF ELEMENTS WITH GIVEN CURRENT DISTRIBUTION $I(l)$ AND ARBITRARY ORIENTATION $\hat{p}^{(1)}$

Having determined what essentially amounts to the dyadic Green's function for a double infinite array, it is now a simple matter to obtain the total vector field $\bar{E}$ for an array with a given current distribution $I_{00}(l)$ on the reference element, as shown in Fig. 4.3. Anticipating later elements with more than one orientation $\hat{p}$, we have

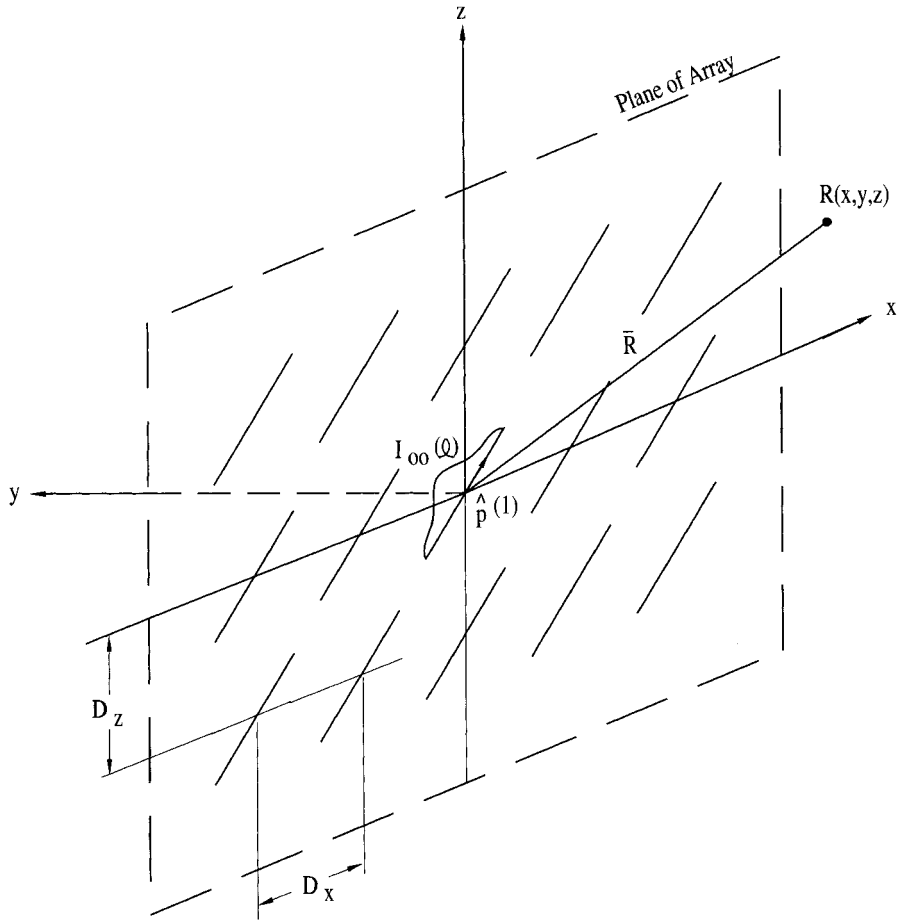

FIGURE 4.3. Double infinite array of elements with current distribution $I_{00}(l)$ and arbitrary orientation $\hat{p}^{(1)}$.

denoted the present element orientation by $\hat{p}^{(1)}$ resulting in $\bar{e}_{\pm}^{(1)}$ as determined by Eq. (4.31).

We further note that the derivation above assumes that the Hertzian reference element was located at the origin. We need to modify Eq. (4.30) to include arbitrary source location $\bar{R}''$. Equation (4.30) expresses a Green's function of the form

$$d\bar{E}^{(1)}(0, \bar{R}), \tag{4.32}$$

where the first argument indicates the location of the reference source and the second argument gives the coordinates of the observer.

To obtain the expression for the more general case, namely where the reference source is located at $\bar{R}''$, we note that if source and observer are both shifted in space

by the same amount, the resulting fields are unchanged. Thus

$$d\bar{E}^{(1)}(\bar{R}'', \bar{R}) = d\bar{E}^{(1)}(\bar{R}'' - \bar{R}'', \bar{R} - \bar{R}'') = d\bar{E}^{(1)}(0, \bar{R} - \bar{R}''). \tag{4.33}$$

Therefore the desired expression is obtained simply by replacing $\bar{R}$ with $(\bar{R} - \bar{R}'')$ in (4.30):

$$\bar{R} \to \bar{R} - \bar{R}'' \tag{4.34}$$

in (4.30), yielding

$$d\bar{E}^{(1)}(\bar{R}'', \bar{R}) = I_{00}\, dl \frac{Z}{2D_x D_z} \sum\sum \frac{e^{-j\beta \bar{R}\cdot \hat{r}_\pm}}{r_y} \bar{e}_\pm^{(1)} e^{+j\beta \bar{R}''\cdot \hat{r}_\pm} \qquad \text{for } y \gtrless 0. \tag{4.35}$$

[Equation (4.35) can also readily be verified by noting that $e^{-j\beta \bar{R}\cdot \hat{r}_\pm}$ represents merely plane inhomogeneous waves as will be discussed later.]

To obtain the total field $\bar{E}^{(1)}$ from an entire array with arbitrary element orientation $\hat{p}^{(1)}$ and a given current distribution $I_{00}^{(1)}(\bar{R}'')$ on the reference element, we subdivide this element into arrays of infinitesimal elements of length dl and current amplitude $I^{(1)}(l)$ as illustrated in Fig. 4.4. Since all these infinitesimal elements have the same $\hat{r}_\pm$ as given by Eq. (4.24), they will also have the same field vectors $\bar{e}_\pm^{(1)}$ as given by Eq. (4.31). Thus the total field $\bar{E}^{(1)}$ from the entire array is simply obtained by integration of the given current distribution $I_{00}^{(1)}(\bar{R}'')$ over the entire reference element:

$$\bar{E}^{(1)}(\bar{R}) = \frac{Z}{2D_x D_z} \sum_{k=-\infty}^{\infty} \sum_{n=-\infty}^{\infty} \frac{e^{-j\beta \bar{R}\cdot \hat{r}_\pm}}{r_y} \bar{e}_\pm^{(1)} \int_{\text{Ref. Ele.}} I_{00}^{(1)}(\bar{R}'') e^{j\beta \bar{R}''\cdot \hat{r}_\pm}\, dl \tag{4.36}$$

for $\bar{R}$ in region I or III.

Regions I, II, and III are defined by the tips of the elements as illustrated in Fig. 4.4. Their physical significance will be discussed later.

Expression (4.36) can be made more manageable if we choose a reference point $\bar{R}^{(1)}$ on the reference element. In that event the source point $\bar{R}''$ can be expressed as

$$\bar{R}'' = \bar{R}^{(1)} + \hat{p}^{(1)} l. \tag{4.37}$$

This is illustrated in Fig. 4.4. Substituting (4.37) into (4.36) obtains

$$\bar{E}^{(1)}(\bar{R}) = I^{(1)}\left(\bar{R}^{(1)}\right) \frac{Z}{2D_x D_z} \sum_{k=-\infty}^{\infty} \sum_{n=-\infty}^{\infty} \frac{e^{-j\beta(\bar{R}-\bar{R}^{(1)})\cdot \hat{r}_\pm}}{r_y} \bar{e}_\pm^{(1)} P^{(1)}, \tag{4.38}$$

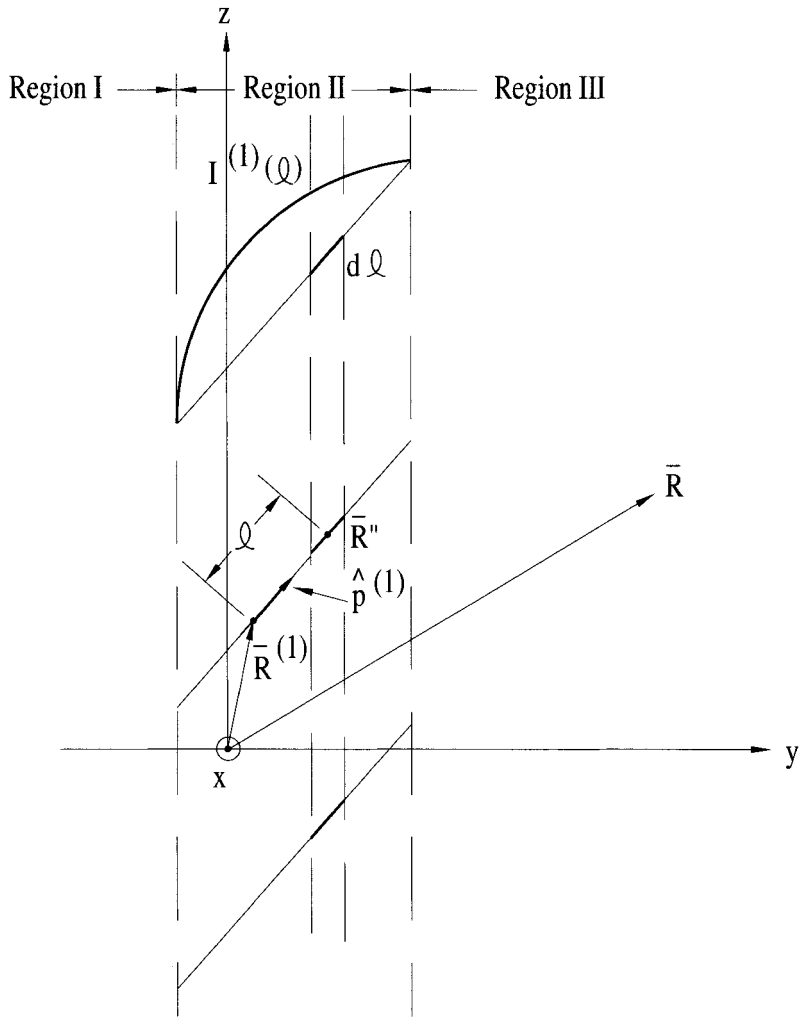

FIGURE 4.4. Total field $E^{(1)}$ from an array with current $I^{(1)}(l)$ and orientation $\hat{p}^{(1)}$ which is obtained by integration of the field $d\bar{E}$ from arrays of Hertzian elements and current amplitudes $I^{(1)}(l)$.

where the pattern function

$$P^{(1)} = \frac{1}{I^{(1)}(\bar{R}^{(1)})} \int_{\text{Ref. Ele.}} I^{(1)}(l) e^{j\beta l \hat{p}^{(1)} \cdot \hat{r}_{\pm}} \, dl \qquad \text{for regions I and III.} \quad (4.39)$$

For region II, see Section 4.9.

4.6 PHYSICAL INTERPRETATION

Physical interpretations of the expressions above are not only interesting in their own right but also a valuable tool in our further development. Let us explore the individual terms in Eq. (4.38).

The exponential term $e^{-j\beta(\bar{R}-\bar{R}^{(1)})\cdot\hat{r}_\pm}$ simply expresses plane waves originating at the reference point $\bar{R}^{(1)}$ and propagating in the directions $\hat{r}_\pm$ as given by Eqs. (4.24) and (4.25). When the summation indexes $(k, n) = (0, 0)$, the direction $\hat{r}_\pm$ becomes

$$\hat{r}_\pm(0, 0) = \hat{x}s_x \pm \hat{y}s_y + \hat{z}s_z. \tag{4.40}$$

That is, it equals the direction $\hat{s}$ of the incident field (forward scattering) and the specular reflected field, as illustrated in Fig. 4.5. These directions will always be present for any periodic surface. However, if the inter-element spacings D_x and D_z are sufficiently large, there may be additional values of (k, n) for which r_y, as given by Eq. (4.25), are real; in other words, propagation will take place in this (these) direction(s) as well. These are denoted grating lobe directions, and one set is illustrated in Fig. 4.5. Higher values of (k, n) will produce imaginary values of r_y corresponding to waves being attenuated as our observation point $\bar{R}(x, y, z)$ moves away from the array as illustrated in Fig. 4.5 (lower half). However, while the phase velocities in the plane of the array are always real, namely $r_x = s_x + k\lambda/D_x$ and $r_z = s_z + n\lambda/D_z$, there is no change of phase in the y-direction for r_y imaginary (i.e., away from the array). These waves are called *evanescent waves*. While their magnitudes are insignificant compared to the propagating modes as one moves away from the array, they are strong and extremely important when we are close to the array elements. They represent electromagnetic energy stored around the elements and will be shown later to be a key factor in determining the imaginary part of the array impedance as well as the shape and the resonant frequency of the reflection and transmission curves of FSSs.

In summary, we can state that the grating lobe indexes (k, n) are those values different from 0, 0, which make r_y as given by Eq. (4.25) positive real. Or more specifically, the onset of grating lobes are determined by

$$r_y = 0 \quad \text{or} \quad \left(s_x + k\frac{\lambda}{D_x}\right)^2 + \left(s_z + n\frac{\lambda}{D_z}\right)^2 = 1. \tag{4.41}$$

This equation is consistent with our discussion about grating lobes in Sections 1.9 and 5.14. It should further be noted that when the summation indexes (k, n) become sufficiently large, we obtain from Eq. (4.25),

$$r_y = \pm j\sqrt{\left(s_x + k\frac{\lambda}{D_x}\right)^2 + \left(s_z + n\frac{\lambda}{D_z}\right)^2 - 1}.$$

The choice of sign depends on whether our observation point $\bar{R}$ is located in region I or region III. By physical reasoning it is obvious that the field should not go to infinity

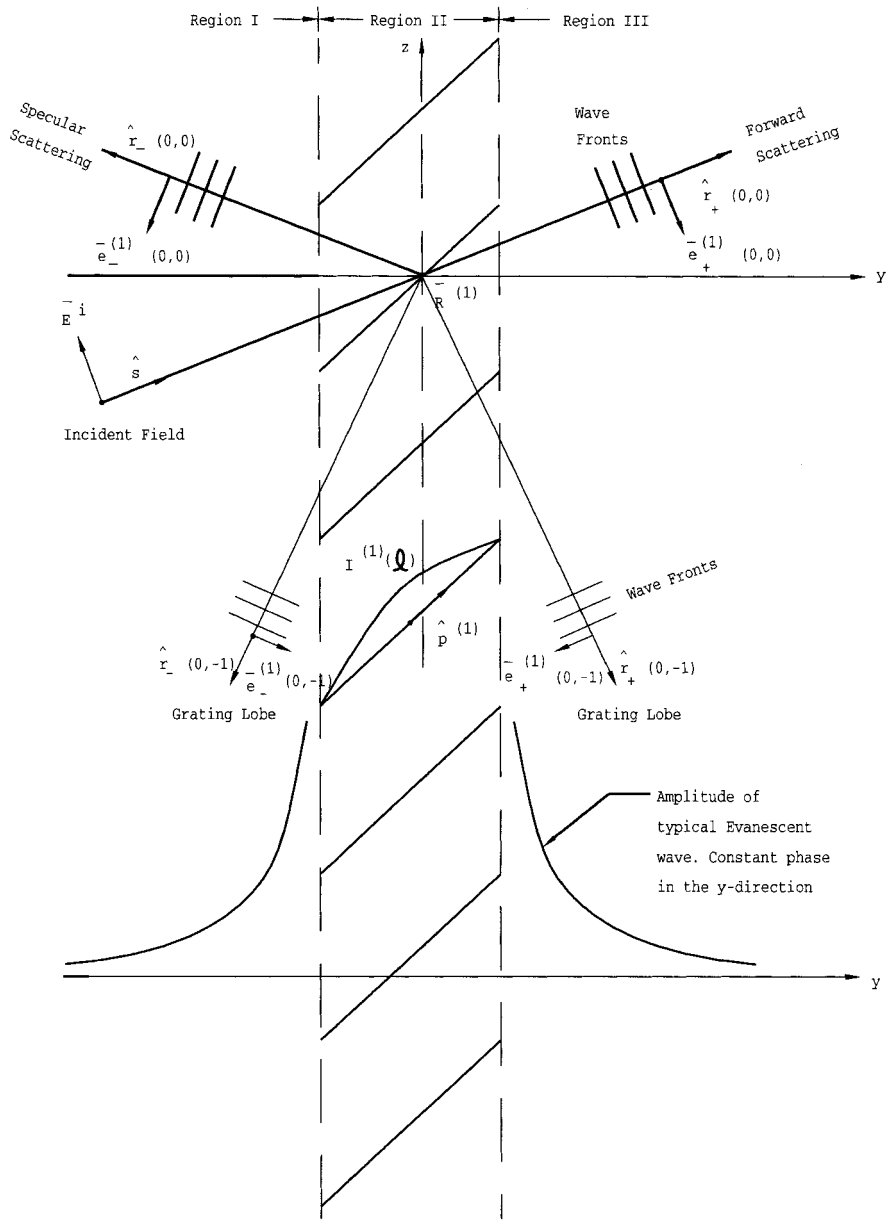

FIGURE 4.5. Illustration of the plane wave spectrum $\hat{r}_{\pm}$ emanating from an array with element orientation $\hat{p}^{(1)}$ and current distribution $I^{(1)}(l)$. *Top:* propagating modes showing the specular reflected, forward, and a finite number of grating lobes if D_x and D_z are large enough. *Bottom:* Evanescent waves shown to fall off exponentially as we move away from the array with no change of phase.

as we move away from the array. By inspection of the exponential term above, it is easy to see that this is the case if we choose $r_y = -j\sqrt{}$ and if we define $\hat{r}_\pm$ as given by Eq. 4.24. (This conclusion can of course also be arrived at by a purely mathematical argument. However, if one is lucky enough to arrive at the correct sign, it is usually an indication that an even number of sign errors were committed!)

We finally remind the reader that we started our investigation by finding the vector potential $d\bar{A}$ for a double infinite array of Hertzian dipoles by simply adding them element by element, namely summing over row number m and column q. We often refer to this as the element or the spatial space.

By repeated use of Poisson's sum formula (4.9), we transformed this double infinite series in element space m, q into another double infinite series in (k, n)-space. As seen above, this merely constitutes an expansion into plane, inhomogeneous waves each with directions $\hat{r}_\pm$ determined by the summation indexes (k, n); in other words, it has nothing to do with the individual elements whatsoever. We often refer to this new space as the spectral domain, or in this book simply the (k, n)-space. The values of (k, n) where r_y is real (i.e., corresponds to propagating waves) are often referred to as *real space*, while similarly those values leading to imaginary r_y (i.e., evanescent waves) are denoted *imaginary space*.

Recall the field vector $\bar{e}_\pm^{(1)}$ and pattern function $P^{(1)}$ given by Eqs. (4.31) and (4.39), respectively. For propagating waves (i.e., r_y real) it is easy to verify that $\bar{e}_\pm^{(1)}$ will be orthogonal to $\hat{r}_\pm$, real and pointing downward as indicated by Fig. 4.5 top. Note that $\bar{e}_\pm^{(1)}$ is not a unit vector but actually less than unity in real space because $\hat{p} \times \hat{r}_\pm = |\hat{p}||\hat{r}_\pm| \sin(\hat{p}, \hat{r})$. However, in imaginary space the situation becomes more complex so further discussion about this subject is postponed until Section 4.8. It should merely now be stated that in general $\bar{e}_\pm^{(1)}$ will diverge for $k, n \to \infty, \infty$. However, luckily it is to be multiplied with the exponential term $e^{-j\beta(\bar{R}-\bar{R}')\cdot\hat{r}_\pm}$ that is more strongly convergent in (k, n)-space than anything else. (See also Problem 4.4 concerning this issue.)

Let us now remind the reader that the field from the array was given by (4.38) and (4.39). It is extremely interesting to compare this expression with the far field for a single element similar to the reference element, as shown in Fig. 4.6 top, namely having the same orientation $\hat{p}^{(1)}$ and same current $I^{(1)}(l)$. Let us denote the direction to the point of observation $\bar{R}$ by the unit vector $\hat{R}$. It is then well known that the far field from the single element is given by

$$\bar{E}_{\text{far}}^{(1)}(\bar{R}) = I^{(1)}\left(\bar{R}^{(1)}\right) \frac{jZ}{2\lambda} \frac{e^{-j\beta|\bar{R}-\bar{R}^{(1)}|}}{|\bar{R}-\bar{R}^{(1)}|} \bar{e}_{\text{far}}^{(1)} P_{\text{far}}^{(1)}, \tag{4.42}$$

where

$$\bar{e}_{\text{far}}^{(1)} = \left(\hat{p}^{(1)} \times \hat{R}\right) \times \hat{R} \tag{4.43}$$

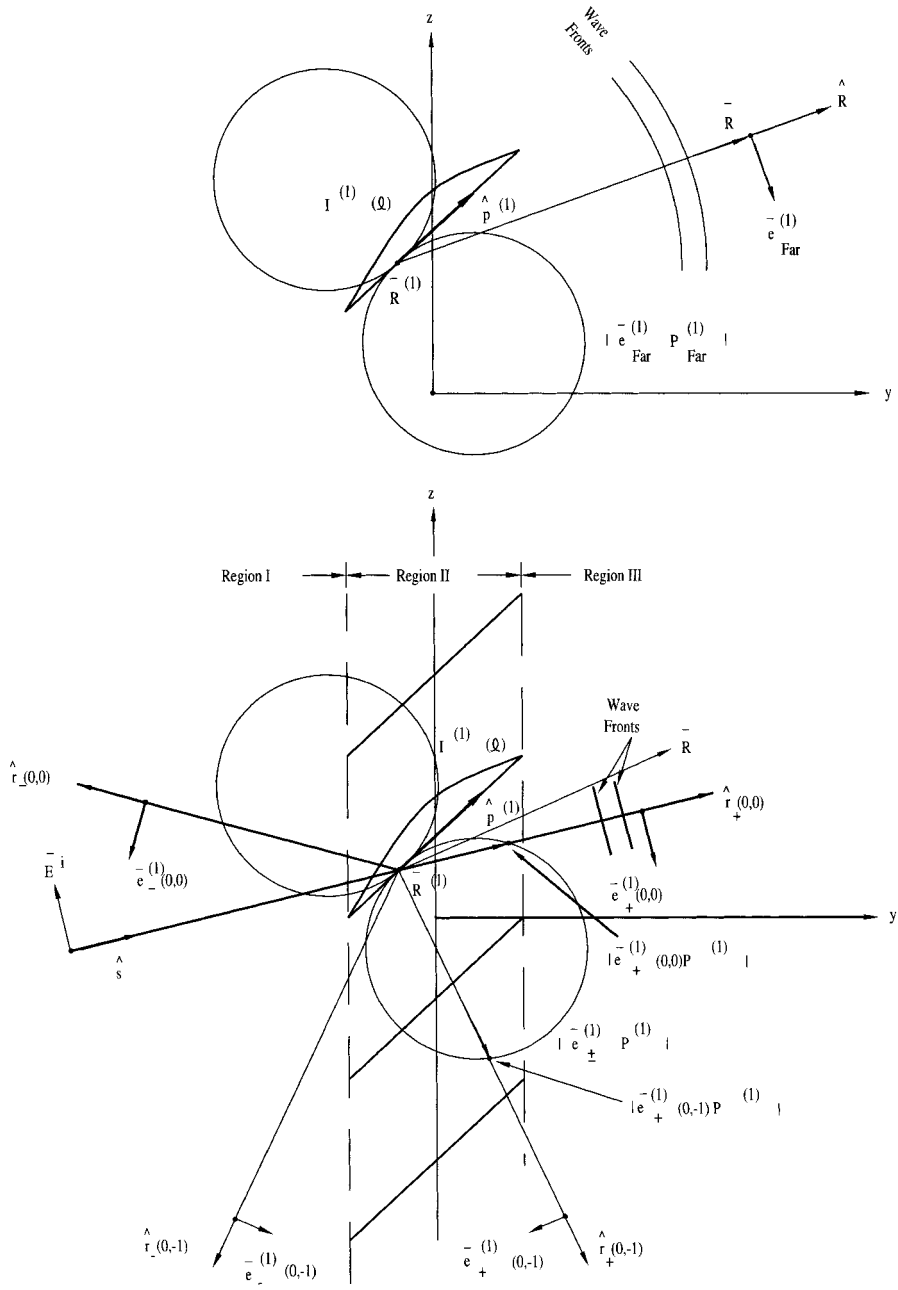

FIGURE 4.6. The far field from a single element shown at the top is given by $|\bar{e}^{(1)}_{\text{far}} P^{(1)}_{\text{far}}|$. Similarly the plane wave spectrum for the array shown at the bottom is weighted by the same function $|\bar{e}^{(1)}_{\pm} P^{(1)}|$ in the discrete directions $\hat{r}_{\pm}$, even for the evanescent waves which can be considered as being merely grating lobes in imaginary space.

and

$$P_{\text{far}}^{(1)} = \frac{1}{I^{(1)}\left(\bar{R}^{(1)}\right)} \int_{\text{Single Ele.}} I^{(1)}(l) e^{+j\beta l \hat{p}^{(1)} \cdot \hat{R}}\, dl. \tag{4.44}$$

The similarity between (4.38) and (4.39) referring to a double infinite array and (4.42), (4.43), and (4.44) referring to a single element is somewhat confusing.

First of all, the exponential term in the element expression (4.42) denotes a spherical wave emanating from $\bar{R}^{(1)}$ and not a plane wave spectrum as was the case for the array. Further the relative magnitude of the far field is given by $\left|\bar{e}_{\text{far}}^{(1)} P_{\text{far}}^{(1)}\right|$ where we recognize that $\left|\bar{e}_{\text{far}}^{(1)}\right| = \sin(\hat{p}, \hat{R})$ simply is the well known obliquity factor associated with a Hertzian element. In the array case shown in Fig. 4.6 bottom, the factor $\left|\bar{e}_{+}^{(1)}(0, 0) P^{(1)}\right|$ still denotes the same pattern as for the single element above; however, it acts only as a weight function for the waves in the spectral directions $\hat{r}_{\pm}$.

Note further that the single element pattern is subject to direct measurement in real space, but only the spectral directions continue from the real into imaginary space. In fact the pattern function $P^{(1)}$ [see Eq. (4.39)] for planar elements (i.e., $p_y = 0$) is basically unchanged when passing into the imaginary space; for example, it remains real for straight segments with symmetric modes. Suppose that $I^{(1)}(l) = I_0$ for $|l| < l_1$; then the pattern function $P^{(1)}$ is typically a simple $\sin x/x$ pattern as illustrated in Fig. 4.7. However, as we mentioned above, the field vector $\bar{e}_{\pm}^{(1)}$ will

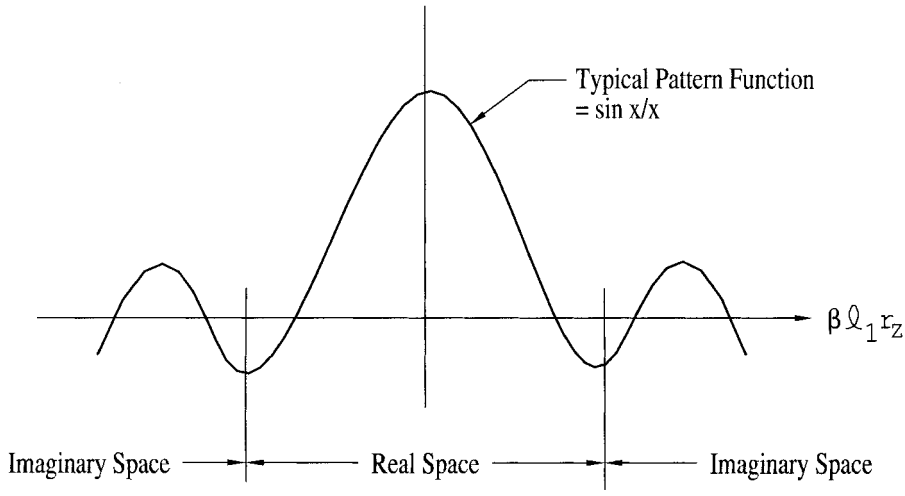

FIGURE 4.7. Typical pattern function $P^{(1)}$ as calculated from (4.39). The pattern function is completely "unfazed" when going from real to imaginary space if the element is planar, $p_y = 0$.

become complex as we pass into the imaginary space. This is one of many reasons why we have chosen to keep $\bar{e}_{\pm}^{(1)}$ and $P^{(1)}$ separate.

Variation with angle of incidence is also interesting. While the field of both the single element and will vary with $e_{\pm}^{(1)} P^{(1)}$, there will, in the array case, also be a strong variation as caused by r_y. We will later show that r_y plays a central role in the behavior of all periodic surfaces. Note further that the spherical waves from a single element are attenuated like $|\bar{R} - \bar{R}^{(1)}|^{-1}$, whereas the plane propagating waves (real space) in the array case are not attenuated at all. The reason is of course that we are never in the far field of an infinite structure. In fact, while the single element expressions (4.42) to (4.44) are valid only in the far field, the array expressions (4.38) to (4.39) are valid everywhere in regions I and III, and for planar elements region II disappears. As mentioned above, it is the evanescent waves that will dominate as our point of observation moves closer to the array.

4.7 INDUCED VOLTAGES IN A LINEAR ANTENNA

4.7.1 By a Single Plane Wave

Applying (4.38) to determine the field from a periodic structure assumes that we know the current $I^{(1)}(\bar{R}^{(1)})$ at the terminals $\bar{R}^{(1)}$. We also assume that we know the current distribution in order to determine $P^{(1)}$ from (4.39). If that is not the case, we must divide the elements up into mathematical sections like it is done in the method of moments (to be discussed later; see also Section 3.5).

In the case of a phased array, we impress the currents from individual generators (for an infinite array it makes no difference whether we use constant current or constant voltage generators). Thus we can in general assume that we know the current $I^{(1)}(\bar{R}^{(1)})$. However, if the structure is exposed to an incident field, we must determine the voltages induced in the elements and subsequently the element currents.

Let the linear antenna depicted in Fig. 4.8 be oriented in the direction $\hat{p}^{(1')}$ and have the current distribution $I^{(1')t}(l)$ when transmitting from the terminals at $\bar{R}^{(1')}$. If this antenna is exposed to a field $\bar{E}(\bar{R})$, then the induced voltage $V^{(1')}(\bar{R}^{(1')})$ will according to basic antenna theory [e.g., see Kraus [26], Schellkunoff [27], or the author's own antenna notes] be given by

$$V^{(1')} = \frac{1}{I^{(1')t}(\bar{R}^{(1')})} \int_{\text{Element } 1'} \bar{E}(\bar{R}) \cdot \hat{p}^{(1')t} I^{(1')t}(l)\, dl, \tag{4.45}$$

where $I^{(1')t}(\bar{R}^{(1')})$ denotes the terminal current[1]. Let the field $\bar{E}(\bar{R})$ be an incident plane wave propagating in the direction $\hat{s}$ as shown in Fig. 4.8:

$$\bar{E}(\bar{R}) = \bar{E}^i e^{-j\beta \bar{R} \cdot \hat{s}}. \tag{4.46}$$

[1]Note that (4.45) is actually valid for arbitrary shaped elements.

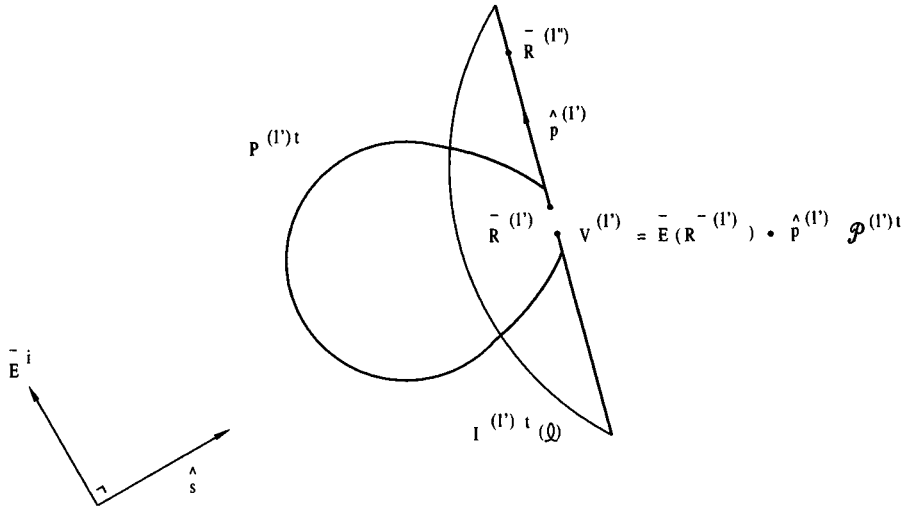

FIGURE 4.8. When a linear antenna with orientation $\hat{p}^{(1')}$ is exposed to an incident plane wave $\bar{E}^i$, we obtain the terminal voltage $V^{(1')} = \bar{E}^i \cdot \hat{p}^{(1')}\mathcal{P}^{(1')t}$ where $\mathcal{P}^{(1')t}$ is given by (4.50).

Substituting (4.46) into (4.45) we have

$$V^{(1')}(\bar{R}^{(1')}) = \bar{E}^i \cdot \hat{p}^{(1')} \frac{1}{I^{(1')t}(\bar{R}^{(1')})} \int_{\text{Element } 1'} I^{(1')t}(l) e^{-j\beta \bar{R}^{(1'')} \cdot \hat{s}}\, dl \qquad (4.47)$$

where $\bar{R}^{(1'')}$ denotes the position vector for an arbitrary point on the element along $\hat{p}^{(1')}$, namely

$$\bar{R}^{(1'')} = \bar{R}^{(1')} + \hat{p}^{(1')} l, \qquad a < l < b \qquad (4.48)$$

where a and b correspond to the endpoints of element $1'$. Substituting (4.48) into (4.47) yields

$$V^{(1')}(\bar{R}^{(1')}) = \bar{E}(\bar{R}^{(1')}) \cdot \hat{p}^{(1')} P^{(1')t}, \qquad (4.49)$$

where

$$P^{(1')t} = \frac{1}{I^{(1')t}(\bar{R}^{(1')})} \int_{\text{Element } 1'} I^{(1')t}(l) e^{-j\beta l \hat{p}^{(1')} \cdot \hat{s}} dl. \qquad (4.50)$$

$P^{(1')t}$ denotes the far field pattern of element $1'$ excluding the cosine of the angle between $\hat{p}^{(1')}$ and $\bar{E}(\bar{R}^{(1')})$. This is consistent with our definition earlier of the pattern function $P^{(1')}$ as given by (4.39).[2] Note also that in spite of the fact that we are cal-

[2]Note the difference in sign in the exponents of (4.39) and (4.50).

culating the voltage $V^{(1')}(\bar{R}^{(1')})$ under receiving conditions, the current distribution used in (4.50) is the one present under transmitting conditions. This apparent paradox is easily understood by the fact that the law of reciprocity was used in deriving (4.45). Equation (4.49) constitutes a very simple formula for obtaining the induced voltage in a linear antenna when exposed to an incident plane wave. It should be compared to the more well-known formula yielding the received power, namely

$$P_{\text{Rec}} = \frac{\lambda^2}{4\pi} G \frac{|E^i|^2}{Z}, \tag{4.51}$$

where G equals antenna gain. Both of these formulas are fundamental. For some reason (4.49) seems to be less known than (4.51). However, in this book we will make extensive use of the former, noting that (4.51) unfortunately contains no phase information.

4.7.2 By a Plane Wave Spectrum

Consider now the situation shown in Fig. 4.9 where an infinite array with element orientation $\hat{p}^{(1)}$ and current distribution $I^{(1)}(l)$ is producing a spectrum $\hat{r}_\pm$ of plane, inhomogeneous waves. Somewhere in region III is located an element with orientation $\hat{p}^{(1')}$ and transmitting current distribution $I^{(1')t}(l)$. This element may be a reference element of another array (shown in broken line), or it may simply be an individual external element that can be moved around for any purpose. We seek the voltage induced in the external element as caused by the field of array 1. This is a simple matter, since each of the plane inhomogeneous waves in the spectrum $\hat{r}$ will induce voltages in the external element as given by (4.49). Since all these quantities are scalars, they are added in simple algebraic fashion. Denoting the total voltage induced in element 2 as caused by all the currents in array 1 by $V^{1',1}$, we readily obtain, by substituting (4.38) into (4.49),

$$V^{1',1} = I^{(1)}(\bar{R}^{(1)}) \frac{Z}{2D_x D_z} \sum_{k=-\infty}^{\infty} \sum_{n=-\infty}^{\infty} \frac{e^{-j\beta(\bar{R}^{(1')} - \bar{R}^{(1)}) \cdot \hat{r}_\pm}}{r_y} \cdot \hat{p}^{(1')} \cdot \bar{e}_\pm^{(1)} P^{(1')t} P^{(1)} \qquad \text{for regions III and I.} \tag{4.52}$$

We finally define the so-called array mutual impedance $Z^{1',1}$ and obtain from (4.52),

$$Z^{1',1} = -\frac{V^{1',1}}{I^{(1)}(\bar{R}^{(1)})} = -\frac{Z}{2D_x D_z} \sum_{k=-\infty}^{\infty} \sum_{n=-\infty}^{\infty} \frac{e^{-j\beta(\bar{R}^{(1')} - \bar{R}^{(1)}) \cdot \hat{r}_\pm}}{r_y} \hat{p}^{(1')} \cdot \bar{e}_\pm^{(1)} P^{(1')t} P^{(1)} \qquad \text{for regions III and I.} \tag{4.53}$$

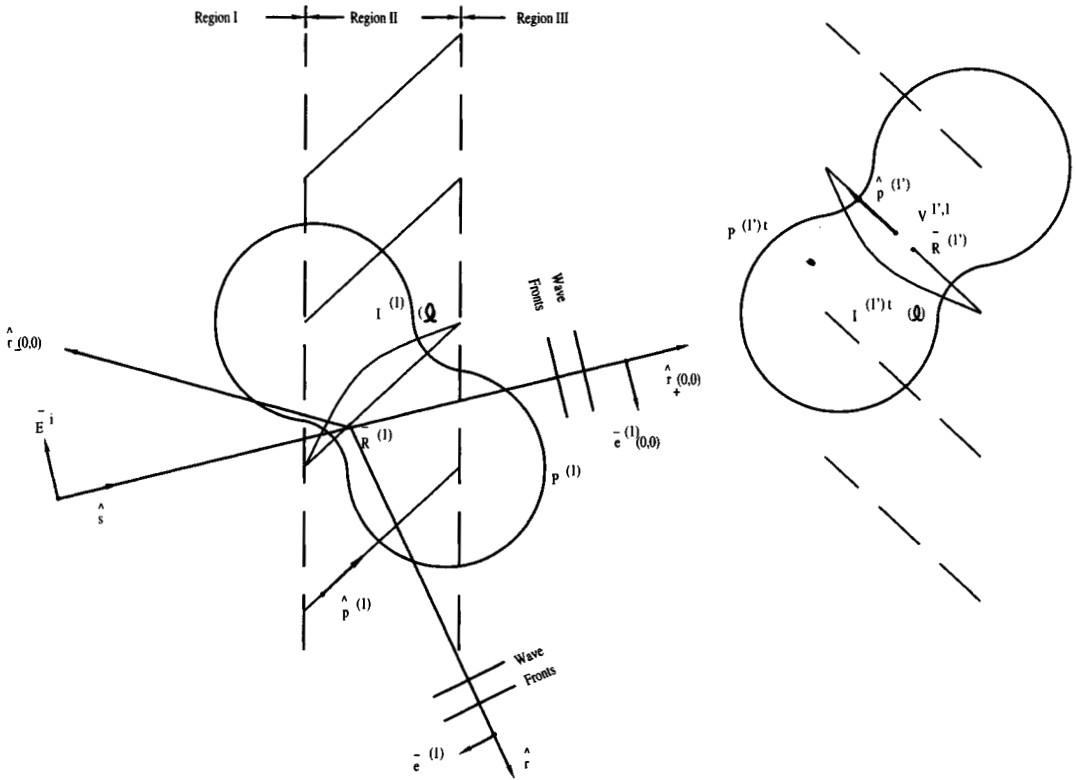

FIGURE 4.9. An external linear antenna with orientation $\hat{p}^{(1')\pm}$ is exposed to a plane wave spectrum $\hat{r}$ from an array. Each of the plane waves induces a voltage in the external element as shown in Fig. 4.8.

The product $\hat{p}^{(1')} \cdot \bar{e}_{\pm}^{(1)}$ can be written in an alternative form. From

$$\bar{e}^{(1)} = [\hat{p}^{(1)} \times \hat{r}] \times \hat{r}$$

we obtain from the vector identity (where we have dropped the $\pm$ subscript for brevity)

$$[\bar{A} \times \bar{B}] \times \bar{C} = (\bar{A} \cdot \bar{C})\bar{B} - (\bar{B} \cdot \bar{C})\bar{A}:$$

$$\bar{e}^{(1)} = (\hat{p}^{(1)} \cdot \hat{r})\hat{r} - \hat{r} \cdot \hat{r}\hat{p}^{(1)} = (\hat{p}^{(1)} \cdot \hat{r})\hat{r} - \hat{p}^{(1)} \tag{4.54}$$

We now define (see Fig. 4.10)

$$_{\perp}\hat{n} = \frac{\hat{n}_D \times \hat{r}}{|\hat{n}_D \times \hat{r}|} = \frac{-\hat{x}r_z + \hat{z}r_x}{\sqrt{r_x^2 + r_z^2}} \tag{4.55}$$

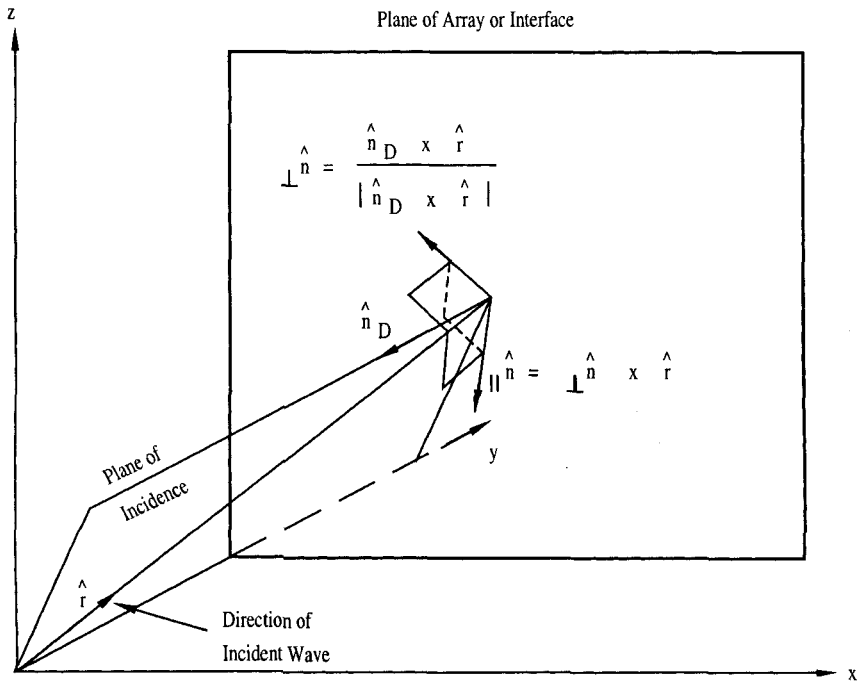

FIGURE 4.10. The plane of incidence is determined by the direction of incidence $\hat{r}$ and the inward unit vector $\hat{n}_D$ to the array. $_{\perp}\hat{n}$ is defined as orthogonal to the plane of incidence and $_{\parallel}\hat{n}$ as orthogonal to $_{\perp}\hat{n}$ and $\hat{r}$.

and

$$\|\hat{n} = \perp\hat{n} \times \hat{r} = \frac{1}{\sqrt{r_x^2 + r_z^2}}\left[-\hat{x}r_x r_y + \hat{y}(r_x^2 + r_z^2) - \hat{z}r_y r_z\right], \tag{4.56}$$

where $\hat{n}_D$ is normal to the plane of the array, namely equal to $-\hat{y}$. We next decompose $\bar{e}^{(1)}$ along $\perp\hat{n}$ and $\|\hat{n}$; that is, for arbitrary $\hat{p}$,

$$\perp\bar{e} = \perp\hat{n}\left[(\hat{p}\cdot\hat{r})(\hat{r}\cdot\perp\hat{n}) - \hat{p}\cdot\perp\hat{n}\right] = -\perp\hat{n}(\hat{p}\cdot\perp\hat{n}), \tag{4.57}$$

$$\|\bar{e} = \|\hat{n}\left[(\hat{p}\cdot\hat{r})(\hat{r}\cdot\|\hat{n}) - \hat{p}\cdot\|\hat{n}\right] = -\|\hat{n}(\hat{p}\cdot\|\hat{n}), \tag{4.58}$$

where we have used the fact that $\hat{r}\cdot\perp\hat{n} = 0$ and $\hat{r}\cdot\|\hat{n} = 0$. Substituting (4.57) and (4.58) into (4.53) obtains

$$Z^{1',1} = \frac{Z}{2D_x D_z}\sum_{k=-\infty}^{\infty}\sum_{n=-\infty}^{\infty}\frac{e^{-j\beta(\bar{R}^{(1')}-\bar{R}^{(1)})\cdot\hat{r}_+}}{r_y} \tag{4.59}$$

$$\cdot\left[\perp P^{(1)}\cdot\perp P^{(1')t} + \|P^{(1)}\|P^{(1')t}\right] \qquad \text{for element } 1' \text{ in region III.}$$

where the pattern components are defined as

$$\underset{\|}{\perp} P^{(1)} = \hat{p}^{(1)}\cdot\underset{\|}{\perp}\hat{n}P^{(1)} \tag{4.60}$$

and

$$\underset{\|}{\perp} P^{(1')t} = \hat{p}^{(1')}\cdot\underset{\|}{\perp}\hat{n}P^{(1')t}. \tag{4.61}$$

By decomposing the incident field $\bar{E}^i$ along $\perp\hat{n}$ and $\|\hat{n}$, we can similarly write (4.49) in an alternate form:

$$V^{(1')}\left(\bar{R}^{(1')}\right) = \bar{E}\left(\bar{R}^{(1')}\right)\cdot\hat{p}P^{(1')t}$$

$$= \perp E\,\hat{p}^{(1')}\cdot\perp\hat{n}P^{(1')t} + \|E\,\hat{p}^{(1')}\cdot\|\hat{n}P^{(1')t}.$$

Or by use of (4.61) we write

$$V^{(1')}\left(\bar{R}^{(1')}\right) = \perp E\perp P^{(1')t} + \|E\|P^{(1')t}. \tag{4.62}$$

4.8 MORE PHYSICAL INSIGHT

The array mutual impedance as given by (4.59) is extremely interesting to analyze more closely.[3] First of all, we observe that the distance $\bar{R}^{(1')} - \bar{R}^{(1)}$ is simply multiplied by the wave spectrum $\hat{r}_+$.

[3]In this book we often use just the notation "mutual impedance" when working with arrays, since the classical mutual impedance between elements is used only when specifically indicated.

4.8.1 Real Space: r_y Positive Real

For these directions the exponential term constitutes a simple phase delay with real as well as imaginary components as one would expect. Further let us consider the term in (4.59):

$$\frac{1}{r_y}\left[{}_{\perp}P^{(1)}{}_{\perp}P^{(1')t} + {}_{\parallel}P^{(1)}{}_{\parallel}P^{(1')t}\right]$$
$$= \frac{1}{r_y}\left[(\hat{p}^{(1)} \cdot {}_{\perp}\hat{n})(\hat{p}^{(1')} \cdot {}_{\perp}\hat{n})P^{(1)}P^{(1')t} + (\hat{p}^{(1)} \cdot {}_{\parallel}\hat{n})(\hat{p}^{(1')} \cdot {}_{\parallel}\hat{n})P^{(1)}P^{(1')t}\right]. \tag{4.63}$$

Inspection of (4.55) and (4.56) readily shows that ${}_{\perp}\hat{n}$ as well as ${}_{\parallel}\hat{n}$ are always real in real space and so are $P^{(1)}$, $P^{(1')t}$ for straight segments with even modes as well as r_y. In other words, (4.63) will always be real in real space.

4.8.2 Imaginary Space: r_y Negative Imaginary

In this case the exponential term in (4.53) is real. So are $P^{(1)}$, $P^{(1')t}$ and ${}_{\perp}\hat{n}$. However, ${}_{\parallel}\hat{n}$ will in general be complex. Let us specifically examine the most important case, namely the planar array where $p_y^{(1)}$ and $p_y^{(1')} = 0$. In that event we see from (4.56) that

$$\hat{p}^{(1)} \cdot {}_{\parallel}\hat{n} = \frac{r_y}{\sqrt{r_x^2 + r_z^2}}\left[p_x^{(1)}r_x - p_z^{(1)}r_z\right], \tag{4.64}$$

since every term in (4.64) is real except that r_y, $\hat{p}^{(1)} \cdot {}_{\parallel}\hat{n}$ will be pure imaginary for $p_y^{(1')} = 0$.

Thus (4.63) has in imaginary space the following signs:

$$\frac{1}{r_y}\left[(\hat{p}^{(1)} \cdot {}_{\perp}\hat{n})(\hat{p}^{(1')} \cdot {}_{\perp}\hat{n})P^{(1)}P^{(1')t} + (\hat{p}^{(1)} \cdot {}_{\parallel}\hat{n})(\hat{p}^{(1')} \cdot {}_{\parallel}\hat{n})P^{(1)}P^{(1')t}\right]$$
$$= \frac{1}{-\text{imag}}\left[\text{real} \cdot \text{real} + \text{imag} \cdot \text{imag}\right]$$
$$= \frac{1}{-\text{imag}}\left[\text{real} - \text{real}\right]; \tag{4.65}$$

that is to say, it is purely imaginary. When the two terms in brackets are equal, we have resonance, and similarly we have either a capacitive or inductive impedance when they are different. We will return to this subject several times later in this book.

4.9 REGION II

So far we have considered the cases only where the point of observation $\bar{R}$ is located in either regions I and III. If the elements are planar ($p_y = 0$), region II will disappear and all the equations given above for regions I and III are completely adequate. However, if the elements are tilted out of the plane of the array, things are more complicated as illustrated in Fig. 4.11. The reason is simply that the plane wave spectrum starting on each Hertzian array will have both left- and right-going waves. Thus a point of observation somewhere in region II will be exposed to right-going

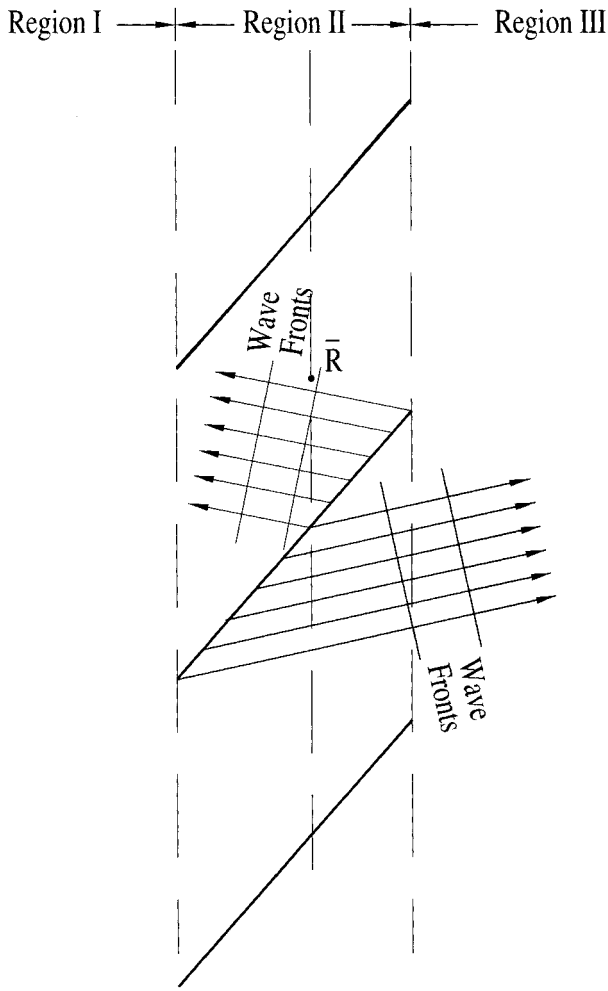

FIGURE 4.11. A point of observation $\bar{R}$ in region II will be exposed by left-going waves from the part of the elements located to the right of $\bar{R}$, and vice versa for the part located to the left.

waves originating on the part of the Hertzian elements that are located to the left and similarly to left-going waves from all the Hertzian arrays located to the right. It leads to a nested integral that conceptually is simple but rather tedious to solve. It has been done by several of the author's graduate students (now successful professionals). Arrays with tilted elements have found some use as spatial filters (transparent when the direction of incidence $\hat{s}$ equals the element orientation $\hat{p}$); see Errol English [28]. Brian Kent considered square loops orthogonal to the plane of the array in a stratified medium [29], while Kwong Ng [30] considered the Clavin element, which is a slot array with protruding monopoles (of arbitrary tilt) that provide scan independence. Jim Lin [31] considered arrays of inverted V-dipoles including the feed lines. This problem was also solved by Schuman et al. [32]. Finally Rob Andrè [33] devised a unique approach by considering triple infinite arrays.

In this book we are primarily interested in the planar case[4] and will therefore not cover region II much further but refer to the references given above. However, we will still treat the arbitrary tilted array in Chapter 5 where we will introduce a stratified medium. We do this primarily for tutorial reasons as observed later.

4.10 SELF-IMPEDANCE OF A SINGLE ELEMENT AND OF ARRAYS

Consider a single dipole element of finite thickness being center fed by a single voltage generator V as shown in Fig. 4.12 top-left. This element is admittedly a little fat so that we may better show how to evaluate the input impedance $Z_{\text{in}} = V/I$ shown in Fig. 4.12 right. We split up the continuous surface of the original dipole into discrete current fibers i, each fed by voltage generators V. The mutual impedance between fibers 0 and n is denoted $Z_{0,n}$ where we recall that we use subscripts when referring to the mutual impedance between elements (fibers). Writing the generalized Ohm's law for fiber 0 (as was done in (3.3)), we obtain

$$V = Z_{0,0} i_0 + i \sum_{n=1}^{N} Z_{0,n} \sim i \sum_{n=1}^{N} Z_{0,n}, \tag{4.66}$$

where $Z_{0,0}$ denotes the self-impedance of fiber 0. Since the fiber thickness is infinitely thin, the self-reactance of this fiber is infinite resulting in negligent fiber current i_0. Thus the total current $I_{\text{tot}} = Ni$ and

$$Z_{\text{in}} = \frac{V}{I_{\text{tot}}} = \frac{V}{Ni}. \tag{4.67}$$

Substituting (4.66) into (4.67), we have

$$Z_{\text{in}} = \frac{1}{N} \sum_{n=1}^{N} Z_{0,n}. \tag{4.68}$$

[4]But still with arbitrary element shapes in the plane of the array (see Chapter 2).

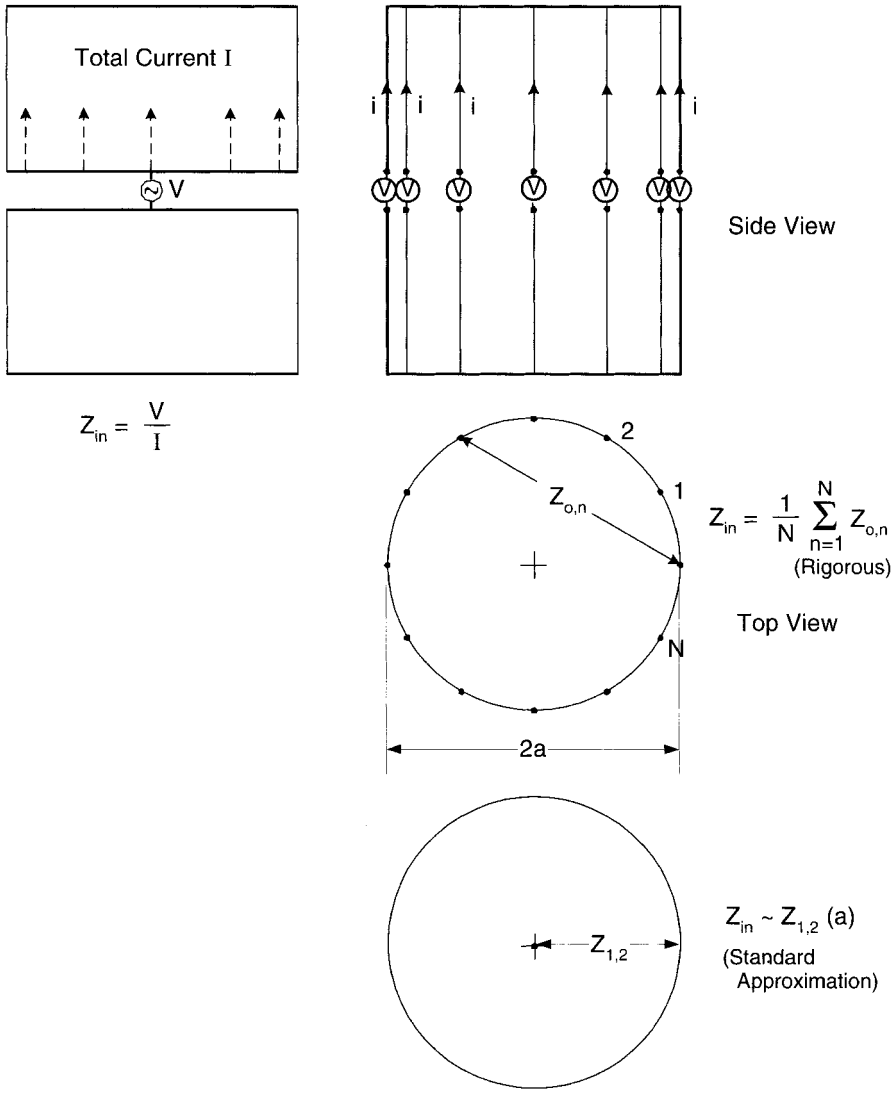

FIGURE 4.12. *Top-left:* The input impedance Z_{in} of a dipole is defined as the ratio between the terminal voltage V and the total current I. *Top-right* and *middle:* Z_{in} is calculated by splitting the total surface current up into fibers 0–N with mutual impedance $Z_{0,n}$. Then $Z_{\text{in}} = \frac{1}{N}\sum_{n=1}^{N} Z_{0,n}$. *Bottom-right:* A standard approximation yields Z_{in} as the mutual impedance between two fibers at a distance of one wire radius, but may not be valid for tilted elements located in an array.

Equation (4.68) is completely rigorous if $N \to \infty$; that is, the summation goes into an integral. However, it can be shown that (4.68) can be approximated by merely the mutual impedance between two elements placed a wire radius apart as shown in Fig. 4.12 bottom. This approximation is standard procedure in the ordinary method of moments.

When dealing with periodic structures, the approach is basically the same as in the single-element case. Namely we merely bring the external element (e.g., in Fig. 4.9) within a wire radius a of the reference element. This is perfectly allright as long as the elements are located in the plane of the array, meaning that $p_y = 0$. The external element can be located in front of or in back of the reference element as well as to the sides (in the plane of the array). However, when the elements are nonplanar ($p_y \neq 0$), the external element must be placed at least in four positions simultaneously, and then the average must be taken, as indicated by (4.68). The reason for this procedure is simply that the field around and close to the element may vary significantly in the tilted case. (For examples of this technique, see [28, 29, 30, 31, 32].)

In summary, we may state that the self-impedance of a planar array is obtained from (4.59) simply by placing the external element at $\bar{R}^{(2)} - \bar{R}^{(1)} = \hat{y}a$:

$$Z_A = \frac{Z}{2D_x D_z} \sum_{k=-\infty}^{\infty} \sum_{n=-\infty}^{\infty} \frac{e^{-j\beta a r_y}}{r_y} \left[{}_{\perp}P_{\perp}P^t + {}_{\parallel}P_{\parallel}P^t \right] \tag{4.69}$$

where we have dropped the element superscript since both pattern functions refer to the array reference element. As discussed above, if there are no grating lobes, all the terms in (4.69) will be imaginary except the term $k = n = 0$, namely

$$R_A = ReZ_A = \frac{Z}{2D_x D_z} \frac{1}{r_y} \left[{}_{\perp}P_{\perp}P^t + {}_{\parallel}P_{\parallel}P^t \right] \tag{4.70}$$

where we have put $e^{-j\beta a r_y} \sim 1$. Note that for planar elements ${}_{\perp}^{\parallel}P$ and ${}_{\perp}^{\parallel}P^t$ are always conjugates when evaluating the self-impedance [see (4.39) and (4.50)]. In imaginary space r_y becomes large, and the exponential term must be retained. It is remarkable that R_A (4.70) can be expressed in closed form by just one term. (See also Problem 4.4.)

4.11 EXAMPLES

The derivation above has admittedly been somewhat lengthy and at times tedious. Hopefully the following examples will illustrate how simply a periodic structure can be evaluated and at the same time give physical insight.

4.11.1 Example I: Scattering from an Array of z-Directed Elements

Consider an array located in the xz-plane with z-directed elements of radius a, loaded at their center with a load impedance Z_L. This configuration is exposed to an inci-

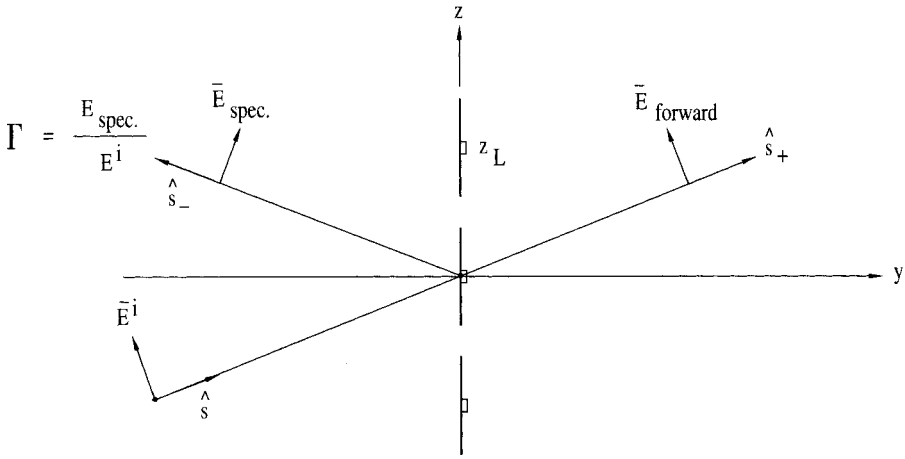

FIGURE 4.13. A double infinite array of z-directed elements with load impedance Z_L is being exposed to an incident plane wave. A re-radiated field will be produced in the specular as well as the forward directions.

dent plane wave propagating in the direction $\hat{s}$ as shown in Fig. 4.13. We seek the reflection coefficient Γ in the specular direction.

The voltage V induced at the "terminals" is given by (4.49) with $\hat{p} = \hat{z}$:

$$V = \bar{E}^i \cdot \hat{z} P^t \tag{4.71}$$

where P^t denotes the pattern function for the reference element under transmitting condition (even if we are actually receiving!); see (4.50). Denoting the terminal impedance by Z_A as given by (4.69), we readily find the terminal current I_A from Thevenin's equivalent circuit:

$$I_A = \frac{V}{Z_A + Z_L}. \tag{4.72}$$

We further assume that we know the form of the current distribution $I(l)$ under receiving (scattering) condition and consequently the pattern function P as given by (4.39). (If that is not the case, see Sections 3.5 and 4.13.) The scattered (reradiated) field is then given by (4.38), or by application of (4.57), (4.58), and (4.60):

$$\bar{E}(\bar{R}) = -I_A \frac{Z}{2D_x D_z} \sum_{k=-\infty}^{\infty} \sum_{n=-\infty}^{\infty} \frac{e^{-j\beta \bar{R}\cdot \hat{r}_\pm}}{r_y} \left[{}_\perp\hat{n}_{\pm\perp} P + {}_\parallel\hat{n}_{\pm\parallel} P \right]. \tag{4.73}$$

Expression (4.73) constitutes the entire reradiated spectrum from the array, namely propagating as well as evanescent waves. Typically we are interested only in the field at some distance from the array where all the evanescent waves have died out and only the propagating waves are left. If we further assume that the inter-element spacings D_x and D_z are so small that no grating lobes are present in the

frequency band of interest [see (4.41)], we will only encounter the waves reflected in the specular and forward directions. Substituting (4.72) into (4.73) for $k = n = 0$, we obtain for the specular field $\bar{E}_{\text{spec}}$ in the direction $\hat{s}_-$,

$$\bar{E}_{\text{spec}} = -\frac{V}{Z_A + Z_L}\frac{Z}{2D_xD_z}\frac{1}{r_y}\left[{}_{\perp}\hat{n}_-{}_{\perp}P + {}_{\parallel}\hat{n}_-{}_{\parallel}P\right]e^{-j\beta\bar{R}\cdot\hat{s}_-} \qquad \text{for } y < 0. \tag{4.74}$$

We now limit our investigation to where the plane of incidence is either in the H-plane (xy-plane) or the E-plane (yz-plane) as shown in Fig. 4.14.

Also we require the incident field $\bar{E}^i$ to be oriented as

$$\bar{E}^i = {}_{\perp}\hat{n}E^i \quad \text{for H-plane scan,} \tag{4.75}$$

$$\bar{E}^i = {}_{\parallel}\hat{n}E^i \quad \text{for E-plane scan.} \tag{4.76}$$

[Equations (4.75) and (4.76) are consistent with $\bar{E}^i$ being a plane wave.] Substituting (4.75) and (4.76) into (4.71) and making use of (4.61) yields

$$V = \bar{E}^i \cdot \hat{z}P^t = \begin{cases} E^i{}_{\perp}P^t & \text{for H-plane scan,} \\ E^i{}_{\parallel}P^t & \text{for E-plane scan.} \end{cases} \tag{4.77}$$

Substituting (4.77) into (4.74) yields for the reflection coefficient for the H- and E-planes

$$\begin{matrix}{}_{\perp} \\ {}_{\parallel}\end{matrix}\Gamma = \frac{E_{\text{spec}}(0)}{E^i(0)} = -\frac{1}{Z_A + Z_L}\frac{Z}{2D_xD_z}\frac{1}{r_y}\begin{cases}{}_{\perp}P{}_{\perp}P^t & \text{for H-plane scan} \\ {}_{\parallel}P{}_{\parallel}P^t & \text{for E-plane scan}\end{cases}. \tag{4.78}$$

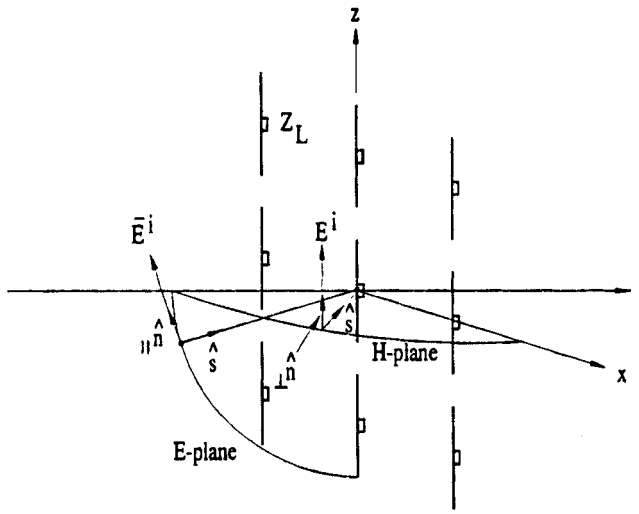

FIGURE 4.14. Same double infinite array as shown in Fig. 4.13 but the incident plane wave is being restricted to the principal planes.

Comparing (4.70) and (4.78) and noting that ${}_{\parallel}P_{\parallel}P^t = 0$ for the H-plane scan and ${}_{\perp}P_{\perp}P^t = 0$ for the E-plane scan in real space, we can write (4.78) as

$$\begin{matrix}\perp \\ \parallel\end{matrix}\Gamma = -\frac{R_A}{Z_A + Z_L} = -\frac{R_A}{R_A + (jX_A + Z_L)} \tag{4.79}$$

for principal planes only, that is, and no grating lobes. Inspection of (4.79) shows that $\begin{matrix}\perp \\ \parallel\end{matrix}\Gamma = -1$ only for $Z_L = -jX_A$; in other words, Z_L must be pure imaginary and tune out X_A to produce a resonance. If Z_L has a real component, $|\Gamma| < 1$.

It is simple to verify that an equivalent circuit of (4.79) consists of merely the impedance $jX_A + Z_L$ over a transmission line with characteristic impedance $2R_A$ as shown in Fig. 4.15.

It is important to note that R_A as well as X_A vary with angle of incidence. Thus so will Γ. If the inter-element spacings D_x/λ and D_z/λ are small, the variation of X_A will be small. However, R_A will always vary significantly unless the array is located in a stratified medium; see Chapter 5.

Thus, to understand the behavior of the scattering properties of frequency selective surfaces as well as phased arrays, it is of utmost importance to study R_A. It will be the subject of the next example.

4.11.2 Example II: Investigation of R_A

The general expression for the real part of the terminal impedance Z_A is given by (4.70). As in the previous example our array consists of z-directed elements as shown in Fig. 4.14, and we also limit our investigation to the H- and E-planes. We further assume the elements to be Hertzian in nature, namely of very short length Δl with constant current.

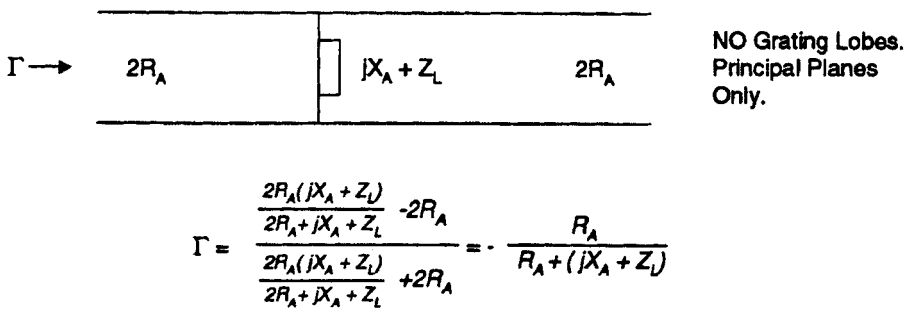

FIGURE 4.15. The equivalent circuit for the array shown in Fig. 4.14. Only valid for the principal planes and for no grating lobes.

H-Plane Scan (xy-Plane)

$$
\begin{aligned}
{}_{\perp}P^t &= \hat{z} \cdot {}_{\perp}\hat{n}P^t = \Delta l, \\
{}_{\parallel}P^t &= \hat{z} \cdot {}_{\parallel}\hat{n}P^t = 0.
\end{aligned}
$$

Thus from (4.70),

$$
R_A = \frac{Z}{2D_xD_z}\frac{\Delta l^2}{r_y} = \frac{Z}{2D_xD_z}\frac{\Delta l^2}{\cos\eta}, \tag{4.80}
$$

for no grating lobes where η is the angle measured from broadside; see Figs. 2.1 and 4.16 bottom, where $r_y = \cos\eta$.

E-Plane Scan (yz-Plane)

$$
\begin{aligned}
{}_{\perp}P^t &= \hat{z} \cdot {}_{\perp}\hat{n}P^t = 0, \\
{}_{\parallel}P^t &= \hat{z} \cdot {}_{\parallel}\hat{n}P^t \sim r_y\Delta l.
\end{aligned}
$$

Thus

$$
R_A = \frac{Z}{2D_xD_z}\frac{r_y^2\Delta l^2}{r_y} = \frac{Z}{2D_xD_z}\Delta l^2\cos\eta, \tag{4.81}
$$

for no grating lobes. Thus we observe that R_A will increase like $1/\cos\eta$ in the H-plane and decrease like $\cos\eta$ in the E-plane as illustrated in Fig. 4.16.

Understanding this variation of R_A with scan angle is fundamental when working with FSS as well as phased arrays. Although the elements considered here were Hertzian in nature, it is important to realize that longer or more complex elements all have the same fundamental behavior. (The pattern factors P and P^t never vary much with scan angle η in real space unless very long or complex.) Besides, a larger element leads in general to larger D_x and D_z, namely to larger variation of X_A with scan angle (earlier onset of grating lobes), and thus larger variation of the resonant frequency (the gangbuster and square spiral arrays are the exceptions). This is the number one problem in FSS design. Keeping the inter-element spacings D_x and D_z small requires small elements. This can be accomplished by some kind of element loading Z_L (see Section 2.3; see also Section 5.13.1 for actual calculated cases).

4.11.3 Example III: Variation of Γ with Scan Angle

Having determined the variation of R_A with scan angle, it is now a simple matter to obtain an estimate of Γ as given by (4.79). We will assume that the element spacings D_x and D_z are small enough for X_A to vary only with frequency and not significantly with angle of incidence (typically $< 0.35\lambda$). Conversely, R_A will not vary much with frequency but, as we saw in example II, significantly with angle of incidence η.

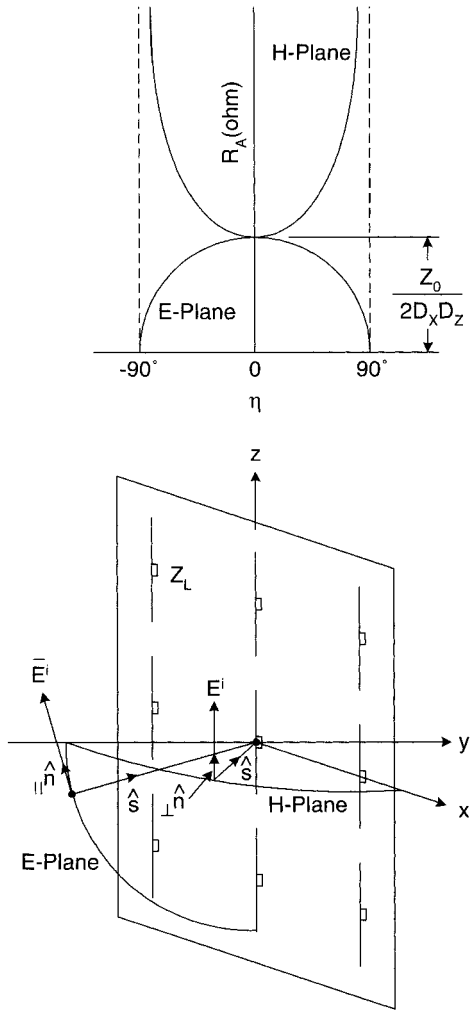

FIGURE 4.16. *Top*: the variation with scan angle of the terminal resistance R_A for an array of Hertzian-like elements (*bottom*). Note how the E- and H- planes vary completely opposite each other.

Inspection of (4.79) then readily shows that the typical reflection coefficient curves will look like those shown in Fig. 4.17 where we show these curves for normal and 60° in the H- and E-planes. Since $\cos 60° = 0.5$, we readily observe that these curves double their bandwidth in the H-plane ($\perp$-plane) and vice versa in the E-plane ($\|$-plane). This bandwidth variation is basic for all FSS designs. This author is not aware of a single planar element that is able to make much more than a dent in this problem. It is possible to turn to three-dimensional elements such as the Clavin element investigated by Ng [30] or the inverted V-dipole investigated by Lin [31].

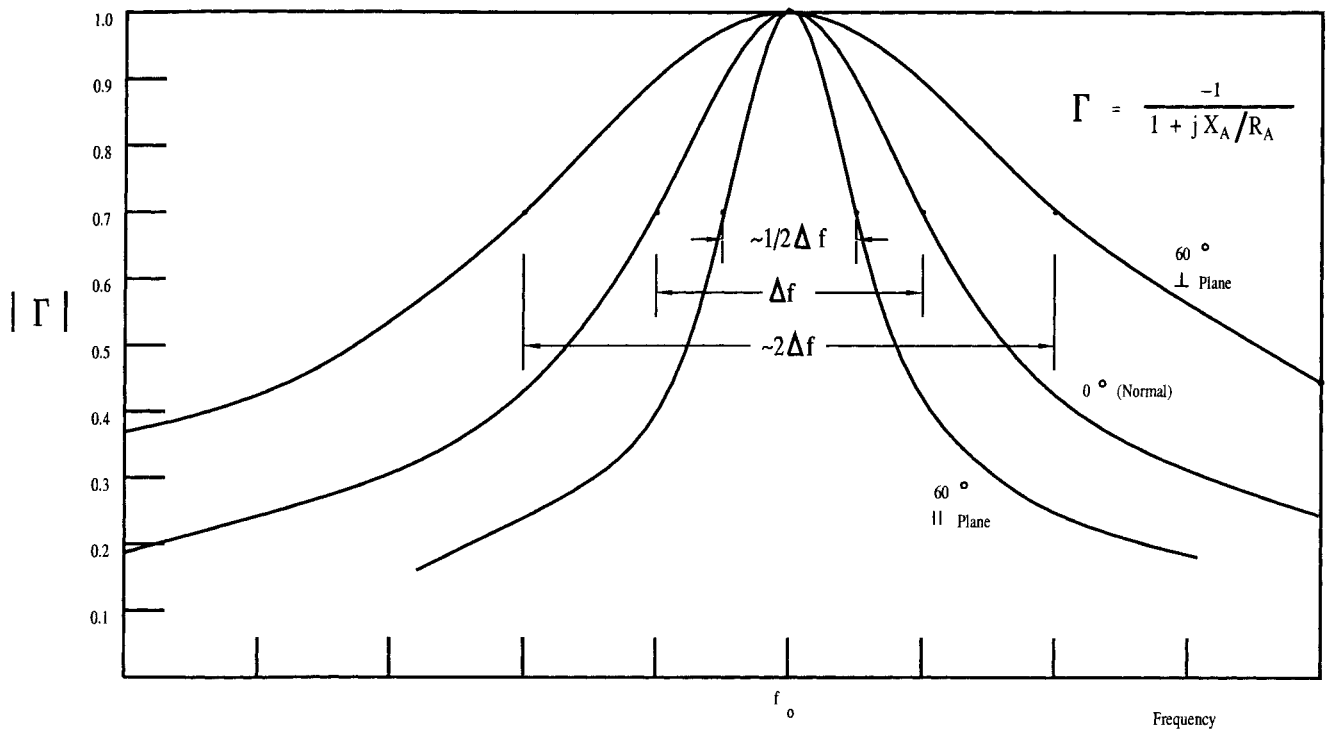

FIGURE 4.17. Typical reflection curves for a periodic structure where X_A varies very little with angle of incidence, since D_x and $D_z < 0.35\lambda$. Note the inherent bandwidth variation with angle of incidence as caused by variation of R_A.

However, the simplest and most elegant solution is to place the array in a stratified dielectric medium. We will study this subject in Chapter 5.

4.11.4 Example IV: Scan Impedance Z_A as a Function of Scan Angle; Surface Waves

In example II above we investigated the real part R_A of the complex scan impedance Z_A as a function of scan angle, meaning our periodic surface is active. We will now examine the entire scan impedance Z_A at a fixed frequency when the scan angle varies from broadside and all the way into the imaginary space.

By programming (4.69), we readily obtain Z_A for a typical array of z-directed elements as shown in Figs. 4.17 and 4.18. We simply scan horizontally by varying s_x through the values 0, $\frac{1}{2}$, and $\frac{\sqrt{3}}{2}$ corresponding to the scan angles 0°, 30°, and 60° from broadside, respectively. For $s_x = 1$ corresponding to grazing, radiation Z_A has a singularity. However, for $s_x > 1$, Z_A becomes purely imaginary, reaching its lowest value for $s_x = \frac{1}{2}(\lambda/D_x) = 2.082$ corresponding to $\beta D_x s_x = \pi$. For higher values of s_x, Z_A simply returns along the imaginary axis into real space at $s_x = \lambda/D_x - 1 = 3.164$ along the same path it followed coming in. Note, however, that for $2.08 < s_x < 3.164$ the surface wave goes in the negative direction.

When Z_A is located on the imaginary axis, the fields surrounding the array will consist of only evanescent waves; that is, no energy radiates from the array, which accounts for Z_A being purely imaginary. For the specific value $s_x = 1.33$, we observe that $Z_A = 0$. This simply implies that the impressed element voltages V_n can be equal to zero and the field surrounding the array can still exist once they have been put in motion. This situation constitutes a surface wave, and more specifically a *free surface wave* as opposed to *forced surface waves* associated with values of s_x when Z_A is imaginary and $\neq 0$; that is, $V_n \neq 0$ in order for them to exist. They basically look like the free ones but must constantly be forced ahead by the element generators V_n. (See also Chapters 5 and 6.)

We remind the reader that the evanescent waves cannot excite an antenna located in the "far" field. Conversely, by reciprocity we conclude that a "distant" antenna (producing an incident plane wave) cannot excite a surface wave. While this is exact for an infinite array as considered so far, it becomes much more complicated when the array is finite. In that case the surface wave will simply start radiating in an endfire mode along the plane of the array and can consequently be picked up by a distant antenna.

Conversely, an incident plane wave can excite a surface wave along the finite array in addition to the ordinary Floquet currents as expressed by (4.2). These two sets of currents will in general have different phase velocity resulting in a ripple of the total currents as one moves along the array. This situation is typical of all *finite arrays*. The key to alleviate this problem will in general be to suppress the surface wave radiation, for example, by use of suitable loads placed at the end of the finite array.

We finally note that had we performed the calculations in Fig. 4.18 at a somewhat higher frequency such as 10 GHz, all the values for Z_A would have been pushed

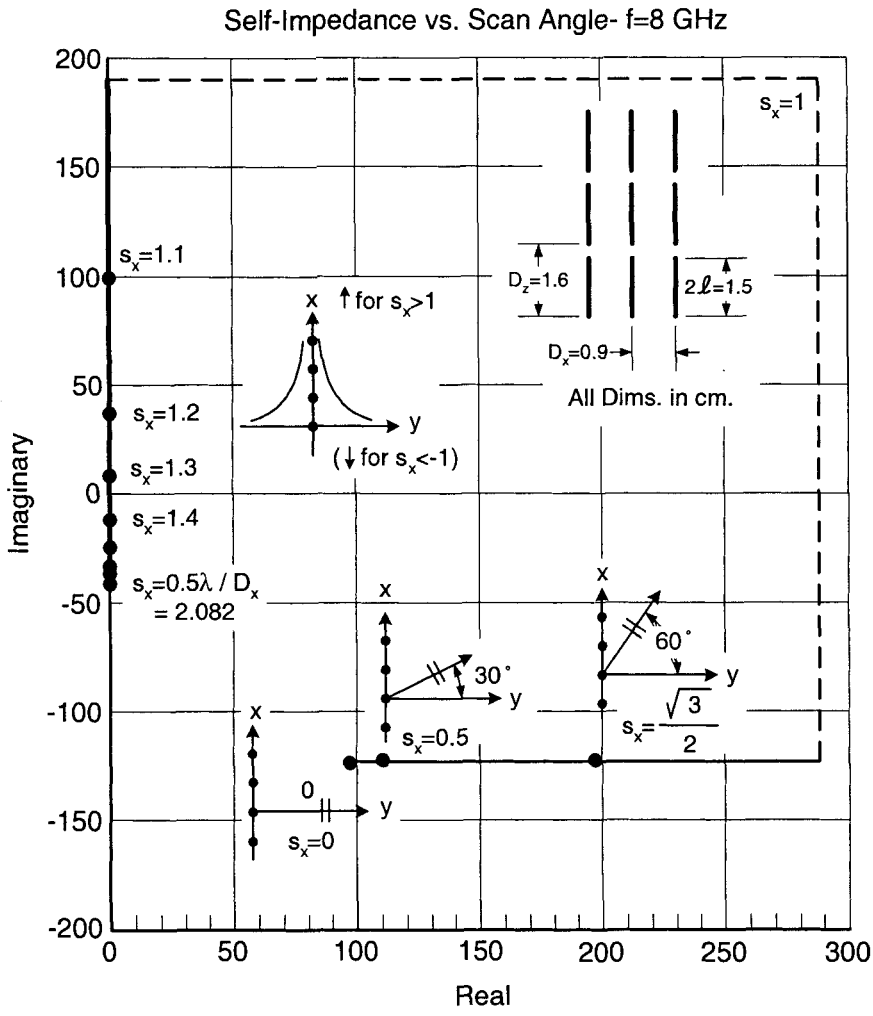

FIGURE 4.18. The scan impedance Z_A (schematic) for an array of z-directed elements at 8 GHz as a function of s_x, cosine to the scan angle. For $1 < s_x < 3.164$ Z_A is purely imaginary and the field surrounding the array consists of only evanescent waves. Their sum can be interpreted as a surface wave. $D_x/\lambda < \frac{1}{2}$.

upward by about $j120$ ohm. More specifically that means that the imaginary values of Z_A for $s_x > 1$ would simply always be above the real axis; no free surface wave could exist at that frequency. Typically surface waves producing array resonances are encountered at frequencies 10% to 30% below the resonance and for small values of D_x.

Alternatively, if the elements were loaded capacitively with $\sim -j120\ \Omega$, a surface wave at 10 GHz would be possible. If the elements were loaded inductively,

the possibility is reduced. Surface waves are even more prominent when a stratified dielectric medium is added (see Chapters 5 and 6).

4.12 PLANAR ELEMENTS OF ARBITRARY SHAPE

So far we have considered only straight elements of arbitrary orientation $\hat{p}^{(1)}$. However, in Chapter 2 we presented a variety of elements that, with few exceptions, was not in that category whatsoever. In this section we will expand the general theory to include planar elements of arbitrary shape.

4.12.1 Total Radiated Field from an Array with Segmented Elements

In Fig. 4.19 we show an array of elements comprised of two sections with orientations $\hat{p}^{(1)}$ and $\hat{p}^{(2)}$. Notice that the two arrays associated with each section have the same inter-element spacings D_x and D_z. Thus they will have the same plane wave spectrum $\hat{r}_\pm$ as given by (4.24) and (4.25). We further choose $\bar{R}^r$ as the reference point where the two segments meet and denote the element current $I(l)$ at this point by $I(\bar{R}^r)$. Then, by a simple extension of (4.38), we obtain for the total field $\bar{E}^t$ at $\bar{R}$,

$$\bar{E}^t(\bar{R}) = I(\bar{R}^r)\frac{Z}{2D_xD_z}\sum_{k=-\infty}^{\infty}\sum_{n=-\infty}^{\infty}\frac{e^{-j\beta(\bar{R}-\bar{R}^r)\cdot\hat{r}_\pm}}{r_y}\left[\bar{e}_\pm^{(1)}P^{(1)} + \bar{e}_\pm^{(2)}P^{(2)}\right]$$

$$\text{for } y \gtrless 0, \tag{4.82}$$

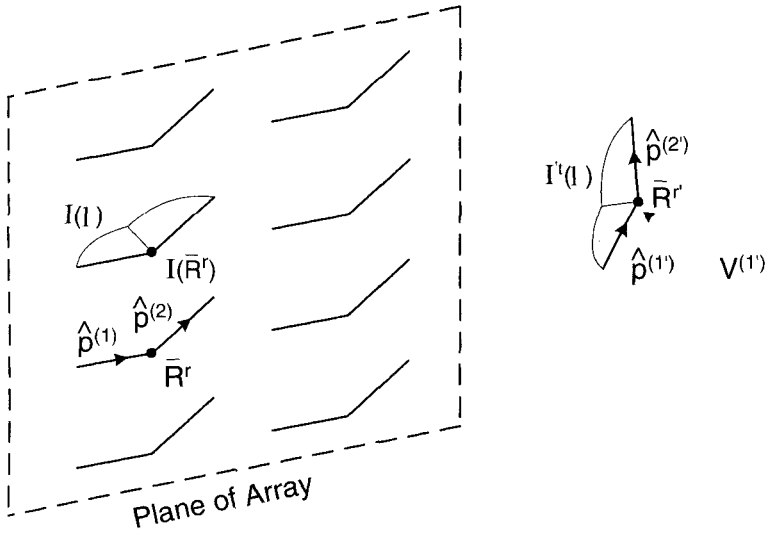

FIGURE 4.19. An array with elements comprised of two sections with orientations $\hat{p}^{(1)}$ and $\hat{p}^{(2)}$. Also shown is an external element with orientations $\hat{p}^{(1')}$ and $\hat{p}^{(2')}$.

where the field vector from (4.31) is $\bar{e}_{\pm}^{(1)} = \left[\hat{p}^{(1)} \times \hat{r}_{\pm}\right] \times \hat{r}_{\pm}$ and analogous for $\bar{e}_{\pm}^{(2)}$ by substituting $\hat{p}^{(2)}$ for $\hat{p}^{(1)}$ while $P^{(1)}$ is obtained from (4.39) as

$$P^{(1)} = \frac{1}{I(\bar{R}^r)} \int_{\text{Section 1}} I(l) e^{j\beta l \hat{p}^{(1)} \cdot \hat{r}_{\pm}} dl \tag{4.83}$$

and analogous for $P^{(2)}$ by substituting $\hat{p}^{(2)}$ for $\hat{p}^{(1)}$ and integrating over section 2. The two field vectors $\bar{e}_{\pm}^{(1)}$ and $\bar{e}_{\pm}^{(2)}$ will in general not only have different amplitudes but also different directions. However, the unit vectors ${}_{\perp}\hat{n}$ and ${}_{\parallel}\hat{n}$ depend only on $\hat{r}_{\pm}$ and the normal to the array; see (4.55) and (4.56). They will therefore be independent of the element orientation $\hat{p}^{(1)}$ and $\hat{p}^{(2)}$. Thus it is pertinent to decompose the field vectors $\bar{e}_{\pm}^{(1)}$ and $\bar{e}_{\pm}^{(2)}$ along ${}_{\perp}\hat{n}$ and ${}_{\parallel}\hat{n}$. By use of (4.57) and (4.58), we can write (4.82) as

$$\begin{aligned}
\bar{E}^t(\bar{R}) &= -I(\bar{R}^r) \frac{Z}{2D_x D_z} \sum_{k=-\infty}^{\infty} \sum_{n=-\infty}^{\infty} \frac{e^{-j\beta(\bar{R}-\bar{R}^r)\cdot\hat{r}_{\pm}}}{r_y} \Big[{}_{\perp}\hat{n} \Big[\left(\hat{p}^{(1)} \cdot {}_{\perp}\hat{n}\right) P^{(1)} \\
&\quad + \left(\hat{p}^{(2)} \cdot {}_{\perp}\hat{n}\right) P^{(2)} \Big] + {}_{\parallel}\hat{n} \Big[\left(\hat{p}^{(1)} \cdot {}_{\parallel}\hat{n}\right) P^{(1)} + \left(\hat{p}^{(2)} \cdot {}_{\parallel}\hat{n}\right) P^{(2)} \Big] \Big] \\
&= -I(\bar{R}^r) \frac{Z}{2D_x D_z} \sum_{k=-\infty}^{\infty} \sum_{n=-\infty}^{\infty} \frac{e^{-j\beta(\bar{R}-\bar{R}^r)\cdot\hat{r}_{\pm}}}{r_y} \\
&\quad \Big[{}_{\perp}\hat{n} \left({}_{\perp}P^{(1)} + {}_{\perp}P^{(2)} \right) + {}_{\parallel}\hat{n} \left({}_{\parallel}P^{(1)} + {}_{\parallel}P^{(2)} \right) \Big] \text{ for } y \gtrless 0,
\end{aligned} \tag{4.84}$$

where ${}_{\perp}^{\parallel}P^{(1)}$ and ${}_{\perp}^{\parallel}P^{(2)}$ are defined by an extension of (4.60).

4.12.2 Induced Voltage in a Segmented Element

Consider now an external element comprised of two sections with orientation $\hat{p}^{(1')}$ and $\hat{p}^{(2')}$ and reference point $\bar{R}^{r'}$ determined by the intersection point of the two segments as also shown in Fig. 4.19. Denoting the current under transmitting conditions by $I'^t(l)$, we obtain by an extension of (4.49) for the induced voltage when exposed to an incident plane wave

$$V^{(1')}(\bar{R}^r) = \bar{E}(\bar{R}^{r'}) \cdot \left[\hat{p}^{(1')} P^{(1')t} + \hat{p}^{(2')} P^{(2')t} \right], \tag{4.85}$$

where $P^{(1')t}$ and $P^{(2')t}$ are defined by extension of (4.50). Substituting (4.84) into (4.85) for $\bar{E}^t(\bar{R})$, we have

$$\begin{aligned}
V^{(1')}(\bar{R}^{r'}) &= -I(\bar{R}^r) \frac{Z}{2D_x D_z} \sum_{k=-\infty}^{\infty} \sum_{n=-\infty}^{\infty} \frac{e^{-j\beta(\bar{R}^{r'}-\bar{R}^r)\cdot\hat{r}_{\pm}}}{r_y} \\
&\quad \cdot \Big[\Big[\hat{p}^{(1')} \cdot {}_{\perp}\hat{n} P^{(1')t} + \hat{p}^{(2')} \cdot {}_{\perp}\hat{n} P^{(2')t} \Big] \Big[{}_{\perp}P^{(1)} + {}_{\perp}P^{(2)} \Big]
\end{aligned}$$

$$+\left[\hat{p}^{(1')}\cdot {}_{\parallel}\hat{n}\,P^{(1')t}+\hat{p}^{(2')}\cdot {}_{\parallel}\hat{n}\,P^{(2')t}\right]\left[{}_{\parallel}P^{(1)}+{}_{\parallel}P^{(2)}\right]\Big]$$

$$\text{for } y \gtrless 0. \tag{4.86}$$

Extending (4.61) finally yields

$$V^{(1')}(\bar{R}^{r'}) = -I(\bar{R}^{r})\frac{Z}{2D_xD_z}\sum_{k=-\infty}^{\infty}\sum_{n=-\infty}^{\infty}\frac{e^{-j\beta(\bar{R}^{r'}-\bar{R}^{r})\cdot\hat{r}_{\pm}}}{r_y}$$
$$\cdot\Big[\Big[{}_{\perp}P^{(1')t}+{}_{\perp}P^{(2')t}\Big]\Big[{}_{\perp}P^{(1)}+{}_{\perp}P^{(2)}\Big]$$
$$+\Big[{}_{\parallel}P^{(1')t}+{}_{\parallel}P^{(2')t}\Big]\Big[{}_{\parallel}P^{(1)}+{}_{\parallel}P^{(2)}\Big]\Big]. \tag{4.87}$$

4.12.3 Mutual Impedance $Z^{1',1}$ for Arrays with Segmented Elements

Finally we obtain from (4.87) the mutual impedance $Z^{1',1}$:

$$Z^{1',1} = -\frac{V^{(1')}(\bar{R}^{r'})}{I(\bar{R}^{r})}$$
$$= \frac{Z}{2D_xD_z}\sum_{k=-\infty}^{\infty}\sum_{n=-\infty}^{\infty}\frac{e^{-j\beta(\bar{R}^{r'}-\bar{R}^{r})\cdot\hat{r}_{\pm}}}{r_y}\Big[\Big[{}_{\perp}P^{(1')t}+{}_{\perp}P^{(2')t}\Big]$$
$$\cdot\Big[{}_{\perp}P^{(1)}+{}_{\perp}P^{(2)}\Big]+\Big[{}_{\parallel}P^{(1')t}+{}_{\parallel}P^{(2')t}\Big]\Big[{}_{\parallel}P^{(1)}+{}_{\parallel}P^{(2)}\Big]\Big]. \tag{4.88}$$

The expression for the mutual impedance as given by (4.88) is valid for two sections on all elements. However, the extension to an arbitrary number of segments on all elements is easily obtained by simply adding more pattern components ${}_{\perp}^{\parallel}P^{(n)}$ and ${}_{\perp}^{\parallel}P^{(n')t}$ in the brackets in (4.85). In that most general case we can then write (4.88) as

$$Z^{1',1} = \frac{Z}{2D_xD_z}\sum_{k=-\infty}^{\infty}\sum_{n=-\infty}^{\infty}\frac{e^{-j\beta(\bar{R}^{r'}-\bar{R}^{r})\cdot\hat{r}_{\pm}}}{r_y}\Big[{}_{\perp}P^{c't}\cdot{}_{\perp}P^{c}+{}_{\parallel}P^{c't}\cdot{}_{\parallel}P^{c}\Big] \tag{4.89}$$

where we have defined the composite pattern components as

$${}_{\perp}^{\parallel}P^{c} = {}_{\perp}^{\parallel}\hat{n}\cdot\Big[\hat{p}^{(1)}P^{(1)}+\hat{p}^{(2)}P^{(2)}+\cdots+\hat{p}^{(p)}P^{(p)}\Big] \tag{4.90}$$

and

$${}_{\perp}^{\parallel}P^{c't} = {}_{\perp}^{\parallel}\hat{n}\cdot\Big[\hat{p}^{(1')}P^{(1')t}+\cdots+\hat{p}^{(p')}P^{(p')t}\Big]. \tag{4.91}$$

The reference points $\bar{R}^r$ and $\bar{R}^{r'}$ can be chosen arbitrarily for each element but usually such that the evaluation of the pattern components is simplified as much as possible.

The expression for $Z^{1',1}$ is crucial for calculation of the scattering performance of FSS with elements of arbitrary shape. These expressions are the backbone of the PMM program. See also Section 3.5.

4.13 COMMON MISCONCEPTIONS

4.13.1 Interpretation of Plane Wave Expansion

Perhaps the most common misunderstanding of the plane wave expansion or PMM as given, for example, by (4.38) is that it constitutes a sum of spherical waves (the direction cosine r_y is confused by some to be a distance parameter). It just cannot be emphasized enough that $\hat{r}$ constitutes directions of the plane inhomogeneous waves and not rays. As a consequence of this thinking, it often puzzles the casual reader how a voltage can be induced in an external element that is not located somewhere in the directions $\hat{r}_{\pm}$. Again, as shown for example in Fig. 4.9, we go out of our way to remind the reader that plane waves have infinitely wide wave fronts that eventually will hit everything!

A related question is: At what distance from the array is our field expression (4.38) valid? Since the pattern function P looks like a simple far field pattern, it is often assumed that in order to be rigorous, the point of observation should be located at least at some "respectable" distance from the array (when dealing with infinite arrays, we will never be in the far field in the classical sense). Actually, as we move closer to the array, we will start to pick up the evanescent waves. Their amplitude are proportional to P and $\hat{p} \cdot_{\perp\!\!\!\parallel} \hat{n}$ but evaluated in imaginary space. Certainly the field expression will blow up at the center of the infinitely thin element fibers like all wire antennas in general will do. But the field expression is completely valid everywhere thanks to the evanescent waves. (See also Sections 4.10 and 5.15.4, as well as Problems 4.4 and 4.5.)

4.13.2 Current Distribution

Another concern is that the approach taken here is based on unknown assumptions, in particular the shape of the current distributions $I(l)$ and $I(l)^t$ under receiving and transmitting conditions, respectively. To this, it should be emphasized that the approach taken here is completely exact if $I(l)$ and $I(l)^t$ both are known in shape. True, we may not always know these or even be able to estimate a reasonable approximation. In that event we simply split up the elements into shorter mathematical segments, each with its own assumed current distributions called *modes*. If these segments are short (0.10–0.30λ), $I(l)$ and $I(l)^t$ on each segment becomes practically the same and the same modes are used for both (we recommend in general the sinusoidal mode for both). We then treat the problem as if it consists of as many arrays as

there are modes. Solving this configuration of arrays is as accurate as the method of moments. In fact we always use this approach when doing actual computer calculations, for example, as in the element calculations shown in Chapter 2. However, the physical insight is better appreciated when we use the total currents $I(l)$ and $I(l)^t$ (one "mode"). Note that the general expression for Γ, as given by (4.79), was obtained without any assumption of $I(l)$ and $I(l)^t$ except that they existed. Not before we actually make a detailed calculation of Γ for arbitrary incidence do we need to resort to the method of moments. Actually this approach is crucial in the design of the dielectric profile of a hybrid radome, for example (as discussed in Chapter 7). The more exact calculations are then done subsequently as the basic layout is known.

Note also that Γ in Fig. 4.15 becomes zero only for $Z_L = \infty$, namely for an open circuit. Obviously this is not quite correct since even short half-elements will scatter some energy (Raleigh region). Our mistake here is that our assumption of a sinusoidal current distribution as shown in Fig. 4.20 left breaks down when $Z_L = \infty$ as shown to the right. Of course these concerns are automatically taken care of when we use the method of moments as discussed earlier.

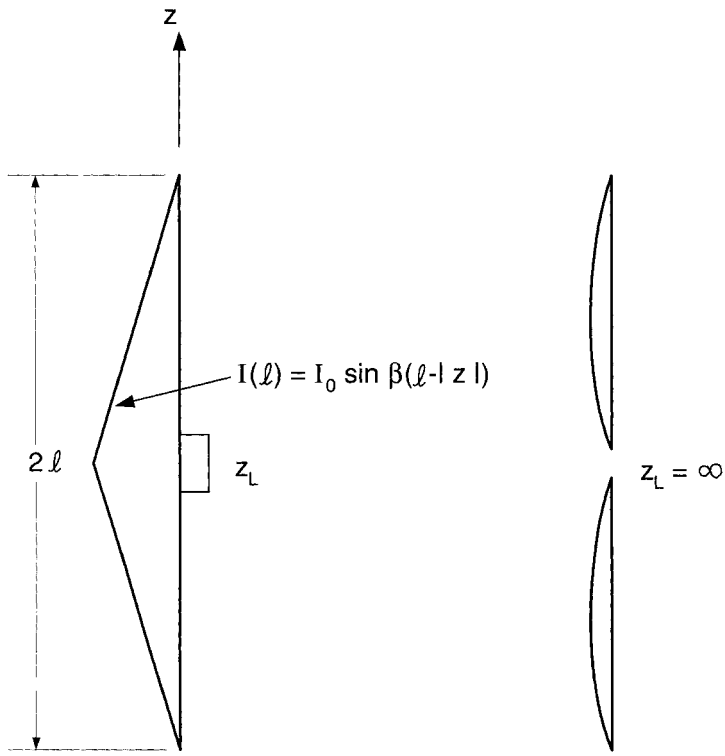

FIGURE 4.20. Typical current distribution on a loaded element for $|Z_L| < |Z_A|$, *left*, and for $Z_L = \infty$, *right*.

4.13.3 Concept of Unit Cells

It will be observed from our derivation above that nowhere do we restrict ourselves to the elements being bounded to an area sometimes referred to as a *unit cell.* And why should we? Our entire derivation is simply based on the array grid (rectangular or skewed) with elements of arbitrary shape and orientation. Period! But certainly, the elements should not overlap? Actually, while "real" elements touching or crossing each other would be a disaster, the elements in our derivations may actually cross each other and yield the "correct" result as long as we do not put a connector mode between the two elements. A typical example is shown in Fig. 2.35 top, where tripoles are actually crossing each other without a connector mode. The practical execution would be to simply split up the elements putting half on each side of a very thin dielectric sheet.

Of course the designer should be aware when such an indiscretion occurs. That is just another good reason for always printing out a picture of the actual desired array.

The unit cells concept derives from the theory of waveguides. While it makes sense in that case (obviously), we have no need for it here. How would you, for example, define a unit cell for the anchor element in Fig. 2.12, not to mention the square spiral in Fig. 2.14? Any approach that cannot handle overlapping elements of arbitrary shape has a serious flaw.

4.13.4 Length of Element Segments

From our first encounter with infinitesimal calculus, we learned to approximate curves by decomposing them into straight segments. Mathematically we obtained perfect accuracy by letting the length of the segments go to zero. As a result of this thinking, there is often a strong tendency to use many short segments when modeling the elements of a periodic surface. However, as shown, for example, by Lee Henderson, in his dissertation [2], this is in general not a good idea. First of all, small segments lead to many segments. This simply means that a very large matrix has to be inverted [e.g., see Fig. 3.9 and (3.23)]. And everyone knows how time-consuming this can be! But what is perhaps worse is the fact that the computation time for calculating the self-impedance of each small segment goes up considerably as we make the segments shorter. A physical explanation is obtained by inspection of the formulas for the self impedance given, for example, by (4.89) to (4.91) which typically contains one or more pattern functions as depicted in Fig. 4.9. As the summation indexes (k, n) increase, we quickly move into imaginary space when the various terms of (4.89) are multiplied by the pattern functions that typically have sidelobes with values considerably lower than the main beam; that is, the pattern functions will in general help the convergence of (4.89). As the elements become shorter, the sidelobes move further out into imaginary space crippling the convergence.

Thus in general it is better to use somewhat long segments ($< 0.6\lambda$) that eventually can be bent (as discussed in Section 4.12). In short, great accuracy and short computation time is obtainable by using long overlapping bent segments. See also [2–7].

4.14 CONCLUDING REMARKS

We have obtained an expression for the mutual impedance between two planar arrays, both of which may have elements of arbitrary shape. Basically it consists of a plane wave expansion with a finite number of propagating and an infinite number of evanescent waves. The directions $\hat{r}_{\pm}$ depend only on the inter-element spacings D_x/λ and D_z/λ. The waves in each direction are weighted with the product of the orthogonal and parallel pattern components for the reference elements, namely ${}_{\perp}P^{(1)}{}_{\perp}P^{(1')t} + {}_{\parallel}P^{(1)}{}_{\parallel}P^{(1')t}$. For planar straight elements with symmetric current, this product will always be real. However, for the evanescent waves, r_y becomes imaginary. The self-impedance of the array is obtained from the mutual impedance expression by simply placing the reference element and the external element at a distance equal to one wire radius. This implies that if we have only one propagating mode set (i.e., no grating lobes) the real part $R_A = ReZ_A$ consists of only one term corresponding to $k = n = 0$. All other terms are imaginary. We also demonstrated by examples how R_A and X_A play a vital role in understanding the fundamental nature of periodic structures, and this will become even more important in design applications shown later, for example, in band filter designs in Chapters 7 and 8. We finally remind the reader that two of the most important features of all antennas are their impedance and radiation pattern. These are usually calculated separately without any obvious connection between them. What is interesting is that we have shown that for a double infinite periodic structure, the impedance and the radiation pattern are directly dependent on each other. This has a strong similarity to some early papers by Wasylkiwskyj and Kahn [34, 35] for single minimum scattering elements that correspond to an array with infinite large inter-element spacings. Also the plane wave expansion as presented here is reminiscent of the grating lobe expansion. However, while the latter has certain restrictions on current distribution and element orientation, the present formulation treats current distributions as well as element orientations that are completely arbitrary.

4.15 PROBLEMS

4.1 Grating Lobe Diagrams Consider an infinite array with element orientation $\hat{p} = \hat{z}$ and element length $2l = 0.50\lambda$. Consider further two cases of inter-element spacings:

Case I: $D_x = 0.35\lambda \quad D_z = 0.60\lambda$

Case II: $D_x = 0.70\lambda \quad D_z = 0.60\lambda$

Find:

a. The scan angles for which grating lobe(s) first occur when scanning only in the E-plane and only in the H-plane, respectively, for both cases I and II.

b. Find and plot the curves in the s_x, s_z-plane for which the onset of grating lobe(s) occurs for fixed values of k, n. Show the curves for $k = 0, \pm 1, \pm 2$, and $n = 0, \pm 1, \pm 2$. Indicate the real space as well as part of the invisible space for cases I and II. Check your answers against item 1 above.

Alternatively, we could have plotted these curves in the r_x, r_z-plane. Both representations are valid and have advantages and disadvantages. See also Section 5.14.

4.2 The Pattern Function and R_A For the same array as given in Problem 4.1 above,

a. Find the pattern function P^t. Plot it in the interval $-5 < s_x < 5$ for $s_z = 0, n = 0$ and in the interval $-5 < s_z < 5$ for $s_x = 0, k = 0$. Indicate the boundary between the real and imaginary spaces.

Assume that the current distribution $I^t(z) = I_0 \sin \beta(l - |z|)$.

b. Plot $\hat{p} \cdot {}_{\perp}\hat{n}$ and $\hat{p} \cdot {}_{\parallel}\hat{n}$ in the same intervals for s_x and s_z as in item *a* above.

c. Finally, plot R_A in the same ranges as above for both cases I and II. Compare with Problem 3.1 and Section 4.11.2. *Note:* Comments on physical observations are always welcome.

4.3 Alternative Evaluation of R_A Based on Physical Insight

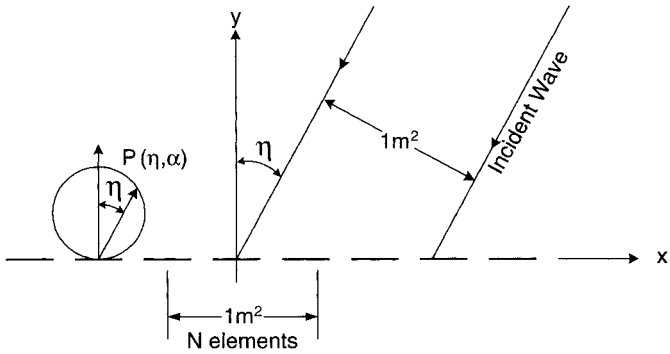

Fig. P4.3

Let an infinite planar array be exposed to an incident plane wave at an angle of incidence equal to η as shown. We denote the radiation pattern of a single element by $P(\eta, \alpha)$, while the scan impedance $Z_A = R_A + j0$ (as seen in the array).

a. What is the received power per element proportional to, as expressed by the element pattern function P and the scan resistance R_A?

b. We further denote the number of elements per m^2 of the array area by N. What is the number of elements inside 1 m^2 of the incident plane wave at incident angle η?

c. Find the total received power by the array elements inside a wave cross section of 1 m^2 expressed by N, $\cos\eta$, P, and R_A. We assume that all incident power is absorbed, nothing reflected.

d. Find the functional dependence of R_A on P and $\cos\eta$.

e. For a simple Hertzian element we can assume that

$$P \propto \begin{cases} 1 & \text{for H-plane scan,} \\ \cos\eta & \text{for E-plane scan.} \end{cases}$$

Find the functional dependence of R_A on $\cos\eta$, and compare with Section 4.11.2 as well as Problem 4.2.

f. If we require R_A to be independent of the scan angle η, find what condition we must impose on P.

The old timers were quite familiar with this reasoning. They had no fancy theories, but they had physical insight.

4.4 Convergence Test Consider an array of z-directed dipoles of length $2l \sim 0.5\lambda$ and radius a located in air. You are to investigate the convergence properties of the self-impedance

$$Z^{1,1} = \frac{Z_0}{2D_x D_z} \sum_k \sum_n \frac{e^{-j\beta a r_{0y}}}{r_{0y}} \left[{}_{\perp}P_{0\perp}P_0^t + {}_{\parallel}P_{0\parallel}P_0^t \right]$$

for the following cases:

Case I For k fixed, let $n \to \infty$ and investigate the asymptotic behavior of r_{0y}, $e^{-j\beta a r_{0y}}$, ${}_{\perp}P_{0\perp}P_0^t$, ${}_{\parallel}P_{0\parallel}P_0^t$ and $Z^{1,1}$ for the following current distributions:

a. $I(z) = I_0$ for $-l < z < l$.

b. $I(z) = I_0 \sin\beta(l + \delta - |z|)$ for $-l < z < l$ where δ typically is ~ 0.1 to $0.2l$.

c. $I(z) = I_0 \sin\beta(l - |z|)$ for $-l < z < l$.

Case II For n fixed let $k \to \infty$, and investigate the asymptotic behavior for the same components as in case I above. Note which current distribution will and will not converge if the wire radius a equals zero.

This problem shows that the exponential term is the key factor in bringing about convergence. While it is OK to put the wire radius a equal to zero for the

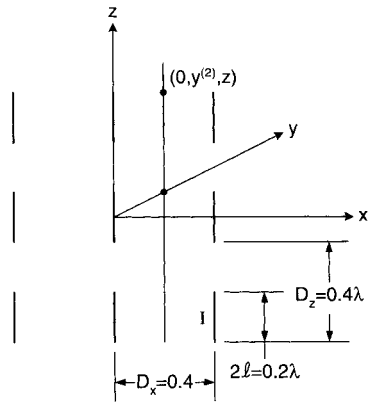

Fig. P4.5

propagating term(s), it is absolutely essential to use the effective wire radius for all the evanescent terms.

4.5 The Electrical Field Surrounding an Array of Hertzian Dipoles Given an array with z-directed Hertzian-like elements with constant currents I and dimensions as shown in Fig. P4.5 above. Find and plot the x-, y-, and z-components of the E-field along the vertical lines

$$\bar{R}^{(2)} = (0, y^{(2)}, z), \qquad -\infty < z < \infty$$

for $y^{(2)}$ =0.04, 0.1, 0.4, and 0.8λ. What happens when $y^{(2)} \to 0$? Show the contributions from real space ($k = n = 0$) and the imaginary space ($k, n \neq 0, 0$) separately. Next sketch or plot the total E-field in the yz-plane based on your results for the x-, y-, and z-components.

An interesting question is: How does the field plot change as the element length $2l$ grows bigger? What happens if the current becomes more realistic, such as sinusoidal?

Note: Our investigation here pertains to the field surrounding an array of *infinitely thin* current elements.

For a more realistic array the field at the element tips, for example, will depend strongly on the actual wire radius. For a more in-depth (and easier) investigation about this subject, see Chapter 10 on power handling of periodic surfaces.

4.6 Poynting's Vector(s) for a Hertzian Array. We have in the text determined the $\bar{E}$- as well as the $\bar{H}$-field for an array of arbitrarily oriented Hertzian elements. Based on these expressions, determine the Poynting vector for the

k, n mode. Determine the direction if $p_y \equiv 0$, that is, for planar elements. Does this direction of the Poynting vector surprise you?

Will there be any mode coupling (average), for example, between mode k, n and $k + 1, n$. *Hint:* Consider the mode coupling between, for example, the principal mode and a grating lobe. Or attack the problem purely mathematically. Also compare this result with the impedance term(s) for surface waves discussed in Section 5.11.

5

DIPOLE ARRAYS IN A STRATIFIED MEDIUM

5.1 INTRODUCTION

In the previous chapter we investigated the scattering properties of one or more FSSs in free space. However, it was already pointed out in Chapter 1 that a periodic structure without any dielectric not only is unrealistic but also in general undesirable because dielectric slabs can be used extensively to *shape* the reflection and transmission curves. In particular, they play a vital role in designing band-pass filters with constant bandwidth for all angles of incidence and polarizations as will be investigated in Chapter 7. They are also used in the design of band-stop filters as treated in Chapter 8.

In the present chapter we will introduce the modifications and extensions to the theory treated in Chapter 4 to do justice to these objectives. More specifically, we will determine the mutual impedance between an array with element orientation $\hat{p}^{(1)}$ and an external element with orientation $\hat{p}^{(1')}$ located anywhere in a stratified medium, as shown in Fig. 5.1. We will assume that the external element is always located in either region I or III.

The case when the external element is located in region II will not be treated here. Instead, see References [28–33].

5.2 A PLANE WAVE INCIDENT UPON A DIELECTRIC INTERFACE

As an introduction, we consider a plane wave propagating in the direction $\hat{r}_1$ in a medium with characteristic impedance Z_1 and propagation constant β_1, as shown in

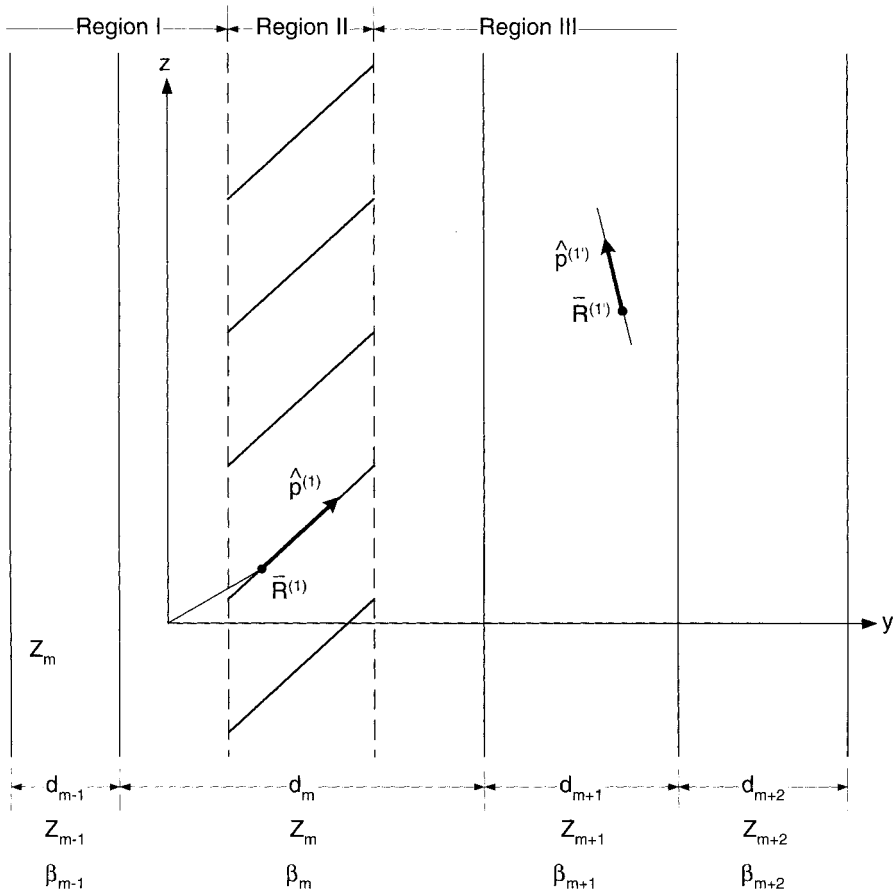

FIGURE 5.1. An array with element orientation $\hat{p}^{(1)}$ and an external element with orientation $\hat{p}^{(1')}$ is located arbitrarily in a stratified medium.

Fig. 5.2:

$$\bar{E}(\bar{R}) = \bar{E}^i e^{-j\beta_1 \bar{R}\cdot\hat{r}_{1-}}, \qquad y < 0. \tag{5.1}$$

Upon reaching medium 2 at $y = 0$ with characteristic impedance Z_2 and propagation constant β_2, it is partly reflected in the specular direction $\hat{r}_{1-}$ (negative going) and partly refracted into medium 2 as a plane wave propagating in the positive direction $\hat{r}_{2+}$:

$$\bar{E}^t(R) = \bar{E}^t e^{-j\beta_2 \bar{R}\cdot\hat{r}_{2+}}, \qquad y > 0. \tag{5.2}$$

The boundary conditions at the interface now require that the total tangential fields on each side of the boundary must be equal not only in amplitude but also in phase.

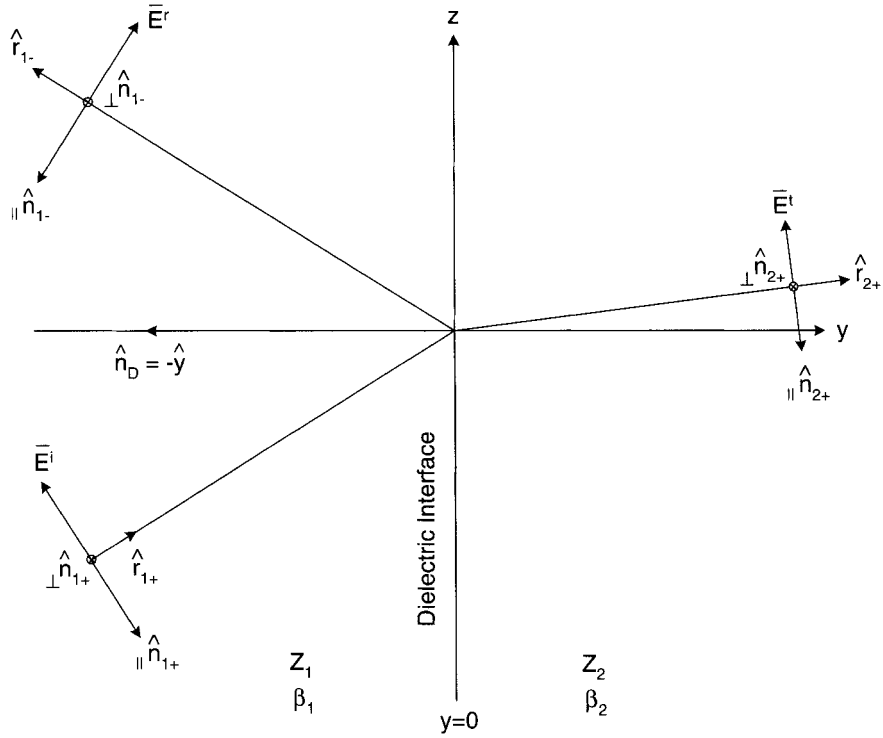

FIGURE 5.2. A plane wave $\bar{E}^i$ with direction of propagation $\hat{r}_{1+}$ is incident upon a dielectric interface. It is reflected in the direction $\hat{r}_{1-}$ and transmitted into medium 2 in the direction $\hat{r}_{2+}$.

Mathematically we have for the x- and z-directions, respectively,

$$\beta_2 r_{2x} = \beta_1 r_{1x} \quad \text{or} \quad r_{2x} = \frac{\beta_1}{\beta_2} r_{1x}, \tag{5.3}$$

$$\beta_2 r_{2z} = \beta_1 r_{1z} \quad \text{or} \quad r_{2z} = \frac{\beta_1}{\beta_2} r_{1z}. \tag{5.4}$$

Finally, since $\hat{r}_2$ is a unit vector,

$$r_{2y} = \sqrt{1 - r_{2x}^2 - r_{2z}^2}. \tag{5.5}$$

Equations (5.3) to (5.5) completely determine the propagation direction $\hat{r}_{2+}$ in medium 2 if $\hat{r}_{1+}$ is known.

Associated with each of these directions are orthogonal and parallel unit vectors defined in accordance with earlier definitions given in Chapter 4 (Section 4.7.2):

$$\perp\hat{n}_{1+} = \frac{\hat{n}_D \times \hat{r}_{1+}}{|\hat{n}_D \times \hat{r}_{1+}|} = \frac{-\hat{x}r_{1z} + \hat{z}r_{1x}}{\sqrt{r_{1x}^2 + r_{1z}^2}} = \frac{-\hat{x}r_{2z} + \hat{z}r_{2x}}{\sqrt{r_{2x}^2 + r_{2z}^2}} = \perp\hat{n}_{2+} = \perp\hat{n}_{1-} \tag{5.6}$$

where use has been made of (5.3) and (5.4). Now

$$\parallel\hat{n}_{1+} = \perp\hat{n}_{1+} \times \hat{r}_{1+} = \frac{1}{\sqrt{r_{1x}^2 + r_{1z}^2}}\left[-\hat{x}r_{1x}r_{1y} + \hat{y}(r_{1x}^2 r_{1y}^2) - \hat{z}r_{1y}r_{1z}\right], \tag{5.7}$$

$$\parallel\hat{n}_{2+} = \perp\hat{n}_{2+} \times \hat{r}_{2+} = \frac{1}{\sqrt{r_{2x}^2 + r_{2z}^2}}\left[-\hat{x}r_{2x}r_{2y} + \hat{y}(r_{2x}^2 r_{2z}^2) - \hat{z}r_{2y}r_{2z}\right]. \tag{5.8}$$

Note from (5.6) that we always have

$$\perp\hat{n}_{1+} = \perp\hat{n}_{2+} = \perp\hat{n}_{1-}.$$

(Thus the direction signs + or − can actually be dropped for $\perp\hat{n}$.) However, by inspection of (5.7) and (5.8) we note that in general $\parallel\hat{n}_{1+} \neq \parallel\hat{n}_{2+}$. Further, for the wave reflected in the specular direction $\hat{r}_{1-}$, we define the parallel vector as

$$\parallel\hat{n}_{1-} = -\perp\hat{n}_1 \times \hat{r}_{1-} \tag{5.9}$$

as also shown in Fig. 5.2.

The motivation for this choice is simply that it leads to a reflection coefficient of −1 when an E-field is incident upon a perfect conductor. It is also consistent with our definition of the orthogonal vector being the same for the reflected signal and the incident signal. The unit vectors $\perp\hat{n}_{1-}$, $\hat{r}_{1-}$, and $\parallel\hat{n}_{1-}$ associated with the negative-going waves constitute a left-hand coordinate system in contrast to the system associated with all the positive-going waves. This choice has not resulted in any problem. In fact it is natural for a reflected field. Note further that we use a subscript every time we refer to a particular medium and a superscript when referring to particular element segments.

5.3 ARRAYS AND EXTERNAL ELEMENTS LOCATED IN INFINITE MEDIUM Z_m

We now consider an array with element orientation $\hat{p}^{(1)}$ and an external element with orientation $\hat{p}^{(1')}$ both located in a medium with intrinsic impedance Z_m as shown in Fig. 5.3. We seek an expression for the voltage induced in the external element as caused by the currents on the arrays. We will apply a simple modification of the case treated in Chapter 4 dealing with free space Z_0 rather than Z_m. Let us denote the directions of the plane wave spectrum in medium m by $\hat{r}_{m\pm}$ and the position vectors for the reference point of the array and the external element by $\bar{R}^{(1)}$ and

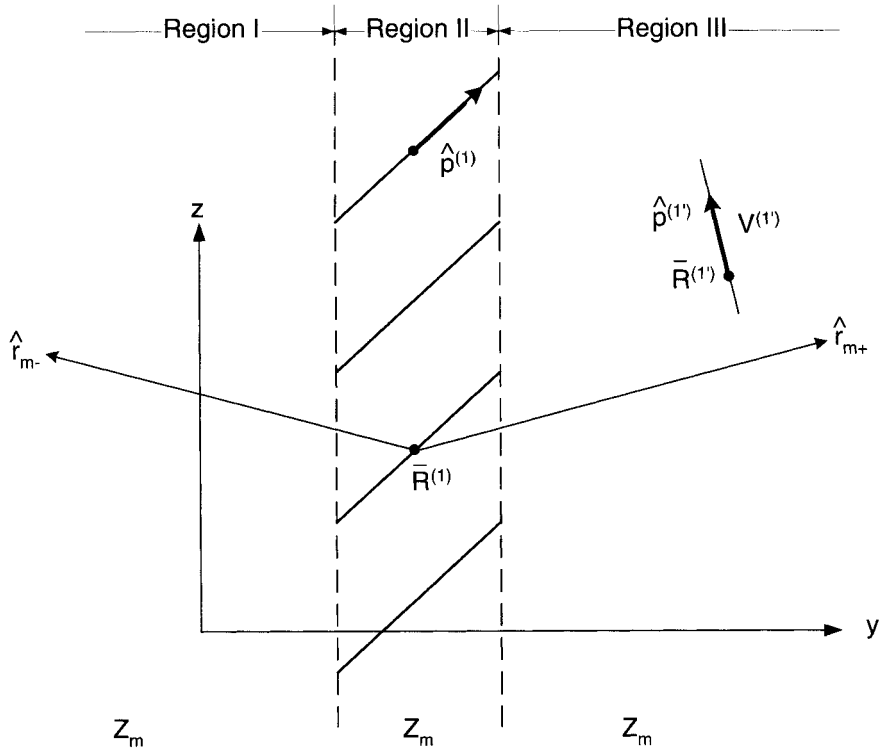

FIGURE 5.3. An array with element orientation $\hat{p}^{(1)}$ and an external element with orientation $\hat{p}^{(1')}$ located in infinite medium with intrinsic impedance Z_m.

$\bar{R}^{(1')}$, respectively. Then by modification of (4.59), we readily find that

$$V_{Di\pm}^{(1')} = -I^{(1)} \frac{Z_m}{2D_x D_z} \sum_k \sum_n \frac{e^{-j\beta_m(\bar{R}^{(1')} - \bar{R}^{(1)})\cdot \hat{r}_{m\pm}}}{r_{my}}$$
$$\left[{}_{\perp}P_{m\pm}^{(1)} {}_{\perp}P_{m\pm}^{(1')t} + {}_{\parallel}P_{m\pm}^{(1)} {}_{\parallel}P_{m\pm}^{(1')t} \right] \tag{5.10}$$

for regions III and I, respectively, where the pattern components [see (4.60) and (4.61)] are

$${}_{\substack{\perp \\ \parallel}}P_{m\pm}^{(1)} = \hat{p}^{(1)} \cdot {}_{\substack{\perp \\ \parallel}}\hat{n}_{m\pm} P_{m\pm}^{(1)}, \tag{5.11}$$

$${}_{\substack{\perp \\ \parallel}}P_{m\pm}^{(1')t} = \hat{p}^{(1')} \cdot {}_{\substack{\perp \\ \parallel}}\hat{n}_{m\pm} P_{m\pm}^{(1')t}, \tag{5.12}$$

and where the pattern factor [see (4.39)] is

$$P_{m\pm}^{(1)} = \frac{1}{I^{(1)}(\bar{R}^{(1)})} \int_{\text{Element}} I^{(1)}(l) e^{j\beta_m l \hat{p}^{(1)}\cdot \hat{r}_{m\pm}} dl \tag{5.13}$$

and where + goes with region III and − goes with region I [also see (4.50) for $P_{m\pm}^{(1)t}$]. The notation $V_{Di\pm}^{(1')}$ is an indication that the signal goes directly to the external element as opposed to being reflected by a dielectric interface as will be analyzed in the next section.

5.4 ARRAYS AND EXTERNAL ELEMENTS LOCATED IN A SEMI-INFINITE MEDIUM

Let us next, as shown in Fig. 5.4, take the first step toward a stratified medium by introducing a dielectric interface at $y = b_m$. The intrinsic impedances are denoted by Z_m and Z_{m+1} and the propagation constants by β_m and β_{m+1} for $y \gtrless b_m$, respectively. Assuming that the array as well as the external element are both located in medium m as shown we readily conclude that all the waves in spectrum $\hat{r}_{m+}$ will be incident upon the dielectric interface $y = b_m$ where they will be reflected in

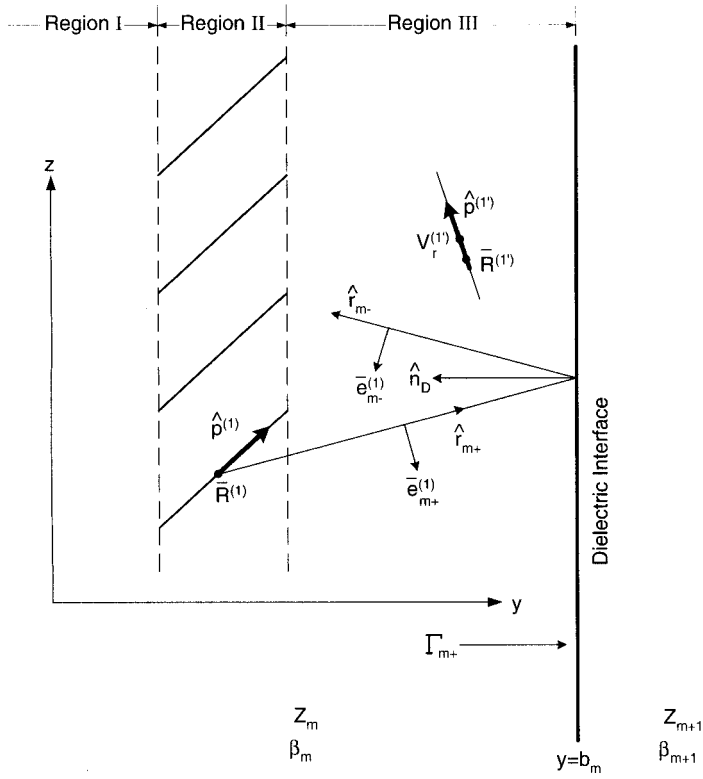

FIGURE 5.4. An array with element orientation $\hat{p}^{(1)}$ and an external element with orientation $\hat{p}^{(1')}$ both located in the semi-infinite medium Z_m with interface at $y = b_m$.

the directions $\hat{r}_{m-}$ with the Fresnel reflection coefficients ${}_{\perp}^{\parallel}\Gamma_{m,m+1}$ or ${}_{\perp}^{\parallel}\Gamma_{m+}$. (See Appendix C for Fresnel reflection coefficients.[1])

For the voltage $V_r^{(1')}$ induced in the external element by the reflected waves only in addition to $V_{Di\pm}^{(1')}$ as given by (5.10), we find that

$$V_r^{(1')} = -I^{(1)} \frac{Z_m}{2D_x D_z} \sum_k \sum_n \frac{e^{-j\beta_m(\bar{R}^{(1')} - \bar{R}^{(1)})\cdot \hat{r}_{m+}}}{r_{my}} e^{-j2\beta_m(b_m - y^{(1')})r_{my}}$$
$$\left[{}_{\perp}P_{m+}^{(1)} {}_{\perp}P_{m-}^{(1')t} {}_{\perp}\Gamma_{m+} + {}_{\parallel}P_{m+}^{(1)} {}_{\parallel}P_{m-}^{(1')t} {}_{\parallel}\Gamma_{m+} \right], \tag{5.14}$$

where $\bar{R}^{(1)}$ may be anywhere in medium m (i.e., $y < b_m$). Note in (5.14) that we have used $+$ in the pattern factors $P_{m+}^{(1)}$ because the signal leaves the array in the directions $\hat{r}_{m+}$ while we must use $-$ in the pattern factor $P_{m-}^{(1)t}$ because the signal arrives at the external element in the directions $\hat{r}_{m-}$.

5.5 ARRAYS AND EXTERNAL ELEMENTS LOCATED IN A SLAB

As the next step toward a stratified medium we are now, as shown in Fig. 5.5, introducing a dielectric interface at $y = b_{m-1}$ in addition to the interface at $y = b_m$. The intrinsic impedance and the propagation constant for $y < b_{m-1}$ is denoted by Z_{m-1} and β_{m-1}, respectively, while the media parameters for $y > b_{m-1}$ remain the same as in Fig. 5.4. The Fresnel reflection coefficient for a plane wave incident upon the interface $y = b_{m-1}$ from medium m is denoted $\Gamma_{m,m-1}$ or Γ_{m-}.

We are now going to experience multiple bounces from the two interfaces where the field emanating in the direction $\hat{r}_{m+}$ will be reflected first from the interface $y = b_m$ and subsequently from $y = b_{m-1}$ each of which are followed by infinitely many bounces. The negative going spectrum $\hat{r}_{m-}$ will be reflected in a similar fashion.

5.6 BOUNCE MODE ORGANIZATION

The bounce modes can be organized a number of ways. However, we have found the organization shown in Fig. 5.6 both practical and useful.

At the top we have the wave emanating from the array and hitting the external element *directly* without any reflection included. Thus this contribution is to be treated just like the medium extended to infinity. On the other hand, as discussed earlier, the expression will depend on which region we are in as indicated in Figs. 5.5 to 5.6, left and right.

[1]The reflection coefficients ${}_{\perp}^{\parallel}\Gamma_{m,m+1}$ or ${}_{\perp}^{\parallel}\Gamma_{m+}$ refer to the incident E-field. In Chapters 6 and 7 we will deal with slot arrays and find it convenient to refer to the incident H-field. The associated reflection coefficients are denoted by ${}_{\perp}^{\parallel}{}^{H}\Gamma_{m,m+1}$ or ${}_{\perp}^{\parallel}{}^{H}\Gamma_{m+}$. When no superscript H is given, we refer to the E-field. In some cases we emphasize that we are referring to the E-field by using the notation ${}_{\perp}^{\parallel}{}^{E}\Gamma_{m+}$.

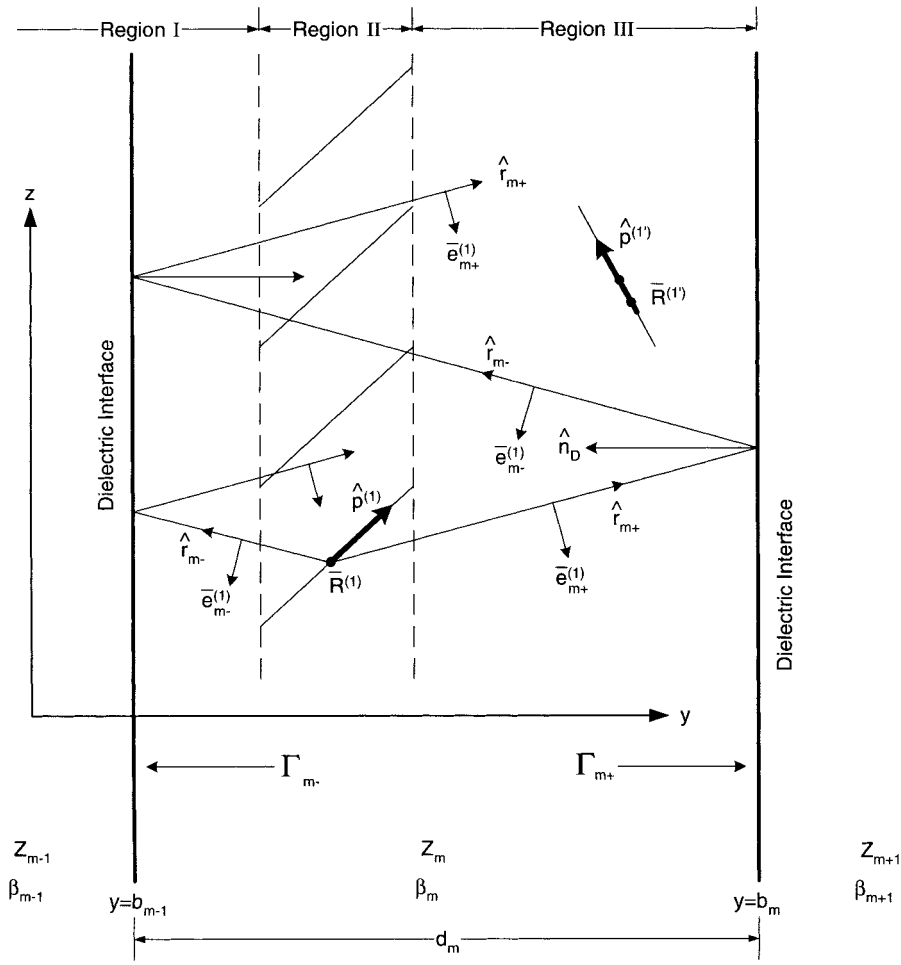

FIGURE 5.5. An array with element orientation $\hat{p}^{(1)}$ and an external element with orientation $\hat{p}^{(1')}$ both located in a slab with intrinsic impedance Z_m.

Next, in Fig. 5.6 (middle and bottom) follow the four reflected bounce modes. To the left we have the two single bounced (SBc) and to the right the two double bounced (DBc). It will further be noted that the modes are denoted—if they *arrive* at $\bar{R}^{(1')}$ in the negative y-direction and similarly for the positive. It will further be recognized that each of these four bounce modes are followed by an infinite number of subsequent bounces which, as we will see below, can be summed in closed form. Note further that $\bar{R}^{(1')}$ can be anywhere in slab d_m as far as the four bounce modes are concerned.

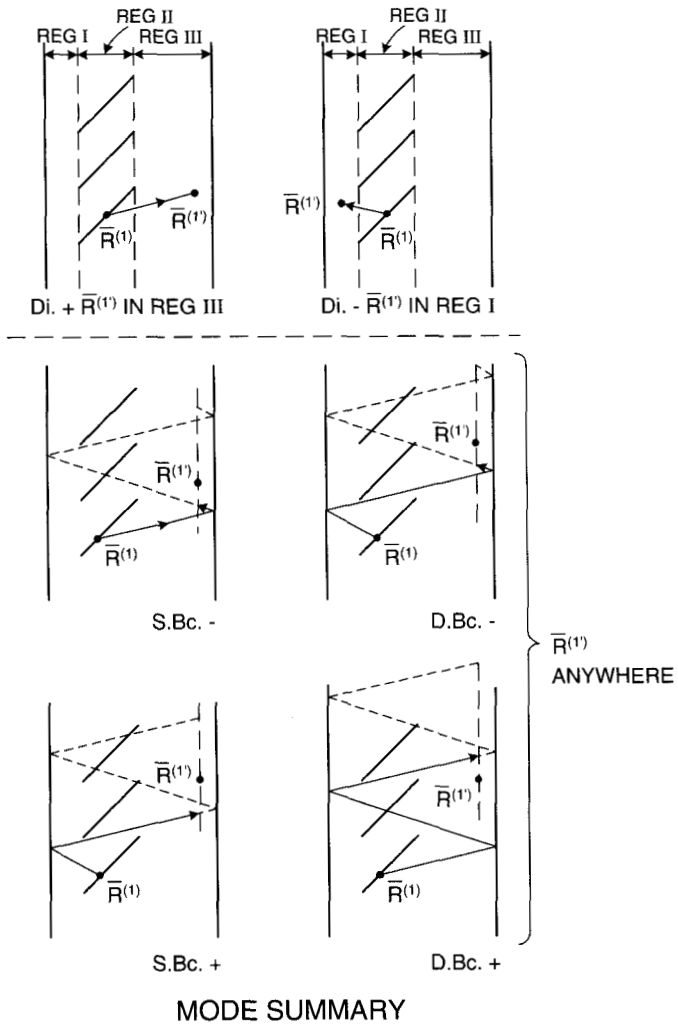

FIGURE 5.6. Organization of the various modes in a slab. *Top-left:* Direct $(Di+)$ going positive. *Top-right:* Direct $(Di-)$ going negative. *Middle-left:* Single bounce $(SBc-)$ going negative. *Middle-right:* Double bounce $(DBc-)$ going negative. *Bottom-left:* Single bounce $(SBc+)$ going positive. *Bottom right:* Double bounce $(DBc+)$ going positive.

5.6.1 Single-Bounce Mode in the Negative y-Direction

The single-bounce mode is going in the negative y-direction as shown in Fig. 5.7 for $\bar{R}^{(1')}$ in region III. However, as we will see later, in that event it is simplest to use $\hat{r}_{m+}$; we will use $\hat{r}_{m-}$ if $\bar{R}^{(1')}$ is in region I.

The first wave emanating from the array will travel toward the interface $y = b_m$ where it will be reflected with the reflection coefficient Γ_{m+}. It will arrive at $y =$

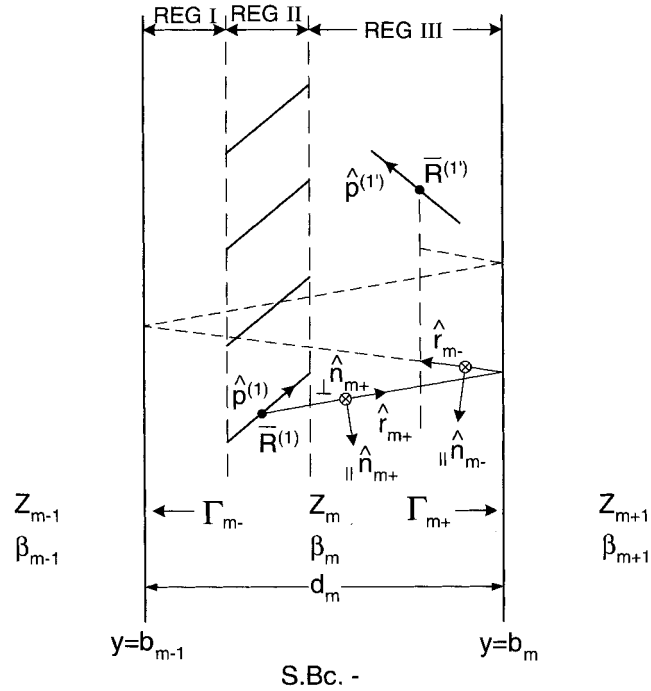

FIGURE 5.7. Single bounce mode ($SBc-$) going in the negative y-direction.

$R_y^{(1')}$ with the relative value $\Gamma_{m+} \cdot e^{-j2\beta_m(\bar{R}^{(1')}-\bar{R}^{(1)})\cdot\hat{r}_{m+}} \cdot e^{-j2\beta_m(b_m-\bar{R}_y^{(1')})r_{my}}$. It will then continue to $y = b_{m-1}$ where it will be reflected with the reflection coefficient Γ_{m-}, next to $y = b_m$ with Γ_{m+}, until it arrives at $y = \bar{R}^{(1')} \cdot \hat{y}$ with an additional delay of $e^{-j2\beta_m d_m r_{my}}$, and so on.

We readily find for the voltage $V_{S-}^{(1')}$ induced in the external element by the single bounce in the negative y-direction:

$$V_{S-}^{(1')} = -I^{(1)} \frac{Z_m}{2D_x D_z} \sum\sum \frac{e^{-j\beta_m(\bar{R}^{(1')}-\bar{R}^{(1)})\cdot\hat{r}_{m+}}}{r_{my}} e^{-j2\beta_m(b_m-y^{(1')})r_{my}}$$

$$\left[{}_{\perp}P_{m+}^{(1)} {}_{\perp}P_{m-}^{(1')t} {}_{\perp}\Gamma_{m+} \left[1 + {}_{\perp}\Gamma_{m-}\Gamma_{m+} e^{-j2\beta_m d_m r_{my}} + \cdots \right] \right.$$

$$\left. + {}_{\parallel}P_{m+}^{(1)} {}_{\parallel}P_{m-}^{(1')t} {}_{\parallel}\Gamma_{m+} \left[1 + {}_{\parallel}\Gamma_{m-}\Gamma_{m+} e^{-j2\beta_m d_m r_{my}} + \cdots \right] \right].$$

By the geometric series for $|x| < 1$,

$$1 + x + x^2 + \cdots = \frac{1}{1-x},$$

we obtain

$$V_{S-}^{(1')} = -I^{(1)} \frac{Z_m}{2D_x D_z} \sum\sum \frac{e^{-j\beta_m(\bar{R}^{(1')}-\bar{R}^{(1)})\cdot\hat{r}_{m+}}}{r_{my}} e^{-j2\beta_m(b_m-y^{(1')})r_{my}}$$
$$\left[{}_{\perp}P_{m+}^{(1)} {}_{\perp}P_{m-}^{(1')t} {}_{\perp}\Gamma_{m+} {}_{\perp}W_m + {}_{\parallel}P_{m+}^{(1)} {}_{\parallel}P_{m-}^{(1')t} {}_{\parallel}\Gamma_{m+} {}_{\parallel}W_m \right] \tag{5.15}$$

for $\bar{R}^{(1')}$ anywhere and where the Wronskian is defined as

$$\begin{matrix}\perp \\ \parallel\end{matrix} W_m = \frac{1}{1 - \begin{matrix}\perp \\ \parallel\end{matrix}\Gamma_{m+} \begin{matrix}\perp \\ \parallel\end{matrix}\Gamma_{m-} e^{-j2\beta_m d_m r_{my}}}. \tag{5.16}$$

5.6.2 Double-Bounce Mode in the Negative *y*-Direction

For the double-bounce mode in the negative y-direction, we readily find as above by inspection of Fig. 5.8 that

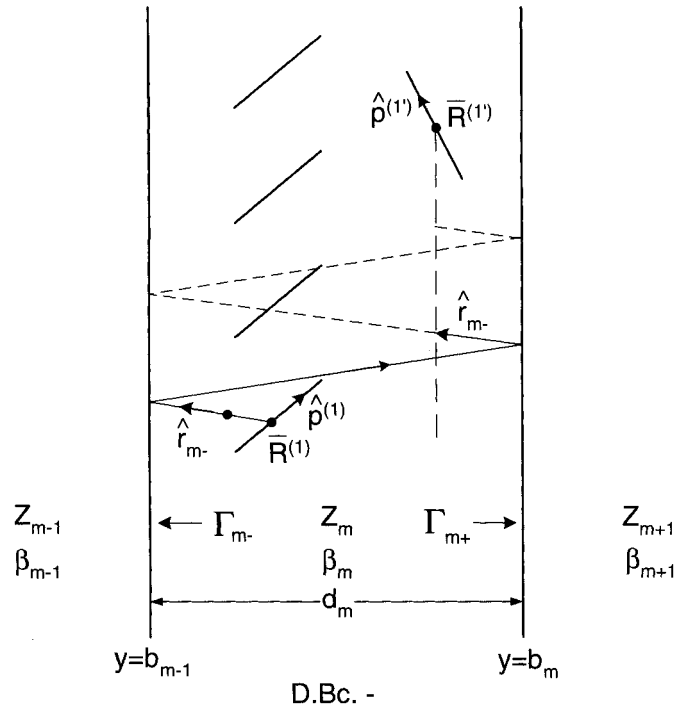

FIGURE 5.8. Double bounce mode ($DBc-$) going in the negative y-direction.

$$V_{D-}^{(1')} = -I^{(1)} \frac{Z_m}{2D_x D_z} \sum\sum \frac{e^{-j\beta_m(\bar{R}^{(1')}-\bar{R}(1))\cdot\hat{r}_{m+}}}{r_{my}}$$
$$e^{-j2\beta_m(y^{(1)}-b_{m-1})r_{my}} e^{-j2\beta_m(b_m-y^{(1')})r_{my}}$$
$$\left[{}_{\perp}P_{m-}^{(1)} {}_{\perp}P_{m-}^{(1')t} {}_{\perp}\Gamma_{m+} {}_{\perp}\Gamma_{m-} {}_{\perp}W_m + {}_{\parallel}P_{m-}^{(1)} {}_{\parallel}P_{m-}^{(1')t} {}_{\parallel}\Gamma_{m+} {}_{\parallel}\Gamma_{m-} {}_{\parallel}W_m \right] \tag{5.17}$$

for $\bar{R}^{(1')}$ located anywhere and where ${}_{\perp}^{\parallel}W_m$ is given by (5.16).

5.6.3 Single-Bounce Mode in the Positive y-Direction

For the single-bounce mode in the positive y-direction we obtain by inspection of Fig. 5.9,

$$V_{S+}^{(1')} = -I^{(1)} \frac{Z_m}{2D_x D_z} \sum\sum \frac{e^{-j\beta_m(\bar{R}^{(1')}-\bar{R}^{(1)})\cdot\hat{r}_{m+}}}{r_{my}} e^{-j2\beta_m(y^{(1)}-b_{m-1})r_{my}}$$
$$\left[{}_{\perp}P_{m-}^{(1)} {}_{\perp}P_{m+}^{(1')t} {}_{\perp}\Gamma_{m-} {}_{\perp}W_m + {}_{\parallel}P_{m-}^{(1)} {}_{\parallel}P_{m+}^{(1')t} {}_{\parallel}\Gamma_{m-} {}_{\parallel}W_m \right] \tag{5.18}$$

for $\bar{R}^{(1')}$ located anywhere.

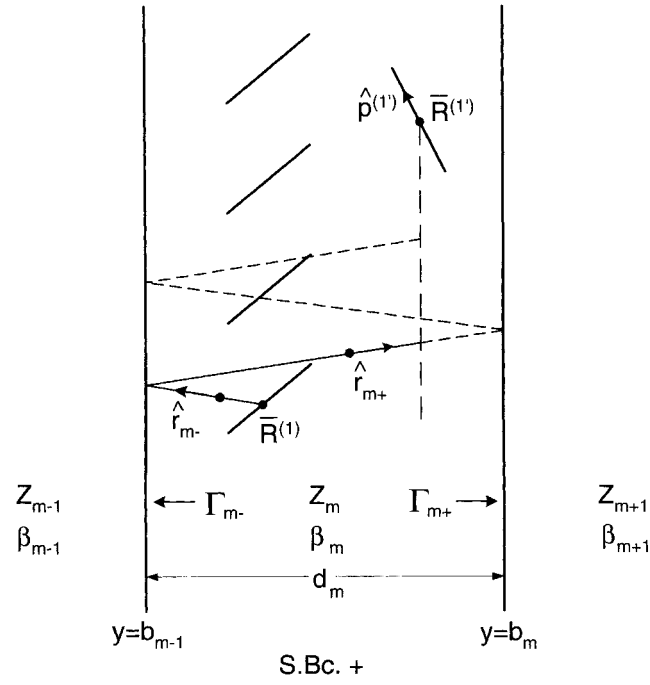

FIGURE 5.9. Single bounce mode ($SBc+$) going in the positive y-direction.

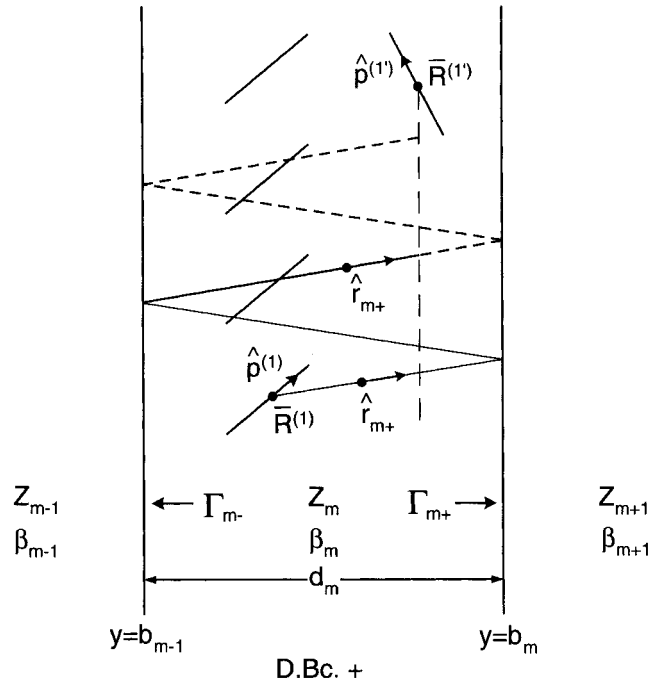

FIGURE 5.10. Double bounce mode ($DBc+$) going in the positive y-direction.

5.6.4 Double-Bounce Mode in the Positive y-Direction

For the double-bounce mode in the positive y-direction, we obtain by inspection of Fig. 5.10,

$$V_{D+}^{(1')} = -I^{(1)} \frac{Z_m}{2D_x D_z} \sum\sum \frac{e^{-j\beta_m(\bar{R}^{(1')}-\bar{R}^{(1)})\cdot\hat{r}_{m+}}}{r_{my}} e^{-j2\beta_m d_m r_{my}}$$
$$\left[{}_{\perp}P_{m+}^{(1)} {}_{\perp}P_{m+}^{(1')t} {}_{\perp}\Gamma_{m+} {}_{\perp}\Gamma_{m-} {}_{\perp}W_m + {}_{\parallel}P_{m+}^{(1)} {}_{\parallel}P_{m+}^{(1')t} {}_{\parallel}\Gamma_{m+} {}_{\parallel}\Gamma_{m-} {}_{\parallel}W_m \right] \tag{5.19}$$

for $\bar{R}^{(1')}$ located anywhere.

5.7 TOTAL VOLTAGE $V_{Tot+}^{(1')}$ INDUCED BY WAVES IN POSITIVE AND NEGATIVE y-DIRECTIONS

We saw above that the expressions for the voltages induced by the reflected waves were valid everywhere in slab d_m. However, the expression yielding the induced voltage for the direct wave depends in general on the location of the external element.

Thus further investigation will be split up into whether $\bar{R}^{(1')}$ is in region I or region III.

5.7.1 $\bar{R}^{(1')}$ Located in Region III

When $\bar{R}^{(1')}$ is located in region III, we have a total of three positive traveling waves, namely the direct wave given by (5.10) where the + sign is applied in region III, and the two reflected waves given by (5.18) and (5.19). By addition of these three equations, we find that for the *positive-going waves*

$$
\begin{aligned}
V_{Tot+}^{(1')} &= V_{Di+}^{(1')} + V_{D+}^{(1')} + V_{S+}^{(1')} \\
&= -I^{(1)} \frac{Z_m}{2D_x D_z} \sum_k \sum_n \frac{e^{-j\beta_m(\bar{R}^{(1')} - \bar{R}^{(1)})\cdot \hat{r}_{m+}}}{r_{my}} \\
&\quad \Big[{}_{\perp}P_{m+}^{(1)} {}_{\perp}P_{m+}^{(1')t} [1 + {}_{\perp}\Gamma_{m+} {}_{\perp}\Gamma_{m-} e^{-j2\beta_m d_m r_{my}} {}_{\perp}W_m] \\
&\quad + {}_{\parallel}P_{m+}^{(1)} {}_{\parallel}P_{m+}^{(1')t} [1 + {}_{\parallel}\Gamma_{m+} {}_{\parallel}\Gamma_{m-} e^{-j2\beta_m d_m r_{my}} {}_{\parallel}W_m] + e^{-j2\beta_m (y^{(1)} - b_{m-1}) r_{my}} \\
&\quad [{}_{\perp}P_{m-}^{(1)} {}_{\perp}P_{m+}^{(1')t} {}_{\perp}\Gamma_{m-} {}_{\perp}W_m + {}_{\parallel}P_{m-}^{(2)} {}_{\parallel}P_{m+}^{(1')t} {}_{\parallel}\Gamma_{m-} {}_{\parallel}W_m] \Big].
\end{aligned} \tag{5.20}
$$

By making use of (5.16), we note that

$$
1 + {}_{\substack{\perp \\ \parallel}}\Gamma_{m+} {}_{\substack{\perp \\ \parallel}}\Gamma_{m-} {}_{\substack{\perp \\ \parallel}}W_m e^{-j2\beta_m d_m r_{my}} = {}_{\substack{\perp \\ \parallel}}W_m. \tag{5.21}
$$

Substituting (5.21) into (5.20) yields

$$
\begin{aligned}
V_{Tot+}^{(1')} &= -I^{(1)} \frac{Z_m}{2D_x D_z} \sum_k \sum_n \frac{e^{-j\beta_m(\bar{R}^{(1')} - \bar{R}^{(1)})\cdot \hat{r}_{m+}}}{r_{my}} \\
&\quad \Big[{}_{\perp}P_{m+}^{(1')t} [{}_{\perp}P_{m+}^{(1)} + {}_{\perp}P_{m-}^{(1)} {}_{\perp}\Gamma_{m-} e^{-j2\beta_m (y^{(1)} - b_{m-1}) r_{my}}] {}_{\perp}W_m \\
&\quad + {}_{\parallel}P_{m+}^{(1')t} [{}_{\parallel}P_{m+}^{(1)} + {}_{\parallel}P_{m-}^{(1)} {}_{\parallel}\Gamma_{m-} e^{-j2\beta_m (y^{(1)} - b_{m-1}) r_{my}}] {}_{\parallel}W_m \Big].
\end{aligned} \tag{5.22}
$$

for $\bar{R}^{(1')}$ located in region III. Similarly we find that for total voltage induced by the *two negative traveling waves* by addition of (5.15) and (5.17),

$$
\begin{aligned}
V_{Tot-}^{(1')} &= -I^{(1)} \frac{Z_m}{2D_x D_z} \sum_k \sum_n \frac{e^{-j\beta_m(\bar{R}^{(1')} - \bar{R}^{(1)})\cdot \hat{r}_{m+}}}{r_{my}} \\
&\quad \Big[{}_{\perp}P_{m-}^{(1')t} {}_{\perp}\Gamma_{m+} {}_{\perp}W_m e^{-j2\beta_m (b_m - y^{(1')}) r_{my}} \\
&\quad [{}_{\perp}P_{m+}^{(1)} + {}_{\perp}P_{m-}^{(1)} {}_{\perp}\Gamma_{m-} e^{-j2\beta_m (y^{(1)} - b_{m-1}) r_{my}}]
\end{aligned}
$$

$$+ {}_{\parallel}P_{m-}^{(1')t}{}_{\parallel}\Gamma_{m+\parallel}W_m e^{-j2\beta_m(b_m-y^{(1')})r_{my}}$$
$$[{}_{\parallel}P_{m+}^{(1)} + {}_{\parallel}P_{m-}^{(1)}{}_{\parallel}\Gamma_{m-}e^{-j2\beta_m(y^{(1)}-b_{m-1})r_{my}}]\Big] \tag{5.23}$$

for $\bar{R}^{(1')}$ located in region III.

Before proceeding, it is interesting to note that the negative-going wave in (5.23) could have been obtained from the positive traveling wave given by (5.22) simply by multiplication of $\Gamma_{m+}e^{-j2\beta_m(b_m-R_y^{(1')})r_{my}}$ and changing $P_{m+}^{(1')t}$ to $P_{m-}^{(1')t}$ as one would expect.

The total voltage $V_{Tot}^{(1')t}$ induced in the external element from the positive and negative waves is obtained by addition of (5.22) and (5.23) for $\bar{R}^{(1')}$ located in region III:

$$V_{Tot}^{(1')} = V_{Tot+}^{(1')} + V_{Tot-}^{(1')}$$
$$= -I^{(1)}\frac{Z_m}{2D_xD_z}\sum_k\sum_n \frac{e^{-j\beta_m(\bar{R}^{(1')}-\bar{R}^{(1)})\cdot\hat{r}_{m+}}}{r_{my}}$$
$$\Big[[{}_{\perp}P_{m+}^{(1)} + {}_{\perp}P_{m-}^{(1)}{}_{\perp}\Gamma_{m-}e^{-j2\beta_m(y^{(1)}-b_{m-1})r_{my}}]$$
$$[{}_{\perp}P_{m+}^{(1')t} + {}_{\perp}P_{m-}^{(1')t}{}_{\perp}\Gamma_{m+}e^{-j2\beta_m(b_m-y^{(1')})r_{my}}]_{\perp}W_m$$
$$+[{}_{\parallel}P_{m+}^{(1)} + {}_{\parallel}P_{m-}^{(1)}{}_{\parallel}\Gamma_{m-}e^{-j2\beta_m(y^{(1)}-b_{m-1})r_{my}}]$$
$$[{}_{\parallel}P_{m+}^{(1')t} + {}_{\parallel}P_{m-}^{(1')t}{}_{\parallel}\Gamma_{m+}e^{-j2\beta_m(b_m-y^{(1')})r_{my}}]_{\parallel}W_m\Big] \tag{5.24}$$

for $\bar{R}^{(1')}$ located in region III.

The total voltage $V_{Tot}^{(1')}$ induced in the external element from the positive and negative waves for $\bar{R}^{(1')}$ located in Region I can be obtained by the same procedure as above. However, it is simpler to apply symmetry considerations to (5.24) directly and obtain

$$V_{Tot}^{(1')} = -I^{(1)}\frac{Z_m}{2D_xD_z}\sum_k\sum_n \frac{e^{-j\beta_m(\bar{R}^{(1')}-\bar{R}^{(1)})\hat{r}_{m-}}}{r_{my}}$$
$$\Big[[{}_{\perp}P_{m-}^{(1)} + {}_{\perp}P_{m+}^{(1)}{}_{\perp}\Gamma_{m+}e^{-j2\beta_m(b_m-y^{(1)})r_{my}}]$$
$$[{}_{\perp}P_{m-}^{(1')t} + {}_{\perp}P_{m+}^{(1')t}{}_{\perp}\Gamma_{m-}e^{-j2\beta_m(y^{(1')}-b_{m-1})r_{my}}]_{\perp}W_m$$
$$+[{}_{\parallel}P_{m-}^{(1)} + {}_{\parallel}P_{m+}^{(1)}{}_{\parallel}\Gamma_{m+}e^{-j2\beta_m(b_m-y^{(1)})r_{my}}]$$
$$[{}_{\parallel}P_{m-}^{(1')t} + {}_{\parallel}P_{m+}^{(1')t}{}_{\parallel}\Gamma_{m-}e^{-j2\beta_m(y^{(1')}-b_{m-1})r_{my}}]_{\parallel}W_m\Big] \tag{5.25}$$

for $\bar{R}^{(1')}$ located in region I.

5.8 GENERAL STRATIFIED MEDIUM WITH NONPLANAR ELEMENTS

We now make the extension to the complete general stratified case shown in Fig. 5.11. An array with reference point $\bar{R}^{(1)}$ is located anywhere in an arbitrary slab m in the stratified medium. We seek the voltage induced in an external element with reference point $\bar{R}^{(1')}$ located somewhere in another slab m'.

Just as in the single slab case treated earlier in Sections 5.5, 5.6, and 5.7, the plane wave spectrum $\hat{r}_{\pm}$ will be reflected from the interfaces $y = b_{m-1}$ and $y = b_m$ and bounce back and forth between these two interfaces. However, in addition the positive going waves will be partly transmitted into medium $m+1$ where they will be partly reflected and eventually find their way back to the array in slab m. Obviously this is just the beginning of a general mass confusion, since all other interfaces will partly reflect and transmit as well. The same is true when the negative-going waves reach all the interfaces to the left of $y = b_{m-1}$.

It is important that the designer realize that this problem must be solved completely rigorously in order to properly assess the transmission and reflection coefficient at resonance of a periodic surface (e.g., a transmission coefficient of 0.997 is unacceptable if it really is 1.000).

Fortunately this dilemma can be solved completely and exactly by using the concept of effective reflection and transmission coefficient for a stratified medium as

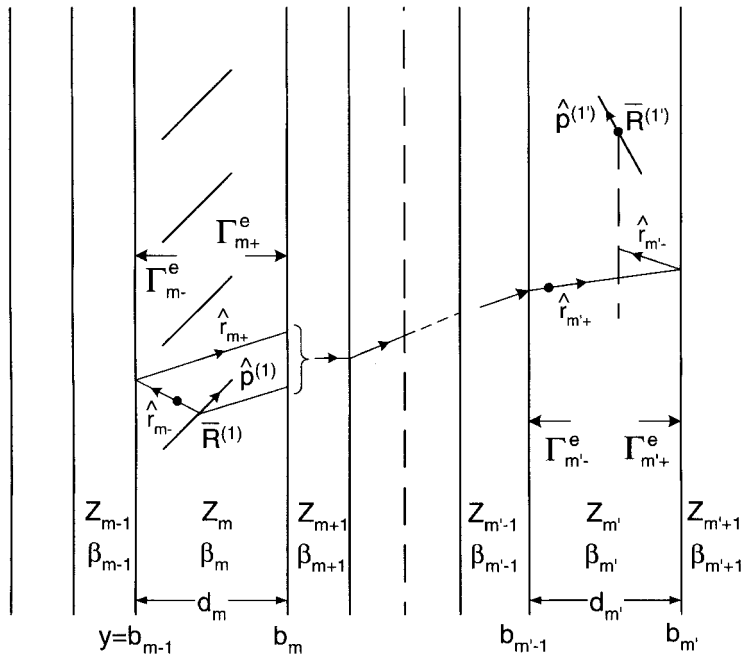

FIGURE 5.11. General stratified case: An array in slab m with element orientation $\hat{p}^{(1)}$ induces a voltage in a external element with orientation $\hat{p}^{(1')}$ located in slab m'.

discussed in Appendix D. As shown there in detail, the trick is simply to start an iterative procedure at the right end of the stratified medium and add one slab at a time until slab m, which contains the arrays, is reached. At each interface we determine the so-called effective reflection and transmission coefficients as given by (D.14) and (D.15), respectively. It is emphasized that this approach completely takes into account all bounces.

Thus the sum of all the right-going waves in slab m in Fig. 5.11 is obtained precisely in the same way as was done earlier for the single-slab case treated in Section 5.7 except that we simply use the effective reflection and transmission coefficients at the interfaces $y = b_{m-1}$ and b_m instead of merely the Fresnel coefficients. From (5.22) modified to the right-going *field* rather than the induced *voltages* (consult (4.73) modified to medium m) we readily obtain

$$\begin{aligned}\bar{E}_+^{Total}(\bar{R}) = -I^{(1)}(\bar{R}^{(1)})\frac{Z_m}{2D_xD_z}\sum_k\sum_n \frac{e^{-j\beta_m(\bar{R}-\bar{R}^{(1)})\cdot\hat{r}_{m+}}}{r_{my}} \\ \Big[{}_{\perp}\hat{n}_{m+}[{}_{\perp}P_{m+}^{(1)} + {}_{\perp}P_{m-}^{(1)}{}_{\perp}\Gamma_{m-}^{e}e^{-j2\beta_m(y^{(1)}-b_{m-1})r_{my}}]_{\perp}W_m^e \\ +{}_{\parallel}\hat{n}_{m+}[{}_{\parallel}P_{m+}^{(1)} + {}_{\parallel}P_{m-}^{(1)}{}_{\parallel}\Gamma_{m-}^{e}e^{-j2\beta_m(y^{(1)}-b_{m-1})r_{my}}]_{\parallel}W_m^e\Big] \qquad (5.26)\end{aligned}$$

where the effective Wronskian is given analogous to (5.16) as

$$\begin{matrix}{}_{\perp}\\{}_{\parallel}\end{matrix}W_m^e = \frac{1}{1 - \begin{matrix}{}_{\perp}\\{}_{\parallel}\end{matrix}\Gamma_{m-}^{e}\begin{matrix}{}_{\perp}\\{}_{\parallel}\end{matrix}\Gamma_{m+}^{e}\,e^{-j2\beta_m d_m r_{my}}}. \qquad (5.27)$$

We find that a plane wave $E_{b,m}$ incident upon interface $y = b_m$ will produce *one* positive- and *one* negative-going wave in slab m' producing a total field at $\bar{R}^{(1')}$:

$$\begin{aligned}\bar{E}_{m'}(\bar{R}^{(1')}) = \Big[{}_{\perp}\hat{n}_{m'}{}_{\perp}E_{b,m}{}_{\perp}\tau_{m+}^{e}{}_{\perp}\tau_{m+1,+}^{e}\cdots{}_{\perp}\tau_{m'-1,+}^{e} \\ [1 + {}_{\perp}\Gamma_{m'+}^{e}e^{-j2\beta_{m'}(\hat{y}b_{m'}-\bar{R}^{(1')})\cdot\hat{r}_{m'}}] \\ +{}_{\parallel}E_{b,m}{}_{\parallel}\tau_{m+}^{e}{}_{\parallel}\tau_{m+1,+}^{e}\cdots{}_{\parallel}\tau_{m'-1,+}^{e}\frac{r_{my}}{r_{m'y}} \\ [{}_{\parallel}\hat{n}_{m'+} + {}_{\parallel}\hat{n}_{m'-}{}_{\parallel}\Gamma_{m'+}^{e}e^{-j2\beta_{m'}(\hat{y}b_{m'}-\bar{R}^{(1')})\cdot\hat{r}_{m'}}]\Big] \\ e^{-j\beta_{m+1}d_{m+1}r_{m+1,y}}\cdots e^{-j\beta_{m'-1}d_{m'-1}r_{m'-1,y}}e^{-j\beta_{m'}(y^{(1')}-b_{m'-1})r_{m'y}}.\end{aligned} \qquad (5.28)$$

By application of (5.28) on (5.26), we obtain for the total field in slab m':

$$\bar{E}_{m'}(\bar{R}^{(1')}) = -I^{(1)}(\bar{R}^{(1)})\frac{Z_m}{2D_xD_z}\sum_k\sum_n \frac{e^{-j\beta_m(\hat{y}b_m-\bar{R}^{(1)})\cdot\hat{r}_{m+}}}{r_{my}}$$

$$\Big[\perp\hat{n}_{m'+}[\perp P_{m+}^{(1)} + \perp P_{m-}^{(1)}\perp\Gamma_{m-}^{e} e^{-j2\beta_m(y^{(1)}-b_{m-1})r_{my}}]\perp W_m^e$$

$$\perp\tau_{m+}^{e}\perp\tau_{m+1,+}^{e}\cdots\perp\tau_{m'-1,+}^{e}[1 + \perp\Gamma_{m'+}^{e} e^{-j2\beta_{m'}(\hat{y}b_{m'}-\bar{R}^{(1')})\cdot\hat{r}_{m'+}}]$$

$$+ [\parallel P_{m+}^{(1)} + \parallel P_{m-}^{(1)}\parallel\Gamma_{m-}^{e} e^{-j2\beta_m(y^{(1)}-b_{m-1})r_{my}}]\parallel W_m^e$$

$$\parallel\tau_{m+}^{e}\parallel\tau_{m+1,+}^{e}\cdots\parallel\tau_{m'-1,+}^{e}\frac{r_{my}}{r_{m'y}}$$

$$[\parallel\hat{n}_{m'+} + \parallel\hat{n}_{m'-}\parallel\Gamma_{m'+}^{e} e^{-j2\beta_m(\hat{y}b_{m'}-\bar{R}^{(1')})\cdot\hat{r}_{m'+}}]\Big]$$

$$e^{-j\beta_{m+1}d_{m+1}r_{m+1,y}}\cdots e^{-j\beta_{m'-1}d_{m'-1}r_{m'-1,y}} e^{-j\beta_{m'}(\bar{R}^{(1')}-\hat{y}b_{m'-1})\cdot\hat{r}_{m'}}. \tag{5.29}$$

The voltage induced in an element located at $\bar{R}^{(1')}$ and with orientation $\hat{p}^{(1')}$ is readily obtained by application of (4.49) and (4.50) modified to medium m'. From (5.29) we readily get

$$V^{(1')} = -I^{(1)}(\bar{R}^{(1)})\frac{Z_m}{2D_xD_z}\sum_k\sum_n\frac{e^{-j\beta_m(\hat{y}b_m-\bar{R}^{(1)})\cdot\hat{r}_{m+}}}{r_{my}}$$

$$\Big[[\perp P_{m+}^{(1)} + \perp P_{m-}^{(1)}\perp\Gamma_{m-}^{e} e^{-j2\beta_m(y^{(1)}-b_{m-1})r_{my}}]\perp W_m^e$$

$$\perp\tau_{m+}^{e}\perp\tau_{m+1,+}^{e}\cdots\perp\tau_{m'-1,+}^{e}[\perp P_{m'+}^{(1')t} + \perp P_{m'-}^{(1')t}\perp\Gamma_{m'+}^{e} e^{-j2\beta_{m'}(\hat{y}b_{m'}-\bar{R}^{(1')})\cdot\hat{r}_{m'+}}]$$

$$+[\parallel P_{m+}^{(1)} + \parallel P_{m-}^{(1)}\parallel\Gamma_{m-}^{e} e^{-j2\beta_m(y^{(1)}-b_{m-1})r_{my}}]\parallel W_m^e$$

$$\parallel\tau_{m+}^{e}\parallel\tau_{m+1,+}^{e}\cdots\parallel\tau_{m'-1,+}^{e}\frac{r_{my}}{r_{m'y}}[\parallel P_{m'+}^{(1')t} + \parallel P_{m'-}^{(1')t}\parallel\Gamma_{m'+}^{e} e^{-j2\beta_{m'}(\hat{y}b_{m'}-\bar{R}^{(1')})\cdot\hat{r}_{m'+}}]\Big]$$

$$e^{-j\beta_{m+1}d_{m+1}r_{m+1,y}}\cdots e^{-j\beta_{m'-1}d_{m'-1}r_{m'-1,y}} e^{-j\beta_{m'}(\bar{R}^{(1')}-\hat{y}b_{m'-1})\cdot\hat{r}_{m'}}. \tag{5.30}$$

for $\bar{R}^{(1')}$ in region III. The case where $\bar{R}^{(1')}$ is located in region I is readily obtained from (5.30) by symmetry as was done earlier.

5.9 GENERAL STRATIFIED MEDIUM WITH PLANAR ELEMENTS

The derivation above has addressed the case where the array elements and the external elements have arbitrary (i.e., nonplanar) orientation $\hat{p}^{(1)}$ and $p^{(1')}$, respectively, and the external elements are located either entirely in region I or in region III.

However, by far most applications deal with elements that are planar, $p_y^{(1)} = p_y^{(1')} = 0$, but may otherwise be arbitrarily oriented. In that event considerable simplification results, namely

$$\begin{matrix}\perp \\ \parallel\end{matrix} P_{m+}^{(1)} = \begin{matrix}\perp \\ \parallel\end{matrix} P_{m-}^{(1)} = \begin{matrix}\perp \\ \parallel\end{matrix} P_{m}^{(1)}, \tag{5.31}$$

$$\begin{matrix}\perp \\ \parallel\end{matrix} P_{m'+}^{(1')t} = \begin{matrix}\perp \\ \parallel\end{matrix} P_{m'-}^{(1')t} = \begin{matrix}\perp \\ \parallel\end{matrix} P_{m'}^{(1')t}, \tag{5.32}$$

and region II simply disappears. Applying (5.31) and (5.32) to (5.30) yields

$$V^{(1')} = -I^{(1)}(\bar{R}^{(1)}) \frac{Z_m}{2D_x D_z} \sum_k \sum_n \frac{e^{-j\beta_m(\hat{y}b_m - \bar{R}^{(1)})\cdot\hat{r}_{m+}}}{r_{my}}$$

$$\left[\perp P_m^{(1)} \perp P_{m'}^{(1')t} \perp T_{m-m'} + \parallel P_m^{(1)} \parallel P_{m'}^{(1')t} \frac{r_{my}}{r_{m'y}} \parallel T_{m-m'} \right]$$

$$e^{-j\beta_{m+1}d_{m+1}r_{m+1,y}} \cdots e^{-j\beta_{m'-1}d_{m'-1}r_{m'-1,y}} e^{-j\beta_{m'}(\bar{R}^{(1')} - \hat{y}b_{m'-1})\cdot\hat{r}_{m'}} \tag{5.33}$$

where the generalized transformation function $\begin{matrix}\perp \\ \parallel\end{matrix} T_{m-m'}$ responsible for transferring the signal from slab m to slab m' is given by

$$\begin{matrix}\perp \\ \parallel\end{matrix} T_{m-m'} = [1 + \begin{matrix}\perp \\ \parallel\end{matrix} \Gamma_{m-}^{e} e^{-j2\beta_m(y^{(1)} - b_{m-1})r_{my}}] \begin{matrix}\perp \\ \parallel\end{matrix} W_m^e$$

$$\begin{matrix}\perp \\ \parallel\end{matrix} \tau_{m+}^{e} \begin{matrix}\perp \\ \parallel\end{matrix} \tau_{m+1,+}^{e} \cdots \begin{matrix}\perp \\ \parallel\end{matrix} \tau_{m'-1,+}^{e} [1 + \begin{matrix}\perp \\ \parallel\end{matrix} \Gamma_{m'+}^{e} e^{-j2\beta_m(b_{m'} - y^{(1')})r_{m'y}}]. \tag{5.34}$$

5.10 SCAN INDEPENDENCE: SINGLE ARRAY IN A SINGLE SLAB

As a good fundamental application of these general cases, let us consider a single planar array with element orientation $\hat{z}$ and located at the distance x in a single slab of thickness d_1 and intrinsic impedance Z_1 as shown in Fig. 5.12.

The array impedance Z_A is readily obtained from (5.33) by noting that

$$Z_A = -\frac{V^{(1')}}{I^{(1)}} \tag{5.35}$$

and by placing the primed element a wire radius a away from the unprimed element. We then obtain

$$Z_A = \frac{Z_1}{2D_x D_z} \sum_k \sum_n \frac{e^{-j\beta_1 a r_{1y}}}{r_{1y}} \left[\perp P_1 \perp P_1^t \perp T_1 + \parallel P_1 \parallel P_1^t \parallel T_1 \right], \tag{5.36}$$

where

$$\begin{matrix}\perp \\ \parallel\end{matrix} T_1 = \frac{\left[1 + \begin{matrix}\perp \\ \parallel\end{matrix} \Gamma_{1-} e^{-j2\beta_1 a_1 r_{1y}}\right] \left[1 + \begin{matrix}\perp \\ \parallel\end{matrix} \Gamma_{1+} e^{-j2\beta_1(d_1 - a_1)r_{1y}}\right]}{1 - \begin{matrix}\perp \\ \parallel\end{matrix} \Gamma_{1-} \begin{matrix}\perp \\ \parallel\end{matrix} \Gamma_{1+} e^{-j2\beta_1 d_1 r_{1y}}}. \tag{5.37}$$

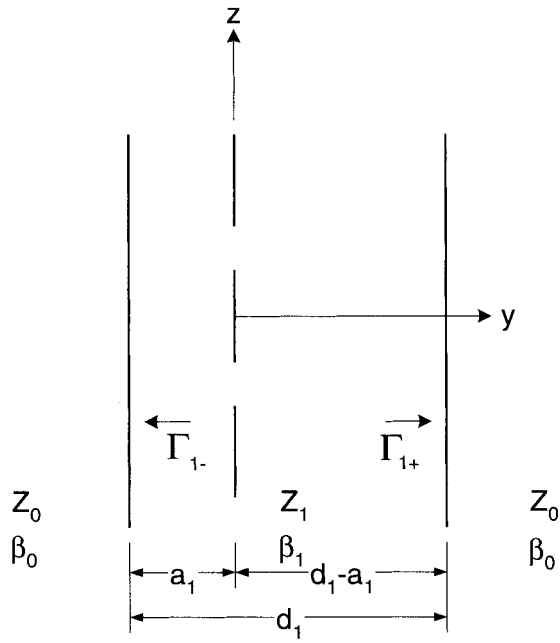

FIGURE 5.12. Single dielectric slab of thickness d_1 with a planar array in the xz-plane with z-oriented elements as shown.

As was done earlier in Section 4.8, we will analyze the situation depending on whether r_y is real or imaginary. We will assume that the dimensions a_1 and d_1 are sufficiently large that

$$e^{-j2\beta_1 a_1 r_{1y}} \sim e^{-j2\beta_1 (d_1 - a_1) r_{1y}} \sim 0$$

for all imaginary values of r_{1y}; that is, from (5.37) we have

$$\begin{matrix} \perp \\ \parallel \end{matrix} T_1 \sim 1 \tag{5.38}$$

for r_{1y} imaginary.[2]

We further note that $e^{-j\beta_1 a r_{1y}}$ in (5.36) is real for r_{1y} imaginary, and so is P_1 and P_1^t (see Fig. 4.7) Thus we can conclude that *all* terms in (5.36) are purely imaginary for r_{1y} imaginary, that is, for $(k, n) \neq (0, 0)$ if there are no grating lobes.

Let us denote the sum of all these imaginary terms by jX_A. We then find from (5.36) that

[2]This simplifying assumption is not needed in general. The rigorous theory will easily handle any case, only the equivalent circuit is a little muddy.

$$Z_A = \frac{Z_1}{2D_x D_z}\frac{1}{r_{1y}}\left[{}_{\perp}P_{1\perp}P_1^t \perp T_1 + {}_{\parallel}P_{1\parallel}P_{1\parallel}^t T_1\right] + jX_A \tag{5.39}$$

where jX_A is given by (5.36) for $(k, n) \neq (0, 0)$.

Further it is readily shown by inspection that (5.37) can be written as

$$T_1 = \frac{2\dfrac{1+\Gamma_- e^{-j2\beta_1 a_1 r_{1y}}}{1-\Gamma_- e^{-j2\beta_1 a_1 r_{1y}}} \cdot 2\dfrac{1+\Gamma_+ e^{-j2\beta_1 (d_1-a_1) r_{1y}}}{1-\Gamma_+ e^{-j2\beta_1 (d_1-a_1) r_{1y}}}}{2\dfrac{1+\Gamma_- e^{-j2\beta_1 a_1 r_{1y}}}{1-\Gamma_- e^{-j2\beta_1 a_1 r_{1y}}} + 2\dfrac{1+\Gamma_+ e^{-j2\beta_1 (d_1-a_1) r_{1y}}}{1-\Gamma_+ e^{-j2\beta_1 (d_1-a_1) r_{1y}}}} \tag{5.40}$$

where we for simplicity have dropped the $\perp$ and $\parallel$ signs.

Substituting (5.40) into (5.39) yields

$$Z_A = Z_{1-} \,||\, Z_{1+} + jX_A \tag{5.41}$$

where[3]

$$Z_{1\pm} = \frac{Z_1}{2D_x D_z}\frac{1}{r_{1y}}\left[{}_{\perp}P_{1\perp}P_1^t{}_{\perp}T_{1\pm} + {}_{\parallel}P_{1\parallel}P_1^t{}_{\parallel}T_{1\pm}\right] \tag{5.42}$$

and

$$T_{1-} = 2\frac{1+\Gamma_{1-} e^{-j2\beta_1 a_1 r_{1y}}}{1-\Gamma_{1-} e^{-j2\beta_1 a_1 r_{1y}}}, \tag{5.43}$$

$$T_{1+} = 2\frac{1+\Gamma_{1+} e^{-j2\beta_1 (d_1-a_1) r_{1y}}}{1-\Gamma_{1+} e^{-j2\beta_1 (d_1-a_1) r_{1y}}}. \tag{5.44}$$

The function T_{1+} given by (5.44) constitutes a bilinear transformation as a function of $j\beta_1(d_1 - a_1)r_{1y}$ when r_{1y} is constant (then Γ is also a constant). As shown in Appendix A, the loci for T_{1+} will be circles with centers on the real axis and going through the points $1 + |\Gamma_{1+}|/1 - |\Gamma_{1+}|$ and $1 - |\Gamma_{1+}|/1 + |\Gamma_{1+}|$ corresponding to $(d_1 - a_1)r_{1y} = n\frac{\lambda_1}{2}$ and $\frac{\lambda_1}{4}(1 + 2n)$, respectively, as illustrated in Fig. 5.13 top. Also shown in Fig. 5.13 bottom are the typical Fresnel reflection coefficients ${}_{\perp}\Gamma_{1+}$ and ${}_{\parallel}\Gamma_{1+}$ for $Z_1 = \frac{1}{2}Z_0$ as a function of r_{1y} going from $r_{1y} = 1$ ($\theta_1 = 0°$) to $r_{1y} = 0$ ($\theta_1 = 90°$). Inspection of these curves readily shows that the $\perp$ case always will lead to circles larger than the circle for 0° (normal). However, the $\parallel$ case will lead to smaller circles for angles less than the Brewster angle where they reduce to merely a point, and from there on they grow again.

By inspection of ${}_{\perp}^{\parallel}T_{1+}$ as shown in Fig. 5.13 top, it is clear that if the dielectric slab $(d_1 - a_1)$ is going to have maximum effect on the impedance Z_{1+} as given by

[3]Note that Z_1 without any sign still refers to the intrinsic impedance of the slab.

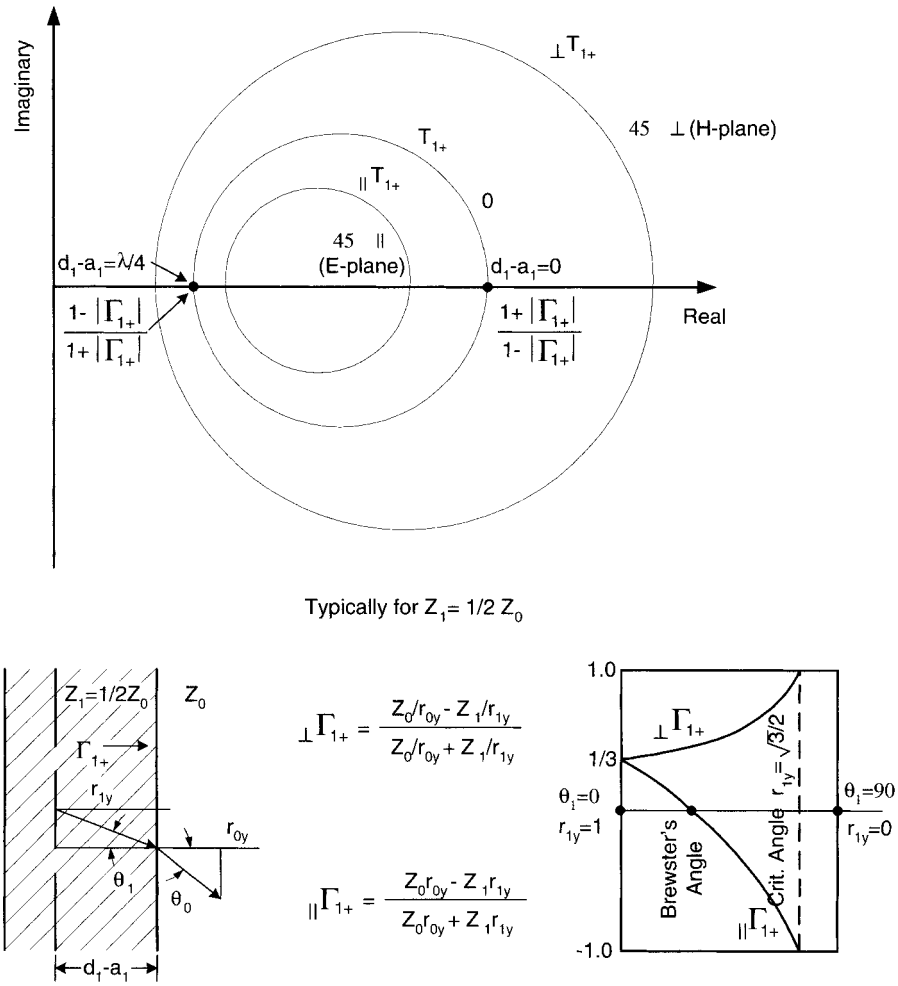

FIGURE 5.13. *Top*: Typical T_{1+}-function plotted in the complex plane for a dielectric slab of thickness $(d_1 - a_1)$. *Bottom-left*: An array in a dielectric slab with $Z_1 = \frac{1}{2}Z_0$ radiating in the directions $\bar{r}_1$ and $\bar{r}_0$ inside the slab Z_1 and in free space Z_0, respectively. *Bottom-right:* Fresnel reflection coefficient Γ_{1+} for a plane wave going from dielectric to free space.

(5.42) through (5.44) we must choose $(d_1 - a_1) \sim \lambda_1/4$ leading to

$$T_{1+} = 2\frac{1-\Gamma_{1+}}{1+\Gamma_{1+}}, \tag{5.45}$$

or by application of (C.7) and (C.8), we have

$$T_{1+} = \begin{cases} 2\dfrac{Z_1}{Z_0}\dfrac{r_{0y}}{r_{1y}} & \text{for } \perp \text{ scan (H-plane scan),} \\ 2\dfrac{Z_1}{Z_0}\dfrac{r_{1y}}{r_{0y}} & \text{for } \parallel \text{ scan (E-plane scan).} \end{cases} \tag{5.46}$$

Further, from (5.11) and (5.12), we find for elements of Hertzian nature (see also Section 4.11.2)

$$\perp P_1 = \perp P_1^t = \hat{z} \cdot \perp \hat{n}_1 P_1 = \begin{cases} \Delta l & \text{for } \perp \text{ scan (H-plane),} \\ 0 & \text{for } \parallel \text{ scan (E-plane),} \end{cases} \tag{5.47}$$

$$\parallel P_1 = \parallel P_1^t = \hat{z} \cdot \parallel \hat{n}_1 P_1 = \begin{cases} 0 & \text{for } \perp \text{ scan (H-plane),} \\ \sim \Delta l r_{1y} & \text{for } \parallel \text{ scan (E-plane),} \end{cases} \tag{5.48}$$

where we have applied (5.13) to yield $P_1 \sim \Delta l$. Substituting (5.46), (5.47), and (5.48) into (5.42), we have

$$Re Z_{1+} \sim \begin{cases} \dfrac{Z_1}{2D_x D_z}\dfrac{1}{r_{1y}}\left[\Delta l^2 \dfrac{2Z_1}{Z_0}\dfrac{r_{0y}}{r_{1y}} + 0\right] & \text{for } \perp \text{ scan,} \\ \dfrac{Z_1}{2D_x D_z}\dfrac{1}{r_{1y}}\left[0 + \Delta l^2 r_{1y}^2 \dfrac{2Z_1}{Z_0}\dfrac{r_{1y}}{r_{0y}}\right] & \text{for } \parallel \text{ scan.} \end{cases} \tag{5.49}$$

Inspection of (5.49) readily shows that if the $\perp$ and $\parallel$ scans are required to yield the *same* impedance $Re Z_{1+}$ at a certain scan angle r_{1y}, we must simply require that

$$\frac{r_{0y}}{r_{1y}} = \frac{r_{1y}^3}{r_{0y}} \quad \text{or} \quad r_{1y}^2 = r_{0y}$$

that is,

$$\cos^2 \theta_1 = \cos \theta_0. \tag{5.50}$$

Further θ_1 and θ_0 are connected by Snell's law:

$$\sin \theta_1 = \frac{1}{\sqrt{\epsilon_{r1}}} \sin \theta_0. \tag{5.51}$$

Solving (5.50) and (5.51) readily yields

$$\epsilon_{r1} = 1 + \cos \theta_0 = 1 + r_{0y}. \tag{5.52}$$

Eq. (5.52) constitutes the condition for scan independence by using a dielectric slab of effective relative dielectric constant ϵ_{r1} and thickness $(d_1 - a_1) \sim \lambda_1/4$ (i.e., minimum change of scan impedance as a function of scan angle).

The impedance Z_{1-} given by (5.42) can be treated analogously to Z_{1+} or terminated in a ground plane placed at a suitable distance x from the array. The value of

ϵ_1 for scan equalization at $\theta_0 = 60°$ ($r_{0y} = \frac{1}{2}$) is, according to (5.52), $\epsilon_1 = 1.5$. *Higher angles are seen to lead to lower values of* ϵ_{r1}. Typical curves for Z_{1+} calculated from (5.49) are shown in Fig. 5.14 for $\epsilon_{r1} = 1.3, 1.5, 1.7$. Finally it should be mentioned that the last term in (5.41), namely jX_A, in general will show a minimal variation with scan angle by keeping the inter-element spacings D_x and D_z small in terms of wavelength.

Scan independence described above may play a very important role when designing arrays of not only dipoles but also other elements as well, and preferably being small. However, perhaps the most remarkable fact is that the same technique also works when using magnetic dipoles (slots) rather than electric ones. This will be discussed in detail in Chapters 6 and 7. (See also Problems 5.2, 6.2 and 6.3.)

5.11 SURFACE WAVES ON PERIODIC STRUCTURES OF ELECTRIC DIPOLES: FREE AND FORCED

Every time a dielectric slab is placed next to any periodic surface there is a general concern about the possibility of surface waves (and rightly so). In this section we address this problem in more detail.

Consider the total scan impedance Z_A as given by (5.36) and (5.37). Each of the terms in this series represents an impedance for a particular mode; that is, all these mode impedances will be connected in a series. Thus, if one of them goes to infinity, all energy supplied by the terminals will go into that mode and leave all the rest of them "cold"; that is, no radiation is possible for these modes.

When we analyzed Z_A above we found it convenient to split it up into the two impedances Z_{1+} and Z_{1-} connected in parallel. When analyzing surface waves, this is in general not to be recommended, since, as we will see, Z_{1+} and Z_{1-} typically become purely imaginary when surface waves occur. Thus, if one impedance becomes infinite, the other can easily take in power, since they are in *parallel*. To be sure, we can easily calculate Z_A from Z_{1+} and Z_{1-}, but when analyzing surface waves, it is in general far easier to stay with the original expressions (5.36) and (5.37).

Let us consider the simple case where an array is located in a slab of thickness d_1 at the distance a_1 from the left interface as shown in Fig. 5.15 top. In that event we have $\Gamma_{1-} = \Gamma_{1+}$, and (5.37) reduces to

$$\underset{\parallel}{\perp} T_1 = \frac{\left[1 + \underset{\parallel}{\perp}\Gamma_{1+}e^{-j2\beta_1 a_1 r_{1y}}\right]\left[1 + \underset{\parallel}{\perp}\Gamma_{1+}e^{-j2\beta_1(d_1-a_1)r_{1y}}\right]}{\left[1 + \underset{\parallel}{\perp}\Gamma_{1+}e^{-j\beta_1 d_1 r_{1y}}\right]\left[1 - \underset{\parallel}{\perp}\Gamma_{1+}e^{-j\beta_1 d_1 r_{1y}}\right]}. \tag{5.53}$$

Inspection of (5.53) readily shows that *singularities* will occur for

$$\underset{\parallel}{\perp}\Gamma_{1+}e^{-j\beta_1 d_1 r_{1y}} = \pm 1 = e^{-jn_1\pi}, \qquad \text{where} \quad n_1 = 0, 1, 2, \ldots, \tag{5.54}$$

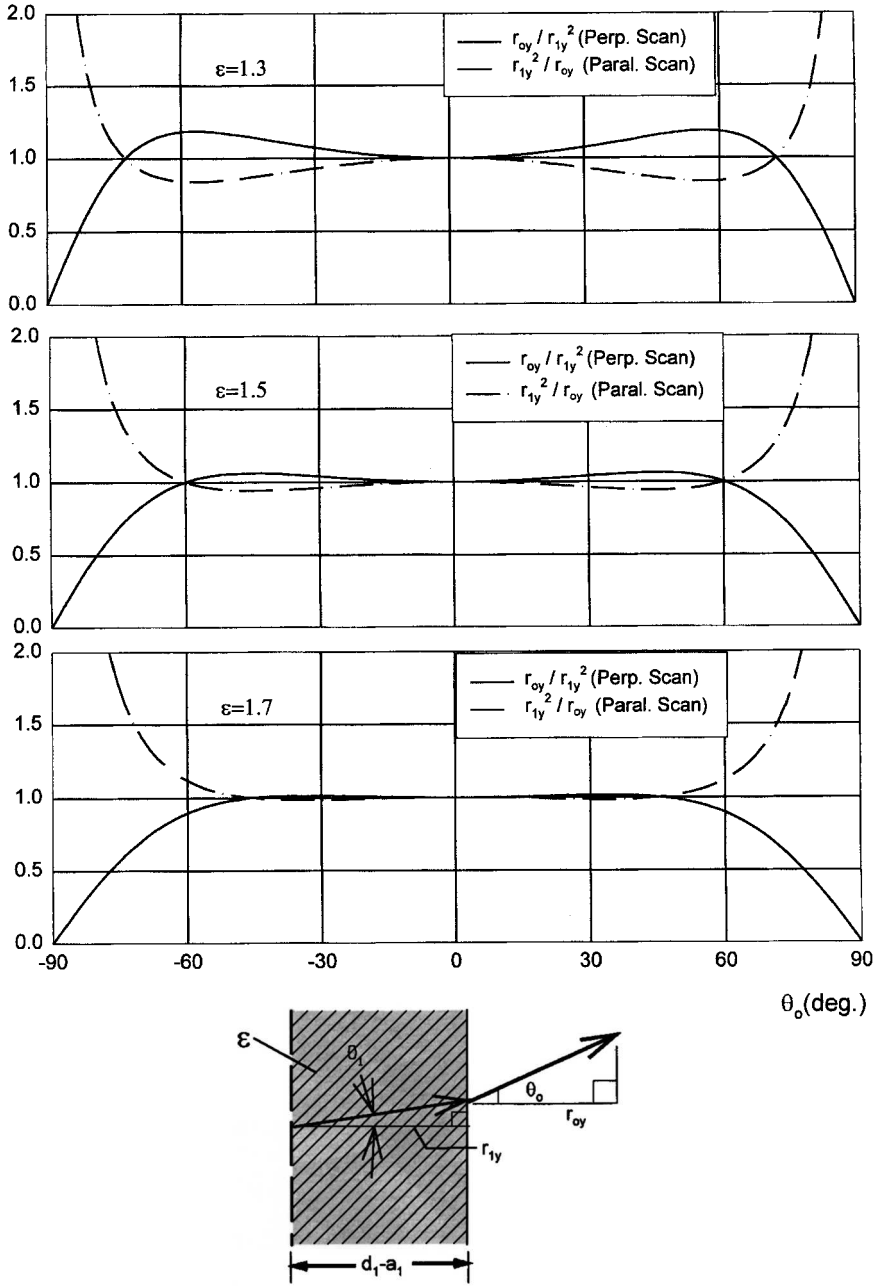

FIGURE 5.14. Typical scan compensation obtained for Z_{1+} by use of a dielectric slab of thickness $\beta_1(d_1 - a_1)r_{1y} \sim \pi/2$ between the dipole array and free space. Complete equalization between $\perp$ and $\parallel$ scan is obtained at an angle determined by ϵ_1 as shown by the three cases; see (5.52). Compare with Fig. 4.16 without dielectric.

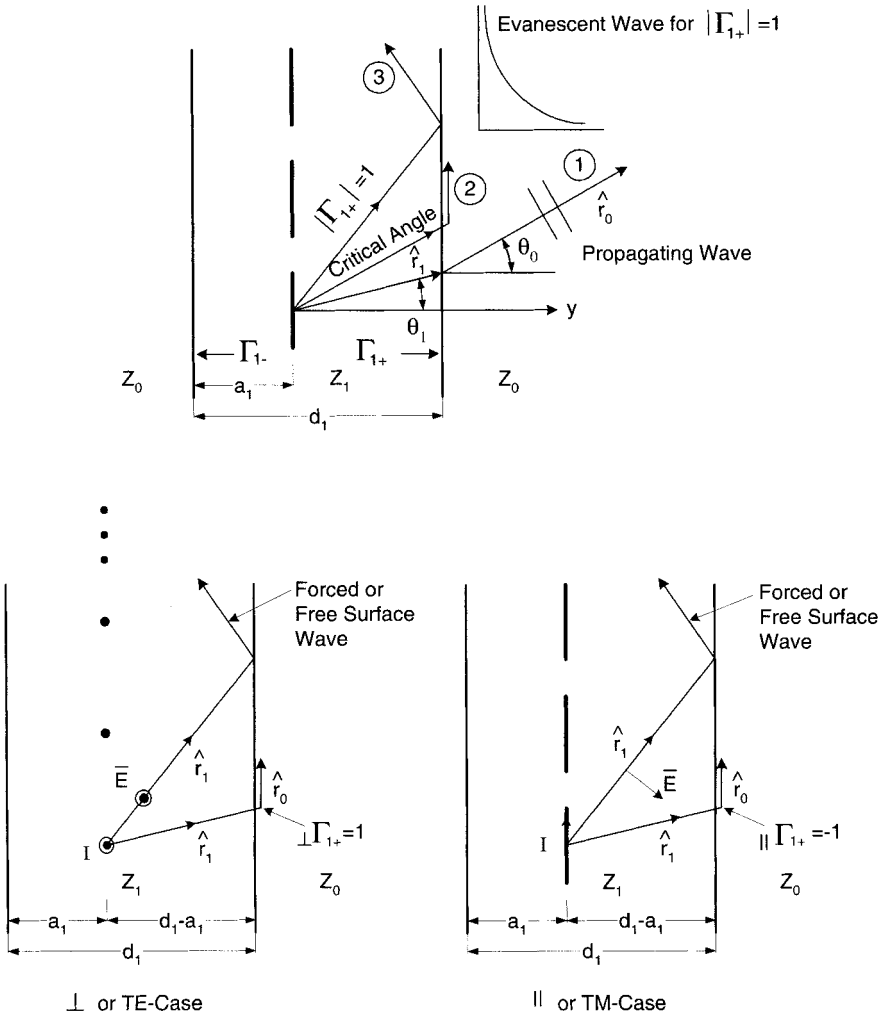

FIGURE 5.15. *Top:* Three different directions of the plane waves(s) emanating from an array in a slab: (1) Angle of incidence smaller than the critical angle leading to a propagating wave in Z_0. (2) Critical angle showing borderline case. (3) Incidence angle larger than the critical angle leading to a trapped wave inside the slab and an evanescent wave outside in Z_0. *Bottom:* Trapped waves for the $\perp$ case (left) and $\|$ case (right).

provided that they are not canceled by corresponding nulls in the numerator, as will be discussed later.

To be sure we may also encounter a singularity for [see Eq. (5.36)]:

$$r_{1y} = 0. \tag{5.55}$$

This case will be discussed in Section 5.12.

A necessary condition for satisfying (5.54) is

$$\left| \begin{matrix} \perp \\ \parallel \end{matrix} \Gamma_{1+} \right| = 1. \tag{5.56}$$

Typically this happens every time a wave goes from a dense medium Z_1 into a less dense medium Z_0 at an angle of incidence such that r_{0y} becomes imaginary.

Again, this situation is illustrated in Fig. 5.15 top, where we show three typical directions of $\bar{r}_1$, namely with directions such that:

1. $\Gamma_{1+} < 1$ (i.e., partially reflected) allowing waves to propagate into Z_0.
2. $|\Gamma_{1+}| = 1$ corresponding to the critical angle, the limiting case between 1 and 3.
3. $|\Gamma_{1+}| = 1$ for all angles greater than the critical angle (i.e., total reflection) allowing only evanescent waves into medium Z_0 to the right. We will split the following investigation up into the $\perp$ and $\parallel$ cases.

Perpendicular Case From Appendix C, Eq. (C.1), we have

$$\perp\Gamma_{1+} = \frac{Z_0 r_{1y} - Z_1 r_{0y}}{Z_0 r_{1y} + Z_1 r_{0y}},$$

and for $r_{0y} = -j|r_{0y}|$ corresponding to total reflection as discussed above, we obtain (we will in the following drop the r in the ϵ_{r1} and μ_{r1}):

$$\perp\Gamma_{1+} = \frac{Z_0 r_{1y} + jZ_1|r_{0y}|}{Z_0 r_{1y} - jZ_1|r_{0y}|} = e^{+j2\tan^{-1}(Z_1/Z_0)(|r_{0y}|/r_{1y})}. \tag{5.57}$$

Substituting (5.57) into (5.54), we have

$$e^{j2\tan^{-1}(Z_1/Z_0)(|r_{0y}|/r_{1y})} e^{-j\beta_1 d_1 r_{1y}} = \pm 1 = e^{-jn_1\pi}, \qquad n_1 = 0, 1, 2, \ldots,$$

or

$$\frac{Z_1}{Z_0}\frac{|r_{0y}|}{r_{1y}} = \tan\left(\beta_1 \frac{d_1}{2} r_{1y} - \frac{\pi}{2} n_1\right). \tag{5.58}$$

Furthermore θ_1 and θ_0 (see Fig. 5.15 top) are related by Snell's law, and recalling that $r_{1y} = \cos\theta_1$, we obtain

$$\frac{\sin\theta_1}{\sin\theta_0} = \frac{1}{\sqrt{\mu_1\epsilon_1}} = \frac{\sqrt{1 - r_{1y}^2}}{\sqrt{1 + |r_{0y}|^2}}$$

or

$$|r_{0y}| = \sqrt{(\mu_1\epsilon_1 - 1) - \mu_1\epsilon_1 r_{1y}^2}. \tag{5.59}$$

Substituting (5.59) into (5.58) yields

$$\sqrt{\left(\beta_0\frac{d_1}{2}\right)^2(\mu_1\epsilon_1 - 1) - \left(\beta_1\frac{d_1}{2}r_{1y}\right)^2} = \frac{1}{\mu_1}\beta_1\frac{d_1}{2}r_{1y}\tan\left(\beta_1\frac{d_1}{2}r_{1y} - \frac{\pi}{2}n_1\right), \quad n_1 = 0, 1, 2, \ldots. \tag{5.60}$$

According to, for example, Harrington [36], (5.60) is merely the characteristic equation for a surface wave with $\perp$ polarization (or the *TE* case) as shown in Fig. 5.15 bottom-left. More on this subject will be given later after we investigate the $\parallel$ case below.

We further evaluate the impedance terms associated with the forced as well as the free surface waves. It is in that event alright to use the form given by (5.42), (5.43), and (5.44).

For any value of r_{1y} leading to $-j|r_{0y}|$, we obtain, by substituting (5.57) into (5.44),

$$_{\perp}T_{1+} = 2\frac{1 + e^{j2\tan^{-1}Z_1/Z_0|r_{0y}|/r_{1y}}e^{-j2\beta_1(d_1-a_1)r_{1y}}}{1 - e^{j2\tan^{-1}Z_1/Z_0|r_{0y}|/r_{1y}}e^{-j2\beta_1(d_1-a_1)r_{1y}}} = 2j\cot{}_{\perp}\Psi, \tag{5.61}$$

where

$$_{\perp}\Psi = \tan^{-1}\frac{Z_1}{Z_0}\frac{|r_{0y}|}{r_{1y}} - \beta_1(d_1 - a_1)r_{1y}.$$

Inspection of (5.42) shows that since r_{1y} as well as $_{\perp}P_1$ ($_{\parallel}P_1$) $_{\perp}P_1^t$ ($_{\parallel}P_1^t$) are purely real for the impedance term considered here while the T-factor given by (5.61) is purely imaginary, this particular impedance term will be *purely imaginary*. The same statement goes for $_{\perp}T_{1-}$. In other words, no real energy can be associated with this particular impedance term. The reason is that this particular direction of $\hat{r}_1$ is totally reflected from the dielectric interface, so that no real energy goes into space Z_0 to the right. In particular, if the surface wave condition (5.60) is satisfied, then that particular impedance term will be infinite; that is, no real energy can go into any other mode since all mode impedances are in series (see introduction of this section). So this particular surface wave will dominate all other modes. We call this a *free surface wave* as opposed to other values of r_{1y} where we still have total reflection at the interface and the impedance terms are purely imaginary but *finite*. They can consequently exist only if they are constantly being "agitated" by the generators driving the array. We call these waves *forced surface waves*. They basically look like the free ones.

Parallel Case From Appendix C we find from (C.2) and proceed as we did above in the $\perp$ case:

$$_{\|}\Gamma_{1+} = \frac{Z_0 r_{0y} - Z_1 r_{1y}}{Z_0 r_{0y} + Z_1 r_{1y}} = \frac{-jZ_0|r_{0y}| - Z_1 r_{1y}}{-jZ_0|r_{0y}| + Z_1 r_{1y}} = -e^{j2\tan^{-1} Z_0/Z_1|r_{0y}|/r_{1y}}. \tag{5.62}$$

Substituting (5.62) into (5.54):

$$e^{j2\tan^{-1}(Z_0/Z_1)(|r_{0y}|/r_{1y})} e^{-j2\beta_1(d_1/2)r_{1y}} = \pm 1 = e^{-j\pi n_1}, \quad \text{where } n_1 = 0, 1, 2, \ldots,$$

or

$$|r_{0y}| = \frac{Z_1}{Z_0} r_{1y} \tan\left(\beta_1 \frac{d_1}{2} r_{1y} - \frac{\pi}{2} n_1\right). \tag{5.63}$$

Finally, substituting Snell's law (5.59) into (5.63) yields

$$\sqrt{\left(\beta_0 \frac{d_1}{2}\right)^2 (\mu_1\epsilon_1 - 1) - \left(\beta_1 \frac{d_1}{2} r_{1y}\right)^2} = \frac{1}{\epsilon_1}\left(\beta_1 \frac{d_1}{2} r_{1y}\right) \tan\left(\beta_1 \frac{d_1}{2} r_{1y} - \frac{\pi}{2} n_1\right), \quad n_1 = 0, 1, 2, \ldots. \tag{5.64}$$

As shown, for example, in Harrington [36], (5.64) is merely the characteristic equation for a surface wave with $\|$ polarization (or *TM*) as shown in Fig. 5.15 bottom-right. Just as described above for the $\perp$ case, we will in the $\|$ case obtain an infinitely high impedance when satisfying (5.64) corresponding to a free surface wave.

In the more general case where a specific direction of $\hat{r}_1$ merely leads to total reflection, we find that by substituting (5.62) into (5.44), similar to the $\perp$ case above,

$$_{\|}T_{1+} = 2\frac{1 - e^{j2\tan^{-1} Z_0/Z_1|r_{0y}|/r_{1y}} e^{-j2\beta_1(d_1 - a_1)r_{1y}}}{1 + e^{j2\tan^{-1} Z_0/Z_1|r_{0y}|/r_{1y}} e^{-j2\beta_1(d_1 - a_1)r_{1y}}} = -2j \tan {}_{\|}\Psi, \tag{5.65}$$

where

$$_{\|}\Psi = \tan^{-1} \frac{Z_0}{Z_1} \frac{|r_{0y}|}{r_{1y}} - \beta_1(d_1 - a_1)r_{1y},$$

leading to a purely imaginary impedance term as was discussed above in the $\perp$ case.

Inspection of the two characteristic equations (5.60) and (5.64) shows them to be identical except for the factors μ_1 and ϵ_1. An easy appreciation of possible solutions of these equations is shown graphically in Fig. 5.16 where we have shown the left side of the equation in the form of a circle and the right side in the form of tan-functions multiplied by their argument. When the two sets of curves intersect, we

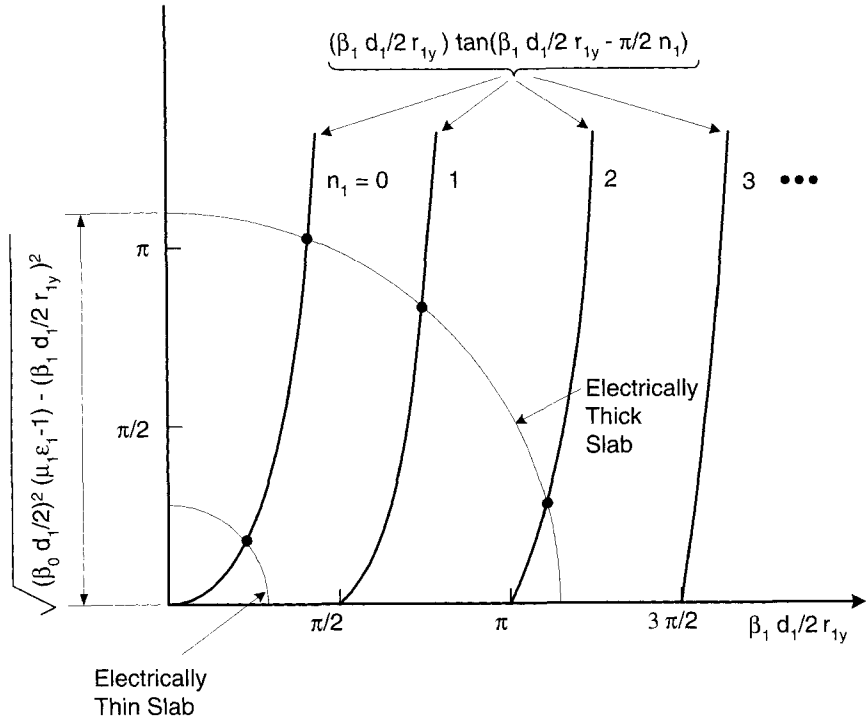

FIGURE 5.16. Graphical determination of free surface waves by the intersection between a circle with radius determined by the electrical thickness of the slab and tangentlike curves as shown. For $a_1 = d_1/2$ (i.e., the array is located in the middle of the dielectric slab) the possible surface waves reduce to $n_1 = 0, 2, \ldots$ for the $\perp$ case and to $n_1 = 1, 3, \ldots$ for the $\parallel$ case.

have a possible solution for a free surface wave. Note that electrically thick slabs lead to many surface wave solutions for both the $\perp$ and $\parallel$ cases.[4]

Inspection of (5.53) also shows that the *nulls* are encountered when

$$\begin{matrix}\perp\\\parallel\end{matrix}\Gamma_1 e^{-j2\beta_1 a_1 r_{1y}} = -1 = e^{-jn_2\pi} \qquad \text{for} \quad n_2 = 1, 3, \ldots \tag{5.66}$$

and

$$\begin{matrix}\perp\\\parallel\end{matrix}\Gamma_1 e^{-j2\beta_1 (d_1 - a_1) r_{1y}} = -1 = e^{-jn_2\pi} \qquad \text{for} \quad n_2 = 1, 3, \ldots. \tag{5.67}$$

Satisfying (5.66) and (5.67) requires that $|\begin{matrix}\perp\\\parallel\end{matrix}\Gamma_1| = 1$ as in the case of singularities.

[4]According to Prof. Robert Kouyoumjian it appears that this approach was first shown by John Brown in 1953 [37]. However, Prof. Stuart Collins informed me that a similar approach was used by L. I. Schiff in quantum mechanics in 1949 [38].

However, contrary to the singularity case, the null here means that no energy is going into this particular mode while plenty can go into the rest of the mode impedances because they are all connected in a series.

An important case is where a null coincides with a singularity and essentially cancels it. Inspection of (5.53) shows this to occur when

$$a_1 = \frac{d_1}{2} + \frac{n_3 \lambda_1}{2r_{1y}}, \qquad n_3 = 0, \pm 1, \pm 2, \ldots. \tag{5.68}$$

We are interested in the most important case of this cancellation case (5.68) where $n_3 = 0$ corresponding to the array being located in the middle of the slab. In that event n_1 in (5.60) is limited to $n_1 = 0, 2, 4, \ldots$ for the $\perp$ case and to $n_1 = 1, 3, \ldots$ in the $\parallel$ case, as also noted in Fig. 5.16. In other words, for a thin slab with the arrays located in the middle, a surface wave is possible only in the $\perp$ case.

Several instructive examples of scan impedances encountering surface waves and onset of trapped as well as free space grating lobe analyses are given in Section 5.13. The reader should also compare the electric dipole case with a similar slot case as discussed in Section 6.7. There are many similarities but also profound differences between these two cases.

5.12 ONSET OF TRAPPED AND FREE SPACE GRATING LOBES

In the previous section we analyzed the nature of surface waves in dielectric and pointed out that free surface waves exist only when the characteristic equations [e.g., (5.60) and (5.64)] are satisfied. However, we also showed that *forced surface waves* are present much more frequently than free surface waves but without disastrous results (they merely add a *finite* imaginary component to Z_A and thus allow some radiation of the principal mode). In this section we analyze just exactly when these various types of surface waves occur and their effect on the scan impedance Z_A.

More specifically, consider Fig. 5.17 showing an array embedded in a dielectric slab with its main beam pointing in a fixed direction (1). If the frequency is low enough, all other waves emanating from this array will be evanescent. However, as we increase the frequency, we will eventually reach the point where a grating lobe inside the dielectric slab is "born" as indicated by (2). Further increase of frequency enables this grating lobe to propagate obliquely toward the dielectric interface where it is totally reflected as shown by (3), since it is incident at an angle greater than the critical angle as indicated by (4). Finally (5) indicates a complete emergence of the grating lobe in free space. We will, as earlier, investigate the $\perp$ and $\parallel$ cases separately.

Further, to gain a broader perspective, we will first consider the case where there is no dielectric.

5.12.1 Onset without Dielectric

For no dielectric $\underset{\parallel}{\perp} T_1 = 1$, and the general expression (5.36) reduces to

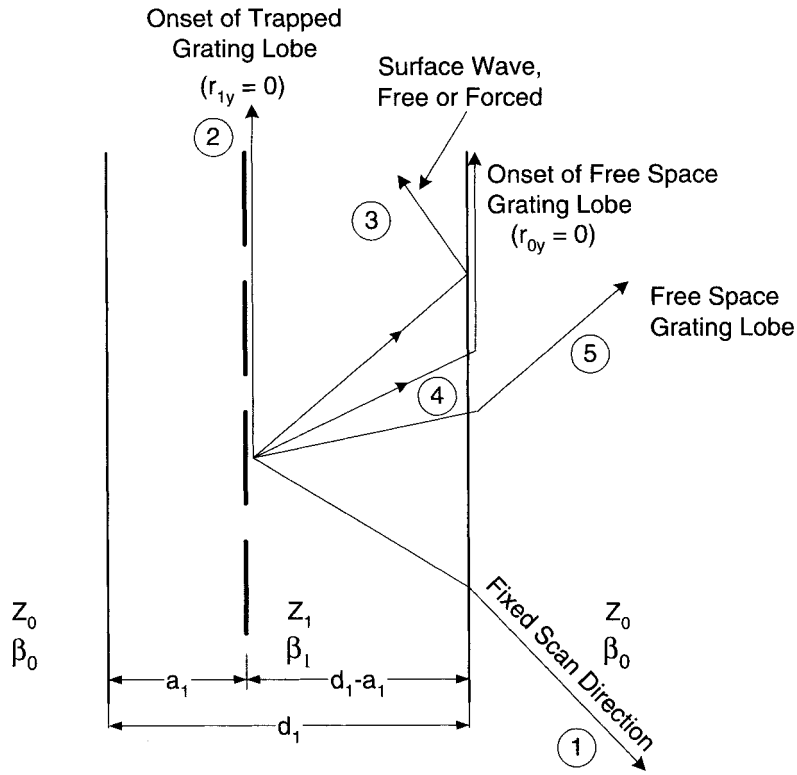

FIGURE 5.17. By keeping a fixed scan direction (1) and increasing the frequency we will first see the onset of a trapped grating lobe (2), and later a forced surface wave (3) that may go into a free surface wave, then onset of free space grating lobe (4), and finally a full fledged grating lobe in free space (5).

$$Z_A = \frac{Z_0}{2D_x D_z} \sum_k \sum_n \frac{e^{-j\beta_1 a r_{0y}}}{r_{0y}} \left[{}_{\perp}P_{1\perp} P_1^t + {}_{\parallel}P_{1\parallel} P_1^t \right]. \tag{5.69}$$

Further, substituting the pattern factor as given by (5.47) yields the following

Perpendicular Scan

$$\Delta Z_{A\ G.L.} \sim \frac{Z_0}{2D_x D_z} \frac{\Delta l^2}{r_{0y}} \to \infty \qquad \text{for} \quad r_{0y} = 0 \quad \text{at the onset of G.L.} \tag{5.70}$$

where $\Delta Z_{A\ G.L.}$ is the impedance terms of the lowest-order evanescent mode in (5.69) that becomes a grating lobe when $r_{0y} \geq 0$.

Similarly, by substituting (5.48), we obtain the following

Parallel Scan

$$\Delta Z_{A\,G.L.} \sim \frac{Z_0}{2D_xD_z}\frac{\Delta l^2}{r_{0y}}r_{0y}^2 \to 0 \quad \text{for} \quad r_{0y} = 0 \text{ (at the onset of a grating lobe).} \tag{5.71}$$

Typical impedance plots of Z_A at the onset of grating lobes are shown in Fig. 5.18 left ($\perp$ scan) and right ($\parallel$ scan), respectively. Note that at the onset of a grating lobe in the $\perp$ case, we not only observe a singularity in the imaginary part of Z_A but also a finite jump in the real part, see Fig. 5.18 top-left. This phenomenon is caused by the fact that we all of a sudden must provide real energy in the grating lobe direction as well. This is in contrast to the $\parallel$ case. Here energy to the grating lobe can only rise slowly as it emerges away from the plane of the array because the element pattern in this case has a null in the grating lobe direction. Thus, in the $\parallel$ case, we only observe a discontinuity for the derivative of Z_A; see Fig. 5.18 top-right. (See also Figs. 5.19 and 5.20 for actual calculated cases.)

5.12.2 Onset with Dielectric Slab

Perpendicular Scan The onset of a trapped grating lobe inside the dielectric slab implies that $r_{1y} = 0$ while $r_{0y} \neq 0$ (see Fig. 5.17). From (5.61) we obtain for $r_{1y} = 0$,

$$\perp T_{1+} = 2\frac{1 + e^{j2\tan^{-1} Z_1/Z_0|r_{0y}|/r_{1y}}}{1 - e^{j2\tan^{-1} Z_1/Z_0|r_{0y}|/r_{1y}}} = \frac{2j}{\tan(\tan^{-1}\frac{Z_1}{Z_0}\frac{|r_{0y}|}{r_{1y}})} = 2j\frac{Z_0}{Z_1}\frac{r_{1y}}{|r_{0y}|}. \tag{5.72}$$

By substituting (5.72) and (5.47) into (5.42), we obtain for the impedance increment caused by the trapped grating lobe

$$\perp\Delta Z_{A\,T.G.L.} = \frac{Z_1}{2D_xD_z}\frac{\Delta l^2}{r_{1y}}(2j)\frac{Z_0}{Z_1}\frac{r_{1y}}{|r_{0y}|} = 2j\frac{Z_0}{2D_xD_z}\frac{\Delta l^2}{|r_{0y}|}. \tag{5.73}$$

Clearly, no discontinuity at the onset of a trapped grating lobe for the $\perp$ case when $r_{1y} = 0$ (unless in the unlikely event $r_{0y} = 0$).

The onset of free space grating lobes implies that $r_{0y} = 0$ (see Fig. 5.17), and from (5.61) we obtain

$$\perp T_{1+} = 2\frac{1 + e^{j\tan^{-1} Z_1/Z_0|r_{0y}|/r_{1y}}e^{-j2\beta_1 d_1/2r_{1y}}}{1 - e^{j\tan^{-1} Z_1/Z_0|r_{0y}|/r_{1y}}e^{-j2\beta_1 d_1/2r_{1y}}} = -2j\cot\left(\beta_1\frac{d_1}{2}r_{1y}\right). \tag{5.74}$$

Substituting (5.74) and (5.47) into (5.42), we obtain for the impedance increment caused by the *free space grating lobe* (FSGL)

$$\perp\Delta Z_{A\,FSGL} = -2j\frac{Z_1}{2D_xD_z}\frac{\Delta l^2}{r_{1y}}\cot\left(\beta_1\frac{d_1}{2}r_{1y}\right), \tag{5.75}$$

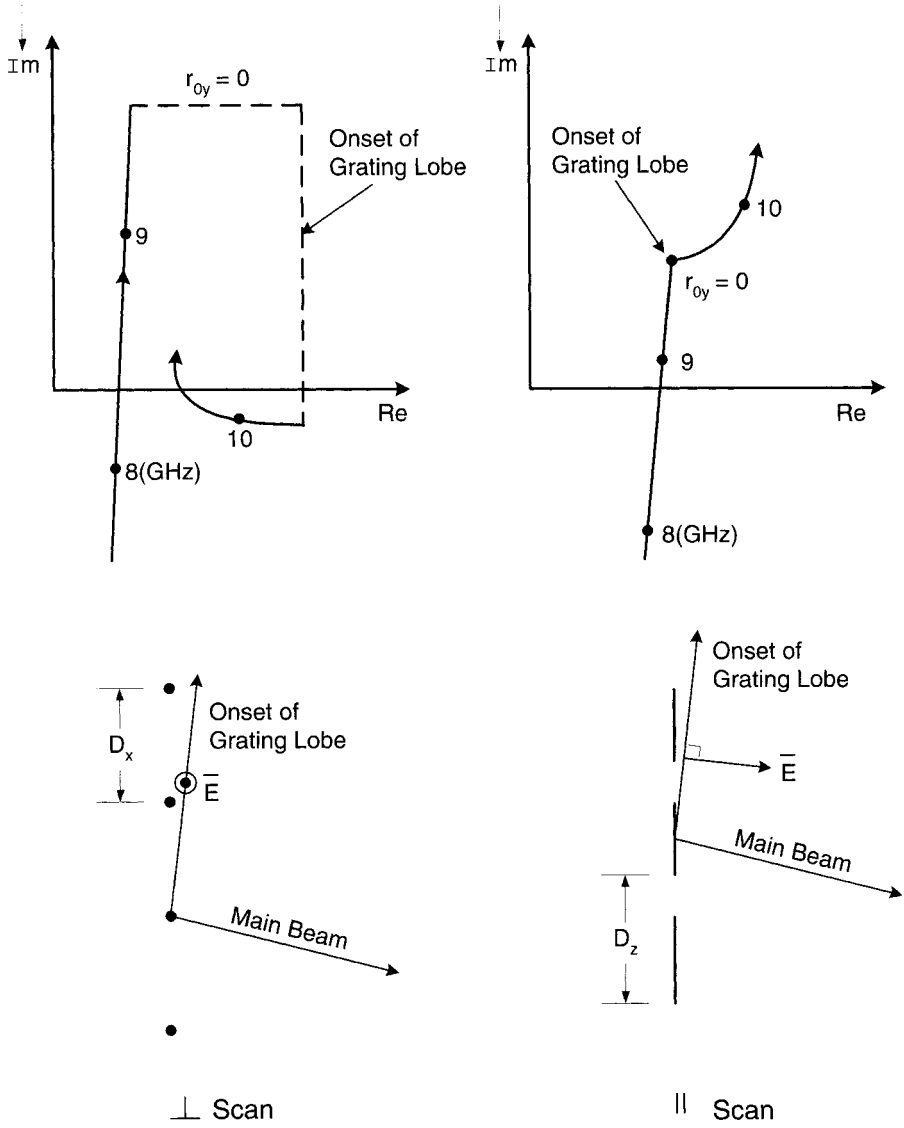

FIGURE 5.18. Onset of grating lobe in the no dielectric case. *Top:* Impedance Z_{1+} for $\perp$ scan (left) and for $\parallel$ scan (right). *Bottom:* Illustration of the arrays and the onset of grating lobes for $\perp$ scan (left) and $\parallel$ scan (right).

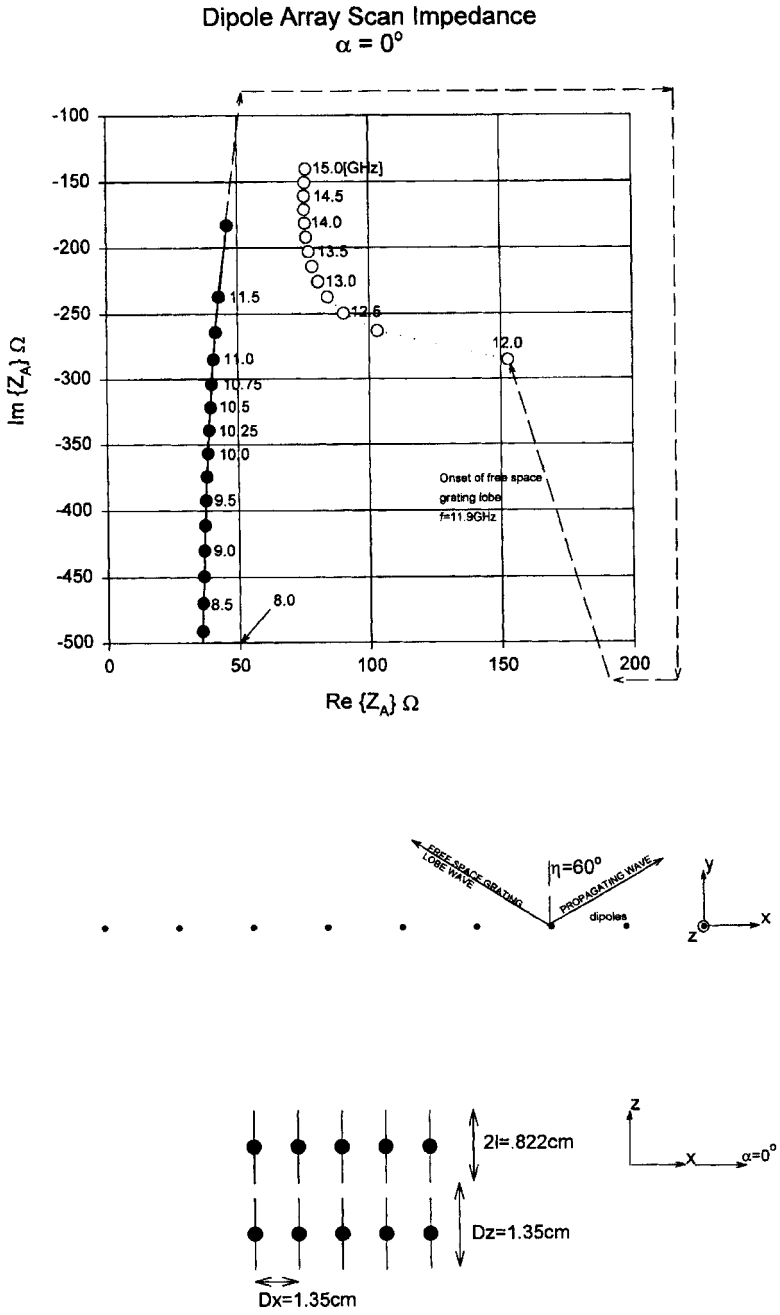

FIGURE 5.19. Complex plot of the scan impedance Z_A for a dipole array without dielectric as shown. Scan angle $\eta = 60°$ in $\perp$ plane (H-plane, $\alpha = 0°$). Note different scales for real and imaginary axes.

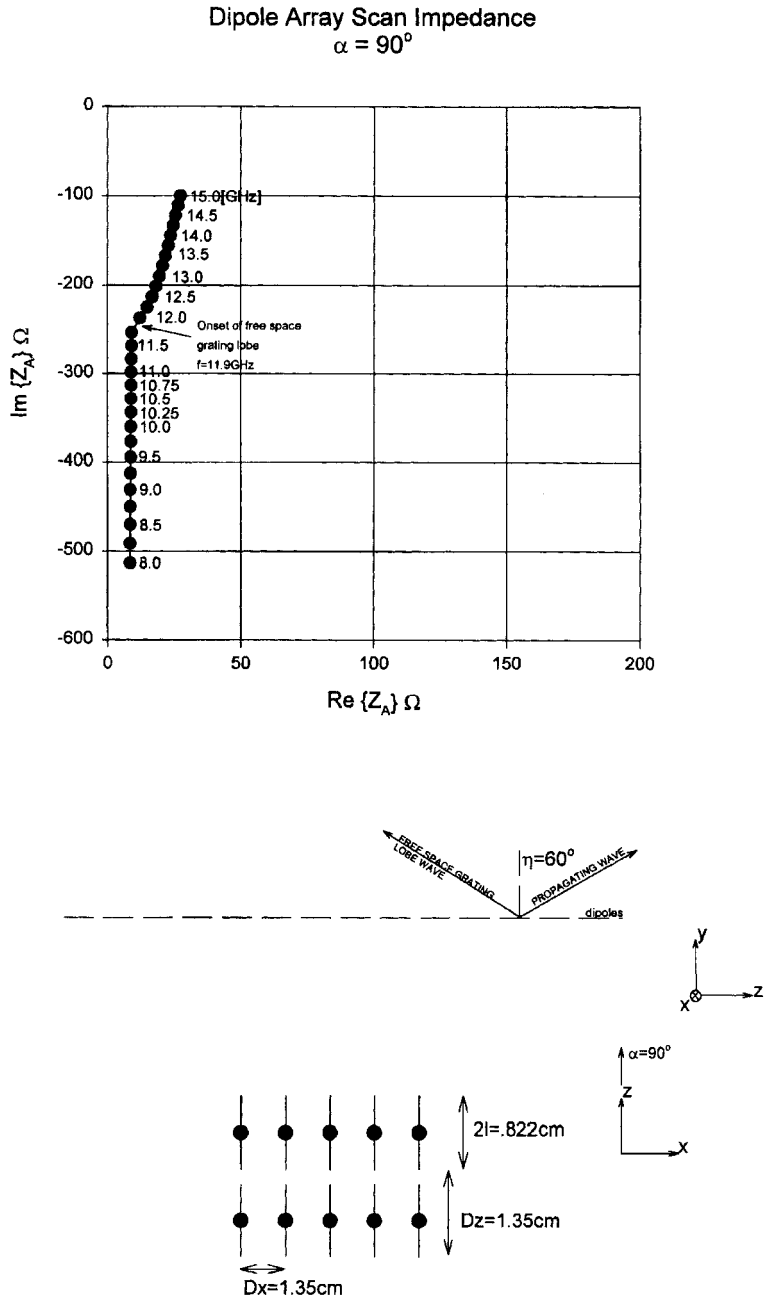

FIGURE 5.20. Complex plot of the scan impedance Z_A for a dipole array without dielectric as shown. Scan angle $\eta = 60°$ in the $\parallel$ plane (E-plane, $\alpha = 90°$). Note different scales for real and imaginary axes.

So no discontinuity at the onset of free space grating lobes when $r_{0y} \to 0$ for $\perp$ scan. However, for $\beta_1 \frac{d_1}{2} r_{1y} = \frac{\pi}{2} n_1 (n_1 = 2, 4, \ldots)$, we have $\cot(\beta_1 \frac{d_1}{2} r_{1y}) = \pm\infty$; we obviously have a pole. This situation, namely $r_{0y} = 0$, corresponds to an incident wave at the critical angle as illustrated in Fig. 5.15 bottom-left. From (5.57) we readily see that in this case ${}_{\perp}\Gamma_{1+} = 1$, corresponding to an open circuit. Thus the input impedance of this particular mode is proportional to $\cot(\beta_1 \frac{d_1}{2} r_{1y})$; it will be infinite when the argument is equal to $\frac{\pi}{2} n_1 \quad (n_1 = 2, 4, \ldots)$ as stated above. This situation simply corresponds to the cutoff of the surface wave modes $(n_1 = 2, 4, \ldots)$ shown in Fig. 5.16.

Parallel Scan The onset of trapped grating lobes inside the dielectric slab implies that $r_{1y} = 0$, while $r_{0y} \neq 0$ (see Fig. 5.17). From (5.65) we then obtain for $r_{1y} = 0$,

$$\begin{aligned} {}_{\parallel}T_{1+} &= 2\frac{1 - e^{j2\tan^{-1} Z_0/Z_1 |r_{0y}|/r_{1y}} e^{-j0}}{1 + e^{j2\tan^{-1} Z_0/Z_1 |r_{0y}|/r_{1y}} e^{-j0}} \\ &= -2j \tan\left(\tan^{-1} \frac{Z_0}{Z_1} \frac{|r_{0y}|}{r_{1y}}\right) = -2j \frac{Z_0}{Z_1} \frac{|r_{0y}|}{r_{1y}}. \end{aligned} \tag{5.76}$$

Substituting (5.76) and (5.48) into (5.42), we obtain for the trapped grating lobe increment:

$${}_{\parallel}\Delta Z_{A\ T.G.L.} = \frac{Z_1}{2D_x D_z} \frac{\Delta l^2}{r_{1y}} r_{1y}^2 (-2j) \frac{Z_0}{Z_1} \frac{|r_{0y}|}{r_{1y}} = -2j \frac{Z_0}{2D_x D_z} \Delta l^2 |r_{oy}|, \tag{5.77}$$

So no discontinuity at the onset of trapped grating lobe for $\parallel$ scan (for $r_{1y} = 0$).

The onset of free space grating lobes implies that $r_{0y} = 0$ (see Fig. 5.17), and from (5.65) we obtain

$${}_{\parallel}T_{1+} = 2\frac{1 - e^{-j0} e^{-j2\beta_1 d_1/2 r_{1y}}}{1 + e^{-j0} e^{-j2\beta_1 d_1/2 r_{1y}}} = 2j \tan\left(\beta_1 \frac{d_1}{2} r_{1y}\right). \tag{5.78}$$

Substituting (5.78) and (5.48) into (5.42), we obtain for the impedance increment due to a free space grating lobe (FSGL),

$${}_{\parallel}\Delta Z_{A\ FSGL} = 2j \frac{Z_1}{2D_x D_z} \Delta l^2 r_{1y} \tan\left(\beta_1 \frac{d_1}{2} r_{1y}\right), \tag{5.79}$$

So no discontinuity at the onset of free space grating lobes for $\parallel$ scan.

However, for $\beta_1 \frac{d_1}{2} r_{1y} = \frac{\pi}{2} n_1 \quad (n_1 = 1, 3, \ldots)$, we obviously obtain a pole. This situation corresponds to a wave incident at the critical angle as illustrated in Fig. 5.15 bottom-right. From (5.62) we obtain ${}_{\parallel}\Gamma_{1+} = -1$ corresponding to a short circuit. Thus the input impedance of this particular mode is proportional to $\tan(\beta_1 \frac{d_1}{2} r_{1y})$; it will be infinite each time the argument is equal to $\frac{\pi}{2} n_1 \quad (n_1 = 1, 3, \ldots)$ as

stated above. We simply observe the cutoff surface wave modes for $n_1 = 1, 3, \ldots$ in Fig. 5.16. For actual calculated cases, see Figs. 5.21 to 5.32.

5.13 EXAMPLES OF SURFACE WAVES AND ONSET OF GRATING LOBES FOR ARRAYS OF ELECTRIC DIPOLES

In this section we give several examples of the scan impedance Z_A of an array of z-directed electric dipoles. We keep the scan angle constant, namely 60°, and show both the H- and E-plane cases, $\alpha = 0°$ and 90°, respectively (see Fig. 2.1).

To gain a better perspective, we start with no dielectric and then show several cases where we increase the thickness d_1 of the dielectric slab. The relative dielectric constant is in all cases 1.6 and the array dimensions are given in each of the figures.

5.13.1 No Dielectric Case

This case is fundamental. It is shown in Fig. 5.19 for the beam fixed at 60° in the H-plane or $\perp$ plane ($\alpha = 0°$; see Fig. 2.1). In Fig. 5.20 the beam is still at 60° but now in the E-plane or $\parallel$ plane ($\alpha = 90°$). Several features are worth noticing. First of all, we have chosen relatively short elements ($2l = 0.822$ cm $\sim \frac{1}{3}\lambda$ at 11 GHz in air). In practice, we could readily tune the elements to resonate at, say, about 10.75 GHz by adding an inductive load of about $j300$ ohm. But why don't we just make the element longer, for example, about $\frac{\lambda}{2}$ at 10 GHz? Because that leads to an element length of about 1.5 cm which exceeds D_z. So why not just increase D_z? Well, that leads to an even earlier onset of grating lobes, surface waves and all that evil. This is just one reason that straight unloaded elements in general are not recommended unless arranged in the gangbuster pattern (see Section 2.2.1). Besides, in this section we just want to show the onset of grating lobes, which is independent of the element length $2l$.

Further, we observe that since $D_x = D_z = 1.35$ cm, the onset of grating lobes is the same for the two planes, namely 11.9 GHz (see Section 1.9). However, in the $\perp$ case (Fig. 5.19) we observe a singularity in the imaginary part of Z_A, while ReZ_A shows a finite jump because we now must provide additional energy in the grating lobe direction (see discussion in Section 5.12.1). However, for the $\parallel$ case in Fig. 5.20, we observe no singularity at all only a change of the slope. This is simply because the element pattern has a null in the direction of the grating lobe at the onset.

Note that ReZ_A at, say, 10.75 GHz amounts to about 40 ohm for the $\perp$ case (Fig. 5.19), while it is around 10 ohm for the $\parallel$ case (Fig. 5.20), approximating a ratio of 4:1. This is in agreement with our prediction discussed in Section 4.11.2 where the ratio is determined to be about $(1/\cos y)/\cos y = 1/(\cos^2 60) = 4$. Although this variation is observed for short straight elements (Hertzian in nature), it must be emphasized that other types of planar elements really cannot change this fundamental observation significantly because the pattern function P for all elements is relatively constant with scan angle.

In other words, the variation of Z_A with scan angle and scan plane is fundamental and not an element question (except for nonplanar). It is simply caused by the projection of the incident E- or H- fields along the plane of the array. For further discussions, see Section 4.11.2. Fortunately we have already shown in Section 5.10 how dielectric slabs placed adjacent to the array can greatly reduce the variation of ReZ_A with scan angle (see Fig. 5.14). Several dielectric cases will be discussed next.

5.13.2 Dielectric Cases

In this section we consider complex impedance plots of Z_A for three different slab thicknesses, namely $d_1 = 1.0$, 1.7, and 2.7 cm for the array positioned in the middle of the slab as well as asymmetrically. We start with the cases where the beam has been fixed at $\eta = 60°$ in the $\perp$ plane or H-plane ($\alpha = 0°$).

Perpendicular Scan First in Fig. 5.21 we show a complex plot of Z_A for the total slab thickness $d_1 = 1$ cm and the array located in the middle. As discussed in Section 5.12.2, we observe that the onset of the trapped as well as the free space grating lobes is smooth without any singularities except the derivative for the free space grating lobe case. We also observe a distinct singularity at $f = 11.1$ GHz corresponding to a surface wave for $\perp$ scan and $n_1 = 0$ as shown in Fig. 5.16. In Fig. 5.22 we have moved the array into an asymmetric position, and as predicted in Section 5.11, the surface waves occur at the same frequency as in the symmetric case.

Next we show in Fig. 5.23 a case where the total slab thickness $d_1 = 1.7$ cm and the array is located in the middle. The onset of the grating lobes is of course unchanged in these two cases. However, note that the surface wave frequency has been lowered from 11.1 to 10.8 GHz (thus an almost doubling of the slab thickness d_1 only lowers the surface wave frequency by about 3%).

The asymmetric case is shown in Fig. 5.24. Note that the surface wave is still at 10.8 GHz. However, we are just starting to see another surface wave at 11.9 GHz corresponding to $\perp$ scan and $n_1 = 1$ in Fig. 5.16. It is observed that we also have onset of a free space grating lobe at the same frequency.

Finally we show in Fig. 5.25 the case where $d_1 = 2.7$ cm and where the array is located in the middle. The surface wave frequency is now lowered slightly to 10.6 GHz. The asymmetric case is shown in Fig. 5.26. The same surface waves appear as before, but in addition we also have a very pronounced wave at $f = 11.3$ GHz corresponding to $\perp$ polarization and $n_1 = 1$ in Fig. 5.16.

Parallel Scan We next present the cases where the beam is pointing 60° from normal but in the $\parallel$ plane or E-plane ($\alpha = 90°$).

In Fig. 5.27 we show the case where the total slab thickness $d_1 = 1$ cm. As predicted from the theory in Fig. 5.16, we see no surface waves, except in the asymmetric case shown in Fig. 5.28 corresponding to $n_1 = 0$. Similarly we show in Fig. 5.29 that the thicker slab $d_1 = 1.7$ cm, and now we observe a surface wave at 11.9 GHz corresponding to $n_1 = 1$. This surface wave is retained for the asymmetric case in Fig. 5.30; however, we also observe an additional surface wave at a lower frequency, namely 11.1 GHz corresponding to $n_1 = 0$.

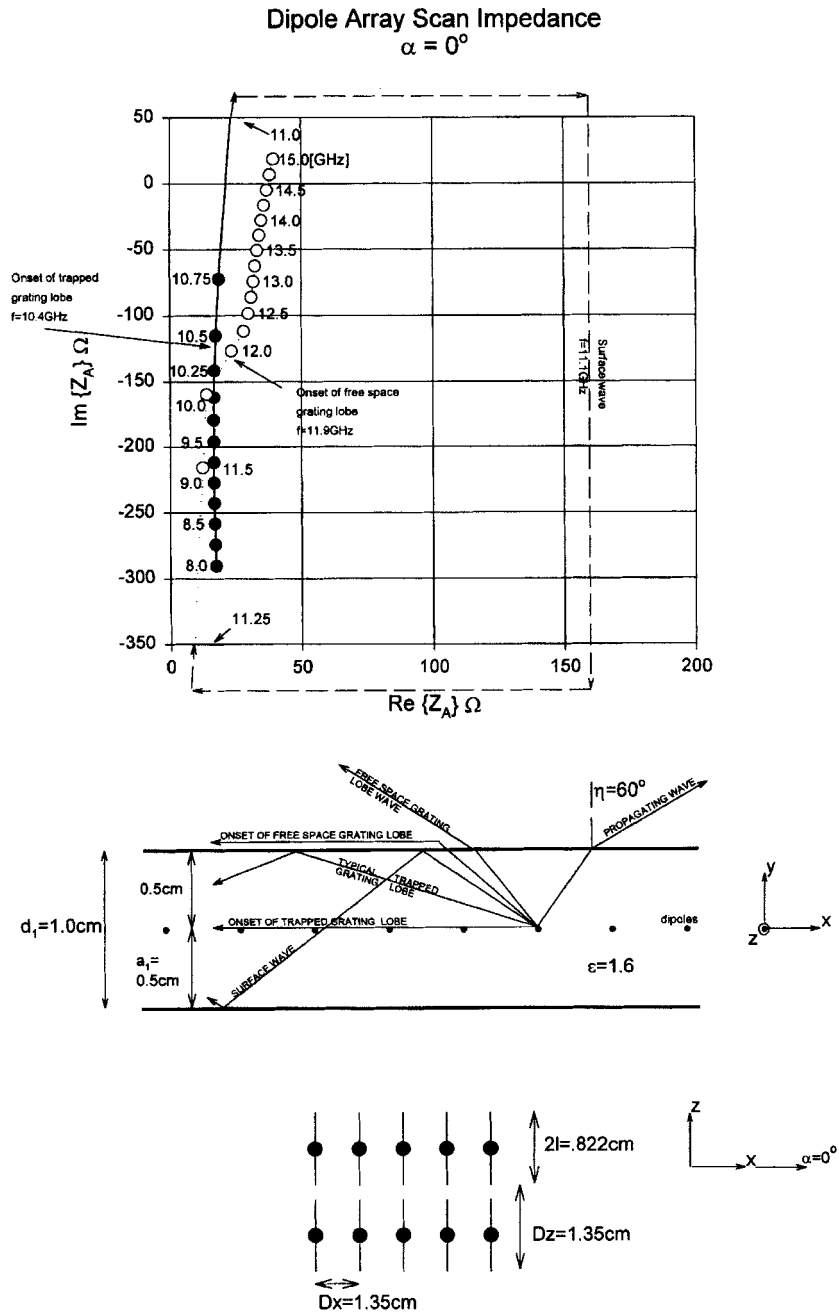

FIGURE 5.21. Complex plot of the scan impedance Z_A for a dipole array in dielectric slab $d_1 = 1.0$ cm, positioned symmetrically, as shown. Scan angle $\eta = 60°$ in the $\perp$ plane (H-plane, $\alpha = 0°$). Note different scales for real and imaginary axes.

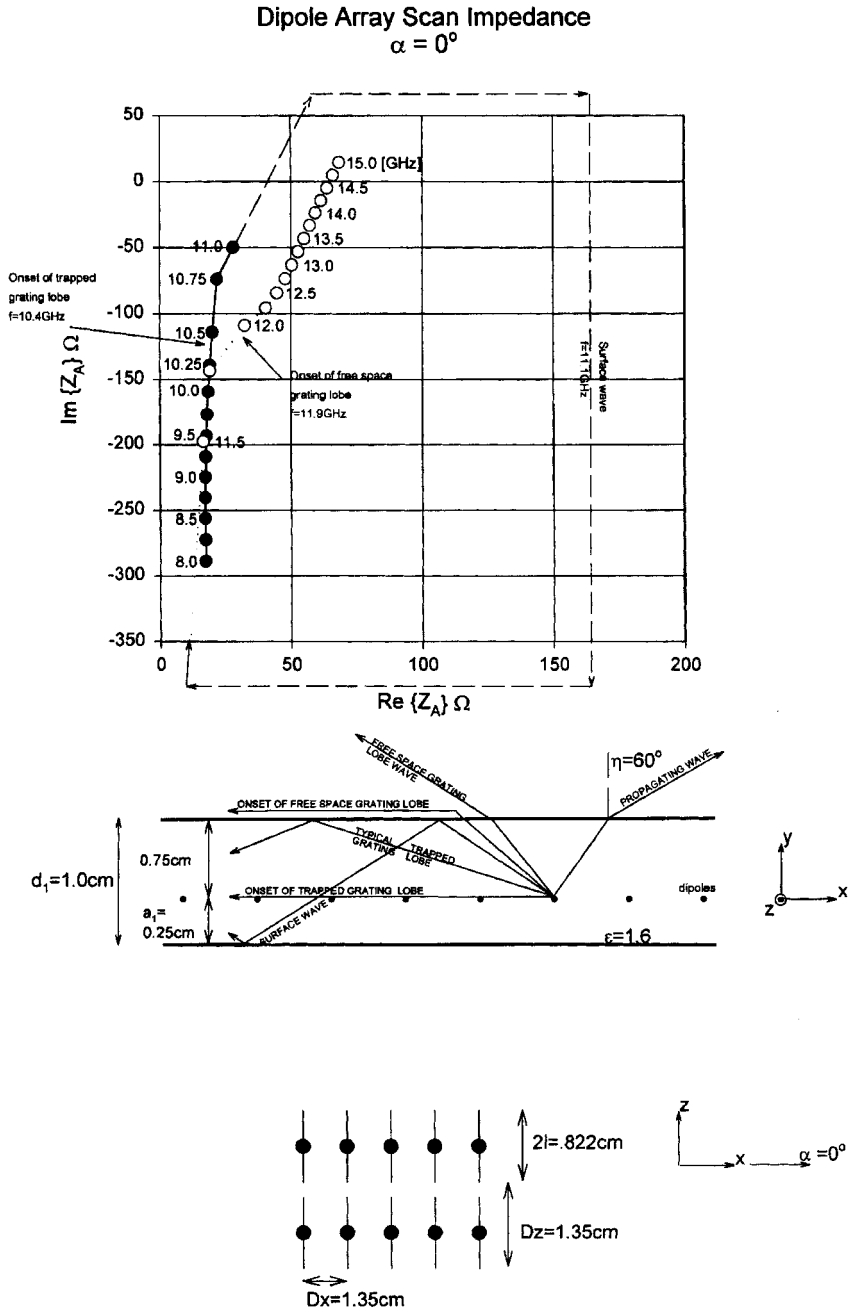

FIGURE 5.22. Complex plot of the scan impedance Z_A for a dipole array in dielectric slab $d_1 = 1.0$ cm, positioned asymmetrically, as shown. Scan angle $\eta = 60°$ in the $\perp$ plane (H-plane, $\alpha = 0°$). Note different scales for real and imaginary axes.

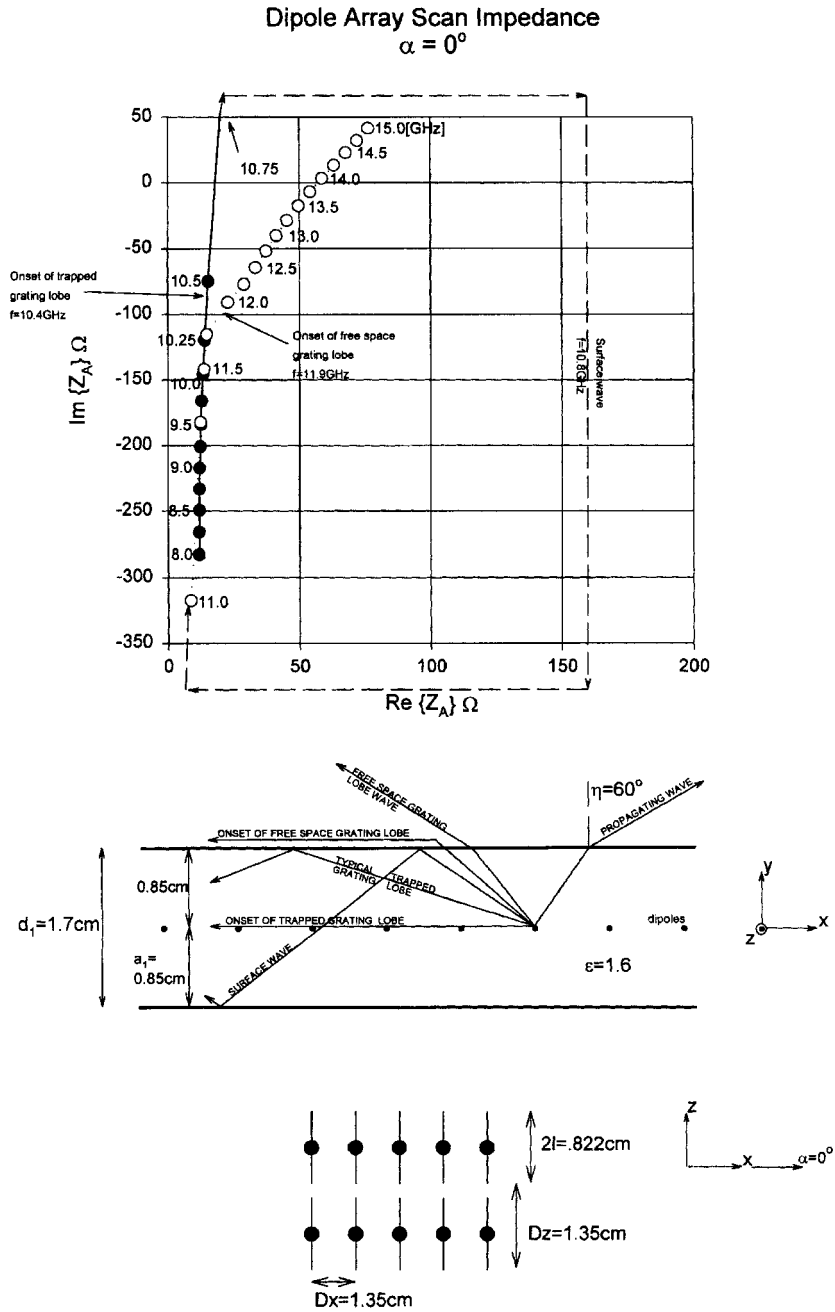

FIGURE 5.23. Complex plot of the scan impedance Z_A for a dipole array in dielectric slab $d_1 = 1.7$ cm, positioned symmetrically, as shown. Scan angle $\eta = 60°$ in the $\perp$ plane (H-plane, $\alpha = 0°$). Note different scales for real and imaginary axes.

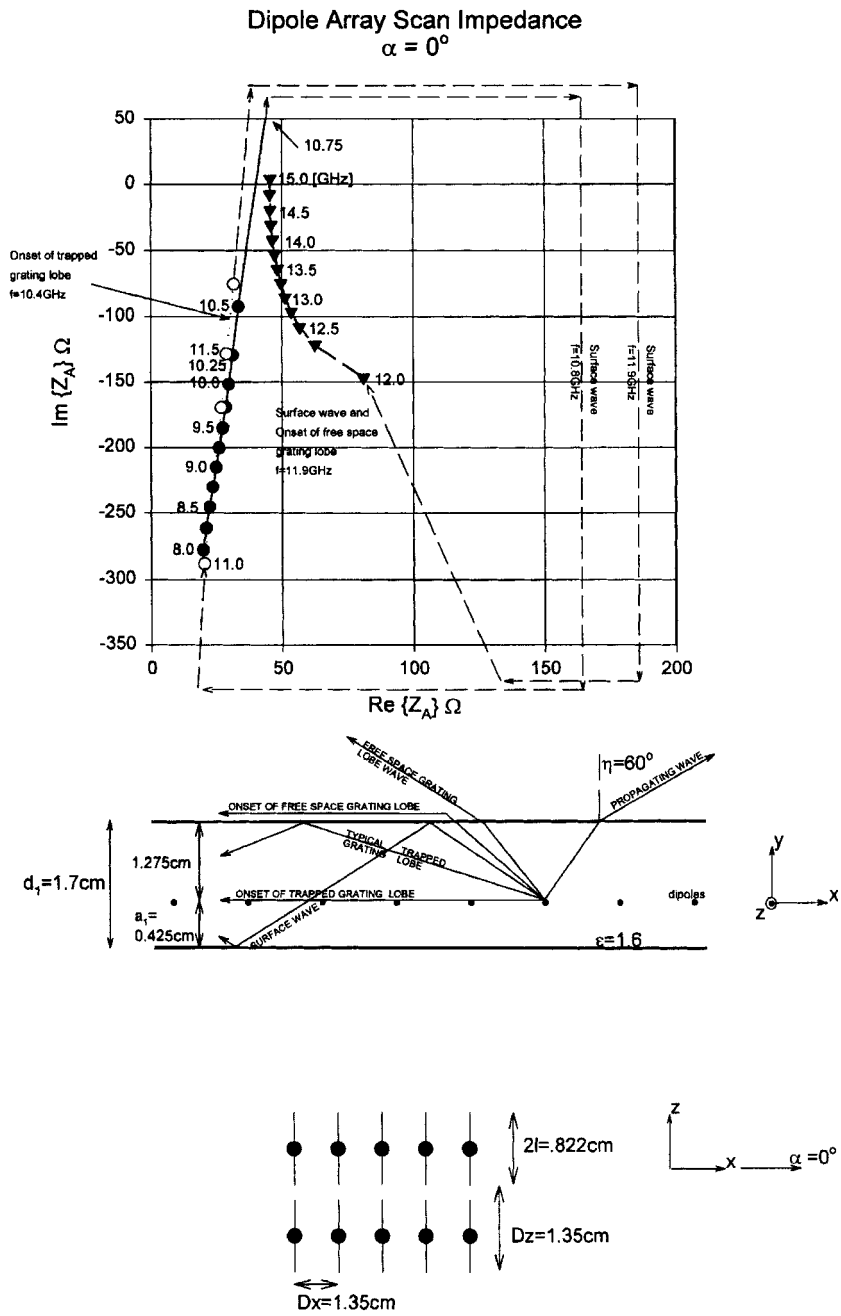

FIGURE 5.24. Complex plot of the scan impedance Z_A for a dipole array in dielectric slab $d_1 = 1.7$ cm, positioned asymmetrically, as shown. Scan angle $\eta = 60°$ in the $\perp$ plane (H-plane, $\alpha = 0°$). Note different scales for real and imaginary axes.

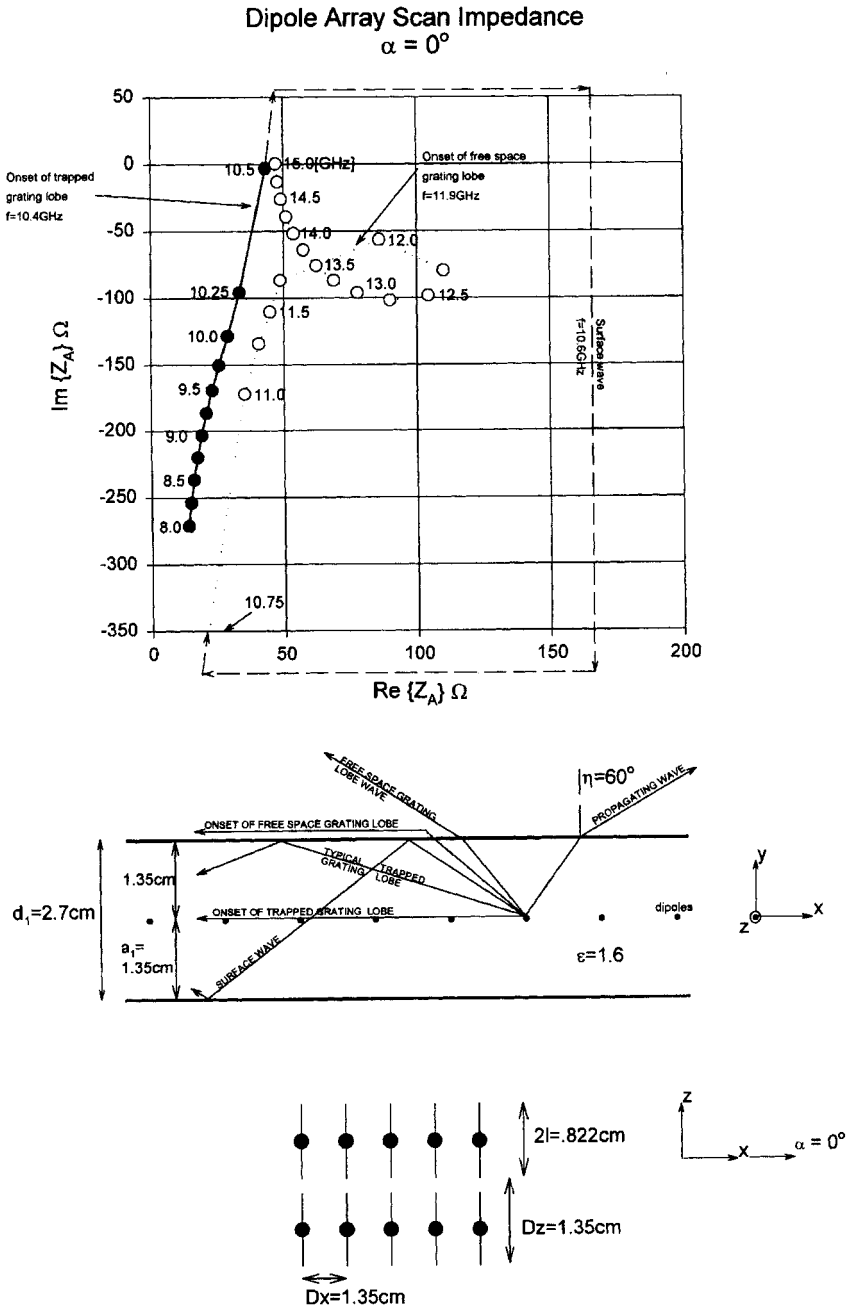

FIGURE 5.25. Complex plot of the scan impedance Z_A for a dipole array in dielectric slab $d_1 = 2.7$ cm, positioned symmetrically, as shown. Scan angle $\eta = 60°$ in the $\perp$ plane (H-plane, $\alpha = 0°$). Note different scales for real and imaginary axes.

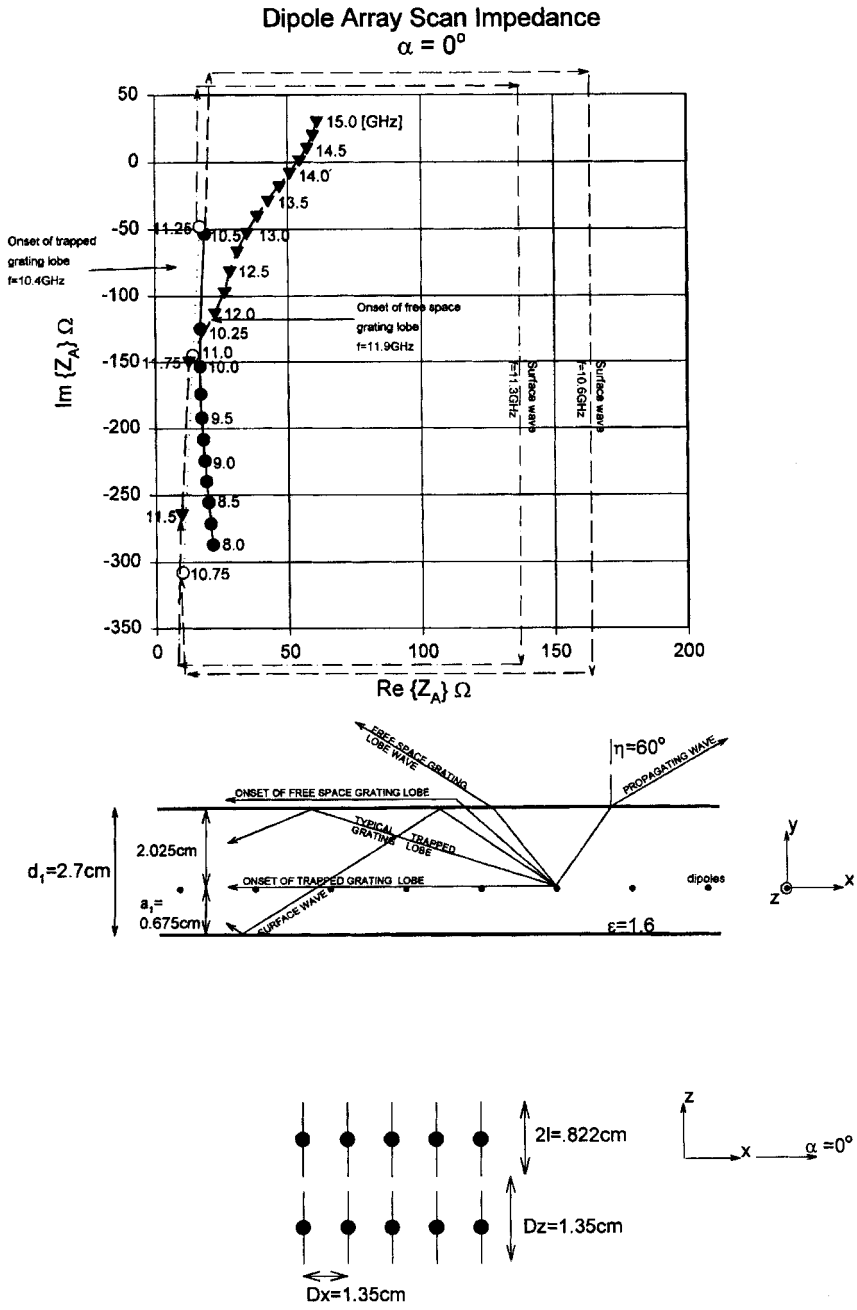

FIGURE 5.26. Complex plot of the scan impedance Z_A for a dipole array in dielectric slab $d_1 = 2.7$ cm, positioned asymmetrically, as shown. Scan angle $\eta = 60°$ in the $\perp$ plane (H-plane, $\alpha = 0°$). Note different scales for real and imaginary axes.

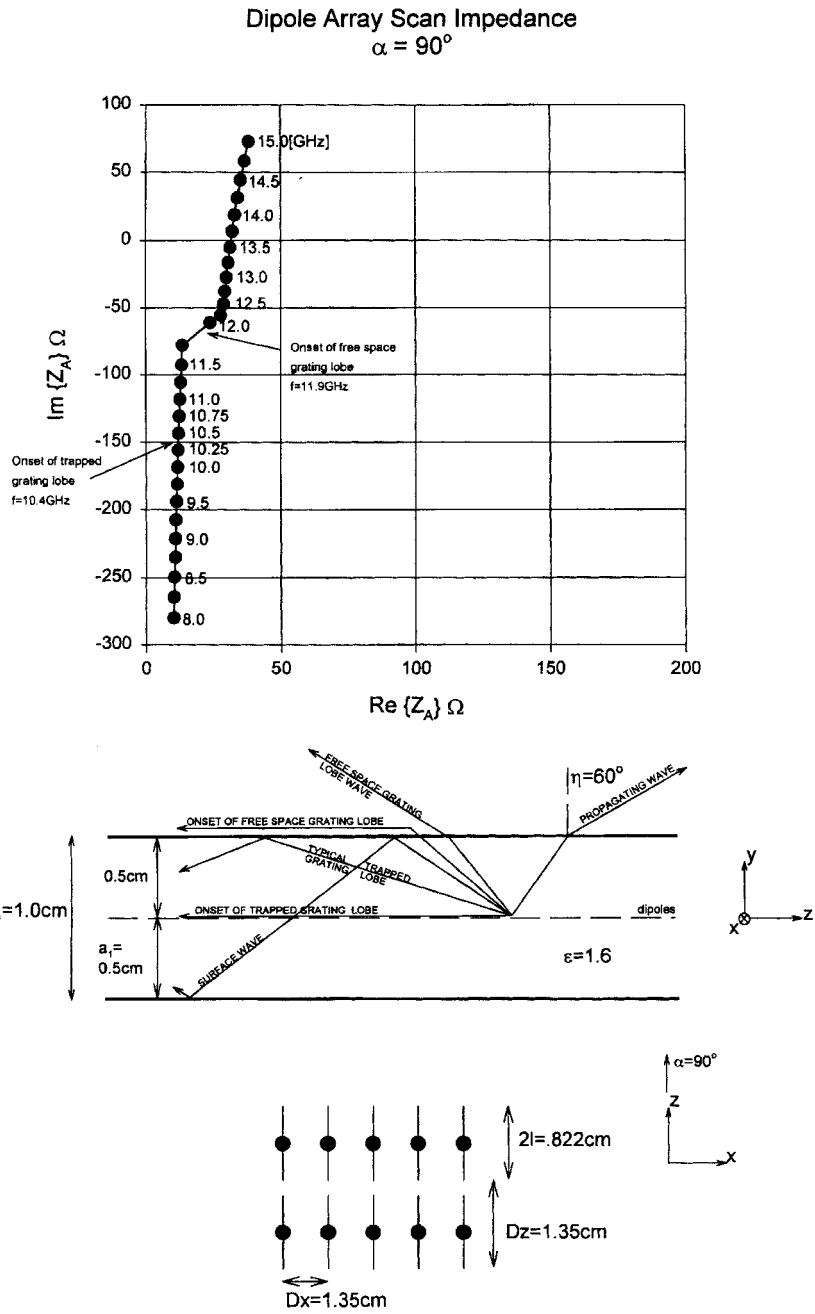

FIGURE 5.27. Complex plot of the scan impedance Z_A for a dipole array in dielectric slab $d_1 = 1.0$ cm, positioned symmetrically, as shown. Scan angle $\eta = 60°$ in the || plane (E-plane, $\alpha = 90°$).

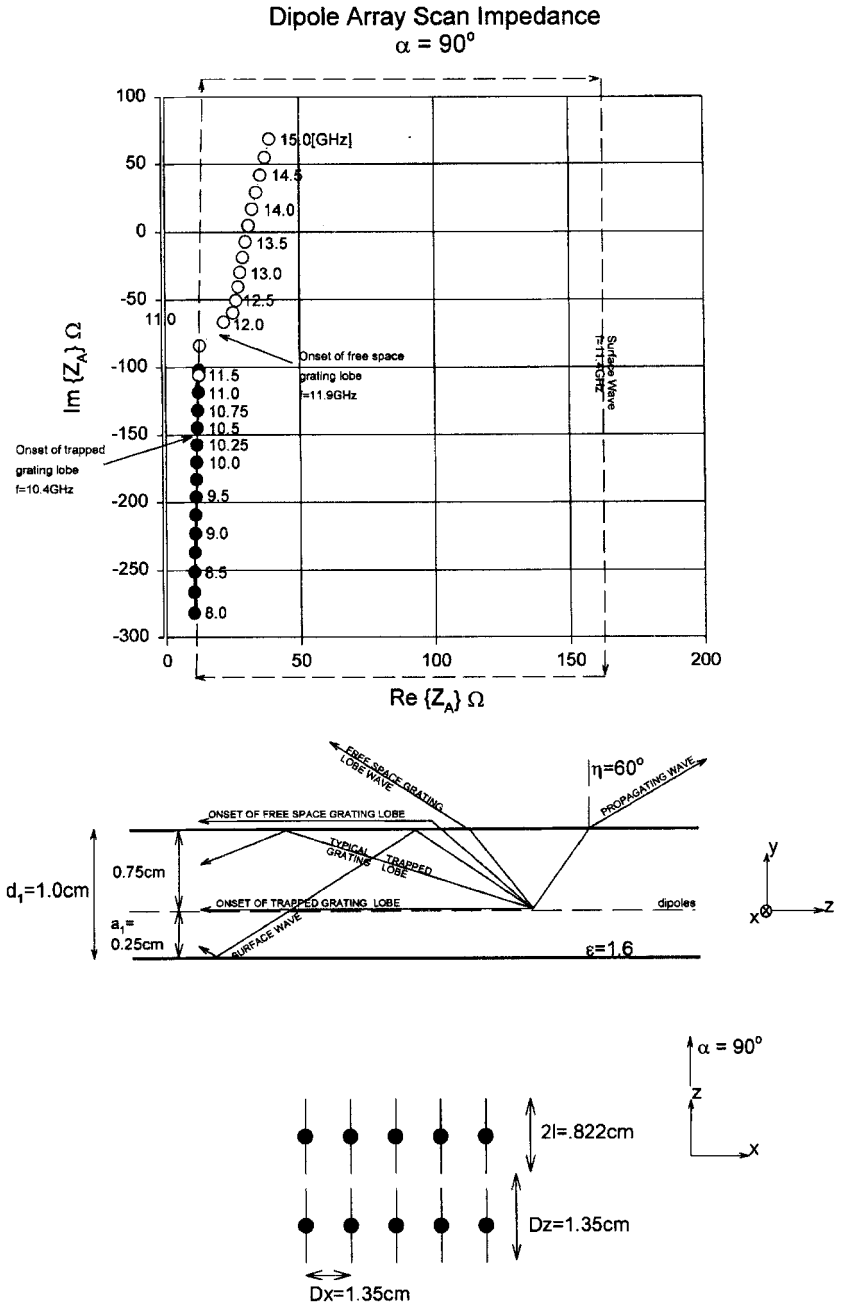

FIGURE 5.28. Complex plot of the scan impedance Z_A for a dipole array in dielectric slab $d_1 = 1.0$ cm, positioned asymmetrically, as shown. Scan angle $\eta = 60°$ in the $\|$ plane (E-plane, $\alpha = 90°$).

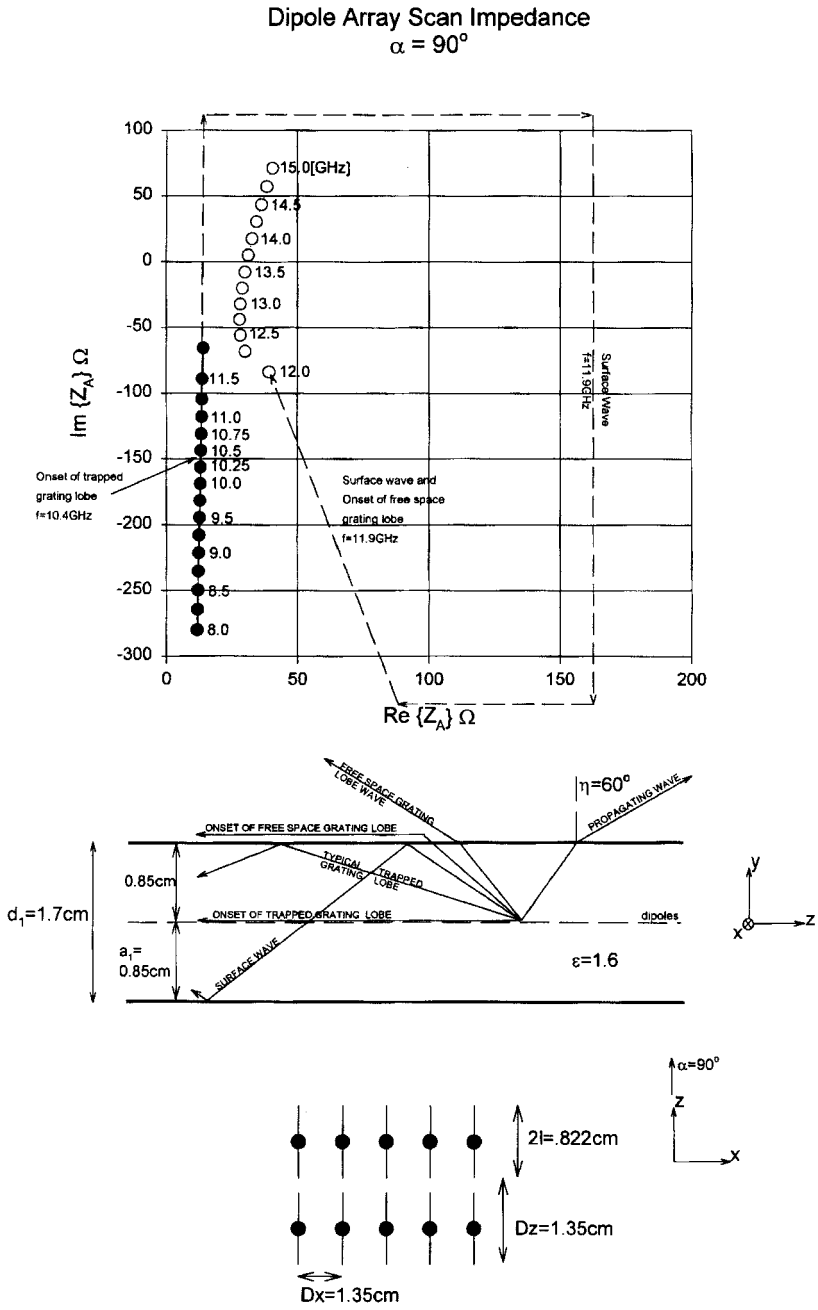

FIGURE 5.29. Complex plot of the scan impedance Z_A for a dipole array in dielectric slab $d_1 = 1.7$ cm, positioned symmetrically, as shown. Scan angle $\eta = 60°$ in the $\|$ plane (E-plane, $\alpha = 90°$).

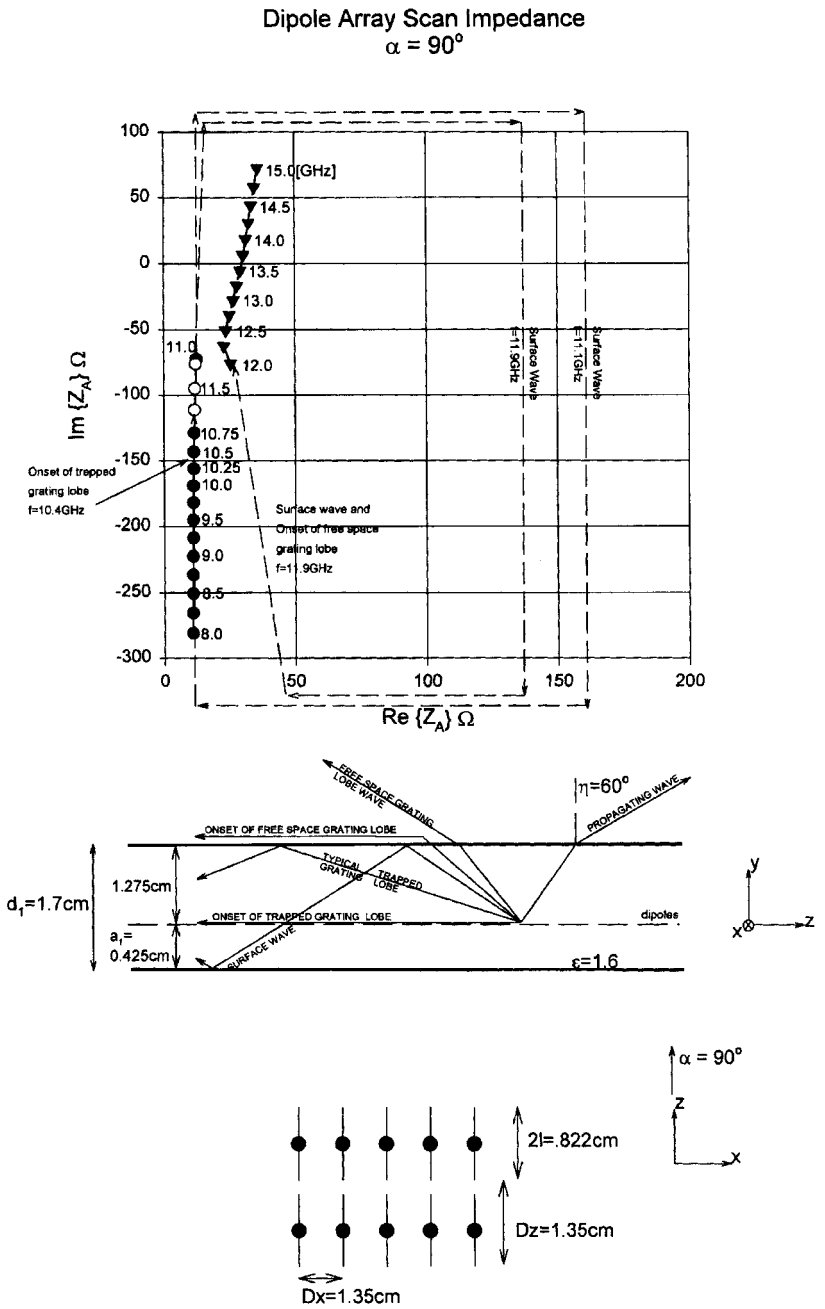

FIGURE 5.30. Complex plot of the scan impedance Z_A for a dipole array in dielectric slab $d_1 = 1.7$ cm, positioned asymmetrically, as shown. Scan angle $\eta = 60°$ in the $\|$ plane (E-plane, $\alpha = 90°$).

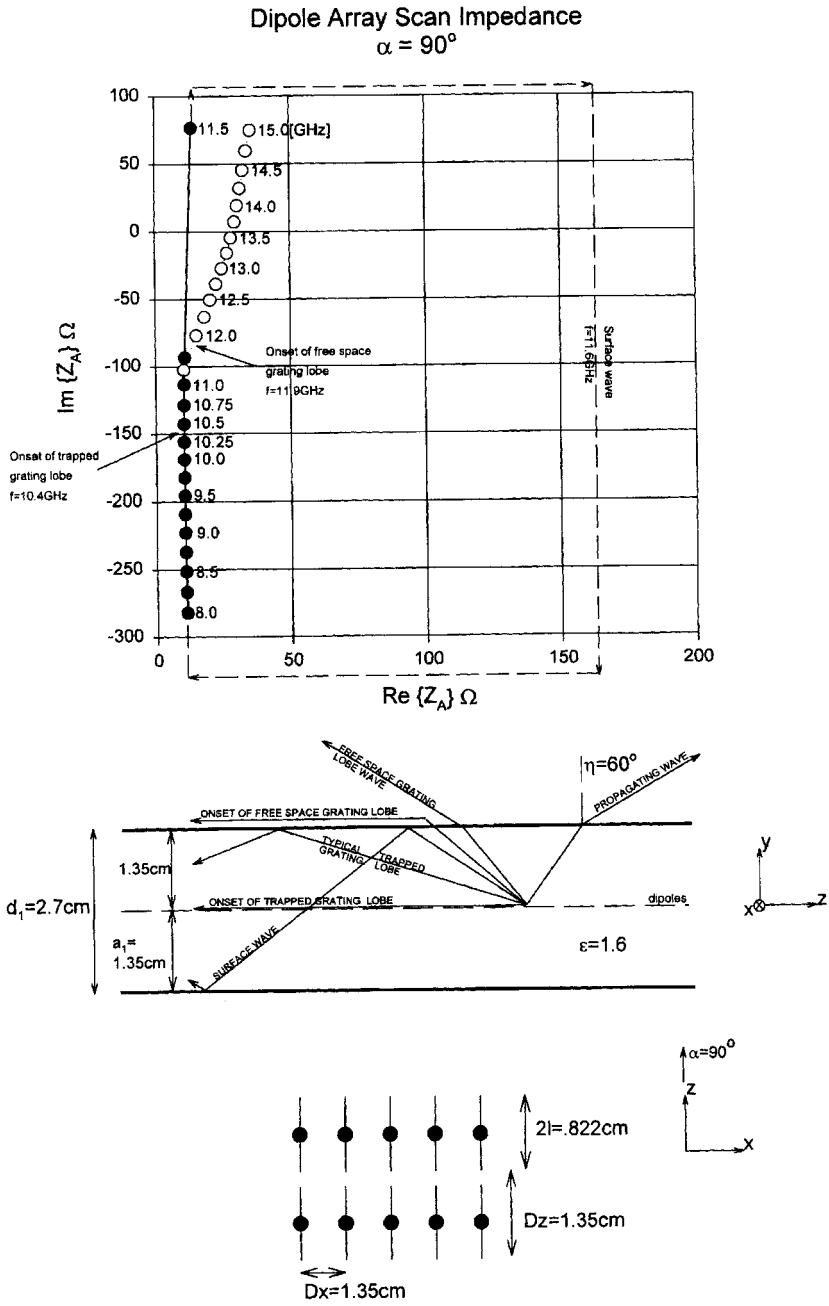

FIGURE 5.31. Complex plot of the scan impedance Z_A for a dipole array in dielectric slab $d_1 = 2.7$ cm, positioned symmetrically, as shown. Scan angle $\eta = 60°$ in the $\|$ plane (E-plane, $\alpha = 90°$).

Finally we show in Fig. 5.31 the case where the array is located symmetrically. Further, we note the additional surface wave at $f = 10.6$ GHz corresponding to $n_1 = 0$, in the asymmetric case shown in in Fig. 5.32.

5.14 GRATING LOBE DIAGRAMS

In the previous section we discussed the onset of trapped as well as free space grating lobes. However, our investigation was limited to the $\perp$ and $\parallel$ scan planes, and since onset of grating lobes in any plane is of intense interest, we will in the following investigate this subject in more detail.

5.14.1 Rectangular Array Grid without Dielectric

It is perhaps easiest to understand grating lobes if we consider an active array of elements being fed by individual generators with the usual linear phase relationship as shown in Fig. 5.33 top.

If we choose $s_x = \frac{1}{2}, s_z = 0$, we obtain $s_y = \sqrt{1 - s_x^2 - s_z^2} = \sqrt{3}/2$, namely a wave propagating in a direction of 30° from normal as shown in Fig. 5.33 middle. Similarly we can choose $s_x = 1, s_z = 0$ leading to $s_y = 0$, namely a wave "propagating" in the endfire direction as shown in Fig. 5.33 middle. (We have here used quotation marks around *propagating* because this case really constitutes a limiting case into an evanescent wave, as we discuss next.)

Further, if we choose, for example, $s_x = 1.28, s_z = 0$, we find that $s_y = \sqrt{1 - 1.28^2} = -j0.8$; that is, a wave being attenuated as we move away from the array or an evanescent wave. While it would be a little tricky to obtain $s_x = 1.28$ for an incident wave (a cosine > 1 ?), it is absolutely no problem for an actively fed array: We merely adjust the phases of the individual voltage generators to whatever we want. It is clear from the example above that the borderline between propagation and evanescent waves is simply

$$s_x^2 + s_z^2 = 1, \tag{5.80}$$

which is a unit circle in the s_x, s_z plane as shown in Fig. 5.33 middle. All values of s_x, s_z inside this circle will produce a propagating wave (visible space) and all values outside will produce evanescent waves (invisible space).

So far we have considered only the principal mode $\hat{s} = \hat{x}s_x + \hat{y}s_y + \hat{z}s_z$. However, from the plane wave expansion in Chapter 4, we know that the complete spectrum from a periodic structure without dielectric is given by

$$\hat{r} = \hat{x}\left(s_x + k\frac{\lambda}{D_x}\right) + \hat{y}r_y + \hat{z}\left(s_z + n\frac{\lambda}{D_z}\right)$$

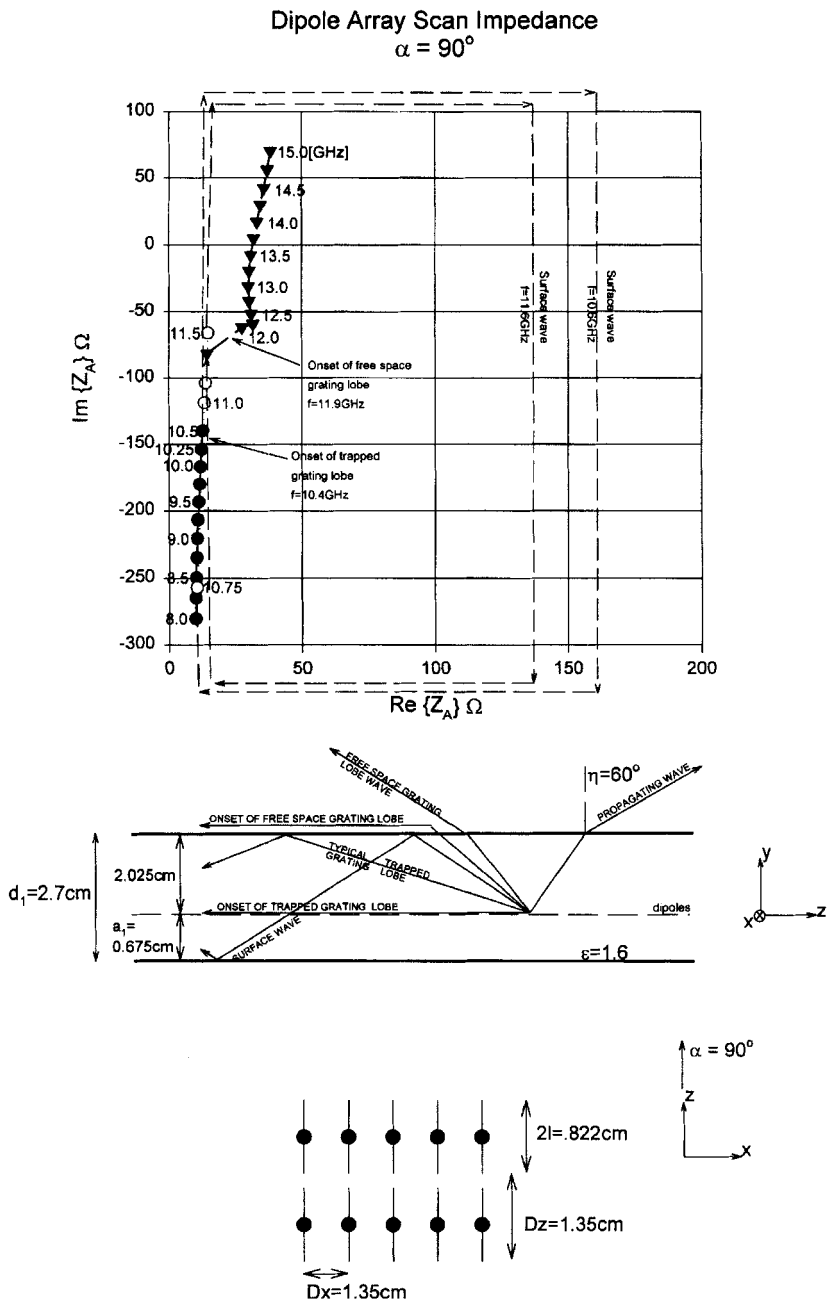

FIGURE 5.32. Complex plot of the scan impedance Z_A for a dipole array in dielectric slab $d_1 = 2.7$ cm, positioned asymmetrically, as shown. Scan angle $\eta = 60°$ in the $\|$ plane (E-plane, $\alpha = 90°$).

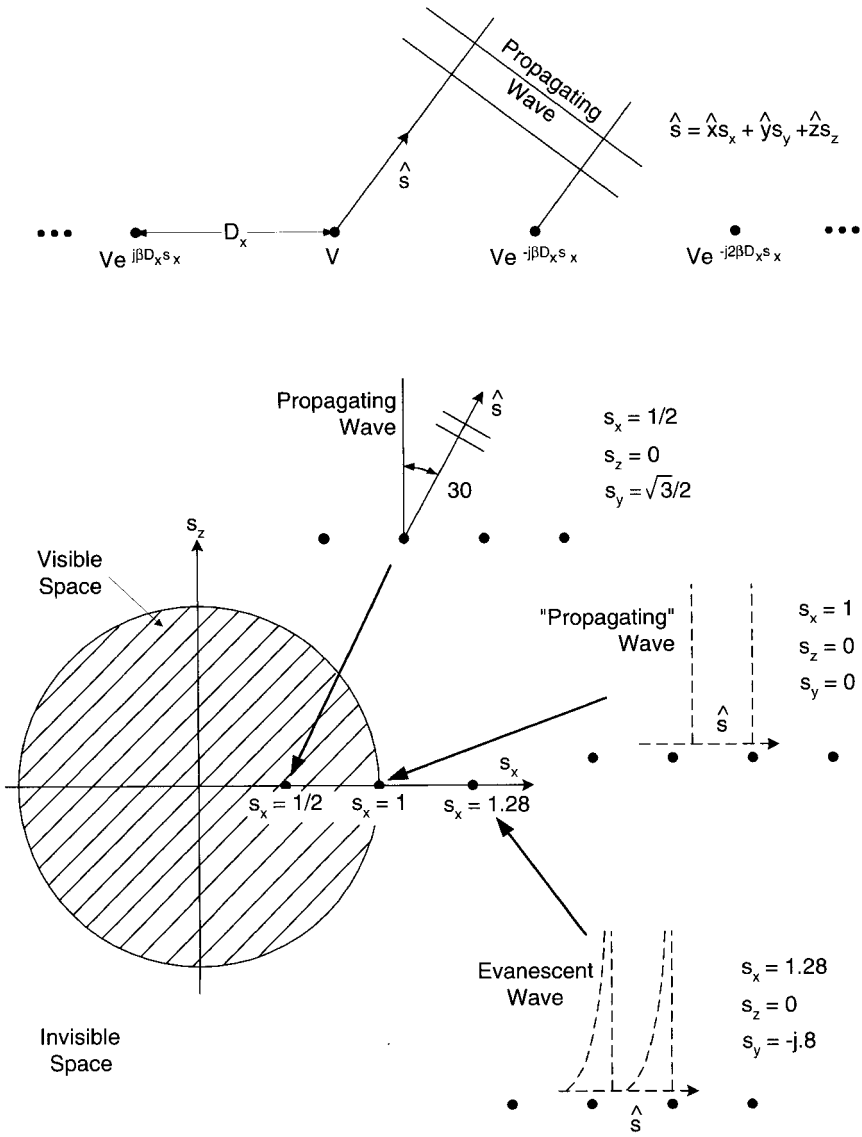

FIGURE 5.33. *Top:* An array is fed from voltage generators with a linear phase variation producing a plane wave in direction $\hat{s}$. *Bottom:* By variation of the phase we can obtain propagating and nonpropagating waves as shown. Propagation is obtained when $s_y = \sqrt{1 - s_x^2 - s_z^2}$ is real, that is, whenever s_x, s_z is inside the unit circle, as shown.

where

$$r_y = \begin{cases} \sqrt{1 - r_x^2 - r_z^2} & \text{for} \quad r_x^2 + r_z^2 \leq 1, \\ -j\sqrt{r_x^2 + r_z^2 - 1} & \text{for} \quad r_x^2 + r_z^2 \geq 1. \end{cases}$$

Thus, as shown in Fig. 5.34, if the principal mode is given by the point (s_x, s_z), then all the higher-order modes will be given by the points $\hat{r}(k, n) = \left(s_x + k\frac{\lambda}{D_x}, s_z + n\frac{\lambda}{D_z}\right)$. As long as these points fall outside the unit circle $s_x^2 + s_z^2 = 1$, they will be in invisible space; in other words, they will be evanescent. If they fall inside, they will propagate.

More specifically, if the principal direction $\hat{r}(0, 0) = (s_x, s_z)$ remains inside the visible space as given by the unit circle $s_x^2 + s_z^2 = 1$, then all the higher-order modes

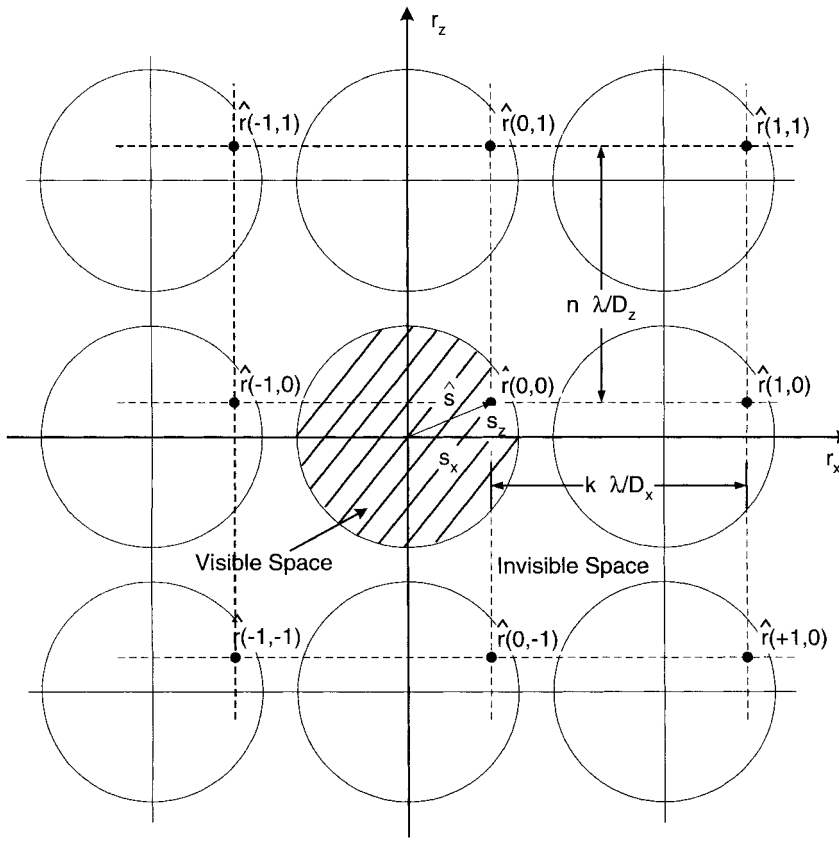

FIGURE 5.34. This figure is an extension of Fig. 5.21 yielding the so-called grating lobe diagram. We have merely added the entire spectrum $\hat{r} = \hat{x}(s_z + k\frac{\lambda}{D_z}) \pm \hat{y}r_y + \hat{z}(s_z + n\frac{\lambda}{D_z})$ and plotted $\hat{r}$ in the (r_x, r_z)-plane. Compare with Fig. 5.36.

will stay inside unit circles with centers at $k\frac{\lambda}{D_x}, n\frac{\lambda}{D_z}$ $(k, n \neq 0, 0)$ as indicated in Fig. 5.34.

If D_x and/or D_z are chosen large, these circles may intersect each other as shown, for example, in Fig. 5.35 where D_x is larger than $\lambda/2$ and D_z is smaller. This leads to crescent-shaped areas inside the visible space (double hatched), and if $\hat{s}$ is inside one of these areas (case 2), we will, for example, have $\hat{r}(-1, 0)$ (case 2′) located inside the other segment. So we will have another propagating wave corresponding to a grating lobe as indicated in Fig. 5.35 bottom.

It is clear that as $\hat{s}$ moves out of the visible region (case 3) one (or more) higher-order modes will move further into the visible region and simply start propagating (case 3′). At this point it becomes academic which is the principal and which is the higher-order direction!

Note that $\hat{s}$ is not restricted to move merely on the r_x-axis as shown but can move around in the entire (r_x, r_z)-plane. Thus a grating lobe diagram is an extremely useful graphical as well as computational way to examine under what conditions grating lobes will occur as far as scan angles r_x and r_z are concerned.

Alternatively, we may also plot a grating lobe diagram in the (s_x, s_z)-plane as shown in Fig. 5.36 rather than in the (r_x, r_z)-plane as shown in Figs. 5.34 and 5.35. Recalling that

$$|r_y| = \sqrt{1 - \left(s_x + k\frac{\lambda}{D_x}\right)^2 - \left(s_z + n\frac{\lambda}{D_z}\right)^2}$$

and that $r_y = 0$ constitutes the limit between propagating and attenuated modes, we readily see that the visible space in Fig. 5.36 is the shaded area inside any of the unit circles as shown. The world seems to be divided between Figs. 5.34 and 5.36.

5.14.2 Skewed Grid without Dielectric

So far we have considered grating lobe diagrams for rectangular grids only as shown in Fig. 5.37 top-left. We remind the reader that the plane wave spectrum in that case was given by

$$\hat{r} = \hat{x}\underbrace{\left(s_x + k\frac{\lambda}{D_x}\right)}_{r_x} \pm \hat{y}r_y + \hat{z}\underbrace{\left(s_z + n\frac{\lambda}{D_z}\right)}_{r_z}.$$

In this section we consider a skewed grid as shown in Fig. 5.37 top-right. As shown in Section 4.3.2, the plane wave spectrum is in that case

$$\hat{r} = \hat{x}\underbrace{\left(s_x + k\frac{\lambda}{D_x} - n\frac{\Delta z}{D_z}\frac{\lambda}{D_x}\right)}_{r_x} \pm \hat{y}r_y + \hat{z}\underbrace{\left(s_z + n\frac{\lambda}{D_z}\right)}_{r_z},$$

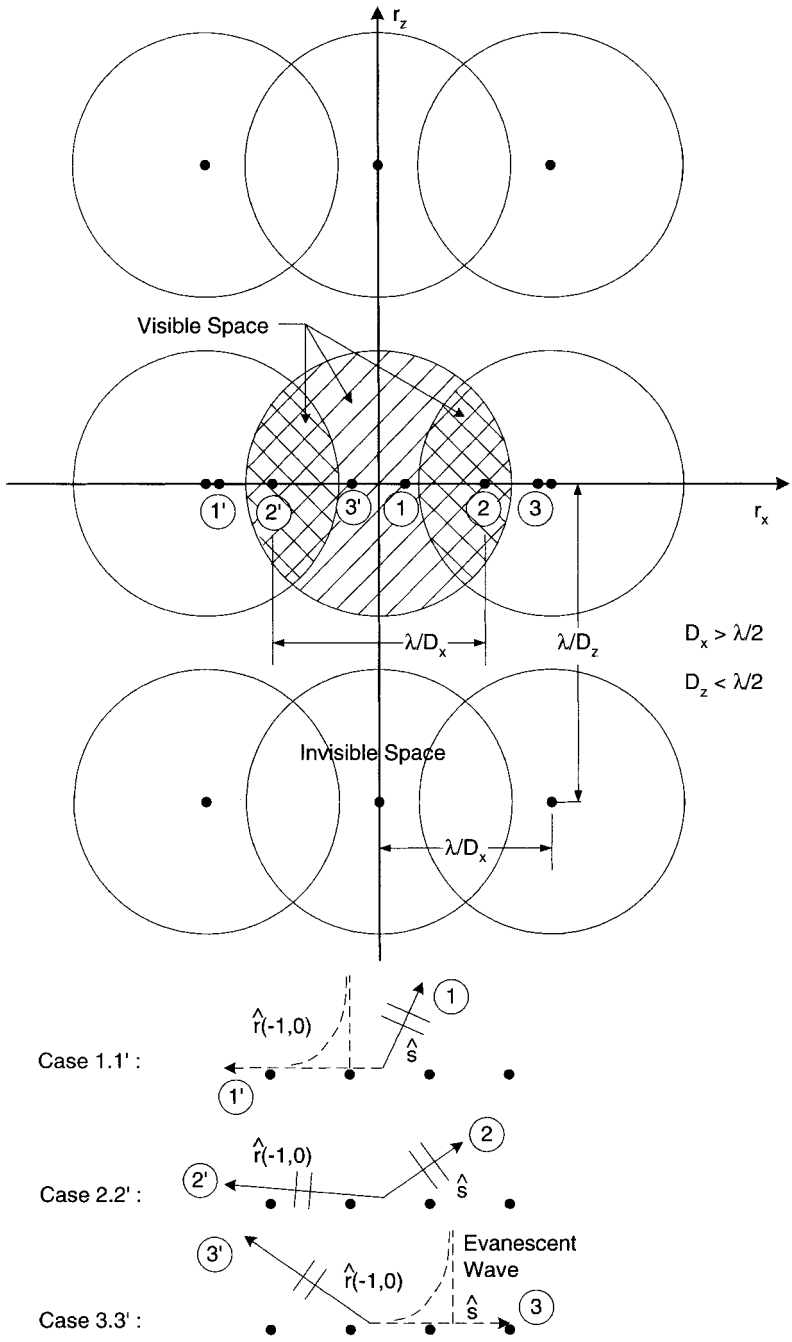

FIGURE 5.35. Grating lobe diagram for $D_x > \lambda/2$ and $D_z < \lambda/2$. By letting $\hat{s}$ vary as shown, the mode $\hat{r}(-1, 0)$ can move into the visible space and produce a grating lobe and even become the "principal" mode itself.

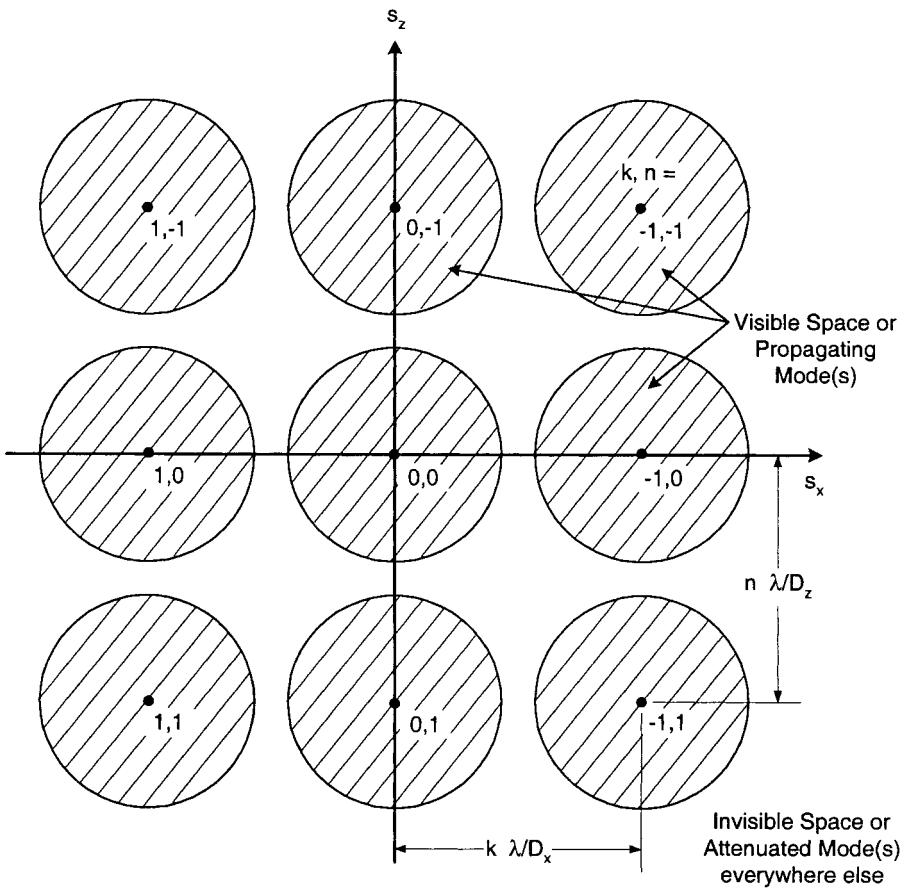

FIGURE 5.36. Grating lobe diagram plotted in the (s_x, s_z)-plane rather than the (r_x, r_z)-plane as shown in Figs. 5.34 and 5.35. If (s_x, s_z) falls inside any of the unit circles, we have propagating mode(s). Otherwise, we do not.

where r_y for both the rectangular and skewed case is given by

$$r_y = \sqrt{1 - r_x^2 - r_z^2}.$$

Inspection of these equations readily leads to the grating lobe diagrams shown in Fig. 5.37 bottom, the rectangular (left) and the skewed grid (right). Note that we in the skewed case can allow a larger D_z than for the rectangluar case before the onset of grating lobes. This conclusion can of course also be obtained by a purely physical argument. (See also Problem 5.4.)

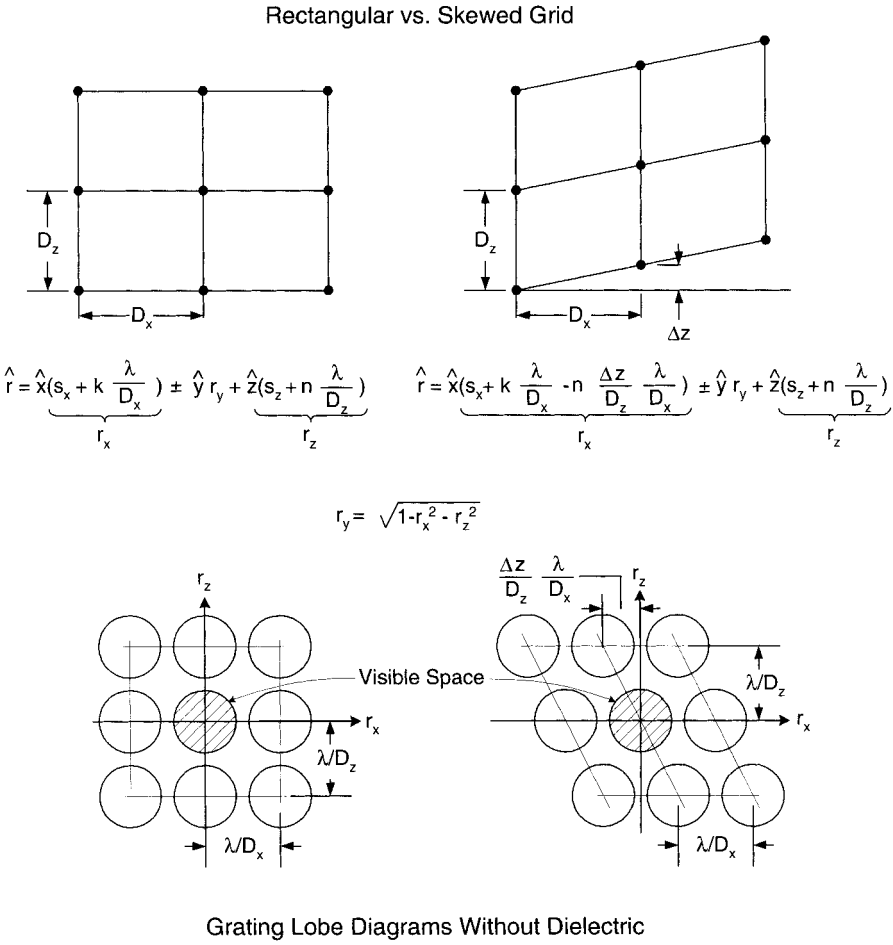

FIGURE 5.37. Effect of the array grid on the grating lobe diagram. *Left:* Rectangular grid. *Right:* Skewed grid.

5.14.3 Any Array Grid with Dielectric

At Fig. 5.38 top, we show a dipole array covered with a dielectric slab with intrinsic impedance Z_1 and thickness d_1. The array elements are phased to produce a direction of propagation $\hat{r}_1$ inside the dielectric slab. In medium Z_0 it is denoted by $\hat{r}_0$ (Snell's law).

The onset of free space grating lobes are simply determined for $\hat{r}_0$ grazing the dielectric slab,

$$r_{0y} = 0 = \sqrt{1 - \left(s_{0x} + k\frac{\lambda_0}{D_x}\right)^2 - \left(s_{0z} + n\frac{\lambda_0}{D_z}\right)^2}.$$

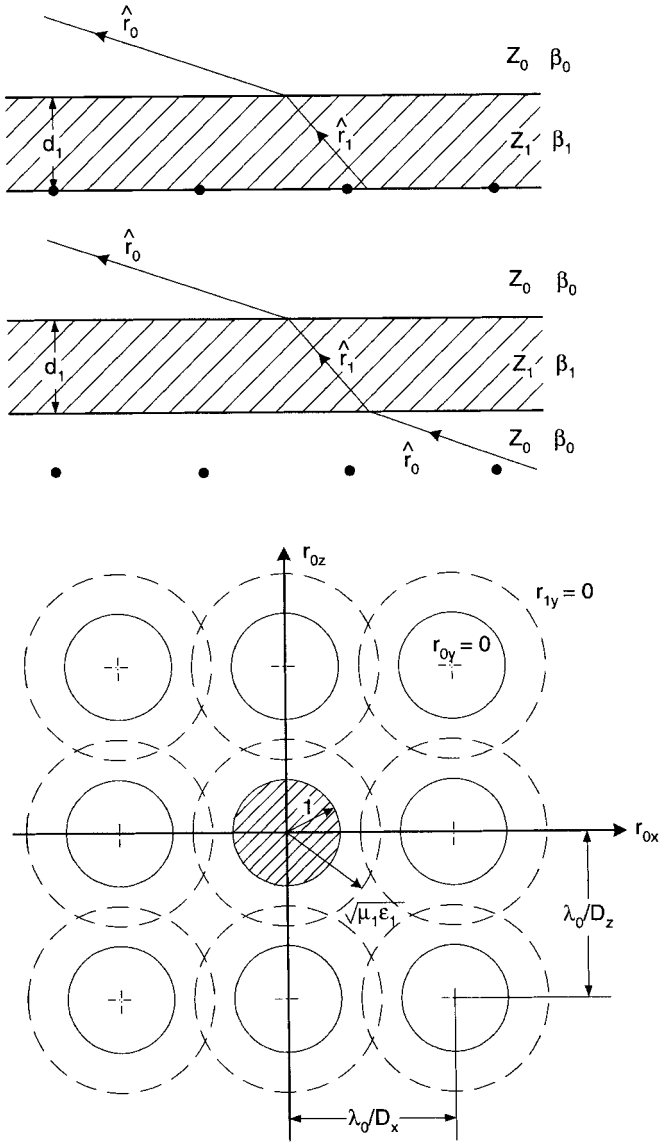

Grating Lobe Diagram With Dielectric

FIGURE 5.38. Placing a dielectric slab upon a *periodic structure* does not change the onset of free space grating lobes (easy to see when lifting the slab away from the array as shown in the middle). However, the onset of trapped grating lobes will take place for $|\hat{r}_0| > 1$, namely when $|\hat{r}_0| = \sqrt{\mu_1 \epsilon_1}$.

The unit circles have centers at $(k\frac{\lambda_0}{D_x}, n\frac{\lambda_0}{D_z})$ just as was seen above in the nondielectric case (Fig. 5.38 bottom). In other words, the onset of free space grating lobes is completely independent of Z_1, β_1, and d_1. This statement usually puzzles readers. However, if we instead consider the case shown in Fig. 5.38 middle, where the slab has been moved above the array, the statement is obvious.

Similarly the onset of trapped grating lobes are determined by

$$r_{1y} = 0 = \sqrt{1 - \left(s_{1x} + k\frac{\lambda_1}{D_x}\right)^2 - \left(s_{1z} + n\frac{\lambda_1}{D_z}\right)^2}$$

and by (5.3) and (5.4),

$$0 = \sqrt{1 - \left[\frac{\beta_0}{\beta_1}\left(s_{0x} + k\frac{\lambda_0}{D_x}\right)\right]^2 - \left[\frac{\beta_0}{\beta_1}\left(s_{0z} + n\frac{\lambda_0}{D_z}\right)\right]^2}.$$

The circles have the same centers as above and radii $= \beta_1/\beta_0 = \sqrt{\mu_1\epsilon_1}$. (This case is also shown in Fig. 5.38 bottom.)

The extension to a skewed grid is readily done by application of the previous section.

5.15 COMMON MISCONCEPTIONS

5.15.1 "Shadow" of an Array

Perhaps the most common misconception in the area of deriving bouncing modes in general is the following:

Take as an example Fig. 5.4, where a plane wave emanating from the array toward the interface $y = b_m$ is being reflected and continues through the array. Considering that an array of dipoles can cast a strong shadow, the astute reader will usually ask: Should there not be some attenuation of the reflected wave as it passes through the dipole array?

We therefore remind the reader that by application of the equivalence principle, we in effect substitute the actual conducting elements with their induced currents. In other words, we remove the conductors entirely leaving merely electric currents. Electric currents do not scatter. In calculating these currents, their values will be dictated by the scattering that obviously takes place. In short, we are solving the problem completely rigorously.

5.15.2 Effect of Dielectric

Another common question is: Since adding dielectric slabs leads to an earlier onset of trapped grating lobes, aren't we really better off without the dielectric? The answer is: Not in general. Recall that adding dielectric to a periodic surface lowers the resonant frequency (See Fig. 1.9 and Appendix E). In other words, if we want

to maintain the original resonant frequency, we can make the elements smaller (at least that is one option). That in turn allows us to reduce the inter-element spacings D_x and D_z, leading to higher onset frequencies of the trapped as well as the free space grating lobes. Since the latter will emerge from the array as if the dielectric were not present (see the discussion in Section 5.14.3), the array with the reduced D_x and D_z will attain a substantially higher onset frequency of free space grating lobes (potentially as much as $\sqrt{\epsilon_1}$ higher). On the other side, the trapped grating lobes will start at roughly the same frequency as the original array without the dielectric. However, they are *trapped*, meaning that they are not hurting us from a backscatter point of view except that they add an extra purely imaginary impedance term in the infinite series. Note that even a thin dielectric layer next to a periodic surface can have a significant effect on the resonant frequency (see Fig. 1.9; no air gap, please!). Such thin dielectric layers are often referred to as *underwear* (dielectric or otherwise). And underwear in general is important! This technique is also called dielectric loading.

5.15.3 Surface Waves

Another often-occuring situation is the following: Having calculated a surface wave to be present at say 11.8 GHz, and being only required to operate up to say 11.6 GHz, will we be all right?

When a surface wave is calculated according to any reputable textbook, one usually refers to a *free surface wave* (whether the designer knows that or not). However, while there can be no doubt that this is where things can (and in general will) go terribly wrong, we clearly see, for example, from Figs. 5.21 through 5.26 that approaching a surface wave leads to very large impedance terms that can be detrimental to impedance properties. Only a detailed examination can show how close one is to total disaster. In other words, things always happen gradually.

5.15.4 On the Distance between Arrays and Dielectric Interface

It should by now be well understood that the spherical wavelets emanating from each element eventually at some distance merge into propagating modes (plane waves) such as the principal mode and eventually grating lobes. We have further shown in this chapter that dielectric interfaces can be analyzed by introducing the classical Fresnel reflection and transmission coefficients valid for plane waves. It is a common misconception that the interface should be located at some distance from the array such that only homogeneous waves are present. The fact is that the dielectric interface can be arbitrary close to the elements. What happens is that the space close to the array will be filled with evanescent waves in addition to the propagating modes. It is significant to note that the classical Fresnel reflection and transmission coefficients given in Appendix C are also valid for all the evanescent waves provided that we use the proper r_y. In short, our approach is completely rigorous for one or more dielectric interfaces placed at an arbitrary distance from the array(s).

5.16 CONCLUDING REMARKS

In this chapter we studied the effect of adding dielectric slabs to a periodic structure of dipoles. There are several reasons for using dielectric. First of all, we will in general need a dielectric to obtain mechanical integrity. But more important are the design possibilities. We demonstrated how use of dielectric slabs can lead to a high degree of impedance scan independence, and this plays a major role in many applications such as phased arrays. We will see in the next two chapters that the dielectric is crucial when designing hybrid radomes with constant bandwidth for all angles of incidence and polarizations.

We also demonstrated the presence of what we called trapped waves or forced surface waves (see Figs. 5.21–5.32). Trapped waves typically emerge as grating lobes inside the dielectric at the same frequency as if the periodic structure had been completely surrounded by infinite media Z_1. Only these grating lobes will be totally reflected from the interface to free space Z_0; that is, they are trapped until the frequency becomes so high that the direction of the trapped grating lobe approaches the critical angle. At higher frequencies they will then emerge in free space as free space grating lobes. That will happen at the same frequency as if the antenna has been placed in free space, namely completely independent of a stratified medium. We also saw that these trapped grating lobes or forced surface waves could become free surface waves. These are the types normally referred to in most textbooks on this subject, for example, Harrington [36]. These free surface waves would add an infinite impedance term in series with the total impedance; in other words, no radiation can take place because all energy will go into the surface wave mode. The impedance term of all forced and free surface waves was purely reactive because no energy could escape into free space for an infinite periodic structure. However, once they became free space grating lobes, energy radiated into free space leading to impedance terms with real as well as imaginary components.

Although the grating lobe diagrams could have been introduced in Chapter 4 for the no dielectric case, it makes more sense to do it in this chapter in order to better emphasize the effect of the dielectric. The grating lobe diagrams are one of the most instructive ways to get a quick (and precise) picture of the rather complicated situation regarding the presence of grating lobes when we are dealing with scan in an arbitrary plane.

5.17 PROBLEMS

5.1 Fresnel Reflection Coefficients in Real and Imaginary Space A plane wave spectrum $\hat{r}_{m+}$ from an array is incident upon the interface between the two semi-infinite media Z_m and Z_{m+1}, as shown in Fig. P5.1. (Assume that s_{mx}, s_{mz}, D_x, and D_z are given as input data in a computer program you may write later.)

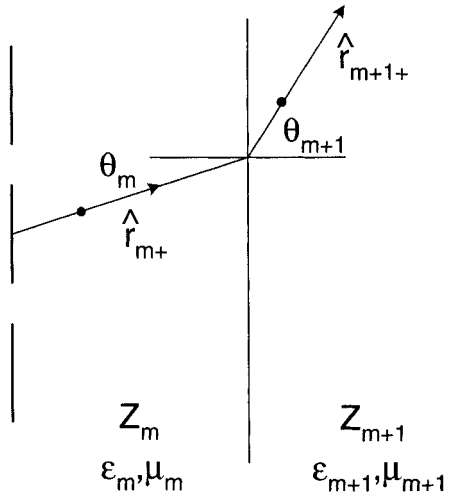

Fig. P5.1

a. Write a computer program yielding ${}^{E}_{\perp\!\!\!\perp}\Gamma_{m+}$ and ${}^{H}_{\perp\!\!\!\perp}\Gamma_{m+}$ as a function of s_{mx}, s_{mz}, k, and n (magnitude and phase). Consult Appendix C.

b. For $\epsilon_1 = 4$, $\mu_1 = 1$, and $\epsilon_2 = 1$, $\mu_2 = 1$ (relative values), plot ${}^{E}_{\perp}\Gamma_{1+}$ and ${}^{E}_{\parallel}\Gamma_{1+}$ in the complex plane (amplitude and phase) in the range $-5 < r_{1x} < 5$ ($r_{1z} = 0$; $k = n = 0$) and also in the range $-5 < r_{1z} < 5$($r_{1x} = 0$; $k = n = 0$).

Indicate the Brewster angle and the critical angle on your plots. Also show the angles θ_1 and θ_2 in the range 0° to 90° on your plots. Finally plot ${}^{H}_{\perp}\Gamma_{1+}$ and ${}^{H}_{\parallel}\Gamma_{1+}$ in the same range as above.

5.2 Scan Compensated Array of Dipoles Given an array of planar dipoles located in a dielectric slab of thickness d_1 and intrinsic impedance Z_1 as shown in the top of Fig. P5.2:

Prove the validity of the equivalent circuit shown at the bottom of the figure, where R_{A0} is the radiation resistance of an array in an infinite medium with Z_0, and R_{A1} is the radiation resistance of the same array in an infinite medium with impedance Z_1.

For the equivalent circuit to be valid we have assumed:

a. No grating lobes.

b. Element length $2l$ so short that $P_0 \sim P_1$, namely independent of medium impedance.

c. The scan is limited to the principal planes.

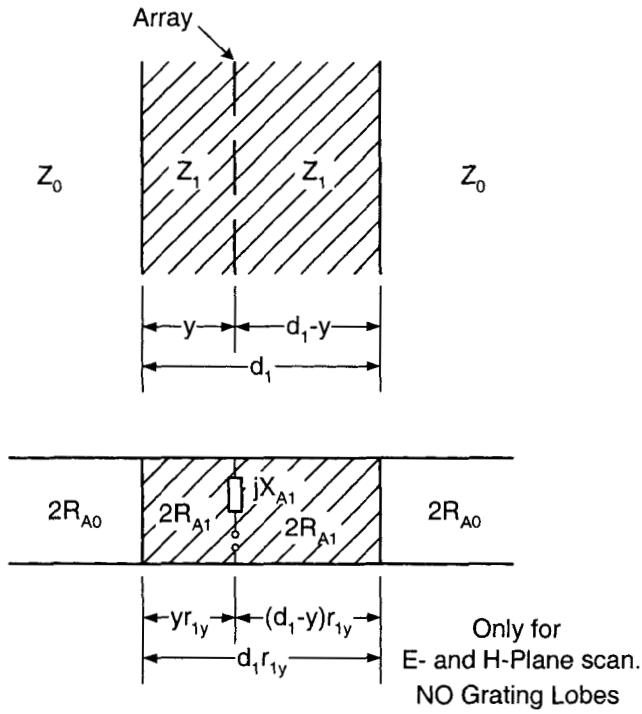

Fig. P5.2

Further:

d. Plot R_{A0} for 0°, 30°, and 60°, in H- and E-planes for $D_x = D_z = 0.35\lambda_0$ and element length $2l = 0.30\lambda_0$.

e. Plot Z_{in} for a transmission line with $Z_c = R_{A0}(0°)/\sqrt{1.5}$ and length $\lambda/4$ terminated in the 5 values above, respectively.

f. Plot Z_{1+} as defined in the text for $Z_1 = Z_0/\sqrt{1.5}$ and thickness $d_1 - y = 0.25\lambda_1$ for 0°, 30°, and 60°, scan angle (air) in the H- and E-planes.
Note the scan compensation.

5.3 Onset of Grating Lobes and Surface Waves Given an active array with inter-element spacings $D_x = D_z = 1.5$ cm, rectangular, and element length $2l = 1.4$ cm:

a. Find the lowest onset frequency for grating lobes when scanning in either of the principal planes and when the array is placed in air.

b. The array is now placed in the middle of a dielectric slab of total thickness $d_1 = 0.2$ cm.
Find the earliest onset of trapped grating lobes as well as free space grating lobes for $\epsilon_1 = 2\epsilon_0$ and $4\epsilon_0$.

c. Estimate the lowest frequency of possible surface waves with respect to the trapped and free space grating lobes calculated above.

d. Write a computer program for determination of the free surface waves for both the orthogonal and parallel scans.

e. Find the exact surface wave frequencies for 60° scan in air in the E- as well as H-planes.

5.4 Skewed versus Rectangular Grid Given a rectangular grid array with $D_x = D_z = \lambda/2$:

a. Plot the element grid next to a grating lobe diagram in the s_x, s_z-plane. Are there any grating lobes in visible space?

b. Skew the grid such that $\Delta z/D_z = 1/2$ but retain the same D_x and D_z as above.

Plot the element grid next to a grating lobe diagram in the s_x, s_z-plane.

c. Determine how much you can increase or decrease D_x as well as D_z in the skewed case so as just *not* to experience any grating lobes in the visible space.

d. Determine how much more distance (in %) between the closest elements you have in the skewed case (c above) and the rectangular case (a above).

6

SLOT ARRAYS IN A STRATIFIED MEDIUM

6.1 BACKGROUND

In the previous chapter we investigated the effect of a stratified medium on an array of electrical dipoles. We demonstrated that dielectric slabs not only have a profound effect on the resonant frequency, but also that it is possible to produce arrays of electric dipoles that retain a fairly constant scan impedance as a function of scan angle in the E- and H-planes (actually in any plane). These properties are important not only when used in their own right as active arrays, they are also a way to produce band-stop filters with bandwidth that is essentially constant for all polarizations and angles of incidence.

In this chapter we investigate in a similar manner the effect of a stratified medium on slot arrays. Such arrangements are important in their own right as active antennas but perhaps even more so as components that enable us to produce band-pass filters with a bandwidth that is essentially constant for all polarizations and angles of incidence.

While this introduction sounds like the dipole and slot cases are identical, the reader should be warned that there are profound (and tricky) differences between the two cases. We will use the duality concept to tie the two cases together.

6.2 DUAL SYSTEMS

The duality concept is well established in electromagnetic theory. An example is shown in Fig. 6.1. To the left we show an electrical system comprised of an array of elements with electrical currents $I^{(1)}(l)$ placed in a dielectric slab of thickness d_1 and with intrinsic impedance Z_1. To the right we show the dual system comprised of elements that have identical geometry to the electrical system but with magnetic currents $M^{(1)}(l)$ instead. The duality principle suggests that if we know, for example,

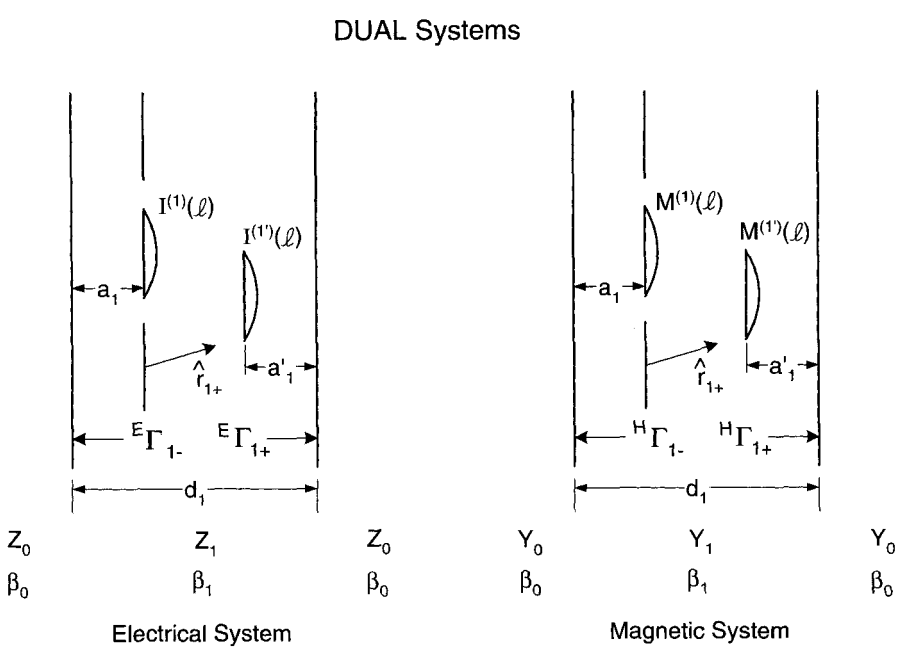

FIGURE 6.1. *Left:* An array with electrical currents $I^{(1)}(l)$ and an external element with current $I^{(1')}(l)$ both located in a slab of thickness d_1 and intrinsic impedance Z_1. *Right:* Same arrangement as the left except that the electrical currents have been replaced with magnetic currents $M^{(1)}(l)$ and $M^{(1')}(l)$ as shown.

the electrical field for the electrical system to the left, then we can readily obtain the magnetic field for the dual magnetic system to the right. More specifically, voltages are interchanged with currents, impedances with admittances, and vice versa. Thus the intrinsic impedance Z_1 in the magnetic system is replaced with the intrinsic admittance Y_1; however, the propagation constant β_1 remains the same for both systems. As an example, let us consider the mutual admittance between the array with reference element at $\bar{R}^{(1)}$ and an external element located at $\bar{R}^{(1')}$ with current $I^{(1')t}$. The elements in the dual system are not in general restricted to being planar. (However, complementary arrays to be presented later must be.) Thus we will restrict our investigation of dual systems to just planar elements. From (5.36) (modified to the mutual impedance rather than the self-impedance) we have with the notation in Fig. 6.1:

$$Z^{2,1} = \frac{Z_1}{2D_x D_z} \sum_k \sum_n \frac{e^{-j\beta_1(\bar{R}^{(1')} - \bar{R}^{(1)})\cdot \hat{r}_{1+}}}{r_{1y}} \left[{}_{\perp}P_1^{(1)} {}_{\perp}P_1^{(1')t} {}_{\perp}^{E}T_{1+} + {}_{\parallel}P_1^{(1)} {}_{\parallel}P_1^{(1')t} {}_{\parallel}^{E}T_{1+} \right] \tag{6.1}$$

where the pattern functions $\underset{\parallel}{\perp} P_1^{(1)}$ and $\underset{\parallel}{\perp} P_1^{(1')t}$ are defined by (5.11) to (5.13). The transformation function for the E-field is defined by

$$\underset{\parallel}{\overset{E}{\perp}} T = \left[1 + \underset{\parallel}{\overset{E}{\perp}} \Gamma_{1-} e^{-j2\beta_1 a_1 r_{1y}}\right]\left[1 + \underset{\parallel}{\overset{E}{\perp}} \Gamma_{1+} e^{-j2\beta_1 a_1' r_{1y}}\right] \underset{\parallel}{\overset{E}{\perp}} W_1, \qquad (6.2)$$

where $\underset{\parallel}{\overset{E}{\perp}} \Gamma_{1\pm}$ refers to the Fresnel reflection coefficient when referring to the E-field [see (C1) and (C2)]. Further $\underset{\parallel}{\overset{E}{\perp}} W_1$ is similarly defined by (5.16), using the reflection coefficients that refer to the E-field.

By duality we then obtain the mutual admittance between the magnetic array and the external element:

$$Y^{2,1} = \frac{Y_1}{2D_x D_z} \sum_k \sum_n \frac{e^{-j\beta_1(\bar{R}^{(1')} - \bar{R}^{(1)})\cdot \hat{r}_{1+}}}{r_{1y}}$$
$$\left[\perp P_1^{(1)} \perp P_1^{(1')t} \underset{\perp}{\overset{H}{}} T_{1+} + \parallel P_1^{(1)} \parallel P_1^{(1')t} \underset{\parallel}{\overset{H}{}} T_{1+}\right] \qquad (6.3)$$

where the pattern functions $\underset{\parallel}{\perp} P_1^{(1)}$ and $\underset{\parallel}{\perp} P_1^{(1')t}$ are evaluated by the same formulas as in the electrical case except that we use the magnetic currents $M^{(1)}(l)$ and $M^{(1')}(l)$, respectively. If we make the reasonable assumption that the shape of the electric and the magnetic currents are the same in the two cases, the pattern functions in the electrical and magnetic cases will be identical (thus the superscripts E and H are not needed).

Furthermore the $\underset{\parallel}{\overset{H}{\perp}} T_{1+}$ functions are calculated identically to $\underset{\parallel}{\overset{E}{\perp}} T_{1+}$, as given by (6.2) except that we must use the Fresnel reflection coefficients for the H-field as given by (C9) and (C10).

Thus we see that properties concerning the magnetic case can readily be obtained from the knowledge already available in the electrical case. The bad news is that a dual case as described above really does not exist: A perfect magnetically conducting element simply cannot be realized. However, in the next section we will consider complementary surfaces where duality will play an important role.

6.3 COMPLEMENTARY SURFACES

We will simply understand complementary surfaces to be two surfaces of a perfectly conducting and thin material with elements of such a shape that if the two surfaces are placed on top of each other they will fill the complete conducting plane. The most important and typical case is that of an array of perfectly conducting, flat dipoles and a slot array made as the negative of the dipole array, such as illustrated in Fig. 1.3.

Complementary surfaces will in general be analyzed by the following approach: Let a single slotted array, as shown in Fig. 6.2 top, be exposed to an incident plane

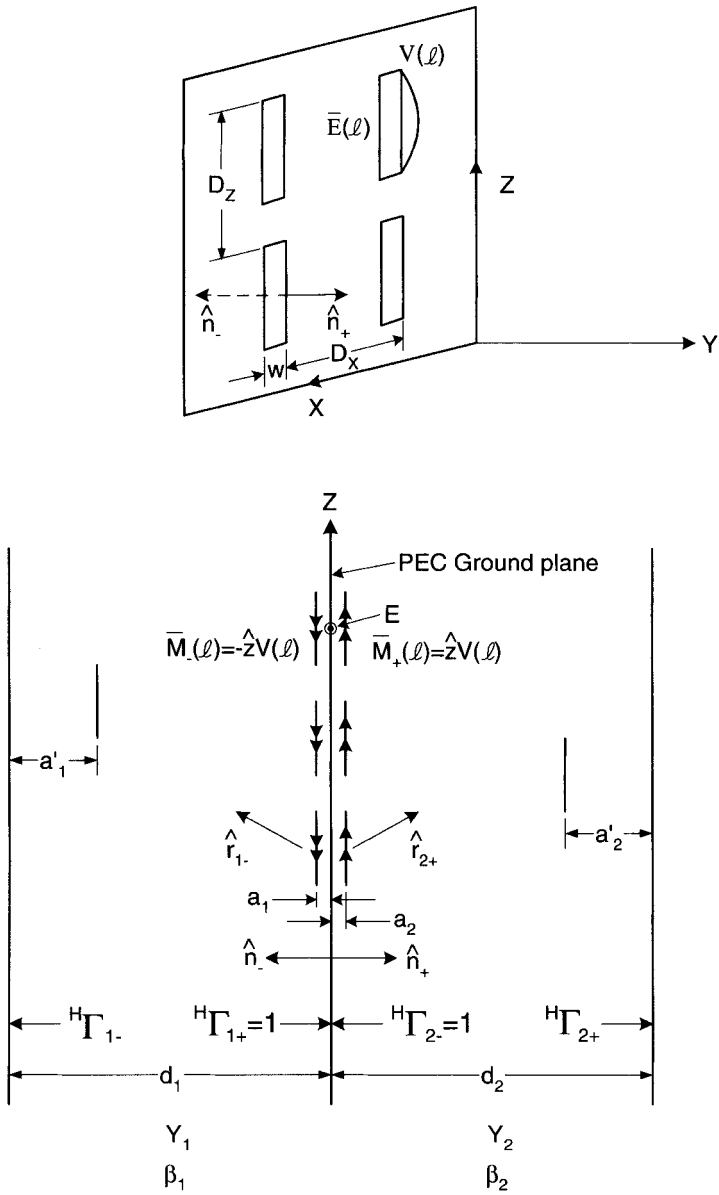

FIGURE 6.2. *Top:* An array of slots exposed to an incident plane wave producing the voltage $V(l)$ in the reference slot. *Bottom:* By the equivalence principle a slot array can be modeled by an array of magnetic currents placed on each side of a PEC ground plane. The slot array is located between slabs of thickness d_1 and d_2 with intrinsic admittances Y_1 and Y_2, respectively.

wave resulting in a voltage distribution $V(l)$ along the slots. If we assume the electric field $\bar{E}$ in the slot to be homogeneous (that's an approximation) and denote the slot width by w, then the electric field along the slot (when choosing $\bar{E}$ to be positive in the x-direction) will be

$$\bar{E} = \hat{x}\frac{V(l)}{w}. \tag{6.4}$$

By the equivalence principle, the electric field $\bar{E}$ is now equivalent to magnetic current density placed on each side of an electrically perfect conducting ground plane:

$$\bar{m}_{\pm} = \bar{E} \times \hat{n}_{\pm} \qquad \text{for } y \gtrless 0, \tag{6.5}$$

where $\hat{n}_{\pm}$ refers to the normal to the ground plane and is pointing into the half-spaces $y \gtrless 0$; see Fig. 6.2 top.

Thus from (6.4) and (6.5) we obtain the total magnetic current in one element:

$$\bar{M}_{\pm} = w\bar{m}_{\pm} = \pm\hat{z}V(l) \qquad \text{for } y \gtrless 0. \tag{6.6}$$

Let us now consider Fig. 6.2 bottom, showing two arrays of magnetic currents in opposite directions placed on each side of a perfectly conducting ground plane placed between two dielectric slabs of thickness d_1 and d_2. From the discussion above it is clear that if the spacings a_1 and $a_2 \to 0$, then these arrays of magnetic currents will simply model an array of slots. Furthermore from (6.3) we obtain the mutual admittance between array 1 to the left and an external element at $\bar{R}^{(1')}$ as

$$Y^{2,1} = \frac{Y_1}{2D_xD_z}\sum_k\sum_n \frac{e^{-j\beta_1(\bar{R}^{(1')}-\bar{R}^{(1)})\cdot\hat{r}_{1-}}}{r_{1y}}$$
$$\left[{}_{\perp}P_1^{(1)}\,{}_{\perp}P_1^{(1')t}\,{}^{H}_{\perp}T_{1-} + {}_{\parallel}P_1^{(1)}\,{}_{\parallel}P_1^{(1')t}\,{}^{H}_{\parallel}T_{1-}\right] \tag{6.7}$$

where the H-version of (6.2) is

$${}^{H}_{\substack{\perp\\\parallel}}T_{1-} = \frac{\left[1 + {}^{H}_{\substack{\perp\\\parallel}}\Gamma_{1-}e^{-j2\beta_1 a_1' r_{1y}}\right]\left[1 + {}^{H}_{\substack{\perp\\\parallel}}\Gamma_{1+}e^{-j2\beta_1 a_1 r_{1y}}\right]}{1 - {}^{H}_{\substack{\perp\\\parallel}}\Gamma_{1-}\,{}^{H}_{\substack{\perp\\\parallel}}\Gamma_{1+}e^{-j2\beta_1 d_1 r_{1y}}}. \tag{6.8}$$

Recalling that the reflection coefficient for the H-field for a PEC ground plane is ${}^{H}_{\substack{\perp\\\parallel}}\Gamma_{1+} = 1$ and if we further let $a_1 \to 0$ in (6.8), we obtain

$${}^{H}_{\substack{\perp\\\parallel}}T_{1-} = 2\frac{1 + {}^{H}_{\substack{\perp\\\parallel}}\Gamma_{1-}e^{-j2\beta_1 a_1' r_{1y}}}{1 - {}^{H}_{\substack{\perp\\\parallel}}\Gamma_{1-}e^{-j2\beta_1 d_1 r_{1y}}}. \tag{6.9}$$

The array's self-admittance $Y_A^{(1)}$ for the array to the left is now readily obtained from (6.7) by simply making use of the well-known fact [39] that a flat element of width w (i.e., the magnetic current modeling the slot) has an equivalent radius equal to $w/4$. Mathematically we set $\bar{R}^{(1')} - \bar{R}^{(1)} = \hat{y}\frac{w}{4}$ and obtain

$$Y_A^{(1)} = \frac{Y_1}{2D_x D_z} \sum_k \sum_n \frac{e^{-j\beta_1 (w/4) r_{1y}}}{r_{1y}}$$
$$\left[{}_{\perp}P_1^{(1)} \, {}_{\perp}P_1^{(1')t} \, {}^{H}_{\perp} T_{1-} + {}_{\parallel}P_1^{(1)} \, {}_{\parallel}P_1^{(1')t} \, {}^{H}_{\parallel} T_{1-} \right] \tag{6.10}$$

where the transformation function ${}^{H}_{\perp\!\!\!\parallel} T_{1-}$ is obtained from (6.9) by simply setting $a_1' \sim d_1$:

$${}^{H}_{\perp\!\!\!\parallel} T_{1-} = 2 \frac{1 + {}^{H}_{\perp\!\!\!\parallel} \Gamma_{1-} e^{-j2\beta_1 d_1 r_{1y}}}{1 - {}^{H}_{\perp\!\!\!\parallel} \Gamma_{1-} e^{-j2\beta_1 d_1 r_{1y}}}. \tag{6.11}$$

The admittance $Y_A^{(2)}$ of the array to the right bordering slab d_2 is obtained analogously to $Y_A^{(1)}$. In (6.10) and (6.11) we merely change subscript 1 to 2 as well as + and −.

The total slot admittance Y_A is simply obtained by noticing that the two admittances $Y_A^{(1)}$ and $Y_A^{(2)}$ are in parallel. Thus

$$Y_A = Y_A^{(1)} + Y_A^{(2)}. \tag{6.12}$$

It is interesting to compare the slot case above with the dipole case, treated earlier in Sections 5.10 and 5.11. The expressions for the two impedances Z_{1-} and Z_{1+} look mathematically quite similar to the admittances $Y_A^{(1)}$ and $Y_A^{(2)}$ at least for the propagating modes. However, although there are obvious similarities between the dipole and the slot cases, there are profound differences, which will be explored next. (See also Problem 6.1.)

6.4 SCAN INDEPENDENCE OF A SLOT ARRAY ADJACENT TO DIELECTRIC SLABS

We saw above how the total admittance Y_A of a slot array simply is the sum of the two admittances $Y_A^{(1)}$ and $Y_A^{(2)}$ (6.12). It is interesting to note that contrary to the electrical dipole case treated earlier in Chapter 5, the two admittances in the slot case are in two distinctly different worlds, namely separated by a perfectly conducting ground plane. Consequently it is completely rigorous to analyze each of these admittances separately, even including the entire imaginary space.

More specifically let us examine $Y_A^{(1)}$ as given by (6.10) where the transformation function is given by

$$\overset{H}{\underset{\parallel}{\perp}} T_{1-} = 2\frac{1 + \overset{H}{\underset{\parallel}{\perp}} \Gamma_{1-} e^{-j2\beta_1 d_1 r_{1y}}}{1 - \overset{H}{\underset{\parallel}{\perp}} \Gamma_{1-} e^{-j2\beta_1 d_1 r_{1y}}}. \tag{6.13}$$

This function $\overset{H}{\underset{\parallel}{\perp}} T_{1-}$ constitutes a bilinear transformation as a function of $\beta_1 d_1 r_{1y}$ provided that the angle of incidence is constant such that the reflection coefficient ${}^H\Gamma_{1-}$ is a constant. As shown in Appendix A, the loci for $\overset{H}{\underset{\parallel}{\perp}} T_{1-}$ will be circles with centers on the real axis and which go through the points $2\frac{1+|{}^H\Gamma_{1-}|}{1-|{}^H\Gamma_{1-}|}$ and $2\frac{1-|{}^H\Gamma_{1-}|}{1+|{}^H\Gamma_{1-}|}$; see Fig. 6.3 top.

At the bottom of the same figure, we show a slot array with a dielectric slab at the left. To the right we show $\overset{H}{\underset{\parallel}{\perp}} \Gamma_{1-}$ for a typical case where $Y_1 = 2Y_0$. Note that $\overset{H}{\underset{\parallel}{\perp}} \Gamma_{1-}$ is mostly negative except for $\perp$ polarization where the angles of incidence are larger than the Brewster angle. By inspection of (6.13), it then follows that $\overset{H}{\underset{\parallel}{\perp}} T_{1-}$ will attain the value $2\frac{1-|{}^H\Gamma_{1-}|}{1+|{}^H\Gamma_{1-}|}$ for slab thickness $\beta_1 d_1 r_{1y} = n_2\pi$ when $n_2 = 0, 1, 2, \ldots$, while for $\beta_1 d_1 r_{1y} = \pi/2 + n_2\pi$ we obtain

$$\overset{H}{\underset{\parallel}{\perp}} T_{1-} = 2\frac{1 + |{}^H\Gamma_{1-}|}{1 - |{}^H\Gamma_{1-}|}. \tag{6.14}$$

Applying (C.15) and (C.16) to (6.14) yields

$$\overset{H}{\underset{\parallel}{\perp}} T_{1-} = \begin{cases} 2\dfrac{Y_1}{Y_0}\dfrac{r_{0y}}{r_{1y}} & \text{for } \perp \text{ scan (E-plane scan)}, \\ 2\dfrac{Y_1}{Y_0}\dfrac{r_{1y}}{r_{0y}} & \text{for } \parallel \text{ scan (H-plane scan)}. \end{cases} \tag{6.15}$$

Similar to the electric dipole case treated in Section 5.10, let us now examine the admittance $Y_A^{(1)}$ of an array of short slots of length Δl oriented in the z-direction and adjacent to a dielectric slab of thickness d_1 as shown in Fig. 6.4. We will examine each of the principal planes separately and we note that the vector signs shown in Fig. 6.4 are consistent with the negative-going waves $\hat{r}_{1-}$ as defined in Section 5.2. Noting that the pattern factors for slots are identical to the electrical dipole case, we readily obtain from (5.47) and (5.48) by further noting from (5.13) that $P_1 \sim \Delta l$:

E-Plane Scan, $\alpha = 0°$ (see Fig. 6.4)

$$\perp P_1^{(1)} = \perp P_1^{(1')t} = \hat{z} \cdot \perp \hat{n}_1 P_1 = \Delta l, \tag{6.16}$$

$$\parallel P_1^{(1)} = \parallel P_1^{(1')t} = \hat{z} \cdot \parallel \hat{n}_1 P_1 = 0. \tag{6.17}$$

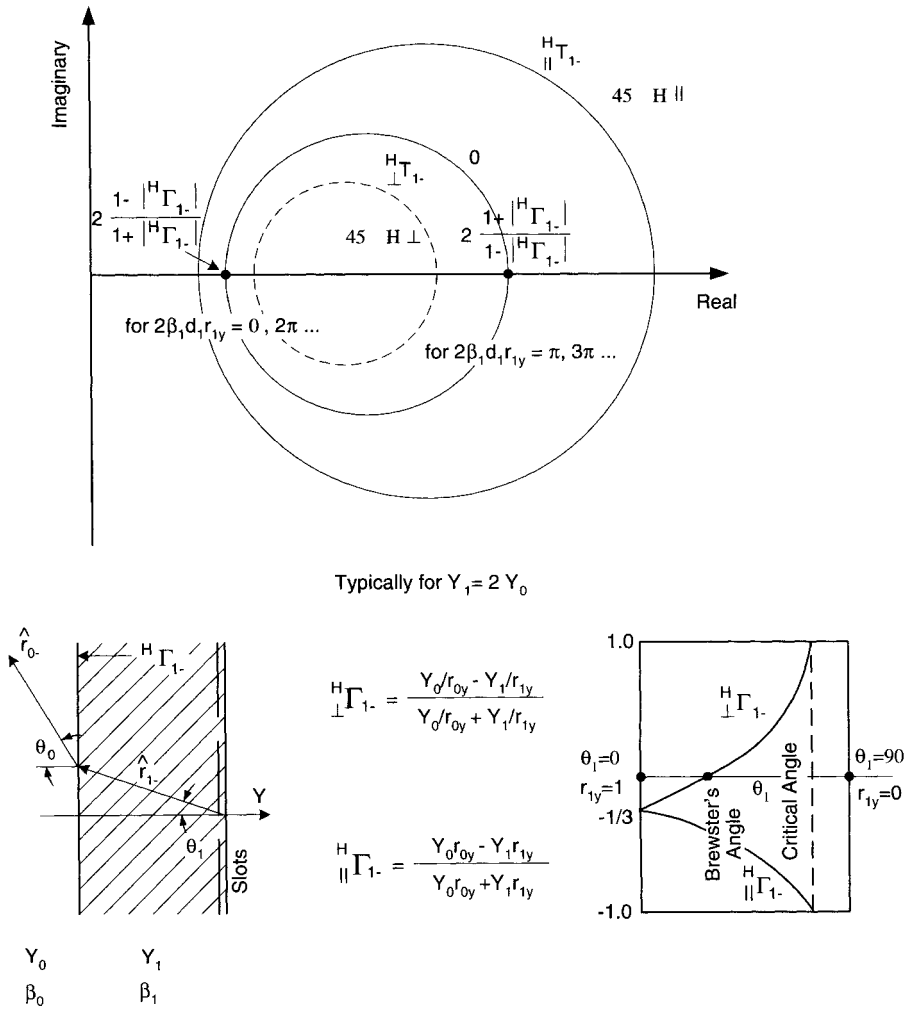

FIGURE 6.3. *Top:* Typical ${}^{H}_{\perp\!\!\!\parallel} T_{1-}$ -function as a function of $\beta_1 d_1 r_{1y}$ where r_{1y} is a constant (i.e., angle of incidence is constant). *Bottom-left:* A slot array emanating the spectrum $\hat{r}_{1-}$ through the slab d_1 to the left side. *Bottom-right:* Reflection coefficient ${}^{H}_{\perp\!\!\!\parallel}\Gamma_{1-}$ for the H-field when going from dielectric to air for $Y_1 = 2Y_0$.

H-Plane Scan, $\alpha = 90°$ (see Fig. 6.4)

$$\perp P_1^{(1)} = \perp P_1^{(1')t} = \hat{z} \cdot \perp \hat{n}_1 P_1 = 0, \tag{6.18}$$

$$\parallel P_1^{(1)} = \parallel P_1^{(1')t} = \hat{z} \cdot \parallel \hat{n}_1 P_1 \sim \Delta l r_{1y}. \tag{6.19}$$

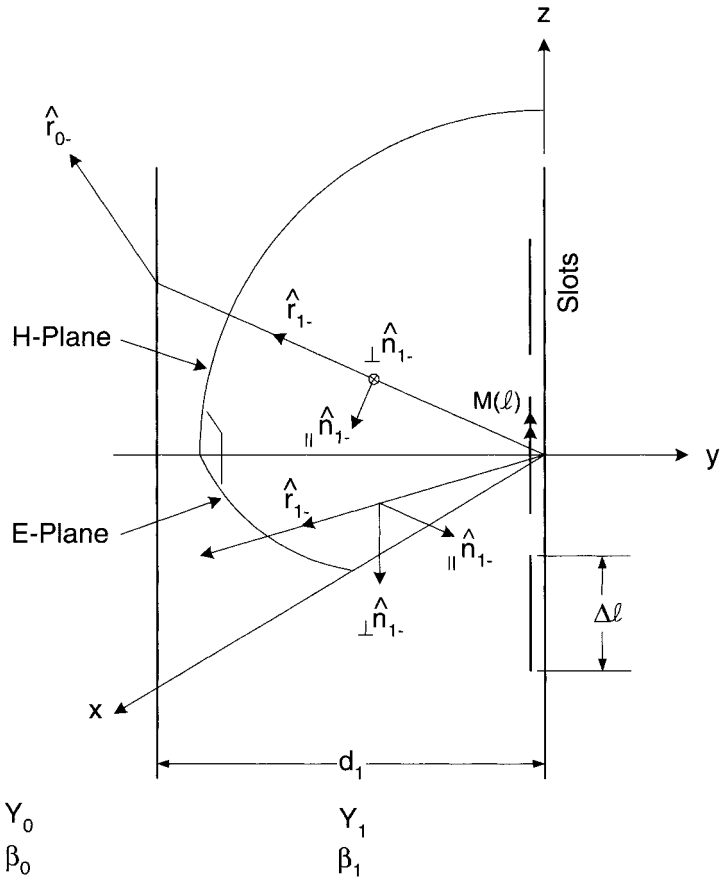

FIGURE 6.4. A slot array adjacent to a slab of thickness d_1 emanates propagating waves $\hat{r}_{1-}$. We show the E-plane and the H-plane, as well as $\perp\!\!\!\parallel \hat{n}_{1-}$.

Substituting (6.15) through (6.19) into (6.10) yields for the real part of $Y_A^{(1)}$ and for no grating lobes

$$Re Y_A^{(1)} \sim \begin{cases} \dfrac{Y_1}{2D_x D_z}\dfrac{1}{r_{1y}}\left[\Delta l^2 2\dfrac{Y_1}{Y_0}\dfrac{r_{0y}}{r_{1y}}\right] & \text{for E-plane scan,} \\ \dfrac{Y_1}{2D_x D_z}\dfrac{1}{r_{1y}}\left[\Delta l^2 r_{1y}^2 2\dfrac{Y_1}{Y_0}\dfrac{r_{1y}}{r_{0y}}\right] & \text{for H-plane scan.} \end{cases} \tag{6.20}$$

Inspection of (6.20) readily shows that in order to obtain the same admittance values in the E- and H-plane at the same scan angle, we must require that

$$\frac{r_{0y}}{r_{1y}} = r_{1y}^2\frac{r_{1y}}{r_{0y}} \quad \text{or} \quad r_{1y}^2 = r_{0y}; \tag{6.21}$$

that is, $\cos^2\theta_1 = \cos\theta_0$. Equation (6.21) is seen to be identical to (5.50) obtained earlier for the electrical dipole case. Thus in the slot case we also obtain scan compensation when we place dielectric slabs on both sides with a relative dielectric constant given by

$$\epsilon_{r1} = \epsilon_{r2} = 1 + \cos\theta_0 = 1 + r_{0y} \quad \text{and} \quad d_1 = d_2 \sim \frac{\lambda_1}{4} \sim \frac{\lambda_2}{4}. \tag{6.22}$$

Typical values of $\epsilon_{r1}(\epsilon_{r2})$ leading to scan compensation are shown in Fig. 5.14 for the electric dipole case. Scan independence for slot arrays plays a crucial role in the design of hybrid radomes with constant bandwidth (as will be described in Chapter 7; see also Problems 6.2 and 6.3).

6.5 ADMITTANCE OF A SLOT ARRAY WITH A DIELECTRIC SLAB TO ONE SIDE AND A GROUND PLANE TO THE OTHER

In Fig. 6.5 we show a case where a slot array is flanked by dielectric slabs with intrinsic admittances Y_1 and Y_2 and thicknesses d_1 and d_2 to the left and right, respectively. Further slab 1 looks out into free space while slab 2 is terminated into a ground plane.

This case is important in its own right as an active antenna. However, it also plays an important role in analyzing hybrid radomes as we will show in detail in Chapter 7.

Basically, the total scan admittance Y_A is given by (6.12) where $Y_A^{(1)}$ is given by (6.10) and (6.11), and analogous for $Y_A^{(2)}$. The trick in analyzing hybrid radomes is now simply that $Y_A^{(1)}$ is split up into appropriate terms. From our basic analysis in Chapter 5, we know the term $k = n = 0$ is the only term that has a real component; all other terms are imaginary (for no grating lobes, of course). However, note that because of $\begin{matrix}\perp \\ \parallel\end{matrix}^H T_{1-}$ being complex as given by (6.11), the term $k = n = 0$ has a real as well as an imaginary component. We will denote these terms by Y_{0re} and Y_{0im}; in other words, from (6.10) we see they are given as

$$Y_{0re}^{(1)} + jY_{0im}^{(1)} = \frac{Y_1}{2D_xD_z}\frac{1}{r_{1y}}\left[\left[{}_\perp P_1^{(1)}\,{}_\perp P_1^{(1')t} Re_\perp^H T_{1-} + {}_\parallel P_1^{(1)}\,{}_\parallel P_1^{(1')t} Re_\parallel^H T_{1-}\right]\right.$$
$$\left. + j\left[{}_\perp P_1^{(1)}\,{}_\perp P_1^{(1')t} Im_\perp^H T_{1-} + {}_\parallel P_1^{(1)}\,{}_\parallel P_1^{(1')t} Im_\parallel^H T_{1-}\right]\right]. \tag{6.23}$$

The rest of the terms in (6.10) are purely imaginary and denoted by

$$Y_{rest}^{(1)} = \frac{Y_1}{2D_xD_z}\sum\sum_{k,n\neq 0,0}\frac{e^{-j\beta_1 w/4r_{1y}}}{r_{1y}}$$
$$\left[{}_\perp P_1^{(1)}\,{}_\perp P^{(1')t}\,{}_\perp^H T_{1-} + {}_\parallel P_1^{(1)}\,{}_\parallel P^{(1')t}\,{}_\parallel^H T_{1-}\right] \tag{6.24}$$

(see also discussion in Section 5.10).

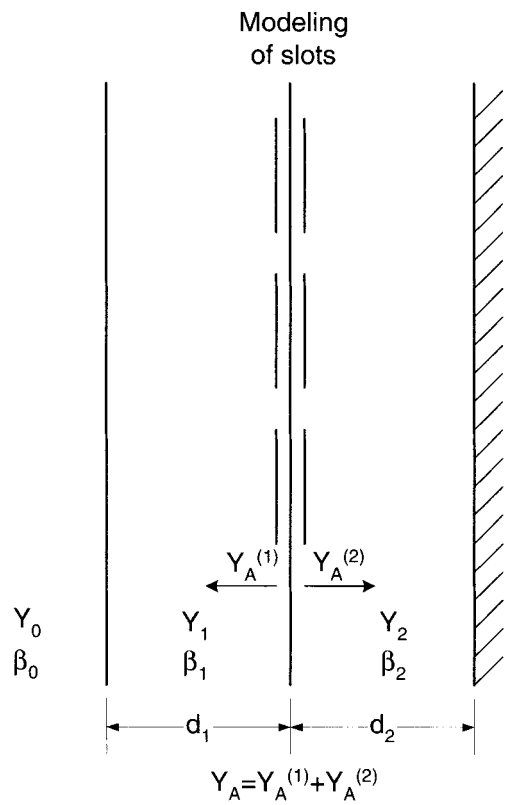

FIGURE 6.5. A slot array flanked by dielectric slabs with thicknesses d_1 and d_2 and intrinsic admittances Y_1 and Y_2 as shown.

An instructive picture of the three components $Y_{0re}^{(1)}$, $Y_{0im}^{(1)}$, and $Y_{0rest}^{(1)}$ is shown in Fig. 6.6 left. Note that $Y_{0re}^{(1)}$ as well as $Y_{0im}^{(1)}$ are sensitive to the slab parameter $\beta_1 d_1 r_{1y}$. The third term $Y_{rest}^{(1)}$ is fairly independent of slab thickness and angle of incidence (unless the slabs become quite thin in terms of wavelength). The reason for this fact is simply that the first two terms are associated with a propagating mode (i.e., $k = n = 0$), while the third term is associated with all the evanescent modes that never really make it to the surface of the slab (or, said another way, they represent energy stored in the immediate neighborhood of the array elements).

The admittance $Y_A^{(2)}$ is given by (6.10) by simply adapting to slab 2. Further in (6.11) we substitute $\beta_2 d_2 r_{2y}$ for $\beta_1 d_1 r_{1y}$, and we also note that ${}^H\Gamma_{2+} = 1$ because of the ground plane. As we did above with $Y_A^{(1)}$, we now split $Y_A^{(2)}$ up into the terms $k = n = 0$ and the rest.

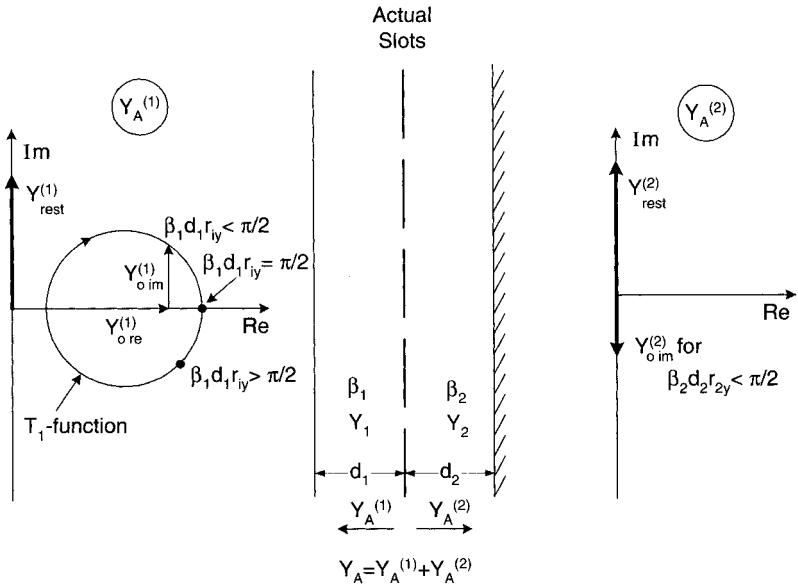

FIGURE 6.6. Total slot admittance $Y_A = Y_A^{(1)} + Y_A^{(2)}$ where $Y_A^{(1)}$ and $Y_A^{(2)}$ look left and right, respectively. $Y_A^{(1)}$ has one real component $Y_{0re}^{(1)}$ and two imaginary components $Y_{0im}^{(1)}$ and $Y_{rest}^{(1)}$, while $Y_A^{(2)}$ has only the purely imaginary components $Y_{0im}^{(2)}$ and $Y_{rest}^{(2)}$.

For the first term $k = n = 0$ we obtain from (6.10) adapted to slab 2:

$$\begin{matrix}H \\ \perp \\ \parallel\end{matrix} T_{2+} = 2\frac{1 + \begin{matrix}H \\ \perp \\ \parallel\end{matrix} \Gamma_{2+} e^{-j2\beta_2 d_2 r_{2y}}}{1 - \begin{matrix}H \\ \perp \\ \parallel\end{matrix} \Gamma_{2+} e^{-j2\beta_2 d_2 r_{2y}}}$$

$$= 2\frac{1 + e^{-j2\beta_2 d_2 r_{2y}}}{1 - e^{-j2\beta_2 d_2 r_{2y}}}$$

$$= -j2\cot(\beta_2 d_2 r_{2y}). \tag{6.25}$$

That is,

$$Y_{0re}^{(2)} = 0, \tag{6.26}$$

$$Y_{0im}^{(2)} = \frac{Y_2}{2D_x D_z}\frac{-j}{r_{2y}}\left[{}_{\perp}P_2^{(1)}\,{}_{\perp}P_2^{(1')t}\,2\cot(\beta_2 d_2 r_{2y}) + {}_{\parallel}P_2^{(1)}\,{}_{\parallel}P_2^{(1')t}\,2\cot(\beta_2 d_2 r_{2y})\right], \tag{6.27}$$

while $Y_{rest}^{(2)}$ is given by (6.24) adapted to slab 2. It should not surprise us that $Y_{0re}^{(2)} = 0$, since no energy can escape to the right because of the ground plane. The other two admittances $Y_{0im}^{(2)}$ and $Y_{rest}^{(2)}$ are shown in Fig. 6.6 right.

In the further analysis we now add the two admittances $Y_{rest}^{(1)}$ and $Y_{rest}^{(2)}$:

$$Y_{rest} = Y_{rest}^{(1)} + Y_{rest}^{(2)}. \tag{6.28}$$

As already noted above, none of these admittances change much with incidence but they change considerably with frequency. On the other hand, $Y_{0re}^{(1)}$ changes little with frequency but may be sensitive to $\beta_1 d_1 r_{1y}$ depending on the value (see scan independence in Section 6.4).

Finally the two imaginary admittances $Y_{0im}^{(1)}$ and $Y_{0im}^{(2)}$ are interesting by the fact that they, to a large degree, can cancel each other as they change with angle of incidence. More specifically, let $\beta_1 d_1 r_{1y} \sim \beta_2 d_2 r_{2y} \sim \frac{\pi}{2}$ for normal angle of incidence (i.e., $r_{1y} = r_{2y} = 1$). For oblique angles of incidence, r_{1y} as well as r_{2y} will be smaller than one. This will move $Y_{0im}^{(1)}$ up in the positive complex plane and $Y_{0im}^{(2)}$ down in the negative half; in other words, we have the possibility that the sum of these two admittances can remain quite stable with angle of incidence. Which simply means the sum of all the imaginary components such that

$$Y_A = Y_{0re}^{(1)} + jy = Y_{0re}^{(1)} + j\left[Y_{rest}^{(1)} + Y_{rest}^{(2)} + Y_{0im}^{(1)} + Y_{0im}^{(2)}\right] \tag{6.29}$$

may remain quite stable with angle of incidence for small inter-element spacings. This is an important observation, since it simply means that the resonant frequency of a multilayered hybrid radome can, if properly designed, remain rather stable with angle of incidence as well as polarization.

We finish this section by emphasizing that the key admittances for analyzing hybrid radomes (as done in Chapter 7) are $Y_{0re}^{(1)}$ as given by the first term on the right of (6.23) and y as defined by (6.29) and should not be confused with the coordinate in the y-direction.

6.6 MUTUAL ADMITTANCE BETWEEN TWO SLOT ARRAYS

In this section we determine the mutual admittance between two adjacent slot arrays as shown in Fig. 6.7. This quantity plays a key role in the determination of the transmission and reflection properties of a general N-layer hybrid radome (as will be investigated later in Chapter 7 and also used in Appendix B).

The two slot arrays are modeled as magnetic dipole arrays placed on each side of perfectly conducting ground planes as explained earlier in the beginning of this chapter and as illustrated in Fig. 6.7. The mutual admittance $Y^{2,1}$ between the two slot arrays is given simply by the mutual admittance between the two inside magnetic dipole arrays. From (6.7) we find after a trivial change of the pertinent parameters that

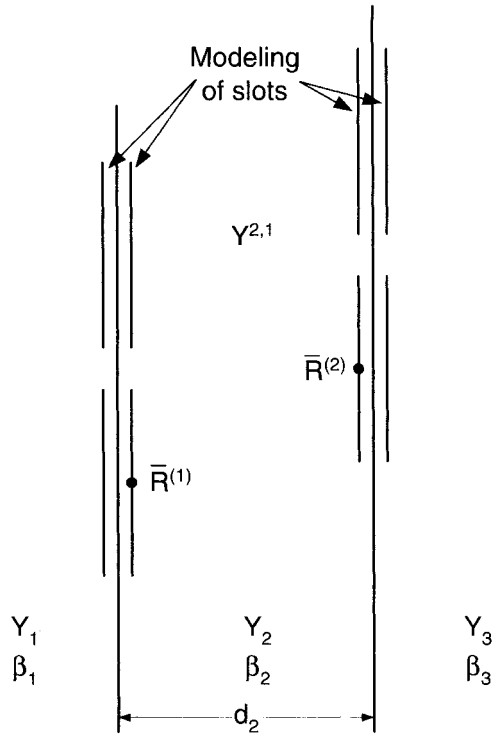

FIGURE 6.7. Two adjacent slot arrays are modeled by magnetic dipole arrays placed on each side of perfectly conducing ground planes as shown. The mutual admittance $Y^{2,1}$ between the two slot arrays is determined solely as the mutual admittance between the two inside magnetic arrays.

$$Y^{2,1} = \frac{Y_2}{2D_x D_z} \sum_k \sum_n \frac{e^{-j\beta_2(\bar{R}^{(2)}-\bar{R}^{(1)})\cdot\hat{r}_{2+}}}{r_{2y}} \left[{}_{\perp}P_2^{(1)}\, {}_{\perp}P_2^{(2)t}\, {}^{H}_{\perp}T_{2+} + {}_{\parallel}P_2^{(1)}\, {}_{\parallel}P_2^{(2)t}\, {}^{H}_{\parallel}T_{2+} \right] \tag{6.30}$$

where by modification of (6.8),

$$\begin{aligned} {}^{H}_{\substack{\perp \\ \parallel}}T_{2+} &= \frac{\left[1 + 1 \cdot e^{-j2\beta_2 \cdot 0 \cdot r_{2y}}\right]\left[1 + 1 \cdot e^{-j\beta_2 \cdot 0 \cdot r_{2y}}\right]}{1 - 1 \cdot 1 \cdot e^{-j2\beta_2 d_2 r_{2y}}} \\ &= \frac{4}{1 - e^{-j2\beta_2 d_2 r_{2y}}}. \end{aligned} \tag{6.31}$$

We further write the exponential term in (6.30) as

$$e^{-j\beta_2(\bar{R}^{(2)}-\bar{R}^{(1)})\cdot\hat{r}_{2+}} = e^{-j\beta_2(x^{(2)}-x^{(1)})\cdot r_{2x}} e^{-j\beta_2 d_2 r_{2y}} e^{-j\beta_2(z^{(2)}-z^{(1)})\cdot r_{2z}}. \tag{6.32}$$

Substituting (6.31) and (6.32) into (6.30) yields

$$Y^{2,1} = -\frac{Y_2}{2D_xD_z}\sum_k\sum_n \frac{e^{-j\beta_2(x^{(2)}-x^{(1)})r_{2x}}e^{-j\beta_2(z^{(2)}-z^{(1)})r_{2z}}}{r_{2y}}$$
$$\left[{}_\perp P_2^{(1)}\,{}_\perp P_2^{(2)t} + {}_\parallel P_2^{(1)}\,{}_\parallel P_2^{(2)t}\right]\frac{2j}{\sin(\beta_2 d_2 r_{2y})}. \tag{6.33}$$

If we further assume that the two arrays are positioned opposite each other, $x^{(1)} = x^{(2)}$ and $z^{(1)} = z^{(2)}$, we observe that the exponent in (6.33) equals unity. Thus, for two arrays on the "same level," we observe that the leading term $(k, n = 0, 0)$ in (6.33) is purely imaginary. The higher-order terms are also imaginary because r_{2y} is imaginary, while the pattern components and the T-function are real. Thus $Y^{2,1}$ is purely imaginary.

Even if the two arrays are not on the same level, it is interesting to observe that for arbitrary positioning

$$Y^{2,1} = \left(Y^{1,2}\right)^*. \tag{6.34}$$

As we will see in Chapter 7, from the evaluation of the determinant D_N, determining the transmission properties of an N-layer hybrid radome typically contains the product $Y^{n,m}Y^{m,n}$. Thus from (6.34) we observe that this product is independent of whether the two slot arrays are opposite each other. (This statement applies only to the evaluation of the determinant D_N; however, see also Section 7.7.2 on registration sensitivity.)

6.7 SURFACE WAVES ON PERIODIC STRUCTURES OF SLOTS: FREE AND FORCED

In this section we examine possible singularities of the slot admittances as for example $Y_A^{(1)}$ as given by (6.10). Inspection shows that it will usually happen at the onset of a trapped grating lobe, namely for $r_{1y} = 0$ (see later). Of greater interest are the cases where ${}^H_{\perp\,\parallel}T_{1-}$ goes to infinity [as given by (6.11)],

$$1 - {}^H_{\perp\,\parallel}\Gamma_{1-}e^{-j2\beta_1 d_1 r_{1y}} = 0. \tag{6.35}$$

Evidently a necessary condition for satisfying (6.35) is that

$$\left|{}^H_{\perp\,\parallel}\Gamma_{1-}\right| = 1. \tag{6.36}$$

We split the following investigation into the $\perp$ and $\parallel$ cases as follows:

Perpendicular Case From (C.9) we have

$$\overset{H}{\perp}\Gamma_{1-} = \frac{Y_0 r_{1y} - Y_1 r_{0y}}{Y_0 r_{1y} + Y_1 r_{0y}},$$

and for total reflection $r_{0y} = -j|r_{0y}|$, we obtain

$$\overset{H}{\perp}\Gamma_{1-} = \frac{Y_0 r_{1y} + jY_1|r_{0y}|}{Y_0 r_{1y} - jY_1|r_{0y}|} = e^{j2\tan^{-1}(Y_1/Y_0)|r_{0y}|/r_{1y}}. \tag{6.37}$$

Substituting (6.37) into (6.35), we have

$$e^{j2\tan^{-1}(Y_1/Y_0)|r_{0y}|/r_{1y}} e^{-j2\beta_1 d_1 r_{1y}} = 1 = e^{-j\pi n_1} \qquad n_1 = 0, 2, 4, \ldots,$$

or

$$\frac{Y_1}{Y_0}\frac{|r_{0y}|}{r_{1y}} = \tan\left(\beta_1 d_1 r_{1y} - \frac{\pi}{2} n_1\right). \tag{6.38}$$

Further θ_1 and θ_0 are related by Snell's law (where we have dropped the r in ϵ_{r1} and μ_{r1}):

$$\frac{\sin\theta_1}{\sin\theta_0} = \frac{1}{\sqrt{\mu_1\epsilon_1}} = \frac{\sqrt{1 - r_{1y}^2}}{\sqrt{1 + |r_{0y}|^2}}$$

or

$$|r_{0y}| = \sqrt{(\mu_1\epsilon_1 - 1) - \mu_1\epsilon_1 r_{1y}^2}. \tag{6.39}$$

Substituting (6.39) into (6.38), we have

$$\sqrt{(\mu_1\epsilon_1 - 1) - \mu_1\epsilon_1 r_{1y}^2} = \frac{Y_0}{Y_1} r_{1y} \tan\left(\beta_1 d_1 r_{1y} - \frac{\pi}{2} n_1\right)$$

or

$$\sqrt{(\beta_0 d_1)^2(\mu_1\epsilon_1 - 1) - (\beta_1 d_1 r_{1y})^2} = \frac{1}{\epsilon_1}(\beta_1 d_1 r_{1y}) \tan\left(\beta_1 d_1 r_{1y} - \frac{\pi}{2} n_1\right),$$
$$n_1 = 0, 2, 4, \ldots. \tag{6.40}$$

According to Harrington [36], (6.40) constitutes the characteristic equation for a surface wave in the TM or $\perp$ case as depicted in Fig. 6.8 left.

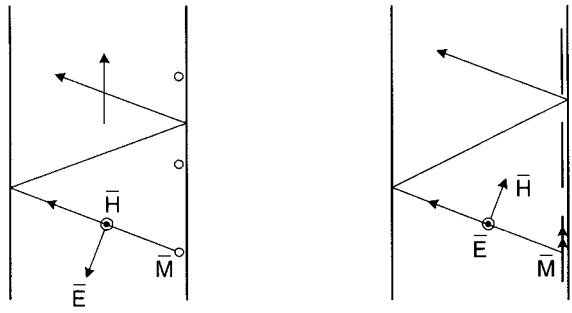

FIGURE 6.8. *Left:* A slot array with currents $\bar{M}$ producing a surface wave in the $\perp$ plane (TM-case). *Right:* A slot array with current $\bar{M}$ producing a surface wave in the $\parallel$ plane (TE case).

Parallel Case From (C.10) we have

$$\overset{H}{\parallel}\Gamma_{1-} = \frac{Y_0 r_{0y} - Y_1 r_{1y}}{Y_0 r_{0y} + Y_1 r_{1y}},$$

and for total reflection $r_{0y} = -j|r_{0y}|$, we obtain

$$\overset{H}{\parallel}\Gamma_{1-} = \frac{-jY_0|r_{0y}| - Y_1 r_{1y}}{-jY_0|r_{0y}| + Y_1 r_{1y}} = -e^{j2\tan^{-1}(Y_0/Y_1)|r_{0y}|/r_{1y}}. \tag{6.41}$$

Substituting (6.41) into (6.35) yields

$$e^{j2\tan^{-1}(Y_0/Y_1)|r_{0y}|/r_{1y}} e^{-j2\beta_1 d_1 r_{1y}} = e^{-j\pi n_1}, \qquad \text{where } n_1 = 1, 3, 5,$$

or

$$\tan^{-1}\frac{Y_0}{Y_1}\frac{|r_{0y}|}{r_{1y}} = -\frac{\pi}{2}n_1 + \beta_1 d_1 r_{1y}$$

$$|r_{0y}| = \frac{Y_1}{Y_0} r_{1y} \tan\left(\beta_1 d_1 r_{1y} - \frac{\pi}{2}n_1\right). \tag{6.42}$$

Substituting Snell's law (6.39) into (6.42), we have

$$\sqrt{(\beta_0 d_1)^2(\mu_1\epsilon_1 - 1) - (\beta_1 d_1 r_{1y})^2} = \frac{1}{\mu_1}(\beta_1 d_1 r_{1y}) \tan\left(\beta_1 d_1 r_{1y} - \frac{\pi}{2}n_1\right),$$

$$n_1 = 1, 3, 5. \tag{6.43}$$

According to Harrington [36], (6.43) is the characteristic equation describing a surface wave of the TE or $\parallel$ case, with respect to the H-field as shown in Fig. 6.8 right.

6.8 COMPARISON OF ELECTRIC DIPOLE AND SLOT CASES

The surface waves for the electric dipole cases were determined by the characteristic equations (5.60) and (5.64) for the $\perp$ and $\parallel$ cases, respectively (with respect to the E-field). Similarly the surface waves for the slot cases were determined by (6.40) and (6.43) for the $\perp$ and $\parallel$ cases, respectively (with respect to the H-field).

Comparison between these four sets of equations reveals that they are basically identical except when noticing that $d_1/2$ in the electric dipole case goes into d_1 or d_2 in the slot case and that the $\perp$ electric case and the $\parallel$ slot case are divided on the right side by μ_1, while the other two equations similarly are divided by ϵ_1 (i.e., we always divide by μ_1 in the TE-cases and by ϵ_1 in the TM-cases). Consequently they can all be solved graphically by the approach discussed in Section 5.11 as shown in Fig. 5.16. Further we may conclude that at least for $\mu_1 = 1$ and low values of ϵ_1, the surface waves in the electric and magnetic (slot) cases are close to each other but are not identical.

Further note that n_1 can attain all integer values in the asymmetric dipole case, while it is restricted in the slot case as given by (6.40) and (6.43).

6.9 ONSET OF TRAPPED AND FREE SPACE GRATING LOBES

In Section 5.12 we investigated in great detail the properties of the Z_A impedance of electric dipole arrays when we experienced onset of either trapped or free space grating lobes. Obviously we have the same interest in the slot array case. The good news is that the typical expression for the electrical dipole case as given, for example, by (5.37) is mathematically of the same form as the admittance for the dual case (or ultimately the slot case) as given, for example, by (6.7) or (6.8). The slot cases treated in this section will behave in essentially the same manner as summarized below:

Without Dielectric

- Discontinuity for onset of grating lobes in the $\perp$ or TM case.
- Only a slope discontinuity for the $\parallel$ or TE case.

With Dielectric

- No discontinuity for the onset of a trapped grating lobe.
- No discontinuity for the onset of free space grating lobes.
- Possibility of slope discontinuity.
- Singularity whenever we excite a free surface wave.

6.10 TYPICAL EXAMPLES OF SURFACE WAVES AND ONSET OF GRATING LOBES FOR ARRAYS OF SLOTS

In Figs. 6.9 through 6.22 we depict several calculated scan admittance curves for slot arrays with and without dielectric slabs.

First we show in Fig. 6.9 the scan admittance for an array of z-directed slots without any dielectric. The direction of the mainbeam is fixed at $\eta = 60°$ from normal and is in the E- or $\perp$-plane; that is, $\alpha = 0°$ as shown in Fig. 6.9 below. We observe onset of a free space grating lobe at 11.9 GHz, where ImY_A makes an infinite jump while ReY_A makes a finite jump to account for the extra energy supplied to the Grating Lobe direction.

Similarly we show in Fig. 6.10 the same configuration as shown in Fig. 6.9, but this time the mainbeam is in the H- or $\|$-plane; that is, $\alpha = 90°$ as shown in Fig. 6.10. Again, we observe the onset of free space grating lobes at 11.9 GHz simply because $D_x = D_z$. However, in the present case we observe no discontinuity in Y_A simply because the element pattern will not let the grating lobes carry any energy right at the onset. Note also that ReY_A are vastly different for the two scan planes shown in Figs. 6.9 and 6.10, respectively. This is for exactly the same reasons as for the electric dipole case discussed in Section 4.11.2.

We next show in Fig. 6.11 the same slot array as above, but this time flanked by dielectric slabs of thickness $d_1 = d_2 = 0.5$ cm and with $\epsilon_1 = \epsilon_2 = 1.6$. The main beam is kept constant at $\eta = 60°$ from normal and in the E- or $\perp$-plane; that is, $\alpha = 0°$ as shown in Fig. 6.11. In contrast to the nondielectric case, we observe no singularity at the onset of the trapped grating lobe at 10.4 GHz but of course one at the free surface wave at 11.4 GHz. Finally we note that the free space grating lobes occur at 11.9 GHz, namely, exactly the same frequency as the onset of grating lobes in the nondielectric case, (compare with Fig. 5.37).

We further show in Fig. 6.12 a case where the total dielectric thickness $d_1 + d_2 = 1.0$ cm as in Fig. 6.11; however, $d_1 = 0.25$ cm and $d_2 = 0.75$ cm. The slot array is now located asymmetrically in the dielectric. We observe onset of trapped grating lobes at 10.4 GHz just like in the case above; however, we also observe two surface wave singularities namely at 11.1 and 11.75 GHz corresponding to the different dielectric slab thicknesses. This is in sharp contrast to the electric dipole case as shown, for example, in Fig. 5.37 where only a single surface wave singularity was encountered and was essentially independent of its location in the total slab. The reasons for this observation are of course clear as predicted earlier when we recall that the slot case really constitutes two distinctly different "worlds" separated by the screen, while the electric case freely lets the waves go through the dipole array as discussed above. The onset of the free space grating lobes does remain the same in all cases, namely at 11.9 GHz, entirely independent of the dielectric properties.

We further show in Figs. 6.13 and 6.14 cases where the total slab thickness $d_1 + d_2 = 1.7$ cm. Figure 6.13 constitutes the symmetric case, leading to only one surface wave singularity at 10.9 GHz, while Fig. 6.14 constitutes the asymmetric case leading to two surface wave singularities, namely slightly below at 10.8 GHz

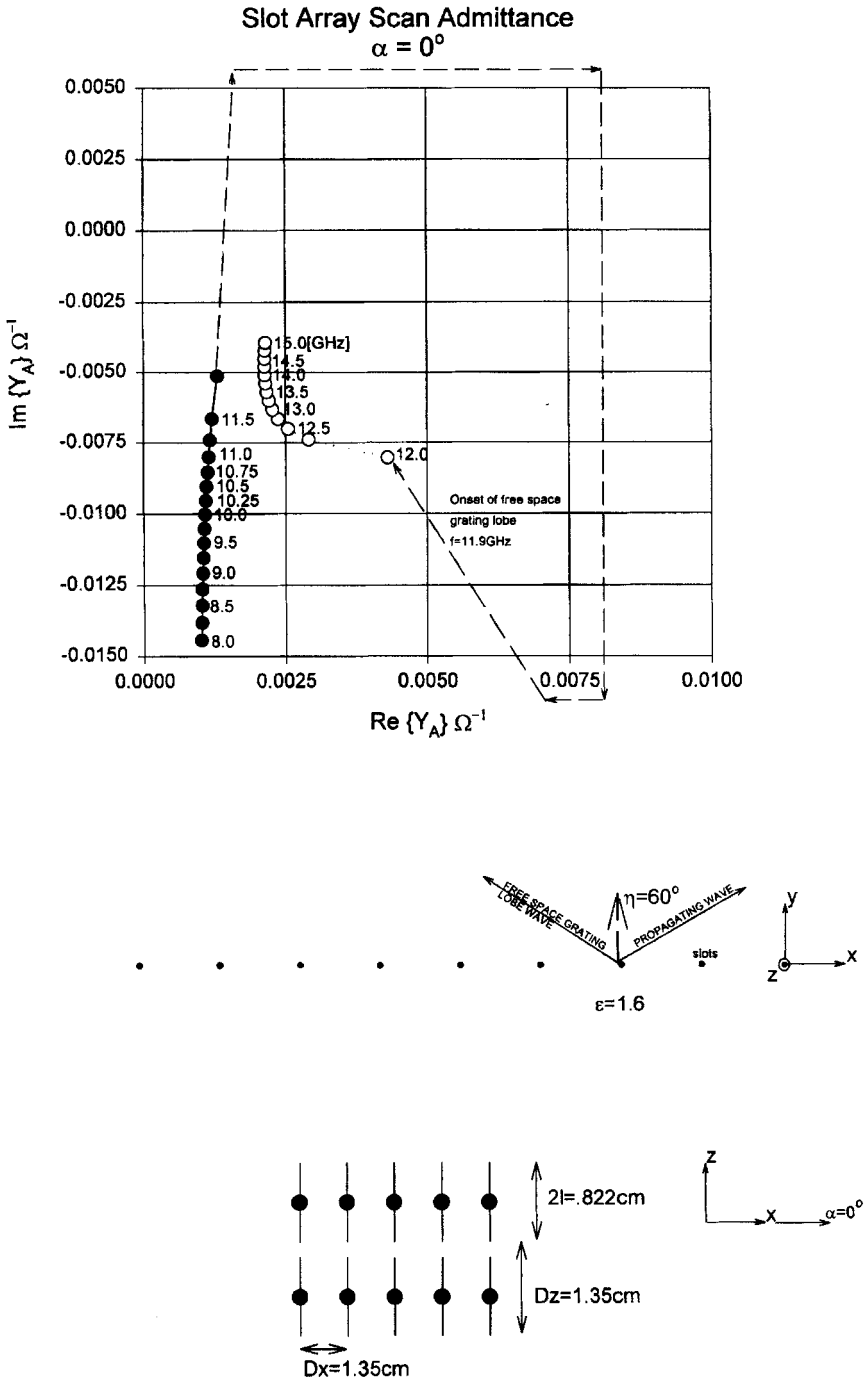

FIGURE 6.9. Complex plot of the scan admittance Y_A for an array of slots without dielectric as shown. Scan angle $\eta = 60°$ in the $\perp$ plane (E-plane, $\alpha = 0°$). Note different scales for real and imaginary axes.

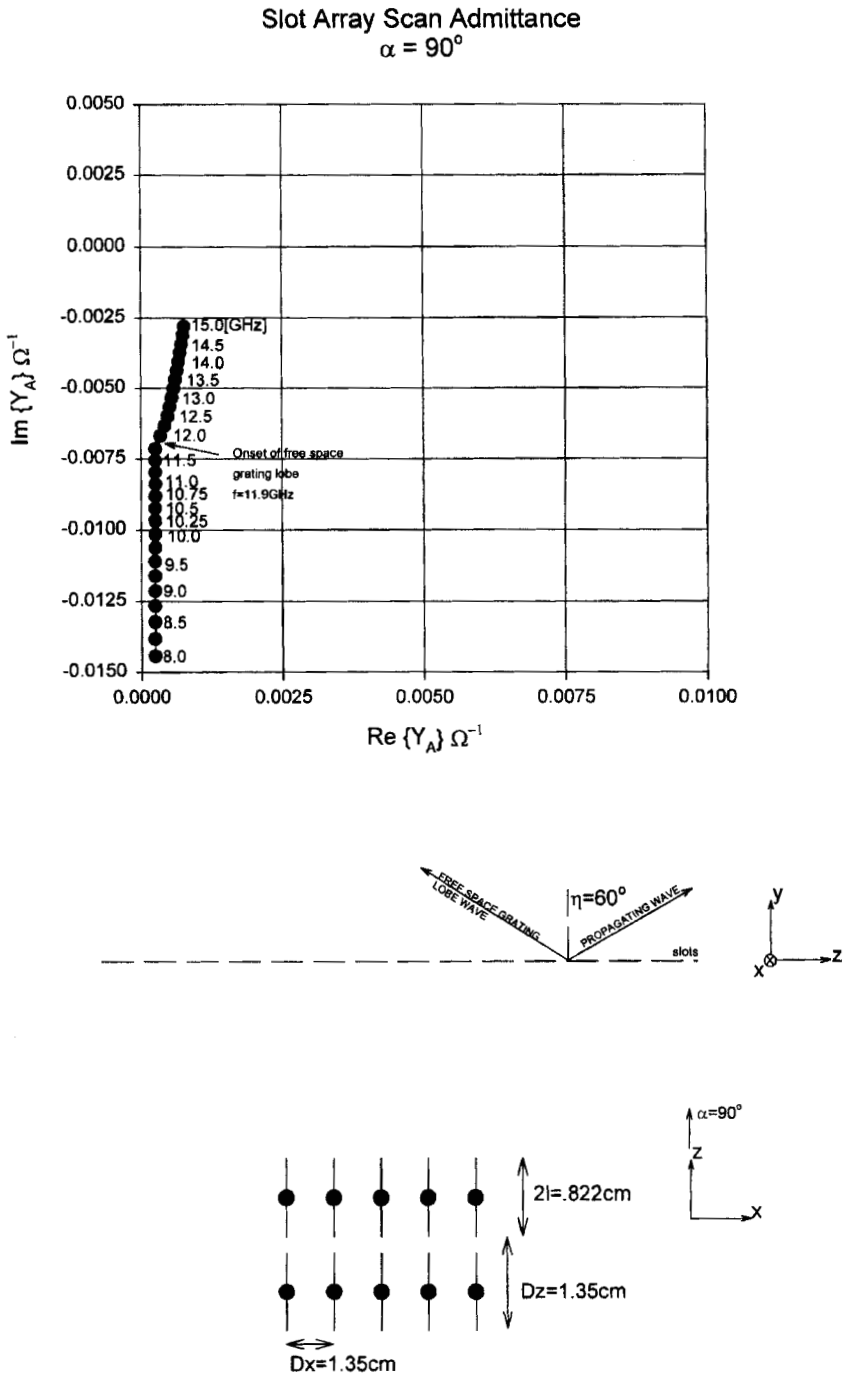

FIGURE 6.10. Complex plot of the scan admittance Y_A for an array of slots without dielectric as shown. Scan angle $\eta = 60°$ in the $\|$ plane (H-plane, $\alpha = 90°$). Note different scales for real and imaginary axes.

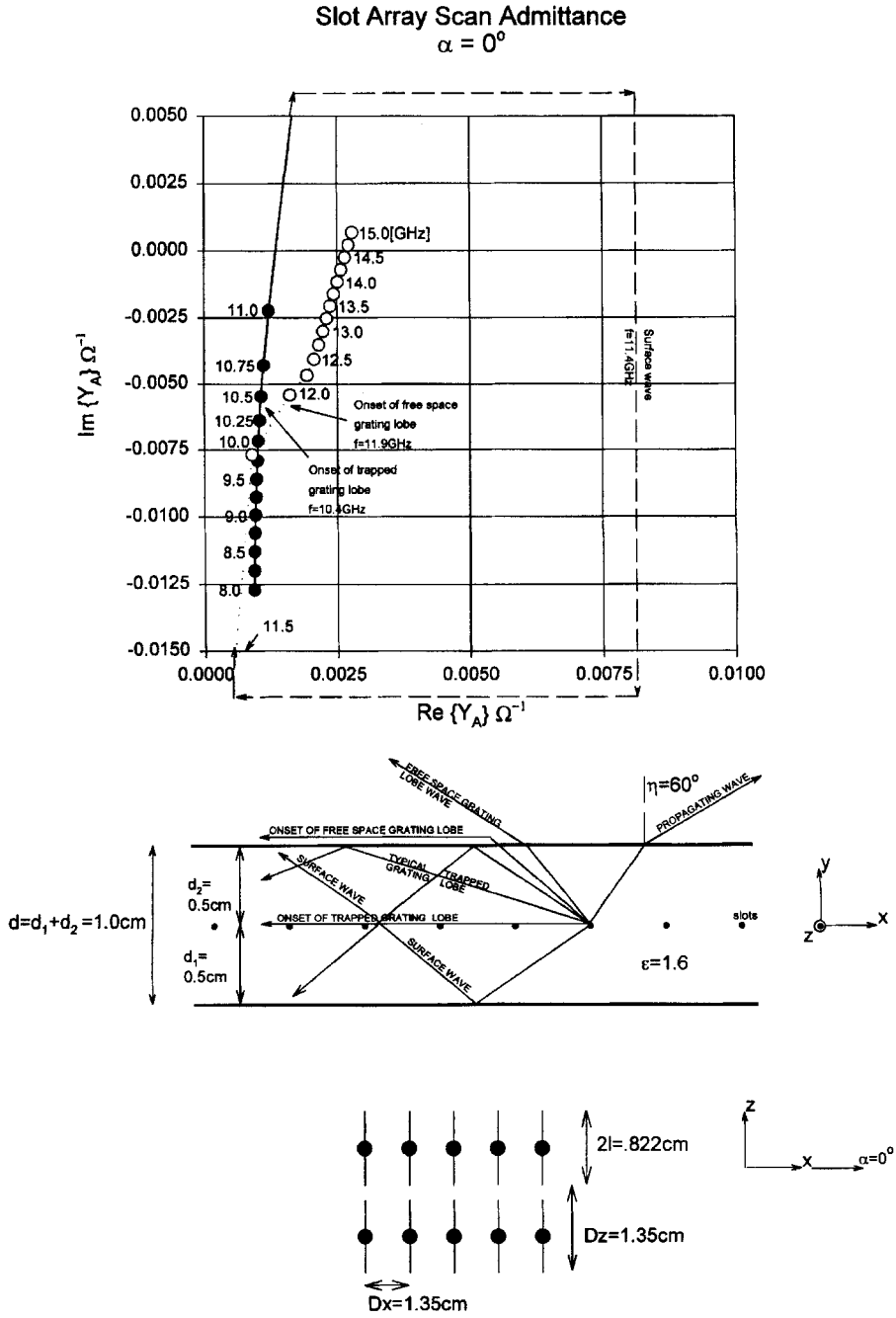

FIGURE 6.11. Complex plot of the scan admittance Y_A for a slot array with identical dielectric slabs on both sides as shown. Scan angle $\eta = 60°$ in the $\perp$ plane (E-plane, $\alpha = 0°$). Note different scales for real and imaginary axes.

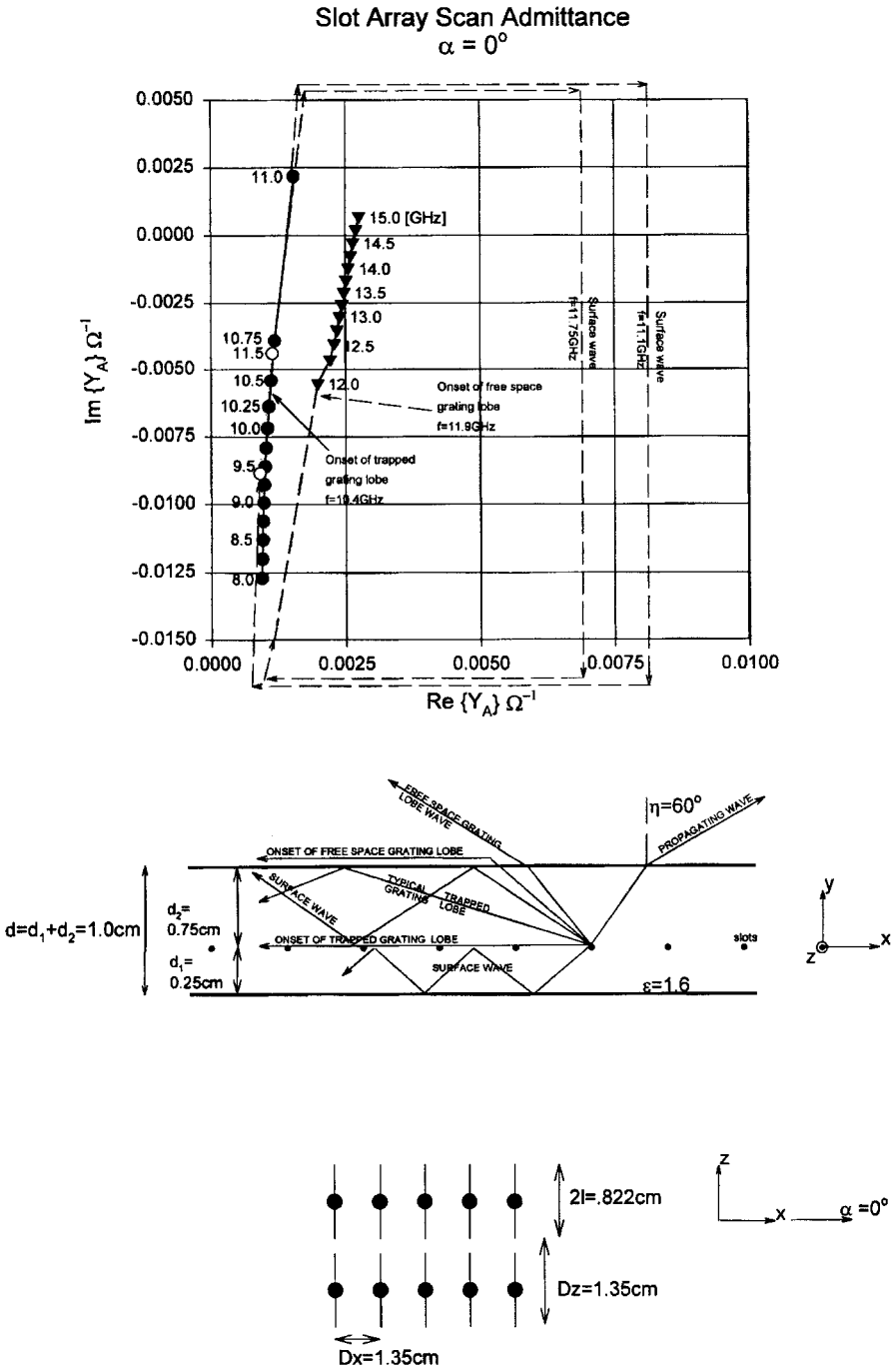

FIGURE 6.12. Complex plot of the scan admittance Y_A for a slot array flanked with dielectric slabs of unequal thicknesses as shown. Scan angle $\eta = 60°$ in the $\perp$ plane (E-plane, $\alpha = 0°$). Note different scales for real and imaginary axes.

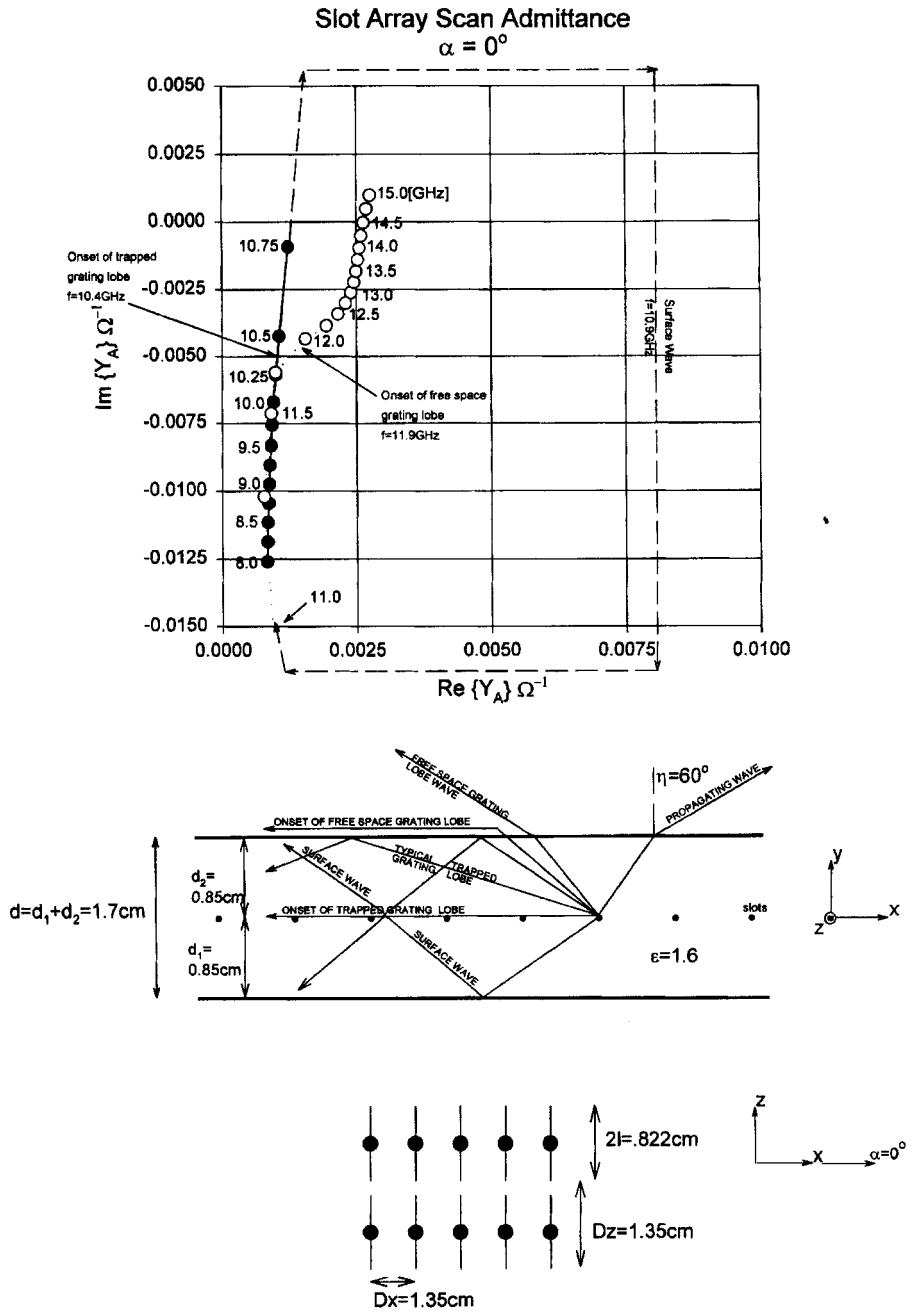

FIGURE 6.13. Complex plot of the scan admittance Y_A for a slot array flanked with identical dielectric slabs as shown. Scan angle $\eta = 60°$ in the $\perp$ plane (E-plane, $\alpha = 0°$).

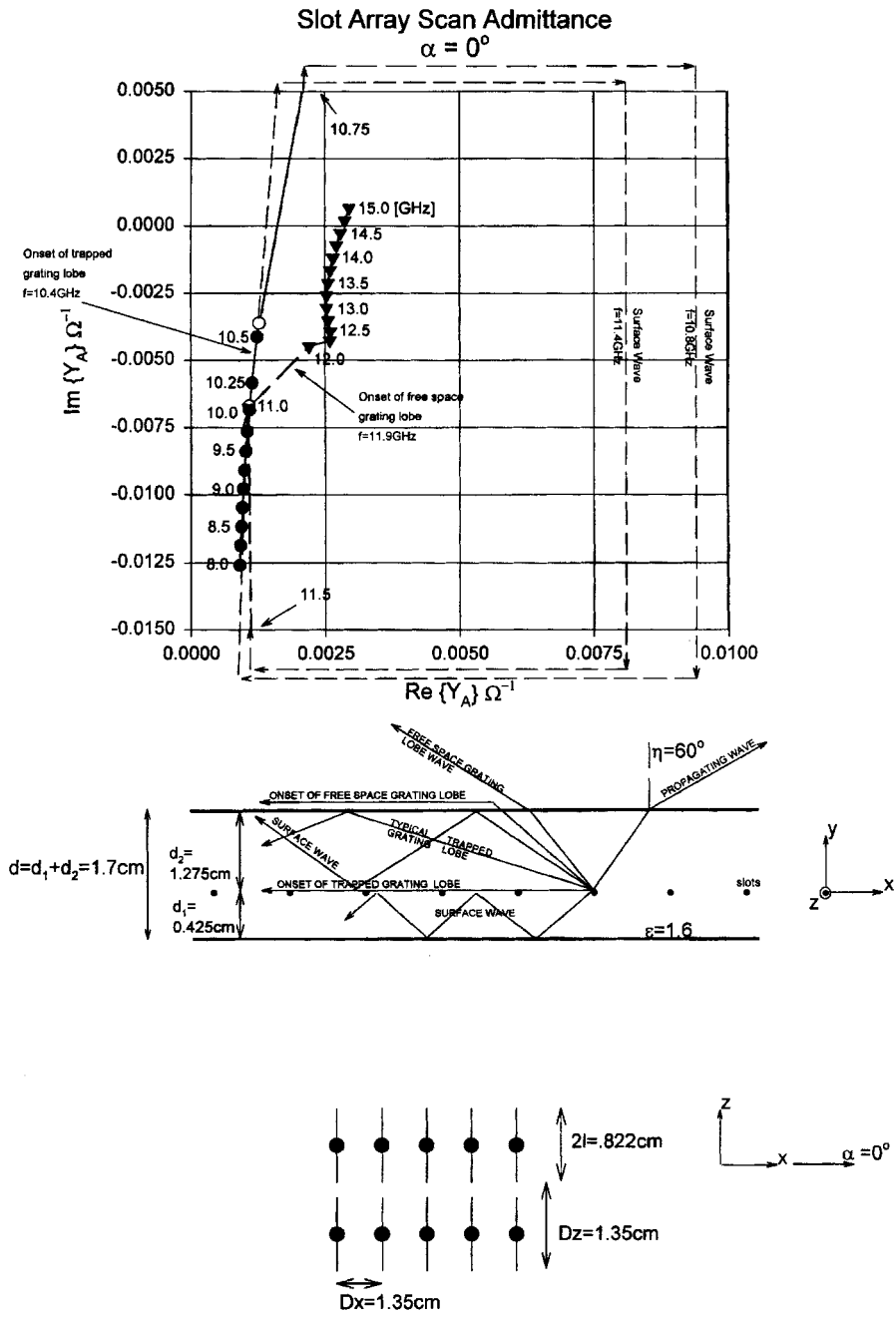

FIGURE 6.14. Complex plot of the scan admittance Y_A for a slot array flanked with dielectric slabs of unequal thickness as shown. Scan angle $\eta = 60°$ in the $\perp$ plane (E-plane, $\alpha = 0°$).

($d_2 = 1.275$ cm) and slightly above at 11.4 GHz ($d_1 = 0.425$ cm). The onset of the trapped as well as the free space grating lobes remains of course the same.

Further increase in the dielectric thickness leads to lower surface wave singularities (although after a while only slightly lower values). The most interesting observation is actually that higher order surface waves eventually will occur. A typical example is shown in Figs. 6.15 and 6.16 for a total slab thickness of $d_1+d_2 = 2.7$ cm.

We next in Figs. 6.17 through 6.22 show a series of cases where the main beam is at $\eta = 60°$ from normal, but located in the H- or ||-plane, that is, $\alpha = 90°$ as shown in all the figures below. As expected, all of the cases are seen to have onset of trapped grating lobes at 10.4 GHz and the free space grating lobes at 11.9 GHz just like in the E-plane case simply because $D_x = D_z = 1.35$ cm.

The symmetric case in Fig. 6.17 shows that the dielectric slabs are too thin to have surface wave singularities. However, the asymmetric case shown in Fig. 6.18 shows that a slab thickness of $d_2 = 0.75$ cm is sufficient to just start a surface wave singularity. In Fig. 6.19 we have $d_1 = d_2 = 0.85$ cm, leading to a more convincing surface wave singularity at around 11.9 GHz which happens to coincide with the onset of free space grating lobes. The asymmetric case shown in Fig. 6.20 clearly shows the presence of a surface wave at 11.4 GHz in the thick slab $d_2 = 1.275$ cm, while the slab $d_1 = 0.425$ cm is just too thin to have a surface wave (agrees with Fig. 6.17 where $d_1 = 0.5$ cm).

Figure 6.21 shows a symmetric case for $d_1 + d_2 = 2.7$ cm where a surface wave is encountered at 11.3 GHz in good agreement with the asymmetric case shown in Fig. 6.20.

Finally we show the asymmetric case in Fig. 6.22 where a surface wave is encountered at 10.9 GHz in the slab $d_2 = 2.025$ cm, while the thin slab $d_1 = 0.675$ cm is just a little bit too thin to carry a surface wave in the H- or ||-plane.

6.11 COMMON MISCONCEPTIONS: THE EFFECT OF DIELECTRIC

Most practitioners of periodic surfaces know well that adding dielectric slabs to an array usually constitutes a breeding ground for surface waves. This is the case whether we deal with arrays of electric or magnetic (slots) *dipoles*. However, what is often poorly understood is a fundamental difference between the two cases, namely that in the electric dipole case the surface waves are determined by the total slab thickness, whereas in the slot case they depend only on the thickness of the individual slabs on each side of the slot array.

A more fundamental question is of course how we can avoid or at least delay surface waves altogether. As we have seen above, a surface wave for an infinite periodic structure will in general be preceded by the onset of a grating lobe. Thus we should simply delay the onset of grating lobes by keeping the inter-element spacings D_x and D_z small (how often have you heard this by now?). This request is usually easy to comply with when we deal with passive periodic surfaces, for example, the hybrid radome as discussed in Chapter 7. However, if the periodic surface is active, for example, for a phased array, it can be a problem simply to get room enough for

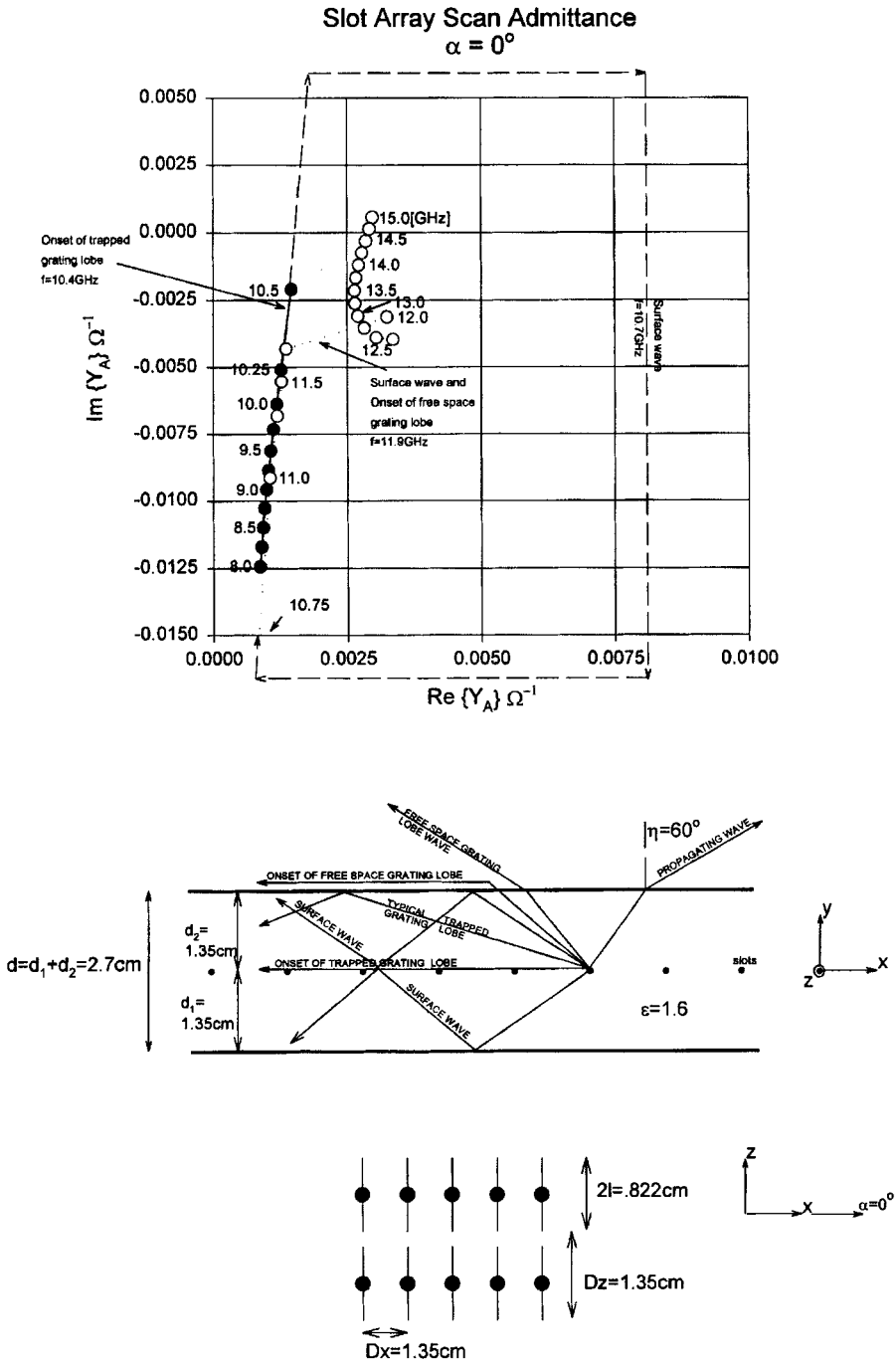

FIGURE 6.15. Complex plot of the scan admittance Y_A for a slot array flanked with identical dielectric slabs as shown. Scan angle $\eta = 60°$ in the $\perp$ plane (E-plane, $\alpha = 0°$).

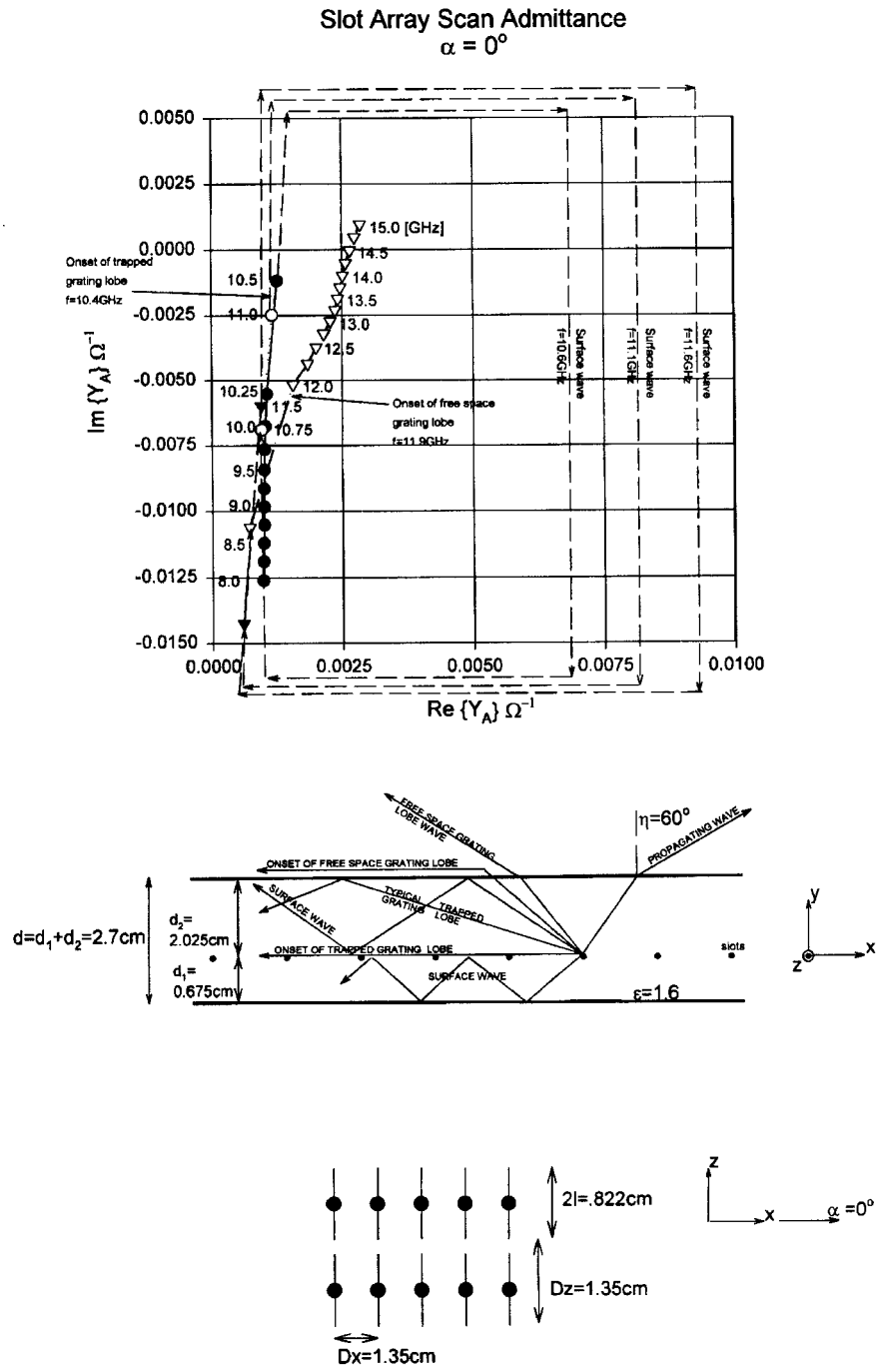

FIGURE 6.16. Complex plot of the scan admittance Y_A for a slot array flanked with dielectric slabs of unequal thicknesses as shown. Scan angle $\eta = 60°$ in the $\perp$ plane (E-plane, $\alpha = 0°$).

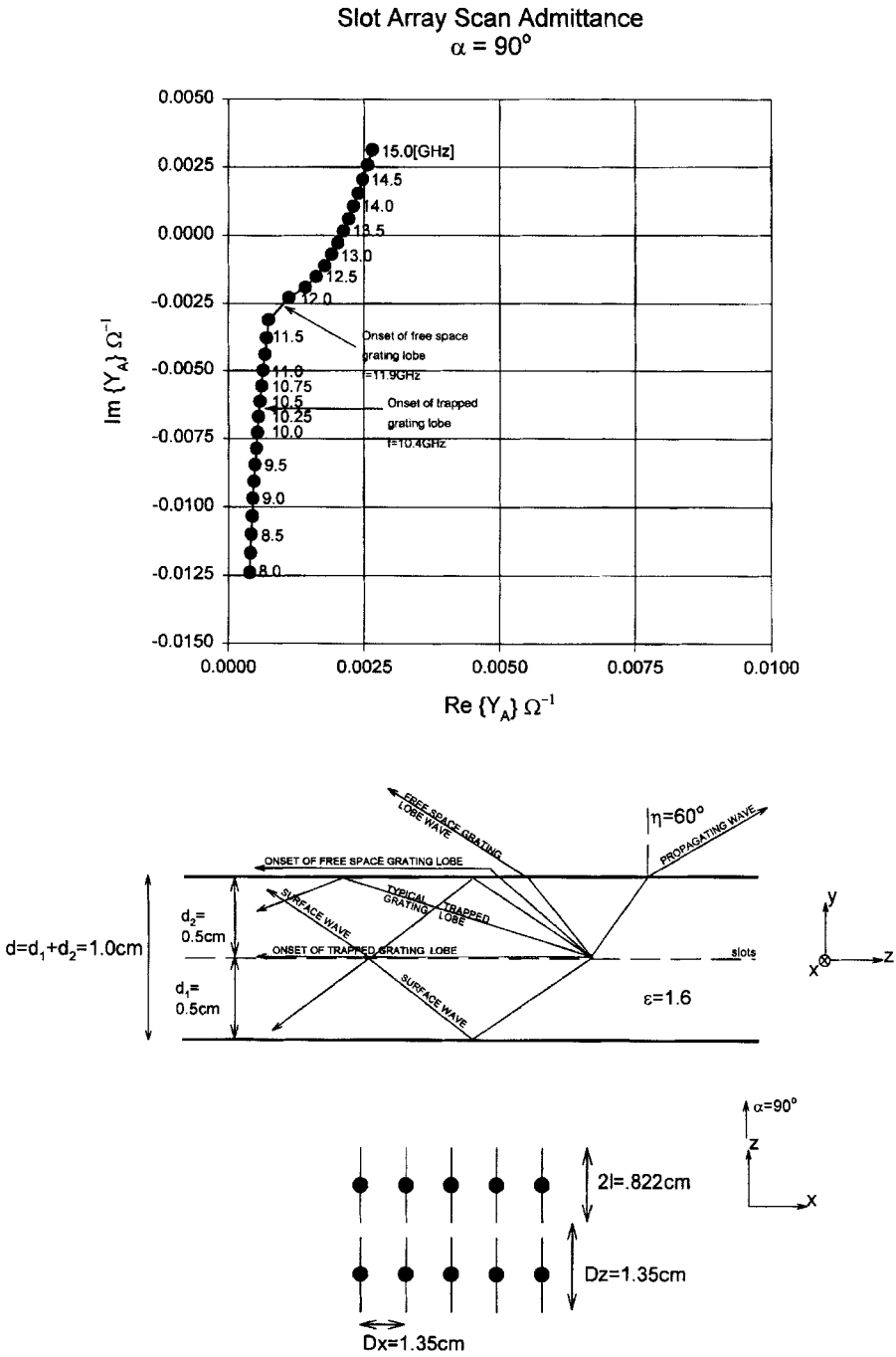

FIGURE 6.17. Complex plot of the scan admittance Y_A for a slot array flanked with identical dielectric slabs as shown. Scan angle $\eta = 60°$ in the $\|$ plane (H-plane, $\alpha = 90°$).

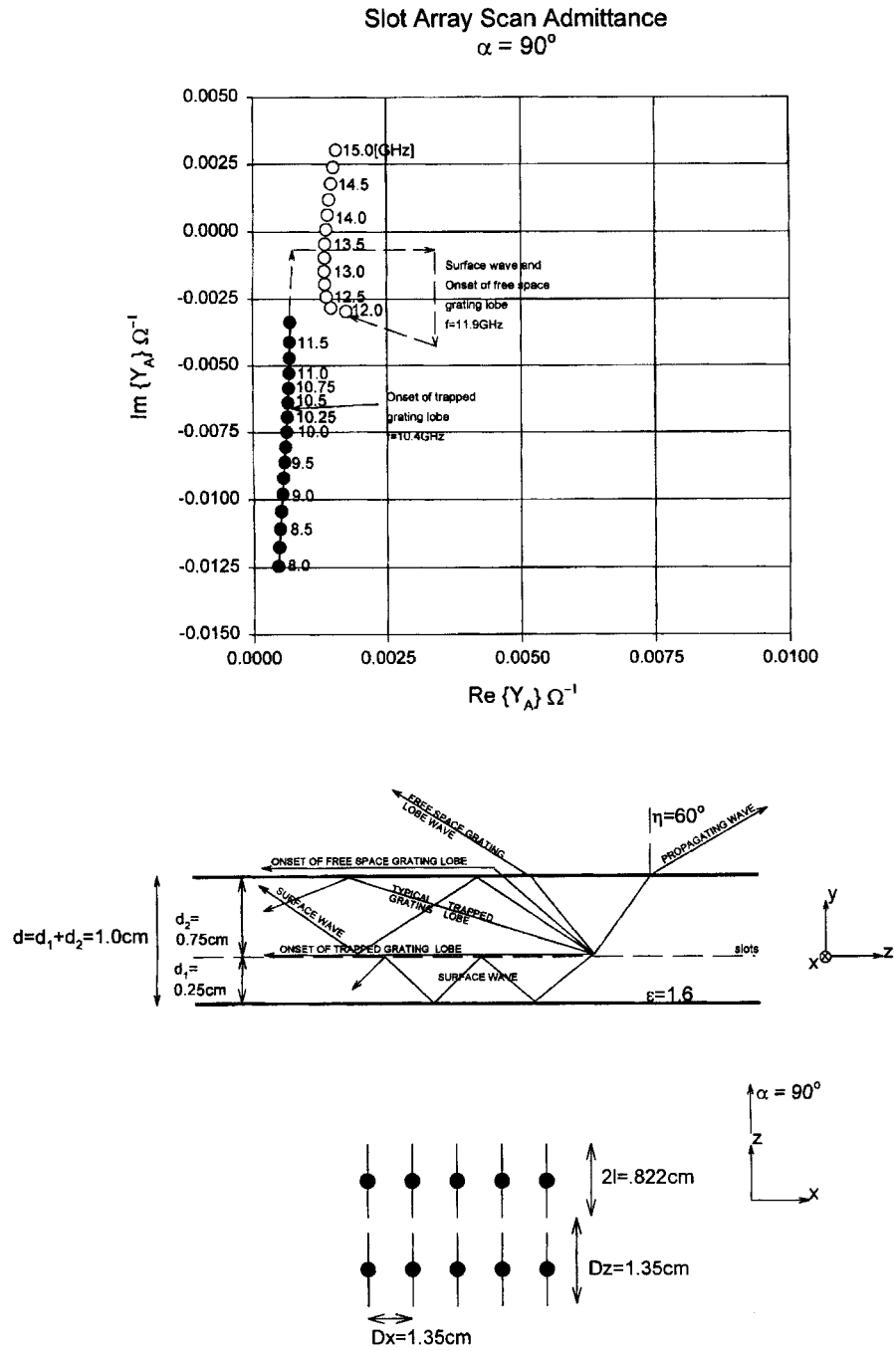

FIGURE 6.18. Complex plot of the scan admittance Y_A for a slot array flanked with dielectric slabs of unequal thicknesses as shown. Scan angle $\eta = 60°$ in the $\|$ plane (H-plane, $\alpha = 90°$).

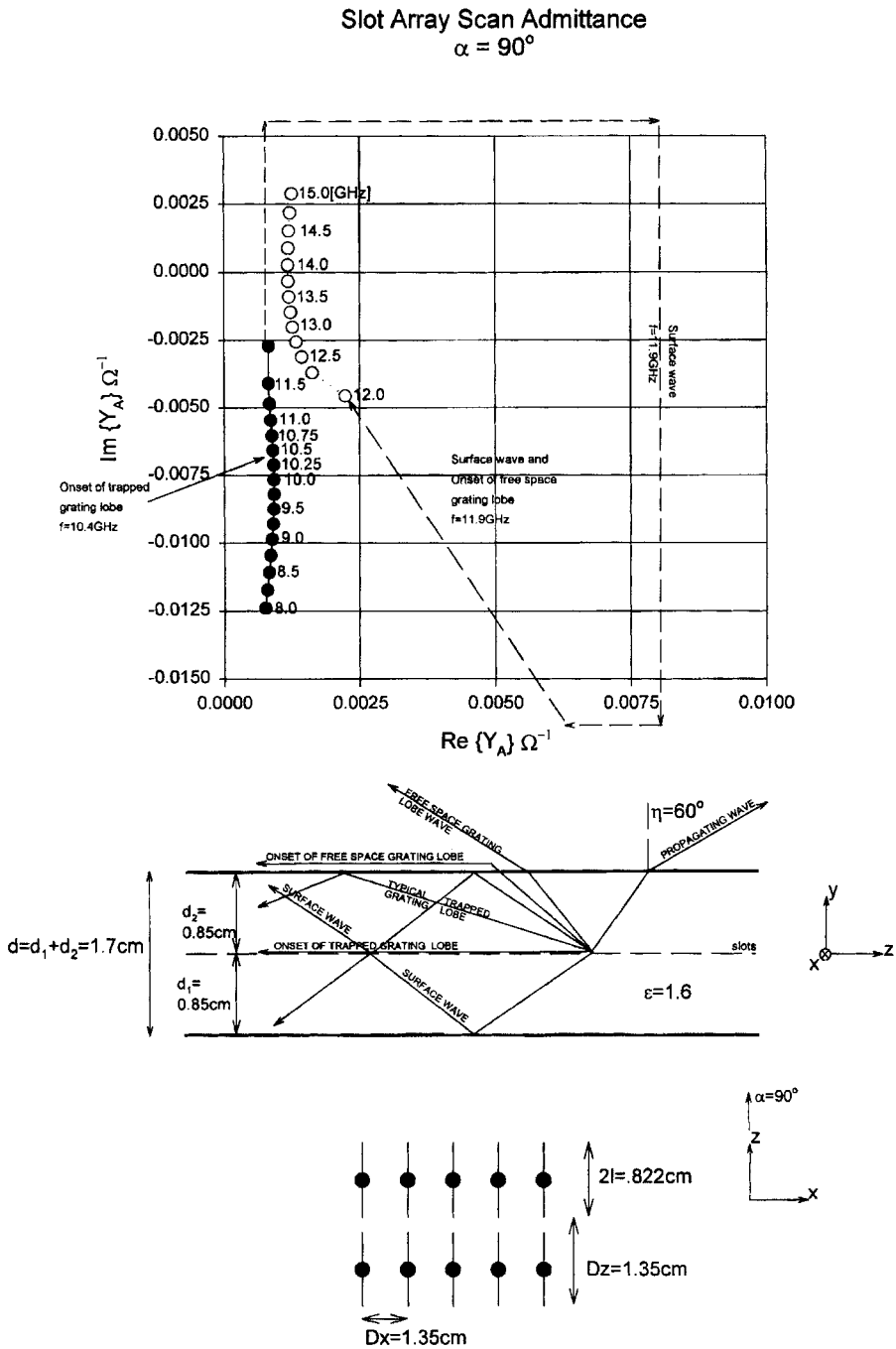

FIGURE 6.19. Complex plot of the scan admittance Y_A for a slot array flanked with identical dielectric slabs as shown. Scan angle $\eta = 60°$ in the $\|$ plane (H-plane, $\alpha = 90°$).

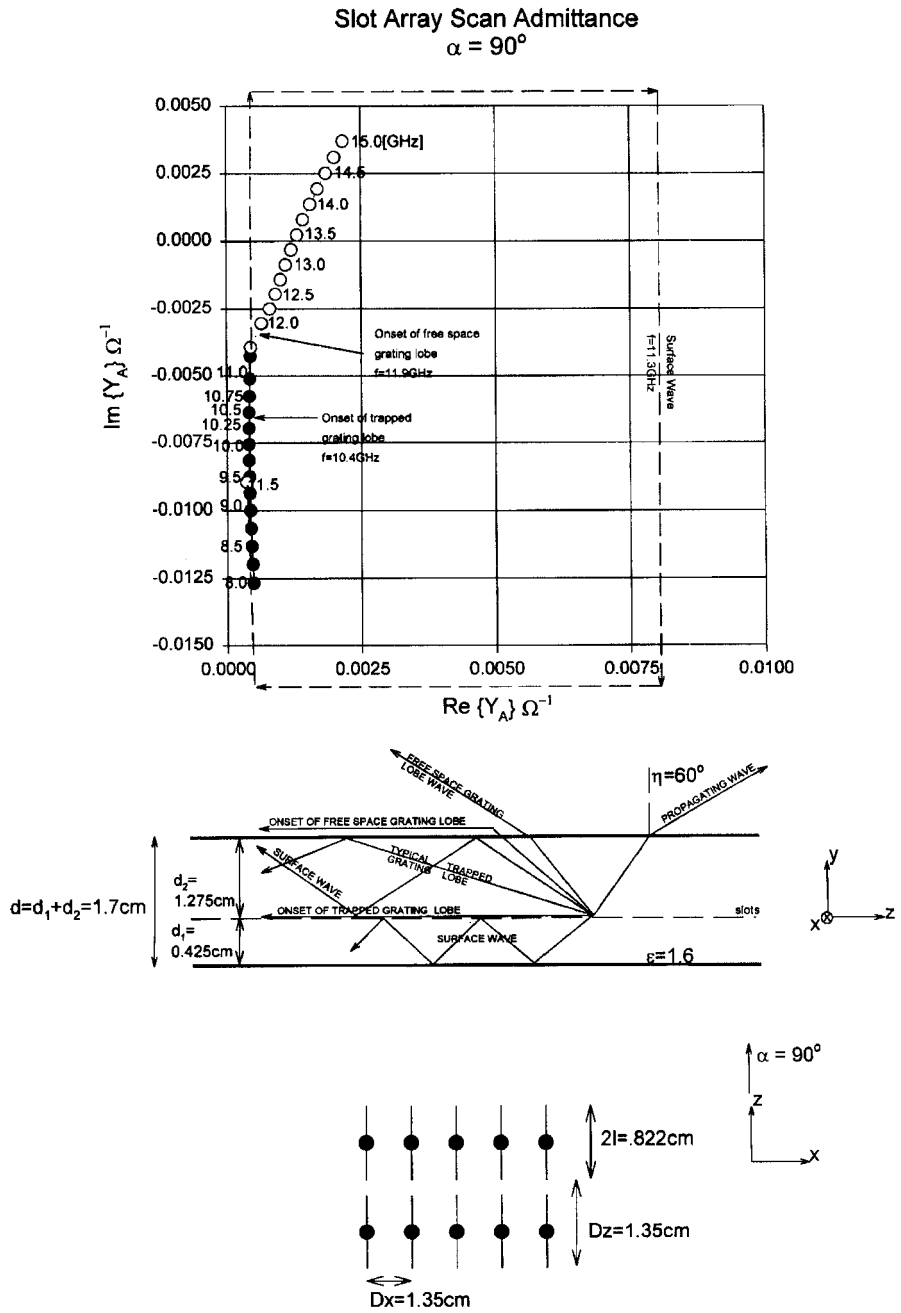

FIGURE 6.20. Complex plot of the scan admittance Y_A for a slot array flanked with dielectric slabs of unequal thicknesses as shown. Scan angle $\eta = 60°$ in the $\|$ plane (H-plane, $\alpha = 90°$).

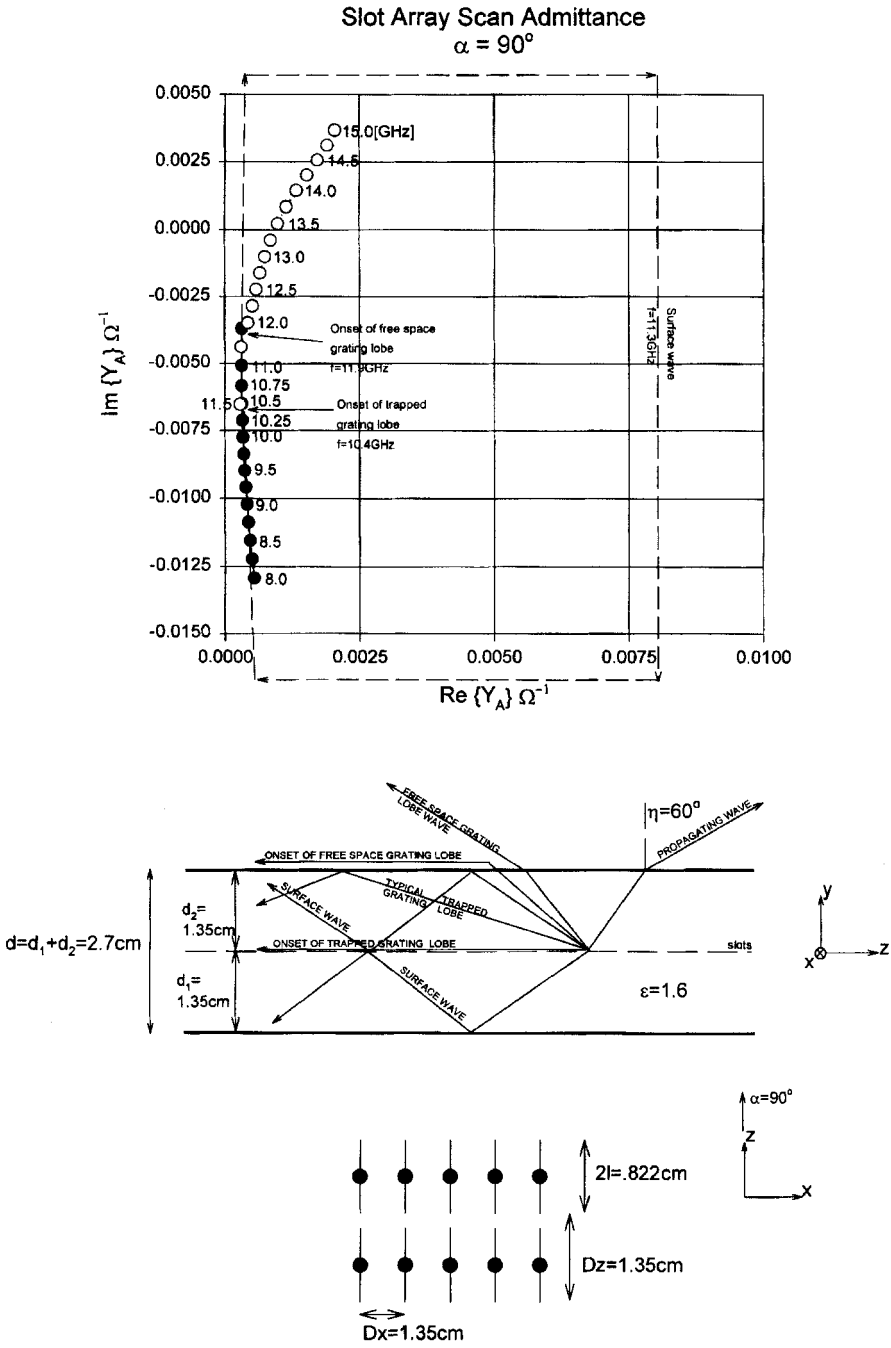

FIGURE 6.21. Complex plot of the scan admittance Y_A for a slot array flanked with identical dielectric slabs as shown. Scan angle $\eta = 60°$ in the $\|$ plane (H-plane, $\alpha = 90°$).

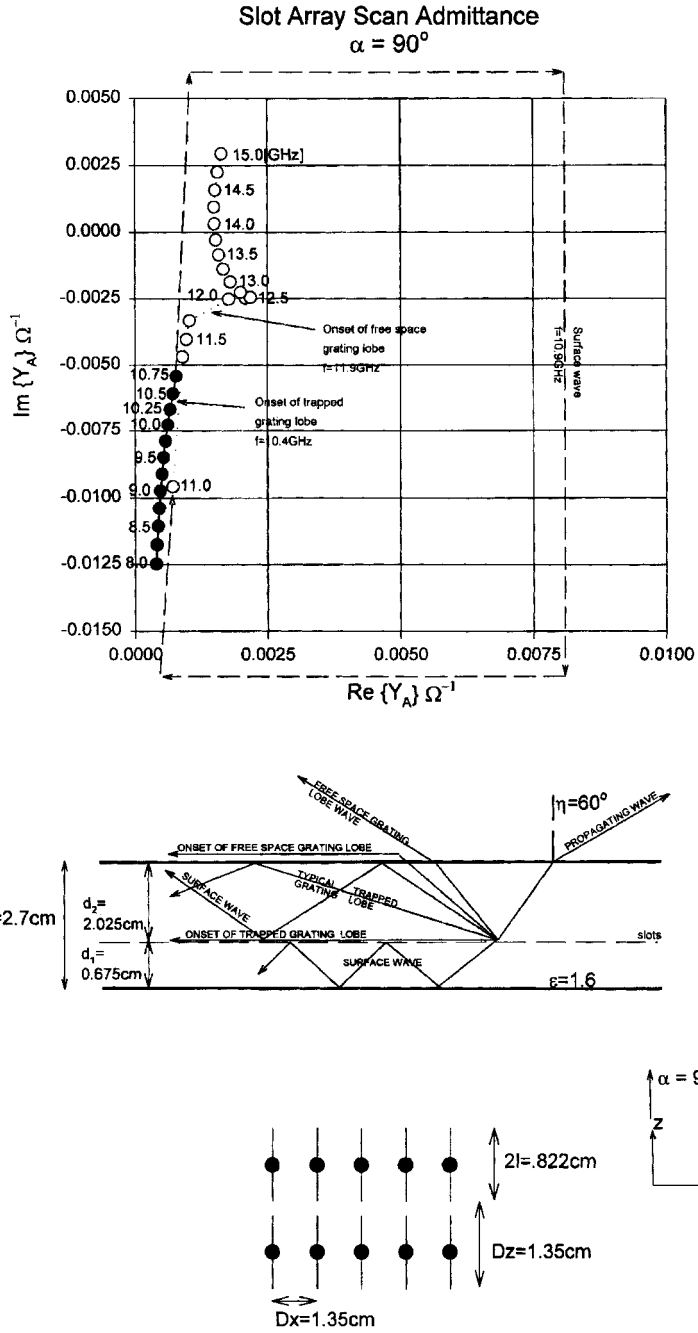

FIGURE 6.22. Complex plot of the scan admittance Y_A for a slot array flanked with dielectric slabs of unequal thicknesses as shown. Scan angle $\eta = 60°$ in the $\|$ plane (H-plane, $\alpha = 90°$).

phase shifters, amplifiers, and so on. The more acute problem becomes to cut down on the number of these devices for economical reasons.

Much research into arrays starts by investigating a single element. This is important and justified in its own right but will often lead to excessive concern over surface waves in general, since a single element with a dielectric slab will show the possibility of exciting every type of surface wave. What is often overlooked is the fact that two or more elements can readily cancel their individual surface waves at least at specific frequencies. However, it is usually much simpler to start with the infinite array where the cancellation is complete as demonstrated above, and then eventually work back from there to a finite array as will be discussed in a future book.

6.12 CONCLUDING REMARKS

We have investigated the behavior of the scan admittance Y_A when it is located in a stratified medium. We found it to be given rigorously as the sum of the admittances to the left and right as seen from the slot array through the slabs. We found that dielectric slabs of proper thickness and proper dielectric constant could produce fairly constant scan admittances as a function of scan angle. In fact we found the stabilizing effect of dielectric slabs to be almost identical to that observed earlier in Chapter 5 for the electric dipole case.

Also similar to the electric case (but not identical), we found that surface waves could be present in the form of trapped grating lobes. While very interesting from a scientific point of view, the onset of trapped grating lobes should in general be avoided in the operating range of the device in question whether it be a phased array or a hybrid radome, which will be discussed in the next chapter. The remedy is of course to make the inter-element spacings D_x and D_z sufficiently small such that the onset of trapped grating lobes is delayed as much as possible. This in turn requires the elements to be small in terms of wavelength or of such a shape that they could be packed close together, as discussed in Chapter 2 (which gives a survey of typical elements that can be used for FSS work).

6.13 PROBLEMS

6.1 Dual and Complementary Arrays: Babinet's Principle

a. Consider a nonplanar array of electric dipoles located in a medium with intrinsic impedance Z_m. Its dual counterpart consists of magnetic dipoles located in the same medium. Show that the scan impedance $Z_{A\text{Elec}}$ of the electric array and the scan impedance $Z_{A\text{Mag}}$ of the magnetic array are related by

$$Z_{A\text{Elec}} \cdot Z_{A\text{Mag}} = Z_m^2.$$

b. We next let the electric array above be planar and denote the scan impedance of its complementary slot array by $Z_{A\text{Slot}}$. Show the relationship

$$Z_{A\text{Elec}} \cdot Z A\text{Slot} = \frac{Z_m^2}{4}.$$

This is an example of the more general Babinet's principle. The equation above can also be written as

$$Z_{A\text{Elec}} = \frac{Z_m^2}{4} Y_{A\text{Slot}}.$$

In other words: $Z_{A\text{Elec}}$ and $Y_{A\text{Slot}}$ look alike in the complex plane. *Note:* The medium Z_m is infinite, not stratified. Also do not forget to rotate E^i (and H^i) by 90° when going from the electric to the slot case. Everyone forgets that at least once in his/her lifetime!

6.2 A Direct and More General Approach to Scan Compensation

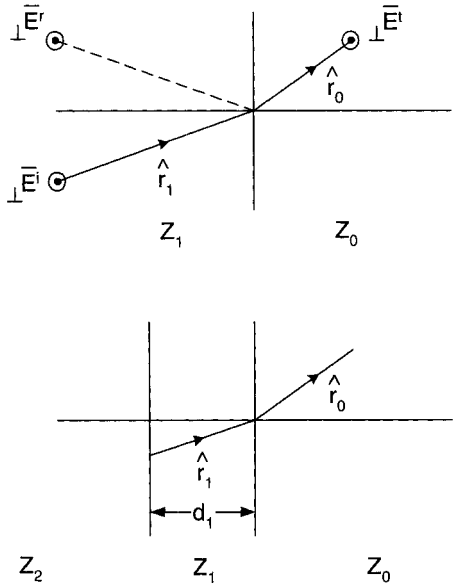

Fig. P6.2

a. Consider a plane wave propagating in the direction $\hat{r}_1$ in medium 1. It is reflected at the interface to medium 0 as shown in Fig. P6.2 top. Inspection of the Fresnel reflection coefficients in Appendix C suggests that the equivalent intrinsic impedance of media 1 and 0 for orthogonal polarization simply are Z_1/r_{1y} and Z_0/r_{0y}, respectively.

Further the input impedance $_{\perp}Z_{0+}$ of medium 0 for orthogonal polarization at the interface is simply equal to the equivalent intrinsic impedance of medium 0 since it is infinite to the right of the interface. Medium 1 is now reduced to a dielectric slab of thickness $d_1 r_{1y} \sim \lambda_1/4$ as shown in Fig. P6.2 bottom. Find the input impedance $_{\perp}Z_{1+}$ of the interface between medium 2 and medium 1 looking right.

b. Repeat part a above for parallel polarization.

c. We now require the input impedances $_{\perp}Z_{1+}$ and $_{\parallel}Z_{1+}$ to be equal at the scan angle θ_0 in medium 0. Find the value of the relative dielectric constant expressed by θ_0.

d. Repeat the cases above for $_{\perp}H$ and $_{\parallel}H$. These cases should by now be obvious, but you cannot be too sure!

e. The conclusion of this investigation is that scan compensation is not uniquely associated with neither dipole or slot arrays but is much more general. For example, as stated in Section 1.7.6, it will also be able to stabilize the performance of a meanderline polarizer with angle of incidence.

6.3 Double- and Multilayered Slabs

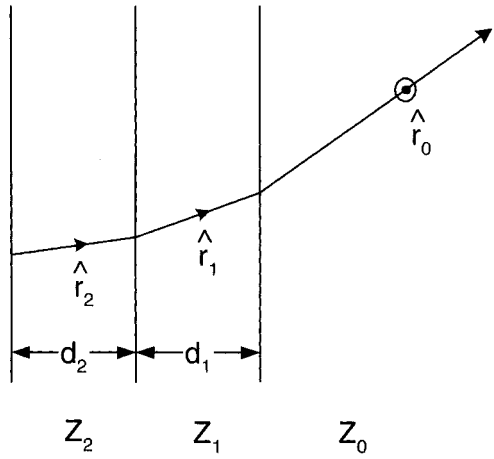

Fig. P6.3

In Problem 6.2 we demonstrated the easy way to arrive at scan compensation when using a single slab d_1. The extension to two or more slabs is of course obvious as indicated in Fig. P6.3. In the case of a double transformer, a good design criteria is that the impedance level between medium 2 and 1 should be equal to the geometrical average between the impedance levels of medium 1 and medium 2.

Find ϵ_2 and ϵ_1 if we require scan compensation at an angle θ_0 in medium 0. Assume that $d_1 r_{1y} \sim \lambda_1/4$ and $d_2 r_{2y} \sim \lambda_2/4$.

7

BAND-PASS FILTER DESIGNS: THE HYBRID RADOME

7.1 INTRODUCTION

One of the most important applications of periodic surfaces is to design structures with band-pass characteristics. Slot elements are usually applied for this purpose, since they are at least in principle transparent at the resonant frequency and opaque below and somewhat above. In order to obtain band filter characteristics, such as a frequency curve with an almost flat top and a fast roll off, two or more surfaces can be cascaded behind each other as shown in Fig. 7.1.

Although conceptually similar to a classical microwave filter, it should be emphasized that a *space filter* is inherently much more complicated. First of all, a classical filter merely has a pair of input and output terminals and only the frequency is varied at the input while the response is recorded at the output. A space filter, on the other hand, has the incident field arriving at various angles of incidence as well as polarizations. This fact has a profound effect on the transmission properties; in short, the transmission curve will in general change dramatically unless carefully designed. Typical transmission curves for untreated structures will generally be broad in the $\perp$ plane and narrow in the $\parallel$ plane (with respect to the H-plane) as illustrated earlier, for example, in Fig. 1.18 top-right.

The remedy for this short-coming is to use dielectric slabs between the outer slot arrays and free space. Very often the reader assumes that this is somehow merely a consequence of Snell's law. This is not the case. If it were so, we would expect better stability with higher values of ϵ. However, we show in this chapter that not only should ϵ be chosen to be rather low, but the thickness of the dielectric slabs should be around $\lambda_1/4$ adjusted to angle of incidence. In fact we will show that the condition for obtaining constant bandwidth is basically identical to the condition of

obtaining a scan independent Y_A as discussed in Chapter 6. In addition we will show that the dielectric slabs between adjacent slot arrays plays a vital role in controlling the depth of the ripples in the transmission curves.

More specifically, consider the configuration shown in Fig. 7.1. It is comprised of N slotted arrays sandwiched between $N + 1$ dielectric slabs of thickness $d_1, d_2, \ldots, d_{N+1}$ and with intrinsic admittances $Y_1, Y_2, \ldots, Y_{N+1}$, respectively. Each array is provided with elements made up of linear segments $\hat{p}^{1,1}, \hat{p}^{2,1}, \ldots, \hat{p}^{M,1}$ where the first superscript refers to the particular segment and the second superscript to the particular array. The locations of the arrays are given by $y = b_1, b_2, \ldots, b_N$ as shown. It is implicit by this notation that the elements may vary from array to array. However, all inter-element spacings D_x and D_z are identical. The elements can be completely arbitrary, but we will assume that the *shape* of the voltage distribution along the elements remains unchanged with angle of incidence. This is a reasonable assumption for relatively short elements but does not hold for longer elements or at higher frequencies where typically odd modes can (and will) be excited (see Chapter 2). It must, however, be borne in mind that the primary purpose of this investigation is to determine the "dielectric profile" at the operating band where the elements are (or should) be small in terms of wavelength (see Section 2.7). Once a preliminary design has been determined, we can readily re-run the entire band-pass radome over any bandwidth with an adequate number of segment modes as described in Section 4.12 and demonstrated numerous times in this chapter.

A related consideration is the fact that the voltage distribution in general will depend strongly upon the polarization of the incident field. Take, for example, a vertical

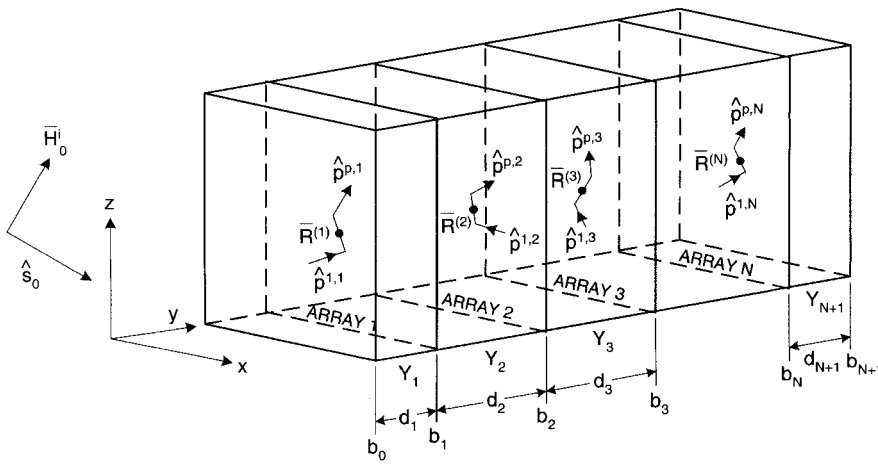

FIGURE 7.1. Transmission of an incident wave $\bar{H}^i_0$ through N slotted arrays sandwiched between $N + 1$ dielectric slabs of thickness $d_1, d_2 \cdots d_{N+1}$ and intrinsic admittances $Y_1, Y_2 \cdots Y_{N+1}$. The slots can be of arbitrary shape and the voltage distribution along each slot is assumed to vary only in amplitude and phase but not in shape. See comments in the text. This combination of FSSs and a stratified medium is often referred to as a hybrid radome.

and a horizontal element crossing each other at their midpoints but without contact (dipole case only). When the incident field is vertically polarized, only the vertical element will be excited, and vice versa for horizontal polarization. However, even if two different modes are excited, depending on the polarization we could readily obtain design information concerning the dielectric profile by simply considering just *one* mode at a time and letting the incident field vary only in the principal plane of that mode. We will of course, as usual, have to check this preliminary design in other planes as well and also apply a suitable number of modes (segments).

This approach might sound somewhat approximate. However, a vast number of such preliminary designs with different elements and various dielectric profiles has been shown to be very close to the final design. This is of course not too surprising when we realize that all the mode segments on an element will have the same T-function.

7.2 MODELING OF AN N-LAYERED HYBRID RADOME

We will analyze the N-layered hybrid radome shown in Fig. 7.1 by use of the duality principle discussed in Chapter 6. We readily arrive at the configuration shown in Fig. 7.2 where each slot array has been modeled by a perfect ground plane with magnetic currents flowing in opposite directions on each side. The dielectric profile is unchanged from the original model shown in Fig. 7.1.

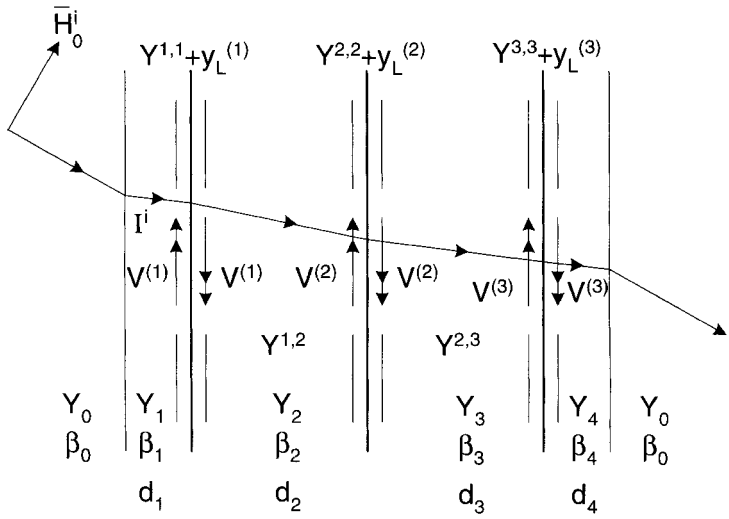

FIGURE 7.2. Modeling of N slot arrays by placing magnetic currents on each side of perfect ground planes. Because of these ground planes we will only have induced currents in array 1 due to the incident field. Similarly there is only mutual admittance between adjacent arrays. Finally the transmitted field comes only from the last slot array.

Let this model be exposed to an incident plane wave with H-field $\bar{H}_0^i$. (Remember: when dealing with magnetic currents, duality tells us to deal with $\bar{H}$ rather than $\bar{E}$.) This wave will induce the current I^i in the element facing the incident wave, that is, the element to the left. No voltage will be induced in the element to the right because the ground plane simply shields it from the incident wave. The same is true for all the other arrays located to the right. However, there will be currents induced in these arrays by the mutual admittances between adjacent arrays, as expressed by $Y^{1,2}, Y^{2,3}, \ldots$, and so on. Note that there is no coupling between for example arrays 1 and 3, nor between 2 and 4, and so on. The self-admittance $Y^{n,n}$ of an arbitrary array is simply defined as the ratio between an impressed current I^n at all the slots and the resulting voltage $V^{(n)}$ when all the other array terminals are *short-circuited* effectively making these merely ground planes. This is consistent with duality of the electric dipole case where all the other arrays are "not there" by simply having all the elements *open-circuited.* Again, this approach assumes that we are dealing with short elements, or if this is not the case, then with short sections as in the method of moments (see Chapter 4).

The general approach is now simply:

1. Determine the current $I^{(i)}$ induced in the first array. As explained above, no current will be induced by the incident wave in any of the other arrays. There will be currents in these only by the mutual admittance between adjacent arrays.
2. By use of the generalized Kirchhoff's law, we next determine the voltages $V^{(n)}$ in the individual arrays.
3. Knowing the slot voltages $V^{(N)}$ for the last array, determine the transmitted signal. No signals will be transmitted from any other array. Similarly from the slot voltage $V^{(1)}$ we can determine the reflected signal. Provided that there are no grating lobes, the sum of the powers of the transmitted and reflected signals should be equal to the incident power (provided the loads $Y_L^{(n)}$ are purely reactive).

7.3 DETERMINATION OF THE TRANSMISSION COEFFICIENT FOR AN N-LAYERED HYBRID RADOME

Based on the outline presented above, we now determine the transmitted as well as the reflected fields from an N-layered hybrid radome.

7.3.1 Determination of the Current $I^{(i)}$ Induced in the First Array by the Incident Field

We have earlier in Section 4.7 shown how a voltage was induced in an electric dipole by an incident E-field as given by (4.49). Decomposing the incident field in orthogonal and parallel components, we may alternatively express the induced voltage by the pattern components ${}_{\perp}P_0^{(1')t}$ and ${}_{\parallel}P_0^{(1')t}$ as defined by (4.61).

Further, we have in Section 4.12 considered elements combined of arbitrary sections, and we showed in Section 4.12.3 that the induced voltages (as well as the scattered fields) could essentially be expressed by replacing the simple pattern components above with the *composite pattern components* as given by (4.90) and (4.91).

Let us next consider a magnetic composite element instead of an electric one. We will assume that it lies in the plane $y = b_1$; however, there are no ground planes or any other arrays. In fact we will assume that the entire space is made up of medium 1 with intrinsic admittance Y_1. Let the value of the incident magnetic field at the element reference point in plane $y = b_1$ be denoted by $\bar{H}^i_{b1}$. Then from (4.49) yielding the induced voltage for an electric element we find, by duality for the induced current I^i in a magnetic element located in medium 1 rather than medium 0, that

$$I^i = \bar{H}^i_{b1} \cdot {}_{\perp}\hat{n}_{1\perp} P^{ct}_1 + \bar{H}^i_{b1} \cdot {}_{\parallel}\hat{n}_{1\parallel} P^{ct}_1, \tag{7.1}$$

where the composite pattern factors ${}_{\substack{\perp \\ \parallel}} P^{ct}_1$ are identical to the electric counterpart given by (4.90) and (4.91), but simply modified to medium 1 as explained in Section 5.3:

$${}_{\substack{\perp \\ \parallel}} P^{ct}_1 = {}_{\substack{\perp \\ \parallel}}\hat{n}_1 \cdot \left[\hat{p}^{(1)} P^{(1)t}_1 + \hat{p}^{(2)} P^{(2)t}_1 + \cdots + \hat{p}^{(p)} P^{(p)t}_1\right]. \tag{7.2}$$

Let us next place a PEC ground plane at $y = b_1$, while we introduce a dielectric interface at $y = b_0$ as was originally the case; see Figs. 7.1 and 7.2. Let us further denote the incident H-field impinging upon the interface $y = b_0$ by $\bar{H}^i_{b0}$. Then, from the dual version of the general formula (D.18), we find for the magnetic field at $y = b_1$ that

$$\begin{aligned}\bar{H}^i_{b1} = \Bigg[& {}_{\perp}\hat{n}_{1+}\left(\bar{H}^i_{b0} \cdot {}_{\perp}\hat{n}_{0+}\right) {}^{H}_{\perp}\mathcal{T}^e_{0+}\left[1 + {}^{H}_{\perp}\Gamma_{1+} e^{-j2\beta_1(b_1-b_1)r_{1y}}\right] \\ & + \left(\bar{H}^i_{b0} \cdot {}_{\parallel}\hat{n}_{0+}\right) {}^{H}_{\parallel}\mathcal{T}^e_{0+} \frac{r_{0y}}{r_{1y}}\left[{}_{\parallel}\hat{n}_{1+} + {}_{\parallel}\hat{n}_{1-} {}^{H}_{\parallel}\Gamma_{1+} e^{-j2\beta_1(b_1-b_1)r_{1y}}\right]\Bigg] e^{-j\beta_1 d_1 r_{1y}}\end{aligned} \tag{7.3}$$

where from (D.7),

$${}^{H}_{\substack{\perp \\ \parallel}}\mathcal{T}^e_{0+} = \frac{{}^{H}_{\substack{\perp \\ \parallel}}\mathcal{T}_{0+}}{1 - {}^{H}_{\substack{\perp \\ \parallel}}\Gamma_{1-} {}^{H}_{\substack{\perp \\ \parallel}}\Gamma_{1+} e^{-j2\beta_1 d_1 r_{1y}}}. \tag{7.4}$$

Further, with ${}^{H}_{\substack{\perp \\ \parallel}}\Gamma_{1+} = 1$, and denoting $\bar{H}^i_{b0} \cdot {}_{\substack{\perp \\ \parallel}}\hat{n}_{0+} = {}_{\substack{\perp \\ \parallel}} H^i_{b0}$, we obtain from (7.3),

$$\bar{H}^i_{b1} = \left[{}_{\perp} H^i_{b0\perp} {}^{H}_{\perp}\mathcal{T}^e_{0+} 2 {}_{\perp}\hat{n}_{1+} + \bar{H}^i_{b0\parallel} {}^{H}_{\parallel}\mathcal{T}^e_{0+} \frac{r_{0y}}{r_{1y}}\left[{}_{\parallel}\hat{n}_{1+} + {}_{\parallel}\hat{n}_{1-}\right]\right] e^{-j\beta_1 d_1 r_{1y}}. \tag{7.5}$$

We finally substitute (7.5) into (7.1):

$$I^i = \left[{}_{\perp}H^{i\ H}_{b0\perp}\mathcal{T}^e_{0+}2_{\perp}P^{ct}_1 + {}_{\parallel}H^{i\ H}_{b0\parallel}\mathcal{T}^e_{0+}2\frac{r_{0y}}{r_{1y}}{}_{\parallel}P^{ct}_1 \right] e^{-j\beta_1 d_1 r_{1y}}, \tag{7.6}$$

where the $\parallel$ component is readily obtained by noticing that ${}_{\parallel}\hat{n}_{1+}$ interact with the incident field going to the right while ${}_{\parallel}\hat{n}_{1-}$ similarly interact with the field reflected from the array.

7.3.2 Determination of the Slot Voltages $V^{(n)}$

After having determined the current I^i induced in the reference elements of array 1 by the incident field, we are now ready to find the slot voltages $V^{(n)}$ at the "terminals" of the various slot arrays.

By Kirchhoff's law we find for array 1 that

$$I^i = \left(Y^{1,1} + Y_L^{(1)}\right) V^{(1)} + Y^{1,2}V^{(2)}, \tag{7.7}$$

where $Y^{1,1}$ denotes the self-admittance as seen by the reference element in array 1 with all the other elements in the same array excited in a Floquet manner (see Chapter 3). Further all elements in the other arrays should have $V^{(n)} = 0$; that is, all other arrays effectively act as ground planes. This case was discussed extensively in Section 6.5 where it was denoted by Y_A as illustrated in Figs. 6.5 and 6.6. In this chapter we use the notation $Y^{n,n}$ for the nth slot array as illustrated in Fig. 7.2. The load admittance $Y_L^{(1)}$ can conceptually be any admittance either in the form of a lumped device or in a form as discussed in Section 2.3. (In actual calculations where we use several mode sections to model arbitrary shaped elements, typically $Y_L^{(1)} = 0$. However, when analyzing a complex structure it is very expedient to keep a load admittance at hand.)

Finally $-Y^{1,2}V^{(2)}$ is simply the current induced in array 1 as caused by the slot voltage $V^{(2)}$ of array 2. The mutual admittance $Y^{1,2}$ is determined with the elements in array 1 short-circuited consistent with determination of the self-admittance as explained above. The self as well as the mutual admittances are simply obtained by duality and the appropriate T-functions as described in Chapter 6 and also in the beginning of this chapter.

Note that the mutual admittance between array 1 and arrays $3, 4, \ldots \equiv 0$ because of the "ground planes" between them.

Similarly in array 2 there will be no induced current by the incident field. By Kirchhoff's law we find that

$$0 = Y^{2,1}V^{(1)} + \left(Y^{2,2} + Y_L^{(2)}\right) V^{(2)} + Y^{2,3}V^{(3)}, \tag{7.8}$$

where the various admittances are defined consistently with the definitions given above. By induction we can write the following matrix equation for the N-layers of arrays:

$$\begin{bmatrix} \left(Y^{1,1}+Y_L^{(1)}\right) & Y^{1,2} & 0 & \cdots & 0 \\ Y^{2,1} & \left(Y^{2,2}+Y_L^{(2)}\right) & Y^{2,3} & & 0 \\ 0 & Y^{3,2} & \left(Y^{3,3}+Y_L^{(3)}\right) & Y^{3,4} & 0 \\ \vdots & & & \ddots & \vdots \\ 0 & \cdots & \cdots & Y^{N,N-1} & \left(Y^{N,N}+Y_L^{(N)}\right) \end{bmatrix} \begin{bmatrix} V^{(1)} \\ V^{(2)} \\ \vdots \\ \vdots \\ V^{(N)} \end{bmatrix} = \begin{bmatrix} I^i \\ 0 \\ \vdots \\ \vdots \\ 0 \end{bmatrix}. \tag{7.9}$$

By Cramer's rule we further obtain from (7.9) for the slot voltage $V^{(N)}$:

$$V^{(N)} = \frac{1}{D_N} \begin{vmatrix} \left(Y^{1,1}+Y_L^{(1)}\right) & Y^{1,2} & 0 & \cdots & I^i \\ Y^{2,1} & \left(Y^{2,2}+Y_L^{(2)}\right) & Y^{2,3} & \cdots & 0 \\ \vdots & & \ddots & & \\ \vdots & & & \ddots & 0 \\ 0 & \cdots & 0 & Y^{N,N-1} & 0 \end{vmatrix}, \tag{7.10}$$

where the determinant

$$D_N = \begin{vmatrix} \left(Y^{1,1}+Y_L^{(1)}\right) & Y^{1,2} & 0 & \cdots & 0 \\ Y^{2,1} & \left(Y^{2,2}+Y_L^{(2)}\right) & Y^{2,3} & \cdots & 0 \\ \vdots & & \ddots & \vdots & \\ 0 & \cdots & 0 & Y^{N,N-1} & \left(Y^{N,N}+Y_L^{(N)}\right) \end{vmatrix}. \tag{7.11}$$

It is easily shown by application of simple rules from the theory of determinants that (7.10) can be written as

$$V^{(N)} = I^i \frac{(-1)^{N-1}}{D_N} Y^{2,1} Y^{3,2} \cdots Y^{N,N-1}. \tag{7.12}$$

The slot voltages $V^{(n)}$ in general could of course be obtained similarly to (7.12). However, to determine the transmitted field, we only need to find $V^{(N)}$, since no radiation in the space $y \geq b_N$ takes place from any of the other arrays. Only determination of $V^{(1)}$ may be of interest in order to find the reflected signal.

7.3.3 Determination of the Transmitted Field

Having determined the slot voltages $V^{(N)}$ for the last array it is now a simple matter to obtain the field radiated in the space $y > b_{N+1}$. This situation is illustrated in Fig. 7.3 showing the last array N located at $y = b_N$ and bounded by the slab of thickness d_{N+1}.

Applying the duality principle to (5.29) for the principal mode only, we readily obtain at the point of observation $\bar{R}^{(1')}$:

$$\begin{aligned}\bar{H}_0(\bar{R}^{(1')}) = V^{(N)} \frac{Y_{N+1}}{2D_x D_z} \frac{e^{-j\beta_{N+1} d_{N+1} r_{N+1y}}}{r_{N+1y}} \\ \left[{}_{\perp}\hat{n}_0 \left[{}_{\perp}P^c_{N+1+} + {}_{\perp}P^c_{N+1-} {}^{H}_{\perp}\Gamma_{N+1-} e^{-j2\beta_{N+1}\cdot 0} \right] \right. \\ {}^{H}_{\perp}W_{N+1} {}^{H}_{\perp}\mathcal{T}_{N+1+}[1+0] \\ + \left[{}_{\parallel}P^c_{N+1+} + {}_{\parallel}P^c_{N+1-} {}^{H}_{\parallel}\Gamma_{N+1-} e^{-j2\beta_{N+1}\cdot 0} \right] \\ \left. {}^{H}_{\parallel}W_{N+1} {}^{H}_{\parallel}\mathcal{T}_{N+1+} \frac{r_{N+1y}}{r_{0y}} [{}_{\parallel}\hat{n}_{0+} + {}_{\parallel}\hat{n}_{0-} \cdot 0] \right] \\ e^{-j\beta_0(\bar{R}^{(1')} - \hat{y}b_{N+1})\cdot \hat{r}_0}. \end{aligned} \tag{7.13}$$

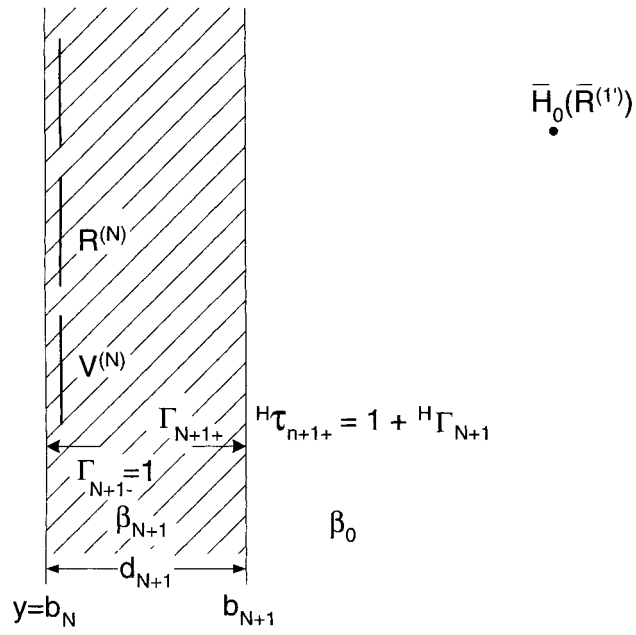

FIGURE 7.3. Transmitted field $\bar{H}_0(\bar{R}^{(1')})$ emanating solely from the array to the right of ground plane N located at $y = b_n$.

where ${}^{H}_{\perp\!\!\!\perp\!\!\!\parallel} W_{N+1}$ is the H-version of (5.27). Specializing (7.13) to planar elements such that (see 5.31)

$$ {}_{\perp\!\!\!\perp\!\!\!\parallel} P^{c}_{N+1+} = {}_{\perp\!\!\!\perp\!\!\!\parallel} P^{c}_{N+1-} = {}_{\perp\!\!\!\perp\!\!\!\parallel} P^{c}_{N+1}, \tag{7.14} $$

and also noticing that ${}^{H}_{\perp\!\!\!\perp\!\!\!\parallel}\Gamma_{N+1-} = 1$, we readily obtain from (7.13) the expression

$$ \begin{aligned} \bar{H}_0(\bar{R}^{(1')}) = V^{(N)} \frac{Y_{N+1}}{2D_x D_z} & \frac{e^{-j\beta_{N+1} d_{N+1} r_{N+1y}}}{r_{N+1y}} \\ & \left[{}_{\perp}\hat{n}_{0\perp} P^{c}_{N+1} 2^{H}_{\perp} W_{N+1} {}^{H}_{\perp} \mathcal{T}_{N+1+} + \right. \\ & \left. {}_{\parallel}\hat{n}_{0\parallel} P^{c}_{N+1} 2^{H}_{\parallel} W_{N+1} {}^{H}_{\parallel} \mathcal{T}_{N+1+} \frac{r_{N+1y}}{r_{0y}} \right] \\ & e^{-j\beta_0(\bar{R}^{(1')} - \hat{y} b_{N+1})\cdot \hat{r}_0}. \end{aligned} \tag{7.15} $$

We next substitute into (7.15) the expression for $V^{(N)}$ as given by (7.12):

$$ \begin{aligned} \bar{H}_0(\bar{R}^{(1')}) = \frac{Y_{N+1}}{2D_x D_z} & \frac{e^{-j\beta_{N+1} d_{N+1} r_{N+1y}}}{r_{N+1y}} I^{i} \frac{(-1)^{N-1}}{D_N} Y^{2,1} Y^{3,2} \cdots Y^{N,N-1} \\ & \left[{}_{\perp}\hat{n}_{0\perp} P^{c}_{N+1} 2^{H}_{\perp} W_{N+1} {}^{H}_{\perp} \mathcal{T}_{N+1+} + \right. \\ & \left. {}_{\parallel}\hat{n}_{0\parallel} P^{c}_{N+1} 2^{H}_{\parallel} W_{N+1} {}^{H}_{\parallel} \mathcal{T}_{N+1+} \frac{r_{N+1y}}{r_{0y}} \right] \\ & e^{-j\beta_0(\bar{R}^{(1')} - \hat{y} b_{N+1})\cdot \hat{r}_0}, \end{aligned} \tag{7.16} $$

where I^{i} is given by (7.6).

Equation (7.16) basically determines the transmitted field $\bar{H}(\bar{R}^{(1')})$ when the front array of the hybrid radome is exposed to an incident field $\bar{H}^{i}_{0}$.

However, the reason for the derivation above is not so much to find the transmission coefficient as it is to analyze the expression to obtain *design information*. (More modes are used when we just calculate.)

7.4 ANALYSIS OF THE HYBRID RADOME

Inspection of (7.16) leaves little doubt that a completely rigorous analysis probably would be difficult to manage. However, we will demonstrate a design approach that, although approximate in nature, has yielded crucial guidance in producing hybrid radomes with essentially constant bandwidth with angle of incidence, as well as fast roll-off and a flat top.

First of all, we notice in (7.16) that the composite pattern factors ${}_{\perp}^{\parallel}P_{N+1}^{c}$ change relatively little with frequency, and the same is true for ${}_{\perp}^{\parallel}{}^{H}W_{N+1}$ ${}_{\perp}^{\parallel}{}^{H}\mathcal{T}_{N+1}$. Thus the bracket in (7.16) is fairly constant with change of frequency. The same is true for I^i as given by (7.6); in fact it is seen to be quite similar to the terms in the bracket.

Finally it can also be verified by direct calculation that the mutual admittance terms $Y^{2,1}, Y^{3,2}, \ldots Y^{N,N-1}$ are in general also fairly insensitive to frequency variations. In fact the only terms in (7.16) that really changes dramatically with frequency around resonance is in general the determinant D_N. Consequently we have investigated D_N, with the details given in Appendix B. Basically a hybrid radome can be designed such that it is symmetric around its center plane in all respects, that is, the slot arrays as well as the dielectric profile. Or it can be more or less arbitrary. These designs are referred to as the *symmetric* and the *nonsymmetric* cases, respectively.

Both of these designs have been investigated and it can be stated that the symmetric designs in general are far superior to the nonsymmetric designs from an electrical design point of view. Consequently we are here going to concentrate on the symmetric case and only give a short resumé about the nonsymmetric case. For details see [40].

7.4.1 Symmetric Hybrid Radome

We show in Appendix B that the magnitude of the determinant $|D_N|$ in the symmetric case is given by

$$|D_N| = 2Y_{0re}^{1,1}\left|Y^{2,1}\right|\left|Y^{3,2}\right|\cdots\left|Y^{N,N-1}\right|\sqrt{1+\mathcal{P}_N^2}, \tag{7.17}$$

where $Y_{0re}^{1,1} = ReY^{1,1}(k = n = 0)$, as explained in Section 6.5, and $\mathcal{P}_N$ is a polynomial of order N as a function of Y defined by (6.29) and is derived in Appendix B for $N = 1$ to 5.

Substituting (7.17) into (7.16) and noticing symmetry ($Y_{N+1} = Y_1$, etc.) we find that

$$\left|\bar{H}_0(\bar{R}^{(1')})\right| = \frac{Y_1}{2D_xD_z}\frac{1}{r_{1y}}\frac{|I^i|}{2Y_{0re}^{1,1}\sqrt{1+\mathcal{P}_N^2}}$$
$$\left|{}_{\perp}\hat{n}_{0\perp}P_1^c 2_{\perp}^{H}W_{N+1}{}_{\perp}^{H}\mathcal{T}_{N+1} + {}_{\parallel}\hat{n}_{0\parallel}P_1^c 2_{\parallel}^{H}W_{N+1}{}_{\parallel}^{H}\mathcal{T}_{N+1}\frac{r_{1y}}{r_{0y}}\right|. \tag{7.18}$$

The further investigation of (7.18) now falls into two cases: the incident H-field being either $\perp$ or $\parallel$ to the plane of incidence.

Orthogonal Polarization For orthogonal polarization we have ${}_{\parallel}H_{b0}^{i} = 0$ and (7.6) reduces to

$$I^i = {}_{\perp}H^i_{b0}\,{}^H_{\perp}\mathcal{T}^e_{o+}\,2_{\perp}P^{ct}_1 e^{-j\beta_1 d_1 r_{1y}} \tag{7.19}$$

In order for any radome to have at least the potential for lossless transmission, we must require no cross-polarization in the transmitted field. From (7.18) we see that it requires that

$${}_{\parallel}P^c_1 = 0. \tag{7.20}$$

Substituting (7.19) and (7.20) into (7.18) yields

$$\frac{\left|\bar{H}_0(\bar{R}^{(1')})\right|}{\left|{}_{\perp}H^i_{b0}\right|} = \frac{Y_1}{2D_xD_z}\frac{1}{r_{1y}}\frac{\left|{}^H_{\perp}\mathcal{T}^e_{0+}\,2_{\perp}P^{ct}_1\,{}_{\perp}P^c_1\,2^H_{\perp}W_{N+1}\,{}^H_{\perp}\mathcal{T}_{N+1+}\right|}{2Y^{1,1}_{0re}\sqrt{1+\mathcal{P}^2_N}}, \tag{7.21}$$

where from (7.4) with ${}^H_{\parallel}\Gamma_{1+} = 1$,

$${}^H_{\perp}\mathcal{T}^e_{0+} = \frac{{}^H_{\perp}\mathcal{T}_{0+}}{1-{}^H_{\perp}\Gamma_{1-}e^{-j2\beta_1 d_1 r_{1y}}} = \frac{1-{}^H_{\perp}\Gamma_{1-}}{1-{}^H_{\perp}\Gamma_{1-}e^{-j2\beta_1 d_1 r_{1y}}}. \tag{7.22}$$

Further

$${}^H_{\perp}W_{N+1} = \frac{1}{1-{}^H_{\perp}\Gamma_{N+1+}e^{-j2\beta_{N+1}d_{N+1}r_{N+1y}}} = \frac{1}{1-{}^H_{\perp}\Gamma_{1-}e^{-j2\beta_1 d_1 r_{1y}}} \tag{7.23}$$

and

$${}^H_{\perp}\mathcal{T}_{N+1+} = 1+{}^H_{\perp}\Gamma_{N+1+} = 1+{}^H_{\perp}\Gamma_{1-}. \tag{7.24}$$

Also, for the $\perp$ plane by adaptation of (6.23),

$$Y^{1,1}_{0re} = \frac{Y_1}{2D_xD_z}\frac{1}{r_{1y}}{}_{\perp}P^c_1\,{}_{\perp}P^{ct}_1 2Re\frac{1+{}^H_{\perp}\Gamma_{1-}e^{-j2\beta_1 d_1 r_{1y}}}{1-{}^H_{\perp}\Gamma_{1-}e^{-j2\beta_1 d_1 r_{1y}}}. \tag{7.25}$$

Substituting (7.22), (7.23), (7.24), and (7.25) into (7.21) yields

$$\frac{\left|\bar{H}_0(\bar{R}^{(1')})\right|}{\left|{}_{\perp}H^i_{b0}\right|} = \left|\frac{(1-{}^H_{\perp}\Gamma_{1-})(1+{}^H_{\perp}\Gamma_{1-})}{\left(1-{}^H_{\perp}\Gamma_{1-}e^{-j2\beta_1 d_1 r_{1y}}\right)^2}\right| \left[Re\frac{\left(1+{}^H_{\perp}\Gamma_{1-}e^{-j2\beta_1 d_1 r_{1y}}\right)}{\left(1-{}^H_{\perp}\Gamma_{1-}e^{-j2\beta_1 d_1 r_{1y}}\right)}\right]^{-1}\frac{1}{\sqrt{1+\mathcal{P}^2_N}}. \tag{7.26}$$

Further (without subscripts and superscripts) and assuming Γ is real, we readily see that

$$Re\frac{1+\Gamma e^{-j2\beta_1 d_1 r_{1y}}}{1-\Gamma e^{-j2\beta_1 d_1 r_{1y}}} = Re\frac{1+\Gamma e^{-j2\beta_1 d_1 r_{1y}}}{1-\Gamma e^{-j2\beta_1 d_1 r_{1y}}}\frac{1-\Gamma e^{+j2\beta_1 d_1 r_{1y}}}{1-\Gamma e^{+j2\beta_1 d_1 r_{1y}}}$$

$$= \frac{1-\Gamma^2}{\left|1-\Gamma e^{-j2\beta_1 d_1 r_{1y}}\right|^2}. \tag{7.27}$$

Substituting (7.27) into (7.26) yields for the transmission coefficient curve

$$_{\perp}T.C. = \frac{\left|\bar{H}_0(\bar{R}^{(1')}\right|}{\left|_{\perp}H^i_{b0}\right|} = \frac{1}{\sqrt{1+\mathcal{P}_N^2}}. \tag{7.28}$$

Parallel Polarization For parallel polarization we have $_{\perp}H^i_{b0} = 0$, and from (7.6) we then obtain

$$I^i = {}_{\parallel}H^i_{b0\parallel}{}^H\mathcal{T}^e_{0+}2\frac{r_{0y}}{r_{1y}}{}_{\parallel}P^{ct}_1 e^{-j\beta_1 d_1 r_{1y}}. \tag{7.29}$$

Further we will require no cross-polarization:

$$_{\perp}P^c_1 = 0. \tag{7.30}$$

Substituting (7.29) and (7.30) into (7.18) and proceeding as we did above in the orthogonal case, we obtain

$$_{\parallel}T.C. = \frac{\left|\bar{H}_0(\bar{R}^{(1')}\right|}{\left|_{\parallel}H^i_{b0}\right|} = \frac{1}{\sqrt{1+\mathcal{P}_N^2}}. \tag{7.31}$$

Shape of the Transmission Curves Considering the complexity at the start of the derivation of the transmission curves above, it is perhaps somewhat surprising how simple the final result looks as exemplified by (7.28) and (7.31) for the principal planes only, and assuming no cross-polarization. However, as any student of classical network theory knows, this is quite typical for a classical filter.

The extremes of (7.28) or (7.31) are obtained by differentiation with respect to the frequency, that is, y yielding

$$2\mathcal{P}_N\frac{d\mathcal{P}_N}{dy} = 0 \tag{7.32}$$

with roots

$$\mathcal{P}_N = 0 \tag{7.33}$$

corresponding to unit transmission (i.e., maximum transmission) and

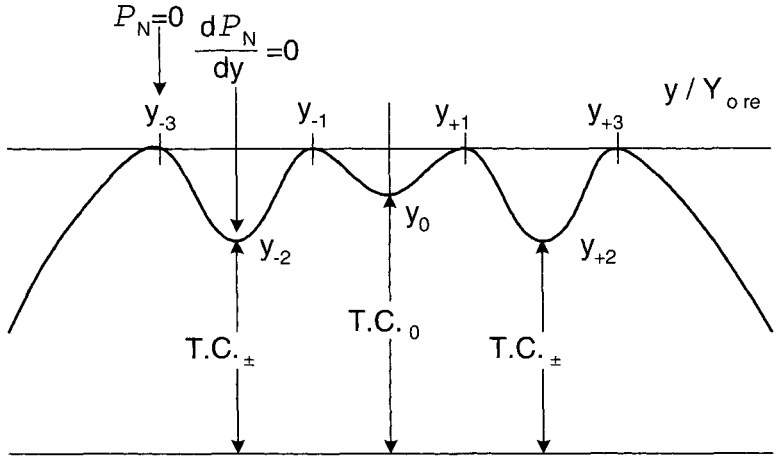

FIGURE 7.4. Typical schematic transmission curve for a symmetric hybrid radome for $N = 4$. Note that in general we obtain neither a Chebyshev nor a Butterworth design. However, the maxima are determined by $\mathcal{P}_N = 0$ and the minima by $d\mathcal{P}_N/dY = 0$. They are located symmetrically around the center frequency.

$$\frac{d\mathcal{P}_N}{dy} = 0 \tag{7.34}$$

corresponding to minimum transmission as illustrated in Fig. 7.4. (Note that y given by (6.29) is not a coordinate and varies considerably more with frequency than Y_{0re} and $Y^{n,m}$.)

As shown in Appendix B, the polynomial $\mathcal{P}_N$ is of order N where N equals the number of slotted arrays. Thus from (7.33) and (7.34) we conclude that the symmetric hybrid radome will at most have N maxima with unit transmission and $N - 1$ minima with a depth depending on the design as explained below. It is possible, however, that some or all roots of (7.33) and (7.34) can coincide or not even exist; see later. Outside the band-pass region the transmission coefficient will asymptotically behave like $T.C. \sim 1/\mathcal{P}_N$; that is. the larger the number of N slot arrays, the higher is the order of $\mathcal{P}_N$ and thus the faster the roll-off. We will present various cases ranging from $N = 1$ to $N = 5$ in Section 7.5.

7.4.2 Nonsymmetric Hybrid Radome

The details of the nonsymmetric hybrid radome are given in [40] and will not be covered here, primarily because it in general is inferior to the symmetric case. It suffices to state that the transmission coefficients in the principal planes are given formally by

$$|T.C.| = \frac{1}{\sqrt{1 + \mathcal{P}_N^2 + \mathcal{P}_{NNS}^2}}, \tag{7.35}$$

where $\mathcal{P}_N$ is the same polynomial as found in the symmetric case above and $\mathcal{P}_{NNS}$ is another polynomial depending on the nonsymmetric design but also of order N.

Evidently, to obtain unit transmission, we must require both $\mathcal{P}_N$ and $\mathcal{P}_{NNS}$ to be equal to zero at the same time. This results in an extra design constraint that makes working with nonsymmetric designs cumbersome. For more details see [40]. The polynomials $\mathcal{P}_{NNS}$ are given in Appendix B for $N = 2$ and 3.

7.5 SPECIFIC CASES

7.5.1 $N = 1$: Monoplanar Symmetric Hybrid Radome

(For the asymmetric case, see Problems 7.1 and 7.2.)

This case is obviously the most simple and consequently has some importance at least on that merit alone. From (B.8) we have

$$\mathcal{P}_1^2 = \frac{y^2}{Y_{0re}^2},$$

that is, for the transmission coefficient,

$$T.C. = \frac{1}{\sqrt{1 + (y^2/Y_{0re}^2)}}, \tag{7.36}$$

in both principal planes and for no cross-polarization.

Unit transmission is obtained for $y = 0$. However, y as well as Y_{0re} will in general change dramatically with angle of incidence which in turn will change the transmission curves. Clearly, in order to have invariance with angle of incidence, we must require just that of both y and Y_{0re} (or at least of their ratio).

Both of these parameters have been investigated in Chapter 6 where we showed that Y_{0re} can be made fairly scan independent by use of dielectric slabs adjacent to the slot array, while the variation of y is minimized by using small inter-element spacings.

We will in the following show several calculated examples that will illustrate the effect of dielectric slabs upon periodic surfaces.

Example First, we show in Fig. 7.5 an array made of four-legged loaded slot elements as discussed in Section 2.3.1. At the top we show the array without any dielectric. We note that the 5 dB bandwidth varies about 6.5:1 at 70° angle of incidence. At the bottom we show the same array with dielectric slabs on each side, and we now observe that the bandwidth variation is reduced to less than 1.4:1. We also note that the resonant frequency is more stable with angle of incidence. Further improvement is possible but will not be discussed in this book.

While this design is neither particularly good nor very practical, it does illustrate the general effect of dielectric on slotted surfaces. However, the designer must be

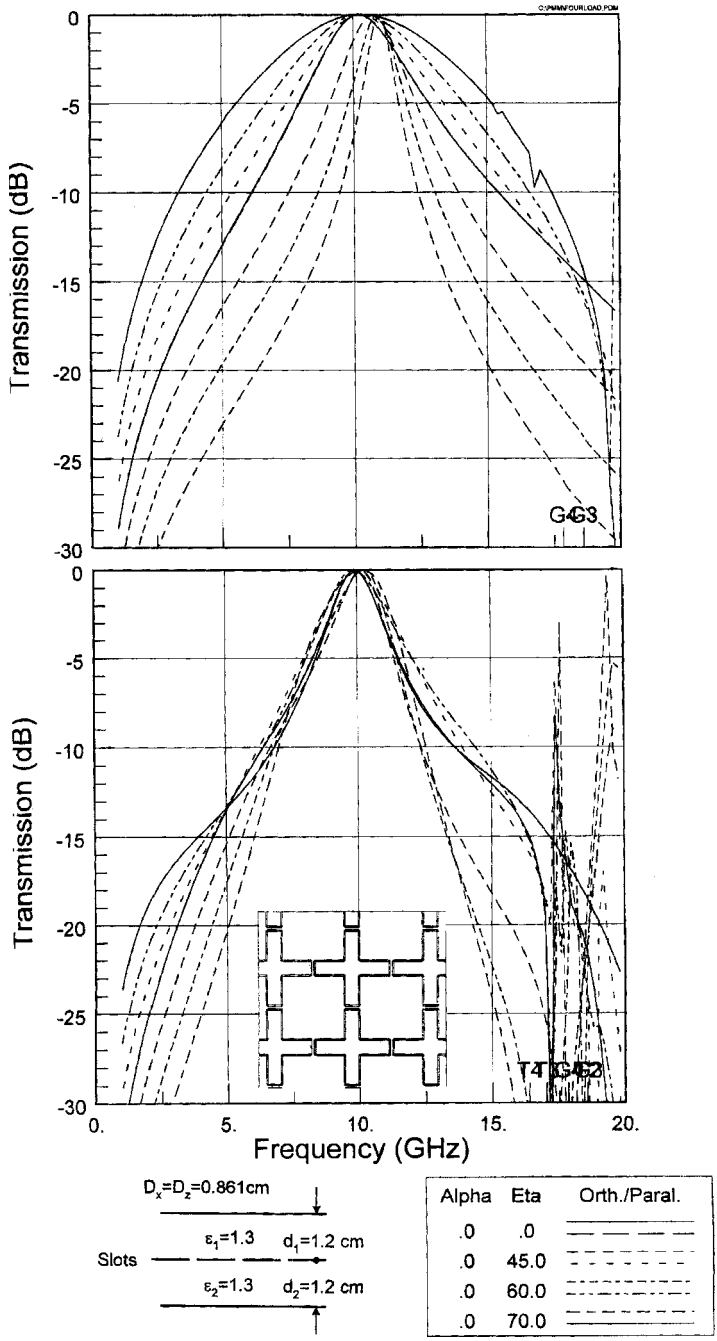

FIGURE 7.5. Transmission curves for an array of four-legged loaded slots as shown in insert. *Top:* Without dielectric slabs. *Bottom:* With dielectric slabs with $\epsilon_1 = \epsilon_2 = 1.3$ and $d_1 = d_2 = 1.2$ cm. Note: Stabilization of the bandwidth as well as the resonant frequency with angle of incidence.

aware that blindly adding dielectric slabs does not automatically take care of all the problems that might plague periodic surfaces.

For example, we show in Fig. 7.6 a slotted array of tripoles as discussed in Section 2.2.2. At the top we show the slot array without any dielectric, and we immediately observe that we have modal interaction nulls at around 16 to 18 GHz. Obviously adding dielectric slabs similar to the one above is not going to cure this problem (as shown in Fig. 7.6 bottom), although we see an excellent stabilization at frequencies below the resonance. (See also Problems 7.1 and 7.2.)

Further someone might think that what is good for a slot array is also good for a dipole array. Although that expectation often is justified (see Section 8.11), the designer should always be acutely aware of the "physics" of his/her problem. As an example, we show in Fig. 7.7 the *dipole* version of the four-legged loaded slot array in Fig. 7.5 (i.e., we show the reflection rather than the transmission). The two nondielectric cases at the top of these figures are of course identical as they should be according to Babinet's principle; see Section 1.4. The dielectric cases shown at the bottom are seen to be vastly different, although some bandwidth stabilization takes place in the dipole case around resonance. The reason for this messed-up dipole case is that reflection takes place not only from the conducting elements but also from the dielectric slabs. In fact for higher angles of incidence for parallel polarization (with respect to $\bar{E}$) the backscatter from the elements is so weak that the dielectric backscatter cancels it and produces nulls above and below the resonant frequency.

It is by no means suggested that the dipole design in Fig. 7.7 is particularly useful for anything, except perhaps writing a useless paper!

Surface Waves (Spurious Resonances) Returning to Fig. 7.5, we notice some spurious resonances at 17 to 20 GHz. These are simply caused by a very fast variation of y when surface waves are encountered as discussed in general in Chapter 6. Consider for example Fig. 6.11 where $ImY_A \to \infty$ (i.e., $y \to \infty$) when we encounter a surface wave. From (7.36) we readily see that it results in $T.C. = 0$. Further in Fig. 6.11 we see that y will come up from $-j\infty$ and resonate once more which is what is producing the sharp spurious resonances eventually followed or preceded by free space grating lobes. Usually these resonances are not of great concern, since they in general are very sharp and consequently strongly reduced by even a minor amount of loss, either from the dielectric or the resistivity of the elements.

Alternatively, they could eventually be moved out of the frequency range of interest. This is left as an exercise for the reader.

7.5.2 $N = 2$: Biplanar Symmetric Hybrid Radome

This case is by far the most important as far as applications are concerned. It will therefore be discussed in more detail than any other case. From (B.12),

$$\mathcal{P}_2 = \frac{1}{2}\frac{Y_{0re}}{|Y^{1,2}|}\left[\left(\frac{y}{Y_{0re}}\right)^2 - \left(\frac{|Y^{1,2}|^2}{Y_{0re}^2} - 1\right)\right], \tag{7.37}$$

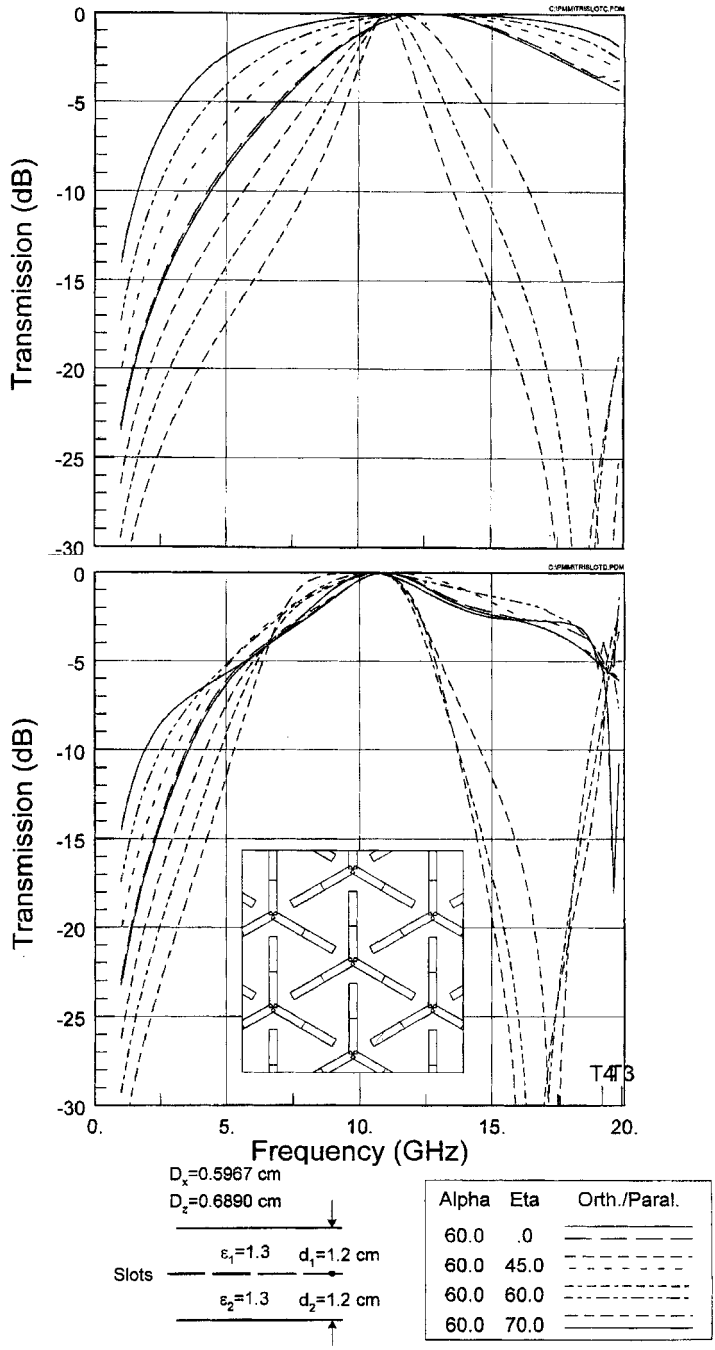

FIGURE 7.6. Transmission curves for an array of tri-slots as shown in insert. *Top:* Without dielectric slabs. *Bottom:* With dielectric slabs with $\epsilon_1 = \epsilon_2 = 1.3$ and $d_1 = d_2 = 1.2$ cm (same as in Fig. 7.5). A modal interaction null at around 17 GHz cannot be eliminated by dielectric slabs.

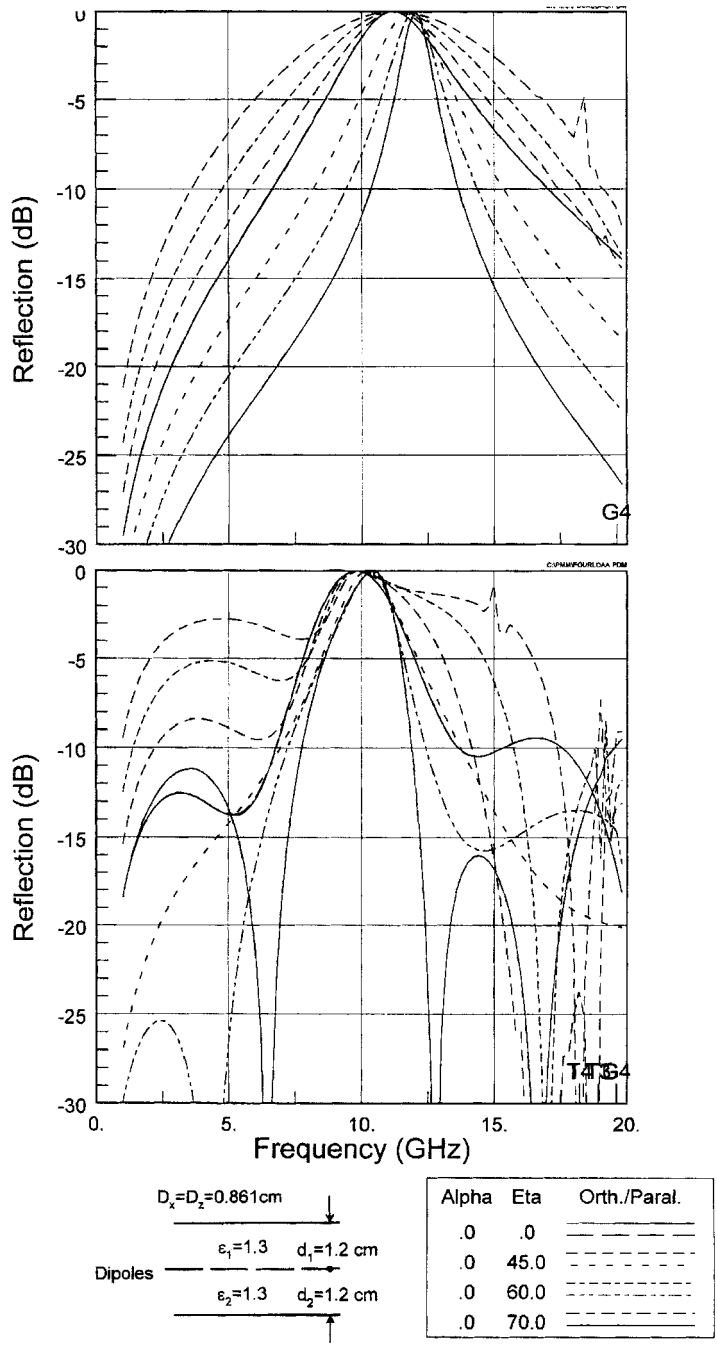

FIGURE 7.7. Reflection curves for a dipole array complementary to the slot array in Fig. 7.5. *Top:* Without dielectric slabs. *Bottom:* With dielectric slabs with $\epsilon_1 = \epsilon_2 = 1.3$ and $d_1 = d_2 = 1.2$ cm (same as in Figs. 7.5 and 7.6). The design at the bottom makes no claim to any practical value.

where we in this symmetric case for brevity have denoted

$$y = y^{1,1} = y^{2,2},$$
$$Y_{0re} = Y_{0re}^{1,1} = Y_{0re}^{2,2}.$$

According to (7.33) we obtain unit transmission for $\mathcal{P}_2 = 0$, namely from (7.37) for

$$y_{\pm 1} = Y_{0re}\sqrt{\left(\frac{|Y^{1,2}|}{Y_{0re}}\right)^2 - 1}. \tag{7.38}$$

Further, according to (7.34) we obtain minima for $d/dy\mathcal{P}_2 = 0$, yielding $Y_0 = 0$ with transmission coefficient

$$T.C._0 = \frac{1}{\sqrt{1 + \dfrac{Y_{0re}^2}{4|Y^{1,2}|^2}\left[\dfrac{|Y^{1,2}|^2}{Y_{0re}^2} - 1\right]^2}} = \frac{2}{\dfrac{|Y^{1,2}|}{Y_{0re}} + \dfrac{Y_{0re}}{|Y^{1,2}|}}. \tag{7.39}$$

Although the derivation above is straightforward and simple, it gives the designer the tools and analysis which enables him to produce superior hybrid radomes.

First in Fig. 7.8 we show some typical schematic transmission curves as a function of y/Y_{0re} for various values of the normalized coupling $|Y^{1,2}|/Y_{0re}$.

For example, for $|Y^{1,2}|/Y_{0re} = 1.5$ we obtain according to (7.39) a transmission coefficient

$$T.C._0 = 0.925 \qquad \text{(curve } a\text{)},$$

and from (7.38) we obtain unit transmission for

$$\frac{y_{\pm 1}}{Y_{0re}} = \pm 1.12.$$

Similarly for $|Y^{1,2}|/Y_{0re} = 1$ we obtain

$$y_{\pm 1} = y_0 = 0$$

with

$$T.C._{\pm 1} = T.C._0 = 1$$

as shown in Fig. 7.8 by curve b. Finally for $|Y^{1,2}|/Y_{0re} < 1$ we obtain only one maximum for $y_0 = 0$ with a transmission coefficient less than one (not shown).

The first of these cases where the mutual coupling $|Y^{1,2}| > Y_{0re}$ is called the *overcritical* or Chebyshev design, while the second case where $|Y^{1,2}| = Y_{0re}$ is called the *critical*, or Butterworth case. Finally, the third case is called the undercritical case (name withheld by request!).

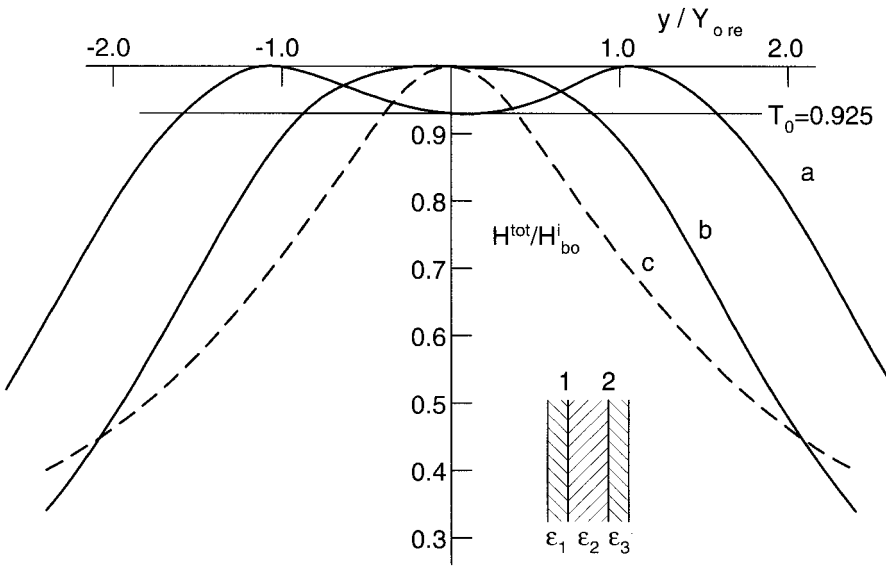

FIGURE 7.8. Typical schematic transmission curves for a symmetric biplanar hybrid radome ($N = 2$). *Curve a*: Chebyshev design with the valley in the middle 0.925 deep. $|Y^{1,2}| = \frac{3}{2}Y_{0re}$ (overcritical coupling). *Curve b*: Butterworth design (maximally flat). $|Y^{1,2}| = 1.0Y_{0re}$ (Critical Coupling). *Curve c*: Single layer alone producing either curve *a* or *b* depending on the mutual admittance $|Y^{1,2}|$.

Obviously the designer must take care to maintain values of $|Y^{1,2}|/Y_{0re}$ that are within strict limits to avoid too deep a valley between the two peaks. However, we also observe by inspection of (7.38) that in order for $y_{\pm 1}$ to be scan independent (i.e., have constant bandwidth), we must also require Y_{0re} to be scan independent. Fortunately this is by now "old hat." Of course we simply have to choose the proper ϵ_1 and d_1 of the outer dielectric slabs as discussed in Chapter 6. Recall that Y_{0re} exists only when looking out. Toward the other slot array it is zero because the "ground plane" is there.

Let us summarize: To make a symmetric hybrid radome that has constant bandwidth with angle of incidence and a flat top, we must require the following:

1. Y_{0re} must be scan independent, for example, by use of dielectric slab(s). There are other ways (see [28, 29, 30, 31]), but this is by far the simplest and best approach.
2. We must choose a mutual admittance $Y^{1,2}$ between the two slot arrays such that we maintain a fairly constant ratio $|Y^{1,2}|/Y_{0re}$ for all scan angles. Typical values would be $|Y^{1,2}|/Y_{0re} \sim 0.98 - 1.1$, where 1.1 corresponds to a transmission loss of $T.C._0 = 0.995$ or 0.02 dB. While this value sounds extremely conservative, the reason for this will be clear when reflection properties are discussed in Section 7.7.1. (See also Fig. 7.17.)

3. The resonant frequency should be as constant with scan angle as possible. This is primarily accomplished by using small elements resulting in small inter-element spacings D_x and D_z (see Chapter 2).

The mutual admittance $Y^{2,1}$ is discussed in detail in Section 6.6 where it is shown that

$$Y^{2,1} = \frac{Y_2}{2D_xD_z} \sum_k \sum_n \frac{e^{-j\beta_2(\bar{R}^{(2)}-\bar{R}^{(1)})\cdot\hat{r}_2}}{r_{2y}} \left[{}_{\perp}P_2^{c(2)t} {}_{\perp}P_2^{c(1)} + {}_{\parallel}P_2^{c(2)t} {}_{\parallel}P_2^{c(1)} \right] \frac{-2je^{j\beta_2 d_2 r_{2y}}}{\sin(\beta_2 d_2 r_{2y})}. \tag{7.40}$$

Comparison between Y_{0re} as defined in Section 6.5 for $|Y^{2,1}|$ given by (7.40) shows that for the principal mode their difference is essentially due to the terms Y_2/Y_1 and $1/\sin(2\beta_2 d_2 r_{2y})$. If we choose $d_2 r_{2y} \sim \lambda_2/4$, we see that the variation of the last terms as a function of $\beta_2 r_{2y}$ is minimum, in particular if we choose not to have a low value of Y_2 such that the variation of r_{2y} is minimized due to Snell's law.

In other words, our requirement that Y_{0re} be scan-independent in order to obtain a constant bandwidth is consistent with our requirement that the ratio $|Y^{1,2}|/Y_{0re}$ also be basically scan independent to obtain a transmission curve with a flat top (i.e., provided that you make intelligent choices of the many parameters involved and not leave that to a mindless computer!).

Note also that there will in general be two distances of $d_2 r_{2y}$ on each side of the 90° value that satisfy the ratio requirement 2 above. In general, one should choose the larger distance, since that results in lower values of the evanescent waves.[1] If these have practically died out at the distance d_2, it simply means that the two slot arrays can be registered arbitrarily with respect to each other without requiring the slots in the two arrays to be on top of each other or some other impractical requirement when building real radomes. This problem is called *registration sensitivity*; it is discussed further in Section 7.7.3.

Example: Calculated Biplanar Hybrid Radome (Symmetric) Actual calculated transmission curves for a hybrid radome with $N = 2$ are shown in Fig. 7.9, bottom. The two identical slot arrays are made of four-legged loaded elements just as shown earlier in the monoplanar case in Fig. 7.5. The dielectric profile is seen to consist of outer layers with $\epsilon_1 = \epsilon_3 = 1.3$ and thickness $d_1 = d_3 = 1.1$ cm. In other words, they are chosen to yield scan independence as explained in Section 6.4 and also as used in the monoplanar case discussed earlier. However, the center slab is chosen with a considerably higher dielectric constant, namely $\epsilon_2 = 1.9$ while $d_2 = 0.6$ cm. Actual calculations of the mutual admittance between the two arrays

[1] There are of course many values of $d_2 r_{2y}$ that will satisfy our coupling requirement due to the periodic nature of $\sin(\beta_2 d_2 r_{2y})$. However, values of $(\beta_2 d_2 r_{2y}) \sim 3/2\pi$ are not in general recommended because the factor r_{2y} will reduce the factor $\beta_2 d_2 r_{2y}$ excessively at higher angles of incidence.

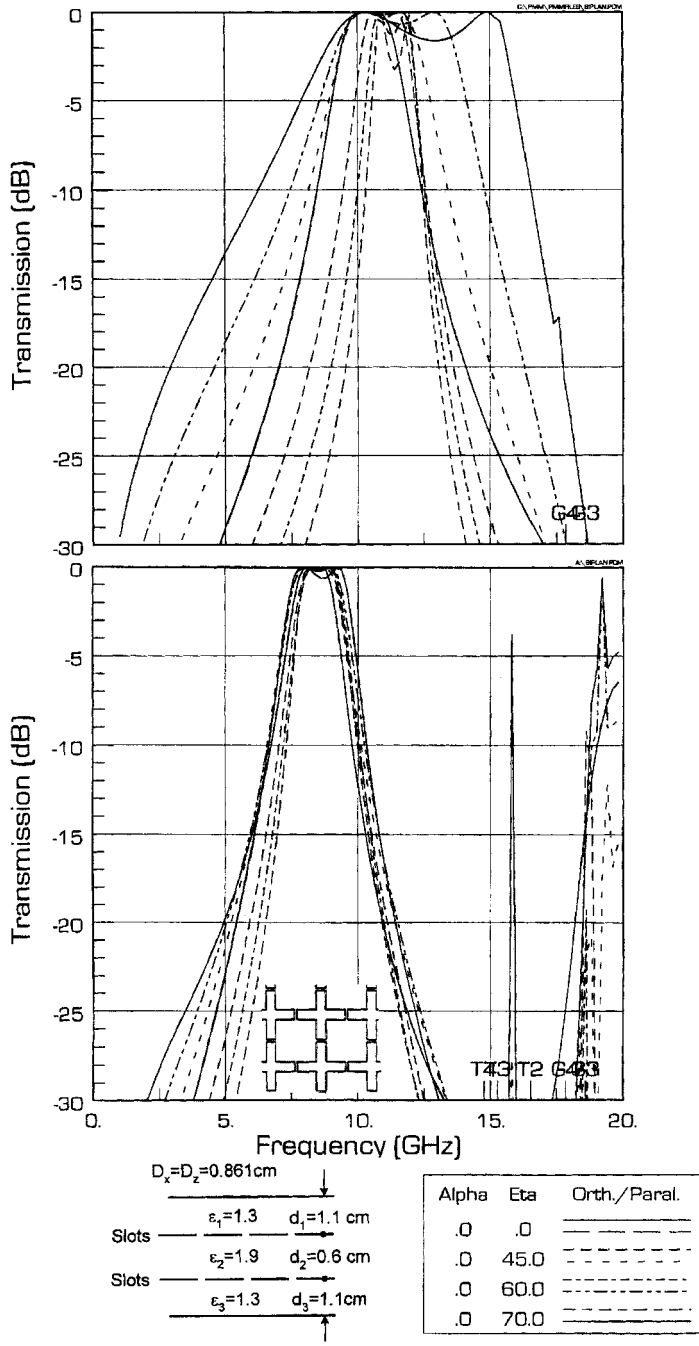

FIGURE 7.9. Calculated transmission curves by the PMM program for a symmetric biplanar hybrid radome of four-legged loaded elements using 8 section modes. *Top:* Without any dielectric slabs. *Bottom:* With a dielectric profile as shown. The tops of the resonant curves have very low ripples except for normal angle of incidence.

shows it to be very close to Y_{0re} as it should be in order to obtain only a small dip between the two peaks. The number of mode sections were 8, the number of Floquet modes typically around 40 (the PMM program shuts off automatically when a preset level of accuracy is reached).

For comparison we also show in Fig. 7.9 top the same array without any dielectric. The effect of the dielectric is seen to be no less than spectacular. Without dielectric the bandwidth is seen to vary about 6:1, while it is reduced to about 1.4:1 when dielectric is added (70° angle of incidence). We also observe better stability of the resonant frequencies with angle of incidence. It should be noted that the top of the transmission curve is quite flat (at least to the eye) with the exception of normal angle of incidence. This is usually all right when designing forward-looking radomes with reasonably high fineness ratio (see Fig. 1.11). In that case the direction of the beam seldom scans far enough to be incident normal to the surface.

The top of the transmission curve can be made flatter. However, it is a much better idea to monitor the reflected field as explained in Section 7.8.1. This is precisely the point where a computerized optimization process would be in order, although the optimization can still be done better and faster by monitoring $|Y^{1,2}|$ and Y_{0re}.

Finally we notice the onset of trapped grating lobes from around 15 GHz and up. They start earlier than in the monoplanar case (see Fig. 7.5) simply because the dielectric slab in the middle has a higher dielectric constant ($\epsilon_2 = 1.9$ instead of $\epsilon_1 = 1.3$). They are preceded by complete absence of signal, namely caused by the so-called *Luebbers' anomaly* as explained in Section 7.7.3. At higher frequencies we observe spurious resonances. They are as in the monoplanar case related to the onset of surface waves. Because of their narrow bandwidth, they are usually very fragile and sensitive to even small loss and consequently not of extreme importance (they also change dramatically with angle of incidence). If they are a problem, they are easily pushed out of sight (left as an exercise for the student).

7.5.3 $N = 3$: Triplanar Symmetric Hybrid Radome

From symmetry we have

$$y^{1,1} = y^{3,3} = y \quad \text{and} \quad Y_{0re}^{1,1} = Y_{0re}^{3,3} = Y_{0re}. \tag{7.41}$$

Here we will assume that the center array has the same resonant frequency as the two other ones but a different bandwidth or slope:

$$y^{2,2} = a_2 y. \tag{7.42}$$

(The requirement that all arrays have the same resonant frequency can always be fulfilled at least at one angle of incidence by simply tuning the elements. However, maintaining the same resonant frequency for all angles of incidence and polarizations is often difficult. See the comments in Section 7.8.7.)

From Appendix B we then obtain by substituting (7.41) and (7.42) into (B.15),

$$\mathcal{P}_3 = \frac{a_2 Y_{0re}}{2|Y^{1,2}|^2} y \left[\left(\frac{y}{Y_{0re}} \right)^2 - \left(\frac{2|Y^{1,2}|^2}{a_2 Y_{0re}^2} - 1 \right) \right]. \tag{7.43}$$

Unit transmission (max) is according to (7.33) given for $\mathcal{P}_3 = 0$; that is, from (7.43),

$$y = y_0 = 0 \tag{7.44}$$

and

$$y = y_{\pm 2} = \pm Y_{0re} \sqrt{\frac{2|Y^{1,2}|^2}{a_2 Y_{0re}^2} - 1}. \tag{7.45}$$

Further, the minima are according to (7.34) given by $d\mathcal{P}_3/dy = 0$, or from (7.43) by the equation

$$3 \left(\frac{y}{Y_{0re}} \right)^2 - \left(\frac{2|Y^{1,2}|^2}{a_2 Y_{0re}^2} - 1 \right) = 0$$

with roots

$$y = y_{\pm 1} = \pm \frac{1}{\sqrt{3}} Y_{0re} \sqrt{\frac{2|Y^{1,2}|^2}{a_2 Y_{0re}^2} - 1}. \tag{7.46}$$

The transmission coefficient at $y_{\pm 1}$ is obtained by substituting (7.46) into (7.31):

$$T.C._{\pm 1} = \frac{1}{\sqrt{1 + \left[\frac{2}{a_2} \frac{|Y^{1,2}|^2}{Y_{0re}^2} - 1 \right]^3 \Big/ \left[27 \frac{|Y^{1,2}|^4}{a_2^2 Y_{0re}^4} \right]}}. \tag{7.47}$$

Typical schematic transmission curves for $N = 3$ are shown in Fig. 7.10 and discussed later. By inspection of (7.44), (7.45), and (7.46), we note the following relationships:

$$y_0 = r_T \cos 90°, \tag{7.48}$$

$$y_{\pm 1} = r_T \cos 60°, \tag{7.49}$$

$$y_{\pm 2} = r_T \cos 30°, \tag{7.50}$$

which are located as the projections from equal arcs on a circle as illustrated in Fig. 7.11. Also shown in the figure is a typical transmission curve which must always be a Chebyshev form (i.e., equal ripple) for $N = 3$, since the roots are located as determined by (7.49) to (7.50). The radius r_T of the root circle is easily determined

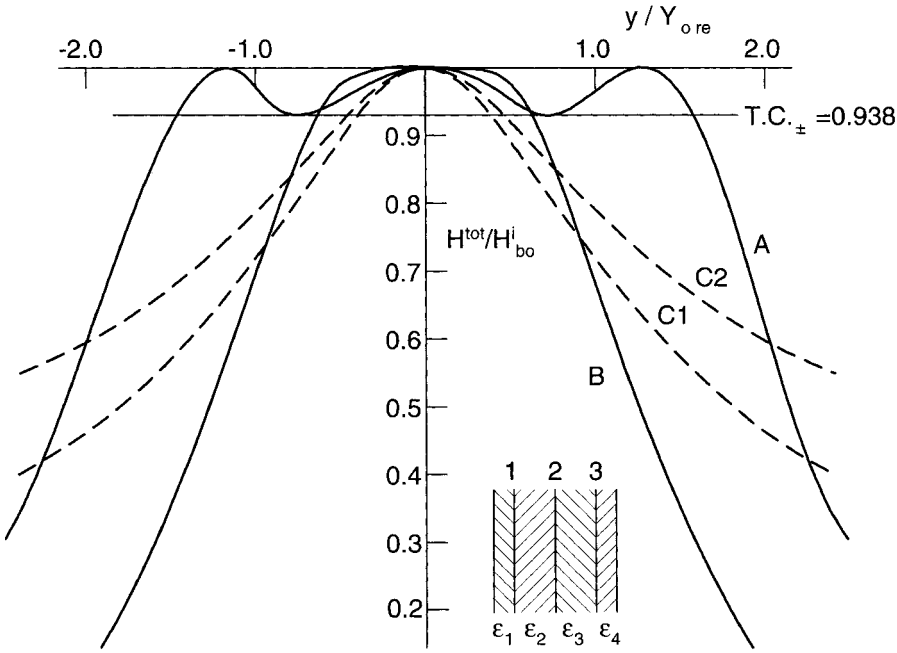

FIGURE 7.10. Typical schematic transmission curves for a symmetric triplanar hybrid radome ($N = 3$). *Curve A:* Chebyshev design with two valleys 0.938 deep, $T.C._{\pm 1} = 0.938$. $|Y^{1,2}| = Y_{0re}$ and $a_2 = \frac{2}{3}$. *Curve B:* Butterworth design (maximally flat). $|Y^{1,2}| = Y_{0re}$ and $a_2 = 2$. *Curve C1*: Transmission curve for the first (third) array alone producing the Chebyshev design (curve *A*). *Curve C2*: Transmission curve for the center array alone used to produce the Chebyshev design (curve *A*).

by substituting (7.46) into (7.50):

$$r_T / Y_{0re} = \frac{2}{\sqrt{3}} \sqrt{\frac{2}{a_2} \frac{|Y^{1,2}|^2}{Y_{0re}^2} - 1} \tag{7.51}$$

[substituting for $y_{\pm 2}$ in (7.50) leads to the same value of r_T].

We finally show in Table 7.1 various Chebyshev designs obtained simply by choosing various values for the relative bandwidth factor a_2 of the middle layers, and choosing $|Y^{1,2}|^2 / Y_{0re}^2 = C$.

Observe that $a_2 = 2C$ makes $r_T / Y_{0re} = 0$; that is, it makes the roots y_0, $y_{\pm 1}$, and $y_{\pm 2}$ equal to zero. So we have the well-known Butterworth filter being maximally flat. For $a_2 < 2C$ we see from (7.51) that the root circle increases; that is, the bandwidth increases and makes the valleys of the transmission curve deeper. For $a_2 > 2C$ the roots $y_{\pm 1}$ and $y_{\pm 2}$ disappear, but the root $y_0 = 0$ remains yielding unit transmission. By inspection of (7.43), we observe that the bandwidth becomes smaller. We finally show in Fig. 7.9 for $N = 3$ a Chebyshev curve A with the minimum transmission coefficient $T.C._{\pm 1} = 0.938$. A Butterworth curve B is also shown. The

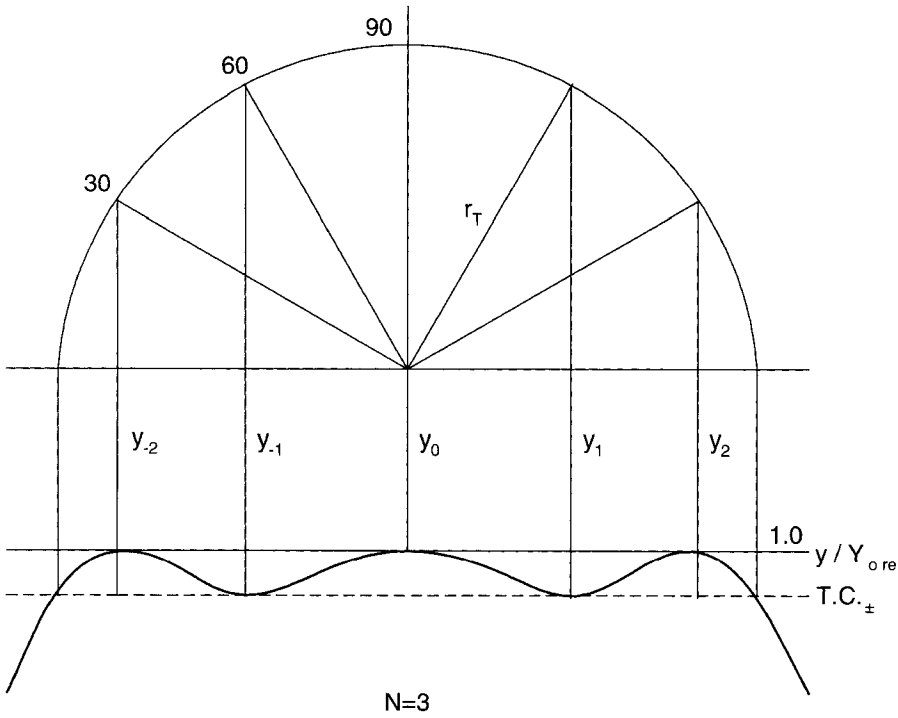

FIGURE 7.11. Construction of the maxima and minima of a symmetric triplanar Chebyshev design ($N = 3$).

transmission curves $C1$ for the first (third) and the second $C2$ individual layer alone used to produce the Chebyshev curve above is also shown. The Butterworth curve is produced by $C1$, and a narrower curve as the second layer ($a_2 = 2$). Observe how the Chebyshev design is approximately three times wider than the first layer alone, while the Butterworth yields approximately the same bandwidth (the price we must pay for smaller ripples).

TABLE 7.1. Various Chebyshev Designs for $N = 3$

	Butterworth	$\lvert Y^{1,2}\rvert^2/Y_{0re}^2 = C$					
	$a_2 = 2C$	$a_2 = 1C$	$a_2 = \frac{3}{4}C$	$a_2 = \frac{2}{3}C$	$a_2 = \frac{1}{2}C$	$a_2 = \frac{1}{3}C$	$a_2 = \frac{1}{4}C$
r_T/Y_{0re}	0	1.154	1.492	1.637	2.000	2.583	3.060
y_0/Y_{0re}	0	0	0	0	0	0	0
$y_{\pm1}/Y_{0re}$	0	0.578	0.747	0.820	1.000	1.294	1.530
$y_{\pm2}/y_{0re}$	0	1.000	1.293	1.414	1.732	2.236	2.646
$T.C._{\cdot\pm1}$	1.0	0.980	0.955	0.938	0.895	0.812	0.746

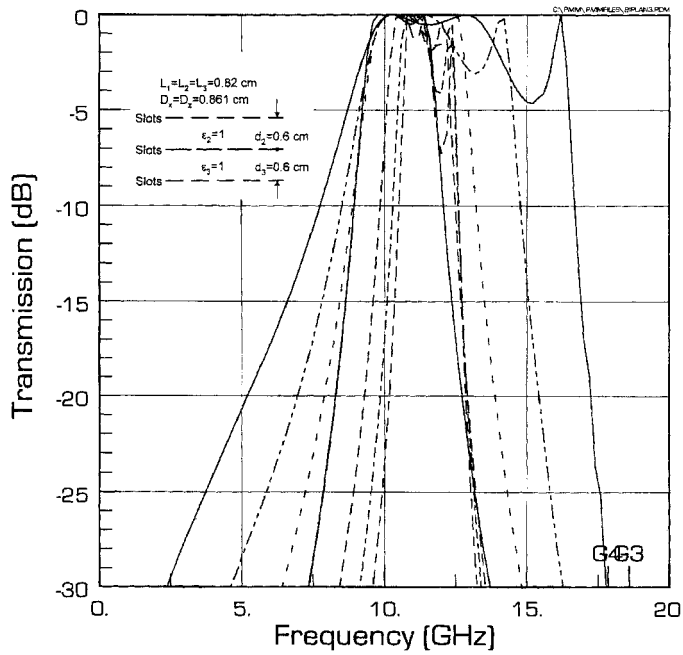

FIGURE 7.12. Calculated transmission curves for a symmetric triplanar hybrid radome of four-legged loaded elements using 8 section modes. *Top*: Without any dielectric slabs. *Bottom*: With a dielectric profile as shown and array elements reduced to maintain the same resonance frequency. Would be a good starting point, not a great radome panel. Optimizers of the world unite. Start your engines!

Note further that since everything in Table 7.1 is expressed in terms of Y_{0re}, it is important to keep Y_{0re} as independent of angle of incidence as possible, as discussed earlier.

Example: Calculated Triplanar Hybrid Radome (Symmetric) Typical calculated transmission curves for triplanar slot designs are shown in Fig. 7.12. At the top we show the no-dielectric case for three identical slot arrays of four-legged loaded elements with the same dimensions as used earlier for the mono- and biplanar cases. The dielectric triplanar case is shown in Fig. 7.12 bottom. Merely adding the dielectric slabs would make this design resonate at a somewhat lower frequency. To make comparison easier, we have moved the resonant frequency back to around 10 GHz by simply scaling the dimensions of arrays 1 and 3. The center array is bounded by dielectric slabs with $\epsilon_2 = \epsilon_3 = 1.9$ on both sides and must consequently be reduced more in order to also resonate around 10 GHz. This was done by further reduction of the element size as shown in the insert but leaving D_x and D_z the same as the two outer arrays in order not to violate Floquet's periodicity requirement. The bandwidth stability is excellent but a closer look at the top shows ripples at 70° angle of incidence. In that respect the triplanar is not as good as the biplanar design, although

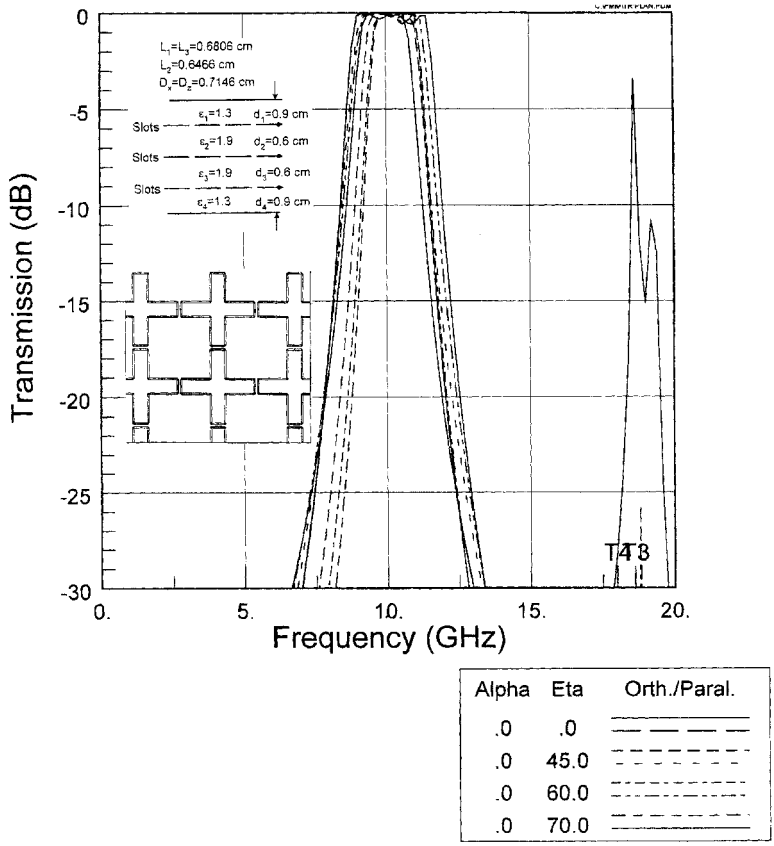

FIGURE 7.12. (*Continued.*)

it is seen to roll off faster as expected (see also Fig. 7.19). The spurious resonances located at frequencies higher than in the biplanar case are due to the reduced D_x and D_z.

7.5.4 $N \geq 4$: Multilayered Cases

Cases for $N = 4$ and 5 have been investigated in the symmetric cases, however, the design philosophy in the general symmetric multilayered case can readily be predicted based on these two cases.

As an example, let us consider the symmetric case for $N = 5$. The polynomial $\mathcal{P}_5$ is given in Appendix B and by proceeding as in the two- and three-layered cases earlier, we readily obtain a typical transmission curve as shown in Fig. 7.13. We note that all the maxima and minima are located symmetrically around the center frequency y_0 where we have a maxima (for N odd we have a maximum in the middle, for N even

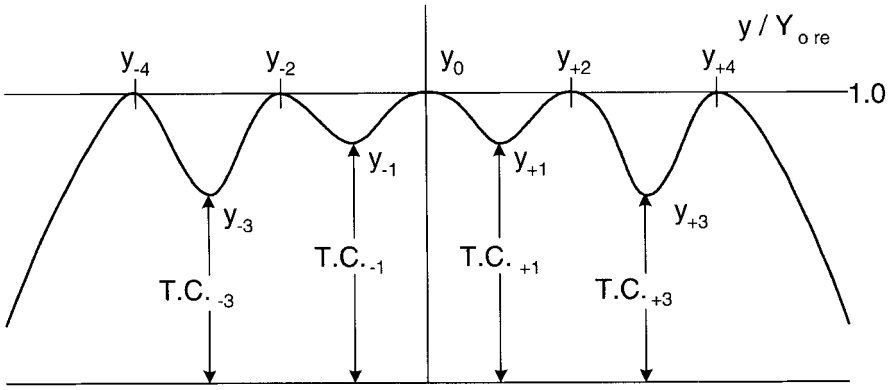

FIGURE 7.13. Typical schematic transmission curves for a symmetric design with five arrays ($N = 5$). To produce Chebyshev and Butterworth designs, further constraints are required.

we have a minimum). We notice, however, that the depth of these symmetric minima are not necessarily the same, although all the maxima exhibit unit transmission. By requiring the depth of all the minima to be equal, namely by imposing additional requirements on the array parameters as well as the dielectric profile, it is possible to arrive at the schematic transmission curve shown in Fig. 7.14, namely a Chebyshev design of order 5. The readers interested in further detail are referred to [40] where design tables for $N = 4$ and 5 similar to Table 7.1 are given. A few features should be emphasized that are common to all symmetric space filters:

1. The outer dielectric layers serve essentially to stabilize the bandwidth with angle of incidence and polarization regardless of the number of arrays. They should be chosen first.
2. The bandwidth is essentially determined by the bandwidth of the individual slot arrays.
3. The depths of the minima are essentially determined by the relative array bandwidth and the dielectric profile.

Note also that $N = 2$ and 3 always produce Chebyshev designs as long as they are symmetric. Further constraints are necessary in the symmetric multilayered case. See also comments in Section 7.8.7.

7.6 "HONEYCOMB" AND THICK SCREEN RADOMES

7.6.1 Honeycomb Panels

We have so far considered only the classical hybrid radome comprised of N slot arrays located in a stratified medium as shown in Fig. 7.1. The transport or coupling of

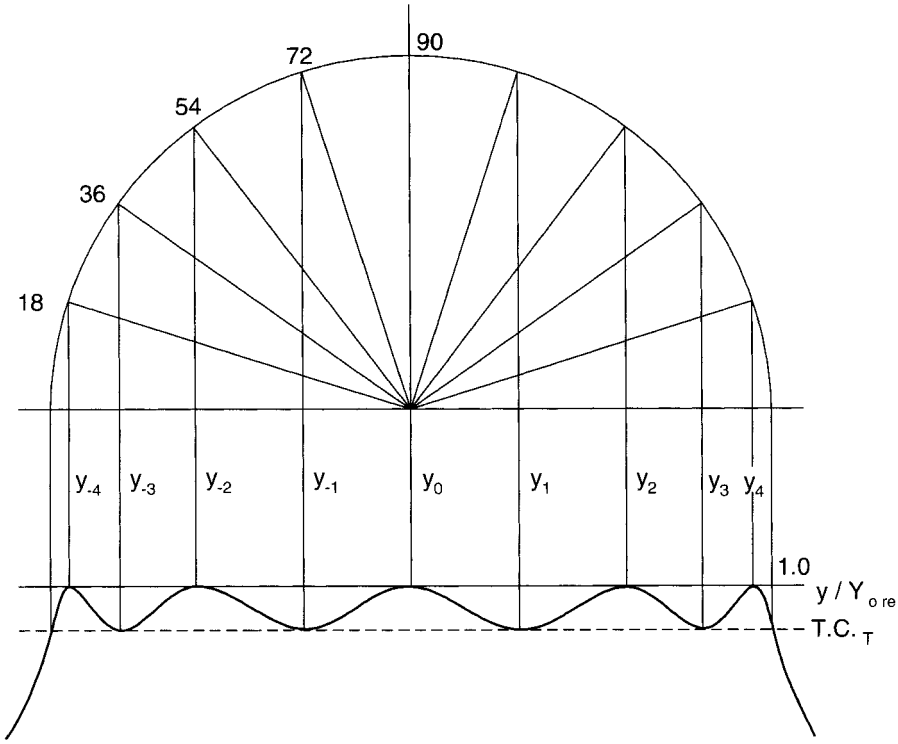

FIGURE 7.14. Construction of the maxima and minima for a Chebyshev design with $N = 5$ layers (symmetric).

energy from one slot array to the next is simply via the mutual admittances between adjacent arrays.

However, an alternative approach would be to connect the elements in adjacent arrays with some form of transmission lines, for example, waveguides. An example of such a biplanar design with square waveguides is seen in Fig. 7.15.

Basically the shape of the waveguides can be anything; it can be round, hexagonal even loaded, and so on. In fact the original thought was to use hexagonal waveguides, so the design would look like the well-known honeycomb design with conducting walls. Thus we could at least in principle obtain a very strong and lightweight panel without using dielectric between adjacent slot arrays (but still use dielectric slabs on the outer sides).

Despite a seemingly sound technical principle, the honeycomb panels never became very popular, mostly for practical reasons. Foremost was the requirement that adjacent slot arrays be placed rather precisely opposite each other to fit into the waveguides. This is a somewhat cumbersome requirement that is unnecessary for the classical design without waveguides as long as it is designed correctly (see Section 7.7.2 on registration sensitivity). For curved surfaces we would further require

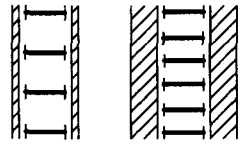

"Honeycomb" Types

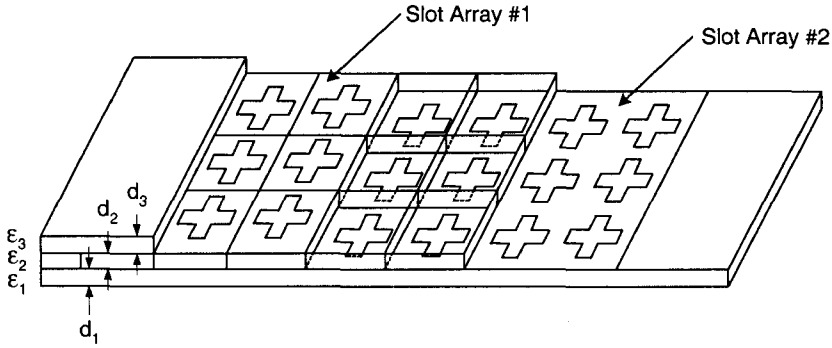

FIGURE 7.15. An example of a honeycomb panel. In this case it is comprised of two slot arrays where the opposing elements are connected by waveguide sections. These are in this case square but were originally intended to be shaped as honeycombs. This was intended to produce a panel that was lightweight and strong at the same time.

array designs with different inter-element spacings, again a requirement not called for in the plain design.

The analysis of the honeycomb panel amounts to rather minor modifications of the approach given already for the ordinary hybrid radome. In fact we merely have to change the mutual admittances between adjacent arrays. This is readily done by recognizing that the field inside the waveguides is comprised of two (or more) plane waves (plus the evanescent waves). The direction of these plane waves is simply adjusted such that the boundary conditions are satisfied at the waveguide walls like all waveguide problems. In other words, on the outside all slot voltages should obey Floquet's theorem, producing the usual spectrum corresponding to the incident wave. However, once inside, they are in their own little "waveguide world" with their own spectrum based on the inside dimensions of the waveguide, but otherwise the same principles apply as to the outside.

For details, see Larson's thesis [41] or Stosic's thesis [42] which not only consider multilayers but also parallel plates rather than waveguides. Also consult Fenn's dissertation [43] and the paper [44].

7.6.2 Thick Screens

Suppose that we reduce the inside of the waveguides above. Obviously that will merely change the mutual admittances between adjacent inside arrays. If we further let our elements be of rectangular shape and let the waveguides shrink until they line up with the outside elements, we have simply an array of rectangular slots in a thick panel. This approach was used by Larson [41] and checked against results obtained earlier by Luebbers who had used a direct mode matching approach [45, 46, 47]. The agreement between the two calculated results as well as measurements were very satisfactory. Further Luebbers had incorporated the ohmic losses and found them to be insignificant unless the panel got very thick (for a good conductor).

The fundamental effect of making panels thicker is that the first resonance exhibits a narrower resonance curve. While this in itself may often be of interest, there are as shown in Chapter 2 many other ways to accomplish just that in a more simple way. Further a thick panel would in general be required to be filled with a dielectric material. Since the thermal expansion coefficient for metal and dielectric often are quite different, minute air cracks would in general occur with unfortunate results (see also Section 2.4).

Finally it will in general be true that the thicker the screen, the more labor-intensive is the manufacturing. Based on these facts it became clear very early, at least to this author, that future designs primarily would be the thin screens sandwiched between dielectric slabs. Here the principle was simply that the dielectric was boss (mechanically), while the thin pliable copper screens would simply follow the expansion of the dielectric.

7.6.3 Receive-Transmit Dipoles Connected via Cables

A related approach is shown in Fig. 7.16. It is seen to consist of dipoles mounted on each side of a groundwall. The idea is simply that one receive an incoming signal on one set of dipoles and transfer it via cables to the dipoles on the other side. The idea is in fact older than the honeycomb panel discussed in Section 7.7.1 dating back to a report by Baechle [48]. According to Leon Peters Jr., it was not very successful, and today we of course know exactly why: When the scan impedance Z_A of the two arrays is changed with angle of incidence, we observe a mismatch loss from the interconnecting cable. The problem can easily be cured by use of dielectric slabs on the outer surfaces. Further the inter-element spacing was much too large.

7.7 SOME SPECIAL TOPICS

7.7.1 Reflection: Image Lobes

So far we have primarily concentrated on the transmission properties of hybrid radomes. However, the reflection properties merit special consideration. The reason for this is illustrated in Fig. 1.11 where a signal emanating from the array is transmitted through the radome as intended (marked "in band"). In addition to the

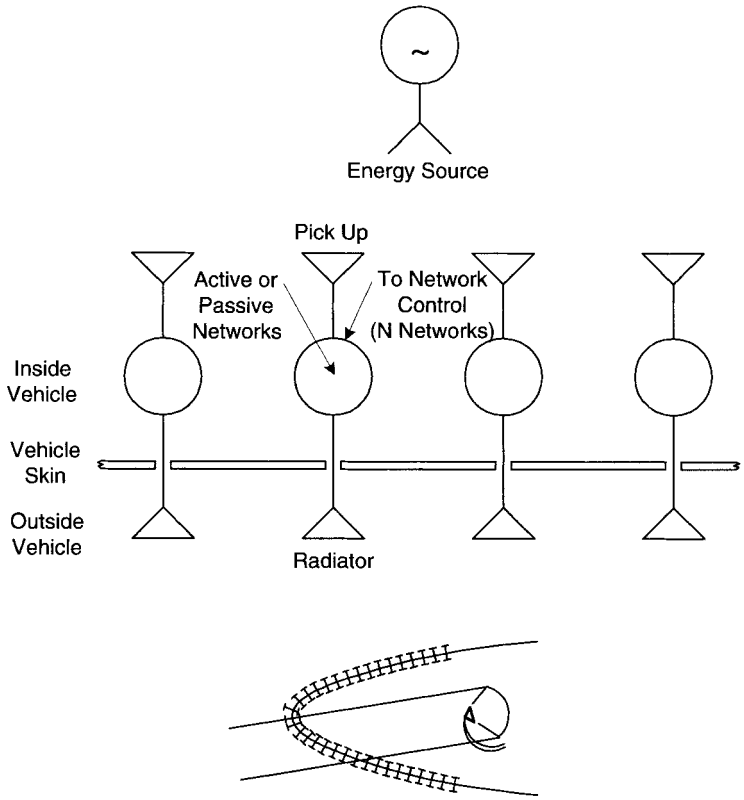

FIGURE 7.16. Concept of the novel metal window.

transmitted field there will also be a field reflected in the bi-static direction as shown. Although the amplitude of this reflected field is small (hopefully!), we realize that it in general will have a direction coinciding with the sidelobes of the antenna. Since that level might be quite low, it becomes obvious that the reflection amplitude should at least be no higher or comparable to the sidelobe level.

As a typical example let us assume that the bi-static reflection coefficient for an infinite hybrid radome is 20 dB. If the shape of the radome is conical as indicated in Fig.1.11, we know from geometrical optics that the reflected field is being reduced by about 6 dB due to spreading. If the radome has double curvature as is the case with an ogival shape, the reflected signal is reduced by an additional 6 dB (i.e., a total of 12 dB). Thus the reflected field will simply create a so-called image lobe that has a peak level of around $20 + 12 = 32$ dB. If this level exceeds the sidelobe level, it could result in false alarms.

Calculation of the reflected field can be done by calculation of the slot voltages in slot array 1 and then finding the reradiated (reflected) signal just as we did for the transmitted field. However, if the radome is lossless, conservation of energy simply

yields for the reflection coefficient

$$R.C. = \sqrt{1 - T.C.^2}. \tag{7.52}$$

As an example let us consider the biplanar case discussed in Section 7.5.2. For the reflection coefficient $R.C._0$ at $y/Y_{0re} = 0$ corresponding to the valley of the transmission curve, we find from (7.52) and (7.39) that

$$R.C._0 = \frac{|Y^{1,2}|/Y_{0re} - Y_{0re}/|Y^{1,2}|}{|Y^{1,2}|/Y_{0re} + Y_{0re}/|Y^{1,2}|}. \tag{7.53}$$

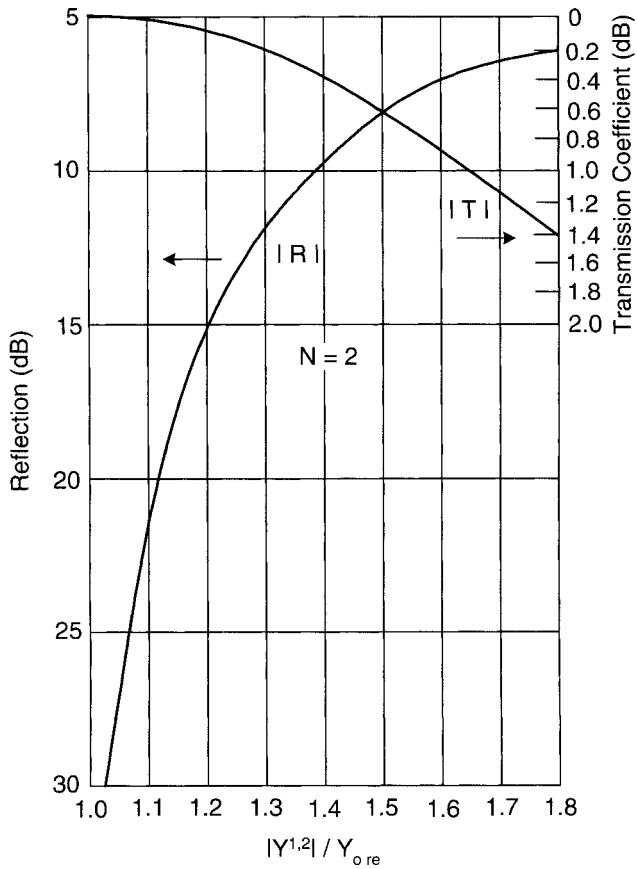

FIGURE 7.17. The necessary (but not sufficient!) conditions that must be imposed on the coupling $|Y^{1,2}|/Y_{0re}$ for the $N = 2$ case to obtain the transmission and reflection level as shown (symmetric design).

We have plotted $T.C._0$ [from (7.39)] as well as $R.C._0$ [from (7.53)] in Fig. 7.17 as a function of $|Y^{1,2}|/Y_{0re}$. We readily observe that to obtain an $R.C._0 > 20$ dB, we must choose $|Y^{1,2}|/Y_{0re} < 1.12$ yielding $T.C._0 <\sim 0.02$ dB.

Obviously, when designing precision radomes, the designer should keep an eye on the reflection curve where the action is, and not to any large degree on $T.C._0$ where very little happens once a certain level is reached. Further illustration of these matters is shown in Fig. 7.18 which shows schematic transmission and reflection curves for a symmetric biplanar hybrid radome as a function of $|Y^{1,2}|/Y_{0re}$.

We finally show in Fig. 7.19 schematic transmission curves for various numbers of slot arrays, namely for $N = 1, 2$, and 3. The 2 and 3 array cases are designed to yield a reflection level of 20 dB. Note the faster falloff as N increases.

7.7.2 Registration Sensitivity

When two periodic surfaces are placed parallel and adjacent to each other, an often asked question is: Should the elements of the two surfaces be on top of each other, or can they be placed arbitrarily with respect to each other?

This question is of great practical importance. For example, when building a hybrid radome, one typically places an FSS and then covers it with a dielectric material. Since dielectric materials in general are opaque, it becomes cumbersome, if not impossible, to keep track of where the elements actually are located. Further, for a curved surface we really have an additional complexity.

The simplest way to alleviate this problem is to design the periodic assembly in such a way that the transmission and reflection properties will exhibit only minute changes as a function of element alignment. We refer to this phenomena as registration sensitivity, and we now plan to examine it in some detail.

Whatever the number of layers in a hybrid radome, we have shown that the maximum transmission as well as the minimum reflection coefficient basically depend only on the ratio $|Y^{1,2}|/Y_{0re}$. For example, the biplanar case is given by (7.39), the triplanar case by (7.47), while the quadru- and quintaplanar cases are given in [40]. We further note that Y_{0re} has nothing to do with registration of the panels whatsoever. Thus we only need to examine $Y^{1,2}$ as a function of registration. Let us denote the position vector for the two reference elements by $\bar{R}^{(1)} = \hat{x}x^{(1)} + \hat{y}y^{(1)} + \hat{z}z^{(1)}$ and $\bar{R}^{(2)} = \hat{x}x^{(2)} + \hat{y}y^{(2)} + \hat{z}z^{(2)}$. Then the mutual admittance $Y^{2,1}$ is according to (6.33) given by

$$Y^{2,1} = \frac{Y_2}{2D_xD_z}\sum_k\sum_n \frac{e^{-j\beta_2(x^{(2)}-x^{(1)})r_{2x}}e^{-j\beta_2(z^{(2)}-z^{(1)})r_{2z}}}{r_{2y}}$$
$$\left[{}_\perp P_2^{(1)}\,{}_\perp P_2^{(2)t} + {}_\parallel P_2^{(1)}\,{}_\parallel P_2^{(2)t}\right]\frac{2j}{\sin(\beta_2 d_2 r_{2y})}. \tag{7.54}$$

where $d_2 = y^{(2)} - y^{(1)}$. Alternatively, (7.54) can be written

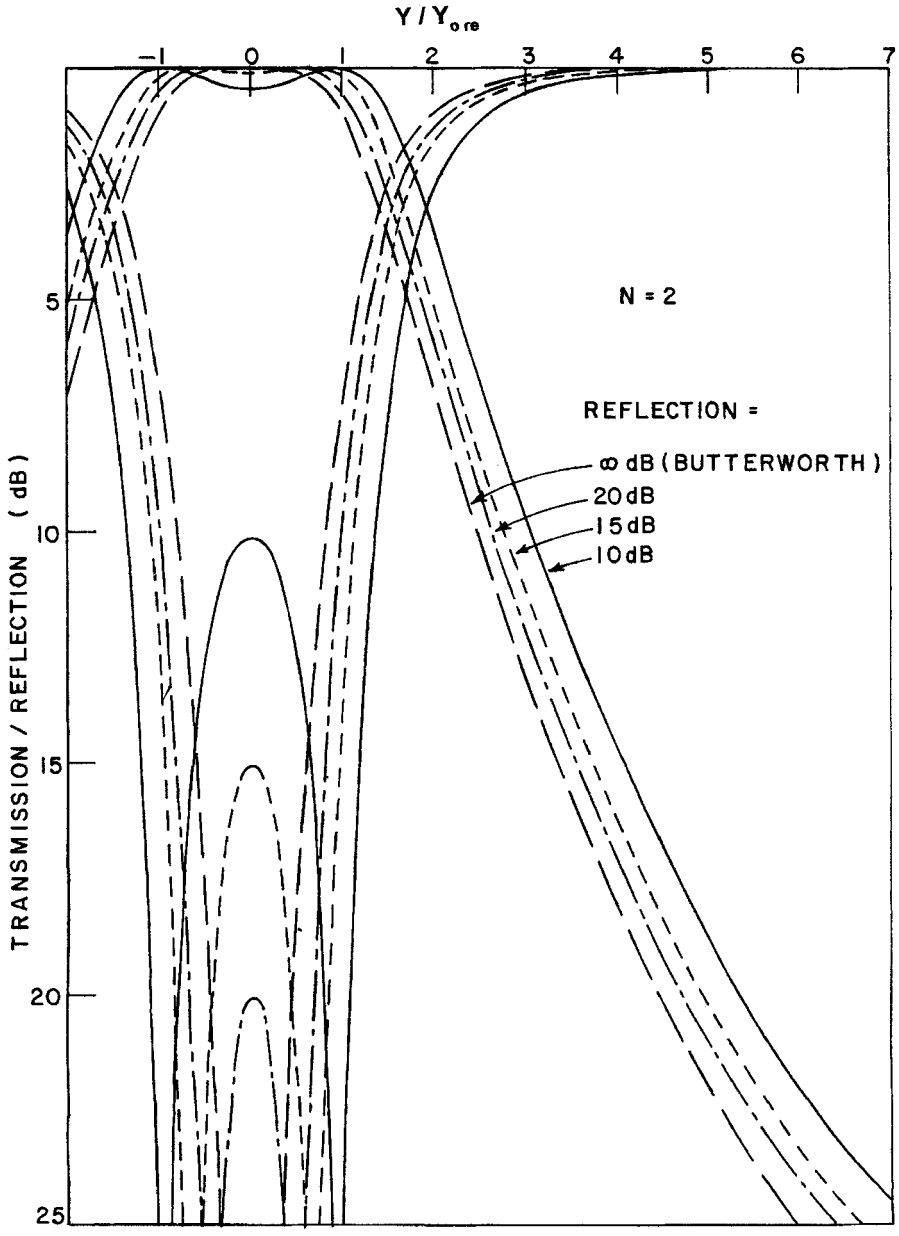

FIGURE 7.18. Schematic transmission and reflection curves for the symmetric $N = 2$ layers case. Four designs are shown: Butterworth and three Chebyshev cases with maximum reflection levels of 10, 15, and 20 dB, respectively.

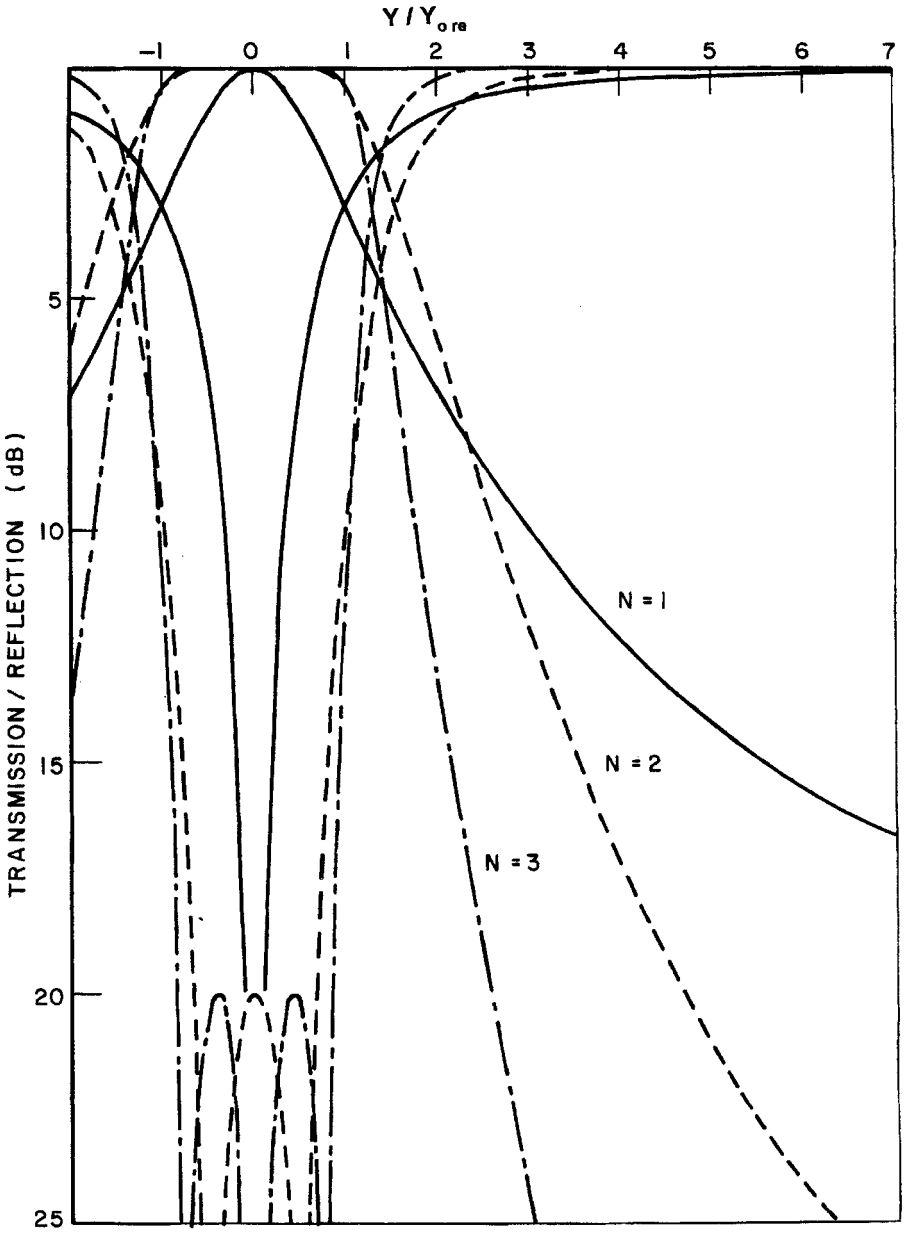

FIGURE 7.19. Schematic transmission and reflection curves for $N = 1, 2$, and 3 layers. The 2- and 3-layered cases have both been designed for a maximum reflection level of 20 dB.

$$Y^{2,1} = \frac{Y_2}{2D_xD_z}\sum_k\sum_n \frac{e^{-j\beta_2(x^{(2)}-x^{(1)})r_{2x}}e^{-j\beta_2(z^{(2)}-z^{(1)})r_{2z}}}{r_{2y}}$$
$$\left[{}_\perp P_2^{(1)}\,{}_\perp P_2^{(2)t} + {}_\parallel P_2^{(1)}\,{}_\parallel P_2^{(2)t}\right]\frac{-4e^{-j\beta_2 d_2 r_{2y}}}{1-e^{-j2\beta_2 d_2 r_{2y}}}. \tag{7.55}$$

We further recall that the plane wave spectrum in (7.54) as well as (7.55) consist of a single propagating mode for $k, n = 0, 0$ (when there are no grating lobes) and an infinite number of evanescent modes. The propagating mode is in general easiest to analyze by using (7.54). Similarly the evanescent modes can in general be estimated simplest by using (7.55), in particular if the array separation $d_2 >\sim \lambda_2/4$. In this case we typically have

$$e^{-j\beta_2 d_2 r_{2y}} << 1 \qquad \text{for } k, n \neq 0, 0. \tag{7.56}$$

Note that for the slot mutual admittance $Y^{2,1}$ both the propagating $(k, n = 0, 0)$ as well as the evanescent modes are purely imaginary.

We further recall that

$$r_{2x} = s_{2x} + \frac{k\lambda_2}{D_x} \quad \text{and} \quad r_{2z} = s_{2z} + \frac{n\lambda_2}{D_z}. \tag{7.57}$$

In particular, for $k, n = \pm 1, 0$ we obtain from (7.55) and use of Euler's law in conjunction with (7.56) and (7.57):

$$\text{Modes} \quad (\pm 1, 0) = \frac{Y_2}{2D_xD_z}e^{-j\beta_2(x^{(2)}-x^{(1)})s_{2x}}e^{-j\beta_2(z^{(2)}-z^{(1)})s_{2z}}\frac{1}{r_{2y}(\pm 1, 0)}$$
$$2\cos\left(\beta_2(x^{(2)}-x^{(1)})\frac{\lambda_2}{D_z}\right)$$
$$\left[{}_\perp P_2^{(1)}\,{}_\perp P_2^{(2)} + {}_\parallel P_2^{(1)}\,{}_\parallel P_2^{(2)}\right]_{k,n=\pm 1,0} 4e^{-j\beta_2 d_2 r_{2y}(\pm 1,0)} \tag{7.58}$$

as depicted in Fig. 7.20. By use of (5.6), (5.7), (5.11), and (5.12), it is easy to show that for z-directed elements

$$\left[{}_\perp P_2^{(1)}\,{}_\perp P_2^{(2)} + {}_\parallel P_2^{(1)}\,{}_\parallel P_2^{(2)}\right]_{k,n=\pm 1,0} = \left[{}_\perp P_2^{(1)}\,{}_\perp P_2^{(2)} + {}_\parallel P_2^{(1)}\,{}_\parallel P_2^{(2)}\right]_{k,n=0,0}. \tag{7.59}$$

From (7.58) and (7.54) we then find by use of (7.59) for the ratio between the lowest-order evanescent mode $k, n = \pm 1, 0$ and the propagating modes: $k, n = 0, 0$:

$$\frac{\text{Modes} \quad (\pm 1, 0)}{\text{Mode} \quad (0, 0)} = \frac{r_{2y}(0, 0)}{r_{2y}(\pm 1, 0)}2\cos\left(\beta_2(x^{(2)}-x^{(1)})\frac{\lambda_2}{D_x}\right)$$
$$\frac{4e^{-j\beta_2 d_2 r_{2y}(\pm 1,0)}}{2j}\sin\left(\beta_2 d_2 r_{2y}(0, 0)\right). \tag{7.60}$$

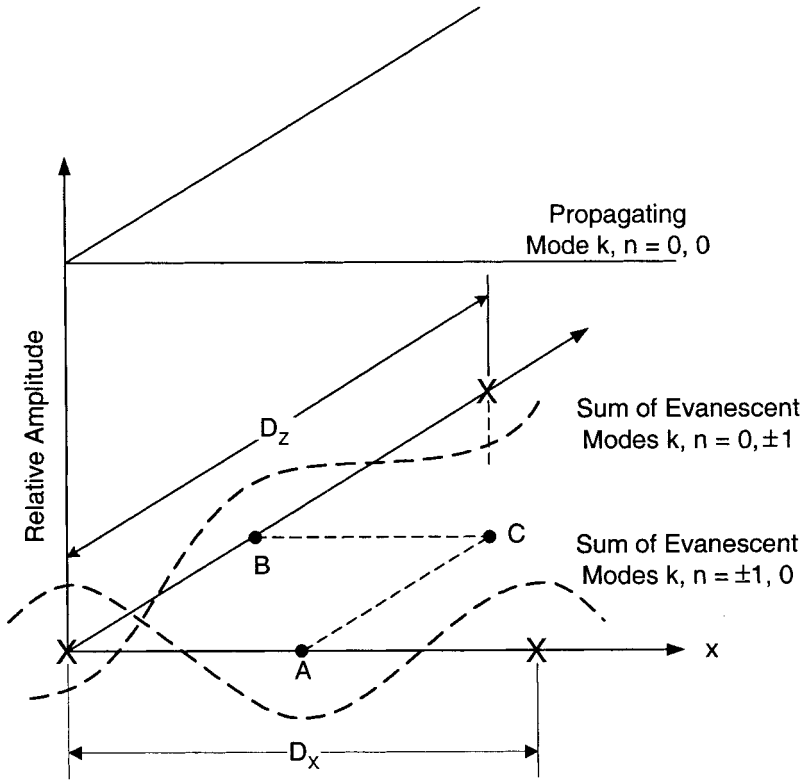

FIGURE 7.20. Typical behavior of the lowest-order evanescent modes.

If the elements of the two arrays are placed on top of each other, we have

$$x^{(2)} - x^{(1)} = 0 \qquad \text{i.e., } \cos\beta_2(x^{(2)} - x^{(1)})\frac{\lambda_2}{D_x} = 1. \tag{7.61}$$

Further, if they are interlaced by $x^{(2)} - x^{(1)}$ (point A in Fig. 7.20), we find that

$$\cos\beta_2\frac{D_x}{2}\frac{\lambda_2}{D_x} = -1. \tag{7.62}$$

Thus the maximum variation is then obtained from (7.60) by use of (7.61) and (7.62):

$$\frac{\text{Modes}\quad(\pm1, 0)}{\text{Mode}\quad(0, 0)} = \frac{r_{2y}(0, 0)}{r_{2y}(\pm1, 0)}2 \cdot 2\frac{4e^{-j\beta_2 d_2 r_{2y}(\pm1,0)}}{2j}\sin\left(\beta_2 d_2 r_{2y}(0, 0)\right). \tag{7.63}$$

Let us now further assume that $d_2 \sim \frac{1}{3}\lambda_2$ (typical). For $r_{2y}(0, 0) = 1$, we have

$$\sin\left(\beta_2 d_2 r_{2y}\right) = 0.95. \tag{7.64}$$

Substituting (7.64) and (7.63) for $r_{2y} = 1$ yields

$$\frac{\text{Modes} \quad (\pm 1, 0)}{\text{Mode} \quad (0, 0)} = 7.6 \frac{e^{-\beta_2 d_2 |r_{2y}(\pm 1, 0)|}}{|r_{2y}(\pm 1, 0)|}, \tag{7.65}$$

where

$$|r_{2y}(\pm 1, 0)| = \sqrt{\left(\frac{\lambda_2}{D_x}\right)^2 - 1}. \tag{7.66}$$

Typically let us require the reflection coefficient to be better than around 22 dB. From Fig. 7.17 we then see that we must require $|Y^{1,2}|/Y_{0re} \leq 1.1$. We further stipulate that the reflection coefficient should vary no more than a couple of dB. From Fig. 7.17 we then observe that $|Y^{1,2}|/Y_{0re}$ should vary no more than about $\pm 2\%$, for a total variation of 4%. Substituting this value into (7.65) yields

$$0.04 = 7.6 \frac{e^{-\beta_2 d_2 |r_{2y}(\pm 1, 0)|}}{|r_{2y}(\pm 1, 0)|} \qquad \text{for a } \pm 2 \text{ dB variation around 22 dB.} \tag{7.67}$$

Solving (7.67) for $d_2 = \frac{1}{3}\lambda_2$ yields with (7.66),

$$D_x \sim 0.34\lambda_2 \tag{7.68}$$

for a reflection of 22 ± 2 dB.

If we make a displacement along the z-axis (point B in Fig. 7.20), the approach remains the same as for the x-axis above except that the left side of (7.59) is multiplied by $r_{2y}^2(0, \pm 1)$ [show this by use of (5.6), (5.7), (5.11),and (5.12)].

Thus (7.67) should be modified to

$$0.04 = -7.6 \frac{-\beta_2 d_2 |r_{2y}(0, \pm 1)|}{|r_{2y}(0, \pm 1)|} |r_{2y}(0, \pm 1)|^2. \tag{7.69}$$

Solving (7.69) for $d_2 = \frac{1}{3}\lambda_2$ yields, when substituting D_z for D_x (7.66),

$$D_z \sim 0.29\lambda_2 \tag{7.70}$$

for a reflection of 22 ± 2 dB.

Note that the negative sign in (7.69) originates from

$$\left(-j r_{2y}(0, \pm 1)\right)^2 = -|r_{2y}(0, \pm 1)|^2.$$

This is observed in Fig. 7.20 for the variation along the z-axis. Thus we may anticipate that the change in reflection is rather small when the elements are located halfway between *both* the x- and z-directions (i.e., point C in Fig. 7.20).

The calculations above are only approximate. However, the conclusion is quite clear: Keeping the inter-element spacings D_x and D_z of a periodic surface small

($<\sim 0.30\lambda_2$) is extremely important when designing high-quality radomes. Obviously only a handful of elements will qualify, most notoriously, the loop types shown in Fig. 2.2, group 2, and also group 1, the center connected or N-poles. Least suitable is group 3, the solid interior or plate types.

Typically one can obtain two (or more) values of d_2 yielding the proper value of $Y^{1,2}$, namely one a little below $\lambda_2/4$ and one slightly above. However, we should realize that the greatest attenuation of the evanescent waves comes from the exponential term $e^{-j\beta_2 d_2 r_{2y}}$. Thus from a registration sensitivity point of view, it will in general be preferable to choose the larger value of d_2. However, we do not choose $d_2 > \lambda_2/2$, since this in general leads to instability with angle of incidence. Put in simple terms, a spacing of $d_2 = \lambda_2/2$ will at normal incidence have $\beta_2 d_2 r_{2y} = \pi$, and for 60° in Y_2 be equal to $\pi/2$. These two cases will in general be the extreme opposites of each other and lead to profound differences of the transmission curves as the angle of incidence varies.

7.7.3 Luebbers' Anomaly

We note that the leading term of $Y^{2,1}$ as given by (7.41) is negative imaginary. This observation is in general of no great consequence, since we really only need the magnitude of $Y^{1,2}$ when calculating the transmission [see (7.17)].

However, when the lowest-order evanescent mode is about to become a grating lobe, we readily observe by inspection of (7.40) that it will have a positive imaginary singularity. In other words, some time before the onset of a grating lobe in d_2, we will have the leading term and the lowest-order evanescent wave canceling each other resulting in zero coupling $Y^{1,2}$. From (7.37) we readily see that it results in $\mathcal{P}_2 \to \infty$; that is, the transmission coefficient equals zero. This null is highly unusual because most grating lobe related phenomena in periodic surfaces occur after the onset of the grating lobe, while this phenomenon takes place before the onset.

It is called Luebbers' anomaly [45, 46, 47] after one of the author's former students who first demonstrated its presence by calculation. When the radome panel was mechanically improved, the anomaly was first actually measured. Like many nulls it is highly temperamental.

7.8 COMMON MISCONCEPTIONS ABOUT THE DESIGN OF HYBRID RADOMES

7.8.1 Choice of Elements

Typically the inexperienced engineer will start the design of hybrid radomes by asking the classical question: What is the best element?

Well, is it just that simple! Consider as an example the monoplanar cases in Section 7.5.1. If one is merely interested in the frequency range from resonance downward, both the four-legged loaded and the three-legged unloaded elements shown

in Figs. 7.5 and 7.6, respectively, do a fair job. However, if we are interested in the range from the resonance and upward, the three-legged might be a disaster because of the modal interaction nulls around 17 GHz. On the other hand, as shown in [49], the three-legged element is superior to the four-legged loaded element with respect to cross-polarization. And the list goes on. In other words, many questions must be asked before the original question can be answered. (For an extensive review of elements, see Chapter 2.)

7.8.2 Dielectric Profile

Another typical misconception is that the transmission curves are primarily determined by the slot arrays alone and that the dielectric between them merely serves as spacers only and consequently should have as low a dielectric constant as possible, like foam with $\epsilon < 1.1$. Well, inspection of several transmission curves with and without dielectric slabs should quickly instruct the reader to the contrary, as illustrated in Figs. 7.5, 7.6, 7.7, 7.9 and 7.12. (See also a very instructive series of cases shown in Fig. 1.18.) In other words, the dielectric profile plays the most important role in the design of hybrid radomes in maintaining a constant bandwidth and a flat top; in fact it does in periodic surfaces in general.

7.8.3 Inter-element Spacings

Every novice in the area of periodic surfaces (and phased arrays) knows that the variation with angle of incidence is caused by the mutual coupling between adjacent elements. (Actually the mutual element coupling is independent of the incident angle. It is merely the phases of the induced element currents that changes with angle of incidence.)

It is further well known that the mutual coupling decreases as we increase the inter-element spacings. So why should we not try to increase the inter-element spacings to reduce mutual coupling?

The reason is very simply that this will lead to earlier onset of grating lobes (see Section 1.9). As we saw in Chapter 6, the onset of grating lobes can in some scan planes lead to $y \rightarrow \infty$ which will produce a very characteristic grating lobe null in the transmission curves. Such a null is very powerful; it in fact is so powerful that it can push the original resonant frequency lower. In particular, if the onset of grating lobes moves lower in frequency with angle of incidence, the lower resonant frequency, will cause an instability of the resonant frequency with angle of incidence.

The conclusion is clear: Use small inter-element spacings which simply require use of small elements (see Chapter 2).

One might ask: So what exactly happened with the increased mutual admittance between elements? Well, the magnitude does go up, but only the *real* part which leads to a higher value of Y_{0re}, namely more bandwidth. The *imaginary* part is reduced leading to stability of the resonant frequency with angle of incidence.

This really should not surprise us. Recall how Wheeler [50] in the early days used continuous current sheets rather than elements when modeling arrays. His sheets had no reactance, only radiation resistance.

7.8.4 Mutual Admittance $Y^{1,2}$

The importance of choosing a proper value of $Y^{1,2}$ or any other mutual admittance in the general N-layered case was demonstrated several times in this chapter. The mutual admittance plays a key role in obtaining a sufficient small valley in the Chebyshev design, or more precisely in obtaining a low level of reflection (see Section 7.7.1).

Quite often the designer thinks that a lower value of $|Y^{1,2}|$ is obtained merely by increasing the array separation d_2. Obviously this expectation is based on the mutual admittance between two single elements which is reduced proportional to $1/d_{12}$ or $1/d_{12}^2$. In the large array case, however, we are basically dealing with plane waves that never change amplitude. In fact, in this case, we are dealing with plane waves bouncing between the two slot arrays. That results in a mutual admittance that has a minimum for $\beta_2 d_2 r_{2y} \sim \pi/2$, while it increases for shorter or longer separations of d_2; see (7.40) and Section 6.6. Conclusion: Use the expression for $Y^{1,2}$, not your intuition. (Intuition is great, we all rely on it to a large extent. However, we must hone it every day to conform with the realities of life and not to comply with some cockeyed idea or misconception.)

7.8.5 Practicality of the Designs

It is by now fairly clear that in order to obtain a constant bandwidth with angle of incidence we must, regardless of element type, number of arrays or thickness of the FSS screens, use outer dielectric slabs of rather low dielectric constant and a thickness of around 0.3λ (at least as long as the elements are planar). The reaction of many people is quite simple that "we just don't have dielectric constants that low, and if we do, it is not mechanically suitable."

Well, one approach would of course be to put the materials engineers to work! While this author cannot comment on what materials scientists might be able to come up with, he can at least emphatically state that there are solutions to this problem so simple that they are left as an exercise for the student.

7.8.6 On Optimization

Everyone in this day and age has certainly heard something about optimization programs. There is an abundance of approaches out there, many of them with very imaginative names, some of them even referring to what at least used to be unspeakable: sex!

Now let there be no doubt that this writer is not at all opposed to that subject. On the contrary, how else would we all be here. However, it should be applied at the proper place and proper time.

More specifically, none of the designs presented in this chapter were arrived at by an optimization process. They are the results of analysis which derives from the Greek word *analyein*, meaning to take something apart and to investigate each of its components.

Certainly there can be no doubt that every design in this chapter could benefit from going through an optimization process. In fact, for a serious application, this writer strongly recommends just that and has done so himself many times.

However, to arrive from say Fig. 7.9 top to the design at the bottom by pure optimization would be rather questionable because we most likely would have to calculate a substantial part of many, many cases.

An upper limit of this number can be estimated by the following line of thought for $N = 2$. Let us assume that we are smart enough to limit our investigation to the symmetric case and assume that the dielectric constant $\epsilon_1 = \epsilon_3$ should vary all the way from $\epsilon_1 = 1$ to 4 in steps of 0.1; that is, we would have to run through $4/0.1 = 40$ cases. Each of these should be tested for slab thicknesses ranging from say 0.1λ to 0.6λ in steps of at least 0.025λ, that is, $0.5/0.025 = 20$ cases. Similarly the slab in the middle should be tested with about the same density or $40 \times 20 = 800$ cases.

Thus the total number of test cases would at most be $800^2 = 640{,}000$ at each angle of incidence and polarization. A fast program and computer are needed here. However, in real life the worst is that most inexperienced designers most likely would not even start with something as inferior looking as Fig. 7.9 top, where the bandwidth as well as the resonant frequency varies all over. In fact a computer program would most likely recognize this transmission curve as "bad" and not allow it to go on in the "mating game." Further there may be numerous false alarms on the way to "perfection." For example, it is entirely possible to use $\epsilon_1 = \epsilon_3 = 4$ with an electric thickness of $\sim 0.1\lambda$ to obtain limited success. Inspection of the T-function, however, will readily show that this will result in a large imaginary impedance component for higher oblique angles of incidence. Now that can easily be tuned out by the reactance of the slot array. The problem is simply that such a design fails for even moderate angles of incidence variations and/or polarizations. Again, the computer readily gets hooked by this apparently "good" solution.

Furthermore most designers would probably not even pay much attention to the dielectric profile but instead concentrate on the "mysteries" of the various element designs and dimensions where typically the inter-element spacings D_x and D_z, and the like, are varied all over without any respect for grating lobe nor stability of the resonant frequency and cross-polarization. In short, it would be a challenge even for a very fast computer to sort out this mess. Typically one of the biggest problems in this optimization procedure is for the designer to state to the computer what is "good" and what is "bad." It is simply not unusual that the "best" result is obtained by mating two "bad" parents! (See also Chapter 9 on circuit analog absorbers.)

7.8.7 Biplanar versus Multilayered Designs

Most readers expect the multilayered hybrid radome to have a faster roll-off and possible smaller ripples on the top than for example a biplanar design. The analysis presented in the chapter certainly proves them to be correct; see Fig. 7.19. However, the analysis contains an element of deception (well, after all, this is the author's primary business).

The problem with the three-layered design lies in (7.42), namely that we assume that

$$y^{2,2} = a_2 y.$$

Clearly, we merely state that the array admittance $y^{2,2}$ in the middle has the same resonant frequency as the outer arrays and a slope relative to these determined by a_2. This condition can always be satisfied at some angle of incidence and polarization. However, as we change the angle of incidence, both $y^{2,2}$ and y will change somewhat with frequency and unfortunately not necessarily by the same amount. In other words, the inside array does not "track" the two outside arrays with angle of incidence and polarization. And why should they? After all, the outer arrays are in an environment with free space to one side (via a dielectric slab) and a ground plane to the other, namely the middle array with the slots short-circuited. And the middle array is bounded by ground planes to each side. In other words, the relationship between $y^{2,2}$ and y looks approximately as

$$y^{2,2} = a_2 y + \Delta(s_x, s_z), \tag{7.71}$$

where $\Delta(s_x, s_z)$ is the tracking term depending on the angle of incidence. A close investigation has shown that the reflection level for arrays of three or more arrays is quite sensitive to $\Delta(s_x, s_z)$. To put it in simple terms, not until we learn to keep $\Delta(s_x, s_z)$ sufficiently low will it be worthwhile to use an optimization process on multiple layers, unless inferior reflection levels can be tolerated.

When these matters are discussed with my many friends in industry, I often get a polite look that clearly say something like "Well, young man (!), we have more money and bigger computers than you have!" While I certainly agree with that, I still have to see a good solution to this problem. In fact, if anyone out there figures it out, my advice would be: "Don't tell anyone! Just call me! I will be at your doorstep the next morning!"

7.8.8 Thick Screen Radomes

When working with thick panels the designer will often focus primarily on the element types. Typically the designer starts with circular holes filled with a dielectric material usually with high ϵ. This may lead to a design suitable for his or her particular need, but very often the designer will go on to more sophisticated elements such as circular holes filled with a dielectric and a center conductor, that is, looking similar to a coaxial cable seen from the end.

This new design may well look quite superior to the first case, and one is tempted to immediately conclude that the second element is far superior to the first. Actually this is because we have merely transformed the plate element into a loop element which is far superior anytime to the first element type (see Section 2.4). However, one of the author's colleagues tried it out and was not particularly impressed. Why the discrepancy? Well, someone forgot or did not think that it was important to mention that the "good" panel must have dielectric slabs on the outside, which happened to

have a thickness of about $0.3\lambda_\epsilon$ and $\epsilon_r \sim 1.5$. As we have investigated in great detail several times before, these slabs can lead to scan independence as the angle of incidence varies. Since the mutual admittance between the two inside arrays located at each end of the "waveguides" is distinctly scan independent no matter what is done inside the waveguides, it becomes clear that in order to satisfy (7.38) and (7.39) for scan independence, the outside array must also be scan independent. In other words, while it is necessary to use a "good" element, such as the loop element (it is small!), it is not sufficient. We must also use properly designed dielectric slabs on the outside. Again, the fact is simply that no matter what fancy stuff you may put inside the waveguides, they are inherently scan independent while the outside is scan dependent unless compensated. No amount of mindless computations can ever make up for that. (To be sure , some elements are just a little better than others with respect to having constant bandwidth, but for angles greater than 45° much more powerful medicine is needed!)

Finally: How does the thick panel design compare with a typical classical hybrid radome design? Well, I have not seen a thick panel design better than the biplanar design shown in Fig. 7.9. And I regret that I cannot even show how good that one can really be!

7.8.9 Accuracy of the Analysis

Quite often designers of hybrid radomes are surprised to find that the approximate analysis presented earlier yields design guidance as accurate and reliable as it does. We remind the reader that this is based on the assumption that the current distribution on the elements does not change shape but only amplitude and phase as the angle of incidence change. This requirement is satisfied reasonably well for a four-legged loaded element in Fig. 7.5 but not for the three-legged element in Fig. 7.6 when the odd mode distorts the current distribution for oblique angle of incidence.

Thus the analysis fails in the latter case, and we do not observe a constant bandwidth with angle of incidence. As stated several times before, the trick is to use elements so compact that only the fundamental current distribution is likely at least in the resonant region.

We emphasize that all the calculated curves were obtained using the PMM program with an appropriate number of section modes. However, there is in general very little to be gained by using an optimization process once the fundamental design based on the analysis above is laid out.

7.9 CONCLUDING REMARKS

In this chapter we have considered the transmission properties of slotted periodic surfaces in a stratified medium. We found that a reasonably stable resonant frequency with angle of incidence could be obtained by keeping the inter-element spacings D_x and D_z relatively small in terms of a wavelength. Further we demonstrated that

the bandwidth of the transmission curves without dielectric compensation in general varied significantly with angle of incidence and polarizations (actually as much as $1/\cos^2 \eta = 1/\cos^2 70 = 11{:}1$ unless something else reduces the bandwidth, e.g., modal interaction nulls or the onset of grating lobes).

We have further demonstrated that adding dielectric slabs on the outside of all narrow-band space filters whether they are monoplanar or multiplanar can be designed to reduce the typical bandwidth variation from as much as 6.5:1 to less than 1.5:1 (for 70° angle of incidence, $\perp$ or $\parallel$ polarization). The value of the dielectric constant as well as the slab thickness, or in short the dielectric profile is extremely important. To some extent it depends on the element type, but typical values of ϵ would be < 1.6 and with a thickness of about 0.25λ to $0.45\lambda_1$. When multiplied with r_{1y} the electrical thickness would typically be around $\lambda_1/4$. It is essential to choose this thickness (at least approximately), since we rely on an impedance transformation as expressed by the transformation function T_1.

We also demonstrated that the flatness (or the ripples) depended on the dielectric profile in general as well as the inter-array spacings.

But the most important issue (at least to this writer) is the approach we took to obtain these results. None were arrived at by optimization, neither simple nor more sophisticated. Instead, we analyzed the workings of almost every major component that could possibly go into the design of a hybrid radome. In particular, we found that the outer dielectric slabs were almost totally responsible for maintaining a constant bandwidth regardless of the number of slot arrays. Moreover the electrical properties, such as the dielectric constants ϵ_n and slab thicknesses d_n, were determined within a rather narrow range (e.g., ϵ_1 should be chosen rather low such as less than 1.6). Further the top of the resonant curve should be flat. Had we instead optimized a biplanar design, it may not have provided us with much of a clue about how to attack the multilayered designs. Nor would the designer be likely to filter out what is caused by element dimensions and types and what is related to the dielectric profile. Remember, everything has to be just right for *all* angles of incidence and polarizations.

Now, could a nondielectric case such as the biplanar case in Fig. 7.9, top, have been improved by proper use of an optimization process? The answer is: Certainly. Everything can eventually be made better in some respect. However, we would never obtain significant equalization of the bandwidth for orthogonal and parallel polarization. Use of a circular or hexagonal loop would bring only a minor improvement to the table, still far short of what is needed at high angles of incidence. Thus there is simply very little incentive for optimizing a design that simply is known a priori (or should have been known) not to be able to show much promise.

But what about relaxing the constant bandwidth requirement and be happy with just a flat top of the transmission curve? Well as we have seen in the analysis earlier the dip of the transmission curve depends essentially on the ratio $|Y^{1,2}|/Y_{0re}$. Now, since Y_{0re} varies significantly with angle of incidence (for no outer dielectric) and since $|Y^{1,2}|$ is fairly constant with angle of incidence, it is clear that the ratio between these two parameters will quickly move out of the proper (very narrow) range required for maintaining a flat top (i.e., low reflection).

The conclusion of the discussion above is: Don't waste valuable computer time and power calculating and optimizing designs that the designer should know ahead of time can never produce anything but mediocre results.

This writer views with some concern today's tendency to rely too much on decisions made solely by computers that do not have the necessary insight to make the right choices except in certain relatively simple cases.

7.10 PROBLEMS

7.1 General Monoplanar Hybrid Radome Given, a single FSS comprised of z-directed slots. It is bounded to the left by a dielectric slab of thickness d_1 and to the right by another of thickness d_2 as shown in Fig. P7.1. The intrinsic admittances of both slabs are Y_1. A plane wave with direction of propagation $\hat{r}_0$ is incident upon this panel from the left.

We will investigate the transmission properties of this panel for no grating lobes. We will limit our analysis to the principal planes and will as usual denote the pattern components by $\underset{\|}{\perp} P_1$ and $\underset{\|}{\perp} P_1^I$.

a. Find the current I^i induced in the FSS reference element.

b. Find the slot voltage at the reference point expressed by I^i and $Y_A = Y_{A1} + Y_{A2}$.

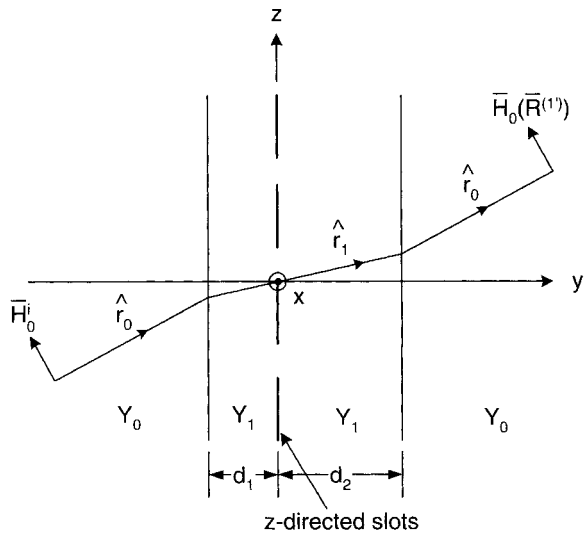

Fig. P7.1a

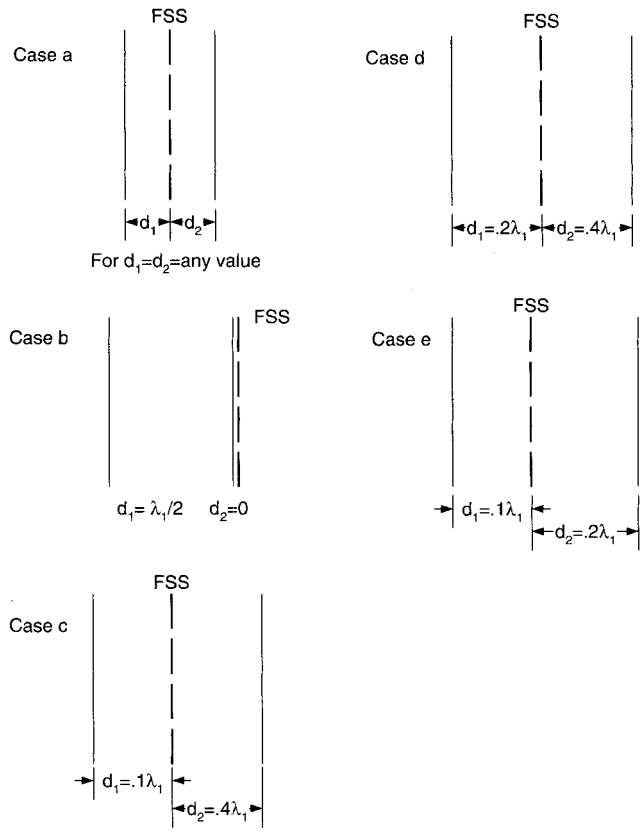

Fig. P7.1b

c. Find the field $\bar{H}_0(\bar{R}^{(1')})$ at point $\bar{R}^{(1')}$ located so far from the radome panel that only the propagating mode is present. Express $\bar{H}_0(\bar{R}^{(1')})$ by V, pattern components, $\underset{\perp}{\overset{H}{\underset{\parallel}{}}} W_1$, $\underset{\parallel}{\perp}\tau_{2+}$, and so on.

d. If we tune the FSS for the best possible transmission, prove that the magnitude of the transmission coefficient in that case is given by

$$\frac{\bar{H}_0(\bar{R}^{(1')})}{\underset{\parallel}{\perp} H_{b0}} = \underset{\parallel}{\perp}\hat{n}_0 \frac{2}{\left|1 - \underset{\parallel}{\overset{H}{\perp}}\Gamma_{1-}e^{-j2\beta_1 d_1 r_{1y}}\right| + \left|1 - \underset{\parallel}{\overset{H}{\perp}}\Gamma_{1-}e^{-j2\beta_1 d_2 r_{1y}}\right|}$$

(for principal planes only and no grating lobes!).

e. Find the condition for lossless transmission assuming the FSS is tuned for best transmission. Assume normal angle of incidence.

f. The condition in item e should reveal that not even a simple FSS located in a stratified medium is assured perfect transmission. To further illustrate this point use condition e to pinpoint which designs below are lossless (under best conditions) and which are not.

This problem illustrates the superiority of a symmetric versus an asymmetric design.

7.2 Equivalent Transmission Line Approach An alternate (and physically very appealing) way to check the transmission properties of a hybrid radome is to use the equivalent transmission line approach shown in Fig. P7.2 for a monoplanar radome panel. You simply find the input impedance (use a Smith chart). If it is in the center at Y_0, the panel is lossless; otherwise, it is not!

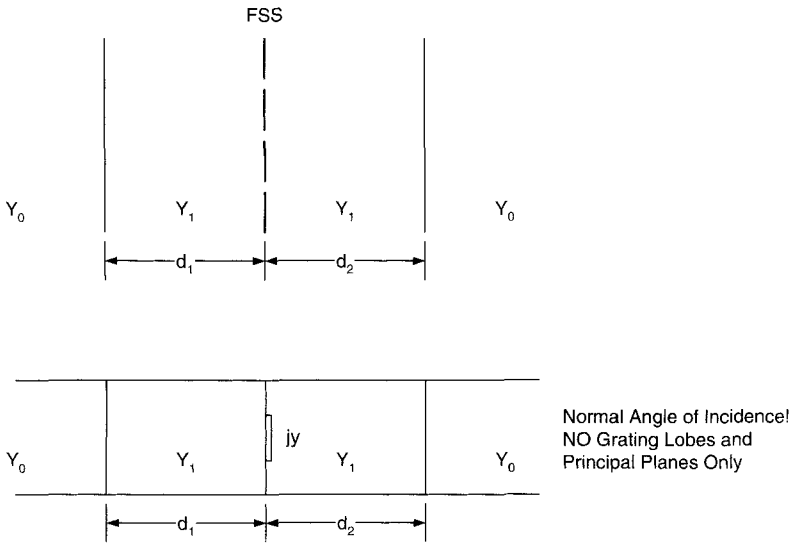

Fig. P7.2

Check all the cases in Problem 7.1. *Note:* The FSS susceptance jy can be adjusted to any value leading to maximum transmission. (See also Fig. 1.18.)

7.3 Biplanar Symmetric Hybrid Radome Ideally the transmission through a hybrid radome should be obtained using real FSS elements and the computer program PMM. However, since it is not readily available, we will resort to the transmission line approach as shown in Fig. P7.3.

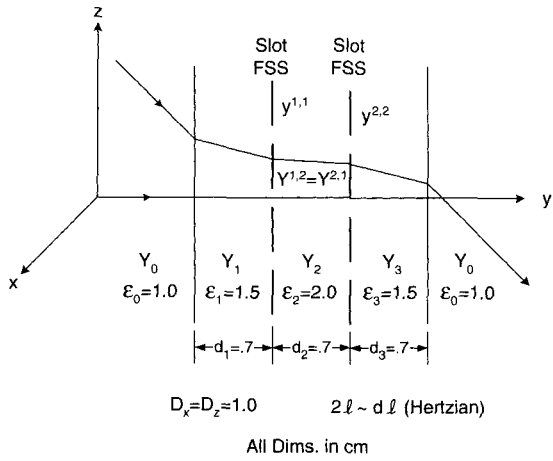

Fig. P7.3

You are required to find the transmission curves $|\mathcal{T}|$ for the biplanar hybrid radome design shown above. However, we suggest to use a simplified approach that will avoid the necessity of writing a computer program based on the plane wave expansion (PWE).

We will assume z-directed slots. We have for the transmission curve for a biplanar symmetric hybrid radome:

$$|\mathcal{T}| = \frac{1}{\sqrt{1+\mathcal{P}_2^2}}, \tag{P7.3-1}$$

where the polynomial $\mathcal{P}_2$ is given by

$$\mathcal{P}_2 = \frac{|Y^{1,2}|}{2Y_{ore}}\left[\left(\frac{y}{|Y^{1,2}|}\right)^2 - \left(1-\left(\frac{Y_{ore}}{|Y^{1,2}|}\right)^2\right)\right] \tag{P7.3-2}$$

and where

$$Y_{ore} = ReY^{1,1} = ReY^{2,2} = Re\frac{Y_1}{2D_xD_z}\frac{1}{r_{1y}}\left[{}_{\perp}P_1^2{}_{\perp}T_1 + {}_{\parallel}P_1^2{}_{\parallel}T_1\right]. \tag{P7.3-3}$$

Further the mutual admittances $Y^{1,2} = Y^{2,1}$ are approximated by using only the leading term in the PWE; that is, $k = n = 0$,

$$Y^{1,2} \sim \frac{Y_2}{2D_xD_z}\frac{e^{-j\beta d_2 r_{2y}}}{r_{2y}}\left[{}_{\perp}P_2^2{}_{\perp}T_2 + {}_{\parallel}P_2^2{}_{\parallel}T_2\right], \tag{P7.3-4}$$

where

$$\begin{matrix}\perp \\ \parallel\end{matrix} T_2 = \frac{\left[1+\Gamma e^{-j0}\right]\left[1+\Gamma e^{-j0}\right]}{1-\Gamma\Gamma e^{-j2\beta_2 d_2 r_{y2}}} = \frac{4}{e^{-j\beta_2 d_2 r_{y2}} 2j \sin \beta_2 d_2 r_{y2}} \qquad (\Gamma = 1). \tag{P7.3-5}$$

Finally we approximate $ImY^{1,1}$ by

$$y = ImY^{1,1} = ImY^{2,2} = C_1(f - f_0), \tag{P7.3-6}$$

where $Y^{1,1}$ is the total admittance of the FSS including ground plane effects from the other FSS, load admittance (if any), and so on. That is, you do not have to go into the imaginary space. C_1 is a constant to be determined later. $f_0 = 10$ GHz denotes the resonance frequency.

It is suggested that you proceed as follows:

a. For a given r_{0y} determine r_{1y} and r_{2y} (see Section 5.2).

b. Evaluate P_1 and P_2 in visible space in mediums 1 and 2, respectively, assuming the elements to be Hertzian elements of length $dl = 0.2D_x$ and constant current. You may later assume P_1 and P_2 to be scan independent in visible space.

c. Evaluate $_\perp P_1$ and $_\parallel P_1$ as well as $_\perp P_2$ and $_\parallel P_2$.

d. Evaluate $_\perp T$ and $_\parallel T$ for slabs 1 and 2 [compare with (P7.3-5) above].

e. Evaluate and plot Y_{ore} at $f_0 = 10$ GHz for angles of incidence 0 to 80° in both principal plane. (*Note:* This is scan independence.)

f. Evaluate and plot $|Y^{1,2}|$ given by (P7.3-4) at $f = 10$ GHz for angles of incidence 0 to 80° in both principal planes. (*Note:* Does not change much with scan angle.)

g. In (P7.3-6) choose the constant C_1 such that at $f = 1.1f_0$ we obtain y equal to Y_{ore} (at f_0 and normal incidence); that is, $y = C_1(1.1 - 1.0)f_0 = Y_{ore}$.

h. Finally evaluate $|\mathcal{T}|$ as given by (P7.3-1) and (P7.3-2) in the frequency range $f = 0.5f_0$ to $1.5f_0$ for normal, 30° and 60° in both principal planes. Use the values in this range for Y_{ore} and $Y^{1,2}$ as obtained at 10 GHz for 0°, 30° and 60°, respectively. (*Note:* The bandwidth is scan independent.)

8

BAND-STOP AND DICHROIC FILTER DESIGNS

8.1 INTRODUCTION

In the previous chapter we investigated designs of band-pass filters. We saw how they in general were made from slotted surfaces sandwiched between dielectric slabs as shown in Fig. 8.1.

In this chapter we investigate band-stop filters. They are in general made of band-stop arrays, namely of the *dipole* type, and they may similarly to the band-pass designs also be cascaded in a stratified medium as shown in Fig. 8.2.

Thus the two cases typically look quite similar; in fact some might say they look like complements of each other. However, the reader should be warned right at the start that there are differences so profound between the two cases that little design experience can be transferred from one to the other case.

More specifically, Fig. 8.1 shows a typical biplanar band-pass design at the top and the schematic transmission and reflection curves at the bottom. Similarly Fig. 8.2 shows a biplanar band-stop design at the top and the schematic reflection and transmission curves at the bottom. Note that these two cases may look similar around their maximum values, namely exhibiting two maxima with unit value and separated by a valley between them. However, while the band-pass design in general will go to zero at frequencies above and below (except for some spurious resonances at higher frequencies; see Fig. 7.9), the band-stop case will typically also go to zero but then show a maximum with less than unit value below and above the resonant region (these smaller maxima are sometimes referred to as "ears"). The reason for this rather profound difference is that an assembly of slot arrays transmits only from the last array as explained in Section 7.2. In an assembly of dipole arrays on the other side, the incident field will not only induce a voltage in each dipole array, but

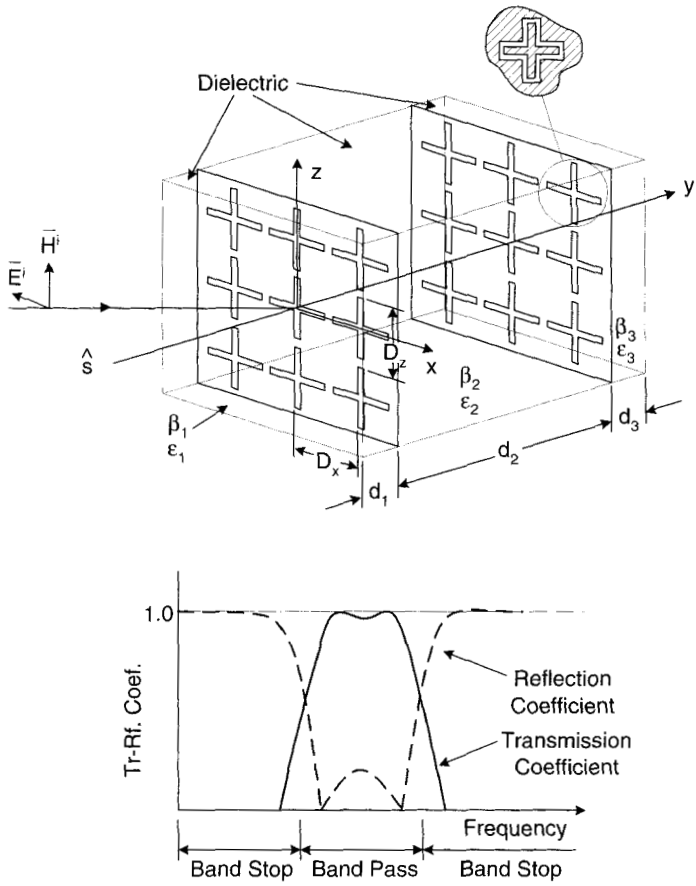

FIGURE 8.1. Compensated band-pass filter. Most band-pass as well as band-stop filters will in general change dramatically with polarization and angle of incidence. Use of a stratified dielectric medium can dramatically reduce this variation in both cases as long as we are dealing with relatively small bandwidths as discussed in Chapter 7.

each array will also scatter in the forward as well as the backscatter direction. The net result is that the various array fields can interfere and produce nulls (called *array interference nulls*), in particular in the case of two arrays and to a lesser degree with more arrays.

The reader should also be reminded that the outer dielectric slabs in a band-pass design essentially serve the purpose of obtaining an almost constant bandwidth for all angles of incidence and polarizations; see Fig. 7.9. In contrast, the outer dielectric slabs in a band-stop design with large bandwidth do not necessarily serve such a function; in fact they may have very little effect on the reflection coefficient in the band-stop region where the FSSs basically act like short circuits across a transmission line.

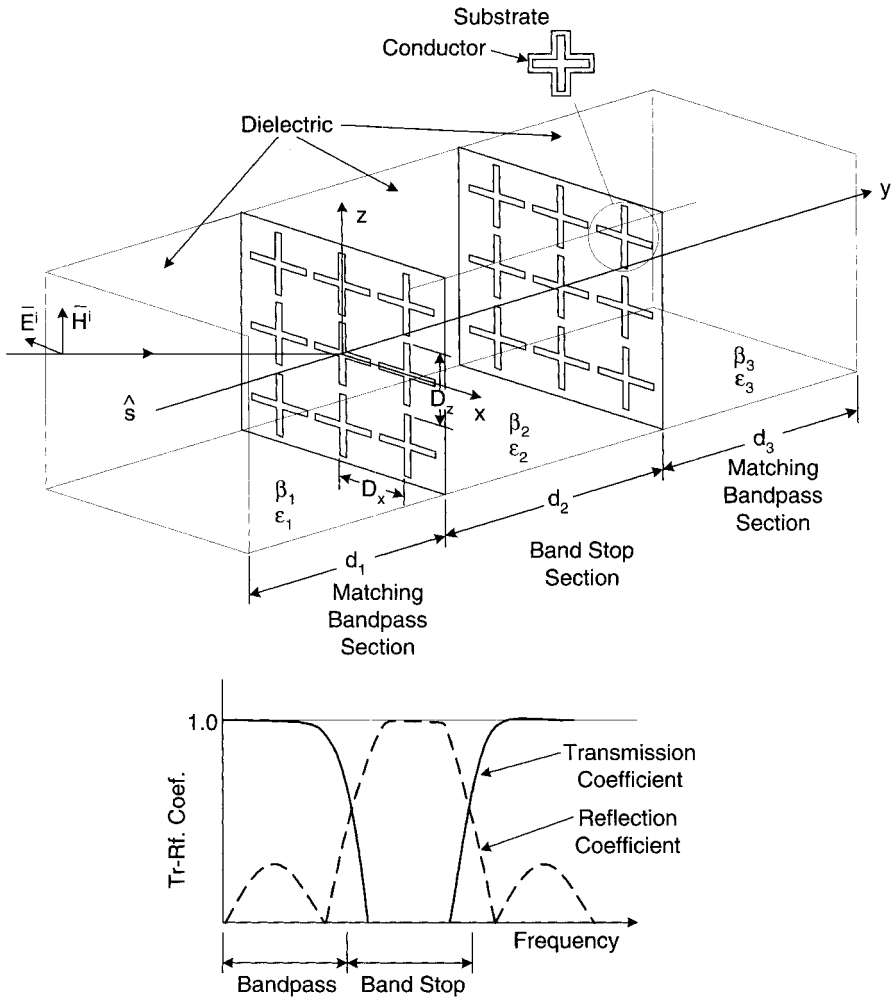

FIGURE 8.2. Although this band-stop filter with large bandwidth may look similar to the band-pass filter in Fig. 8.1, the purpose of the outer dielectric slabs in this case is primarily to improve the transmission in the band-pass region. However, see also Section 8.11 dealing with band-stop filters with narrow bandwidth.

When the band-stop filter is basically transparent, the outer dielectric slabs may merely serve as matching sections. Thus they may be designed simply to produce an input impedance as close to that of the surrounding media as possible (i.e., in general Z_0). This goal is often accomplished best by use of several dielectric slabs of various thickness and dielectric constants.

Also, while band-pass filters typically may be designed for a relative narrow frequency range (typical 3–25%), a broadband band-stop filter is often required to show band-stop characteristics in a frequency range exceeding an octave. Consequently a

band-stop filter for broadband applications will typically use element types having much larger bandwidth than its band-pass counterpart. We will, however, also show examples of band-stop filters designed for narrow-band application, as seen in Section 8.11. There the outer dielectric slabs serve essentially the same purpose as in the hybrid radome case, namely to stabilize the bandwidth for all angles of incidence and polarizations. In other words, they act more like the compensated band-pass filters discussed in Chapter 7.

8.2 APPROACH

From the introduction above it is clear that the typical band-stop filter with large bandwidth is basically made of two or three parts:

1. The actual band-stop section is made of one or more FSS arrays of the *dipole* type. These are separated by dielectric slabs.
2. Basically a band-stop filter should ideally be transparent outside the band-stop region.

We will determine the proper thickness and dielectric constants for the dielectric slabs. Then we will investigate the implications of the FSS arrays having the same resonant frequency or being stagger-tuned. A band-stop filter can usually be improved upon by adding matching sections to either one or both sides of the band-stop section. Basically these matching sections can be designed like any classical matching network, namely by using reactive surfaces (FSSs) in combination with dielectric matching transformers. By choosing the proper dielectric constant and thickness of these transformers, it is often possible to avoid the sometimes rather costly reactive surfaces. Also it is usually the purpose of the matching sections to improve the bandwidth where the band-stop filter is transparent.

Like most matching problems, the matching sections are easiest designed by use of the Smith chart. Further, since the dipole arrays for broadband applications typically are spaced far apart from each other, the evanescent waves surrounding each array have usually died out sufficiently before they reach the next one, so the transmission line approach is valid. We will find this approach to be extremely useful in analyzing as well as designing band-stop filters. However, when actually calculating the reflection and transmission curves for the band-stop filters in question, we will of course use the PMM program with an appropriate number of section modes.

8.3 HOW TO CALCULATE THE SCATTERING FROM N ARRAYS OF DIPOLES IN A STRATIFIED MEDIUM

The basic model for our band-stop filter of planar elements is shown in Fig. 8.3. It is comprised of N arrays of *dipoles* located in M dielectric slabs of thickness $d_1 \cdots d_M$

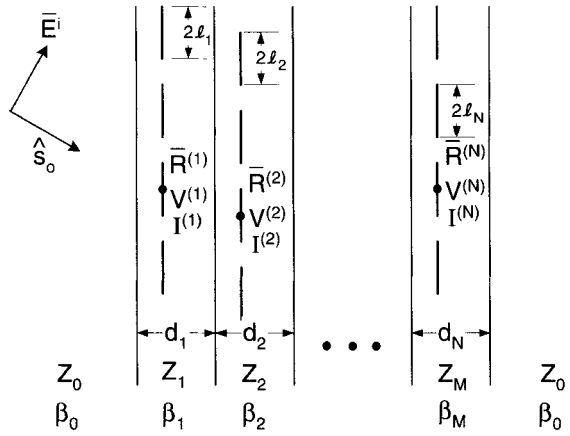

FIGURE 8.3. Basic model for a band-stop filter of planar elements.

and intrinsic impedance $Z_1 \cdots Z_M$ as shown. It is exposed to an incident plane wave with the field vector $\bar{E}^i$ and propagating in the direction $\hat{s}_0$.

Determination of the scattered field is based on the development in Chapter 5 as follows:

1. From (D.18) we determine the total fields at the reference points $R^{(1)} \cdots R^{(N)}$. We then find the induced voltages $V^{(1)} \cdots V^{(N)}$ by use of the approach in Section 5.3.
2. We determine all self- and mutual admittances $Z^{n,n}$ and $Z^{n,m}$ by use of (5.33).
3. We determine all the element currents $I^{(1)} \cdots I^{(N)}$ from the matrix equation

$$\begin{bmatrix} V^{(1)} \\ V^{(2)} \\ \vdots \\ V^{(N)} \end{bmatrix} \tag{8.1}$$

$$= \begin{bmatrix} \left(Z^{1,1} + Z_L^{(1)}\right) & Z^{1,2} & \cdots & Z^{1,N} \\ Z^{2,1} & \left(Z^{2,2} + Z_L^{(2)}\right) & \cdots & Z^{2,N} \\ \vdots & & & \\ Z^{N,1} & \cdots & & \left(Z^{N,N} + Z_L^{(N)}\right) \end{bmatrix} \begin{bmatrix} I^{(1)} \\ I^{(2)} \\ \vdots \\ I^N \end{bmatrix}. \tag{8.2}$$

4. Knowing all element currents $I^{(1)} \cdots I^{(N)}$, it is now a simple matter to find the scattered field as the sum of all the fields scattered from each array. These are obtained by (5.29) modified to planar elements as demonstrated in Section 5.9.

5. We add the scattering from the entire assembly of dielectric slabs as if the wire arrays were not present. This is readily done by calculating the effective reflection and transmission coefficients as explained in Appendix D. (It is interesting to note that if the dielectric slabs are not added to the fields scattered from the arrays, then the arrays will formally have a reflection coefficient larger than one.)

Comparison between the evaluation of the *dipole* case above and the *slot* case in Chapter 7 shows many similarities. However, we also observe a profound difference between the two matrix equations (8.2) and (7.9), namely that the former is full while the latter is banded. This enables us to reduce and analyze (7.9), though this has not been possible for (8.2) in the general case. A further complication is the scattering from the dielectric profile. Only for a single array located arbitrarily in a single slab has it be shown that the unit reflection coefficient is obtained at resonance. For details, see [51, 52, 53]. (These reports are so early that they precede the formal plane wave expansion.)

8.4 CHOICE OF THE ELEMENT TYPE

It is usually the greatest challenge to design band-stop filters with large bandwidth. Once that is mastered, determining the narrow-band designs is a breeze.

Consequently in this chapter we will concentrate primarily on broadband designs. Further, since the bandwidth is primarily determined by the element type, we will after consulting Chapter 2 choose the hexagon element to be used in the design example to follow.

8.5 CHOICE OF ARRAY SEPARATION: ARRAY INTERFERENCE NULLS

We observed in Chapter 2 that no matter how broadband is a single array, it will in general only have one fundamental resonance with perfect reflection (magnitude one). We can improve upon this situation to a significant degree by using two (or more) arrays cascaded after each other as shown earlier in Fig. 8.2. Our first task is to determine the array separation D, which is an important function as illustrated in Fig. 8.4 where we show the reflection curves for normal angle of incidence for array separations $D = 1.0$, 1.5, and 1.8 cm, respectively. We observe first of all a much flatter reflection curve than for a single array. Further we observe three sharp notches in the reflection curve: around $f_L \sim 3$ GHz, around $f_M \sim 7$–11 GHz, and at the high end of the band around $f_H \sim 13$–19 GHz. The locations of these nulls, called array interference nulls, are easily understood if we consider for a moment the equivalent circuit of two identical FSSs separated by a distance D, as shown in Fig. 8.5 (top-left) and a typical reflection coefficient curve with the three notch frequencies f_L, f_M, and f_H as indicated at the top-right. At the bottom of Fig. 8.5 are three Smith charts (with the admittance normalized to Y_0) depicting the key admittances at the

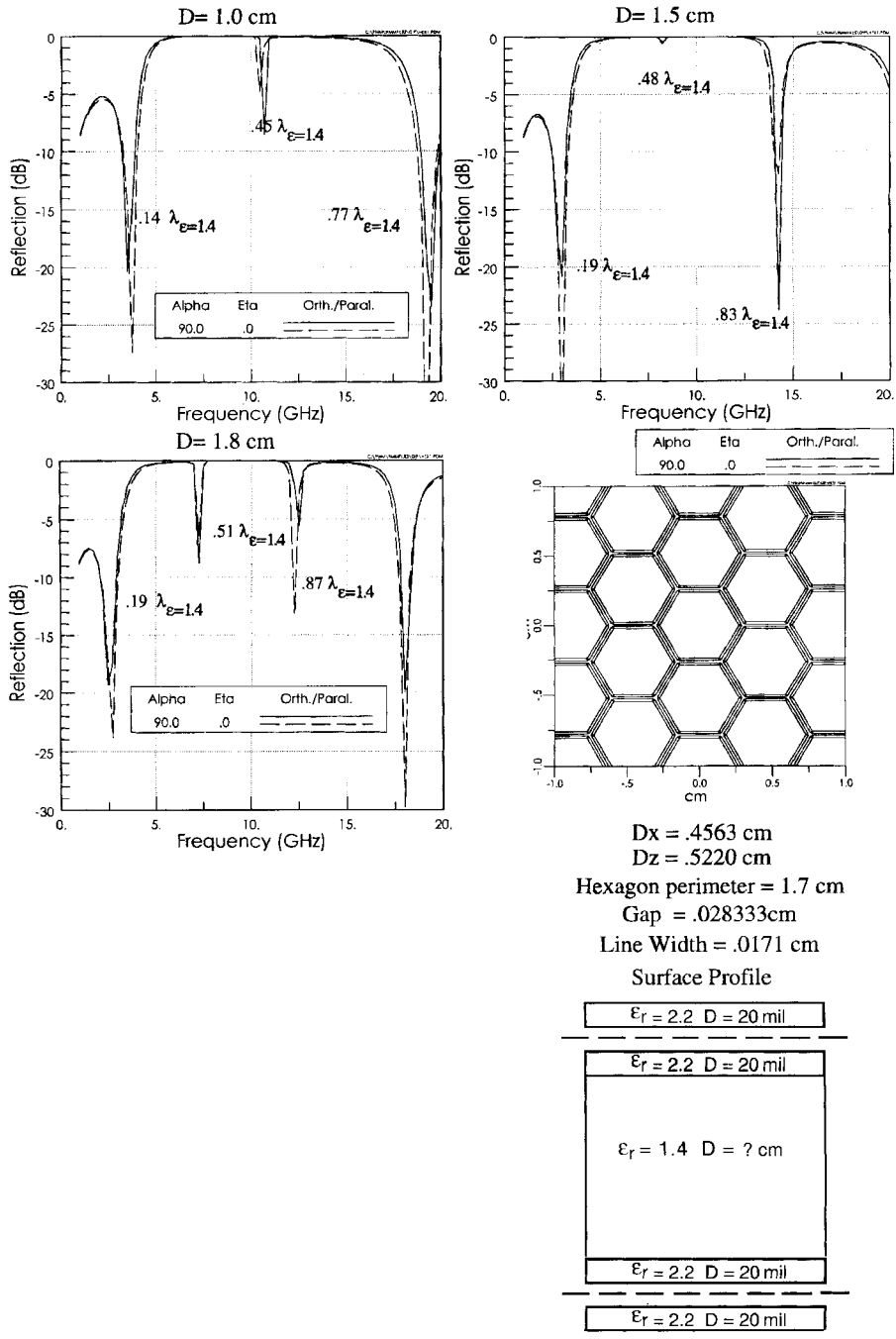

FIGURE 8.4. Reflection coefficient curves for two FSSs connected in cascade as shown in insert to the right, bottom. Array separation is indicated in respective figures. Normal angle of incidence, orthogonal and parallel polarization.

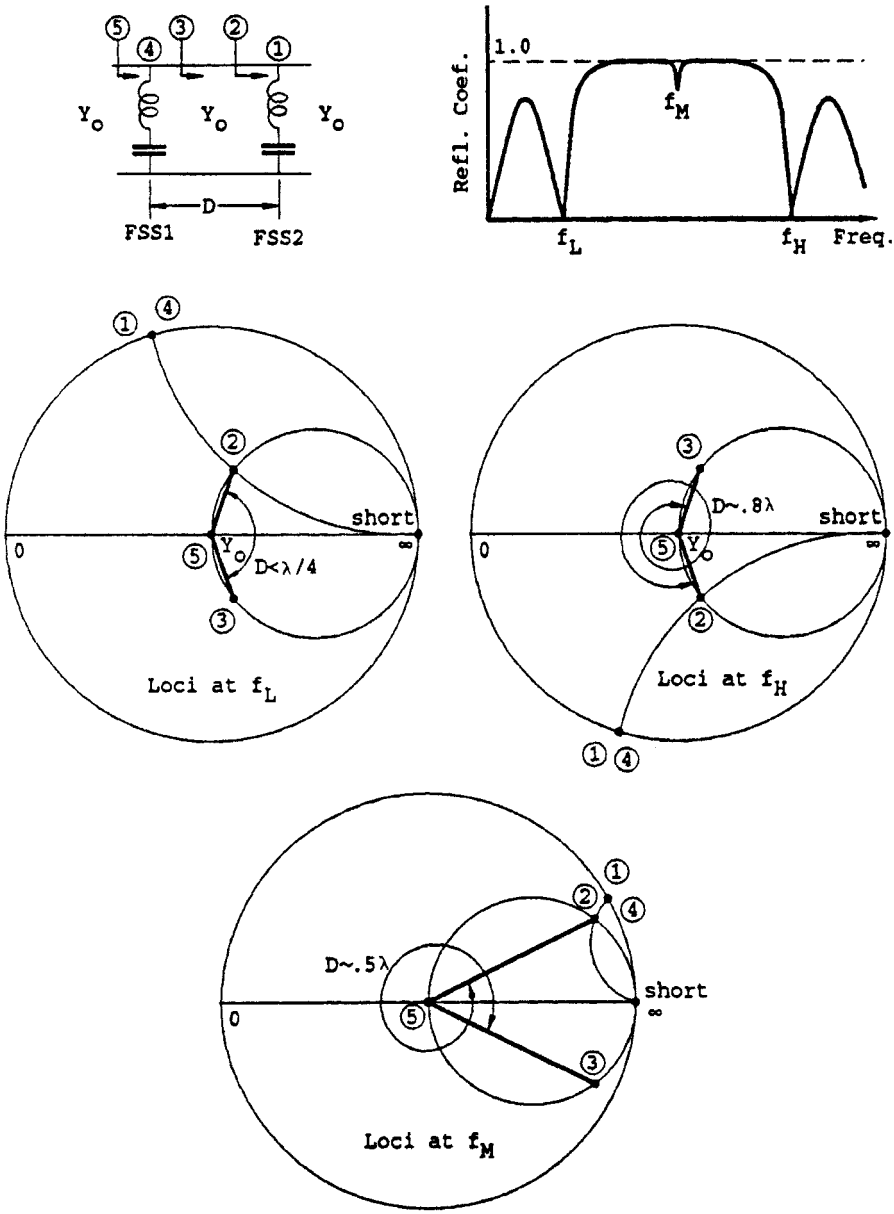

FIGURE 8.5. Typical admittance plots in Smith charts for two FSSs in cascade as shown by equivalent circuit at top to the left.

above three frequencies. Starting from the right in the equivalent circuit and working toward the left, we begin with the free space admittance Y_0 to which we add in parallel the LC-circuit (1) representing FSS 2 and thereby obtaining the admittance (2). This admittance is now rotated by the amount D/λ to yield the transformed admittance (3). We next add the LC-circuit (4) representing the FSS 1. It is easy to see that if (3) and (4) have the same susceptance with opposite signs, their sums (5) will go through the center of the Smith chart corresponding to zero reflection coefficients at the frequencies f_L, f_M, and f_H.

It is further shown that the notch at f_M can also exist when (1) and (4) are slightly below the short-circuit point ∞ and not only slightly above. The rotation D/λ would in that case be slightly smaller than $\lambda/2$. Only if $D/\lambda = 0.5$ exactly where FSS 1 and FSS 2 resonate (i.e., go through ∞) will the notch at f_M disappear (or be "infinitely" narrow if you prefer). Since f_M typically would be located in the middle of the band-stop, it becomes a major design constraint that $D/\lambda = 0.5$ at the FSS resonant frequency. The other notch frequencies f_L and f_H would then have to be moved if desired by other means. Inspection of Fig. 8.4 readily shows that the larger the array separation D, the lower are the two frequencies f_L and f_H, as one would expect.

8.6 CHOICE OF DIELECTRIC BETWEEN ARRAYS

So far we have concerned ourselves only with signals at normal angle of incidence. However, in reality we must demand that our filter work for a large range of angles of incidence and for arbitrary polarization. From the general theory of periodic surfaces, we know that the mathematical expressions for anything involving transmission or reflection from two FSSs separated by the distance D typically contain the form $\beta_\epsilon D \cos \eta_\epsilon$, where

β_ϵ is the propagation constant in the medium ϵ between the two FSSs.

η_ϵ is angle of incidence inside the same medium.

Since α_ϵ is related to the incidence angle α in free space by Snell's law, it is obvious that $\beta_\epsilon D \cos \eta_\epsilon$ will vary less with angle of incidence than if in free space. However, the dielectric will also in general scatter more than merely free space. Thus a compromise must be found, as will be discussed next.

In Fig. 8.6 we show the reflection curves for two FSSs separated by a dielectric medium with dielectric constants 1.0, 1.4, and 1.8 for normal and 45° angle of incidence, orthogonal and parallel polarization. The slab thickness D is in all these three cases adjusted to be approximately $0.5\lambda_\epsilon$ at the resonant frequency of the FSSs and produces a null around 3.5 GHz; that is, we do not have a notch at f_M for normal angle of incidence but a small one for 45°. We further note that the lower notch frequency f_L varies less with angle of incidence as the dielectric constant is increased. However, we also note a higher level of reflection below $f_L \sim 3\ GHz$. This problem will be examined in the next section.

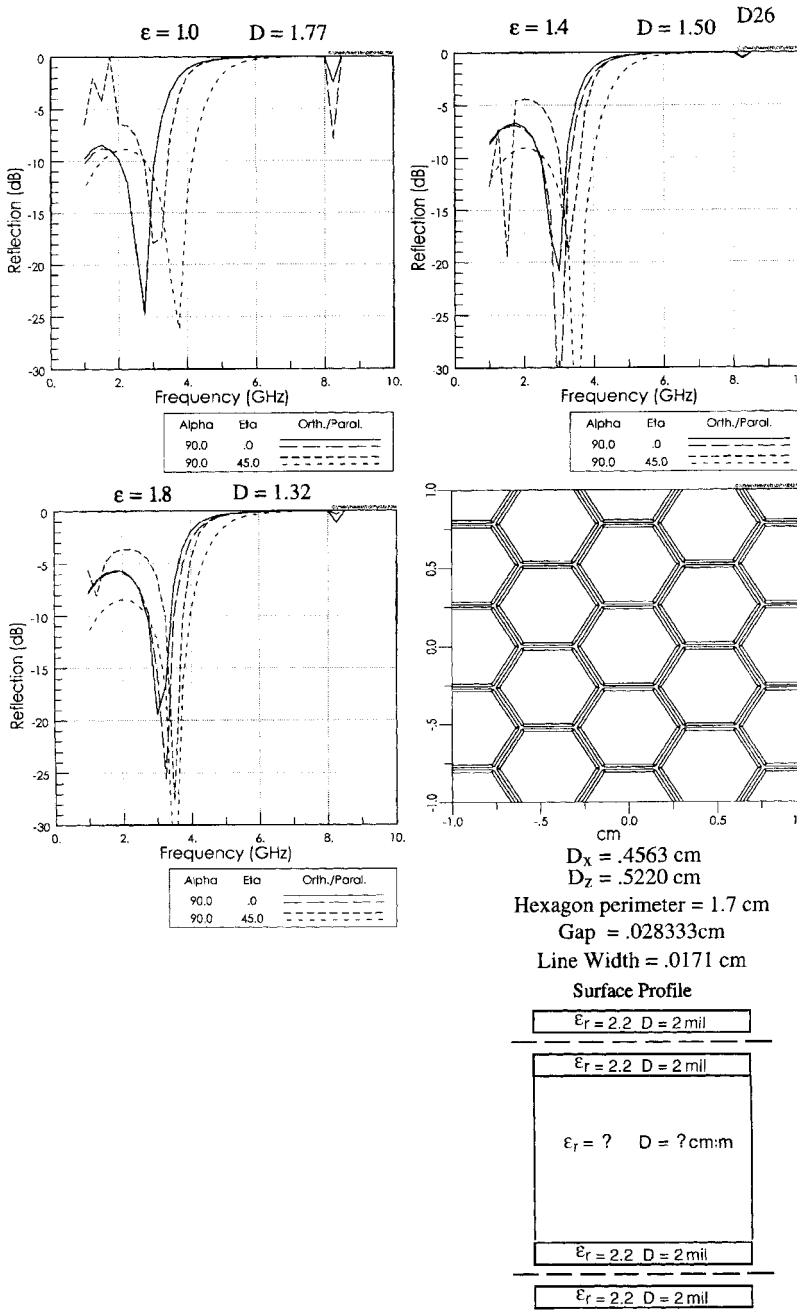

FIGURE 8.6. Lower frequency part of the reflection coefficient curves for two FSS in cascade as shown at the bottom right. The space between the two FSSs is filled with material with dielectric constants $\epsilon = 1.0$, 1.4, and 1.8, respectively, and the array separation D, is adjusted to yield a null around 3.5 GHz for all cases for easy comparison.

8.7 MATCHING IN THE BAND-PASS REGION

So far we have designed a filter able to stop a certain frequency band. It consists basically of two FSSs separated by a dielectric slab. It is important to realize that as long as these two FSSs and the dielectric slab between them are left unchanged, the band-stop feature will essentially remain unchanged as well (no matter what).[1] As a consequence, if we would like to improve the transmission properties in a chosen band-pass, it would be perfectly all right to add any matching network as long as it is done outside the space between the two FSSs.

Thus the next logical step is simply to find the input admittance of the filter in the band-pass region 0–f_L (0–3 GHz in our case) and then design a matching section to be placed on both outer sides of the FSSs. However, we will first show how to optimize the transmission coefficient in the band-pass region without any matching and then as the next step add the matching sections.

8.7.1 Optimizing the Band-Pass Transmission without Use of Separate Matching Sections

Although the transmission properties can readily be computed in the band-pass region, it is quite instructive to sketch the various steps leading to the input admittance in a Smith chart as illustrated in Fig. 8.7.

At the top we show for easy reference the two FSSs separated by the distance D where for simplicity we have assumed the dielectric between them to be air. In case I (left) the two purely reactive FSSs are indicated by the loci (1) and (4) on the rim of the Smith Chart in the frequency range 0–f_L, respectively. Starting from the right and moving left, we first add FSS 2 in parallel to the free space admittance Y_0 and obtain loci (2). Next we rotate clockwise corresponding to the distance D/λ which has been adjusted such that f_L is obtained at our chosen frequency as explained in Fig. 8.5.

Finally we add in parallel to loci (3) the FSS 2 loci (4) and obtain the input admittance (5). Note that we have a perfect match at the notch frequency f_L (again, the distance D was chosen such). It is also easy to see by inspection of the Smith chart that we obtain the greatest mismatch around the frequency $\frac{1}{2}f_L$, as illustrated by the reflection curve at the bottom of Fig. 8.7.

In case II (right) the two FSSs have the same resonant frequency f_M as for case I, but the bandwidth of the two FSSs are slightly smaller. That is, the frequency f_L is located somewhat closer to zero in the Smith chart as noted by inspection. The input admittance (5) is obtained precisely as above. However, it is easy to see that the worst mismatch around $\frac{1}{2}f_L$, has been reduced as observed in both the Smith chart and the reflection coefficient curve at the bottom of Fig. 8.7. We finally illustrate the design principle in Fig. 8.7 by two actually computed cases as shown in Figs. 8.8 and 8.9. If Fig. 8.8 top-left we show the response of a single FSS with a relatively broadband,

[1]The two resonating FSSs act essentially as two short circuits across a transmission line: A short is a short is a short!

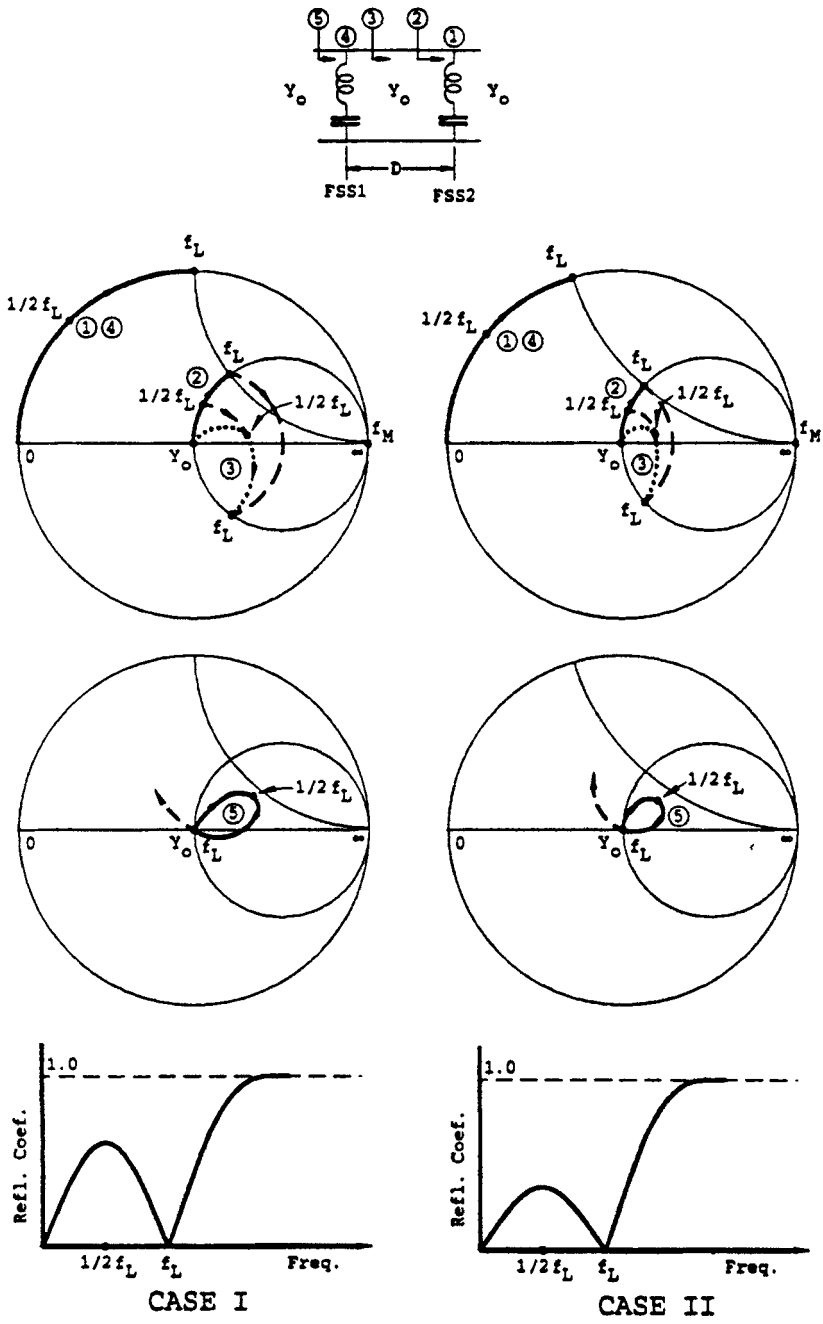

FIGURE 8.7. Typical admittance plots for two cascaded FSSs as indicated in equivalent circuit, top. Case II to the right has a narrower FSS bandwidth than case I. This will produce smaller "ears."

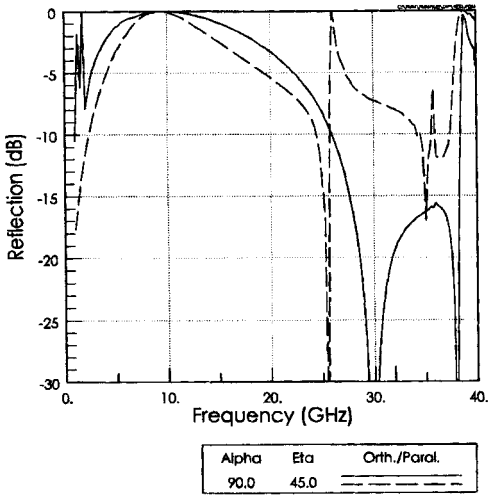

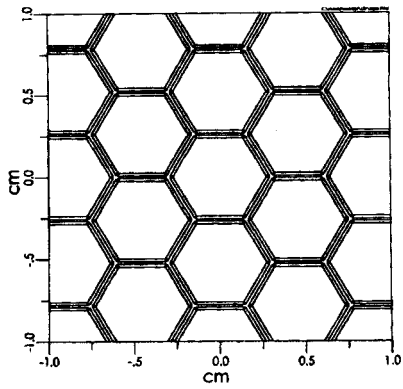

D_x = .4563 cm
D_z = .5220 cm
Hexagon perimeter = 1.7 cm
Gap = .028333cm
Line Width = .0171 cm

Surface Profile

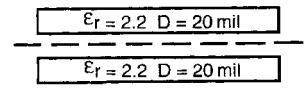

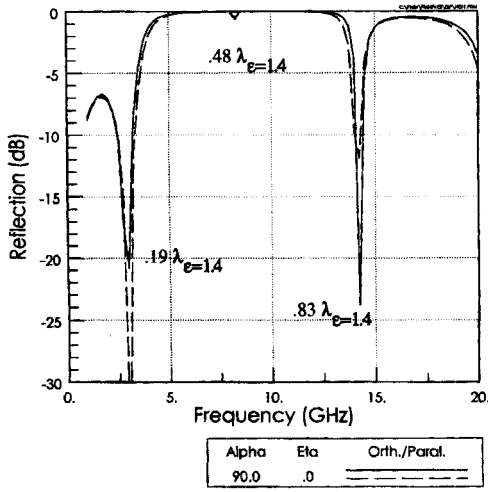

D_x = .4563 cm
D_z = .5220 cm
Hexagon perimeter = 1.7 cm
Gap = .028333cm
Line Width = .0171 cm

Surface Profile

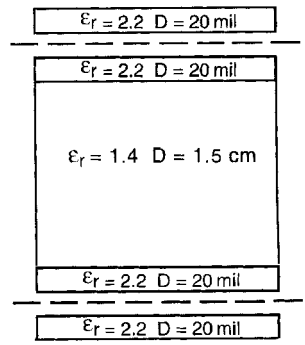

FIGURE 8.8. Actual calculation of reflection of two cascaded FSSs each with reflection curves as shown (*top-left*). Close spacing of the hexagon elements produce a large bandwidth leading to a maximum "ear" level of around 6.5 dB (*bottom-left*). Normal angle of incidence, orthogonal and parallel polarization.

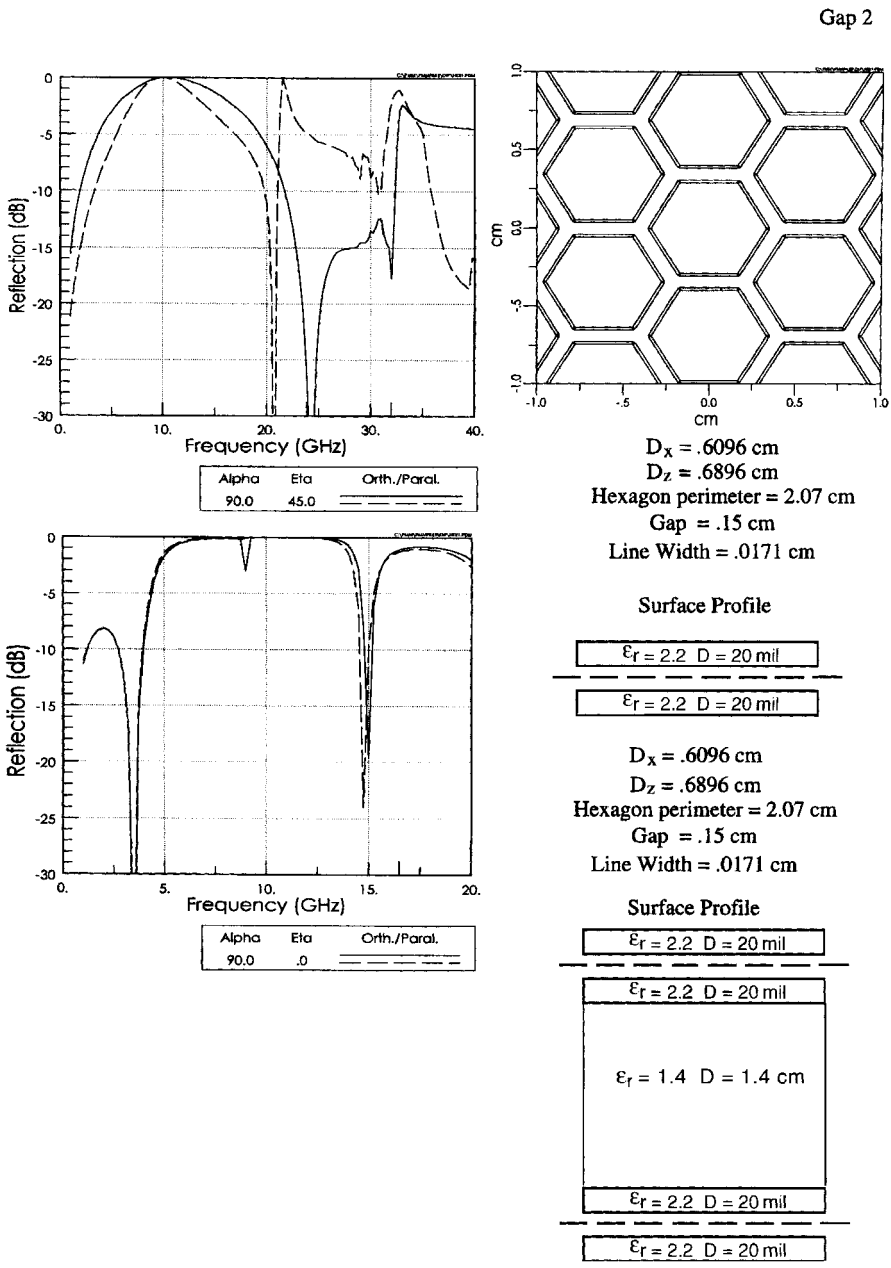

FIGURE 8.9. Basically the same case as in Fig. 8.8 but with larger inter-element spacings leading to a narrower FSS bandwidth (*top-left*) and a maximum "ear" level of about 8.0 dB (*bottom-left*).

while we similarly in Fig. 8.9 top-left show a more narrow-banded response at around 10 GHz. At the bottom of Figs. 8.8 and 8.9 we further show the reflection curves of the broad and narrow-band cases, respectively.

We do indeed obtain better transmission properties at $\frac{1}{2}f_L$ in the narrow-banded case. However, we also lose some bandwidth in the transmission region. Thus a compromise must be reached or a further improvement is introduced, as shown next.

8.7.2 Designing a Matching Section for the Band-Pass Frequencies

We saw above how the transmission at frequencies below f_L could be improved by making the two FSSs more narrow-banded. In this section we will show how further improvement is possible by adding specially designed matching sections on both sides of the band-stop, as shown earlier in Fig. 8.2.

Theoretical Background In the name of simplicity, let us first consider the case where a matching section is placed only to the left of the band-stop section, as shown in Fig. 8.10 (top). The typical input admittance for the band-stop section above looks like curve (5) shown earlier in Fig. 8.7. It is also shown for easy reference in Fig. 8.10 in Smith chart (*a*) (we have chosen case I to more clearly show the concept). How to match a single admittance point of curve (5) to Y_0 is well known. However, in the present case we will attempt to keep a good match at all frequencies between $\frac{1}{2}f_L$ and f_L. In other words, we will design a broadband rather than a narrow-banded matching section.

A relatively simple approach is to use a dielectric slab as shown in Fig. 8.10 top. Let the characteristic admittance of the slab be $1.3Y_0$. Then the admittance at f_L will be rotated clockwise slightly more than 360°, while the $\frac{1}{2}f_L$ admittance will be rotated slightly more than 180° as also shown in Smith chart (*b*). The entire input admittance (6) normalized to $1.3Y_0$ is shown in Smith chart (*c*) while Smith chart (*d*) shows the same admittance but normalized to Y_0. Note how all the frequencies from $\frac{1}{2}f_L$ to f_L fall closer to the center of the Smith chart (Y_0), that is, the lower reflection as seen in Fig. 8.10 bottom-right. We do of course pay a price in higher reflection below $\frac{1}{2}f_L$, but we can usually live with that.

Calculated Examples In order to illustrate the theoretical principles discussed above, we are now going to show some actual calculated results.

First, we show in Fig. 8.11 the reflection coefficient curves for the uncompensated case shown already in Fig. 8.8 where $\bullet = 1.4$ and $D = 1.5$ cm. However, we also in Fig. 8.11 show this case not only for 45° angle of incidence but also for normal as well as 60°, orthogonal and parallel polarization.

We observe that this choice of dielectric slab leads to almost no array interaction null around 10 GHz. However, we also note that the maximum reflection level below 3 GHz is too high to yield good transmission, in particular for orthogonal polarization and higher angles of incidence. As discussed above, the remedy for this calamity is to place dielectric matching slabs on both sides of the band-stop core shown in Fig. 8.12 bottom-right.

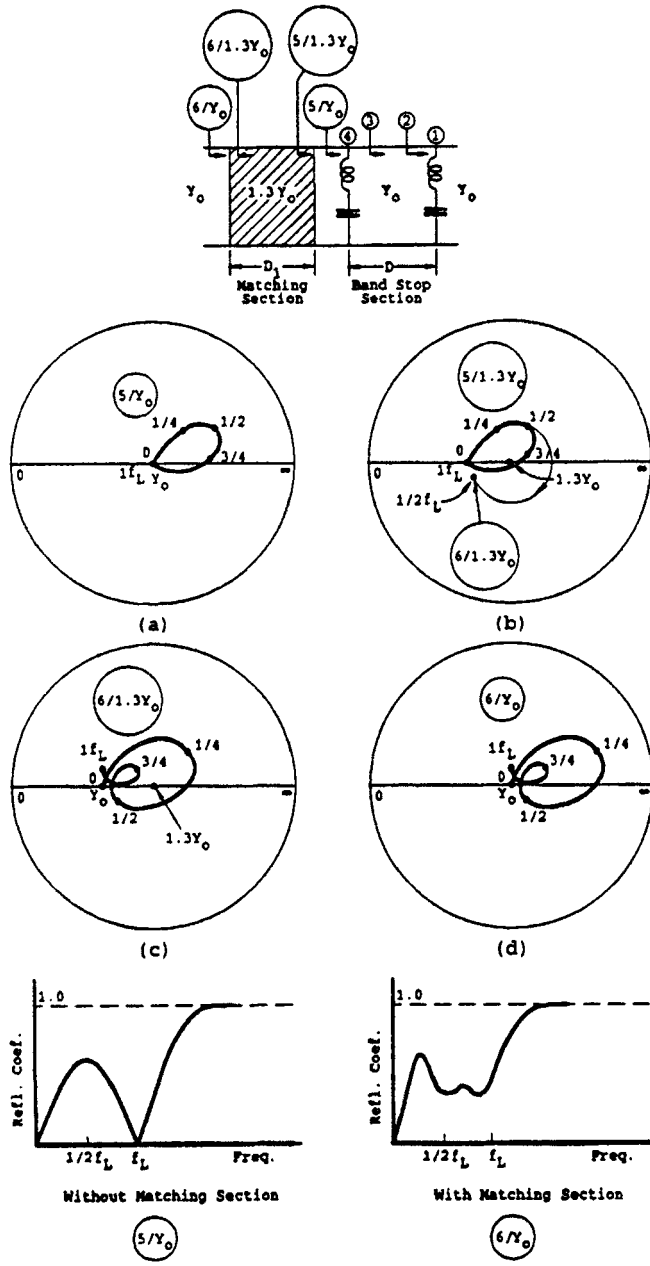

FIGURE 8.10. Typical admittance plots of two cascaded FSSs with and without a dielectric matching plate. For our application use of matching slabs is considered an advantage.

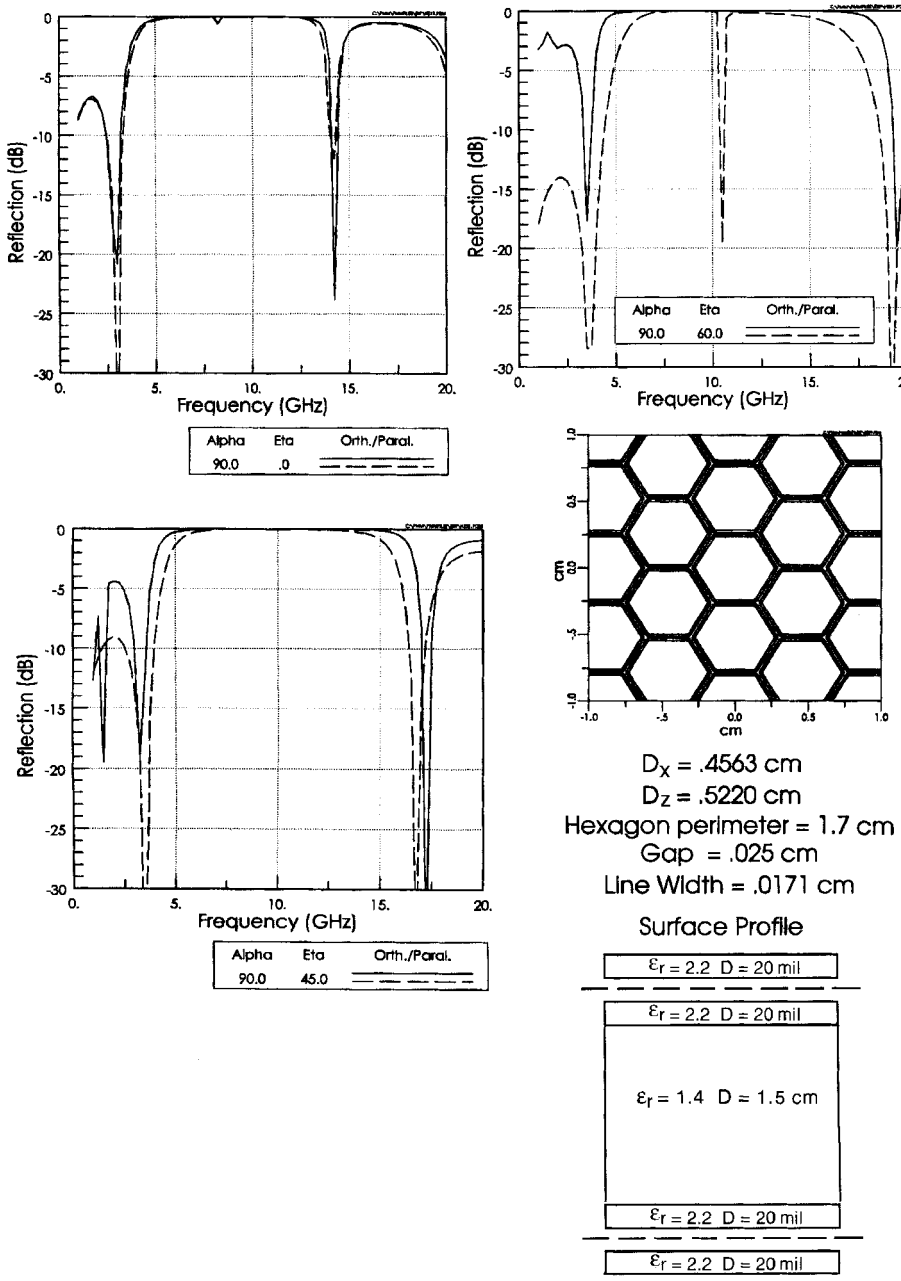

FIGURE 8.11. Reflection curves for the band-stop section without any outer matching plates. Shown for normal, 40° and 60° angles of incidence.

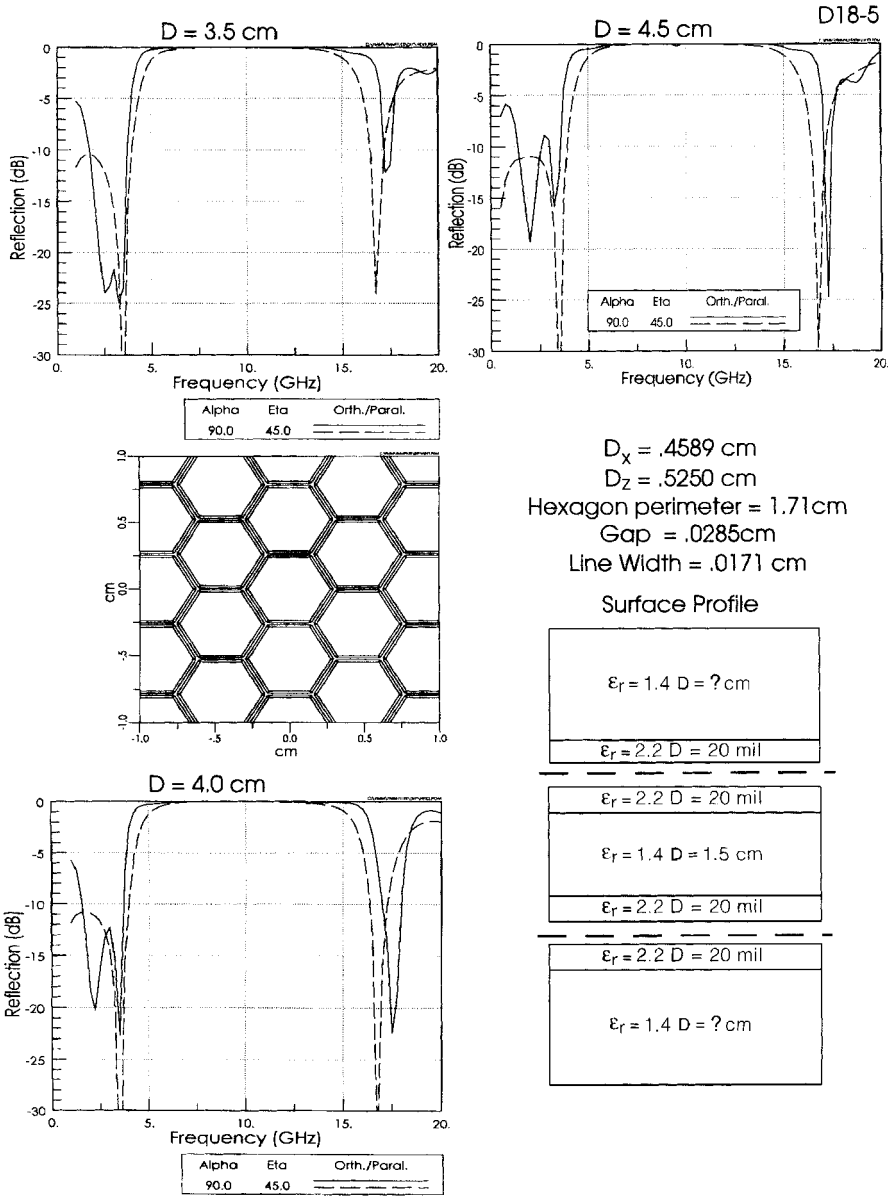

FIGURE 8.12. Reflection curves for the same band-stop core as shown in Fig. 8.11 but with outer dielectric slabs with fixed $\epsilon_r = 1.4$ and for three cases of slab thickness, $D = 3.5$, 4.0, and 4.5 cm. Only the 45° case is shown.

We will first determine the tentative optimal outer slab thickness by fixing ϵ_r at 1.4 and then in Fig. 8.12 show the reflection coefficient curves for three cases, namely for thicknesses 3.5, 4.0, and 4.5 cm. For the sake of expediency we only show these curves for 45° angle of incidence. We observe a significant reduction of the reflection level below 3 GHz for all three thicknesses shown in Fig. 8.12. However, an optimum value for both polarizations seems to be around $D = 4.0$ cm. At 3 GHz that corresponds to an electrical thickness of around $0.47\lambda_\epsilon$ which is in line with our reasoning discussed above.

We next in Fig. 8.13 show the reflection coefficient curves for three different values of the dielectric constant, namely $\epsilon_r = 1.4$, 1.6, and 2.0. In all three cases the slab thickness D was adjusted to be electrically the same as determined above for $\epsilon = 1.4$ (see Fig. 8.12). This leads to the values $D = 4.0$, 3.75, and 3.3 cm for $\epsilon_r = 1.4$, 1.6, and 2.0, respectively.

Again, we note a significant reduction in reflection level below 3 GHz in all three cases. The optimum value of ϵ is estimated to be around $\epsilon_r = 1.6$, and that value will be chosen for further tentative design work. We emphasize that once we get closer to a final design, further optimization of all these values is envisioned (in fact this whole issue at some point becomes a tolerance question).

8.8 EXTENDING THE UPPER FREQUENCY

So far we have designed a band-stop filter comprised of two identical FSSs sandwiched between essentially three dielectric slabs (see Fig. 8.13). This design approach leads to several array interference nulls. One of these at around 10 GHz is basically eliminated by making the array separation electrically equal to one half wavelength at the resonant frequency of the two FSSs (about 10 GHz). This choice leads to only a single null below the resonant frequency (about 3 GHz), which is quite desirable in the present case since it partly ensures a good transmission coefficient at the lower frequencies. There will also be a similar array interference null above the FSS resonance, namely is this case at 17 to 18 GHz, as also shown in Fig. 8.13. In many instances this will be more than adequate and not be cause for concern. However, if it is desirable to raise the upper end of the frequency band, it can be done by adding a third FSS resonating at the upper array interference null (in this case about 17–18 GHz). It should be located outside the space between the two original FSSs; see the remarks in Section 8.4. An example is shown in Fig. 8.14 where the high-frequency array (FSS 2) is seen to be located beneath the original two FSS 1s. More specifically, we show the transmission curves for three cases in Fig. 8.14 where the resonant frequency of FSS 2 has been varied by changing its element perimeter (1.25, 1.30, and 1.35 cm). Observe how such a minor perturbation has a pronounced effect on the level of reflection (more than 10 dB at about 17 GHz). The spacing between FSS 2 and the lower FSS 1 is seen electrically to be close to one quarter wavelength. However, since this spacing does not appear to be critical, we do not show any examples perturbing this spacing.

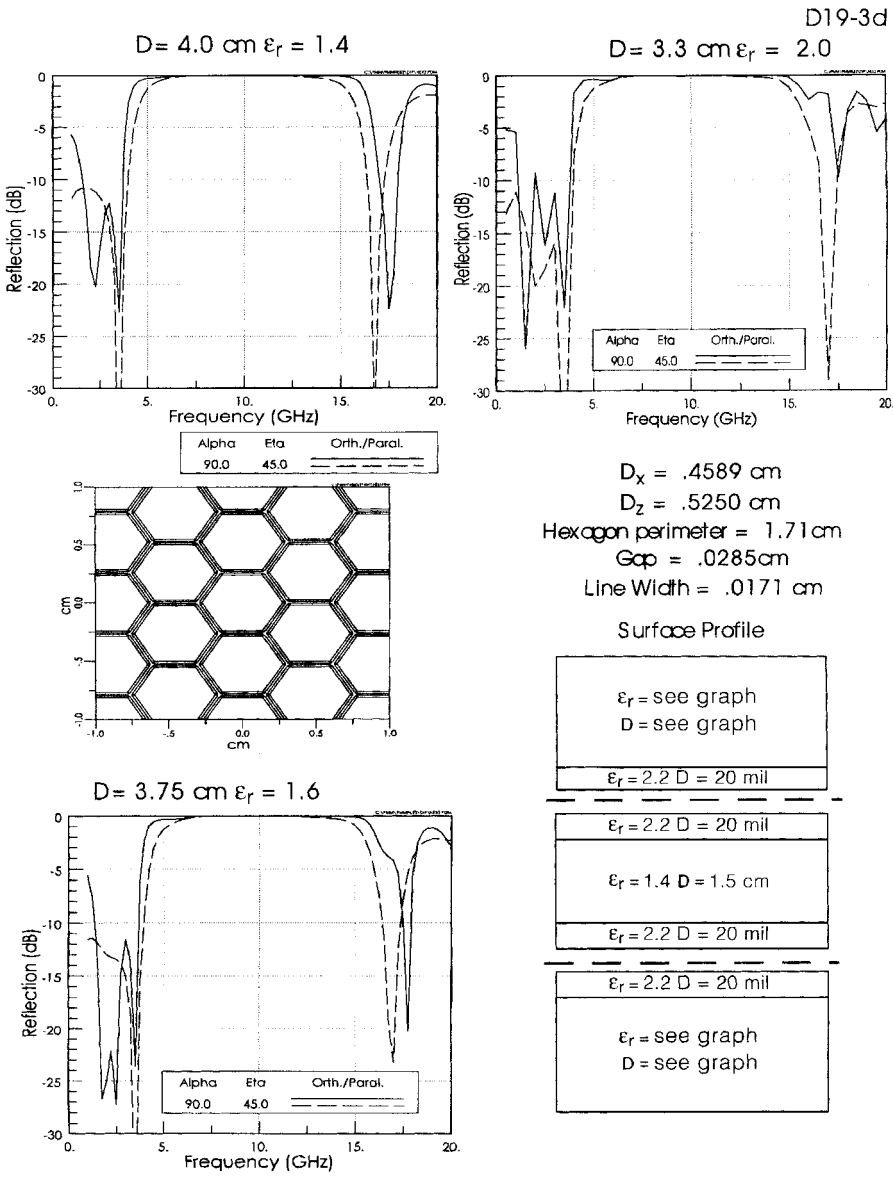

FIGURE 8.13. Reflection curves for the same band-stop core as shown in Fig. 8.11 but for different dielectric constants of the outer slabs, $\epsilon_r = 1.4$, 1.6, and 2.0. The thicknesses D are electrically the same in all three cases.

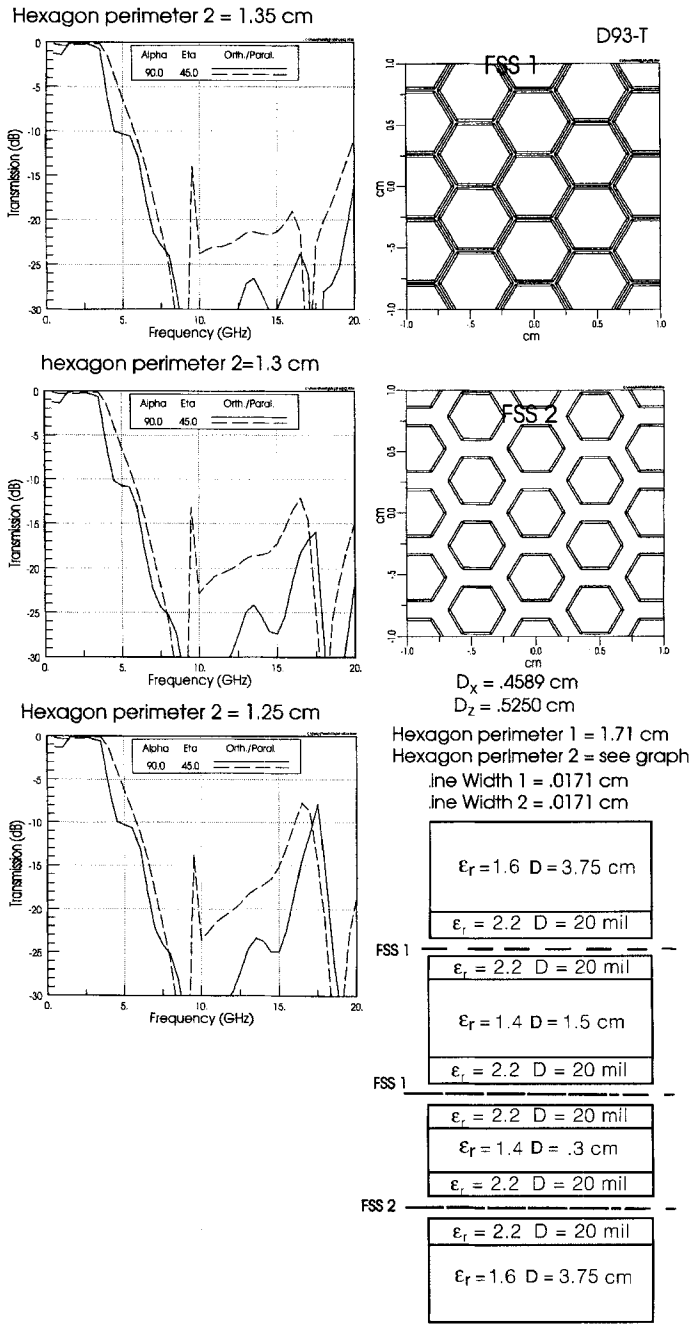

FIGURE 8.14. Transmission curves for the original two FSS 1 design with a third FSS 2 added as shown. The resonant frequency of FSS 2 is varied by changing the element perimeter, 1.35, 130, and 1.25 cm. Note the pronounced effect on the reflection level around 17 GHz.

We finally in Fig. 8.15 show the reflection curves for the case in Fig. 8.14 where the hexagon perimeter of FSS 2 is equal to 1.35 cm. This example should by no means be considered optimized. It only illustrates the general principle of adding an extra FSS 2 to the basic design. Although we have not done so, we see no difficulty adding more FSSs resonating at higher frequencies. In other words, the bandwidth could in principle be extended upward indefinitely, as long as we do not excite grating lobes.

8.9 EFFECT OF STAGGERED TUNING

So far we have only investigated the typical behavior of two FSSs tuned to the same frequency f_M. We found in Sections 8.4 and 8.5 that we would expect in general to see a null in the reflection coefficient curve provided that the separation between the two FSSs differed from $0.5\lambda_M$. If equal to $0.5\lambda_M$, it would disappear.

It is quite common that designers ask the simple question: Could we not obtain a larger band-stop bandwidth by simply making the resonant frequencies of the two FSSs different, in other words, use staggered tuning? The answer to this question is: Certainly, but you pay the price.

In this section we will investigate the effect of staggered tuning. More specifically, let us assume that one FSS is resonating at a lower frequency f_{M-} and the other (symmetric) at f_{M+}, while their separation remains $0.5\lambda_M$ at the original frequency f_M.

8.9.1 Behavior around f_M

In that event the situation will be as shown in Fig. 8.16. At the top-left we show the equivalent circuit of the two FSSs resonating at f_{M-} and f_{M+}, respectively. Below we show a Smith chart normalized to the free space intrinsic admittance Y_0. At the frequency f_M the FSS 2 has the admittance indicated by (1) which, when added to the free space admittance Y_0, yields the combined admittance (2). Next this admittance (2) is rotated along the transmission line of length D which at the frequency f_M happens to be exactly $\lambda/2$, that is, the transformed impedance (3) is exactly on top of (2) as shown. We now add the susceptance (4) to (3). However, since the susceptance (4) of FSS 1 is assumed to be equal but opposite in sign to the susceptance (1) of FSS 2 (at the frequency f_M), the sum admittance (5) must simply go through the center of the Smith chart corresponding to zero reflection coefficient as indicated in the reflection coefficient curve to the right.

The next question is then whether we can affect the null observed above at the frequency f_M in some fashion. Let us assume that the array separation $D < 0.5\lambda_M$ as shown in Fig. 8.4 bottom-left. In that event the transformed admittance (3) will no longer come back to (2) as above but will be located further up in the positive region of the Smith chart as shown. Thus, when the FSS 1 admittance (4) is added, we will no longer end up in the center of the Smith chart as earlier but somewhat off the center of the Smith chart as indicated by (5) corresponding to some reflection as shown in the reflection coefficient curve in Fig. 8.4 bottom-right. The depth of

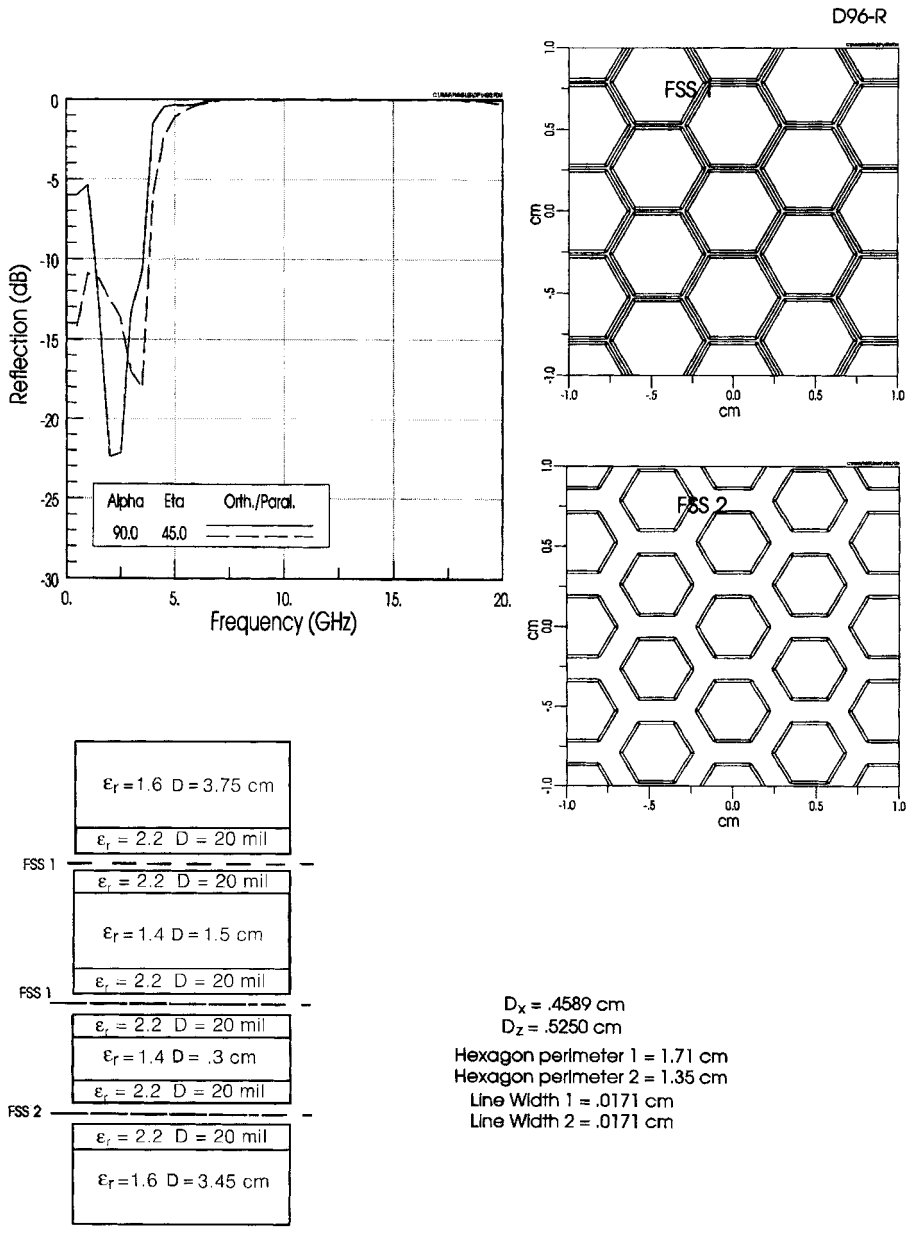

FIGURE 8.15. Transmission and reflection curves for the case in Fig. 8.14 where the element perimeter equals 1.35 cm.

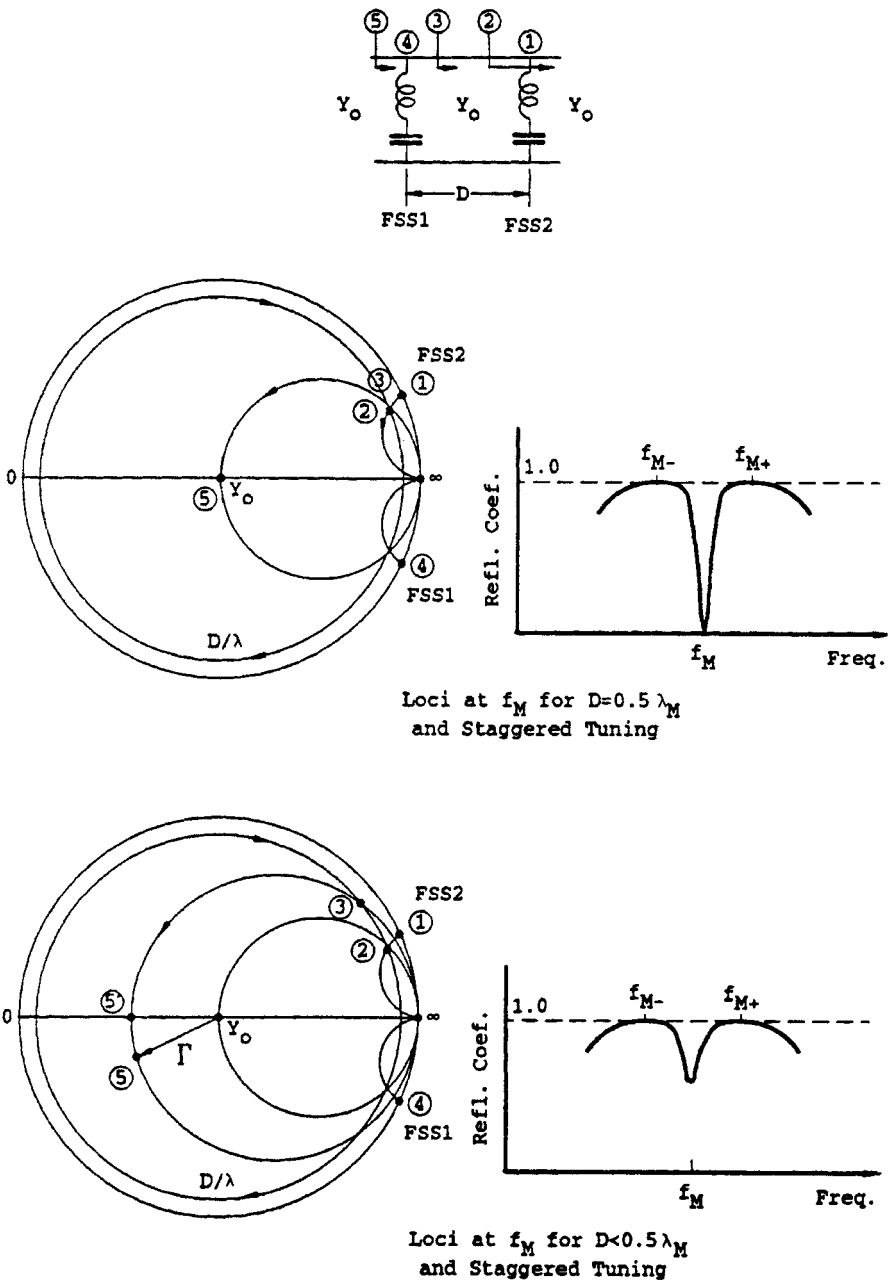

FIGURE 8.16. *Top*: Schematic of a two-layer band-stop filter with FSS 1 $\neq$ FSS 2. *Middle-left*: Smith chart showing the loci at frequency f_M for $D = 0.5\ \lambda_M$. *Right*: Reflection coefficient curve around f_{M-} and f_{M+}. *Bottom-left*: Smith chart showing the loci at frequency f_M for $D < 0.5\lambda_M$. *Right*: Reflection coefficient curve around f_{M-} and f_{M+}.

this depends on the ratio f_{M+}/f_{M-} and on the length of D (the shorter, the less deep it is). It is also easy to see by inspection that in the case where the FSS 1 admittance (4) is chosen in a more general asymmetric way, the closest (5) can get to the center will be position (5′) as shown, so we will never be able to obtain a deep null.

8.9.2 Behavior at f_{M+} and f_{M-}

As illustrated in Fig. 8.17, we will at the frequency f_{M-} have the FSS 2 susceptance (1) at ∞ and so will the sum admittance (2). The transformed admittance (3) will be located somewhere on the rim of the Smith chart regardless of the separation D. Thus, when added to the FSS 1 admittance (4), their sum will also be on the rim of the Smith chart; that is, we will have 100% reflection as indicated in the reflection coefficient curve to the right. Similarly we also obtain perfect reflection at f_{M+}.

8.9.3 Behavior at f_L and f_H

In the event the two FSSs were tuned to the same frequency, we saw in Section 8.4 that a perfect null was obtained at the low and high frequencies f_L and f_H, respectively (see Fig. 8.5). If, on the other hand, the two FSSs are tuned to different frequencies this situation is illustrated for f_L in Fig. 8.17 bottom. Let FSS 1 be tuned to a somewhat higher frequency than FSS 2 as indicated in the Smith chart in Fig. 8.17 bottom, by the susceptances (4) and (1), respectively. Then the sum of (1) and the free space admittance Y_0 will be indicated by (2) which is next rotated into (3) depending on the separation D.

To obtain a sharp null, we must ideally require (3) to be located at the constant conductance circle through Y_0 which is alway possible either by adjustment of the separation D or by change of frequency. However, in any event we also observe that adding (4) to (3) will never land us in the middle of the Smith chart unless (1) equals (4); that is, we will no longer have a clean null in the reflection coefficient curve but a filled in null as indicated in Fig. 8.17 bottom-right.

At the high-frequency f_H the situation is quite similar to f_L; namely, a sharp null is obtained only when the two FSSs are tuned to the same frequency. A sharp null may be an important feature if good transmission is desired either at f_L or f_H.

8.9.4 Summary of Equal versus Staggered Tuning

A systematic display of the difference between equal and staggered tuning is shown in Fig. 8.18. First, at the first row after the schematic we show the equal tuned case ($f_{M-} = f_M = f_{M+}$) with array separation $D = \lambda/2$. We obtain two distinct nulls at f_L and f_H while the middle one at f_M is so narrow it essentially does not exist. Next, in the second row the two FSSs have been tuned symmetrically up to f_{M+} and down to f_{M-}, respectively. Essentially two things happen:

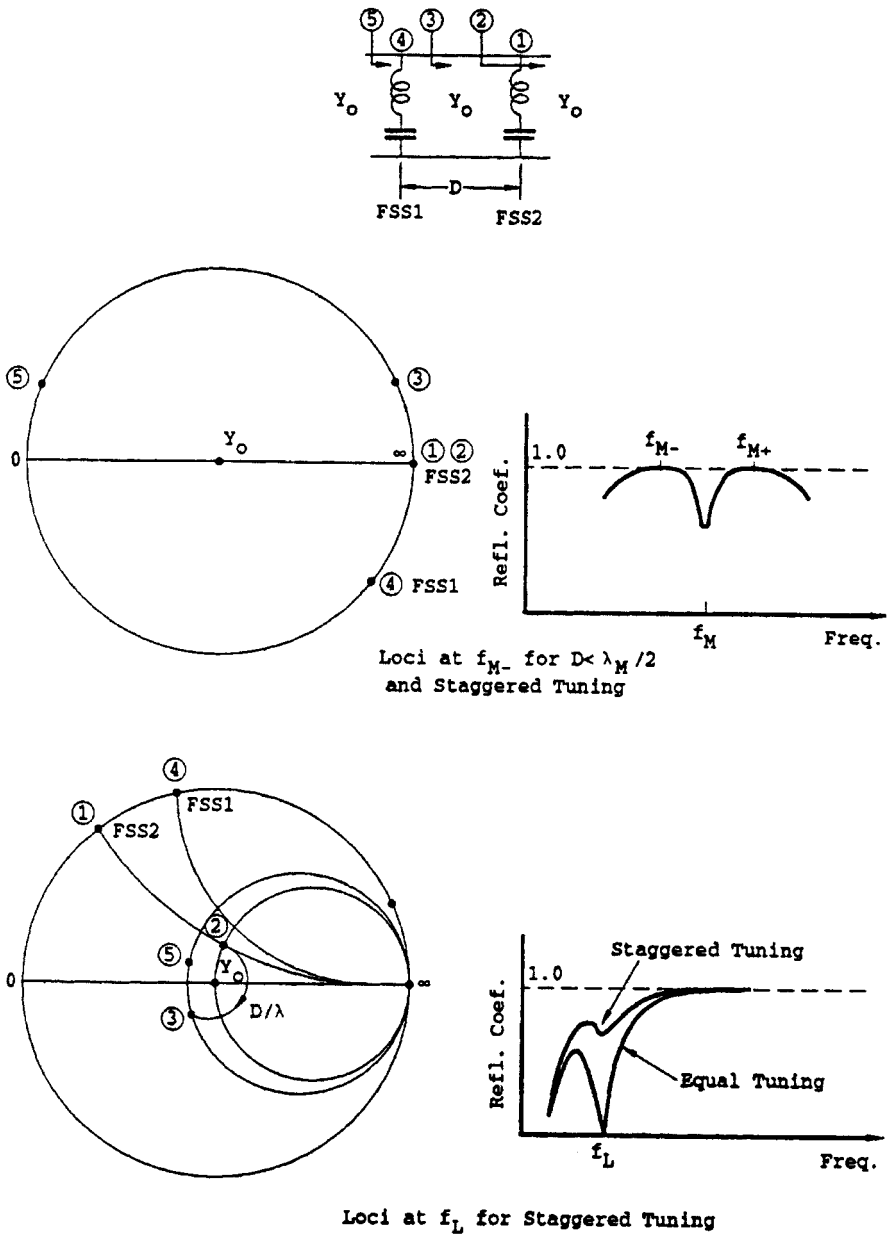

FIGURE 8.17. *Top*: Schematic of a two-layer band-stop filter with FSS 1 $\neq$ FSS 2. *Middle-left*: Smith chart showing the loci at frequency f_{M-} for $D < 0.5\,\lambda_M$. *Right*: Reflection coefficient curve around f_{M-} and f_{M+}. *Bottom-left*: Smith chart showing the loci at frequency f_L. *Right*: Reflection coefficient curve around f_L.

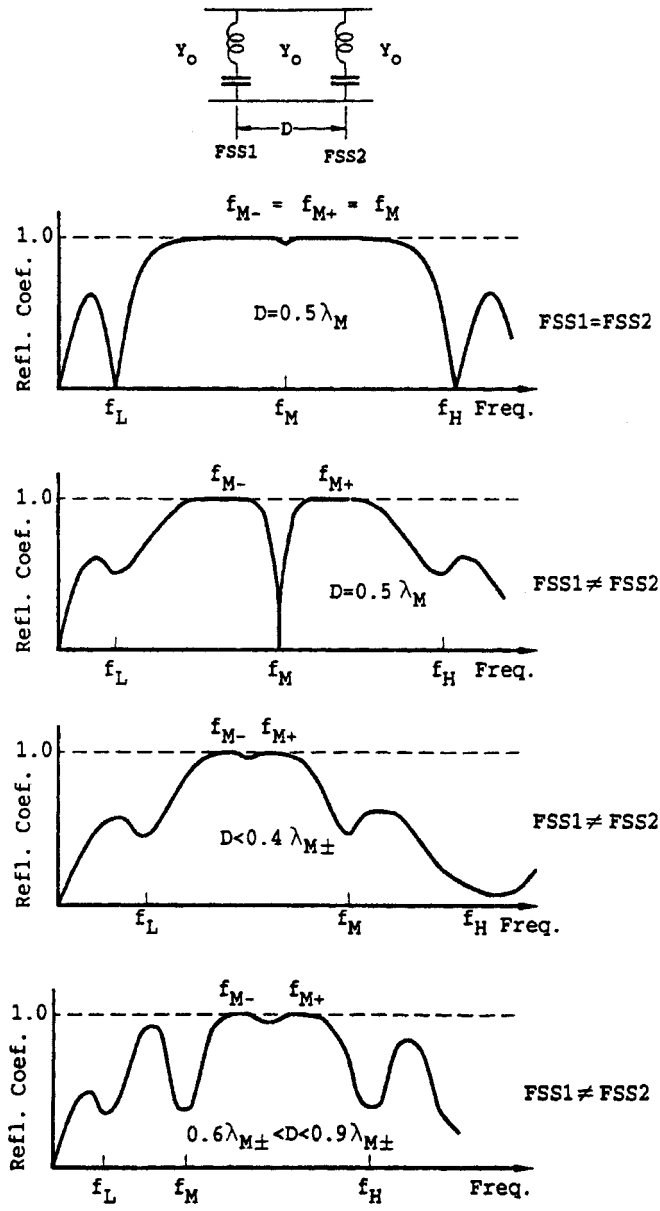

FIGURE 8.18. Summary of staggered band filter design. *Top*: Schematic of a two-layer band-stop filter. *First row*: Reflection coefficient curve for $f_{M-} = f_M = f_{M+}$ and FSS separation equal to $0.5\lambda_M$ (reference case). *Second row*: Reflection coefficient curve for $f_{M-} \neq f_{M+}$ and $D = 0.5\lambda_M$. *Third row*: Reflection coefficient curve for $f_{M-} \neq f_{M+}$ and $D = 0.4\lambda_{M\pm}$. *Fourth row*: Reflection coefficient curve for $f_{M-} \neq f_{M+}$ and $0.6\lambda_{M\pm} < D < 0.9\lambda_{M\pm}$.

1. A distinct null now occurs at f_M, whose width depends of how far f_{M-} and f_{M+} are from each other. We have perfect reflection at both these frequencies.
2. The nulls at f_L and f_H will be filled in.

Further we show in Fig. 8.18, third row, the case where we are still staggered tuned with the same f_{M-} and f_{M+} as before, but the array separation D has been reduced somewhere to $D < 0.4\lambda_{M\pm}$. This results in an upward shift of all three frequencies f_L, f_M, and f_H with the latter f_H typically moving out of the frequency range of interest. However, the midfrequency f_M typically moves up higher than f_{M+} (and is for that reason often mistaken for f_H). The reflection coefficient between f_{M-} and f_{M+} is now merely a gentle valley with a depth depending on the ratio f_{M+}/f_{M-} as well as the array separation D. Note also that the maximum right below f_L is somewhat higher than the previous case (Fig. 8.18 second row). It can be lowered by making the bandwidth of the two FSSs narrower.

Finally we show in Fig. 8.18 bottom row the same staggered tuned case as above but after the FSS separation D has been increased to the range $0.6\lambda_{M\pm} < D < 0.9\lambda_{M\pm}$. This is seen to move all three frequencies f_L, f_M, and f_H downward, similar to the equal tuned cases shown in Fig. 8.4. However, in the staggered case the nulls will (in general) be filled in.

We should further note that if the distance D in the second row case is not $\lambda_M/2$ but slightly different, the null at f_M will be filled in. If f_M moves closer to either f_{M+} or f_{M-}, we will still have perfect reflection at both these two frequencies but some loss around them.

8.9.5 Conclusions on Equal and Staggered Tuning

Since equal tuning effectively takes out f_M if $D = 0.5\lambda_M$ and also yields deep clean nulls at f_L and f_H in contrast to staggered tuning, it appears that equal tuning is preferable to staggered tuning for most applications.

8.10 CONCLUSIONS FOR BAND-STOP FILTER DESIGN WITH BROAD BANDWIDTH

We have in this chapter demonstrated that band-stop filters with large bandwidth (typically 3 to 1, or more) could be produced by using two cascaded broadband FSSs separated by $\lambda/2$ at their resonating frequency. First, it was shown that use of a dielectric slab between the two FSSs could improve the band-stop stability with angle of incidence. However, although higher dielectric was better from a stability point of view, it also leads to higher transmission loss at the frequencies below the band-stop frequencies. Thus a compromise was determined with ϵ_r around 1.4.

Further it was shown that improved matching at the band-pass frequencies leading to lower transmission loss below 3 GHz could be obtained by use of dielectric matching plates placed on the outside of the two FSSs. It was determined that a dielectric constant around 1.6 and a thickness of 3.75 cm ($\sim 0.5\lambda_2$) lead to an average

reflection level of around 15 dB (or 10–30 dB transmission loss) from around 2 to 3.5 GHz for angles of incidence ranging from normal up to 60° (orthogonal and perpendicular polarization).

Finally we demonstrated that adding a third FSS resonating at a higher frequency than the two first (i.e., at about 17 GHz rather than 10 GHz) could extend the band-stop region upward beyond 20 GHz without any effect at the band-pass region below 3 GHz. Although we did not actually demonstrate a further extension of that principle, we see no reason why more FSSs resonating at higher frequencies could not be added and extend the band-stop region upward indefinitely, as long as grating lobes are not excited.

8.11 BAND-STOP FILTER WITH NARROW BANDWIDTH

So far we have investigated band-stop filters with large bandwidth in the band-stop region. In this section we will present a band-stop filter with relatively narrow bandwidth. Actually it is a dichroic surface that is designed to be reflective from around 28 to 30 GHz and transparent from around 18 to 20 GHz and the angle of incidence goes from 0° up to 70°. Basically it will consist of two identical reflecting surfaces resonating around 29 GHz. They are sandwiched between three dielectric slabs as shown in the insert of Fig. 8.19.

8.11.1 Choice of Element

Since this is a narrow-band design it will in general be a good idea to choose a narrow-banded element. Inspection of Chapter 2 suggests the four-legged loaded element is a possible candidate. It is interesting to note that it belongs to the loop family like the hexagon element used earlier in the broadband design. A picture of our element is shown in Fig. 8.20.

8.11.2 Choice of Dielectric Profile

Since this dichroic surface has to work for angles of incidence up to 70° in a relatively narrow-band, it is important to explore the possibility of using dielectric slabs similar to the hybrid radome case discussed in Chapter 7. It should be emphasized, however, that these outer dielectric slabs in the present case work quite differently from the broadband case discussed earlier in this chapter. In the narrow-band case we can simply maintain the "magic" thickness of approximately $\lambda_\epsilon/4$ around the upper-frequency band. In the broadband case the frequency simply varies so much that the electrical thickness varies from almost nothing to more than a full wavelength. As discussed earlier in Section 8.2, the outer dielectric slabs serve primarily as matching devices in the transparent frequency region.

Thus, based on our investigation in Chapter 5, we will choose the dielectric constant of the outer dielectric slabs to be around $\epsilon_1 = \epsilon_3 = 1.3$ with a thickness of about $0.33\lambda_1$ (more than $0.25\lambda_1$ account for $r_{1y} < 1$) at 29 GHz. For the dielectric slab in the middle, we will choose $\epsilon_2 = 2.17$ primarily because it is a value readily

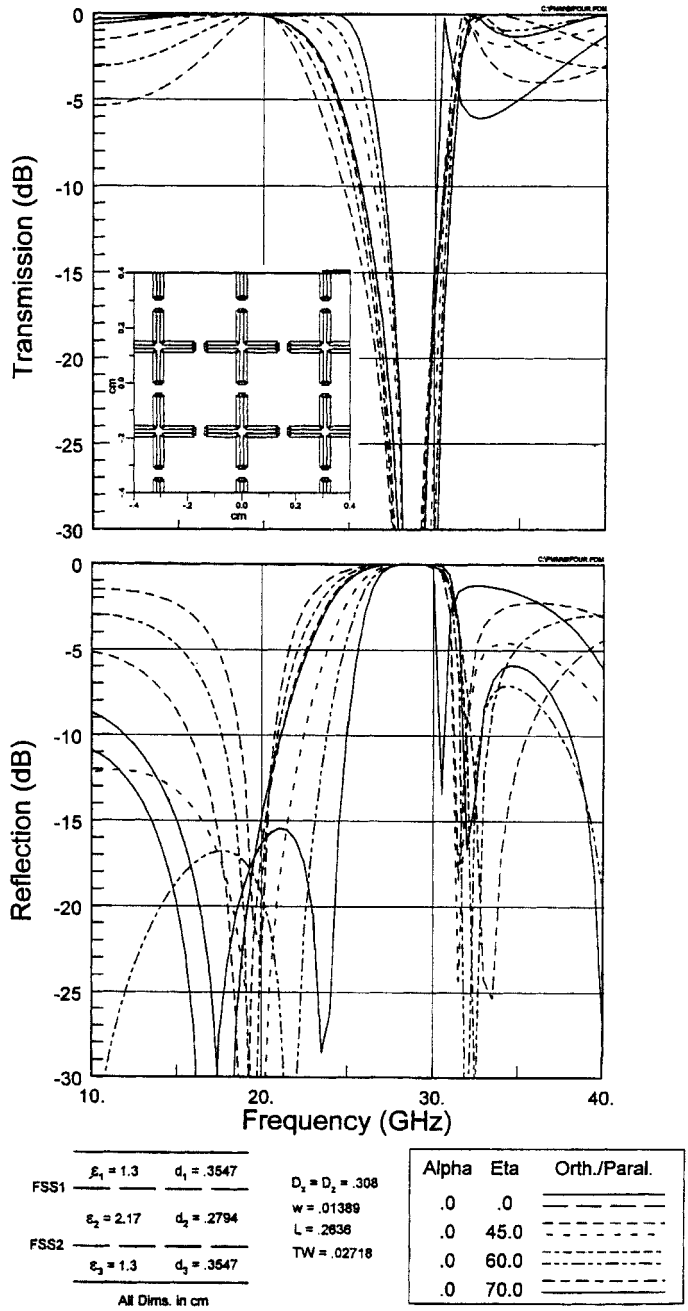

FIGURE 8.19. Typical transmission and reflection curves for a biplanar dichroic design for relatively narrow bands. Therefore the outer dielectric slabs can stabilize the bandwidth.

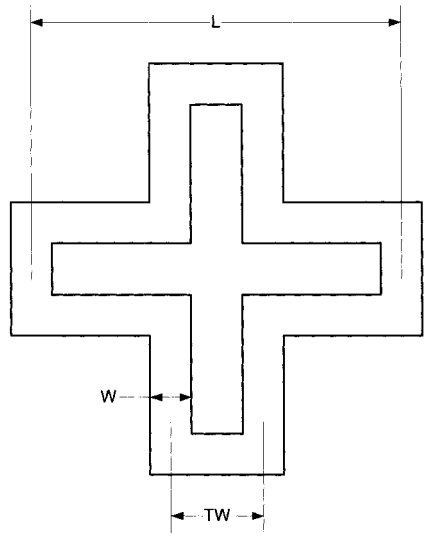

FIGURE 8.20. Detailed drawing of the four-legged loaded element used in the design shown in Fig. 8.19.

available commercially. The thickness should be around $0.3\lambda_2$ to be determined primarily by the transparent frequency range 18–20 GHz. In fact, this design will also exhibit a number of nulls just as we saw in the broadband case earlier in Section 8.5, and as shown there the location of these nulls in the reflection curves are determined primarily by the distance d_2 between the two FSSs. More specifically the null around 20 GHz can be moved up in frequency simply by reducing d_2.

8.11.3 Calculated Reflection and Transmission Curves

Based on the considerations presented above, we have designed the dichroic surface shown in the insert in Fig. 8.19 bottom. It is comprised of two identical FSSs of four-legged loaded elements with dimensions as given.

At the top of Fig. 8.19 we show the transmission curves from 10 to 40 GHz for angles of incidence 0, 45°, 60°, and 70°, orthogonal and parallel polarization. At the bottom of the same figure, we show the reflection curves. A total of eight segments was used on the elements, and speed was not an issue. Apart from minor adjustments no optimization was done. It would be a good place to start.

We finally in Fig. 8.21 show the same design as in Fig. 8.19 but without any dielectric slabs. We observe reasonable reflection properties around resonance which is now around 38 GHz due to the absence of the dielectric. However, the variation of the bandwidth with angle of incidence has deteriorated into unacceptable levels resulting in mediocre transmission at any lower frequency. Returning the design back to 28–30 GHz is easily accomplished by increasing the element size. However, only dielectric can produce the stability with angle of incidence. No need to optimize here.

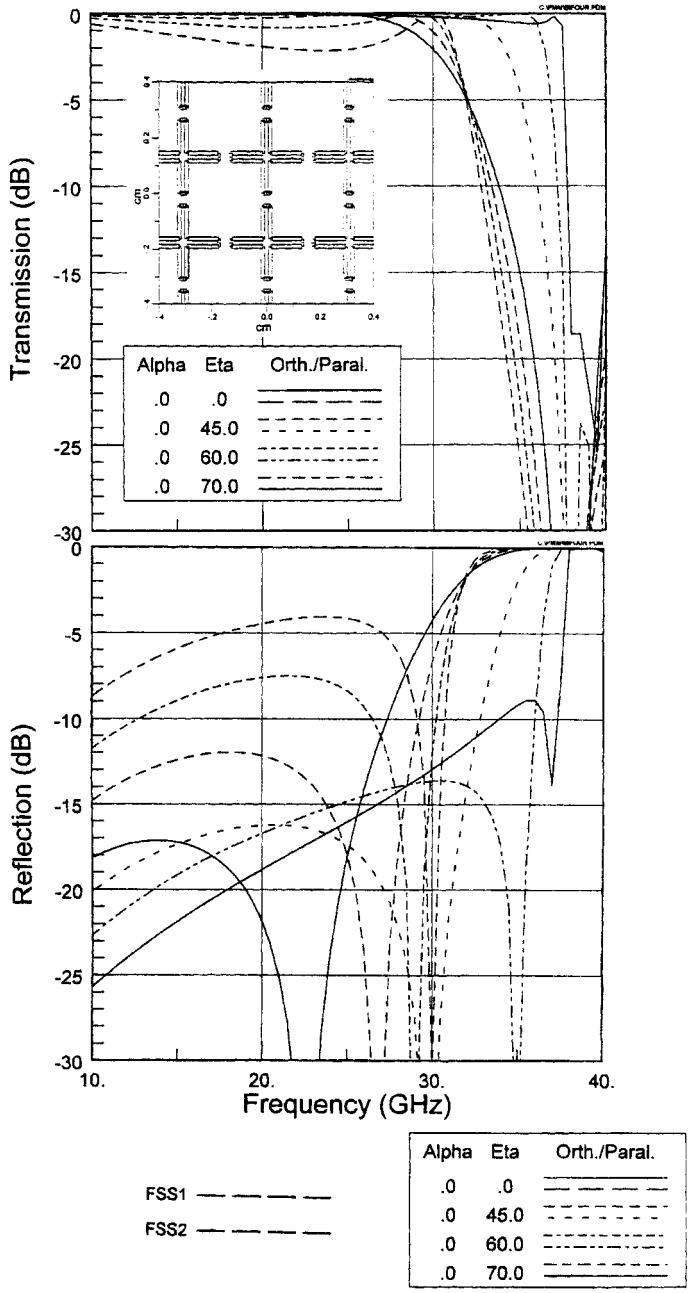

FIGURE 8.21. Same design as in Fig. 8.19 but without any dielectric slabs. It has been reduced to be merely a reasonable reflector at around 39 GHz. However, the constant bandwidth and transmission at lower frequencies is gone (except for 0–45° angles of incidence).

8.12 COMMON MISCONCEPTIONS

8.12.1 Differences between Band-Pass and Band-Stop

Everyone quickly catches on to the concept that band-pass as well as band-stop filters should be built of cascaded arrays of FSSs. In the band-pass case we generally use periodic structures of the slot type. Further, as we have demonstrated so far in this chapter and in Chapter 7, use of a stratified dielectric medium can greatly enhance the performance in both cases.

Because of this similarity between the two cases, it is often erroneously expected that the reflection properties of one case somehow by an obscure "duality concept" mimics the transmission curves of the other. Although there certainly are strong similarities between the two cases, they are in reality profoundly different in many ways. The significant difference is that while the transmission curve for the band-pass case of slot arrays typically will go down rather monotonically below as well as above the band-pass region (see Fig. 7.9), a reflection curve of a biplanar band-stop filter of dipoles will typically go down to zero (or at least a low value) then up again to a maximum value with reflection coefficient less than unit (often referred to as *ears*). These nulls are the result of interference between the individual arrays of dipoles, and they are therefore often referred to as *array interference nulls*. Their location is primarily determined by the array separation $\beta_2 d_2 r_{2y}$; that is, for smaller separation d_2 the interference frequencies will be higher. The same is true for higher angles of incidence, since this will lead to a smaller value of r_{2y}. No array interference nulls are present in the slot case as discussed in detail in Chapter 7.

8.12.2 On the Number of Layers

It is quite common to observe inexperienced designers with an enormous appetite for putting many layers of FSSs into band filter designs. In cases where the bandwidth is large and the roll-off steep, classical filter theory will of course support this notion.

There are at least two reasons for showing some restraint here: One is simply cost; the other is loss and in some cases cooling of the filter, see Chapter 10.

As shown in this chapter, considerable bandwidth can be obtained from just two FSSs if properly designed. It is simply good policy to start there. If more bandwidth is needed, add a third FSS as explained in Section 8.8. Remember that ordinary filter theory must be adapted to angle of incidence variations as well as polarization. Further, evanescent mode coupling cannot alway be ignored as is the case when a simple transmission line approach is used.

8.12.3 On the Bandwidth of "Fat" Elements

It was already mentioned in Section 2.6.2 that while "fatter" dipole elements in general are capable of producing a larger bandwidth, there comes a point when they degenerate into some form of the plate element. These simply do not resonate in general (it is the onset of the grating lobes that makes them look like they resonate).

In this chapter we saw a very vivid demonstration of how a large bandwidth is obtained, namely by using elements of the loop (particularly hexagon) type, where they can be considered simply as being of the solid or plate type that subsequently have been hollowed out as discussed earlier in Section 2.4. It is a rather common misconception that removing the center of the element can't do much. In other words, an element is expected to behave like its own outline. How terribly wrong this simple picture is!

8.13 CONCLUSIONS

We have investigated spatial band-pass and band-stop filters in Chapter 7 and this chapter, respectively. The first type is usually made of slot arrays, and the second, of dipole arrays. We found that for a relatively narrow bandwidth such as 5% to 20%, the use of a stratified dielectric medium is an absolute necessity in both cases in order to obtain a relatively constant bandwidth with angle of incidence (0 to 70° and even higher) and arbitrary polarization.

However, only in the band-pass case did we establish rigorous conditions enabling us to design band-pass filters with constant bandwidth and low reflection in the pass band. The principal reason for this dilemma is that we in the slot case have re-radiation only from the front and back array, while we in the dipole case always have re-radiation from all arrays at the same time. This fact makes dipole arrays inherently more difficult to analyze unless an approximate transmission line model is adopted. In both cases we established that slabs with a relatively low dielectric constant are essential to maintain constant bandwidth with angle of incidence.

We also investigated filters stopping frequencies over a broad frequency range while the band-pass range at the lower frequencies varies. In this case the use of dielectric slabs was favorable but essentially for different reasons than in the narrow-band case. The principal reason is simply that the larger bandwidth makes the dielectric slab thickness considerably outside the range of $\lambda_\epsilon/4$. However, the outer dielectric slabs could be designed to act as matching sections at the lower band-pass frequencies while use of dielectric slabs between adjacent arrays could stabilize the pass band as a function of angle of incidence.

We finally demonstrated a scheme where we added extra arrays of dipoles resonating at higher frequencies. This approach enabled us to extend the stop band upward indefinitely, as long as no grating lobes are excited.

For further reading about FSS with a somewhat different viewpoint, see [54, 55].

8.14 PROBLEMS

8.1 Dichroic FSS

a. Design a dichroic FSS with reflection coefficient close to magnitude one from $f = 6$ to 10.5 GHz and transmission at $f = 2.0$ to 2.1 GHz.

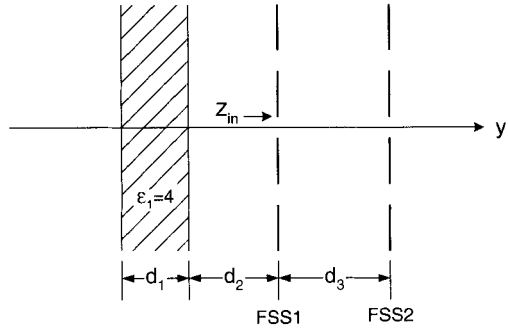

Fig. P8.1(a)

We choose to use two very broadbanded identical FSSs as indicated by FSS1 and FSS2 in Fig. P8.1*a*. The *input impedance* Z_{in} of this combination at FSS1 is shown in the Smith chart in Fig. P8.1*b*. Realizing that the reflection coefficient in a Smith chart is simply the distance from the center of the chart to the frequency point in question, we observe an excellent reflection from about 6 to 10.5 GHz. However, perfect transmission is obtained at around 3.2 GHz and not at 2.0 to 2.1 GHz as desired. Increasing the distance d_3 between the two FSSs would lower the transmission frequency but would also produce an undesirable null in the reflection band.

Alternatively, it is suggested to place a dielectric slab of thickness d_1 and $\epsilon_1 = 4$ at a distance d_2 from the FSS to the left as shown in Fig. P8.1*a*.

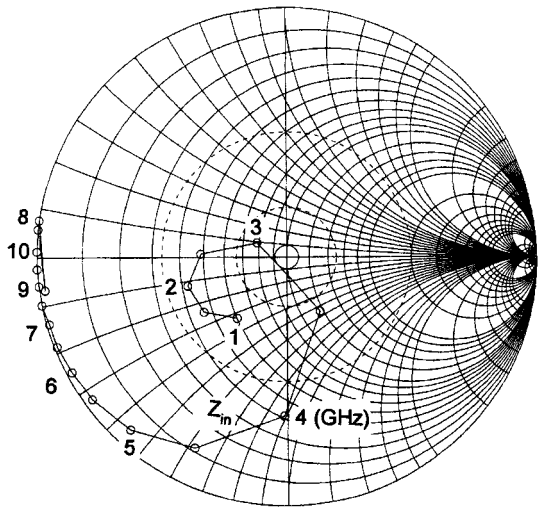

Fig. P8.1(b)

b. Find d_1 and d_2 in cm such that there is good transmission at 2.0 to 2.1 GHz. Can you suggest an alternative matching scheme that would yield larger bandwidth at the transmission band?

c. Explain the "glitch" at around 8 GHz.

9

JAUMANN AND CIRCUIT ANALOG ABSORBERS

9.1 BACKGROUND

So far in this book we have considered periodic surfaces made only of perfectly conducting elements. In this chapter we investigate FSSs made from lossy elements. Such devices are used extensively for producing absorbers that have a smooth surface, are relatively thin in terms of wavelength, and are potentially lightweight.

It is often expected that such devices are inherently narrow-banded because of the resonant nature of the FSS elements. This is, however, not necessarily the case. In fact it is possible to obtain a bandwidth that should be measured in decades rather than octaves. Such surfaces are called *circuit analog* (CA) *absorbers* for reasons that will be explained later. These types of surfaces are actually derived from surfaces that are nonperiodic and simply contain a resistive sheet in front of a ground plane, namely the *Salisbury screen* [56]. If two or more resistive sheets are put in front of each other, we obtain the *Jaumann absorber*. Both of these will be discussed in some detail before our discussion of the actual CA absorbers.

As with our investigation of band-stop filters in Chapter 8, we will also in this chapter make heavy use of the transmission line approach and use of the Smith chart during the design phase. More rigorous calculations then follow via a modified computer program.

9.2 SALISBURY SCREEN

A typical Salisbury screen is depicted in Fig. 9.1 top. It is simply comprised of a resistive sheet mounted one-quarter wavelength in front of a ground plane (all absorbers should in general have a ground plane in the back to prevent any ambiguity as caused by any objects located behind the absorber sheets). This type of absorber

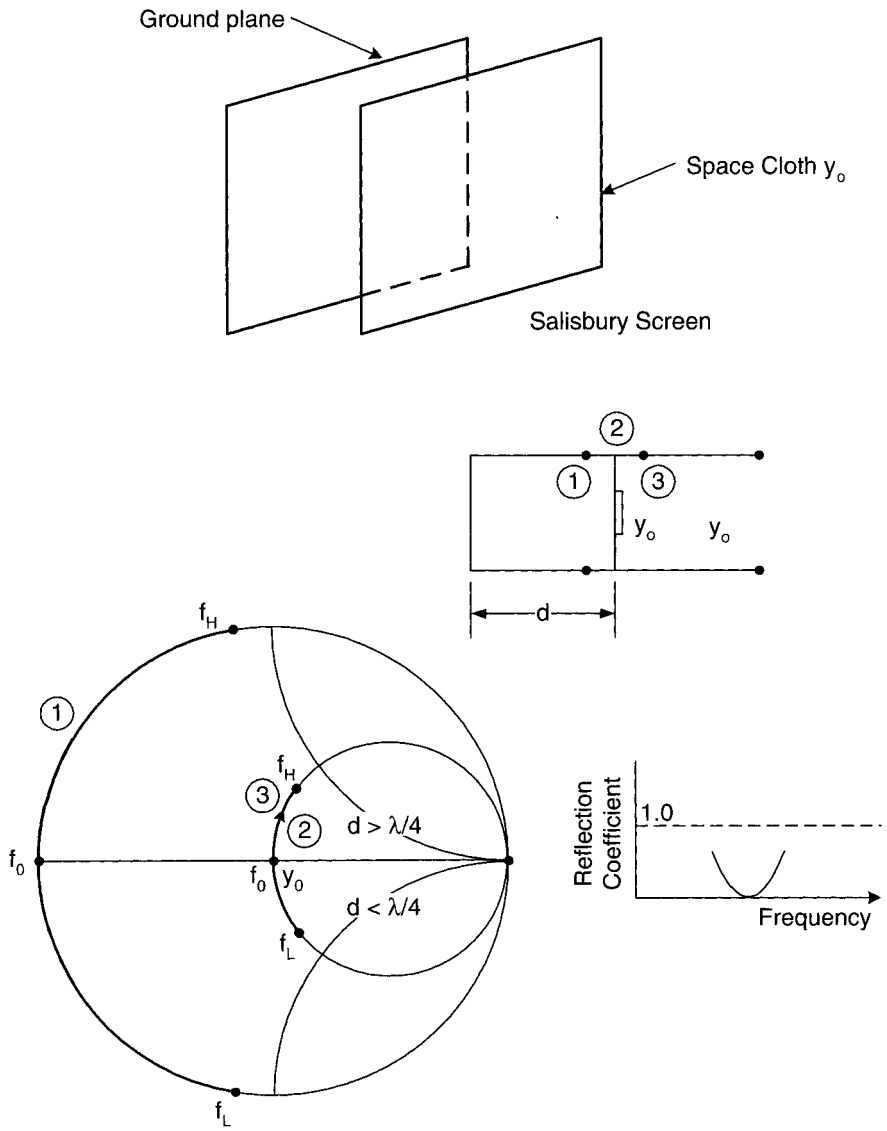

FIGURE 9.1. *Top:* Simple Salisbury screen comprised of a resistive sheet in front of a ground plane. *Middle:* Equivalent circuit. *Bottom-left:* Smith chart showing the derivation of the input admittance as a function of frequency. *Bottom-right:* Reflection coefficient as a function of frequency.

was named after its inventor, W.W. Salisbury of the MIT Radiation Laboratory, who was issued a patent in 1952 [56].

The workings of the Salisbury screen are easily understood by inspection of the equivalent circuit shown in Fig. 9.1 middle. At the frequency where the spacing

from the resistive screen to the ground plane is $\lambda/4$, the input admittance of the equivalent short circuited transmission line denoted (1) is zero. We merely see the resistive screen alone which has an admittance close to that of free space Y_0. In other words we obtain a total input admittance located close to the center of the Smith chart as shown in Fig. 9.1 bottom. However, at lower frequencies the input admittance of the equivalent transmission line (1) becomes inductive, causing the total admittance to be located in the lower half of the Smith chart. A typical reflection curve is readily obtained, as shown in Fig. 9.1 bottom-right. Use of a dielectric slab between the screen and the ground plane leads to a higher input admittance in the equivalent transmission line (1) (except for $\lambda/4$ spacing). Thus this is seen to reduce the bandwidth of the Salisbury screen. Ideally we could use ferrite or some other material with a lower intrinsic admittance than free space Y_0. However, that approach is usually not very popular because of the weight penalty and because better solutions are obtained by other means (as will be discussed later). Use of dielectric and/or a high μ material will of course lead to designs of reduced thickness.

9.3 JAUMANN ABSORBER

The Jaumann absorber is similar to the Salisbury screen except that it is made of two or more homogeneous resistive sheets mounted in front of a ground plane as shown in Fig. 9.2 top. These screens are separated by dielectric slabs of about $\lambda/4$ thickness measured in the respective slabs at the center frequency. Thus the Jaumann absorber can be considered as a simple extension of the Salisbury screen. However, it appears to actually predate the latter by several years. The historical facts are hard to obtain since the Jaumann absorber was invented by J. Jaumann during World War II in Germany. It was apparently used primarily to reduce the radar cross section of submarine snorkels and periscopes.

The workings of a Jaumann absorber with air separations is readily understood by inspection of the Smith charts and the equivalent circuit also shown in Fig. 9.2. The admittance at position (1) looking toward the ground plane in the equivalent circuit is depicted by curve (1) at the rim of the Smith chart in the middle. To this pure reactance we now add the sheet admittance $2Y_0$ as denoted by curve (2). The sum of curves (1) and (2) yields curve (3) where we note that the highest frequency f_H is located in the upper half of the Smith chart while the lowest frequency f_L is located in the lower half. We next rotate curve (3) into curve (4) corresponding to the separation between the two resistive sheets. If we choose this separation to be $\lambda/4$ at the center frequency f_0, we will rotate less than 180° at the lower frequency f_L and more at the higher f_H. The result is seen to be that the frequencies f_L, f_0, and f_H are more clustered together in curve (4) than in curve (3). We finally add the last sheet admittance $0.7Y_0$ as shown in the lower Smith chart in Fig. 9.2 and obtain curve (6). This curve is seen not only to be located at the center of the Smith chart but also to have the frequencies further clustered together due to the nature of the Smith chart. Recalling that the reflection coefficient is simply the distance from the center of the Smith chart to the respective frequency points of curve (6), we readily

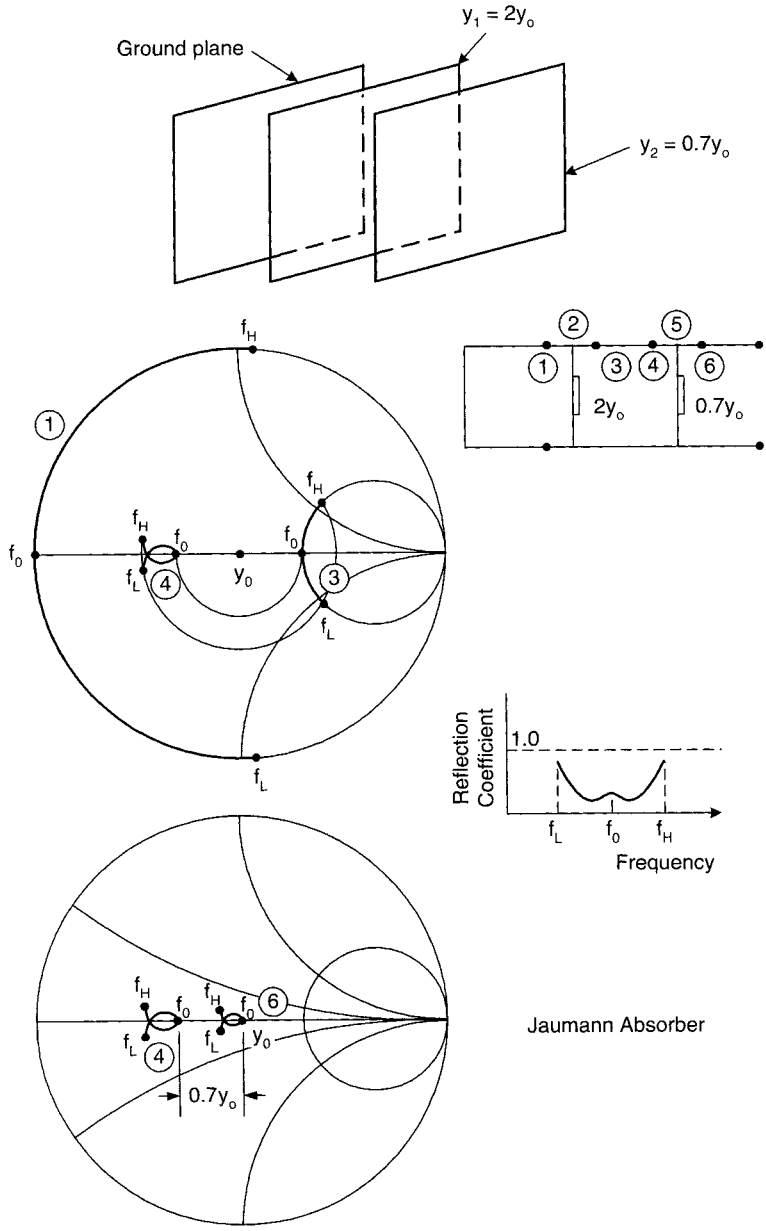

FIGURE 9.2. *Top:* Typical Jaumann absorber comprised of two resistive sheets in front of a ground plane. *Middle:* Smith chart (left) showing the beginning of how to obtain the input admittance of the absorber and equivalent circuit (*right*). *Bottom:* Smith chart (*left*) showing the final calculation of the input admittance and typical reflection coefficient as a function of frequency (*right*).

obtain the typical reflection curve shown in Fig. 9.2 bottom-right. We observe that contraction of the admittance curves (4) and (6) is obtained only when the first sheet admittance $Y_1 > Y_0$. If $Y_1 < Y_0$, no contraction is observed; in fact we cannot even land in the center of the Smith chart unless Y_2 is negative.

The simple example of a Jaumann absorber shown above had air between the resistive sheets. This was chosen to facilitate the calculations in the Smith chart. Under most practical circumstances dielectric slabs will usually be required at least for mechanical reasons. However, use of dielectric cannot only reduce the total thickness of a Jaumann absorber, it can actually extend the bandwidth. This can easily be observed by pursuing the calculations in a Smith chart. An example is shown in Fig. 9.3 where the dielectric constants of 3 and 2 were given as shown in the schematic. Straight forward calculations in the Smith chart easily yield curve 4 that is seen to be centered around Y_0 located at $0.7Y_2$. We easily obtain a reflection level below 20 dB in the frequency range 5 to 15 GHz and for a total thickness of about 1.2 cm. This would be a good place to start an optimization process for the resistive sheets and the optimum values of the intrinsic admittances Y_1 and Y_2.

Note that we have applied a dielectric slab on the outside of the outermost resistive sheets. It serves two purposes. First, it improves the bandwidth of the absorber, and second, it shields the resistive sheet from the environment (this is particularly important in the cases where we use a CA sheet as we will see later). Note also the 30 mil dielectric layer on the very outside of the absorber. It serves primarily as a mechanical protection for the lower dielectric constant material underneath. In general, the more rugged dielectrics have a higher dielectric constant than those with a dielectric constant below 2. It is of course part of the outer matching transformer and is easily compensated for in this case by simply making the thickness of the outer transformer slightly less than one-quarter wavelength.

9.4 CIRCUIT ANALOG ABSORBER

The two absorber types considered above, the Salisbury screen and the Jaumann absorber, were characterized by using purely resistive sheets.

We are now going to consider the so-called CA absorbers. These are characteristically made of sheets that not only contain a resistive component but are reactive as well. This is accomplished by using periodic surfaces made of lossy material, as shown in Fig. 9.4 top. We have in Section 4.11.1 developed the equivalent circuit for an array of lossless elements loaded with Z_L as shown in Fig. 4.15. Based on this circuit, it is fairly obvious that the equivalent circuit for a CA sheet in either principal plane will consist of an RLC series combination as indicated in the equivalent circuit shown in Fig. 9.4 middle. The resistive component is a result of the lossy element material, while the inductance is associated with the straight part of the elements and the capacitance with the gaps between the elements as shown at the top of Fig. 9.4. We emphasize that this equivalent circuit is only an approximation that merely serves to explain the workings and the name of the CA absorber. The more precise calculation will be developed later in Sections 9.5 and 9.6. In fact, as shown later, it is not

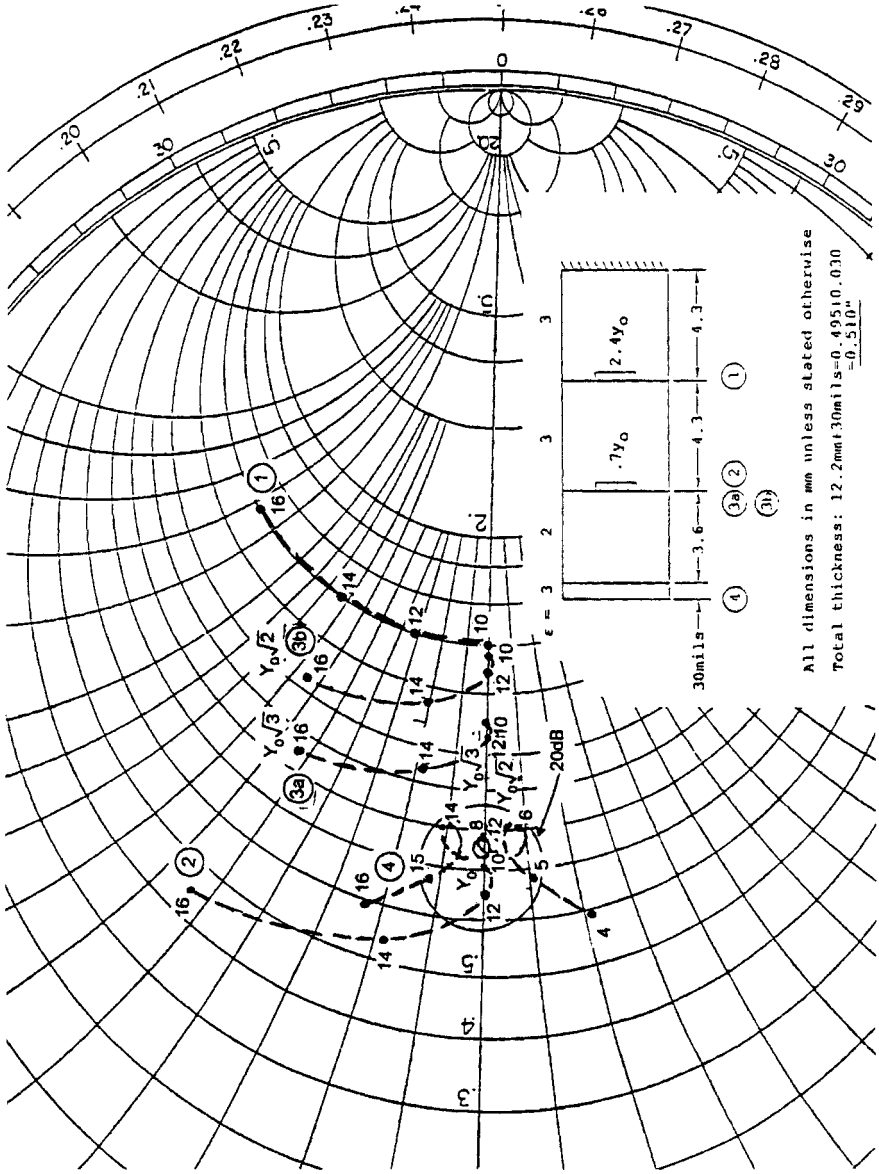

FIGURE 9.3. Smith chart showing calculations of a Jaumann absorber comprised of two resistive sheets sandwiched between three dielectric slabs and an external skin.

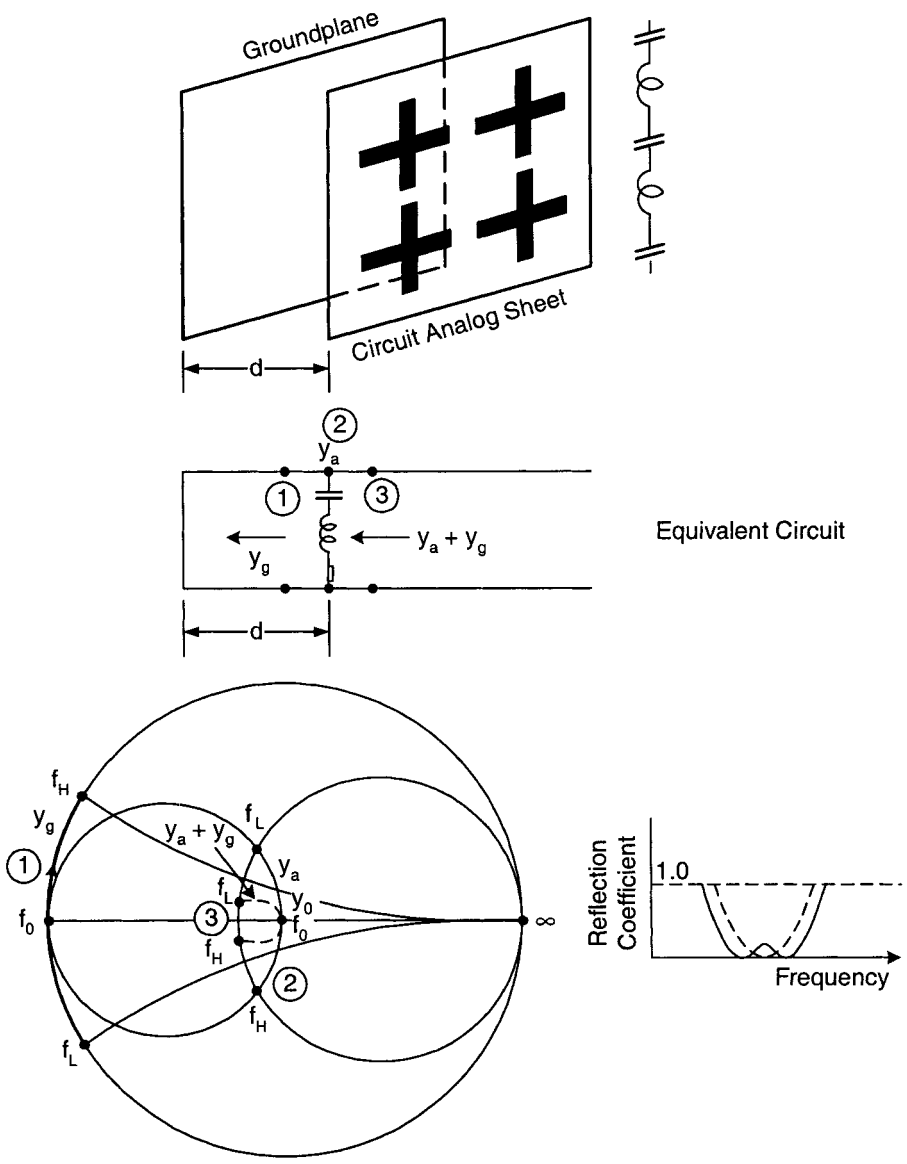

FIGURE 9.4. *Top:* CA absorber comprised of a single CA sheet in front of a ground plane. *Middle:* Equivalent circuit. *Bottom:* Smith chart depicting how to calculate the input admittance (*left*) and typical reflection coefficient as a function of frequency (*right*). The frequencies f_L and f_H denote the lowest and highest frequencies, respectively.

even recommended to obtain the exact equivalent circuit but merely to plot the CA sheet admittance directly on a Smith chart and simply work from there.

Based on these facts, the basic idea of a CA absorber becomes quite clear. At the center frequency f_0 the distance between the ground plane and the CA sheet is approximately $\lambda/4$ while the RLC-series circuit resonates. In other words, it is similar to the simple Salisbury screen discussed earlier. However, at the lower frequency f_L the input admittance Y_g toward the ground plane becomes inductive as indicated by curve (1) of Fig. 9.4 at the rim of the Smith chart, while the RLC sheet Y_a becomes capacitive as indicated by curve (2). The total admittance of the complete CA absorber is simply the sum of Y_a and Y_g, as indicated by curve (3).

We observe that the reactive parts of Y_a and Y_g to a large degree cancel each other resulting in a location for f_L very close to the center of the Smith chart; it leads to a small reflection. The same is true for the higher-frequency f_H.

It is easily noted that choosing the real part of the CA sheet admittance equal to Y_0 is not necessarily the best choice when designing for the largest bandwidth. In fact, if chosen slightly higher than Y_0, it can result in a somewhat higher bandwidth as indicated by the full line reflection curve in Fig. 9.4 bottom-right.

Just like the Jaumann absorber was made of more resistive sheets, a CA absorber can be made from an arbitrary number of CA sheets. A simple example comprised of two CA sheets is shown in Fig. 9.5. The best understanding is obtained by simply calculating the various admittances in the Smith chart starting from the ground plane and continuing to the front. As you progress, you will see where the CA sheets should be modified to obtain the largest bandwidth at the front of the absorber. You next aim to change the dimensions of the CA sheets to obtain these ideal values of the CA sheets.

In short, you first sketch your design in a Smith chart. You next use a computer program (see the following section) simply to reduce the work load and improve accuracy. It is strongly recommended, however, that each additional layer in a Smith chart be plotted in order to keep track of the computation activity.

9.5 RIGOROUS CALCULATIONS OF CIRCUIT ANALOG ABSORBERS

The specular return from an assembly of array of lossy elements located in a stratified medium is calculated basically as for an array of lossless elements (as described in Section 8.3). Certain modifications will be necessary as will be discussed next.

9.5.1 Modifications Due to Element Width

Most applications of FSSs call for elements of relatively small or moderate width. However, some designs involving CA sheets often require so-called fat elements because of a request for large bandwidth.

In the first instance it is well known that a flat element of width w will, to a good approximation, be equal to an element of circular cross-section with radius $w/4$. In the event we are dealing with wide elements or elements with small inter-element

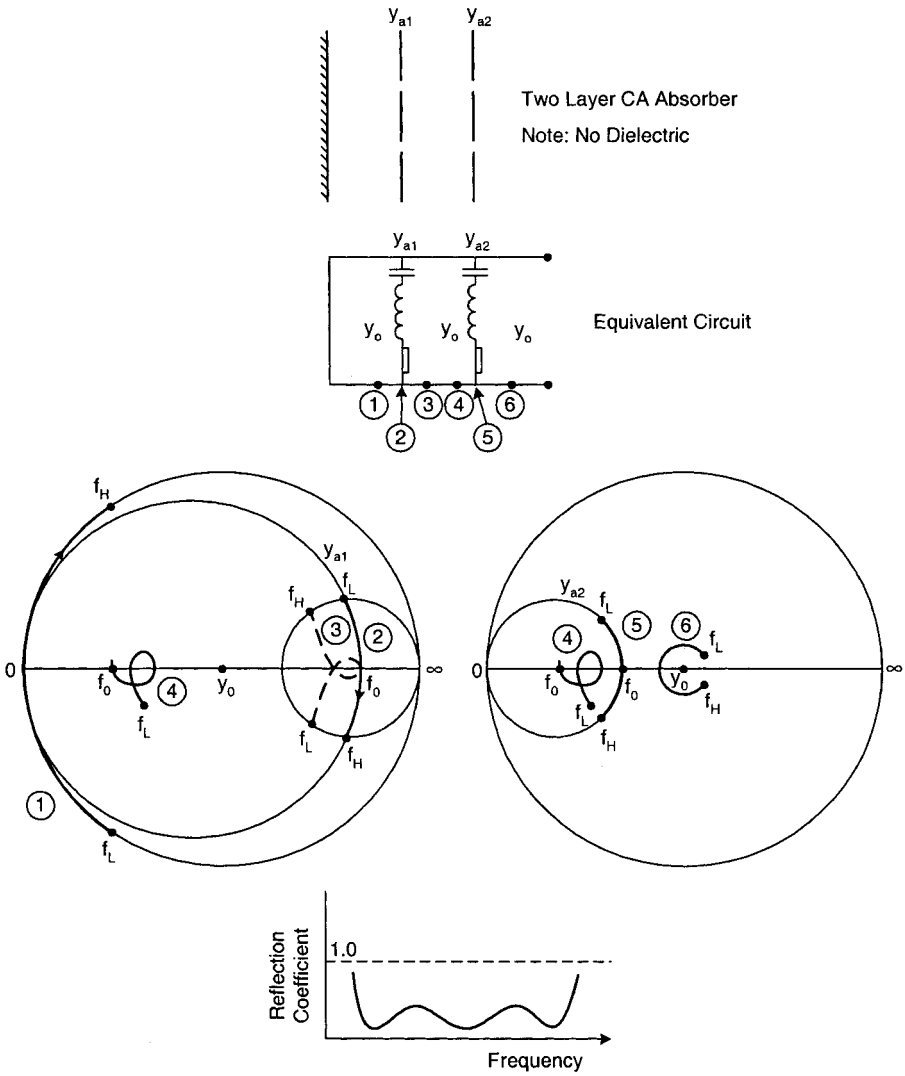

FIGURE 9.5. *Top:* CA absorber comprised of two CA sheets in front of a ground plane. *Middle:* Equivalent circuit (*above*) and two Smith charts showing the calculation of the input admittance (*below*). *Bottom:* Typical reflection curve as a function of frequency. The intricate details of curve (6) are not shown, only an outer bound.

spacing, it is usually more accurate to use the modified approach described in Appendix F. We simply use two-dimensional pattern factors obtained by integrating the assumed current densities under scattering as well as transmission conditions over the entire reference element as expressed by (F.7) and (F.12), respectively. These current densities will be discussed in the next section.

9.5.2 Modifications of the Currents Due to Loss in the Elements

Let us start by considering an array comprised of infinitely long wires, as shown in Fig. 9.6 left. It is exposed to an incident plane wave propagating in the direction $\hat{s}$ as shown. As a result we have traveling waves induced on these wires with the current on the reference wire given by

$$I(z) = I_0 e^{-j\beta z s_z}. \tag{9.1}$$

This equation is always valid for any infinitely long wire. However, the current amplitude I_0 will depend on the wire conductivity. Let us next consider an array of lossless elements of length $2l_1$, as shown in Fig. 9.6 middle. As we saw above, for

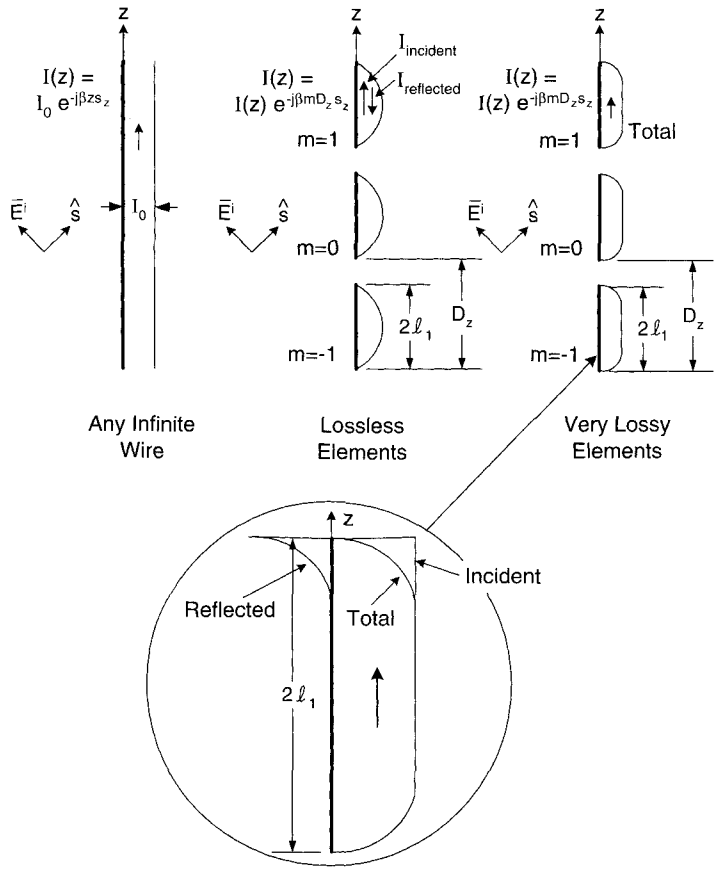

FIGURE 9.6. Current distribution on arrays of: *Left:* Infinitely long wires, with or without loss. *Middle:* Finite elements with no loss. *Right:* Very lossy finite elements with details of current distributions shown in the insert.

the infinitely long wires we will obtain a traveling wave propagating upward (for $s_z > 0$). However, at the upper tips of the elements, there will be a strong reflection resulting in a downward traveling wave. By also applying the boundary condition at the lower tips, we obtain a total current distribution that is basically sinusoidal, although for oblique angle of incidence not necessarily symmetric. Specifically, we obtain from (4.2) the element currents as given by (Floquet's theorem)

$$I_{qm} = I_{oo}(z)e^{-j\beta q D_x s_x} e^{-j\beta m D_z s_z}, \tag{9.2}$$

where $I_{oo}(z)$ denotes the current on the reference element.

Let us finally consider the case when the finite-length elements are made up a highly resistive material as shown in Fig. 9.6 right. As in the lossless case above, we will obtain a wave traveling upward, and again it will be reflected at the upper element tips. However, the reflected wave traveling downward will be strongly attenuated because of loss in the elements as illustrated in the insert of Fig. 9.6. Also shown there is the total element current, which is simply the sum of the incident and the reflected waves. The shape of the currents at the lower element tips is similar to the upper tips because the current will be built up gradually by the incident field.

The pattern functions to be used in our work with CA absorber or wide elements are discussed in Appendix F. The current distribution to be used in the evaluation of these pattern functions should for the CA absorber consist of a traveling wave adapted to the scattering as well as the transmitting case. In practice, it is quite common to approximate the amplitude of the current by a trapezoidal shape (it is a little easier to evaluate in closed form; see also Section 9.5.3, Example 2).

9.5.3 Equivalent Load Resistance Due to Lossy Elements

In the expression for the generalized Ohm's law, we have introduced the load impedance Z_L in the main diagonal terms of the impedance matrix. This impedance may represent any lumped impedance introduced by the designer at the reference point or it may represent the equivalent loss resistance obtained by making the elements of a lossy material as in a CA sheet.

In this section we calculate the equivalent loss resistance for a given conductivity and a given shape of the various current modes that may exist on the lossy elements. Let the ohmic surface resistance per square be denoted by R_S (ohm). In the present discussion, width refers to the element dimension which is transverse to the direction of current flow. Similarly length is associated with the element dimension in the direction of current flow. The dimension l_1 is equal to one-half of the total element length.

Consider the rectangular lossy element shown in Fig. 9.7 with length $2l_1$ and width w. The current is flowing in the $\hat{z}$-direction. Assume the current distribution to be uniform in the direction transverse to current flow [i.e., $\bar{J}^z$ is not dependent on x; i.e., $\bar{J}^z = \bar{J}^z(z)$].

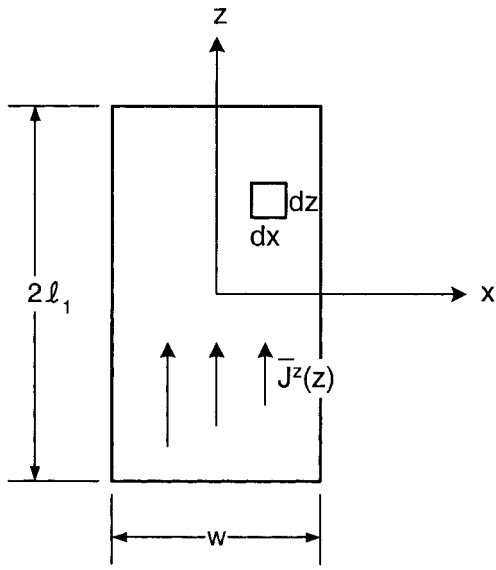

FIGURE 9.7. Lossy elements with current density $J^z(z)$ flowing in the $\hat{z}$ direction.

Noticing that the total resistance for an infinitesimal square $dxdz$ is equal to $R_s dz/dx$ (ohm), we readily find that the infinitesimal power lost per square is

$$\begin{aligned} \Delta P_L &= \left|J^z(z)dx\right|^2 R_s \frac{dz}{dx} \\ &= \left|J^z(z)\right|^2 R_s dx dz. \end{aligned} \tag{9.3}$$

Thus the total power lost per element due to loss in the elements is

$$\begin{aligned} P_L &= R_s \int_{-w/2}^{w/2} \int_{-l_1}^{l_1} \left|J^z(z)\right|^2 dx dz \\ &= wR_s \int_{-l_1}^{l_1} \left|J^z(z)\right|^2 dz \text{ (watts)}. \end{aligned} \tag{9.4}$$

Seen from a gap across the elements at $z = 0$, as shown in Fig. F.2 (Appendix F), this power is lost in an equivalent lumped resistance R'_L,

$$P_L = \left|J^z(0)w\right|^2 R'_L \quad \text{(watts)}. \tag{9.5}$$

Substituting (9.4) into (9.5) yields

$$R'_L = \frac{R_s}{w\,|J^z(0)|^2}\int_{-l_1}^{l_1} |J^z(z)|^2\,dz \quad \text{(ohms)}. \tag{9.6}$$

We next demonstrate the use of (9.6) with two key examples:

Example 1: Sinusoidal Current Distribution Let the current distribution in the z-direction be given by

$$J(z) = J(0)\sin\beta(l_1 - |z|). \tag{9.7}$$

Substituting (9.7) into (9.6) yields

$$\begin{aligned} R'_L &= \frac{R_s}{w\,|J(0)|^2\sin^2\beta l_1}\int_{-l_1}^{l_1} |J(0)|^2\sin^2\beta(l_1 - |z|)dz \\ &= \frac{R_s}{w\sin^2\beta l_1}\left[l_1 - \frac{1}{2\beta}\sin\beta l_1\right] \quad \text{(ohm)}. \end{aligned} \tag{9.8}$$

Example 2: Trapezoidal Current Distribution We saw earlier that the current distribution on very lossy elements was given by a constant current with exponential shape at the ends as shown in the insert in Fig. 9.6. It is often convenient to approximate this current distribution by a trapezoidal shape as shown in Fig. 9.8 where the current distribution is

$$J^z(z) = \begin{cases} \dfrac{J^z(0)}{1-c_1}\left[\dfrac{z}{l_1}+1\right] & \text{for } -l_1 < z < -c_1 l_1, \\ J^z(0) & \text{for } -c_1 l_1 < z < c_1 l_1, \\ \dfrac{J^z(0)}{1-c_1}\left[-\dfrac{z}{l_1}+1\right] & \text{for } c_1 l_1 < z < l_1, \end{cases} \tag{9.9}$$

Substituting (9.9) into (9.6) yields

$$\begin{aligned} R'_L &= \frac{2R_s}{w|J^z(0)|^2}\left[\int_0^{c_1 l_1} J^z(0)^z dz + \frac{|J^z(0)|^2}{(1-c)^2}\int_{c_1 l_1}^{l_1}\left(-\frac{z}{l_1}+1\right)^2 dz\right] \\ &= \frac{2R_s l_1}{3w}(1+2c_1) \quad \text{(ohm)}. \end{aligned} \tag{9.10}$$

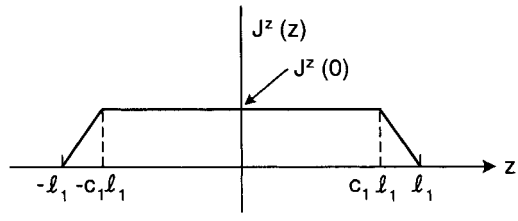

FIGURE 9.8. Trapezoid current distribution.

The parameter c_1 will of course depend on the lossiness of the elements. However, it is not a critical parameter as far as R'_L is concerned. Only it should never be put equal to unity, since the plane wave expansion in that case in general may not converge (see Problem 4.4).

9.5.4 Effect on Load Resistance Due to Orthogonal Strips

Expression (9.10) found above assumed the current to be uniformly distributed across the resistive strip in question. This is usually a good approximation provided that the strips do not change width or exhibit any other irregularity.[1] In many practical cases we are faced with the situation where two sets of strips are placed orthogonal to each other in order to handle arbitrary polarization. If the two sets of orthogonal strips are separated (e.g., by being located on opposite sides of a thin dielectric substrate) the formulas above apply without any modification. However, in many practical applications the two orthogonal strips are made of the same homogeneous resistive sheets where some parts of it have been removed to provide the pattern of two orthogonal strips as shown in Fig. 9.9 top. The figure shows also that the current no longer flows uniformly where two orthogonal strips intersect. Instead, the current buckles, similar to the fringing effects found in a parallel plate capacitor, as shown in Fig. 9.9 bottom. The parallel plate capacitor analogy is approximate, since part of the flux lines originate on the outside of the plates, whereas the currents in the absorber are confined to the resistive strips. However, the parallel plate capacitor analogy yields a good estimate of a lower bound on the new value of R'_L calculated above by (9.6).

According to Weber [57], the fringing for a semi-infinite parallel plate capacitor with plate width equal to plate separation increases the total dielectric flux by 31% over the nonfringing case. In the present case we have fringing on both sides of the capacitor (see Fig. 9.9 bottom), so we can consider this case as made up of two semi-infinite cases in parallel where the plate width equals one-half of the plate separation. According to Weber [57], each of these semi-infinite cases has a 60% increase in flux due to fringing (i.e., the total increases in flux of the total capacitance is also 60%). This in turn means that the total resistance of the square common to the area of two crossing strips (see Fig. 9.9) is reduced from R_s to $R_s/1.6 = 0.63R_s$, namely a reduction of $0.37R_s$ for a single square. Thus, if the orthogonal strips cross each other n_C times within a strip length $2l_1$ (see Fig. 9.9 top), the load resistance as given by (9.10) should be modified to

$$R'_L = \frac{2R_s l_1}{3w}\left[1 + 2c_1 - 1.1\frac{wn_C}{2l_1}\right] \quad \text{(ohm)}. \tag{9.11}$$

Although the approach above is approximate, numerous tests have shown it to be remarkably accurate (and in particular, faster than anything else!).

[1] Using a Sommerfeld distribution is not correct, since the element edges are a bit rounded and not sharp like a knife.

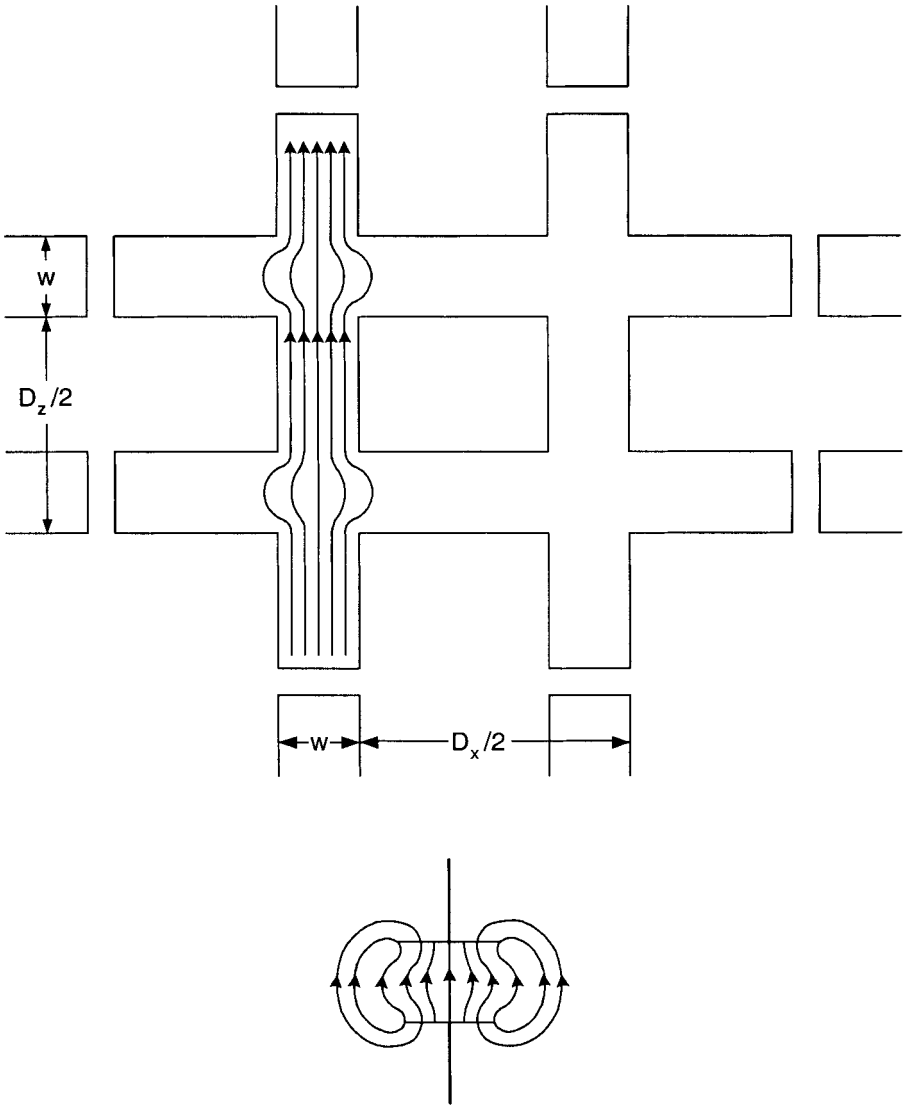

FIGURE 9.9. *Top:* Current flow in the z-direction modified by an orthogonal set of strips. *Bottom:* Current flow approximated as the flux lines in a plate capacitor.

9.6 EFFECT ON Y_a AS CAUSED BY ORTHOGONAL STRIPS

It is well known that the sheet admittance of an array of infinitely long lossless rods is a pure inductance if the E-field of the incident signal is parallel with the rods (no grating lobes, please!). Similarly, if the E-field is orthogonal to the rods, the sheet

admittance will be capacitive. It is quite instructive to apply this observation to the investigation of CA absorbers.

Basically, if the incident field is z-directed (see Fig. 9.10 top), then the z-oriented elements are responsible for producing the series RLC circuit as illustrated in Fig. 9.10 middle. The x-directed elements will produce an equivalent capacitance C_p in parallel with the series RLC circuit as also shown in Fig. 9.10 middle. Finally we show at the bottom of the same figure a Smith chart depicting a typical series RLC loci (full line) and also the total sheet admittance when the susceptance of the parallel capacitance C_p is added (broken line). The effect is of course most notable at the higher frequencies. However, if the conductance becomes sufficiently low, the total sheet admittance can end up entirely in the upper region (capacitive) of the Smith chart; it will not even resonate. This situation illustrates quite vividly how important it is to follow the design in a Smith chart sheet for sheet. Don't leave it up to an optimizer to make important decisions before a basic design is given!

9.7 OBTAINING A CIRCUIT ANALOG ADMITTANCE FROM THE FIELD REFLECTION COEFFICIENT

By application of the modification outlined above on Y_a, we can now obtain the reflection coefficient for CA absorbers comprised of any number of CA sheets located in a stratified medium with or without a ground plane. At this point CA designers are often tempted to play around in front of a computer screen and eventually use an optimization program. It can be stated that designing CA absorbers in a way is simpler than designing, for example, radomes. This is based on the fact that we in general only have severe specifications for normal angle of incidence, while a radome must work for a large range of incidence angles. The creative designer will in general be better off using an equivalent circuit as illustrated in Fig. 9.5. The equivalent CA sheet admittance Y_{a1} for a single sheet is easily obtained from the equivalent circuit shown in Fig. 9.11. The reflection coefficient Γ (E-field) for this single sheet is simply equal to

$$\Gamma = -\frac{(Y_{a1} + Y_0) - Y_0}{(Y_{a1} + Y_0) + Y_0} = -\frac{Y_{a1}}{Y_{a1} + 2Y_0}. \tag{9.12}$$

Solving (9.12) for Y_{a1} yields

$$Y_{a1} = -Y_0 \frac{2\Gamma}{1 + \Gamma}. \tag{9.13}$$

9.8 MANUFACTURING CIRCUIT ANALOG SHEETS

The earliest CA sheets were often made by silk-screening a resistive paste into a pattern on a dielectric substrate. However, it took considerable experience to obtain the proper resistivity and thickness to get the correct resistivity of the elements.

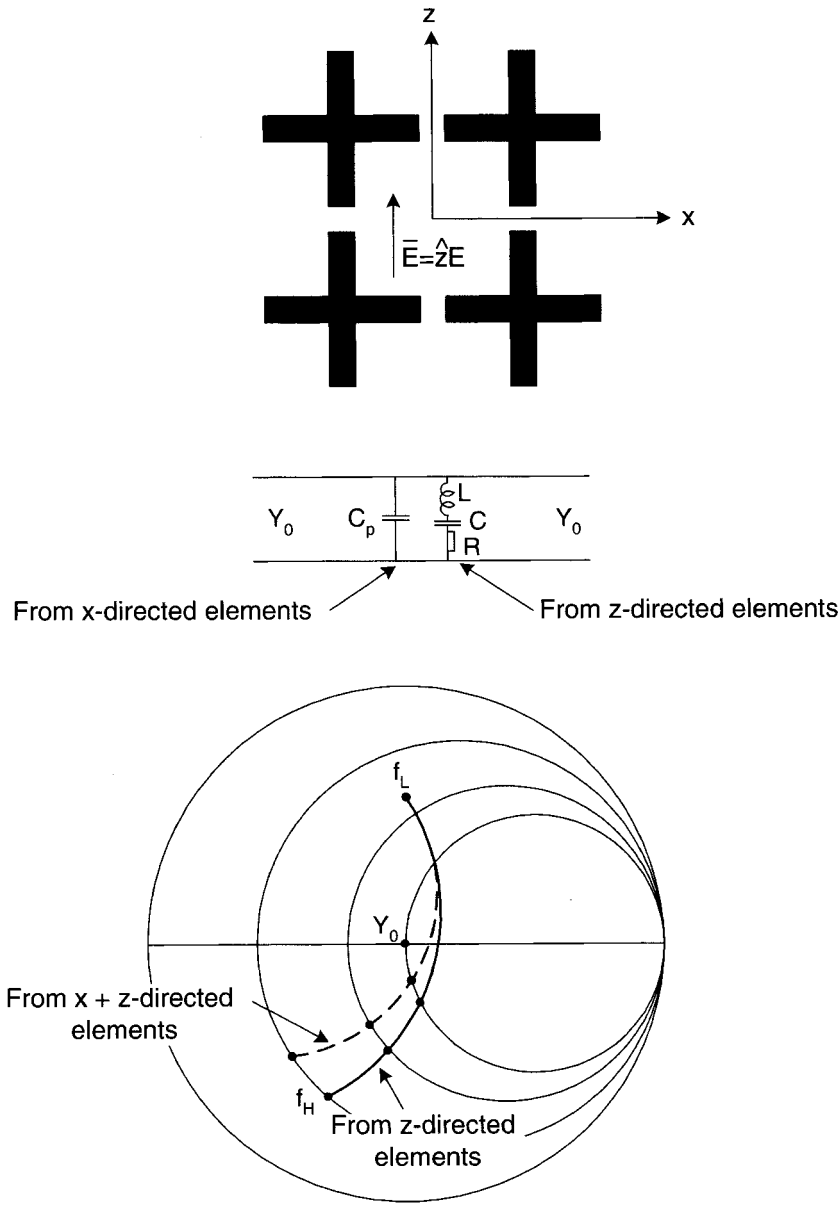

FIGURE 9.10. *Top:* Typical CA sheet exposed to an incident E-field parallel to the z-axis. *Middle:* Equivalent circuit with a series RLC circuit resulting from the z-directed element and parallel capacitance C_p resulting from the orthogonal elements. *Bottom:* Smith chart showing the sheet admittance for the series RLC circuit alone (full line) as well as the total obtained by adding the susceptance of C_p.

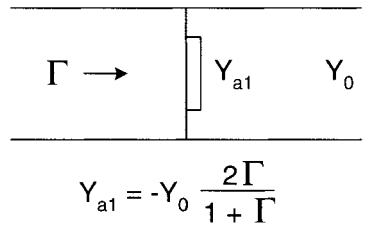

FIGURE 9.11. Single CA sheet in air. By calculating the reflection coefficient Γ for the reflected E-field from our modified code, we can readily obtain Y_{a1} as given by (9.13).

A significant improvement is observed by instead using a thin resistive film obtained by vapor deposition on a suitable dielectric substrate. The CA pattern is subsequently obtained, for example, by photo etching. Since vapor deposition today is capable of producing resistive sheets with very close tolerances and since photo etching also is highly accurate, this approach leads to CA sheets with great repeatability. (See further our concluding remarks in Section 9.10.)

9.9 COMMON MISCONCEPTIONS

9.9.1 Design Approach

It has already been mentioned that the inexperienced designer often is prone to simply using an optimization program to minimize the reflection over a band of frequencies. Unfortunately, this can lead to inferior designs. Typically a very low reflection is obtained only in the middle of the desired frequency range while it is lacking at the ends of the band. Although some improvement can be obtained by addition of a weight function, the real problem is that the designer is getting very little feedback as to *why* the design is inferior. The problem is usually that a broadband CA absorber should be comprised of CA sheets that play each other against one another as illustrated in Fig. 9.5; that is, they have loci relatively far away from the center of the Smith chart such that they cancel each other over a broad frequency band.

If an optimization program is left to its own devices, it has a strong tendency to just place the individual CA sheets closest to the center of the Smith chart. A much better approach is to use a Smith chart and simply start evaluating a possible CA design by starting at the ground plane and adding successive individual CA sheets as obtained from a computer program and subsequent use of (9.13), similar to the example shown in Fig. 9.5. Once a tentative design is obtained in that fashion, it is perfectly all right to use an optimizer provided that the various parameters are allowed only inside relatively small perturbations.

Typically this approach can lead to CA designs with a reflection less than 25 dB over a frequency band exceeding a decade. The total thickness is typically about $\lambda/8$ at the *lowest* frequency, or $\frac{3}{4}\lambda$ at the center frequency (in air).

An added advantage with this approach is that it gives the designer a good feel for how critical a design is. Unfortunately, an actual design cannot be shown.

It should finally be emphasized that the Smith chart approach is justified by the fact that the inter-element spacings are in general small in terms of wavelength. That simply means that the evanescent waves are dying out very fast, which is precisely what is needed when using the transmission line approach in conjunction with a Smith chart.

9.9.2 Phased Arrays versus Circuit Analog Absorbers

It may seem out of order to consider phased arrays at this point. Fundamentally a CA absorber is a passive device exposed to an incident plane wave, whereas a phased array is an active device fed from a human-made generator. However, if we are interested in the RCS of a phased array, the two subjects have much in common. In fact the RCS of a phased array is easily understood from the knowledge of CA absorbers. (For a reference that concentrates on phased arrays, see Hansen [58].)

A typical array of dipoles is shown in Fig. 9.12 left. The elements are fed from a generator via a harness with hybrids. The effect of these hybrids is now that if the array is exposed to an incident plane wave, all the elements will have the same load impedance Z_L that is *independent* of the angle of incidence (see Fig. 9.12 right.) Denoting the array terminal impedance by $Z_A = R_A + jX_A$, we easily obtain the equivalent circuit shown in Fig. 9.12 lower-right. This circuit is basically identical to the CA absorber shown earlier in Fig. 9.4. Thus the conclusion is that the backscatter from an array with a ground plane can be as low as that of a CA absorber, which of course is zero.

When it comes to RCS of an array, it is a common misconception that ideally the ground plane should somehow be removed or at least covered by an absorptive layer. From the equivalent circuit in Fig. 9.11, it should be fairly obvious that an open circuit behind the array instead of the ground plane will simply require $Z_L \sim \infty$ in order to minimize the backscatter, so we basically could not receive any power. If we use an absorber in front of the ground plane its input impedance should be higher than that of free space and so should Z_L such that their parallel combination could be close to Z_0. Of course about half the power may be lost in the absorber. In other words, it would be bad for the antenna gain and could also produce a lot of smoke as well!

9.9.3 Element Gaps

As mentioned earlier, the series capacitance in a CA absorber resides around the gaps between the elements. Further it is well known from fundamental static field theory that the smaller the gaps, the higher is the capacitance, and correspondingly the lower the operating frequency. Since early designers lacked the sophisticated computer programs available today, they were on a more or less intuitive basis promoting the necessity of small gaps (just a few mills). This resulted in CA designs that were very tolerance sensitive, which for years held CA absorbers back. It was later realized that the gaps could be made much larger without significant reduction in capacitance. This is based on the fact that most of the flux lines between two ele-

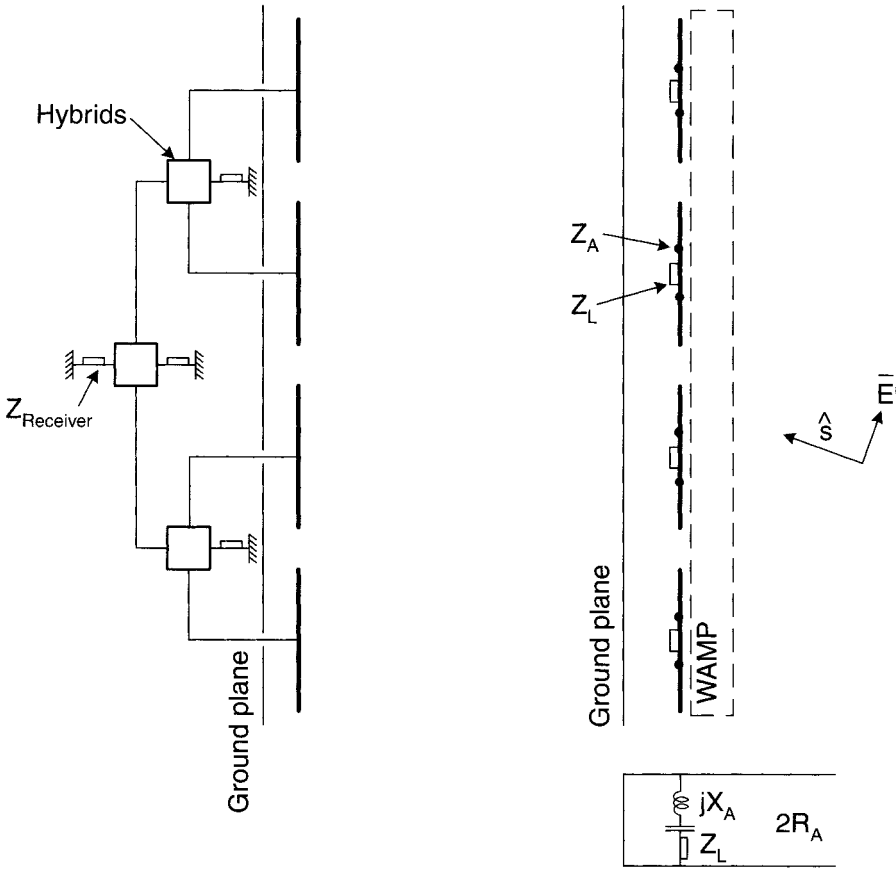

FIGURE 9.12. *Left:* Array of dipoles fed via cables with hybrids. *Right:* Under scattering condition the array acts as a periodic surface of elements with load impedance Z_L. The scan impedance Z_A can be stabilized by use of a side angle matching plate. Also shown is the equivalent circuit. See also Section 5.10.

ments is tied up in the fringe field and not between the tiny areas at the ends of the elements (i.e., most flux lines start at the sides and not at the *ends* of the elements like a plate capacitor). Thus, when the gaps are varied, most of the flux lines attached to the sides will essentially remain unchanged resulting in only a nominal change of capacitance.

9.10 CONCLUDING REMARKS

This chapter started out by considering absorbers constructed of simple resistive sheets sandwiched between dielectric slabs. We next moved on to absorbers where the resistive sheets had been provided with a periodic pattern (CA absorbers). This

added a reactive component to the sheet impedance resulting in a larger bandwidth, although the dielectric slabs in the Jaumann absorber could also be designed to yield improved bandwidth. Circuit analog absorbers with a bandwidth exceeding 10:1 and thickness less than $\lambda/8$ at the lowest frequency are possible. This very often is at odds with designers' intuitions, namely that arrays of *dipoles* are narrow-banded (it depends strongly on how densely the elements are packed).

It is regrettable that neither a finished design nor measurements can be shown. This does not mean that we are lacking in either one of these categories. In fact a very important case was a design for the spy ship *Sea Shadow* [59]. It was designed by the author using the approach put forth in this chapter. It was produced by the Laboratories of N.J. Damascos, Inc. The agreement between calculations and measurements was excellent from the lowest to the highest frequency. Further the design was quite tolerance friendly.

10

POWER HANDLING OF PERIODIC SURFACES

10.1 INTRODUCTION

While our derivation of the periodic moment method has been quite rigorous, the following calculations of power breakdown contain numerous engineering approximations and estimations. Nevertheless they have produced results in satisfactory agreement with measurements (see [60]).

Further, a substantial advantage of the present approach as compared to purely numerical calculations is that it describes the breakdown in terms of the pertinent FSS parameters. Thus, even if approximate, we are getting insight into which parameters to attack to improve the power handling capacity.

Many applications require periodic surfaces to handle high power levels. Like all other microwave devices, they will eventually disintegrate when the power level becomes too high.

There are basically two ways a periodic surface might fail:

1. Under sustained continuous high average power, lossy materials will develop heat and the surface will eventually melt or burn.
2. Under very high peak power, very high electrical fields will develop at the dipoles or slots and arcing will occur which will leave the surface inoperational because the elements are effectively being short-circuited by the arcing.

The first type of deterioration occurs when the average power of the incident signal becomes too high. Communication signals typically fit in this category.

The second situation occurs mainly when we are dealing with a pulsed signal with high peak power. Typical examples are radar with relatively low average power but

high peak power. This situation usually manifests itself by rather spectacular flashes between the elements. It should be avoided unless, as noted by my good friend John Kraus, you are in the advertising business and want to attract a great deal of attention!

Some modern-day radars may have an average power so high that they actually belong in both of the categories.

10.2 BREAKDOWN CAUSED BY HEAT

Lossy dielectric as well as the conductance of the elements will produce heat when exposed to an incident field. As the temperature rises, cooling will eventually spread to the surroundings. When the amount of heat produced by the conductors and the surrounding dielectric equals the heat lost by convection, the temperature will reach a steady state. Obviously the temperature should never be allowed to rise to the point where any of the dielectric or the elements would be damaged.

The greatest amount of heat is usually developed when the elements are resonating. If we at first assume no dielectric or resistive loss, the reflection (for dipoles) or the transmission (for slots) should be very nearly 100%; that is, the mismatch losses are negligible. If we next introduce loss tangents in the dielectric and resistivities in the conductors, we can readily obtain the reflection and transmission losses from a program like PMM. We further readily conclude that they are due entirely to the lossy materials; that is, we can obtain the amount of power produced as heat by the surface if we know the incident power.

To dispense with this heat buildup is sometimes a nasty problem. Often various FSSs are located in a stratified dielectric medium, and the maximum amount of heat production typically takes place in the very neighborhood of the elements. Unfortunately, the surrounding dielectric slabs are usually poor heat conductors preventing the heat to escape. This problem can often be overcome by introduction of air gaps next to the FSS as shown in Fig. 10.1. We note that the FSSs are encapsulated in thin layers of dielectric for protection and possible dielectric loading (*underwear*). However, the electrical effect of the narrow air gaps are minimum and can in general be compensated for by adjustment of the outer dielectric slabs. In some cases it may be necessary to do without *underwear* to improve the heat transfer. In that event loaded elements with a floating center must in general be substituted with, for example, the unloaded three-legged element shown in Fig. 2.2 top, or the special nonfloaters shown in Fig. 2.2 bottom. An example and further discussion is given in [61]. The calculation of the amount of cooling air to be forced through the air gaps is outside the scope of this book. Consult an expert in heat transfer.

10.3 BREAKDOWN CAUSED BY THE ELECTRICAL FIELD IN GENERAL

Any time the electrical field strength surrounding an object reaches a certain value, breakdown will eventually occur whether the surrounding media is air or any other

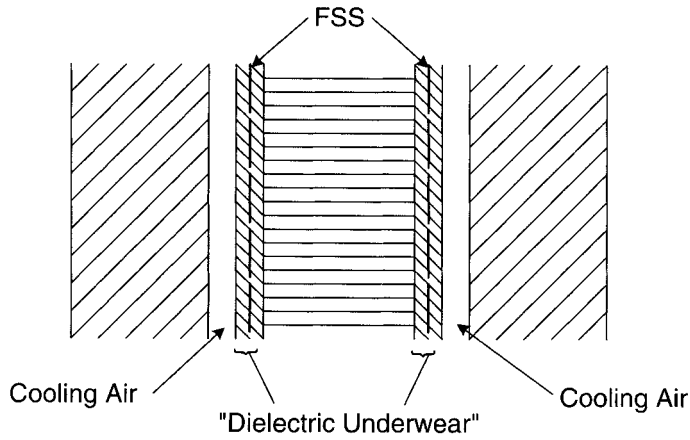

FIGURE 10.1. Typical dichroic surface. Cooling air can be blown in along air ducts close to the FSS encapsulated in dielectric *underwear*.

dielectric. For air, breakdown occurs when the electric field strength is larger than around 30 kV/cm at normal atmospheric pressure. As the air pressure decreases with elevation, so does the breakdown field strength until it reaches a minimum around 10 Torr. Then it goes up again as the air becomes thinner, as illustrated in Fig. 10.2. In a dielectric, breakdown will occur at $\delta 30$ kV/cm where δ is a constant characteristic for the dielectric in question and is called the *dielectric strength*. Contrary to air, the breakdown voltage for a solid dielectric does not depend on the atmospheric pressure.

Many microwave devices have limited power-handling capability because of breakdown, and the devices become inoperable and even completely damaged. For example, an ordinary waveguide can only handle a certain amount of power before it breaks down in the form of an arc between two opposite walls. Any periodic surface has similar limitations that are aggravated by the fact that the field strength present between the elements can be much larger than that of the incident fields, as illustrated in Fig. 10.3. Note how the elements forces the incident field to be concentrated between the elements. The field surrounding the elements must be higher than $\bar{E}^i$; in fact it can be hundreds of times higher, as will be shown in later examples.

As we pointed out several times earlier, complementary surfaces have much in common but also profound differences. A pair is illustrated in Fig. 10.4. To the left we show a four-legged loaded wire element exposed to an incident field. We will obtain the maximum field strength at the tips of the elements and also at the center, as shown. Similarly we show the complementary slot case in Fig. 10.4 right. The maximum field strength is now between the edges of the slots. It is further worth noticing that these areas actually constitute the element loads when the H-field is oriented as shown. Thus we will in the following investigate the wire and slot cases separately.

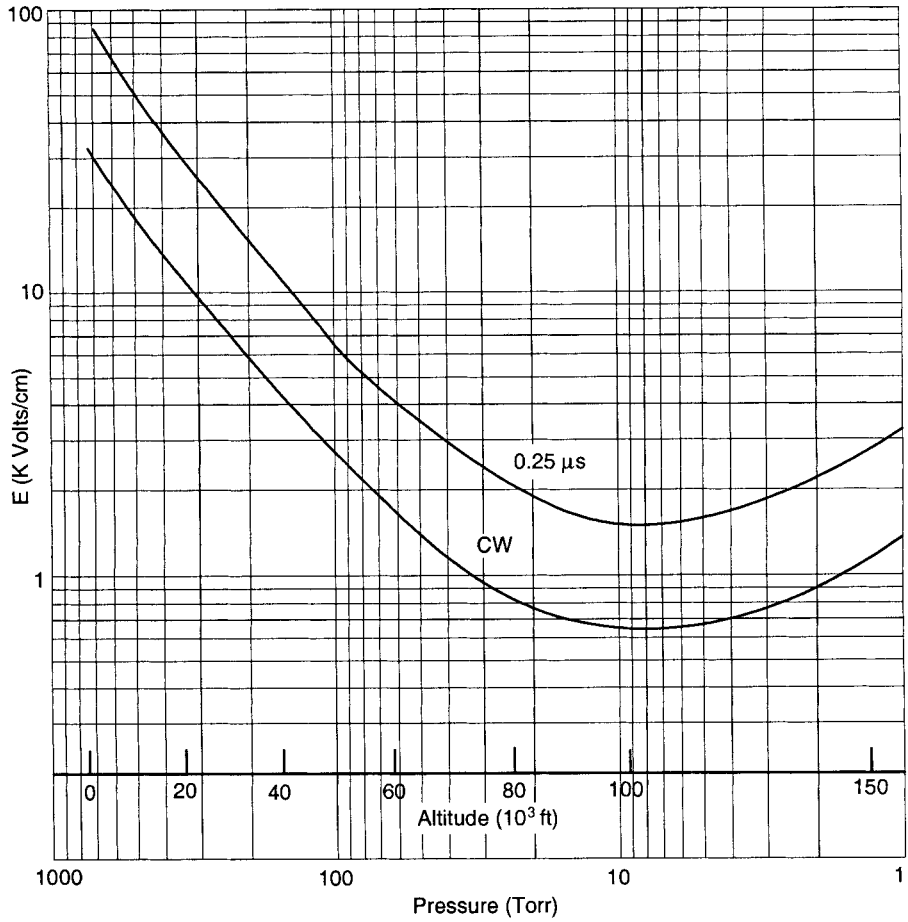

FIGURE 10.2. Required field strength for breakdown in air for CW as well as for a 0.25μs pulse. Frequency = 9.3 GHz and homogeneous field.

10.4 ON VOLTAGE BREAKDOWN OF WIRE ELEMENTS

When analyzing and computing the transmission and reflection properties of an FSS made of an electric conductor of the *wire* type (or *dipole* type), it is essential to find the electrical current $I(l)$ along the element. Associated with the current distribution is a voltage distribution $V(l)$. It is in general not necessary to determine the latter except in the case where one is interested in finding the field strength at any point along the elements. Simply put, if this field strength exceeds the breakdown voltage of the surrounding medium (air or dielectric in general) the FSS becomes inoperable and can even be permanently damaged.

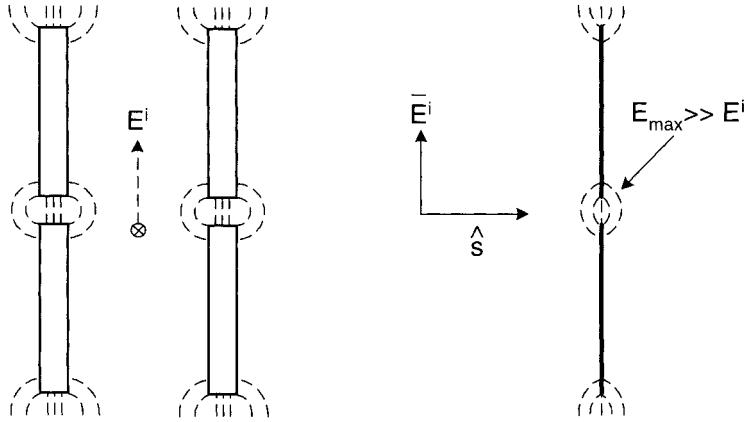

FIGURE 10.3. Illustration of how the maximum field strength in an FSS can be much larger than the incident field.

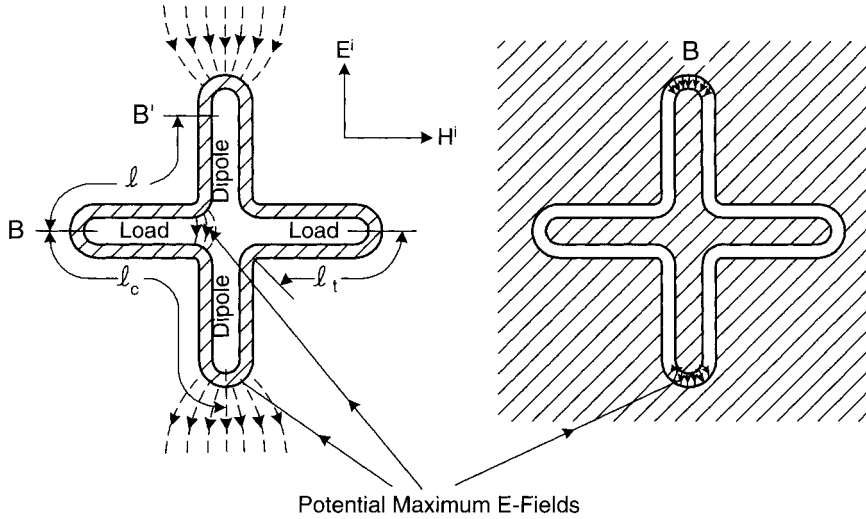

FIGURE 10.4. The greatest potential for field breakdown occurs when the E-fields are maximum. *Left*: Four-legged loaded wire elements. See also Fig. 2.18. *Right*: Complementary four-legged loaded slot element. Note the orientation of the incident E^i- and H^i-fields.

10.4.1 Determination of $V(l)$ along the Elements

If the current distribution $I(l)$ along an element is known, it is a relatively simple matter to determine the voltage distribution $V(l)$. This is based on the fact that an FSS wire element can be viewed as a loaded dipole (as explained in Section 2.3.1) made of a transmission line with a certain characteristic impedance:

$$Z_c = \sqrt{\frac{L_c}{C_c}} \quad \text{(ohm)}, \tag{10.1}$$

where L_c equals inductance per unit of length and C_c equals capacitance per unit of length of the dipole. Further the propagation constant

$$\beta_c = w\sqrt{L_c C_c}. \tag{10.2}$$

From elementary transmission line theory [62] we have

$$jwC_c V(l) = -\frac{dI(l)}{dl}. \tag{10.3}$$

For a typical loaded element as shown in Fig. 10.4 left, the current distribution for an incident vertically polarized E-field as shown would be given approximately by a standing wave along the element as

$$I(l) = I(0)(\cos\beta_c l - \cos\beta_c l_c), \qquad |l| \leq l_c, \tag{10.4}$$

where l equals the distance from point B to the arbitrary source point B', and l_c equals the distance from A to the top or bottom of the element (i.e., equal to one-quarter of the total circumference). $I(0)$ denotes the current at point B. Substituting (10.4) into (10.3) yields

$$V(l) = \frac{\beta_c}{jwC_c} I(0)\sin\beta_c l, \qquad l \leq l_c. \tag{10.5}$$

Applying (10.1) and (10.2) to (10.5) yields

$$V(l) = -jZ_c I(0)\sin\beta_c l, \qquad l \leq l_c. \tag{10.6}$$

Inspection of (10.6) readily shows that $V(l)$ is maximum for $l = l_c$ and further that the highest maximum is obtained for $l_c = \lambda_c/4$, which is for resonance condition as one would expect. Realizing that the element at the top has the opposite voltage of (10.6) corresponding to $l = -l_c$, we obtain from for the total maximum voltage between the tips of two adjacent elements

$$2\,|V_{max}|_{tip} = 2Z_c\,|I(0)_{max}| \quad \text{(volts)}. \tag{10.7}$$

We further note that the terminal voltage V_A at point A is given by (4.64) as

$$V_A = \left[{}_{\perp}E^i \, {}_{\perp}P_0^t + {}_{\parallel}E^i \, {}_{\parallel}P_0^t \right], \tag{10.8}$$

where ${}_{\perp}P_0^t$ and ${}_{\parallel}P_0^t$ denote the pattern components associated with the dipole part of the element as explained in Section 2.3.1. This is the pattern factor for the part of the element parallel to $\bar{E}^i$; see Fig. 10.4.

10.4.2 Determination of $I(0)$

To determine $2\,|V_{max}|_{tip}$ as given by (10.7), we must find $I(0)$ at point B. While this value can be extracted, for example, from the PMM program, it is quite instructive to analyze the parametric behavior as follows:

Let us denote the total impedance of the dipole part by Z_A and the parallel combination of the two loads by Z_L. Then the terminal currents in each side is given by

$$I_A = \frac{1}{2} \frac{V_A}{Z_A + Z_L}. \tag{10.9}$$

The maximum value of I_A is obtained for resonance,

$$I_{A\,max} = \frac{1}{2} \frac{V_A}{R_A}. \tag{10.10}$$

The real part R_A of the scan impedance is obtained, for example, from (4.70):

$$R_A = \frac{Z_0}{2D_x D_z} \frac{1}{r_y} \left[{}_{\perp}P_{0\perp}P_0^t + {}_{\parallel}P_{0\parallel}P_0^t \right]. \tag{10.11}$$

Substituting (10.8) and (10.11) into (10.10) yields

$$I_{A\,max} = \frac{1}{2} E^i \frac{2D_x D_z r_y}{Z_0} \frac{{}_{\perp}P_0^t + {}_{\parallel}P_0^t}{{}_{\perp}P_{0\perp}P_0^t + {}_{\parallel}P_{0\parallel}P_0^t}. \tag{10.12}$$

If we limit the scan to the principal planes, one of the pattern components in (10.12) will be zero (see Section 4.11). In that event it is easy to see that $I_{A\,max}$ will be maximum for normal angle of incidence where $r_y = 1$.

We further note from transmission line theory [63] that

$$I(0)_{max} = \frac{I_{A\,max}}{\cos \beta_c l_t}, \tag{10.13}$$

where l_t is defined in Fig. 10.4 left.

Substituting (10.12) into (10.13), we have

$$I(0)_{max} = E^i \frac{D_x D_z}{Z_0 P_0 \cos \beta_c l_t} \tag{10.14}$$

(for normal angle of incidence).

10.4.3 Characteristic Impedances Z_c and Z_c'

The exact value of the characteristic impedance Z_c along the dipole part of the elements is somewhat problematic, but a reasonable approximation should be quite sufficient for our present use.

When considering the dipole part (parallel to $\bar{E}^i$), the adjacent element currents will be in phase (push push mode) and consequently radiate like an antenna (see Fig. 2.18). In contrast, the load portion where adjacent element sections are out of phase (push pull mode) will consequently behave more like a nonradiating transmission line.

In the first instance (radiating or push push mode) Schellkunoff [64] provides us with the following value:

$$Z_c \sim \frac{60}{\sqrt{\epsilon_1}} \left[-\ln \frac{\beta_c a_{eff}}{4} + 0.116 + Ci 2\beta_c l_t - \frac{\sin 2\beta_c l_t}{2\beta_c l_t} \right], \tag{10.15}$$

where a_{eff} equals the effective wire radius of the two wire dipole section; see Fig. 10.5 for an evaluation. β_c and ϵ_1 are the propagation and relative dielectric constants of the dielectric medium in the immediate neighborhood of the element. For a typical four-legged loaded element, we have for resonant condition $2l_t \sim \lambda_c/4$ yielding $Ci 2\beta_c l_t \sim 0.47$ and $\sin 2\beta_c l_t / 2\beta_c l_t \sim 0.66$; that is, (10.15) reduces to

$$Z_c \sim \frac{60}{\sqrt{\epsilon_1}} \ln \frac{2\lambda_c}{\pi a_{eff}} \quad \text{(ohm)}. \tag{10.16}$$

Further the impedance Z_c' for the push pull mode for the transmission line load is evaluated using [65] in Fig. 10.5

$$Z_c' \sim \frac{120}{\sqrt{\epsilon_1}} \ln \frac{4(a_w + a_t)}{a_w} \quad \text{(ohm)}. \tag{10.17}$$

10.4.4 Maximum Field and the Form Factor α

Substituting (10.14) into (10.7) yields

$$2\,|V_{max}|_{top} = E^i \frac{Z_c}{Z_0} \frac{2D_x D_z}{P \cos \beta_c l_t} \quad \text{(volts)}, \tag{10.18}$$

where Z_c is given by (10.16).

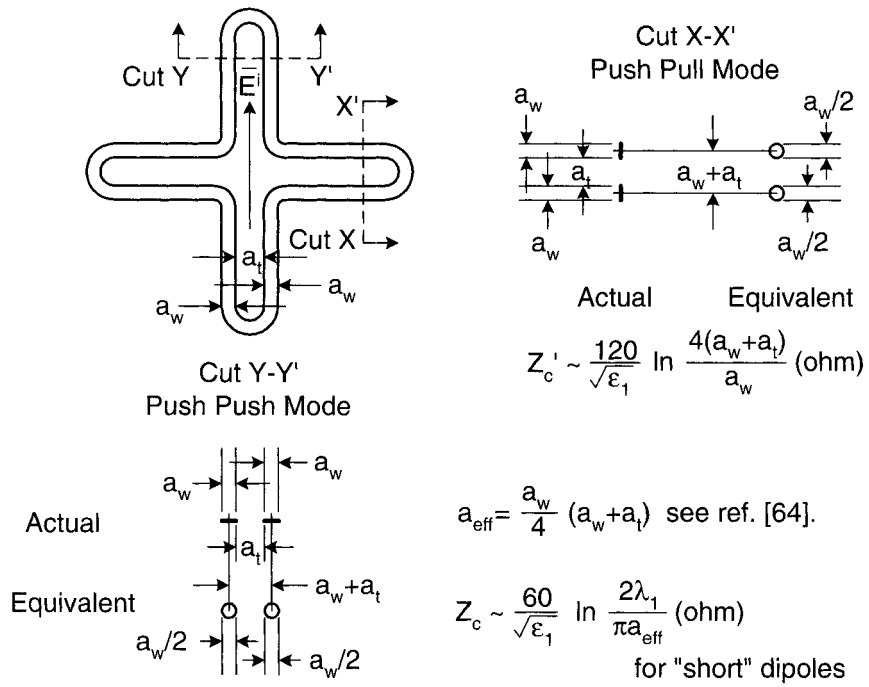

FIGURE 10.5. For a vertical incident E-field the vertical part of the four-legged loaded element can be considered a dipole with push-push current; see Fig. 2.18. The horizontal parts act like a reactive load with push-pull currents.

Having determined the maximum voltage difference between adjacent element tips, our next step is to determine the maximum field strength between these tips. If the voltage difference $2V_{max}$ existed between two parallel plates of infinite extent at spacing $2a_2$, as illustrated in Fig. 10.6 top, the field between them would be homogeneous with the value

$$E_{homo} = \frac{2V_{max\,tip}}{2a_2}. \tag{10.19}$$

In case the two electrodes are nonplanar, there will be an increase or decrease of the electrical field strength compared to E_{homo} as given by (10.19). Basically the field strength is going to increase close to sharp conductors. In particular, we show in Fig. 10.6 a typical four-legged loaded element being exposed to an incident E-field as shown. It results in a maximum voltage $V_{max\,tip}$ as found by (10.18). This field can be expressed as

$$E_{max\,tip} = \alpha E_{homo} = \alpha \frac{2V_{max\,tip}}{2a_2}, \tag{10.20}$$

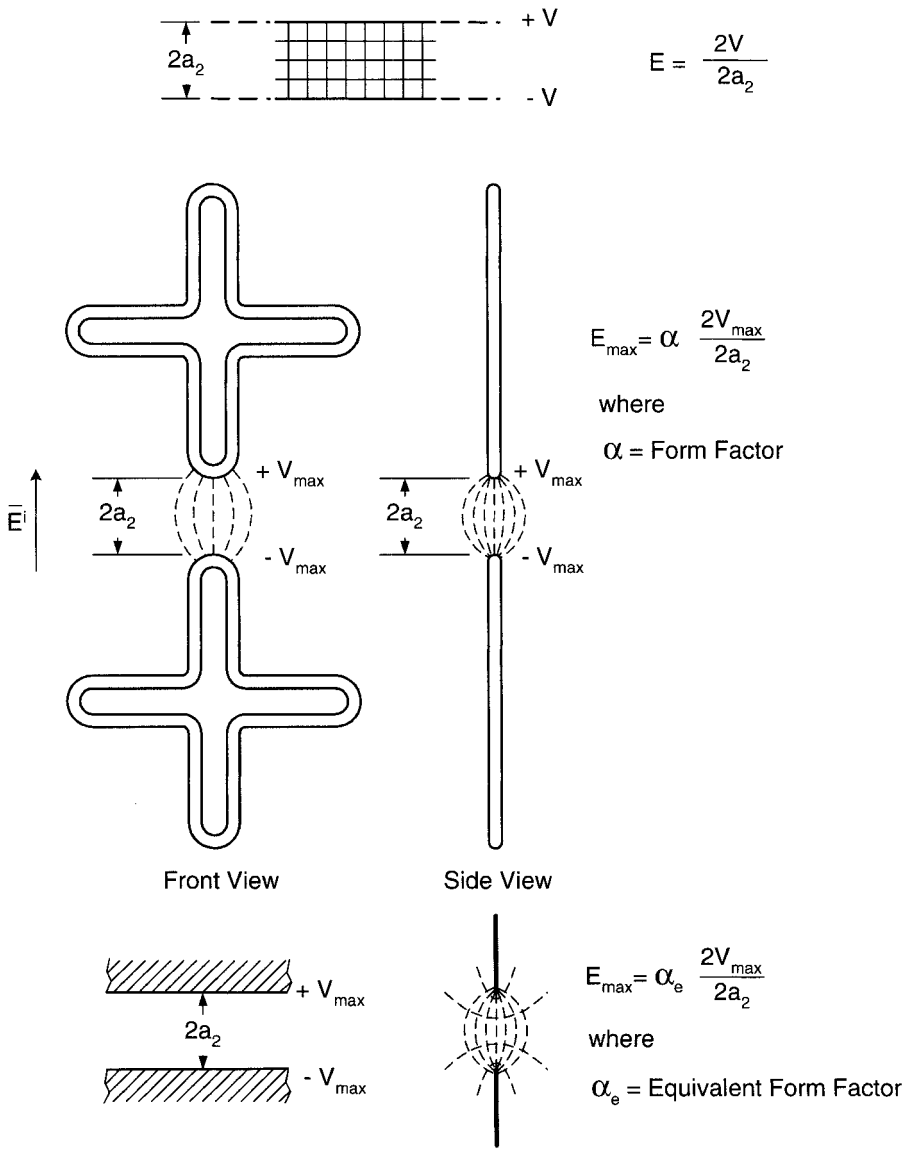

FIGURE 10.6. The field lines between various electrodes. *Top*: The homogeneous field forms between two infinite large plates. *Middle*: The maximum field E_{max} between the tips of two wire elements will in general be the form factor α stronger than the homogeneous case. *Bottom*: The exact field between two infinite thin half-planes can be used to model the field between cylindrical surfaces.

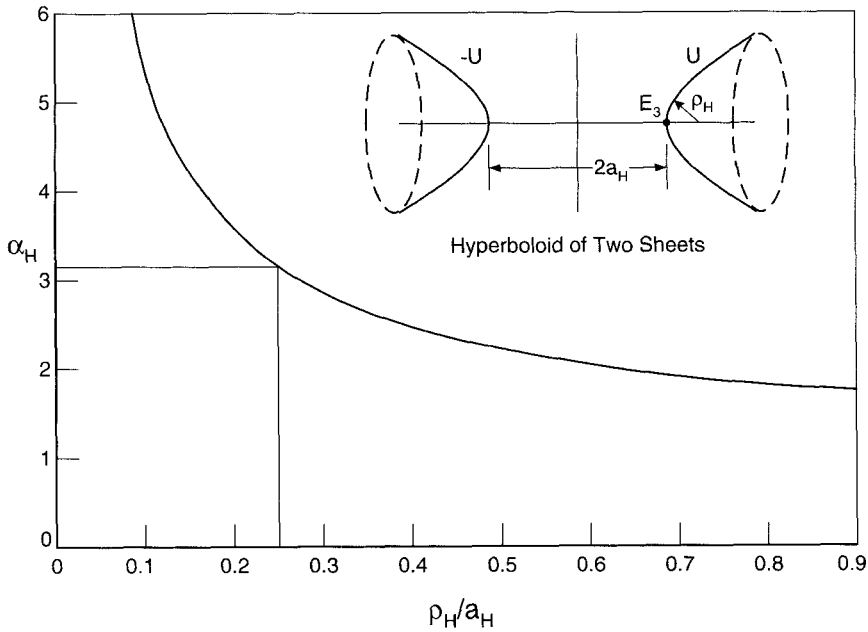

FIGURE 10.7. Form factor α_H for a hyperboloid of two sheets.

where α is a factor indicating how much stronger or weaker the field strength is compared to the homogeneous case. The value of α depends on the shapes of the electrodes involved and it is therefore often called a *form factor*. It is investigated extensively in [60] for a number of classical cases that can be evaluated exactly.

For the benefit of the reader we present here some cases that are most pertinent to our present investigation. In Fig. 10.7 we show the form factor α_H for a hyperboloid as shown in the insert. The radius of curvature is denoted ρ_H, while the smallest distance between the two electrodes is denoted $2a_H$. The corresponding form factor α_H is plotted as a function of ρ_H/a_H.

Similarly we show in Fig. 10.8 the form factor α_h for a pair of hyperbolic cylinders as shown in the insert. Note, that the form factor α_h for this case is considerably smaller than α_H for the hyperboloid case shown in Fig. 10.7. This is simply because the latter case is more pointed than the former.

Finally, we show in Fig. 10.9 the form factor α_c for a convex pair of hyperbolic cylinders as shown in the insert. Also shown for comparison is a coaxial cable.

Our approach is simply to obtain a reasonable approximation for the form factor α as it pertains to our particular element shapes by matching it to one or more of the standard shapes presented above. See the examples given later.

Substituting (10.18) into (10.20) yields

$$E_{max\,tip} = \alpha E^i \frac{Z_c}{Z_0} \frac{D_x D_z}{a_2 P_0 \cos \beta_c l_t} \quad (V/m). \tag{10.21}$$

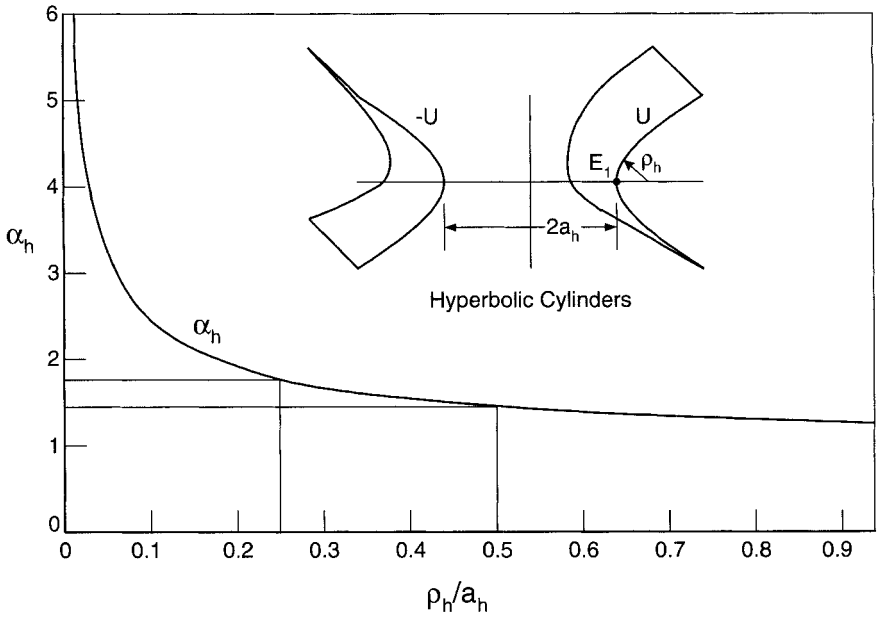

FIGURE 10.8. Form factor α_h for various hyperbolic cylinders as shown.

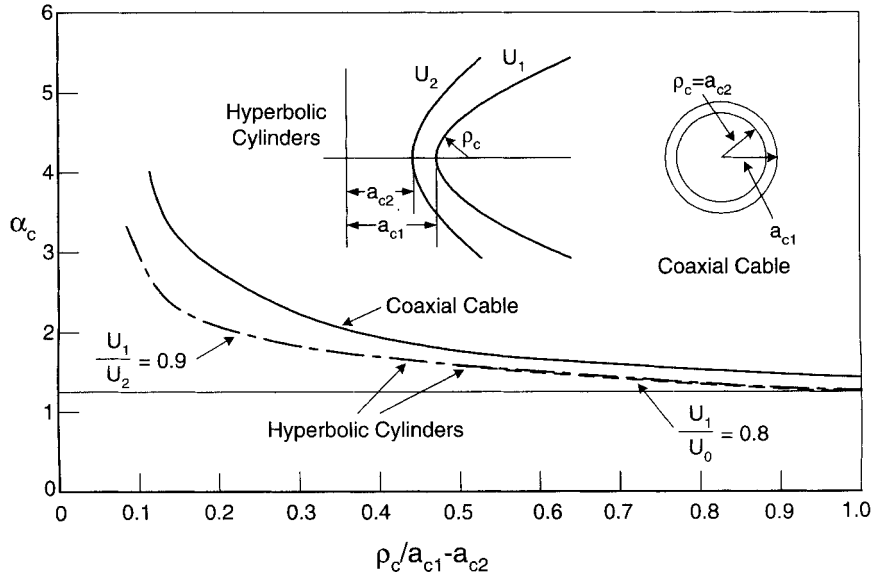

FIGURE 10.9. Form factor α_c for two convex hyperbolic cylinders.

For the field strength at the terminals at point A:

$$E_{max\,term} = \alpha \frac{V_{A\,max}}{a_t} = \alpha \frac{I_{A\,max}|Z_L|}{a_t},$$

where $Z_L = jZ_c' \tan \beta_c l_t$.

For a typical four-legged loaded element we have at resonance $\tan \beta_c l_t \sim 1$ and substituting (10.12) for $I_{A\,max}$ yields

$$E_{max\,term} \sim \alpha E^i \frac{Z_c'}{Z_0} \frac{D_x D_z}{a_t P_0} \tag{10.22}$$

for normal angle of incidence and resonant condition.

We next illustrate the approach by an example.

10.4.5 Example 1: An FSS of Four-Legged Loaded Wire Elements

Let the incident power density be 1 MW/m^2; that is, $E^i = \sqrt{10^6 \cdot 120\pi} = 1.94 \cdot 10^4$ V/m = 194 V/cm.

Further the operating frequency is $f = 10$ GHz ($\lambda_0 = 3$ cm) and typical inter-element spacings, $D_x = D_z = 1$ cm $= 0.33\lambda_0$. Also given is $2l = 0.28\lambda_0 = 0.84$ cm; that is, $2a_2 = D_x - 2l = 0.16$ cm and $\cos \beta_c l_t \sim 0.7$. For element dimensions $a_w = 10$ mills$= 2.54 \cdot 10^{-2}$ cm and a_t =20 mills (see Fig. 10.5), we obtain $a_{eff} = \sqrt{a_w/4(a_w + a_t)} = \sqrt{10(10 + 20)/4} = 8.7$ mills $= 0.020$ cm. This yields from (10.16) and (10.17), respectively,

$$Z_c = \frac{60}{1} \ln \frac{2 \cdot 3}{\pi \cdot 0.020} = 273 \quad \text{(ohm)}$$

and

$$Z_c' = \frac{120}{1} \ln \frac{4(a_w + a_t)}{a_w} = 120 \ln \frac{4(10 + 20)}{10} = 298 \quad \text{(ohm)}$$

If the tips of the elements are rounded (see Fig. 10.5), we obtain a radius of curvature in the plane of the elements equal to $\frac{1}{2}(a_w + a_t) = 15$ mills.

Similarly let the thickness of the copper sheet be equal to 5 mills, yielding a radius of curvature approximately equal to 2.5 mills. The average radius of curvature can then be estimated as

$$\rho = \frac{15 + 2.5}{2} = 8.75 \text{ mills} = 0.02 \text{ cm}$$

or

$$\frac{\rho}{a_2} = \frac{0.02}{0.08} = 0.25.$$

Approximating the tip by a hyperboloid as shown in Fig. 10.7 with $\rho_H/a_H = 0.25$, we see that a reasonable approximation for the form factor is $\alpha_H = 3.2$.

Substituting the values above into (10.21), we have

$$E_{max\,tip} = \alpha_H E^i \frac{Z_c}{Z_0} \frac{D_x D_z}{a_2 P_0 \cos \beta_c l_t}$$

$$= 3.2 \cdot 194 \frac{273}{377} \frac{1 \cdot 1}{\frac{1}{2} 0.16 \cdot 0.28 \cdot 0.7} = 28.6 \quad \text{(kV/cm)}.$$

For the input area of the loads (see Fig. 10.4) we have

$$\frac{2\rho}{a_t} = \frac{5}{20} = 0.25.$$

Using Fig. 10.8, we find that $\alpha_h = 1.8$. Thus, from (10.22),

$$E_{max\,term} = \alpha_h E^i \frac{Z_c'}{Z_0} \frac{D_x D_z}{a_t P_0}$$

$$= 1.8 \cdot 194 \frac{298}{377} \frac{1 \cdot 1}{0.051 \cdot 0.28} = 19.4 \quad \text{(kV/cm)}.$$

We emphasize that the field strength above is for resonant condition and normal angle of incidence. When the elements are nonresonating, the field strength will in general be considerably lower.

10.4.6 How to Increase the Power Handling of Wire Elements

Considering the fact that the breakdown field strength for air at normal atmospheric pressure is 30 kV/cm (see Fig. 10.2), it is quite clear that the values obtained in the example above are not only marginal but simply lacking a conservative safety factor. Thus let us investigate what can be done to improve upon this situation.

Inspection of (10.21) for $E_{max\,tip}$ would suggest that the gap $2a_2$ between the elements be increased. However, this will in turn lead to a lower value of ρ_H/a_H, and from Fig. 10.7 we observe that the form factor α_H will increase, meaning that it will partly cancel the benefit of increasing a_2. Thus only a moderate improvement is possible by that approach.

We reach a similar conclusion for $E_{max\,term}$ given by (10.22) if we increase a_t.

Another possibility would be to increase the thickness 2ρ of the element sheet. Inspection of Fig. 10.7 shows that doubling of the thickness from 5 to 10 mills would reduce α_H from about 3.2 to 2.1; that is, a reduction in field strength for $E_{max\,tip}$ of about $2.1/3.2 = 0.68$. The reduction for $E_{max\,term}$ is seen to be about $1.5/1.8 = 0.83$. Had we originally used a thinner sheet thickness such as 3 mills, we would have been on a much steeper part of the curve for α_H and α_h, so the improvement would have been spectacular!

However, the real problem begins if the FSS has to be airborne without pressurization. At an altitude of 70,000 feet the breakdown field strength in air has been reduced to approximately 1 kV/cm at CW; see Fig. 10.2. Basically only one remedy will do, encapsulation of the FSS in a dielectric. To be sure, we need in general only a relatively small thickness, comparable to the gap spacing $2a_2$ between the elements (or the tongue width a_t; whatever is biggest). Some of the benefits of this *underwear* have been pointed out before; see Section 5.15.2. From a breakdown point of view, the greatest benefit is that the breakdown field strength of most dielectric is considerably higher than that of air, and, best of all, it does not depend on altitude.

But there is another substantial advantage, namely that the length of the elements will be reduced by about $\sqrt{\epsilon_c}$ when we maintain the same resonant frequency; see Fig. 1.9 or Appendix E. In (10.21) it simply means that Z_c, D_x, D_z, and P_0 can all be reduced by about $\sqrt{\epsilon_c}$. The net reduction in $E_{max\,tip}$ is ϵ_c if we choose to leave the tip distance a_2 basically unchanged, and about $\sqrt{\epsilon_c}$ if a_2 is scaled by $\sqrt{\epsilon_c}$ as well. (Note that Z_0 remains essentially unchanged simply because the *underwear* is quite thin as seen from the T-factor.) A typical value for ϵ_c would be about 3.3; thus the reduction in the breakdown field strength can be substantial. The same conclusion is seen to hold true for $E_{max\,term}$ as given by (10.22). See also discussion in Section 10.8.1.

10.5 ON VOLTAGE BREAKDOWN OF SLOT ELEMENTS

10.5.1 Determination of the Slot Voltage

We will consider a single slot array being complementary to the wire array discussed in the previous section; see Fig. 10.4. Our approach will follow the one taken earlier in Chapter 7 concerning multilayered radomes in general.

Let us denote the incident H-field by $\bar{H}^i$. Then the induced current is according to (7.6) for no dielectric

$$I^i = 2_\perp H^i{}_\perp P_0^t + 2_\parallel H^i{}_\parallel P_0^t. \tag{10.23}$$

If we further denote the slot admittance at point A by Y_A and the total load admittance at the same point looking up and down the slotted transmission line for Y_L, we readily obtain the voltage V_A of point A:

$$V_A = \frac{I^i}{Y_A + Y_L}. \tag{10.24}$$

The maximum value for V_A is obtained for resonance condition:

$$V_{A\,max} = \frac{I^i}{G_A} \tag{10.25}$$

when, according to (6.10) and (6.12),

$$G_A = 4\frac{Y_0}{2D_xD_z}\frac{1}{r_y}\left[{}_\perp P_{0\perp} P_0^t + {}_\parallel P_{0\parallel} P_0^t\right]. \tag{10.26}$$

For the voltage at the end of the transmission line at point B, we have from simple transmission line theory [65] the expression

$$V_{B\,max} = \frac{V_{A\,max}}{\cos\beta_c l_t}. \tag{10.27}$$

Limiting ourselves to the principal planes as earlier in the wire case, we recall that one of the pattern components will be equal to zero. In that event it it easy to see that $V_{B\,max}$ will be maximum for normal angle of incidence when $r_y = 1$.

Substituting (10.23), (10.25), and (10.26) into (10.27) yields for normal angle of incidence:

$$V_{B\,max} = \frac{1}{2}H^i\frac{D_xD_z}{Y_0P_0\cos\beta l_t}, \tag{10.28}$$

where the factor $\frac{1}{2}$ is caused by the fact that the total voltage V_{Bmax} is split between two gaps (at the tip of each load).

10.5.2 Determination of the Maximum Field Strength in the Slots

Having determined the maximum voltage $V_{B\,max}$ at the end of each of the slot loads, we are ready to obtain the maximum field strength $E_{B\,max}$ in the same manner as earlier:

$$E_{B\,max} = \alpha\frac{V_{B\,max}}{a_w} = \alpha H^i\frac{D_xD_z}{2a_wY_0P_0\cos\beta_c l_t},$$

or alternatively by $H^i = E^i/Z_0$,

$$E_{B\,max} = \alpha E^i\frac{D_xD_z}{2a_wP_0\cos\beta_c l_t}\ \text{V/m} \tag{10.29}$$

for normal incidence and resonance.

It is interesting to compare (10.29) with (10.21) and (10.22), pertaining to slot versus dipole arrays, respectively. It appears at first glance that the slot array has been favored by a factor of 2 if we assume that $a_w = a_2$ and $Z_c = Z_0$. However, in practice, this situation might be somewhat different as illustrated by the following example. (See also summary in Fig. 10.10.)

10.5.3 Example 2: An FSS of Four-Legged Loaded Slot Elements

Let the slot array be complementary to the wire case investigated in Example 1 above; that is, D_x, D_z, a_w, P_0, and $\cos\beta_c l_t$, are exactly as evaluated there (see

Fig. 10.4). Further let the incident power density be the same (1 MW/m^2) leading to

$$E^i = 194 \text{ V/cm}.$$

Thus, substituting into (10.29) yields

$$E_{B\,max} = \alpha E^i \frac{D_x D_z}{2a_w P_0 \cos\beta_c l_t}$$

$$= \alpha 194 \frac{1 \cdot 1}{2 \cdot 2.54 \cdot 10^{-2} \cdot 0.28 \cdot 0.7} = \alpha 19.6 \text{ kV/cm}. \qquad (10.30)$$

As usual, we must estimate α by inspection of the Figs. 10.7 to 10.9. Had the ends of the slots been straight rather than rounded, the form factor α could be obtained from Fig. 10.8 with $\rho_H = \frac{1}{2}5 = 2.5$ mills and $a_h = \frac{1}{2}a_w = 5$ mills. Thus $\rho_h/a_h = 2.5/5 = 0.5$ and from Fig. 10.8 we obtain $\alpha_h = 1.5$. Similarly, had the slots been cylindrical sheets following the rounded shape of the elements, we could have used Fig. 10.9 with $\rho_c = \frac{1}{2}a_t = \frac{1}{2}20 = 10$ mills and $a_{c1} - a_{c2} = 10$ mills. Thus we find that $\rho_c/a_{c1} - a_{c2} = 10/10 = 1$ leading to $\alpha_c = 1.2$.

We simply postulate (conservatively) that the actual form factor for the tips of the loads is equal to the product of α_h and α_c. Thus, substituting into (10.30), we have

$$E_{B\,max} = \alpha_h \alpha_c 19.6 \text{ kV/cm}$$

$$= 1.8 \cdot 19.6 = 35 \text{ kV/cm}. \qquad (10.31)$$

Again, as in the wire case, we emphasize that the field strength calculated above is for resonant condition. It will in general be considerably less for nonresonance.

10.5.4 How to Increase the Power Handling of Slot Elements

As in the case of the wire elements treated earlier, the breakdown voltage for the complementary slot array is too large, and improvement is needed.

Inspection of (10.29) readily shows that the only parameter that can possibly be adjusted to a reasonable degree is the slot width a_w. If we double it from 10 to 20 mills, we obtain $\rho_h/a_h = 2.5/10 = 0.25$, and from Fig. 10.8 we obtain a new $\alpha_h = 1.8$ instead of the old one of 1.5. Thus the net reduction of $E_{B\,max}$ is $\frac{1}{2}(1.8/1.5) = 0.6$ times; that is, $E_{B\,max} = 0.6 \cdot 35$ kV/cm $= 21$ kV/cm. This level would be marginally acceptable at atmospheric pressure; see Fig. 10.2. However, if our device becomes airborne, dielectric protection is needed.

As we saw in the wire case earlier, even a thin layer of dielectric (*underwear*) leads to an element reduction of $\sqrt{\epsilon_c}$, which in turn allows us to reduce D_x and D_z by the same factor. Thus the net reduction is seen from (10.29) to be $\sqrt{\epsilon_c}$ if we leave a_w unchanged, and no reduction at all if we also reduce a_w by $\sqrt{\epsilon_c}$.

We do of course, as in the wire case, enjoy the benefit from the dielectric strength of the *underwear* and in particular that it is independent of the atmospheric pressure. (See also comments in Section 10.8.1.)

10.6 COMPARISON OF WIRE AND SLOT FSS

Figure 10.10 shows a summary of the maximum field strength for a typical wire FSS (left) as well as a typical slot FSS (right). Comparison of the two expressions shows that they are quite similar except that the slot version formally amounts to only 25% of the wire version. This conclusion is, however, somewhat deceiving by the fact that the tip spacing $2a_2$ for the wire case typically is considerably larger than the slot width a_w. On the other hand, the form factor α_w for the wire case will typically be larger than the form factor α_s for the slot case. In practice, the result is often that the power handling of the two cases are comparable. Use of dielectric *underwear* is

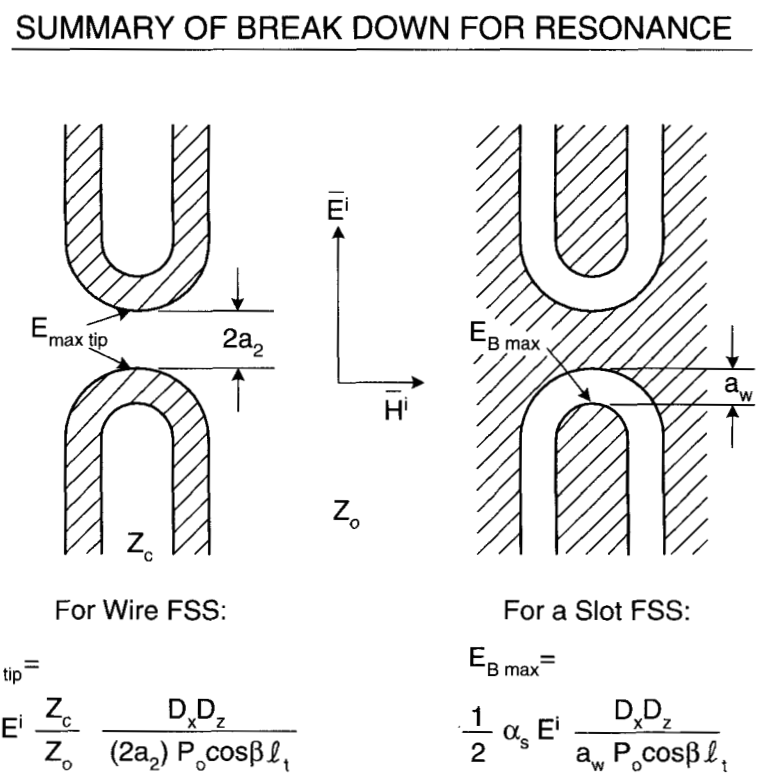

FIGURE 10.10. Comparison of the field strength for a typical four-legged wire FSS (left) as well as a typical four-legged slot FSS (right). Typically the tip spacing $2a_2 >>$ the slot width a_w, leading to comparable power handling despite a formal difference of $2/\frac{1}{2} = \frac{1}{4}$.

strongly recommended for both cases in particular at low atmospheric pressure (see also the comments in Section 10.8.1).

Some improvement may be observed in the wire case by interlacing the elements as shown in Fig. 2.17 provided that the tip spacing is increased somewhat as compared to the rectangular grid shown in Fig. 2.16.

10.7 POWER HANDLING IN A STRATIFIED MEDIUM

The formulas given above for the field strength at certain key points of the FSS elements are valid for a single FSS encapsulated by thin dielectric slabs on both sides (*underwear*) or for no dielectric at all. However, we have several times in this book stressed that practical space filter designs in general require a stratified medium. Thus we will examine the effect of thick dielectric slabs upon the power handling.

A basic idea is obtained by considering a single FSS encapsulated by thin dielectric slabs with relative dielectric constant ϵ_{r1} as shown in Fig. 10.11. Also shown are two dielectric slabs with relative dielectric constant ϵ_{r2} and thickness d_2 mounted on each side of the FSS.

As shown earlier, we need only consider normal angle of incidence. Consequently the simple equivalent transmission line circuit shown in Fig. 10.11 (bottom) will be adequate. If we denote the incident field by $\bar{E}^i$, simple transmission line theory tells us that the E-field at the FSS in the middle will fluctuate between $E^i/\sqrt{\epsilon_{r2}}$ and E^i depending on the slab thickness d_2. Similarly the magnetic field at the FSS will fluctuate between $H^i\sqrt{\epsilon_{r2}}$ and H^i. The following investigations will deal with the wire and slot cases separately.

10.7.1 Wire Case

In the *wire* case we find from (10.7) and (10.13) that

$$2\,|V_{max}|_{tip} = \frac{2Z_c|I_{A\,max}|}{\cos\beta_c l_t} \tag{10.32}$$

where according to (10.10),

$$I_{A\,max} = \frac{1}{2}\frac{V_A}{R_A} \tag{10.33}$$

for resonance. From (10.8) we see that V_A can be reduced by $\sqrt{\epsilon_{r2}}$ when $d_2 = \lambda_2/4$. Further from simple transmission line theory we see that R_A as seen at the FSS can be reduced by a factor of as much as ϵ_{r2}. Thus from (10.33) we see that the net reduction of $I_{A\,max}$ can be as high as ϵ_{r2}, and this is true for $V_{max\,tip}$ and $E_{max\,tip}$ as given by (10.32) and (10.20), respectively. For $d_2 = \lambda_2/2$ we observe no change. Note that Z_c is primarily affected only by the underwear's dielectric constant ϵ_{r1}.

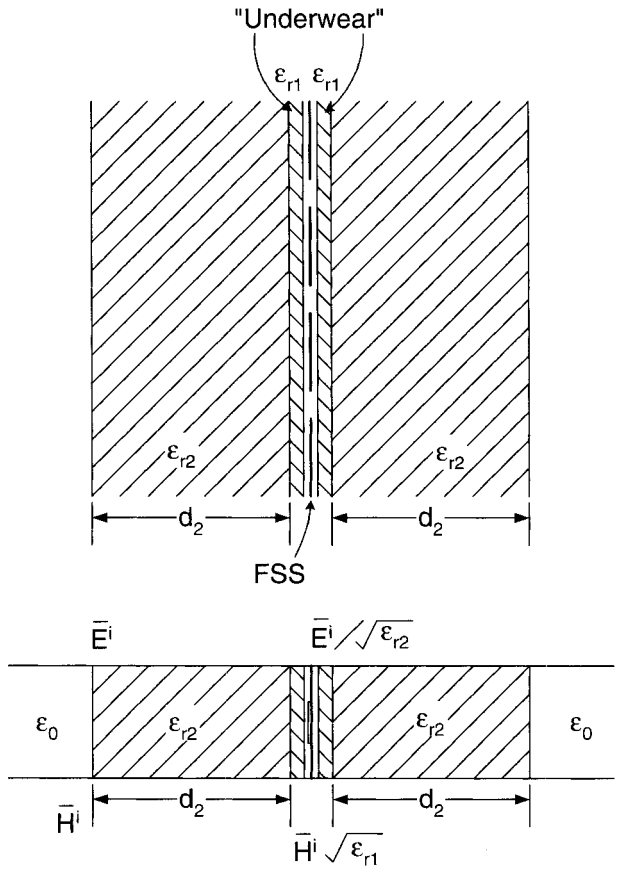

FIGURE 10.11. An FSS with underwear sandwiched symmetrically between two dielectric slabs with relative dielectric constant ϵ_{r2}. The field strength at the element tips can increase with up to $\sqrt{\epsilon_{r2}}$ times the value with just underwear for a wire FSS. For a slot FSS it can decrease by the same factor. Note that no air gaps between the FSS and the underwear is allowed. See also Section 10.8.1.

10.7.2 Slot Case

In the slot case we find from (10.27) and (10.25):

$$V_{B\,max} = \frac{I^i}{G_A \cos \beta_c l_t} \tag{10.34}$$

for resonance. From (10.23) we see I^i will increase as much as $\sqrt{\epsilon_{r2}}$ for $d_2 = \lambda_2/4$. From simple transmission line theory we further see that G_A in that case will increase with the factor ϵ_{r2}. Thus from (10.34) we see that $V_{B\,max}$ can be reduced by $\sqrt{\epsilon_{r2}}$, and the same then holds true for $E_{B\,max}$.

10.7.3 Comparing the Wire and Slot Cases

From the investigation above we learn that a pair of symmetric slabs with relative dielectric constant ϵ_{r2} mounted next to an FSS with underwear can in the wire case amplify the maximum field strength by a factor up to $\sqrt{\epsilon_{r2}}$, while we in the slot case observe a reduction down to $1/\sqrt{\epsilon_{r2}}$. It is left as an exercise to treat the case where we have a large dielectric slab to only one side but still underwear around the FSS. Consider both cases where the incident field comes from the left or the right side.

10.8 COMMON MISCONCEPTIONS

10.8.1 On Dielectric Underwear

Use of thin dielectric sheets placed on each side of the elements (*underwear*) was introduced in Section 5.12.2. Their importance has been stressed several times since. In this chapter we pointed out their beneficial effect in enhancing the power handling capacity of an FSS in general.

It is, however, not uncommon that researchers arrive at a different conclusion. Typically an FSS (wires or slots) is etched on a thin dielectric substrate with one side open into free space. It has been tested and found inadequate in handling sufficient power before voltage breakdown. The designer correctly concludes that a thin dielectric slab should be added to the open side. To general dismay, one often finds that the power capacity has been reduced.

To understand what is most likely the problem consider Fig. 10.12 top. We show a plate capacitor filled partly with dielectric (ϵ_1) and partly with air (ϵ_0), with the fields E_0 and E_1, respectively. If the plate voltage is V volts and the thicknesses a and b are as defined in Fig. 10.12, then by static approximation,

$$E_0 b + E_1(a - b) \sim V. \tag{10.35}$$

Further, from continuity of the flux lines, we have

$$\epsilon_0 E_0 = \epsilon_1 E_1. \tag{10.36}$$

From (10.35) and (10.36),

$$E_0 \sim \frac{V}{a} \frac{\epsilon_{r1}}{1 + \frac{b}{a}(\epsilon_{r1} - 1)}, \tag{10.37}$$

$$E_1 \sim \frac{V}{a} \frac{1}{1 + \frac{b}{a}(\epsilon_{r1} - 1)}. \tag{10.38}$$

We have also plotted E_0 and E_1 in Fig. 10.12 for $\epsilon_{r1} = 4$. We observe that E_0 can for $b/a \to 0$ be increased by as much as ϵ_{r1} times the value of the field strength in a homogeneous medium (air or dielectric). Similarly E_1 can be reduced by as much as $1/\epsilon_{r1}$ if $b/a \to 1$. This observation is similar to a voltage divider made of two

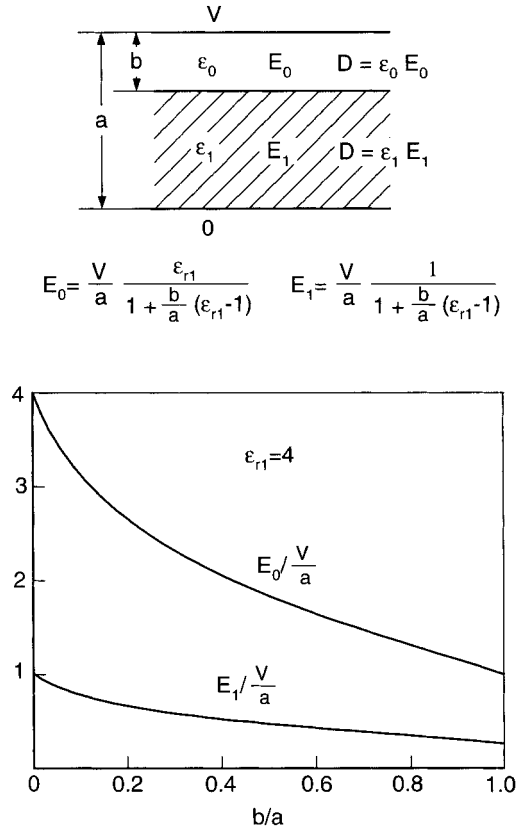

FIGURE 10.12. *Top*: Plate capacitor filled with materials with dielectric constants ϵ_0 and ϵ_1. *Bottom*: Fields E_0 and E_1 normalized to the homogeneous case (all air or all dielectric) plotted as a function of b/a for $\epsilon_{r1} = 4$. Note that the amplification of E_0 goes toward ϵ_{r1} for $b/a \to 0$.

resistors in series: It is the *high-resistance* air section compared to the *low-resistance* dielectric section that takes the brunt.

Let us now return to the FSS shown in Fig. 10.13 left, where typically an FSS (wire or slot) has been covered by an added dielectric slab. Even if firmly pressed toward the FSS such as by using vacuum bags, it is practically impossible to completely avoid minute air cracks. And as we saw above, these air pockets will enhance the field strength almost at the worst possible location.

In short, these air cracks must be avoided by using, for example, a low-loss glue that covers all cracks completely or alternatively a low-loss grease if the FSS must be taken apart. The above calculations are admittedly approximate but still drive home the point: No air gaps, please! Even *underwear* to only one side as shown in Fig. 10.13 right can easily lead to amplification of the field in air next to the FSS.

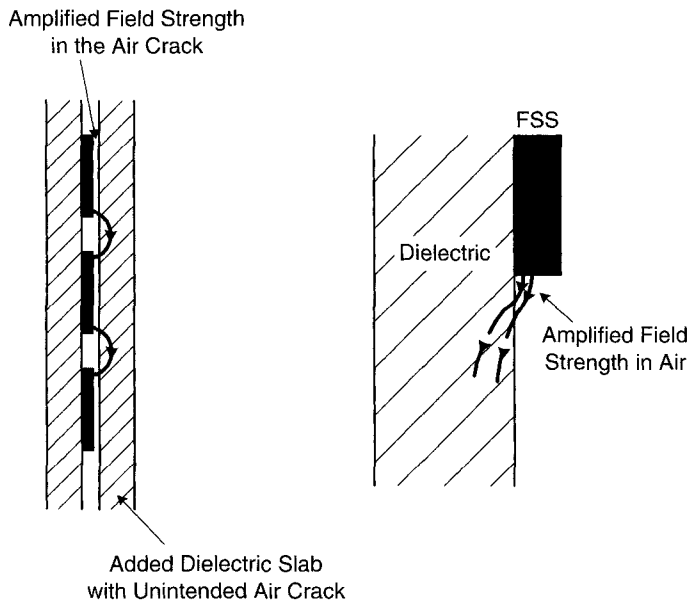

FIGURE 10.13. *Left*: Air cracks inadvertently created next to the FSS, as illustrated in Fig. 10.12, can produce a much higher field strength in air than in the nondielectric case even if the space between the FSS elements is filled with dielectric. *Right*: Similarly, dielectric substrate to only one side can create higher field strength in air than for the nondielectric case.

10.8.2 Effect of Etching

In the calculations above we assumed that the typical slot had a cross section that was fairly smooth and rounded as shown in Fig. 10.14*a*. However, depending on the method of manufacturing, the shape can deviate somewhat. If, for example, the FSS is produced by photo-etching, the cross section can easily look as shown in Fig. 10.14*b* and *c*, corresponding to being too short or too long in the chemical etchant. Obviously these two cases will have a form factor somewhat higher than the ideal shown by Fig. 10.14*a*.

This little detail shows that determination of the breakdown field strength has many uncertainties in addition to the engineering approximations eluded to already. In short, real FSS should always be tested by measurement with the appropriate power as well as air pressure.

10.9 CONCLUDING REMARKS

We have introduced an analytic approach in our investigation of the power handling of FSSs made of wire or slot elements. It contains several engineering approximations. Nevertheless, it has produced numerous results that agree fairly well with early

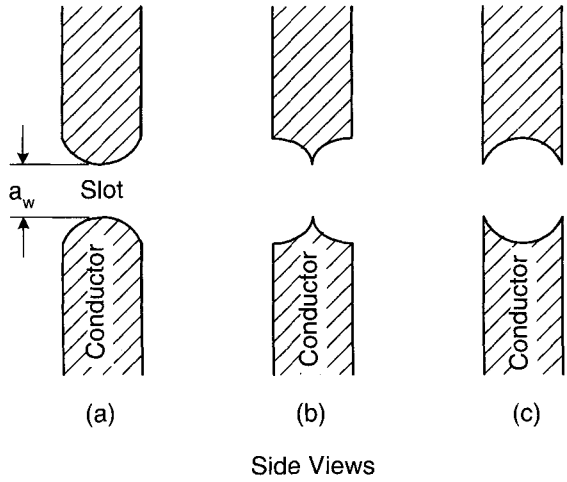

FIGURE 10.14. Cross section of typical slots: (*a*) Desired cross section (approximately); (*b*) time in chemical etchant too short; (*c*) time in chemical etchant too long.

measurements performed in an evacuated waveguide as discussed in [60] (this report was recently declassified). A computational approach is given in [61].

But the biggest value, at least in this author's opinion, is that it enables us to study fairly closely which parameters are important in our pursuit of improving the power handling of FSSs in general.

In the *wire* case the key issue is that the voltage and the field strength are proportional to the *element current* $I(0)$; see (10.7). When placed in a dielectric stratified medium the impedance level may be transferred downward with respect to free space; that is, the element currents are being increased and so is the field strength at the tips or terminals.

In the slot case, however, the key is that the field strength is proportional to the *slot voltage*; see Section 10.5. Again, when placed in a stratified medium, the impedance level may be transformed downward with respect to free space, and so is the slot voltage. Thus the slot field strength may be *reduced* in a stratified medium.

In general, the inter-element spacings D_x and D_z should be as small as possible, whether we are dealing with wire or slot elements. However, in the wire case care must be exercised that the inter-element spacings are not reduced to the point where the tips of the elements get too close to each other. In the slot case we do not have this concern because the breakdown in slots takes place primarily in the slots themselves.

Both wire and slot elements benefit greatly from being totally encapsulated in dielectric of even modest thickness (typically 30 mills for X-band applications). However, it is extremely important not to have any air cracks next to the FSS, since that will lead to a significant reduction of the power handling capacity. Nor is it a good idea to have dielectric to only one side of the FSS—from a power handling point of view.

Who was it that said that we do not need to teach "statics" anymore?

11

CONCLUDING REMARKS AND FUTURE TRENDS

No doubt the approach taken in this book is different from the one followed by many academics. Typically their approach is simply to expand the field from a periodic surface into Floquet modes (as shown in Chapter 4), then apply the appropriate boundary conditions and write a computer program. Dielectric layers may be added, for example, by use of a simple transmission line theory. This approach will lead to correct transmission and reflection coefficients. There is, however, one important aspect missing: physical insight. Unfortunately, this means that a designer in general will have very little to guide him or her on how to develop a periodic surface. Consequently the designer must resort to simply running through a parametric study of element and array dimensions that seem pertinent but, in actuality, are often not. Eventually this search is organized by an optimizing computer program of one sort or another. For a single FSS this approach might be adequate but for more complex multilayered periodic structures, the number of iterations soon can be prohibitive.

In contrast, the approach taken in this book is analytic. This simply means that all components of any complex periodic structure have been examined individually in great detail. Consequently the designer will know what primarily determines the resonant frequency and its stability with angle of incidence. The designer will know what tools to use to obtain constant bandwidth with angle of incidence and polarization. The designer will know the "character" of the various elements, which ones are narrow-banded and which ones are broadbanded, which one produce odd resonances for oblique angles of incident and why. Finally the designer will know how to make adjustments of the bandwidth without changing the general character of the transmission and reflection curves. In other words, the approach taken here is systematic and not trial and error.

The best illustration of these statements is probably the development of the hybrid radome discussed in Chapter 7. There it is shown that an ideal band-pass filter, namely with a flat top and a constant bandwidth for *all angles of incidence* and *all polarizations*, can be obtained *only* by proper use of scan independence of the outer FSS layers regardless of the total number. The simplest approach is to use dielectric matching transformers with an effective dielectric constant less than around 2 (varies somewhat with angle of incidence and element type). One can only speculate on the amount of computer time that has been wasted looking for solutions when the outer dielectric constant was fixed a priori at say 4. That is to say, one cannot pick roses where there aren't any! Besides, approaching a complex design problem with preconceived notions about design values is in general a bad idea. It may at first glance look like good engineering leading to "practical" solutions and weeding out the "unrealistic" cases. To this line of reasoning, let me state categorically: Do not demand before you understand.

Once you know the workings of your problem, it is often just a matter of adding a little ingenuity to turn an "unrealistic" solution into one that is "just right" (with a little luck thrown in at the top).

Eventually we must ask the question: Can superior designs ever be obtained by a computerized optimization program alone? The answer is: In theory, of course (given enough time). In practice, it is not very likely unless you have a good starting point.

In fact, ever since the author got his patent for the hybrid radome in 1978 (see Fig. 1.10), he has been aware of numerous attempts to design radomes with an ideal band-pass characteristic (see Fig. 1.11). He is not aware of any new design that can accommodate more than a very limited range of incidence angles and polarizations.

So the next question is: Should you ever use an optimizer? And the answer is: Certainly, but not before you have a good starting point based on a sound concept. Perhaps my feelings on this subject can best be expressed by the following little vignette: Consider a beautiful Chippendale table with ball and claw feet. It has gracefully curved legs with beautiful carved feet. This is the result of the vision of an artist and executed by a superb craftsman. They were not the result of a computer optimization. However, you may (and should!) treat the legs with a fine sandpaper followed by fine steel wool or pummice powder and an appropriate finish. This will further bring out the beauty and luster of the wood. That is the optimizer!

We finally remind the reader that the primary purpose of the analytic approach is to guide us to workable designs. In many instances we do not have to know the precise current distribution along the elements. We can, for example, obtain rather detailed information about the dielectric profile of a hybrid radome by simply assuming that the shape of the voltage distribution along the slot elements does not change with angle of incidence, only the amplitude and phase do. This assumption may not hold for some elements. They should be left out of consideration, since they in general will lead to inferior designs anyway. Once a tentative design has been established, we can apply the method of moments using the PMM program followed by minor iterations. In fact this is when an optimization program comes in handy.

While the importance of a stratified dielectric medium has been emphasized repeatedly, we are by no means implying that the elements are unimportant. In fact the

choice of proper elements is necessary for a good design but just not sufficient. Always keep in mind that the equivalent circuit of any single periodic surface is merely a transmission line shunted with a reactive element (at best!). Really there is not much one can do with that except change frequency and bandwidth.

Some elements can be designed to have more stable resonance with angle of incidence than others. The key is simply to choose small elements and pack them closely together. That will cut down on the amount of energy stored around the elements. Since the variation of the resonant frequency is directly related to the reactive part of the element impedance, we obtain better stability of the resonant frequency with angle of incidence. The most suitable elements for most applications are the loop types (group 2). The least suitable are the plate types (group 3). They were typically used in early FSS work due to their simplicity, and they still seem to be popular with designers who are more interested in producing papers and numbers rather than useful designs.

We also investigated in great detail the possibility of surface waves in the dielectric medium. We found that they will occur but not before onset of grating lobes inside the dielectric medium. Consequently we can prevent these surface waves by making the inter-element spacing small; that is, we must use small compact elements such as the loop types (group 2). We observed many similarities between the dipole and the slot case but also profound differences. For example, the surface wave resonance depends, in the dipole case, on the total slab thickness (i.e., the sum of dielectric slabs on both sides). In the slot case, however, we found one set of surface waves associated only with the dielectric medium to one side and similarly another set tied in with the other side. We also saw that both the orthogonal and parallel cases could in general exist from the onset frequency and up. However, if a dipole array is located in the middle of the dielectric slab, the parallel case cannot exist.

We emphasize that the surface waves discussed here can occur on infinite as well as finite periodic surfaces. In a future volume we will demonstrate another type of surface waves that can exist only on a finite periodic structure (strictly speaking, these waves will radiate, and they are therefore not surface waves in an exact sense).

11.1 FUTURE TRENDS

Most of the periodic surfaces considered in this book are of infinite extent in two dimensions. However, in real life all surfaces are finite. It is a well-known observation that finite arrays in many respects behave like infinite arrays. There are important differences between the two cases:

1. In a finite array the element currents and scattering at the edges can deviate significantly from those of an infinite array. However, if we are about one or two columns inside the finite array, we experience almost the same currents as for an infinite array. However, some deviation is observed because of another phenomenon, as described in item 2 below.

2. A finite array can in certain cases support waves that look similar to surfaces waves on an infinite array. However, these cannot be excited on an infinite array if the periodic surface is excited by an incident plane wave (i.e., passive mode). Only if they are actively excited can they exist, see Fig. 4.18. However, if the array is finite these "surface waves" can easily be demonstrated by the simple fact that they will radiate primarily from the ends. Furthermore, since these waves travel along the array with a phase velocity quite different from that of the Floquet currents, the two systems will interfere and produce "ripples" along the array. This is observed in [66]. We emphasize that the surface waves observed on finite arrays only are not the same surface waves observed in dielectric slabs adjacent to a periodic surface. These can readily be excited by an incident plane wave on an infinite structure.

This writer is by no means suggesting that all problems concerning infinite arrays have been solved. They have not! He is suggesting, however, that much future research will and should concentrate around the problems unique to finite arrays.

11.2 ENGINEERING EDUCATION

Educating young talent to follow an analytic approach is a lengthy and often frustrating and humiliating process. Only a few engineers are interested enough to start and even fewer finish. The competition is of course coming from the camp who thinks that engineering of the future is merely to obtain an appropriate computer program for their purpose and then basically do a parametric study.

To this I say: Someone has to write the program. And to do this, someone had better know the theory and its interpretation in order for the program to be meaningful and not just numbers crunching. It is difficult to lay out a meaningful parametric study without at least some physical insight.

It is my hope that this book will make contributions in that area.

This Page Intentionally Left Blank

A

BILINEAR TRANSFORMATION

A bilinear transformation is defined as

$$Z = \frac{a + bz}{c + dz}, \tag{A.1}$$

where a, b, c, and d are constants (complex in general) and z is an independent complex variable being mapped into the dependent complex variable Z as illustrated in Fig. A.1.

This type of transformation occurs numerous times in electrical engineering, for example, as dielectric hysteresis, mutual impedance coupling between circuits, transmission line calculations, propagation in a stratified medium, loadspeaker impedance, in the development of the Smith chart, and in particular in the investigation of periodic structures in a stratified medium or more precisely in our analysis of the T-function defined in Chapter 5. It is therefore quite natural that we should investigate this transformation in some detail.

As we start our investigation we should, however, remind the reader of some fundamental laws from circle geometry. They will greatly facilitate the examination of (A.1).

A.1 "POWER OF THE CIRCLE"

Given a circle and a point A from which we draw lines intersecting the circle, as shown in Fig. A.2, it is true that:

Theorem 1 $b_1 c = b c_1$, where b, c, b_1, and c_1 are defined in Fig. A.2.

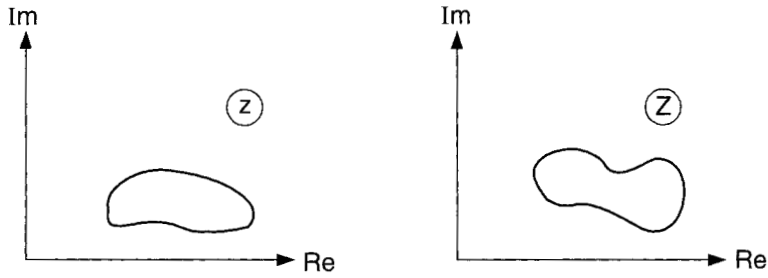

FIGURE A.1. When a complex variable z transverses a curve in the z-plane (*left*) it will image another curve in the complex Z-plane (*right*).

Proof From elementary circle geometry, $\angle ABC = \angle AB_1C_1$; that is, ΔABC and ΔAB_1C_1 are similar, and thus

$$\frac{b_1}{c_1} = \frac{b}{c}$$

or

$$b_1 c = b c_1 \tag{A.2}$$ ■

A.2 INVERSION

Definition of Inversion: Given a circle with radius k and center O as shown in Fig. A.3. Through the arbitrary point P and the center O we draw a line. The point P_1

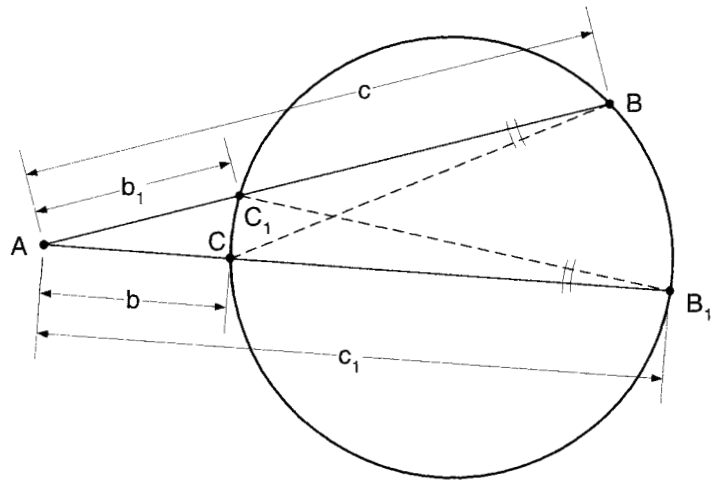

FIGURE A.2. For all lines through A intersecting the circle, $b_1 c = b c_1$ (power of the circle).

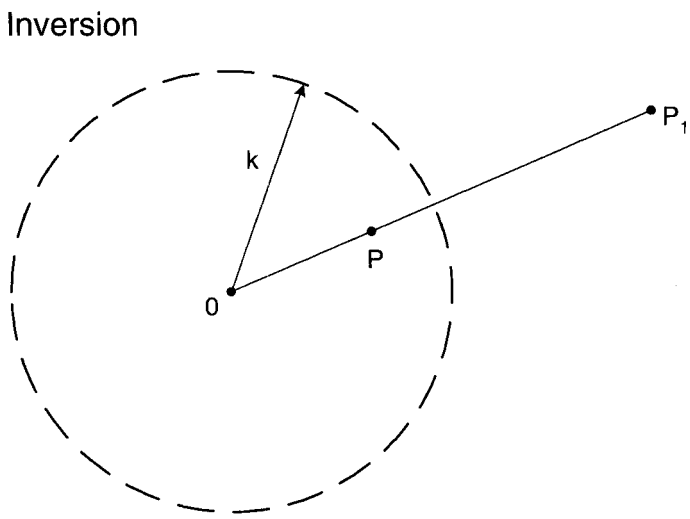

FIGURE A.3. Point P_1 is the inverted point of P in a circle of inversion with radius k if P_1 and P are located on the same radius and $OP \cdot OP_1 = k^2$.

on this radius is called the *inverted point* of P with respect to this circle of inversion with radius k if

$$OP_1 = \frac{k^2}{OP}. \tag{A.3}$$

Theorem 2 If point P transverses a circle, so does point P_1.

Proof Let P transverse the circle C_1 as shown in Fig. A.4. Further let us denote the other intersection between the circle C_1 and the radius OP by P_2.

Then from Theorem 1 above we have

$$OP \cdot OP_2 = c^2, \tag{A.4}$$

where c is a constant defined in Fig. A.4 and not related to any previously defined c. Substituting (A.4) into (A.3) yields

$$OP_1 = \frac{k^2}{OP} = \frac{k^2}{c^2} OP_2 = \text{constant} \cdot OP_2. \tag{A.5}$$

Inspection of (A.5) shows that any figure traced out by P_1 will be similar to the figure traced by P_2. Thus, if P transverses a circle C_1, the inverted point P_1 will transverse the circle C_2 as well.

Or: A circle is always inverted into another circle (as Theorem 2). ■

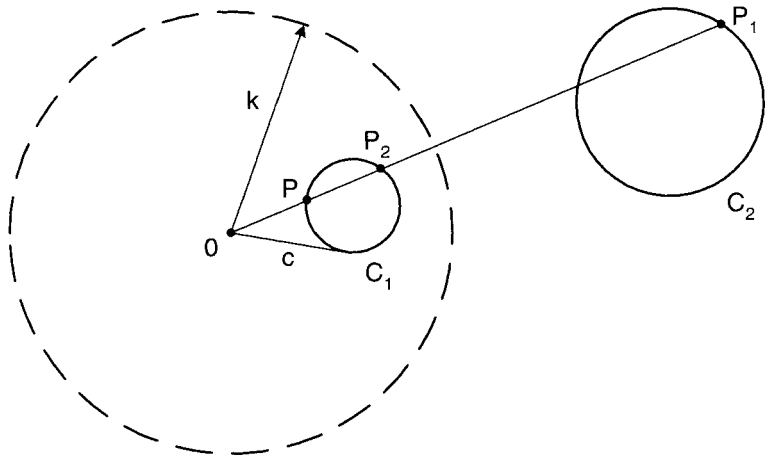

FIGURE A.4. A circle C_1 is always inverted into another circle C_2 which could degenerate into a straight line.

Note: A straight line is merely a circle with an infinite radius; a straight line can be inverted into a circle (or straight line).

A.3 BILINEAR TRANSFORMATION

Theorem 3 If the complex variable z transverse a circle, so will the dependent variable Z given by a bilinear transformation.

Proof Let us first decompose (A.1) as follows:

$$Z = \frac{a + bz}{c + dz} = \frac{a + (c + dz)\frac{b}{d} - c\frac{b}{d}}{c + dz}$$

$$= \frac{a - \frac{b}{d}c}{c + dz} + \frac{b}{d} = \frac{|k|^2 e^{j2\phi}}{c + dz} + \frac{b}{d},$$

or

$$Z = \frac{|k|^2 e^{j2\phi}}{c + dz} + \frac{b}{d}, \tag{A.6}$$

where $ke^{j\phi}$ is a complex constant.

Let z transverse the circle C_1 as shown in Fig. A.5. Then $|z||d|$ will also be a circle C_2 (by similarity) and further multiplication with $e^{j(\phi_z + \phi_d)}$ is merely a rotation; zd will be a circle C_2.

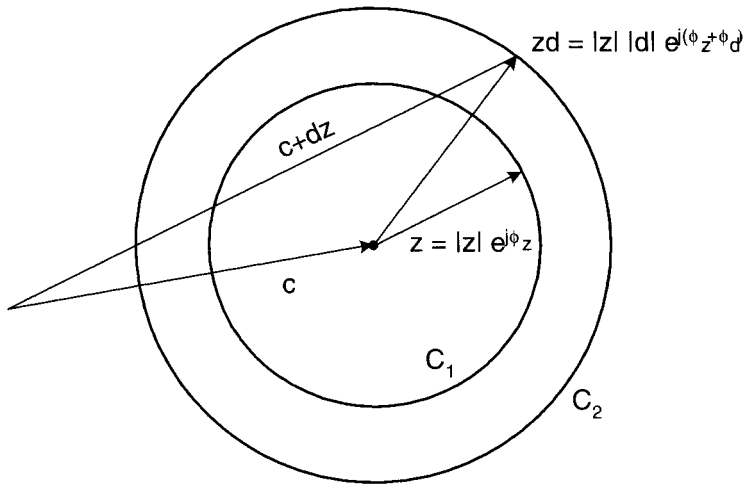

FIGURE A.5. Let z transverse the circle C_1. Then dz will transverse the circle C_2. Further, adding the complex constant c merely amounts to a translation preserving the shape of the circle C_2.

Finally we add the complex constant c to obtain the denominator $c + dz$ in (A.6). This operation is a simple translation as also shown in Fig. A.5; that is, $c + dz$ is also a circle (C_2).

Inspection of (A.6) now shows that we must invert the circle $c + dz$, that is, C_2 into a circle of inversion with radius k.

Further, according to Theorem 2 above, that will produce a new circle C_3 as shown in Fig. A.6. Multiplication with the factor $e^{j2\phi}$ in (A.6) will merely rotate the circle C_3 into a new circle C_4 as also shown in Fig. A.6. We finally add the complex constant $\frac{b}{d}$ [see (A.6)] which clearly preserves the circle C_4 (we merely have a change of the coordinate system's origin). Thus we have shown that for a bilinear transformation (A.1), a circle is always mapped into another circle. ■

Note: We have at this point not concerned ourselves with what specific circle C_4 might be (although we could). That question is in general being solved much easier by transformation of key points provided by (A.1). This procedure will be illustrated by examples.

We should emphasize that this procedure avoids lengthy and complicated calculations.

Theorem 4 The bilinear transformation is conformal.

Primarily Theorem 4 means that if two curves intersect each other at an angle α in the z-plane, then their images in the Z-plane will intersect each other with the same angle α as illustrated in Fig. A.7.

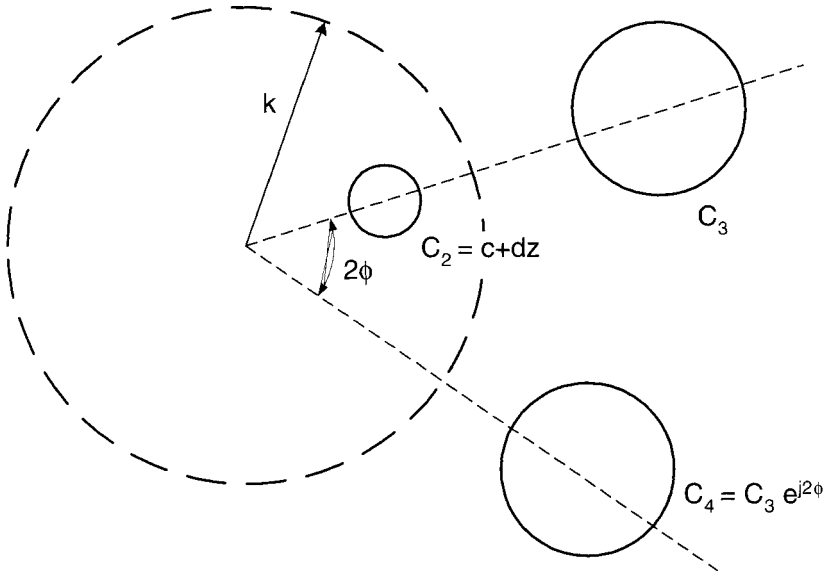

FIGURE A.6. Continuing from Fig. A.5, the circle $C_2 = c + dz$ is now inverted in a circle of inversion with radius k into the circle C_3 that is subsequently rotated into the circle C_4. Thus, if the input of a bilinear transformation in the z-plane is a circle, so is the output in the Z-plane.

Proof For any analytic function $f(z)$ (which is the bilinear transformation) it is true that if a curve in the z-plane has a tangent at point z_0, then the tangent to the image in the Z-plane is obtained from the one in the z-plane by rotation of $\angle f'(z_0)$ in the positive direction.

Thus, if two curves in the z-plane intersect each other at an angle α, then the tangents to their images will both be obtained by rotation of the same angle $\angle f'(z)$;

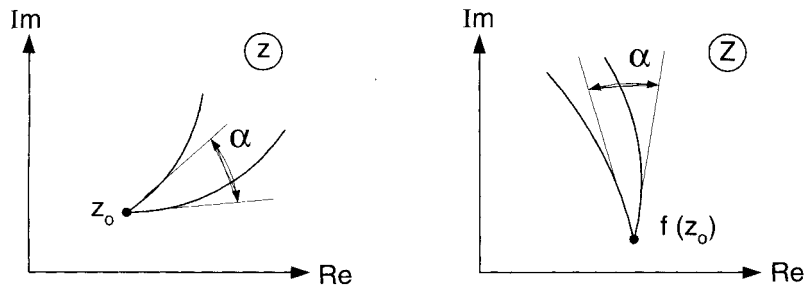

FIGURE A.7. For any analytic function such as the bilinear transformation, it is true that if two curves in the z-plane intersect each other at an angle α, their image curves in the Z-plane will do the same.

that is, the angle between the two intersecting curves in the Z-plane is still α as illustrated in Fig. A.7. ■

Further, from the definition of $f'(z)$, for any analytic function:

$$\left|f'(z)\right| = \lim_{\Delta \to 0} \frac{|\Delta Z|}{|\Delta z|} = \text{constant},$$

so not only are the intersecting angles preserved but also the scaling. In other words, an analytic function like the bilinear transformation is conformal.

A.4 EXAMPLES OF BILINEAR TRANSFORMATIONS

The impedance at a distance d from a dielectric interface or a simple form of the T-function is defined in Chapter 5. The input impedance Z_{in} at the distance d from an interface with reflection coefficient Γ, as shown in Fig. A.8, is well known:

$$Z_{in} = \frac{E_{tot}}{H_{tot}} = Z_1 \frac{1 + \Gamma e^{-j2\beta_1 d}}{1 - \Gamma e^{-j2\beta_1 d}}, \tag{A.7}$$

or

$$Z_{in} = Z_1 \frac{1 + \Gamma z}{1 - \Gamma z} \qquad z = e^{-j2\beta_1 d}. \tag{A.8}$$

Clearly, (A.7) constitutes a bilinear transformation where the input for the independent variable z in a circle, namely, $e^{-j2\beta_1 d}$, when $\beta_1 d$ varies.

Thus, according to Theorem 3, Z_{in} must also be a circle.

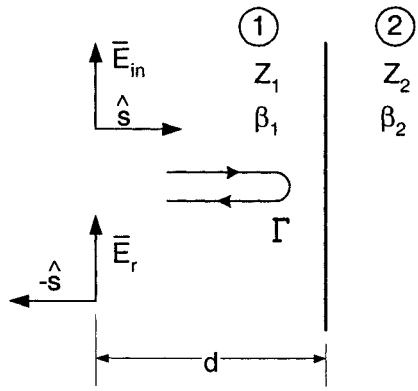

FIGURE A.8. A wave incident upon the interface between two semi-infinite media with intrinsic impedances Z_1 and Z_2, respectively, will be reflected with the reflection coefficient $\Gamma = (Z_2 - Z_1)/(Z_2 + Z_1)$.

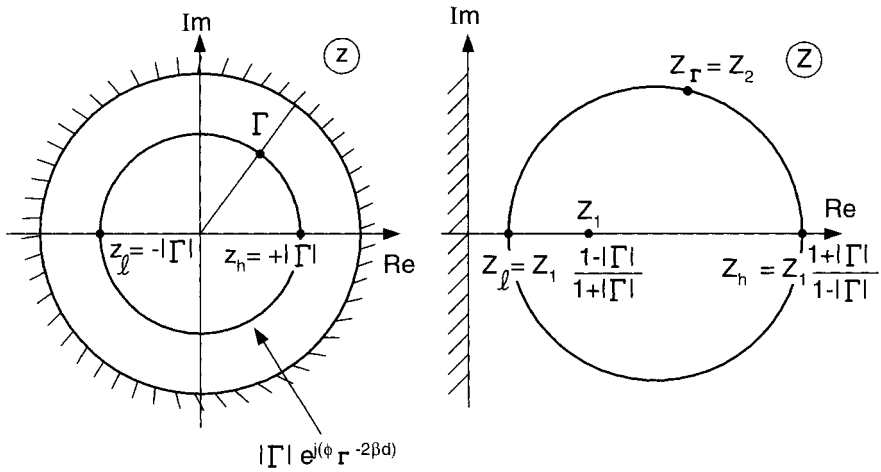

FIGURE A.9. *Left*: As z transverse a circle $|z| = |\Gamma|$, it will intersect the points $z_h = +|\Gamma|$ and $z_l = -|\Gamma|$ with the highest and lowest real values, respectively. *Right*: The image points Z_h and Z_l of z_h and z_l, respectively, determine the image circle in the complex Z-plane.

To determine what circle, we merely observe that

$$\Gamma z = |\Gamma|\, e^{j(\phi_\Gamma - 2\beta d)}$$

is a circle with radius $|\Gamma|$ in the z-plane as shown in Fig. A.9 left. This circle is seen to intersect the real axis at two points:

$$z_h = +|\Gamma| \quad \text{and} \quad z_l = -|\Gamma|\,. \tag{A.9}$$

The images in the Z-plane of z_h and z_l are obtained from (A.8) by substituting $z\Gamma = \pm|\Gamma|$, respectively:

$$Z_h = Z_1 \frac{1+|\Gamma|}{1-|\Gamma|} \quad \text{and} \quad Z_l = Z_1 \frac{1-|\Gamma|}{1+|\Gamma|} \tag{A.10}$$

as shown in the Fig. A.9 right.[1] The image circle in the Z-plane must now go through the points Z_h and Z_l, and since the original circle $|\Gamma|\, e^{j(\phi_\Gamma - 2\beta l)}$ in the z-plane intersects the real axis at 90°, so must the image circle in the Z-plane (Theorem 4). Thus the center of the image circle in the Z-plane must be on the line connecting Z_l and Z_h. This completely determines the image circle. (This result can also be obtained by a symmetry argument.)

Note: No long calculations are necessary to find the image circle in the Z-plane. We observe that the point $\Gamma = 0$ in the z-plane is transformed into Z_1 in the Z-plane

[1] We assume Z_1 to be real.

according to (A.8). We also note that the unit circle $|\Gamma| = 1$ is transformed into

$$Z_{in} = Z_1 \frac{1 + e^{+j(\phi_\Gamma - 2\beta l)}}{1 - e^{+j(\phi_\Gamma - 2\beta l)}} = jZ_1 \cot\left(\frac{\phi_\Gamma}{2} - \beta l\right),$$

which is purely imaginary (we assume Z_1 real). In other words, the unit circle $|\Gamma| = 1$ is transformed into the imaginary axis in the Z-plane as indicated in Figs. A.9 and A.10.

Also the point $\Gamma = |\Gamma| e^{j\phi_\Gamma}$ corresponding to $2\beta d = 0$ (i.e., right up against the interface) is transformed into the point Z_Γ:

$$Z_\Gamma = Z \frac{1 + \Gamma}{1 - \Gamma}, \tag{A.11}$$

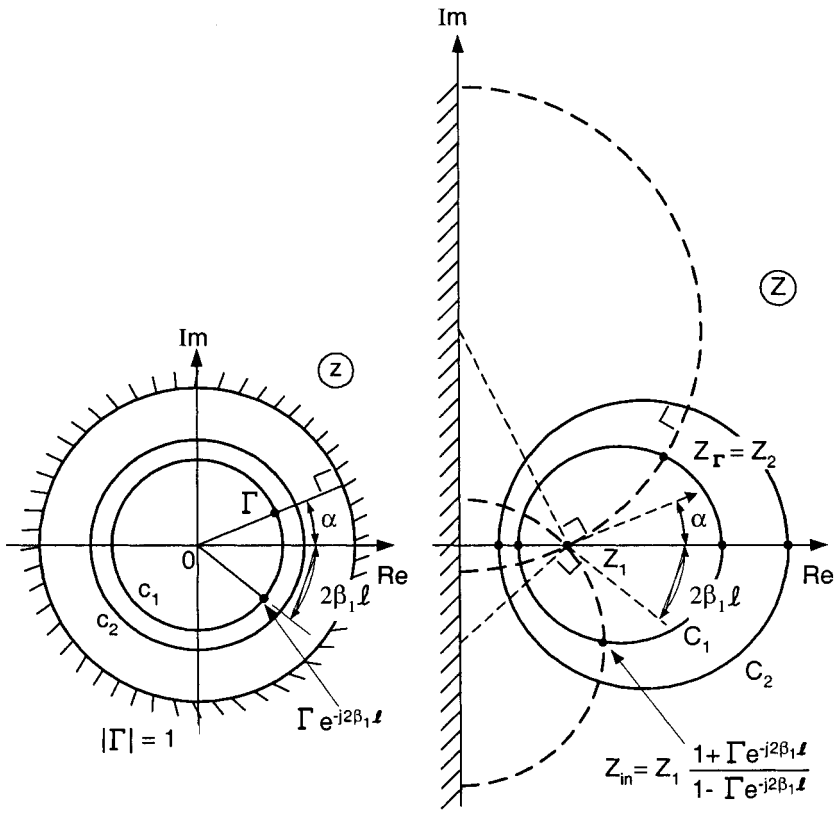

FIGURE A.10. Two concentric circles c_1 and c_2 (*left*) are transformed in the two nonconcentric circles C_1 and C_2 (*right*). Further all radii at the left are transformed into circles through Z_1 with their centers at the imaginary axis (*right*). Note further how all angles are preserved, for example, α.

where

$$\Gamma = \frac{Z_2 - Z_1}{Z_2 + Z_1}. \tag{A.12}$$

Substituting (A.12) into (A.11) yields

$$Z_\Gamma = Z_1 \frac{1 + \frac{Z_2 - Z_1}{Z_2 + Z_1}}{1 - \frac{Z_2 - Z_1}{Z_2 + Z_1}} = Z_1 \frac{Z_2 + Z_1 + Z_2 - Z_1}{Z_2 + Z_1 - Z_2 + Z_1} = Z_1 \frac{2Z_2}{2Z_1} = Z_2, \tag{A.13}$$

which we would expect for $d = 0$.

Further in Fig. A.10 we show how the two concentric circles c_1 and c_2 in the z-plane are transfered into the two nonconcentric circles C_1 and C_2 in the Z-plane.

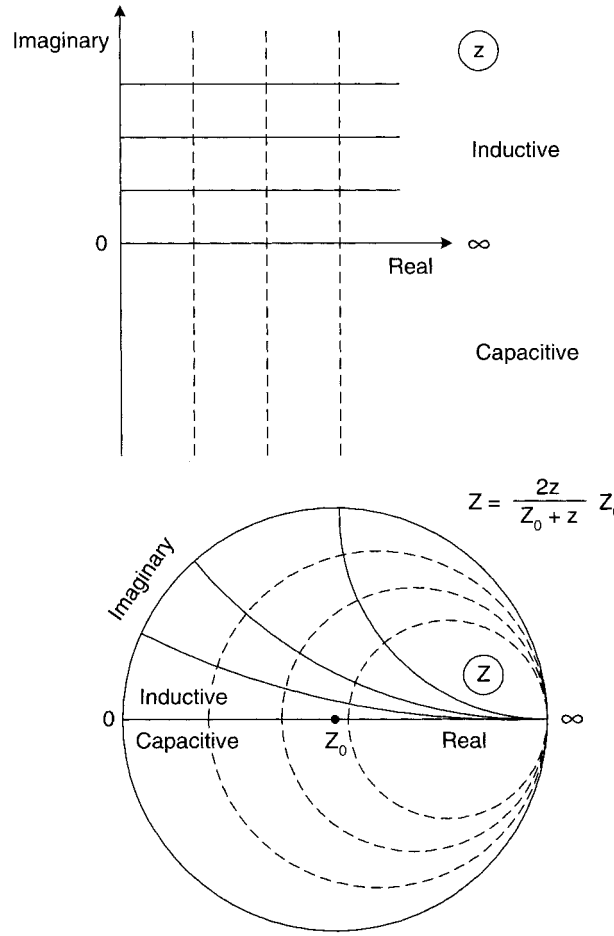

FIGURE A.11. Smith chart summary

We finally note that the images of the radial lines in the z-plane must also be circles (or part of) going through Z_1 (corresponding to O).

Since all radial lines in the z-plane intersect circles like c_1 and c_2 at 90°, they must do the same in the Z-plane (Theorem 4). In particular, they must intersect the imaginary axis at 90°, which means that their center must lie on the imaginary axis.

Also, if the angle between a radial line and the real axis is α (see Fig. A.10), then this angle is preserved in the Z-plane for the tangent to the circle through Z_1 (Theorem 4). This observation completely determines all radial circles as illustrated in Fig. A.10.

A.5 SMITH CHART

Perhaps the most important application of the bilinear transformation is the construction of the Smith chart shown in Fig. A.11. Basically we merely transform the right half z-plane at the top of Fig. A.11 into the inside of the circle shown at the bottom of the same figure by use of the bilinear transformation $Z = Z_0(2z/Z_0 + z)$. Using the various theorems derived earlier, it can easily be seen that the rectangular coordinate system at the top will be transformed into the set of orthogonal circles shown at the bottom. The details are left as an exercise for the student.

This Page Intentionally Left Blank

B

EVALUATION OF THE DETERMINANT D_N

In this appendix we pursue a systematic evaluation of the determinant D_N given by Eq. (7.11) as

$$D_N = \begin{vmatrix} Y^{1,1} + Y_L^{(1)} & Y^{1,2} & 0 & 0 & \cdots & 0 \\ Y^{2,1} & Y^{2,2} + Y_L^{(2)} & Y^{2,3} & 0 & \cdots & 0 \\ 0 & Y^{3,2} & Y^{3,3} + Y_L^{(3)} & Y^{3,4} & \cdots & 0 \\ \cdots & & & & & \\ 0 & \cdots & \cdots & \cdots & Y^{N,N-1} & Y^{N,N} + Y_L^{(N)} \end{vmatrix}. \tag{B.1}$$

As shown in Section 6.5 by (6.29), the self-admittances of the two outside layers consist of a real and imaginary part; that is, by noting the change of notation as explained in Section 7.3.2:

$$Y^{1,1} = Y_{ore}^{1,1} + jy^{1,1}, \tag{B.2}$$

$$Y^{N,N} = Y_{ore}^{N,N} + jy^{N,N}, \tag{B.3}$$

where $Y_{ore}^{1,1}$, as explained in Section 6.5, simply denotes the $k = n = 0$ term taking the real part of $_{\perp}^{\parallel}T$ while $y^{1,1}$ denotes the sum of all the imaginary terms [see (6.29)]. In particular, the self-admittance of any internal layer will be purely imaginary, as shown in Section 6.5, because we have "ground planes" to both sides of the internal arrays:

$$Y^{n,n} = jy^{n,n}, \qquad n = 2, 3, \ldots, (N-1). \tag{B.4}$$

We have further shown in Section 6.6 that all the mutual admittances are purely imaginary unless spaced very close:

$$Y^{n,m} \sim j\left|Y^{n,m}\right| \qquad \text{for all } n \neq m. \tag{B.5}$$

The determinant D_N given by (B.1) above can then be written by application of (B.2), (B.3), (B.4), and (B.5) as

$$D_N = \begin{vmatrix} Y_{0re}^{1,1} + jy^{1,1} & j\left|Y^{1,2}\right| & 0 & 0 & \cdots & 0 \\ j\left|Y^{1,2}\right| & jy^{2,2} & j\left|Y^{2,3}\right| & 0 & \cdots & 0 \\ 0 & j\left|Y^{3,2}\right| & jy^{3,3} & j\left|Y^{3,4}\right| & \cdots & 0 \\ \vdots & & & & & \\ 0 & \cdots & 0 & j\left|Y^{N,N-1}\right| & & Y_{0re}^{N,N} + jy^{N,N} \end{vmatrix}. \tag{B.6}$$

We can now evaluate (B.6) for various values of N.

$N = 1$ (Symmetric Case)

(For the asymmetric case, see Problems 7.1 and 7.2.)

$$D_1 = Y_{0re}^{1,1} + jy^{1,1}, \tag{B.7}$$

or dropping the superscripts,

$$\mathcal{P}_1^2 = \frac{y^2}{Y_{0re}^2}. \tag{B.8}$$

$N = 2$ (General Case)

$$D_2 = Y_{0re}^{1,1}Y_{0re}^{2,2} - y^{1,1}y^{2,2} + \left|Y^{1,2}\right|\left|Y^{2,1}\right| + j\left[Y_{0re}^{1,1}y^{2,2} + Y_{0re}^{2,2}y^{1,1}\right], \tag{B.9}$$

$$|D_2|^2 = 4Y_{0re}^{1,1}Y_{0re}^{2,2}\left|Y^{1,2}\right|\left|Y^{2,1}\right|\left[1 + \mathcal{P}_{2\text{even}}^2 + \mathcal{P}_{2\text{odd}}^2\right], \tag{B.10}$$

where

$$\mathcal{P}_{2\text{even}}^2 = \frac{1}{4Y_{0re}^{1,1}Y_{0re}^{2,2}\left|Y^{1,2}\right|\left|Y^{2,1}\right|}\left[y^{1,1}y^{2,2} - \left|Y^{1,2}\right|\left|Y^{2,1}\right| + Y_{0re}^{1,1}Y_{0re}^{2,2}\right]^2, \tag{B.11}$$

$$\mathcal{P}_{2\text{odd}}^2 = \frac{1}{4Y_{0re}^{1,1}Y_{0re}^{2,2}\left|Y^{1,2}\right|\left|Y^{2,1}\right|}\left[Y_{0re}^{1,1} \quad y^{1,2} - Y_{0re}^{2,2} \quad y^{1,1}\right]^2 \tag{B.12}$$

$N = 3$ (General Case)

$$D_3 = \left[-Y_{0re}^{1,1}y^{2,2}y^{3,3} - Y_{0re}^{3,3}y^{1,1}y^{22} - Y_{0re}^{1,1}\left|Y^{2,3}\right|\left|Y^{3,2}\right| + Y_{0re}^{3,3}\left|Y^{1,2}\right|\left|Y^{2,1}\right|\right]$$
$$+ j\left[Y_{0re}^{1,1}Y_{0re}^{3,3}y^{2,2} - y^{1,1}y^{2,2}y^{3,3} + y^{1,1}\left|Y^{2,3}\right|\left|Y^{3,2}\right| + y^{3,3}\left|Y^{1,2}\right|\left|Y^{2,1}\right|\right] \tag{B.13}$$

$$|D_3|^2 = 4Y_{0re}^{1,1}Y_{0re}^{3,3}\left|Y^{1,2}\right|\left|Y^{2,1}\right|\left|Y^{2,3}\right|\left|Y^{3,2}\right|\left[1 + \mathcal{P}_{3\text{even}}^2 + \mathcal{P}_{3\text{odd}}^2\right], \tag{B.14}$$

where

$$\mathcal{P}_{3\text{even}}^2 = \frac{1}{4Y_{0re}^{1,1}Y_{0re}^{3,3}\left|Y^{1,2}\right|\left|Y^{2,1}\right|\left|Y^{2,3}\right|\left|Y^{3,2}\right|}\left[y^{1,1}y^{2,2}y^{3,3} - \left(-Y_{0re}^{1,1}Y_{0re}^{3,3}y^{2,2}\right.\right.$$
$$\left.\left. + y^{1,1}\left|Y^{2,3}\right|\left|Y^{3,2}\right| + y^{3,3}\left|Y^{1,2}\right|\left|Y^{2,1}\right|\right)\right]^2, \tag{B.15}$$

$$\mathcal{P}_{3\text{odd}}^2 = \frac{1}{4Y_{0re}^{1,1}Y_{0re}^{3,3}\left|Y^{1,2}\right|\left|Y^{2,1}\right|\left|Y^{2,3}\right|\left|Y^{3,2}\right|}\left[y^{2,2}\left(Y_{0re}^{1,1}y^{3,3} - Y_{0re}^{3,3}y^{1,1}\right)\right.$$
$$\left. - \left(Y_{0re}^{1,1}\left|Y^{2,3}\right|\left|Y^{3,2}\right| - Y_{0re}^{3,3}\left|Y^{1,2}\right|\left|Y^{2,1}\right|\right)\right]^2. \tag{B.16}$$

$N = 4$ (Symmetric Case Only)

$$D_4 = \left[\left(y^{1,1}y^{2,2}\right)^2 - \left[-\left(Y_{0re}^{1,1}y^{2,2}\right)^2 + \left(y^{1,1}\left|Y^{2,3}\right|\right)^2 + 2y^{1,1}y^{2,2}\left|Y^{1,2}\right|\left|Y^{2,1}\right|\right]\right.$$
$$\left. + \left[-\left(Y_{0re}^{1,1}\left|Y^{2,3}\right|\right)^2 + \left(\left|Y^{1,2}\right|\left|Y^{2,1}\right|\right)^2\right]\right]$$
$$- 2\left(Y_{0re}^{1,1}\right)^2\left[\left(y^{2,2}\right)^2 - \left(\left|Y^{2,3}\right|\right)^2\right]$$
$$+ 2jY_{0re}^{1,1}\left[-y^{1,1}\left[\left(y^{2,2}\right)^2 - \left|Y^{2,3}\right|^2\right] + y^{2,2}\left|Y^{1,2}\right|\left|Y^{2,1}\right|\right], \tag{B.17}$$

$$|D_4| = 2Y_{0re}^{1,1}\left|Y^{2,1}\right|\left|Y^{3,2}\right|\left|Y^{1,2}\right|\sqrt{1 + \mathcal{P}_4^2}, \tag{B.18}$$

where

$$\mathcal{P}_4 = \frac{1}{2Y_{0re}^{1,1}\left|Y^{2,1}\right|\left|Y^{3,2}\right|\left|Y^{1,2}\right|}\left[\left(y^{1,1}y^{2,2}\right)^2\right.$$

$$- \left[\left(y^{1,1} \left| Y^{2,3} \right| \right)^2 - \left(Y_{0re}^{1,1} y^{2,2} \right)^2 + 2 y^{1,1} y^{2,2} \left| Y^{1,2} \right| \left| Y^{2,1} \right| \right]$$

$$+ \left[\left(\left| Y^{1,2} \right| \left| Y^{2,1} \right| \right) - \left(Y_{0re}^{1,1} \left| Y^{2,3} \right| \right)^2 \right] \Bigg]. \tag{B.19}$$

$N = 5$ (Symmetric Case Only)

$$D_5 = j \Bigg[\Bigg[\left(y^{1,1} y^{2,2} \right)^2 y^{3,3} - \Bigg[\Bigg(- \left(Y_{0re}^{1,1} y^{2,2} \right)^2 y^{3,3} + y^{1,1} y^{2,2} y^{3,3} \left| Y^{1,2} \right| \left| Y^{2,1} \right| \Bigg)$$

$$+ \left(y^{1,1} y^{2,2} y^{3,3} \left| Y^{1,2} \right| \left| Y^{2,1} \right| + 2 \left(y^{1,1} \right)^2 y^{2,2} \left| Y^{2,3} \right| \left| Y^{3,2} \right| \right) \Bigg]$$

$$+ \Bigg[\left| Y^{1,2} \right| \left| Y^{2,1} \right| \left(y^{3,3} \left| Y^{1,2} \right| \left| Y^{2,1} \right| + 2 y^{1,1} \left| Y^{2,3} \right| \left| Y^{3,2} \right| \right)$$

$$- 2 \left(Y_{0re}^{1,1} \right)^2 y^{2,2} \left| Y^{2,3} \right| \left| Y^{3,2} \right| \Bigg] \Bigg]$$

$$- 2 \Bigg[\left(Y_{0re}^{1,1} y^{2,2} \right)^2 y^{3,3} - 2 \left(Y_{0re}^{1,1} \right)^2 y^{2,2} \left| Y^{2,3} \right| \left| Y^{3,2} \right| \Bigg] \Bigg]$$

$$+ \Bigg[2 Y_{0re}^{1,1} y^{1,1} \left(y^{2,2} \right)^2 y^{3,3} - 2 \Bigg[Y_{0re}^{1,1} y^{2,2} y^{3,3} \left| Y^{1,2} \right| \left| Y^{2,1} \right|$$

$$+ 2 Y_{0re}^{1,1} y^{1,1} y^{2,2} \left| Y^{2,3} \right| \left| Y^{3,2} \right| \Bigg] + 2 Y_{0re}^{1,1} \left| Y^{1,2} \right| \left| Y^{2,1} \right| \left| Y^{2,3} \right| \left| Y^{3,2} \right| \Bigg], \tag{B.20}$$

$$|D_5| = 2 Y_{0re}^{1,1} \left| Y^{2,1} \right| \left| Y^{3,2} \right| \left| Y^{2,3} \right| \left| Y^{1,2} \right| \sqrt{1 + \mathcal{P}_5^2}, \tag{B.21}$$

where

$$\mathcal{P}_5 = \frac{1}{2 Y_{0re}^{1,1} \left| Y^{2,1} \right| \left| Y^{3,2} \right| \left| Y^{2,3} \right| \left| Y^{1,2} \right|} \Bigg[\left(y^{1,1} y^{2,2} \right)^2 y^{3,3}$$

$$- \Bigg[2 y^{1,1} y^{2,2} y^{3,3} \left| Y^{1,2} \right| \left| Y^{2,1} \right| + 2 \left(y^{1,1} \right)^2 y^{2,2} \left| Y^{2,3} \right| \left| Y^{3,2} \right|$$

$$- \left(Y_{0re}^{1,1} y^{2,2} \right)^2 y^{3,3} \Bigg]$$

$$+ \Bigg[\left| Y^{1,2} \right| \left| Y^{2,1} \right| \left(y^{3,3} \left| Y^{1,2} \right| \left| Y^{2,1} \right| + 2 y^{1,1} \left| Y^{2,3} \right| \left| Y^{3,2} \right| \right)$$

$$- 2 \left(Y_{0re}^{1,1} \right)^2 y^{2,2} \left| Y^{2,3} \right| \left| Y^{3,2} \right| \Bigg] \Bigg]. \tag{B.22}$$

C

FRESNEL REFLECTION AND TRANSMISSION COEFFICIENTS

In this appendix we present a collection of formulas containing the reflection and transmission coefficients for a plane wave entering from the semi-infinite medium 1 to the semi-infinite medium 2. We denote the direction of propagation in these two media by $\hat{r}_1$ and $\hat{r}_2$, while their wave impedances are denoted by Z_1 and Z_2, respectively. If we refer to the E-field as shown in Fig. C.1, we can denote the reflection coefficient for the orthogonal and parallel components by ${}^{E}_{\perp}\Gamma_{1,2}$ and ${}^{E}_{\parallel}\Gamma_{1,2}$, respectively. Similarly we have introduced ${}^{H}_{\perp}\Gamma_{1,2}$ and ${}^{H}_{\parallel}\Gamma_{1,2}$ when referring to the H-vectors being orthogonal or parallel, respectively, to the plane of incidence. Noting that the y-components r_{1y} and r_{2y} of $\hat{r}_2$ and $\hat{r}_2$ are merely the direction cosines with respect to the y-axis of these vectors, we obtain from the classical Fresnel reflection coefficient (see also the note in Fig. C.1). When referring to the H-Field, we will find that using the admittances $Y_1 = 1/Z_1$ and $Y_2 = 1/Z_2$ leads to a very convenient symmetry.

REFERENCE TO THE E-FIELD

Orthogonal

$$ {}^{E}_{\perp}\Gamma_{1,2} = \frac{Z_2 r_{1y} - Z_1 r_{2y}}{Z_2 r_{1y} + Z_1 r_{2y}} \tag{C.1} $$

Parallel

$$ {}^{E}_{\parallel}\Gamma_{1,2} = \frac{Z_2 r_{2y} - Z_1 r_{1y}}{Z_2 r_{2y} + Z_1 r_{1y}} \tag{C.2} $$

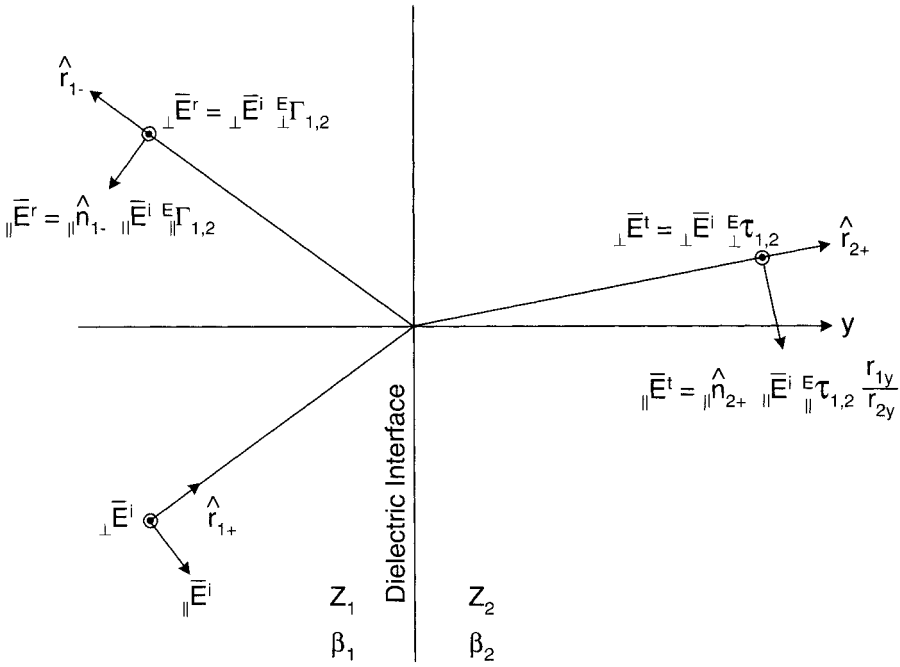

FIGURE C.1. Fresnel reflection coefficients for a plane wave incident upon an interface between two media with intrinsic impedances Z_1 and Z_2, respectively. For definition of $_{\perp}n$ and $_{\parallel}n$, see Sections 5.2 and 4.72. Note that the parallel component of the transmitted signal are multiplied by r_{1y}/r_{2y} in addition to $_{\parallel}\mathcal{T}_{1,2}$. This notation preserves symmetry of the formulas.

Orthogonal

$$ {}^E_{\perp}\mathcal{T}_{1,2} = 1 + {}^E_{\perp}\Gamma_{1,2} = \frac{2Z_2 r_{1y}}{Z_2 r_{1y} + Z_1 r_{2y}} \tag{C.3} $$

Parallel

$$ {}^E_{\parallel}\mathcal{T}_{1,2} = 1 + {}^E_{\parallel}\Gamma_{1,2} = \frac{2Z_2 r_{2y}}{Z_2 r_{2y} + Z_1 r_{1y}} \tag{C.4} $$

Note the obliquity factor r_{1y}/r_{2y} in Fig. C.1.

Orthogonal

$$ 1 - {}^E_{\perp}\Gamma_{1,2} = \frac{2Z_1 r_{2y}}{Z_2 r_{1y} + Z_1 r_{2y}} \tag{C.5} $$

Parallel

$$1 - {}^{E}_{\parallel}\Gamma_{1,2} = \frac{2Z_1 r_{1y}}{Z_2 r_{2y} + Z_1 r_{1y}} \tag{C.6}$$

Orthogonal

$$\frac{1 + {}^{E}_{\perp}\Gamma_{1,2}}{1 - {}^{E}_{\perp}\Gamma_{1,2}} = \frac{Z_2}{Z_1}\frac{r_{1y}}{r_{2y}} \tag{C.7}$$

Parallel

$$\frac{1 + {}^{E}_{\parallel}\Gamma_{1,2}}{1 - {}^{E}_{\parallel}\Gamma_{1,2}} = \frac{Z_2}{Z_1}\frac{r_{2y}}{r_{1y}} \tag{C.8}$$

REFERENCE TO THE H-FIELD

Orthogonal

$${}^{H}_{\perp}\Gamma_{1,2} = \frac{Y_2 r_{1y} - Y_1 r_{2y}}{Y_2 r_{1y} + Y_1 r_{2y}} \tag{C.9}$$

Parallel

$${}^{H}_{\parallel}\Gamma_{1,2} = \frac{Y_2 r_{2y} - Y_1 r_{1y}}{Y_2 r_{2y} + Y_1 r_{1y}} \tag{C.10}$$

Orthogonal

$${}^{H}_{\perp}\mathcal{T}_{1,2} = 1 + {}^{H}_{\perp}\Gamma_{1,2} = \frac{2Y_2 r_{1y}}{Y_2 r_{1y} + Y_1 r_{2y}} \tag{C.11}$$

Parallel

$${}^{H}_{\parallel}\mathcal{T}_{1,2} = 1 + {}^{H}_{\parallel}\Gamma_{1,2} = \frac{2Y_2 r_{2y}}{Y_2 r_{2y} + Y_1 r_{1y}} \tag{C.12}$$

Note the obliquity factor r_{1y}/r_{2y} in Fig. C.1.

Orthogonal

$$1 - {}^{H}_{\perp}\Gamma_{1,2} = \frac{2Y_1 r_{2y}}{Y_2 r_{1y} + Y_1 r_{2y}} \tag{C.13}$$

Parallel

$$1 - {}^{H}_{\parallel}\Gamma_{1,2} = \frac{2Y_1 r_{1y}}{Y_2 r_{2y} + Y_1 r_{1y}} \tag{C.14}$$

Orthogonal

$$\frac{1 + {}^{H}_{\perp}\Gamma_{1,2}}{1 - {}^{H}_{\perp}\Gamma_{1,2}} = \frac{Y_2}{Y_1}\frac{r_{1y}}{r_{2y}} \tag{C.15}$$

Parallel

$$\frac{1 + {}^{H}_{\parallel}\Gamma_{1,2}}{1 - {}^{H}_{\parallel}\Gamma_{1,2}} = \frac{Y_2}{Y_1}\frac{r_{2y}}{r_{1y}} \tag{C.16}$$

RELATIONSHIP BETWEEN Γ^E AND Γ^H

$$ {}^{E}_{\perp}\Gamma_{1,2} = -{}^{E}_{\perp}\Gamma_{2,1} = -{}^{H}_{\parallel}\Gamma_{1,2} = {}^{H}_{\parallel}\Gamma_{2,1}, \tag{C.17}$$

$$ {}^{E}_{\parallel}\Gamma_{1,2} = -{}^{E}_{\parallel}\Gamma_{2,1} = -{}^{H}_{\perp}\Gamma_{1,2} = {}^{H}_{\perp}\Gamma_{2,1}. \tag{C.18}$$

${}^{H}_{\perp}\Gamma_{n,m}$ is obtained from ${}^{E}_{\parallel}\Gamma_{n,m}$ by substituting Y_n and Y_m for Z_n and Z_m, respectively. Compare all orthogonal equations with all parallel equations above. Alternative notations also used frequently in the text for $\perp$-, $\parallel$-, E-, and H-fields:

$$\Gamma_{1,2} = \Gamma_{1+}, \tag{C.19}$$

$$\mathcal{T}_{1,2} = \mathcal{T}_{1+}, \tag{C.20}$$

$$\mathcal{T}_{2,1} = \mathcal{T}_{2-}, \quad \text{etc.} \tag{C.21}$$

D

EFFECTIVE REFLECTION AND TRANSMISSION COEFFICIENTS FOR A STRATIFIED MEDIUM

The field reflected from a single dielectric interface is given by the well-known formulas of Fresnel; see Appendix C. However, if we instead are considering a stratified medium, it is practical to introduce a concept for effective reflection and transmission coefficients. The former is defined as the ratio between the field reflected in the bistatic direction and the field incident upon the dielectric interface with all the stratified medium in place on the transmitted side of the interface in question.

Consider first the simple interface $y = b_m$, shown in Fig. D.1 top, with intrinsic impedance Z_{m+1} for $y > b_m$ and Z_m for $y < b_m$. The Fresnel reflection for a plane wave propagating in the direction $\hat{r}_{m+}$ incident upon this interface is given by (see Appendix C):

$$\underset{\perp}{\overset{E}{}}\Gamma_{m+} = \frac{Z_{m+1}r_{my} - Z_m r_{m+1,y}}{Z_{m+1}r_{my} + Z_m r_{m+1,y}}, \tag{D.1}$$

$$\underset{\parallel}{\overset{E}{}}\Gamma_{m+} = \frac{Z_{m+1}r_{m+1,y} - Z_m r_{my}}{Z_{m+1}r_{m+1,y} + Z_m r_{my}}, \tag{D.2}$$

where the superscript E indicates that we are referring to the E-field. The orthogonal and parallel unit vectors ${}_{\perp}\hat{n}_{m+} = {}_{\perp}\hat{n}_{m-} = {}_{\perp}\hat{n}_m$, and ${}_{\parallel}\hat{n}_{m+}$, ${}_{\parallel}\hat{n}_{m-}$ and ${}_{\parallel}\hat{n}_{m+1,+}$ are as shown in Fig. D.1 and are discussed in detail in Section 4.7.2.

Further the transmission coefficient for interface $y = b_m$ is

$$\underset{\perp \atop \parallel}{\overset{E}{}}\tau_{m+} = 1 + \underset{\perp \atop \parallel}{\overset{E}{}}\Gamma_{m+}. \tag{D.3}$$

We next add another interface to the left at $y = b_{m-1}$, thereby creating a slab of thickness d_m located between two media with intrinsic impedances Z_{m-1} and Z_{m+1}, respectively, as shown in Fig. D.1 bottom.

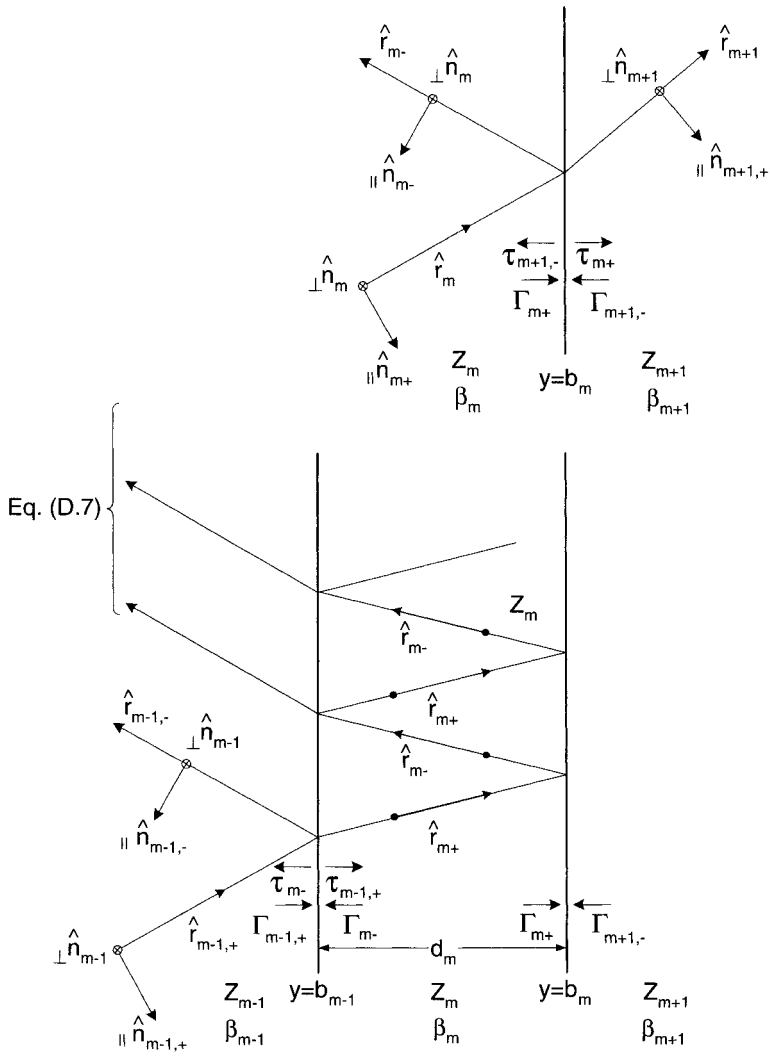

FIGURE D.1.

A plane wave propagating in the direction $\hat{r}_{m-1,+}$ in medium $m-1$ will be transmitted into slab m with transmission coefficient $\tau_{m-1,+}$ and proceed in the direction $\hat{r}_{m+}$ to the interface $y = b_m$, where it will be reflected with reflection coefficient Γ_{m+} back toward interface $y = b_{m-1}$, where it is reflected with reflection coefficient Γ_{m-}, and so on.

For all the right (or positive) going waves in slab m at an arbitrary point of observation $\bar{R}$, we then obtain

$$\bar{E}_{m+}(\bar{R}) = \Big[{}_{\perp}\hat{n}_{m+\perp}E_{b,m-1,+\perp}\tau_{m-1,+}\Big[1 + {}_{\perp}\Gamma_{m+\perp}\Gamma_{m-}e^{-j2\beta_m d_m r_{my}} + {}_{\perp}\Gamma^2_{m+\perp}\Gamma^2_{m-}e^{-j4\beta_m d_m r_{my}} + \cdots\Big] + {}_{\parallel}\hat{n}_{m+\parallel}E_{b,m-1,+\parallel}\tau_{m-1,+}\frac{r_{m-1,y}}{r_{my}}\Big[1 + {}_{\parallel}\Gamma_{m+\parallel}\Gamma_{m-}e^{-j2\beta_m d_m r_{my}} + {}_{\parallel}\Gamma^2_{m-1\parallel}\Gamma^2_{m-}e^{-j4\beta_m d_m r_{my}} + \cdots\Big]e^{-j\beta_m(y-b_{m-1})r_{my}}\Big]. \tag{D.4}$$

SINGLE DIELECTRIC SLAB

From $1 + x + x^2 \cdots = \frac{1}{1-x}$ for $|x| < 1$, we obtain

$$\bar{E}_{m+}(\bar{R}) = \Big[{}_{\perp}\hat{n}_{m+\perp}E_{b,m-1,+}\frac{{}_{\perp}\tau_{m-1,+}}{1 - {}_{\perp}\Gamma_{m+\perp}\Gamma_{m-}e^{-j2\beta_m d_m r_{my}}} + {}_{\parallel}\hat{n}_{m+\parallel}E_{b,m-1,+}\frac{r_{m-1,y}}{r_{my}}\frac{{}_{\parallel}\tau_{m-1,+}}{1 - {}_{\parallel}\Gamma_{m+\parallel}\Gamma_{m-}e^{-j2\beta_m d_m r_{my}}}\Big] e^{-j\beta_m(y-b_{m-1})r_{my}} \tag{D.5}$$

or

$$\bar{E}_{m+}(\bar{R}) = \Big[{}_{\perp}\hat{n}_{m+\perp}E_{b,m-1,+\perp}\tau^e_{m-1,+} + {}_{\parallel}\hat{n}_{m+\parallel}E_{b,m-1,+}\frac{r_{m-1,y}}{r_{my}}{}_{\parallel}\tau^e_{m-1,+}\Big]e^{-j\beta_m(y-b_{m-1})r_{my}}, \tag{D.6}$$

where we have obtained the effective transmission coefficients as

$${}_{\perp\atop\parallel}\tau^e_{m-1,+} = \frac{{}_{\perp\atop\parallel}\tau_{m-1,+}}{1 - {}_{\perp\atop\parallel}\Gamma_{m+}{}_{\perp\atop\parallel}\Gamma_{m-}e^{-j2\beta_m d_m r_{my}}}. \tag{D.7}$$

The sum of all the left-going waves is simply a result of all the right-going waves being reflected at $y = b_m$ with reflection coefficient Γ_{m+}. Thus the sum of the left-going waves in slab m is obtained from (D.6) by multiplication with Γ_{m+}:

$$\bar{E}_{m-}(\bar{R}) = \Big[{}_{\perp}\hat{n}_{m-\perp}E_{b,m-1,+\perp}\tau^e_{m-1\perp}\Gamma_{m+} + {}_{\parallel}\hat{n}_{m-\parallel}E_{b,m-1,+}\frac{r_{m-1,y}}{r_{my}}{}_{\parallel}\tau^e_{m-1\parallel}\Gamma_{m+}\Big]e^{-j\beta_m(2d_m-(y-b_{m-1}))r_{my}}. \tag{D.8}$$

At the interface $y = b_{m-1}$ the sum of these left-going waves, as illustrated in Fig. D.1 bottom, will be transmitted into media $m - 1$ with transmission coefficient τ_{m-}, namely,

$$\bar{E}_{m-}(\bar{R}) = \left[{}_{\perp}\hat{n}_{m-1,-}\, {}_{\perp}E_{b,m-1,+}\, {}_{\perp}\tau^{e}_{m-1}\, {}_{\perp}\Gamma_{m+}\, {}_{\perp}\tau_{m-} \right.$$
$$\left. + {}_{\parallel}\hat{n}_{m-1,-}\, {}_{\parallel}E_{b,m-1,+}\, {}_{\parallel}\tau^{e}_{m-1}\, {}_{\parallel}\Gamma_{m+}\, {}_{\parallel}\tau_{m-} \right] e^{-j2\beta_m d_m r_{my}}. \quad \text{(D.9)}$$

To obtain the total field reflected from interface $y = b_{m-1}$, we must add to (D.9) the field reflected directly from the interface $y = b_{m-1}$, namely,

$$\bar{E}^{\text{Front Refl}} = {}_{\perp}\hat{n}_{m-1,-}\, {}_{\perp}E_{b,m-1,+}\, {}_{\perp}\Gamma_{m-1,+} + {}_{\parallel}\hat{n}_{m-1,-}\, {}_{\parallel}E_{b,m-1,+}\, {}_{\parallel}\Gamma_{m-1,+}. \quad \text{(D.10)}$$

Adding (D.9) and (D.10) yields for the total field reflected at interface $y = b$,

$$\bar{E}_{m-1,-} = {}_{\perp}\hat{n}_{m-1,-}\, {}_{\perp}E_{b,m-1,+} \left[{}_{\perp}\Gamma_{m-1,+} + {}_{\perp}\tau^{e}_{m-1}\, {}_{\perp}\Gamma_{m+}\, {}_{\perp}\tau_{m-} e^{-j2\beta_m d_m r_{my}} \right]$$
$$+ {}_{\parallel}\hat{n}_{m-1,-}\, {}_{\parallel}E_{b,m-1,+} \left[{}_{\parallel}\Gamma_{m-1,+} + {}_{\parallel}\tau^{e}_{m-1} {}_{\parallel}\Gamma_{m+}\, {}_{\parallel}\tau_{m-} e^{-j2\beta_m d_m r_{my}} \right]. \quad \text{(D.11)}$$

Substituting (D.6) into (D.11) and noting that

$$\tau_{m-1,+} = 1 + \Gamma_{m-1,+} \quad \text{and} \quad \tau_{m-} = 1 + \Gamma_{m-} = 1 - \Gamma_{m-1,+}$$

yields for the total effective reflected field at interface $y = b_{m-1}$,

$$\bar{E}_{m-1,-} = {}_{\perp}\hat{n}_{m-1,-}\, {}_{\perp}E_{b,m-1,+}\, {}_{\perp}\Gamma^{e}_{m-1,+} + {}_{\parallel}\hat{n}_{m-1,-}\, {}_{\parallel}E_{b,m-1,+}\, {}_{\parallel}\Gamma^{e}_{m-1,+} \quad \text{(D.12)}$$

where the effective reflection coefficient for interface $y = b_{m-1}$ in the positive direction is obtained as

$${}_{\substack{\perp \\ \parallel}}\Gamma^{e}_{m-1,+} = \frac{{}_{\substack{\perp \\ \parallel}}\Gamma_{m-1,+} + {}_{\substack{\perp \\ \parallel}}\Gamma_{m+} e^{-j2\beta_m d_m r_{my}}}{1 - {}_{\substack{\perp \\ \parallel}}\Gamma_{m+}\, {}_{\substack{\perp \\ \parallel}}\Gamma_{m-} e^{-j2\beta_m d_m r_{my}}} \quad \text{(D.13)}$$

and the effective transmission coefficient ${}_{\substack{\perp \\ \parallel}}\tau^{e}_{m-1,+}$ is given by (D.7).

GENERAL STRATIFIED MEDIUM

Extension to a general stratified medium is now easily done by iteration. For example, when adding another slab of thickness d_{m-1} in front of slab d_m, as shown in Fig. D.2, we readily observe that the effective reflection coefficient at interface $y = b_{m-1}$ in the positive direction is equal to $\Gamma^{e}_{m-1,+}$ as found above by (D.13).

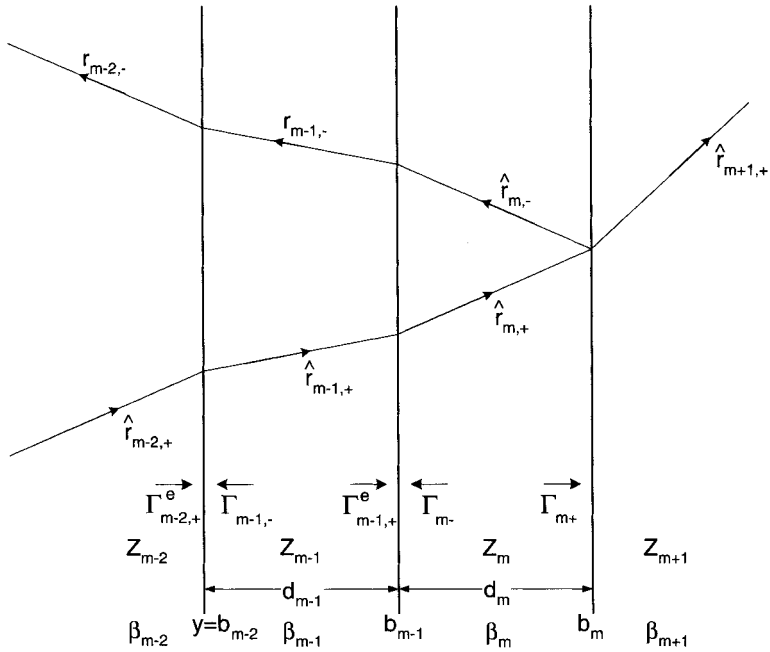

FIGURE D.2.

However, at interface $y = b_{m-2}$ in the negative direction it is simply $\Gamma_{m-1,-}$. Thus, for the effective reflection coefficient at interface $y = b_{m-2}$, we find by extension of (D.13) that

$$\underset{\parallel}{\perp}\Gamma^e_{m-2,+} = \frac{\underset{\parallel}{\perp}\Gamma_{m-2,+} + \underset{\parallel}{\perp}\Gamma^e_{m-1,+} e^{-j2\beta_{m-1}d_{m-1}r_{m-1,y}}}{1 - \underset{\parallel}{\perp}\Gamma^e_{m-1,+}\underset{\parallel}{\perp}\Gamma_{m-1,-} e^{-j2\beta_{m-1}d_{m-1}r_{m-1,y}}}. \tag{D.14}$$

Similarly we find for the new effective transmission coefficient at $y = b_{m-2}$ by extension of (D.7) that

$$\underset{\parallel}{\perp}\tau^e_{m-2,+} = \frac{\underset{\parallel}{\perp}\tau_{m-2,+}}{1 - \underset{\parallel}{\perp}\Gamma^e_{m-1,+}\underset{\parallel}{\perp}\Gamma_{m-1,-} e^{-j2\beta_{m-1}d_{m-1}r_{m-1,y}}}. \tag{D.15}$$

Further extension to an arbitrary number of dielectric slabs is readily obtained by iteration of (D.14) and (D.15). Note, however, that because only one slab is added at the time, we use the effective reflection coefficient only to the right side of the slab and the Fresnel reflection coefficients to the left.

By extension of (D.5) we readily see that the right-going wave in slab $m - 1$ is

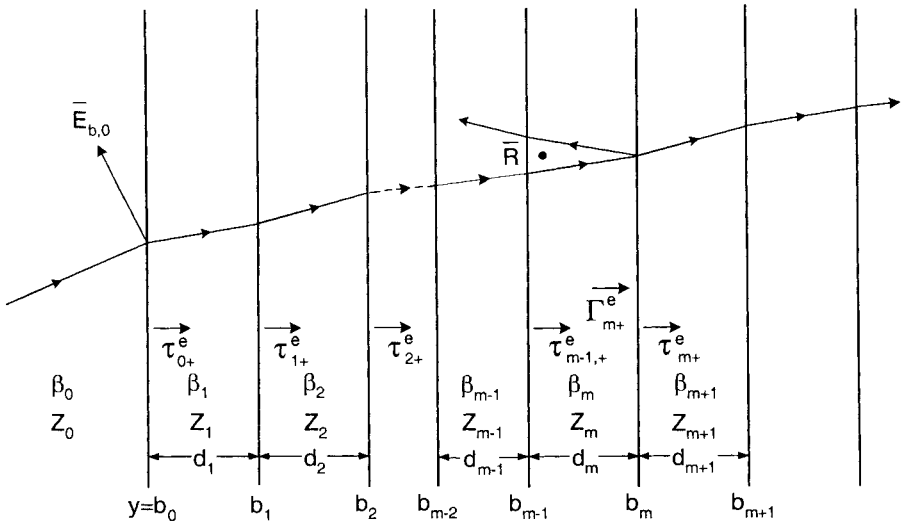

FIGURE D.3.

$$\bar{E}_{m-1,+}(\bar{R}) = \Big[\perp\hat{n}_{m-1,+}\perp E_{b,m-2,+}\perp\tau^{e}_{m-2,+} + \|\hat{n}_{m-1,+}\| E_{b,m-2,+}\|\tau^{e}_{m-2,+}\frac{r_{m-2,y}}{r_{m-1,y}}\Big] e^{-j\beta_{m-1}(y-b_{m-2})r_{m-1,y}}. \tag{D.16}$$

For a general stratified medium shown in Fig. D.3 we readily obtain by repeated use of (D.16) for the field of an arbitrary point $\bar{R}$,

$$\bar{E}_{m+}(\bar{R}) = \Big[\perp\hat{n}_{m+}\perp E_{b,0+}\perp\tau^{e}_{0+}\perp\tau^{e}_{1+}\cdots\perp\tau^{e}_{m-1,+} + \|\hat{n}_{m+}\| E_{b,0+}\|\tau^{e}_{0+}\|\tau^{e}_{1+}\cdots\|\tau^{e}_{m-1,+}\frac{r_{0y}}{r_{my}}\Big] e^{-j\beta_1 d_1 r_{1y}}\cdots e^{-j\beta_{m-1}d_{m-1}r_{m-1,y}} e^{-j\beta_m(y-b_{m-1})r_{my}}, \tag{D.17}$$

where $\bar{E}_{b,0}$ denotes the positive-going incident field in medium 0 at interface $y = b_0$. This positive-going signal $\bar{E}_{m+}(\bar{R})$ given by (D.17) will continue toward the interface $y = b_m$ where it will be reflected with the effective reflection coefficient Γ^{e}_{m+}. It will then propagate back to $\bar{R}$ with a total phase delay of $2\beta_m(b_m - y)r_{my}$. Thus the total field at $\bar{R}$ is given by the sum of the right- and left-going waves as

$$\bar{E}_m(\bar{R}) = \Big[{}_{\perp}\hat{n}_m \, {}_{\perp}E_{b,0} \, {}_{\perp}\tau^e_{0+} \, {}_{\perp}\tau^e_{1+} \cdots {}_{\perp}\tau^e_{m-1,+}$$
$$\Big[1 + {}_{\perp}\Gamma^e_{m+} e^{-j2\beta_m(b_m - y)r_{my}} \Big]$$
$$+ {}_{\parallel}E_{b,0} {}_{\parallel}\tau^e_{0+} \, {}_{\parallel}\tau^e_{1+} \cdots {}_{\parallel}\tau^e_{m-1,+} \frac{r_{0y}}{r_{my}}$$
$$\Big[{}_{\parallel}\hat{n}_{m+} + {}_{\parallel}\hat{n}_{m-} {}_{\parallel}\Gamma^e_{m+} e^{-j2\beta_m(b_m - y)r_{my}} \Big] \Big]$$
$$e^{-j\beta_1 d_1 r_{1y}} \cdots e^{-j\beta_{m-1} d_{m-1} r_{m-1,y}} e^{-j\beta_m (y - b_{m-1}) r_{my}}. \qquad \text{(D.18)}$$

This Page Intentionally Left Blank

E

ESTIMATING THE RESONANT FREQUENCY OF A SINGLE PERIODIC SURFACE: THE CONCEPT ϵ_{eff}

In Chapter 2 we presented calculated resonant curves for a variety of typical elements. These curves were obtained from the PMM code using an appropriate number of section modes. However, not everyone has access to the PMM code. And even if you do, you may simply be interested in estimating the resonant frequency in order to input reasonable dimensions before the correct frequency is obtained by simple iteration.

Although many attempts have been made to produce simple formulas or algorithms to calculate the resonant frequency of a FSS, this author is not aware of any approach that works under all circumstances. In fact he does not believe it is possible. Thus the following rules constitute merely approximate guidelines but they are nevertheless very helpful for the design engineer.

RESONANT FREQUENCY

The resonant frequency of an FSS depends primarily on the dimensions of the individual elements. For example, group 1, the center connected in Fig. 2.2 top, will basically resonate when the largest tip to tip length is approximately equal to $\lambda/2$ as indicated in the case of the tripole. Similarly group 2, the loops types of Fig. 2.2, will resonate when their average circumference is approximately one wavelength long. Group 3, namely the solid interior elements, should similarly be approximately $\lambda/2$ across the elements but can be affected by many other factors. Finally, group 4, the combination elements, is simply too diverse to summarize.

EFFECT OF DIELECTRIC

Furthermore the resonant frequency will depend heavily on the dielectric substrate. For example, dielectric slabs thicker than about $0.05\lambda_\epsilon$ on both sides of the FSS may lower the resonant frequency of an FSS of the *dipole* type with as much as a factor of $\sqrt{\epsilon_r}$. In the *slot* case things are a bit more complicated, since we are now transmitting through the surface with the dielectric substrate acting as a reactively loaded radome.

As the thickness of the dielectric substrate is reduced, the resonant frequency will start to creep up toward the free space resonant frequency. This is a very important range from a practical point of view and in general difficult to estimate.

However, an approximate idea of how the resonant frequency changes with thickness of the substrate can be obtained by introducing the effective dielectric constant ϵ_{eff} instead of ϵ_r. It is basically defined by the change of the static capacitance between two *dipole* halves as shown in the insert of Fig. E.1. The curves for ϵ_{eff} is

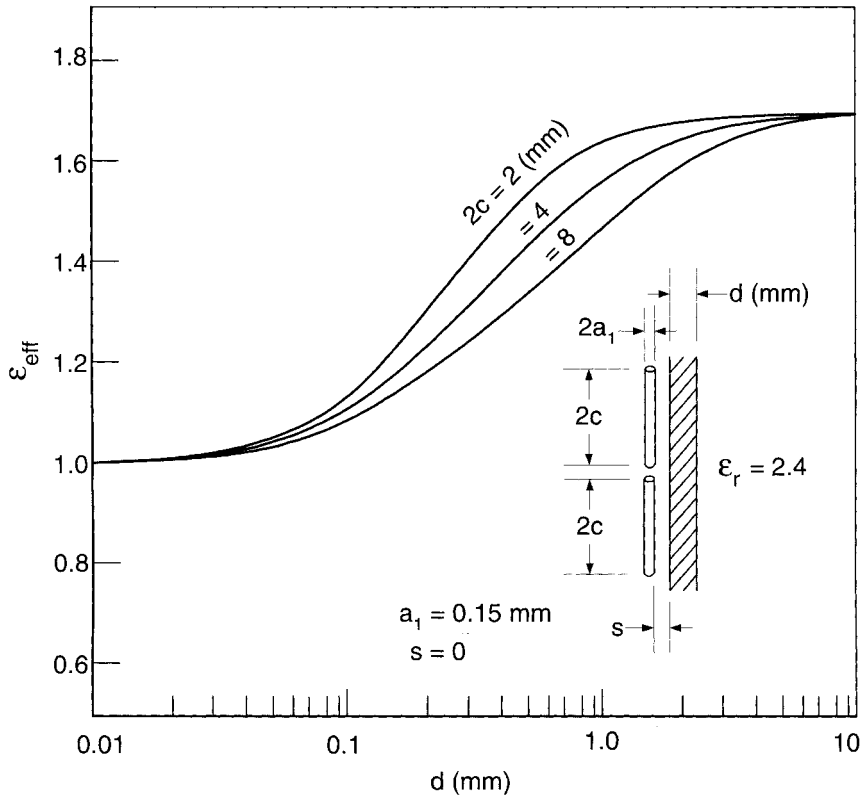

FIGURE E.1. Effective dielectric constant ϵ_{eff} as a function of the thickness d of a substrate located to only one side of colinear *dipoles*, $\epsilon_r = 2.4$. Note, for dielectric to one side only, $\epsilon_{eff} \xrightarrow[d\to\infty]{} \frac{\epsilon_r+1}{2}$. For dielectric to both sides, $\epsilon_{eff} \xrightarrow[d\to\infty]{} \epsilon_r$.

obtained from the theory of dielectric images. For details and computer programs, see [51, 52, 53]. The curves in Fig. E.1 have been calculated for element lengths $2c$ that are typical for the C- and X-band. Observe that the upper limit for ϵ_{eff} is $(1+\epsilon_r)/2$ if the dielectric is placed to only one side of the FSS, while it is simply ϵ_r when placed to both sides. Note also that this maximum value is attained for as little as $d \sim 1.5$ mm or about $0.05\lambda_0$ (not very thick!). Note also that ϵ_{eff} starts to increase when d is as thin as 0.05 mm. This shows that although the evanescent waves may be weak at some distance from the periodic structure, they are extremely strong next to the elements. (Note that evanescent waves represent stored energy closely related to the static field as expressed partly by the capacitance.) In Fig. E.2 we show ϵ_{eff} for two parallel wire sections placed at the distance s from a dielectric slab of thickness d as illustrated in the insert. As the figure shows, when the elements are directly up against the dielectric (i.e., $s = 0$), the effective dielectric constant ϵ_{eff} behaves quite similarly to the colinear case in Fig. E.1. However, we also observe that for an air crack as low as $s = 0.05$ mm, ϵ_{eff} is reduced by about 5% when

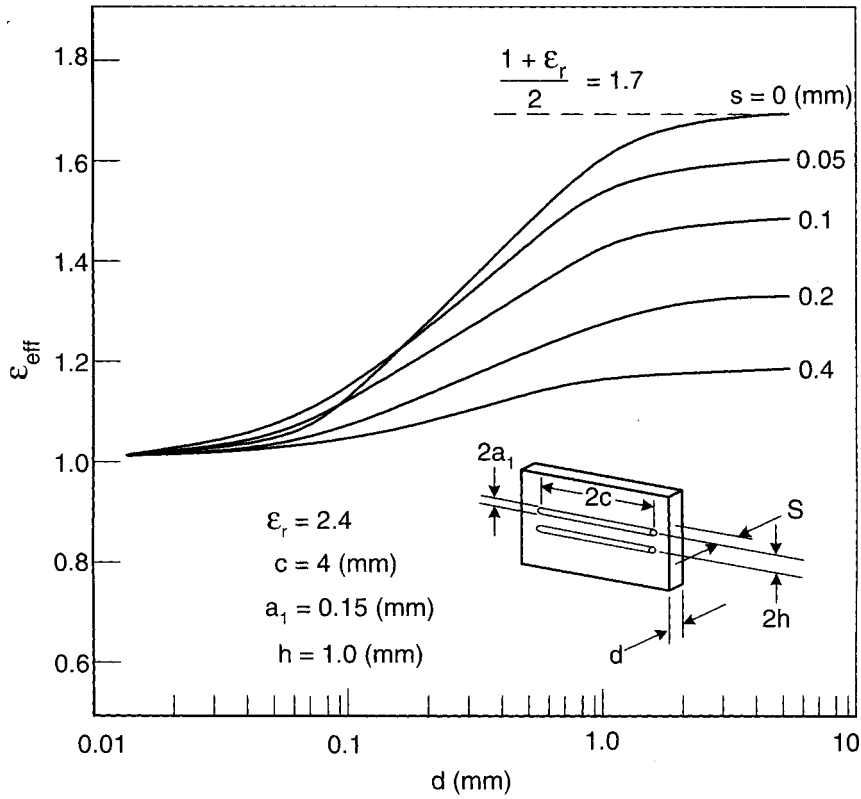

FIGURE E.2. Effective dielectric constant ϵ as a function of slab thickness d for parallel wires. Also shown is the effect of an air gap s between wires and dielectric slab.

$d \sim 1$ mm. The observation is extremely important from a practical point of view. For example, if an FSS is assembled in a dry stack and held too loosely together, we can easily measure a faulty resonant frequency. See also Section 10.8.1.

We finally note that the ϵ_{eff} concept is based on the assumption that the waves along a *dipole* element propagate similarly to a TEM wave. In that case the propagation constant $\beta_{eff} = \sqrt{\epsilon_{eff}\mu}$ can be obtained exactly from the static values obtained above (μ is not affected by the dielectric). As is well known, this is not the case. Nevertheless, the concept ϵ_{eff} has proved to be a valuable tool in estimating the resonant frequency of FSSs in general and has provided much quantitative insight.

BANDWIDTH

The bandwidth of an FSS depends in general largely on the inter-element spacings D_x and D_z. If either D_x or D_z is increased by a relatively small amount, say 10%, the bandwidth will be reduced by about 10%. If they are both increased by the amount, the bandwidth is reduced by about 20%.

However, some elements such as the three- and four-legged loaded elements can also change bandwidth significantly by simply varying the area enclosed by these loop elements, as illustrated by Figs. 2.19 and 2.26. For many elements such variation of the bandwidth takes place with a minimum change of the resonant frequency.

Still, there are notable exceptions. For example, elements with heavy capacitive end loading such as the Jerusalem cross in Fig. 2.12 or the tilted cross element shown in Fig. 2.37 will not only change bandwidth but also resonant frequency when the inter-element spacings D_x and D_z are changed without changing the element dimensions. The reason for that is simply that reduction of D_x and D_z can greatly increase the end capacitance of the elements in particular for the Jerusalem cross. This in turn will significantly lower the resonant frequency.

The hexagon element is also noteworthy in that respect. If the gaps between the elements are reasonably large, the surface will resonate approximately when the element circumference is one wavelength based on ϵ_{eff}. As the elements get closer, the bandwidth will increase. However, the capacitance between adjacent elements will also increase for very close spacing which in turn will force the resonant frequency downward. Thus we must reduce the element circumference to get the resonant back up, typically by as much as 20% to 30%. For examples of this effect, see Figs. 2.27 and 2.28.

F

EXTENSION TO ARRAYS OF WIDE FLAT ELEMENTS

We found in Chapter 4 the field caused by an array of relatively thin elements. In this appendix we modify the theory to include an array made of elements of wide rectangular shape.

RERADIATED FIELD

Consider the array shown in Fig. F.1. It consists of rectangular elements of length $2l_1$ and width w. When exposed to an incident plane wave propagating in the arbitrary direction $\hat{s}$, a current density is induced:

$$\bar{J}(x, z) = \hat{x} J_x(x, z) + \hat{z} J_z(x, z). \tag{F.1}$$

We will investigate the x- and z-directed systems separately starting with the z-directed system.

As we have earlier in Chapter 4, we will denote our point of observation by $\bar{R}$ and a source point somewhere on the reference element by $\bar{r}''$. Then, according to (4.36), the field from an array of infinitesimal elements $dxdz$ and current density $\hat{z} J_z(x, z)$ is given by

$$d\bar{E}\left(\bar{R}^{(1)}\right) = J_z(x, z) dx dz \frac{Z}{2D_x D_z} \sum_k \sum_n \frac{e^{-j\beta \bar{R} \cdot \hat{r}_\pm}}{r_y} \left(\hat{z} \times \hat{r}_\pm\right) \times \hat{r}_\pm e^{j\beta \bar{R}'' \cdot \hat{r}_\pm}. \tag{F.2}$$

The total E-field from the array is then obtained by simply integrating (F.2) over the reference element:

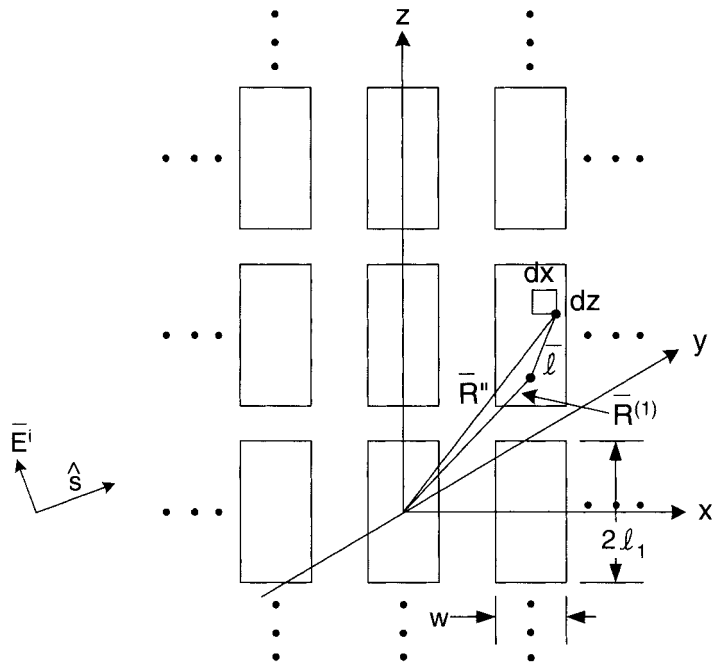

FIGURE F.1. Field from an array of two-dimensional elements obtained by integrating over the entire reference element.

$$\bar{E}\left(\bar{R}^{(1)}\right) = \frac{Z}{2D_x D_z} \sum_k \sum_n \frac{e^{-j\beta \bar{R}\cdot \hat{r}_\pm}}{r_y} \left(\hat{z} \times \hat{r}_\pm\right) \times \bar{r}_\pm$$

$$\int\int_{\text{Ref.Ele.}} J_z(x, z) e^{j\beta \bar{R}''\cdot \hat{r}_{\pm 1}} dx dz. \tag{F.3}$$

Expression (F.3) can be more easily managed if, as we have done earlier in the wire case, we introduce a reference point $\bar{R}^{(1)}$ on the reference element as illustrated in Fig. F.1:

$$\bar{R}^{(1'')} = \bar{R}^{(1')} + \bar{l}, \tag{F.4}$$

where

$$\bar{l} = \hat{x} l_x + \hat{z} l_z. \tag{F.5}$$

Substituting (F.4) into (F.3) yields

$$\bar{E}^{(1)} = I_z(\bar{R}^{(1)}) \frac{Z}{2D_x D_z} \sum_k \sum_n \frac{e^{-j\beta \bar{R}\cdot \hat{r}_\pm}}{r_y} (\hat{z} \times \hat{r}_\pm) \times \hat{r}_\pm \mathcal{P}_z, \tag{F.6}$$

where the two-dimensional scattering pattern factor $\mathcal{P}_z$ is defined as

$$\mathcal{P} = \frac{1}{I_z(\bar{R}^{(1)})^{(1')}} \int \int_{\text{Ref.Ele.}} J_z(x, z) e^{j\beta \bar{l} \cdot \hat{r}_{\pm}} dx dz \tag{F.7}$$

and where $I_z(\bar{R}^{(1')})$ denotes the total current in the z-direction, which is $I_z(R^{(1')} = \int J_z(x, z)dx$ for $z = z^{(1)}$. See Section 9.5 for current distribution on lossy elements.

INDUCED VOLTAGE

The incident field $\bar{E}^i$ propagating in the direction $\hat{s}$ will induce a voltage $V^{(1')}$ across an imaginary gap in the reference element as shown in Fig. F.2. We will find this induced voltage $V^{(1')}$ by application of reciprocity as explained in Section 4.7.

More specifically, we obtain from (4.47)

$$V^{(1')}\left(\bar{R}^{(1')}\right) = \hat{z} \cdot \bar{E}^i\left(\bar{R}^{(1')}\right) \frac{1}{I^{(1')t}\left(\bar{R}^{(1')}\right)} \int_{\text{Elem.}1'} I^{(1')t}(z) e^{-j\beta \bar{R}^{(1'')} \cdot \hat{s}} dz, \tag{F.8}$$

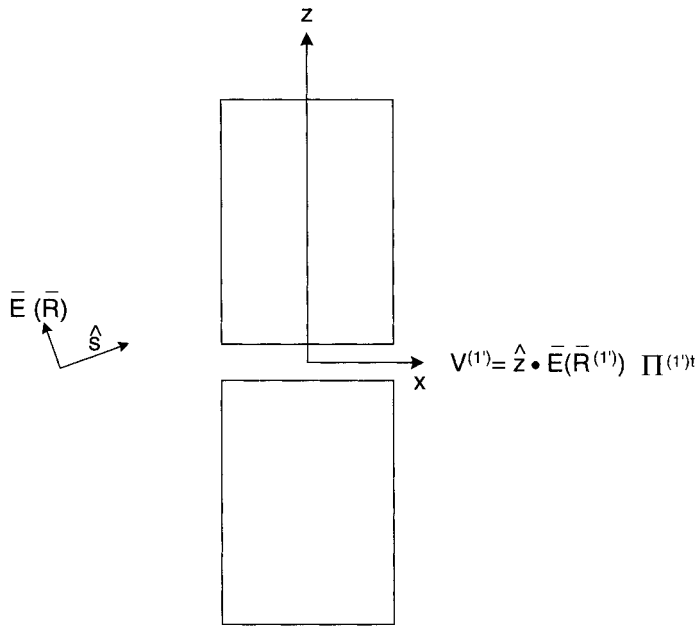

FIGURE F.2. Voltage induced in the reference element by an incident plane wave, which is expressed by the two-dimensional pattern formula $\mathcal{P}^{(1')t}$.

where

$$\bar{R}^{(1'')} = \bar{R}^{(1')} + \hat{z}z \tag{F.9}$$

and

$$I^{(1')t}(z) = \int_{-w/2}^{w/2} J^t(x, z)e^{-j\beta x s_x} d_x. \tag{F.10}$$

Substituting (F.9) and (F.10) into (F.8), we have

$$V^{(1')}\left(\bar{R}^{(1')}\right) = \hat{z} \cdot \bar{E}^i\left(\bar{R}^{(1')}\right) \mathcal{P}^{(1')t}, \tag{F.11}$$

where

$$\mathcal{P}^{(1')t} = \frac{1}{I^{(1')t}\left(\bar{R}^{(1')}\right)} \int\int_{\text{Ref. Elem.}} J_z^{(1')t}(x, z)e^{-j\beta(x\hat{x}r_x + z\hat{z}r_z)} d_x d_z. \tag{F.12}$$

Note that $J_z^{(1')t}$ denotes the current density under transmitting condition.

REFERENCES

1. B. A. Munk and R. D. Fulton, "Transmission Through a Bi-Planar Slot Array Sandwiched Between Three Dielectric Layers, March 1973–Nov. 1975," Tech. Rept. 3622-7, Ohio State Univ. ElectroScience Lab., Dept. of Electrical Eng., Columbus, Feb. 1976.
2. L. W. Henderson, "The Scattering of Planar Arrays of Arbitrary Shaped Slot and/or Wire Elements in a Stratified Dielectric Medium," Ph.D. Dissertation, Ohio State Univ., Dept. of Electrical Eng., Columbus, 1983.
3. L. W. Henderson, "Introduction to PMM," Tech. Rept. 715582-5, Ohio State Univ. ElectroScience Lab., Dept. of Electrical Eng., prepared under contract No. F33615-83-C-1013 for the Air Force Avionics Laboratory, Air Force Wright Aeronautical Laboratories, Air Force Systems Command, Wright-Patterson Air Force Base, OH 45433, Feb. 1986.
4. B. A. Munk and G. A. Burrell, "Plane Wave Expansion for Arrays of Arbitrarily Oriented Piecewise Linear Elements and Its Application in Determining the Impedance of a Single Linear Antenna in a Lossy Half-Space," *IEEE Trans. on Antennas and Propagation, AP-34*(3), 331–343, May 1979.
5. B. A. Munk, G. A. Burrell, and T. W. Kornbau, "A General Theory of Periodic Surfaces in Stratified Media," Tech. Rept. 784346-1, Ohio State Univ. ElectroScience Lab., Dept. of Electrical Eng., prepared under contract AFAL-TR-77-219, Nov. 1977.
6. T. W. Kornbau, "Analysis of Periodic Arrays of Rotated Linear Dipoles, Rotated Crossed Dipoles, and of Biplanar Dipole Arrays in Dielectric," Ph.D. Dissertation, Ohio State Univ., Dept. of Electrical Eng., Columbus, 1984.
7. S. W. Schneider, "On the Scattering Properties of Super Dense Periodic Surfaces," Ph.D. Dissertation, Ohio State Univ., Dept. of Electrical Eng., Columbus, 1992.
8. B. A. Munk, United States Patent 3,789,404, Periodic surface for large scan angles, Jan. 29, 1974.
9. E. L. Pelton and B. A. Munk, United States Patent 3,975,738, Periodic antenna surface of tripole slot elements, Aug. 17, 1976.

10. E. L. Pelton and B. A. Munk, "A Streamlined Metallic Radome," *IEEE Trans. on Antennas and Propagation, AP-22*(6), 799–803, Nov. 1974.

11. Schneider, ibid., p. 177.

12. Schneider, ibid., p. 176.

13. R. B. Kieburtz and A. Ishimaru, "Scattering by a Periodically Apertured Conducting Screen," *IRE Trans. on Antennas and Propagation, AP-9*(6) 506–514, Nov. 1961.

14. S. W. Lee, "Scattering by Dielectric-Loaded Screen," *IEEE Trans. on Antennas and Propagation, AP-19*(5) 656–665, Sept. 1971.

15. C. C. Chen, "Transmission of Microwave through Perforated Flat Plates of Finite Thickness," *IEEE Trans. on Microwave Theory and Techniques, MITT-21*(1), 1–6, Jan. 1973.

16. R. Orta, P. Savi, and R. Tascone, "Numerical Green's Function Technique for the Analysis of Screens Perforated by Multiply Connected Apertures," *IEEE Trans. on Antennas and Propagation, AP-44*(6), 765–776, June 1996.

17. B. A. Munk and T. W. Kornbau, "Monoplanar Arrays of Generalized Three-Legged Elements in a Stratified Dielectric Medium," Tech. Rept. 4346-6 (784346), Ohio State Univ. ElectroScience Lab., Dept. of Electrical Eng., Unclassified AFAL-TR-78-43, Columbus, May 1978.

18. H. E. King, "Mutual Impedance of Unequal Length Antennas in Echelon," *IRE Trans. Antennas and Propagation, AP-5*(3) 306–313, July 1957.

19. M. G. Floquet, "Sur les equations différentielles linéaires a coefficients périodiques," *Annale École Normale Superieur*, pp. 47–88, 1883.

20. R. C. Hansen, *Phased Array Antennas*, Wiley, New York, 1998.

21. A. Papoulis, *The Fourier Integral and Its Applications*, McGraw-Hill, New York, 1962, pp. 47–49.

22. H. Bateman, *Table of Integral Transforms*, Vol. 1, McGraw-Hill, New York, 1954.

23. A. Papoulis, op. cit., pp. 14–15.

24. H. Bateman, op. cit., sec. 1.13.

25. T. W. Kornbau, "Application of the Plane Wave Expansion Method to Periodic Arrays Having a Skewed Grid Geometry," M.Sc. Thesis, Ohio State Univ., Dept. of Electrical Eng., Columbus, 1977.

26. J. D. Kraus, *Antennas*, McGraw-Hill, New York, 1988, Chapter 10, pp. 413–422.

27. S. A. Schelkunoff and H. T. Friis, *Antennas Theory and Practice*, Wiley, New York, 1952, p. 298, Eq. 100, and p. 366, Eq. 26.

28. E. K. English, "Electromagnetic Scattering from Infinite Periodic Arrays of Arbitrarily Oriented Dipole Elements Embedded in a General Stratified Medium," Ph.D. Dissertation, Ohio State Univ., Dept. of Electrical Eng., Columbus, 1983.

29. B. M. Kent, "Impedance Properties of an Infinite Array of Non-planar Rectangular Loop Antennas Embedded in a General Stratified Medium," Ph.D. Dissertation, Ohio State Univ., Dept. of Electrical Eng., Columbus, 1984.

30. K. T. Ng, "Admittance Properties of a Slot Array with Parasitic Wire Arrays in a Stratified Medium," Ph.D. Dissertation, Ohio State Univ., Dept. of Electrical Eng., Columbus, 1985.

31. S. J. Lin, "On the Scan Impedance of an Array of V-Dipoles and the Effect of the Feedlines," Ph.D. Dissertation, Ohio State Univ., Dept. of Electrical Eng., Columbus, 1985.

32. H. K. Schuman, D. R. Pflug, and L. D. Thompson, "Infinite Planar Array of Arbitrarily Bent Thin Wire Radiators," *IEEE Trans. on Antennas and Propagation, AP-32*(4), 364–477, April 1984.

33. R. Andre, "An Analysis Method for Doubly Periodic Nonplanar Antenna Arrays," M.Sc. Thesis, Ohio State Univ., Dept. of Electrical Eng., Columbus, 1985.

34. W. Wasylkiwskyj and W. K. Kahn, "Theory of Mutual Coupling among Minimum-Scattering Antennas," *IEEE Trans. on Antennas and Propagation, AP-18*(2), 204, March 1970.

35. W. Wasylkiwskyj and W. K. Kahn, "Scattering Properties and Mutual Coupling of Antennas with Prescribed Radiation Patterns," *IEEE Trans. on Antennas and Propagation, AP-18*(6), 741, Nov. 1970.

36. R. F. Harrington, *Time-Harmonic Electromagnetic Fields*, McGraw-Hill, New York, 1961, pp. 163–168.

37. J. Brown, "The Types of Waves Which May Exist Near a Guiding Surface," *Proc. of IEE*, Part III, *100*, 363–364, Nov. 1953.

38. L. I. Schiff, *Quantum Mechanics*, McGraw-Hill, New York, 1949, pp. 34–39.

39. *The Microwave Engineer's Handbook and Buyer's Guide*, 1964.

40. B. A. Munk and J. F. Stosic, "Radome Panels of Slotted Arrays Located in a Stratified Dielectric Medium," Tech. Rept. 784346-10, Ohio State Univ. ElectroScience Lab., Dept. of Electrical Eng., Columbus, June 1979 (Contract No. 7633-13-28).

41. C. J. Larson, "Modified Center Layer Metallic Biplanar Radome Design," Tech. Rept. AFAL-TR-78-28, Ohio State Univ. ElectroScience Lab. Rept. RF 4346-2, Columbus, March 1978.

42. J. F. Stosic, "Multilayer Metallic Radome Panel Design with Modified Center Layers," M.S. Thesis, Ohio State Univ., Dept. of Electrical Eng., Columbus, 1980.

43. A. J. Fenn, "Moment Method Calculation of Reflection Coefficient for Waveguide Elements in a Finite Planar Phased Antenna Array," Ph.D. Dissertation, Ohio State Univ., Dept. of Electrical Eng., Columbus, 1978.

44. A. J. Fenn, G. A. Thiele, and B. A. Munk, "Moment Method Analysis of Finite Rectangular Waveguide Phased Arrays," *IEEE Trans. on Antennas and Propagation, AP-30*(4), 554–564, July 1982.

45. R. J. Luebbers, "Analysis of Various Periodic Slot Array Geometries Using Modal Matching," Ph.D. Dissertation, Ohio State Univ., ElectroScience Lab., Dept. of Electrical Eng., Columbus, 1975.

46. R. J. Luebbers and B. A. Munk, "Analysis of Thick Rectangular Waveguide Windows with Finite Conductivity," *IEEE Trans. on Microwave Theory and Techniques, MTT-21*(7), 461–468, July 1973.

47. R. J. Luebbers and B. A. Munk, "Some Effects of Dielectric Loading on Periodic Slot Arrays," *IEEE Trans. on Antennas and Propagation, AP-26*(4), 536–542, July 1978.

48. J. R. Baechle, "Results of Some Preliminary Tests on a Prototype of a Concept in the Integration of the Design of an Antenna and Electromagnetic Window for Aerospace Vehicles," Ohio State Univ., ElectroScience Lab., Dept. of Electrical Eng., Columbus, May 1963.

49. B. A. Munk and R. Emrick, "Design of Dichroic Subreflectors and Its Consequences in a Cassegrain System," Tech. Rept. 726109-2, Ohio State Univ. ElectroScience Lab., Dept. of Electrical Eng., Columbus, July 1993.

50. H. A. Wheeler, "Simple Relations Derived from a Phased Array Antenna Made of an Infinite Current Sheet," *IEEE Trans. on Antennas and Propagation, AP-13*(4), 506–514, July 1965.

51. B. A. Munk, R. J. Luebbers, and T. L. Oliver, "Reflection Properties of a Periodic Array of Dipoles in a Dielectric Slab," Tech. Rept. AFAL-TR-72-381, Ohio State Univ. ElectroScience Lab. Rept. RF 2986-6, Dept. of Electrical Eng., Columbus, Dec. 1972.

52. B. A. Munk, R. J. Luebbers, and T. L. Oliver, "Impedance of Dipole Arrays in Various Dielectric Slab Configurations," Tech. Rept. 2989-5 (AFAL-TR-72-338), Ohio State Univ., ElectroScience Lab., Dept. of Electrical Eng., Columbus, Sept. 1972.

53. B. A. Munk and R. J. Luebbers, "Admittance of Slot Arrays with Various Dielectric Slab Configurations," Tech. Rept. 2989-7 (AFAL-TR-72-380), Ohio State Univ. ElectroScience Lab., Dept. of Electrical Eng., Columbus, Dec. 1972.

54. J. C. Vardaxoglou, *Frequency Selective Surfaces*, Research Studies Press, London 1997.

55. T. K. Wu, *Frequency Selective Surface and Grid Array*, Wiley, New York, 1995.

56. W. W. Salisbury, United States Patent 2,599,944, Absorbent body of electromagnetic waves, June 10, 1952.

57. E. Weber, *Electromagnetic Fields*, Wiley, New York pp. 111–115 and p. 337, 1950.

58. R. C. Hansen, *Phased Array Antennas*, Wiley, New York, 1998.

59. M. A. Dornheim, *Aviation Week* issue on space technology, p. 23, April 26, 1993.

60. B. A. Munk, R. Luebbers, and C.A. Mentzer, "Breakdown of Periodic Surfaces at Microwave Frequencies," Tech. Rept. 2989-1, Ohio State Univ., ElectroScience Lab., Dept. of Electrical Eng., Columbus, June 24, 1971 (AFAL-TR-71-116, contract F33615-70-C-1439, declassified March 30, 1999).

61. Mission Research Corporation, "High Power Multi-Layer Frequency Selective Surfaces," Final Rept., April 1, 1998.

62. J. D. Kraus and D. A. Fleisch, *Electromagnetics with Applications*, 5th Ed., McGraw-Hill, New York, 1999, pp. 119–123.

63. Kraus and Fleisch, ibid., p. 144.

64. Schellkunoff, ibid., p. 236.

65. Kraus and Fleisch, ibid., p. 132.

66. K. A. Shubert and B. A. Munk, "Matching Properties of Arbitrary Large Dielectric Covered Phased Arrays," *IEEE Trans. on Antennas and Propagation, AP-31*(1), 54–59, Jan. 1983.

INDEX